MULTIFUNCTIONAL FLUORENYL-EMBEDDED HELICENES

Ruhee Azim Dawood

Doctor of Philosophy

University of York

Chemistry

October 2023

ABSTRACT

Fluorene – an electron-rich organic polyaromatic molecule containing a central 5-membered ring – has been well-established in the literature as being a versatile, multifunctional building block with tuneable and robust optoelectronic and redox properties. For example, its relatively high photoluminescence quantum yield, its ability to support neutral organic radicals and its ambipolar charge transporting capabilities has warranted its use in the development of advanced light-emitting and charge transporting applications. However, benzannulated derivatives of fluorene are less well-known, despite retaining the optoelectronic behaviours inherent to fluorene, that are boosted by enhanced conjugation through the polyaromatic backbone. In fact, the few examples of *ortho*-fused benzannulated derivatives of fluorene that have been published are shown to possess a non-planar screw-shaped backbone enabling access to properties relating to their inherent chirality.

This Thesis focuses on investigating the fundamental properties of tetra-annulated tetrabenzo[*a,c,g,i*]fluorene (TBF) and its derivatives in order to draw attention to its multifaceted optical and charge conductive behaviours. Particular emphasis is placed on scrutinising the structures that the materials synthesised adopt in the solution- and solid-state and relating these structural findings to their emergent properties. For example, Chapter 2 and Chapter 3 relate how the structures of TBFs appended with a bulky, rigid anthracene substituent, affect their emissive and redox properties, respectively. Then, in Chapter 4, the dynamic interconversion of the polyaromatic backbone of TBFs are interrogated by DFT calculations to inform the design of configurationally stable TBF helicenes for the isolation of chiroptically-active molecules. Finally, Chapter 5 explores how the incorporation of heteroatoms into the TBF framework impacts optical and redox properties. Such chiral fluorescent closed- and open-shell helicenes can lead to a deeper understanding of fundamental spin electronics and molecular magnetics that may benefit the development of advanced light-emitting and memory technologies and hence lead us to a more advanced and sustainable future.

TABLE OF CONTENTS

Author's Declaration

I declare that this thesis is a presentation of original work, and I am the sole author. Unless otherwise stated, the work presented in this thesis is the work of the author. This work has not previously been presented for a degree or other qualification at this University or elsewhere. All sources are acknowledged as references.

Signed: R. A. Dawood

Date: 30 October 2023

ACKNOWLEDGEMENTS

I don't think I'm ever going to have enough, or the right words to express how immensely grateful I am to you, Alyssa. You are the one person I have the most to thank for. You took a chance on me very early on during my undergraduate degree and you made such a positive impression that I couldn't bear to leave the group, the lab and research. Then again, in the final year of my undergraduate studies, you gave me the confidence to believe that I had it in me to pursue a PhD and supported me through all my applications. For as long as I have known you, you have never been satisfied just letting things be "the way they have always been." You have pushed for change on all fronts with creative solutions and that is something I deeply admire and hope to emulate. Thank you for everything that you have taught me, all your support and confidence (even when I maybe didn't feel it myself) and for all the laughs. You always have this effect of brightening up the lab/office space! Everyone I speak to about my PhD knows what a huge impact you have had on my experience and having such a great supervisor allowed me to put my head down and focus on the science. I definitely would not have been able to enjoy this PhD without having you in my corner. I hope I have made you proud :)

Then, I must remember that to get to this point in my life – about to submit my PhD thesis – has been a journey that started well before the 1st of October 2020. Therefore, I must continue these acknowledgements by thanking my parents. You have believed in me and have always pushed and encouraged me to do my best and to keep my faith strong and for that I must say thank you. I know how difficult (in all aspects) it has been for you to have three daughters at university abroad (we miss you so much!), yet you are still abundantly proud and wish us nothing but the best. I have truly been blessed to have such supportive parents. Papa, our Saturday catch ups were everything I needed after a busy long week to reflect on the successes and failures in the lab and thank you so much for showing so much interest in the work I was doing and asking me questions – you challenged me to consider things from different perspectives which really helped with my determination in the lab. Mama, there are so many meals that I would've forgotten to have if you had not called me and sat with me while I began cutting up some onions or if you hadn't given me the motivation to wash my dishes – you always made me smile even when I didn't have the energy for it. I love you both so much.

To the larger Avestro Group team (both past and present), you were the family that I never had in the UK, and I could finally be my authentic self and grow my confidence with you. Pavan, you were more than just a mentor or a friend, and the A-Team lost such a massive integral part of us when you had to leave. I learnt so much from you which I have already been passing along to new researchers I meet, and our deep meaningful conversations will always be treasured. Grant and Fraser, it has always felt like we went through this journey together (because I started my final year undergraduate project in the Avestro Group at the same time that you started your PhDs) and it has been so amazing to see you grow into the people that you are today. You made this experience just that little bit easier! Shana, I really

reason to believe that you are one of the big reasons for my experimental successes. Treat the ones who come after me just as well!

To Raeesa, Amaal and Tahirah – we didn't get to see each other much during my three years of research (what with COVID and trying to find a way to get our schedules to match, etc) but I will always treasure our three weeks at home this April where we were all finally reunited, and I got to learn about all the interesting habits that you'd picked up in the 3–4 years apart. As the eldest of the four sisters (not by much, just seven minutes, I know Raeesa) I am so proud of the strong independent adults you've become, and I know that distance is never going to be able to take away what we have with each other. You are my people. Thank you! Finally, Zain, you were my escape from Chemistry and being in the lab. You constantly reminded me that my life was much bigger than my PhD, reminders that I desperately needed during the tough times when nothing was really working in the lab. You have been patient with me and loved me throughout and I thank you for that.

CHAPTER 1 |
BENZANNULATED FLUORENES

SYNOPSIS
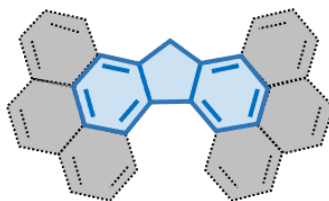
This Chapter focusses on introducing the fluorenyl moiety (highlighted in blue with a solid line in the cartoon above) as a polyaromatic hydrocarbon with highly efficient intrinsic emissive and redox properties that can be utilised effectively in applications related to the advancement of optoelectronic device fabrications from organic molecules. As a result, fluorenes have served as a functional organic small molecule building block to create simple and advanced structural architectures with enhanced properties depending on the nature of the groups attached to it. The advantages of extending the π-system in all directions through benzannulation (as represented in the cartoon in grey) are discussed by highlighting specific examples from the literature. Some of these advantages include accessing systems that possess highly delocalised conjugation pathways and are therefore better suited to stabilising charged and neutral radical states (and even under ambient conditions) with red-shifted optical properties. The discussion then moves towards strategies that researchers have been using to introduce additional functionality to polyaromatic hydrocarbons by careful design of their three-dimensional structures to introduce chiral features through non-planar helically twisted geometries. Helicenes with the fluorenyl moiety embedded into them are discussed for their ability to improve the intrinsic chiroptical properties of these carbon-containing *ortho*-fused polyaromatics. In addition, it is evident from the literature search that researchers have had success with swapping out the carbon containing methylene-bridge in these fluorenyl-embedded helical systems with heteroatoms such as nitrogen and silicon to enhance solution and solid-state optical and redox properties even further. Finally, tetrabenzofluorene (TBF) is introduced as a tetraannulated analogue of fluorene and its remarkable solution and solid-state optical properties, together with its use in metal-organic half-sandwich complexes for synthetic catalytic purposes are discussed. The potential of TBFs to serve as chiroptically active [5]helicene derivatives are discussed based on experiments that are available in the literature, however it is clear that there is additional scope needed to study more thoroughly the fundamental properties of tetrabenzofluorenes and its derivatives.

1.1 FLUORENE: A BRIEF HISTORY

Fluorene, which was first isolated from crude anthracene oil by Berthelot M.[1] in 1867, was named on account of its intense violet fluorescence under UV irradiation. Its structure, described by Barbier P.[1b,2] as a "biphenyl in which two atoms of hydrogen are replaced by an equal volume of methylene" consists of a 5-membered cyclopentadienyl central ring, flanked by two annulated benzene rings (Figure 1.1a). Although it is classed as a polycyclic aromatic hydrocarbon, the central cyclopentadienyl ring is non-aromatic unless reduced to its highly delocalised anionic redox state[3] whereby it obeys Hückel's $4n+2\pi$ electron rule for aromaticity. Early on, the three-dimensional (3D) shape and structure of fluorene was contested,[4–6] but it is known now that fluorene is planar with a C_{2v} symmetric axis by X-ray analyses (Figure 1.1b). In fact, the enhanced conjugation through the biphenyl moiety as a result of the rigidified planar framework endows its ability to absorb and emit in the UV–vis region.[7] Researchers quickly discovered that, owing to the reactivity of the hydrogen atoms in the 9-position (pK_a = 22.6 in DMSO; weakly acidic),[8] fluorene can be derivatised to introduce functionality at the methylene bridged head-position.[9-11] Meanwhile direct substitution around the aromatic benzene rings occurs preferentially in the 2-position and the 7-position.[1b,11,12] Researchers have been able to take advantage of these early advancements in understanding the structure, reactivity, and the intrinsic optoelectronic properties of fluorene to develop novel functional derivatives that have found use as dyes,[13,14] anticancer agents,[15] molecular and ionic photoluminescent sensors,[16,17] electron-accepting materials in organic photovoltaic devices[18] (OPVs) and emissive materials in organic light-emitting diodes (OLEDs),[19, 20] among other uses.[21, 22]
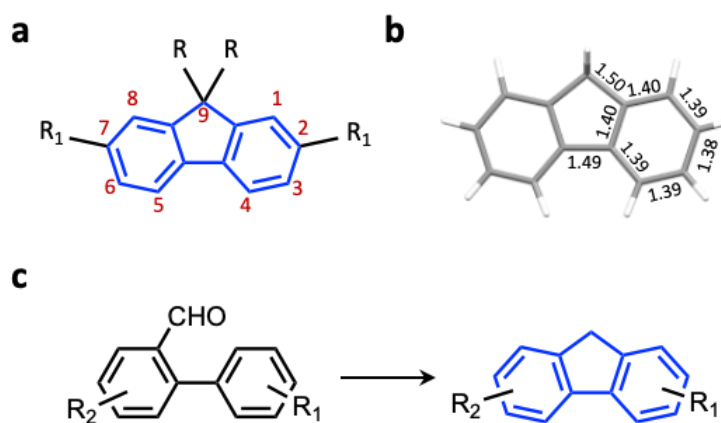
Figure 1.1 (a) Molecular and (b) X-ray crystal structure obtained by Belsky, V. K. et al.[4] of fluorene with substituent numbering labelled in red and C–C bond distances labelled in black. (c) An example of an alternative method to synthesise diverse functionalised fluorenes from a substituted-biphenyl.[7]

1.2 FUNCTIONAL SMALL MOLECULES BASED ON FLUORENE

Synthetic variety has been quite simple to achieve from this small building block with methodologies evolving to enable symmetric and non-symmetric substitutions around all positions on the fluorene core

(where substitution in the 1,8-positions naturally requires smaller sterically bulky groups in the 9-position to be feasible).[23] Substitution at the methylene bridge 9-position is normally utilised to introduce solubilising groups[24] (e.g., branched or linear alkyl groups or aryl groups) and has been especially popular in the development of spirocyclic compounds (i.e., spirofluorenes). Spirofluorenes are efficient light-emitting materials with high colour stability due to their molecular rigidity and efficient electroluminescence due to the ability of the spiro conformation to hinder intermolecular aggregation.[25–27]

Although a popular strategy that is used to take advantage of the robust and reliable properties of fluorene is to incorporate this motif into organic polymers[24,28,29] by reaction in the 2,7-positions, this introductory chapter will focus instead on its use in discrete functional organic small molecules (e.g., in Figure 1.2). Halogenation reactions (to install –Cl, –Br, –I, for example) involving fluorene or its oxidised counterpart fluorenone (Figure 1.2d) followed by subsequent metal-mediated C–C bond formation reactions (e.g., Suzuki–Miyaura, Sonogashira and Stille couplings) account for a majority of the diversity in organic small molecules bearing at least one fluorene unit.[24,30] There exist alternative ways of decorating fluorene with substituents e.g., by careful construction of the fluorenyl core from a functionalised biphenyl building block[7,31] (Figure 1.1c). Careful choice of substituents enables the tuning of frontier molecular orbitals (FMOs) for the desired applicability in optoelectronic devices.[32]

Facile non-symmetric aromatic derivatisation[33] together with the electron-rich nature of the fluorene moiety makes it suitable to use in push–pull donor–acceptor systems as either the π-spacer[34,35] or the electron-donating group. For example, fluorene-based materials have had success in their use in dye sensitised solar cells when fused with other electron-donors such as triarylamines[36] resulting in light-electricity conversion efficiencies of up to 8% for a fully organic system[37] (Figure 1.2c). The coplanar nature of the biphenyl embedded in the fluorene is desirable because it enhances electron delocalisation (i.e., charge transport) between donors and acceptors in push–pull systems compared to π-spacers that twist out of plane of each other (e.g., biphenyls). Push–pull materials have also displayed suitable properties to be used as fluorosensors, nonlinear optical switches and in electro-optical and piezochromic materials.[31]

In addition to push–pull conducive properties, fluorene derivatives and their oxidised counterparts based on fluorenone have exhibited impressive photophysical phenomena including solid-state emission through aggregation induced emission (AIE), room-temperature phosphorescence (RTP), and twisted intramolecular charge transfer (TICT).[31] For example, a fluorene conjugated diphenylamine-oxadiazole derivative **1** (Figure 1.2a), was found to be emissive in the solid state with photoluminescent quantum yields (PLQYs i.e., the ratio between the number of photons emitted by a molecule and the number of photons used to excite the molecule) of 0.41. This impressive solid-state emission was found to be due to a phenomenon known as aggregation induced emission (AIE), which enables their solution-processability for OLED device applications.[38] Further, when functionalised with

heavy atoms such as bromine in the 2,7-positions, fluorene **2** (Figure 1.2b) has been found to show triboluminescent room-temperature phosphorescence (i.e., upon introducing a mechanical stimulus, the material is phosphorescent) that are highly dependent on halogen Br⋯Br interactions.[39] In a separate example, a 2,7-diethylaminophenyl fluorenone **4** (Figure 1.2d) was observed to exhibit different radiative decay mechanisms dependent on solvent polarity; in low polarity solvents, radiative decay from an excimer dominated its emission whereas in higher polarity solvents, TICT emission was observed.[40,41]
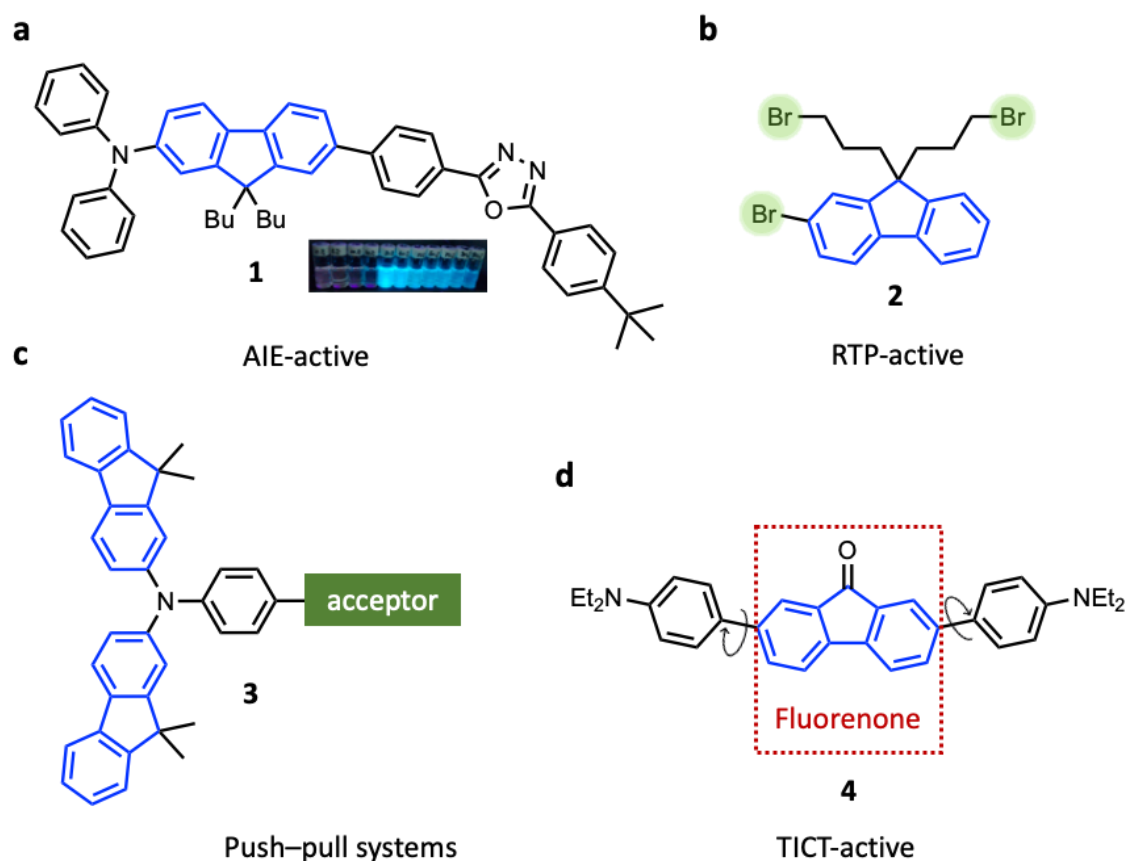
Figure 1.2 Molecular structures of relevant fluorenyl compounds discussed showing complex photophysical properties including (a) aggregation induced emission (AIE);[38] (b) room temperature phosphorescence (RTP);[39] (c) donor–acceptor push-pull systems;[37] (d) twisted intramolecular charge transfer (TICT) processes.[40,41]

Apart from the intrinsic photophysical properties of fluorene, researchers have also been intrigued by its redox behaviour and in particular its tendency to form chemically generated organic radicals. For example, the oxidation properties of 9,9-dialkyl substituted fluorenes were studied and it was observed that under a scanning potential, charged states were preferentially electropolymerising.[42] On the other hand, the properties of radical anion and anionic states of fluorene were studied, and the stability of these states were found to be dependent on the counterion, solvent and temperature.[43] In addition, researchers have been able to enhance the electron-accepting abilities of fluorene to afford strong electron acceptors with fully reversible reduction behaviours.[44] Together, these works highlight the possibility for achieving ambipolar redox properties with fluorene (Figure 1.3a). Notably, fluorene has

been found to be suitable at forming chemically generated neutral organic radicals which can be kinetically stabilised such that they are able to persist under ambient conditions by the inclusion of sterically bulky groups such as anthracenyl and mesityl groups[45–47] (e.g., **5** in Figure 1.3b). For example, the half-life ($\tau_{1/2}$) of an anthracenyl-fluorenyl radical prepared by Nishiuchi, T. et al.[47] was found to be 5.6 days under ambient conditions. Researchers have been able to extract this property from fluorenes to design mechanophores based on arylfluorene radicals.[48]
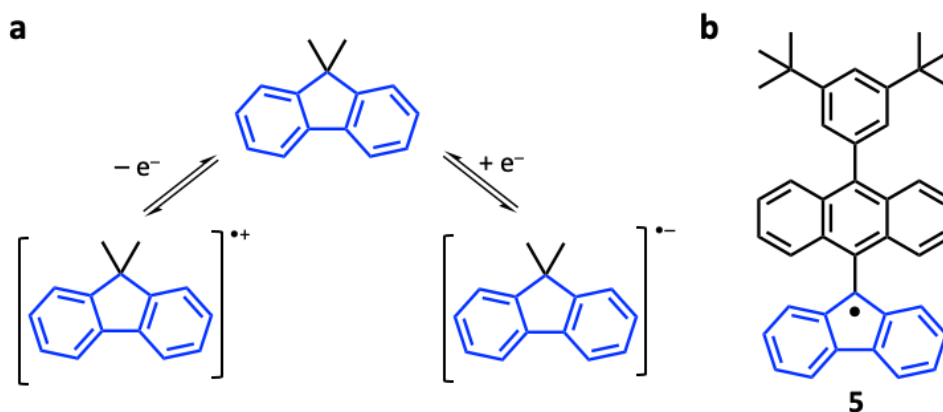
Figure 1.3 (a) Highlighting the ambipolar redox abilities of fluorene. (b) An example of one of the first kinetically stabilised fluorenyl-radicals synthesised and characterised.

There has also been a great tendency for researchers to use fluorene as a building block to construct non-planar and three dimensional (3D) molecular architectures (e.g., macrocycles, molecular rotors, metalla-knots,[49] etc) in their efforts to synthesise and understand the properties of carbon-containing nanostructures.[30,51] In particular, researchers have found that macrocyclisation of dibrominated fluorenes in the 3,6-positions (Figure 1.4a) are more conducive to forming non-linear conformations[51,52] compared to 2,7-derivatives which favour the formation of linear oligomers. For example, macrocyclization of fluorene was found to enhance electron delocalisation to result in globally antiaromatic polyradicaloid systems due to the enforced rigidity and planarity of the molecular structure.[53] This global antiaromatic current is depicted by computationally determined anisotropic induced current (AICD) isosurfaces, shown in Figure 1.4b. 3D molecular structure and in particular conformational switching upon introduction of a mechanical stimulus has also been explored for fluorenylidene-acridanes (an example **7**, is shown in Figure 1.4c) with applications in inkjet printing technologies[54] and selective hole or electron mobilities[55] depending on whether the system adopts a folded and twisted structure[56] (Figure 1.4c). Fluorene in head-substituted fulvalene structures (e.g., compound **8** in Figure 1.4d) has also been used as a stator in the development of light-driven rotary molecular motors when trying to understand the dynamics behind photoisomerization which enables unidirectional rotation about a double bond[57] (Figure 1.4d).
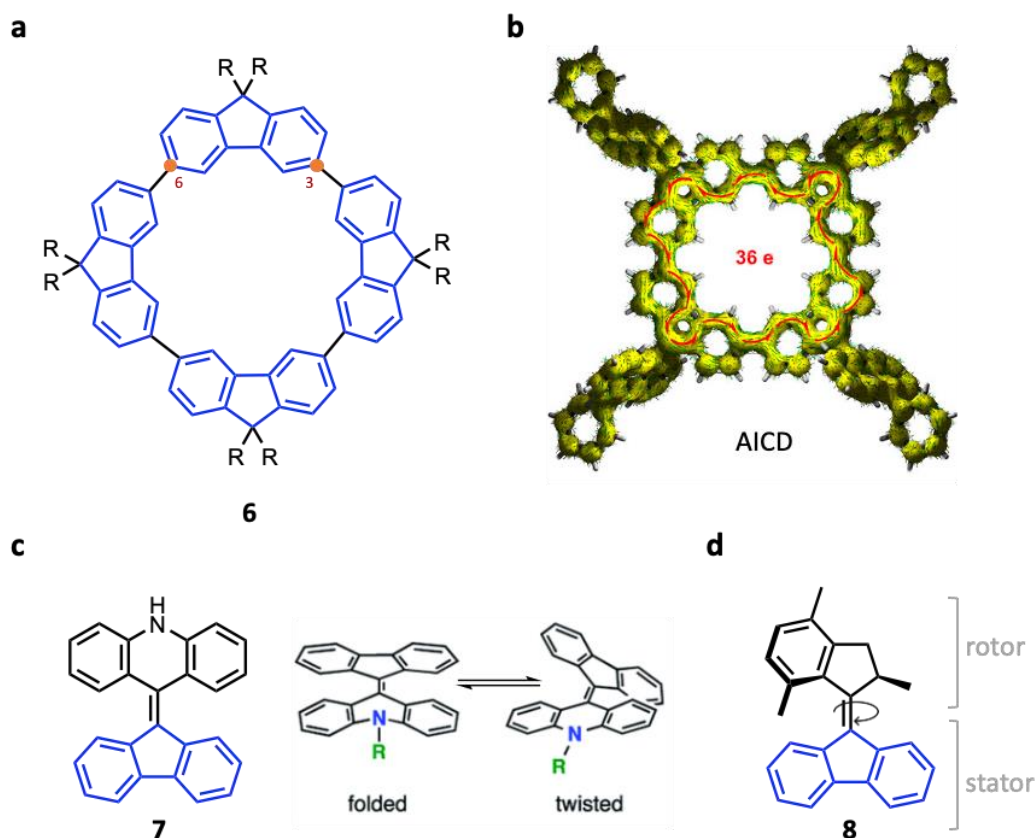
Figure 1.4 (a) Chemical structure of a tetrameric macrocycle synthesised from 3,6-fluorene derivatives and (b) depiction of the computationally calculated AICD global aromatic current experienced by a polyradicaloid macrocycle synthesised from four fluorene units. (c) Chemical structure of fluorenylidene-acridane **7** and a representation of the two conformations it can adopt in the solid state. (d) An example of a molecular rotary motor based on fluorene.

It is evident that fluorene is a versatile and multifunctional building block that has enabled the study of the fundamental and intrinsic properties of rigid and planar polyaromatic small-molecule hydrocarbons where functionalisation allows for easy tuning of these properties. In addition, its incorporation into larger 3D systems has been found to increase the stability of the redox states of fluorene due to enhanced conjugation.

1.3 BENZANNULATED FLUORENES

Given the attractive photophysical and redox properties that are inherent to fluorene, the synthesis and properties analysis of π-extended benzannulated derivatives of fluorene has developed as researchers aim to take advantage of its reliably high PLQYs and reversible redox properties to create organic materials that have found use in advanced optoelectronic and magnetic applications. Benzannulation can occur in either the 1,2-, 2,3- or 3,4-positions[58] (i.e., *a*, *b*, *c* positions respectively) singly to create benzofluorenes (or benzofluorenones)[59] or doubly in a non-symmetric[60] or symmetric fashion to make dibenzofluorenes (examples structures are shown in Figure 1.5). Synthetically, this feat has been achieved through intermolecular metal-catalysed cycloadditions[61] (Figure 1.5a) or intramolecular Diels-Alder reactions[62] (Figure 1.5b) to synthesise 1,2- and 2,3-benzofluorenes **9** and **10** respectively.

Alternatively, Pd-catalysed cascade reactions from a 2,7-diiodofluorene *via* consecutive arylation, cyclisation and aromatisation steps can achieve a variety of symmetric and non-symmetric elongated dibenzo- and benzofluorenes in good yields[63] (Figure 1.5c).
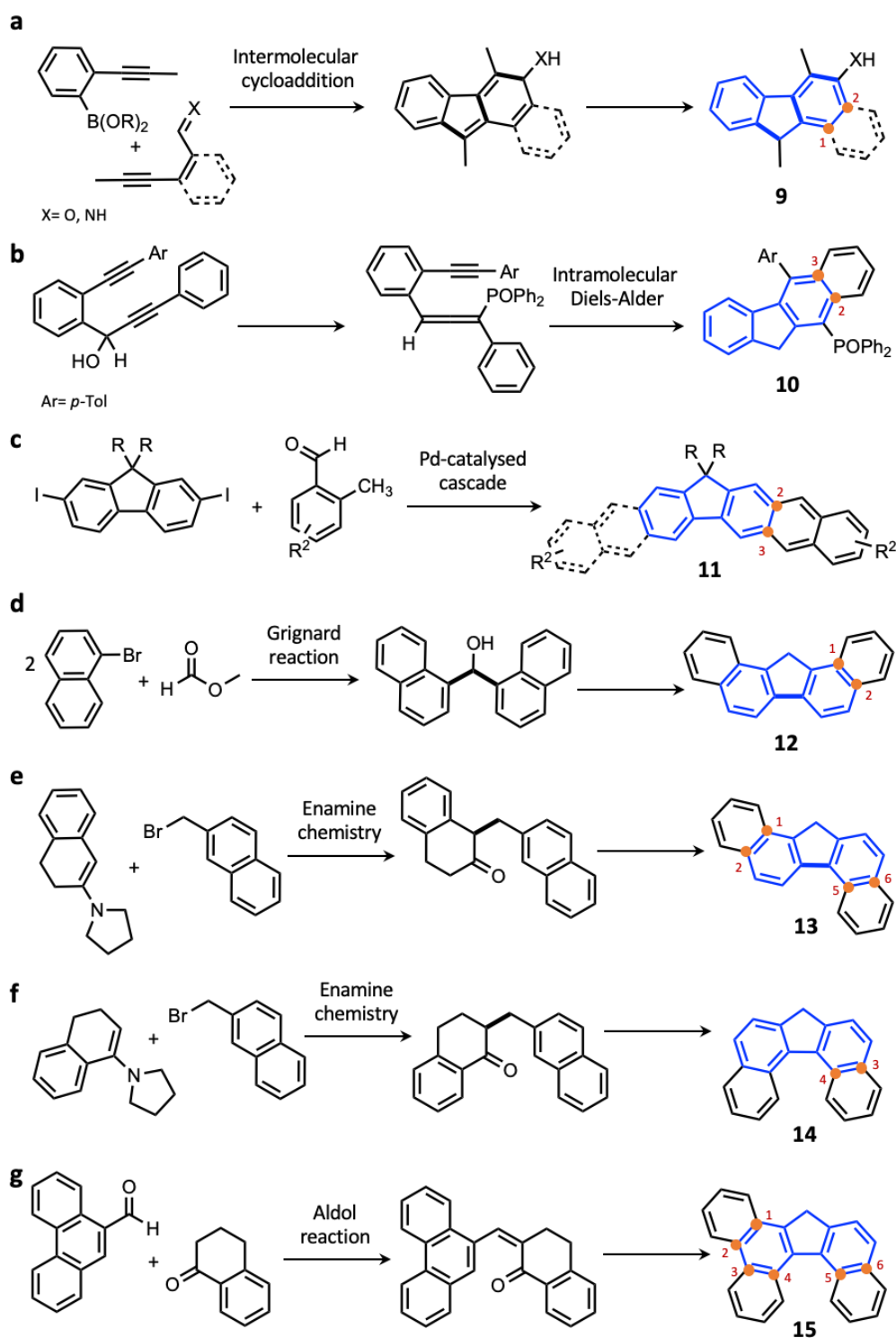
Figure 1.5 Synthetic schemes showing the diversity of methods available to synthesise monobenzofluorenes (e.g., in (a) and (b)), dibenzofluorenes either (c) directly from fluorene or using (d) Grignard or (e), (f) enamine chemistry and (g) tribenzofluorenes such as **15**

With regards to the synthesis of dibenzofluorenes, it is more common to use alternative milder and more efficient synthetic strategies where the fluorene core is stitched together from a variety of polyaromatic molecules (e.g., naphthalene or phenanthrene derivatives) making use of either Grignard[64,65] (Figure 1.5d) or enamine chemistry[64–66] (Figure 1.5e and f) to synthesise 1,2–, 1,2,5,6– and 3,4–dibenzofluorenes **12**, **13** and **14** respectively. Synthetic occurrences in the literature of tribenzofluorenes (e.g., **15**) are sparse and follow similar synthetic routes to dibenzofluorenes, where for example, a base-assisted aldol reaction[67] brings together phenanthrene and naphthalene derivates before successive oxidations to form the fluorenyl-core (Figure 1.5g). π-Extended fluorenes have been used in very similar ways to fluorene, e.g., by incorporating them into polymers,[28,64] long chain oligomers[68] or creating spirobenzofluorene derivatives[69,70] and studying their solution and solid-state emissive and electrochemical properties for use as materials in OLEDs and OFETs as the emissive or charge transporting materials. This section will instead focus on the properties of the parent, small-molecule derivatives of these π-extended fluorenes in a similar manner to the section above.

The absorption spectra of different isomers of benzofluorene and benzofluorenone[71] display features that are less dependent on the electronics of the conjugated backbone and instead reveal interesting structural differences. For example, 3,4-benzofluorene **17** (Figure 1.6) displays an absorption spectrum whose features are significantly different to its 1,2- and 2,3-isomers because its structure is expected to disrupt the planarity of the fluorene backbone as a result of steric clashes between hydrogen atoms on the aromatic core. On the other hand, 1,2-benzofluorenone **16** displays an absorption spectrum whose features do not match its isomers because of the possibility of forming an intramolecular CH···O interaction between the carbonyl and a neighbouring aromatic proton.[72]
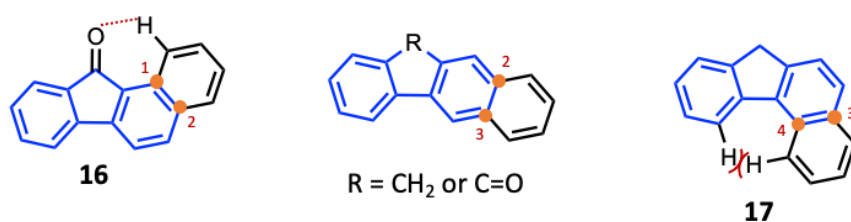
Figure 1.6 Structures of the three possible isomers of benzofluorene (R = CH2) and/or benzofluorenone (R = C=O) where structural differences (highlighted in red) are used to differentiate absorption behaviours.

Benzo- and dibenzofluorenes display a similar blue emission to fluorene with relatively high PLQYs. For example, the PLQY of polymers synthesised using either dibenzofluorene **12**, **13** or **14** as the repeating unit are as high as 0.62 (e.g., **P13**[64] Figure 1.7a), while the $PLQY_{solution}$ for a benzofluorene derivative was found to be up to 0.72[73] (e.g., **19** and **20** Figure 1.7b and c). These π-extended 3,4-benzofluorene derivatives were found to display higher PLQYs compared to a fluorene control, even as solution-processed neat films ($PLQY_{film}$ of up to 0.45 compared to 0.40 with fluorene). Notably, the neat films possess high quantum yields that are only minimally affected by high concentration (i.e., aggregation) with fast radiative decay constants (k_r) which when paired with an enhanced photostability

compared to fluorene compounds in air make them suitable materials for use in lasing applications.[73] Depending on the position of the benzannulation,[61,74] emission of benzofluorenes are typically red shifted compared to fluorene due to the introduction of enhanced conjugation. Tuning of these optical properties can be made with ease with the correct choice of electron donating or accepting groups in particular positions around the extended aromatic surface (for example, **21**[61] in Figure 1.7d) is a near-IR emitter). As a result of precisely understanding the optical properties of benzofluorenes, researchers were able to display its effective sensing of trinitrotoluene (TNT) on a nanomolar scale evident from a loss of emission from the benzofluorene upon titrating in dilute solutions of TNT.[75]
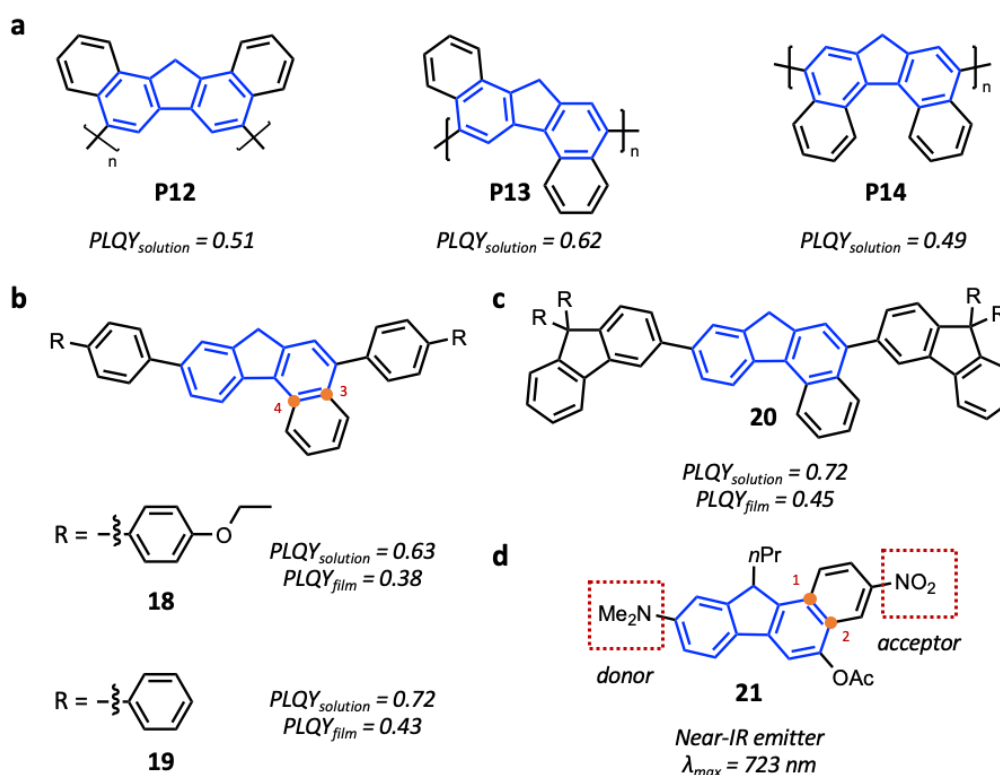
Figure 1.7 Structures of a variety of benzo- and dibenzofluorene derivatives that have been studied for their optical properties in solution and as neat films (where possible, PLQYs are mentioned adjacent to the relevant chemical structures). (d) An example of a benzofluorene containing both donor and acceptor groups substituted to tune its optical properties such that it is a near-IR emitter.

In addition to thoroughly understanding their optical properties, researchers have devoted time to probing the redox behaviour of benzo- and dibenzofluorenes. 1,2-Benzofluorene was found to be a better electron donor than its fully aromatic analogue chrysene (highlighting its oxidative abilities) aided by the polarising effect of the methylene carbon bridge in the cyclopentadienyl ring.[76] In fact, the incidence of intense femtosecond laser pulses leads to the formation of triply and quadruply charged cations of 2,3-benzofluorenes detected by time-of-flight mass spectrometry (before the fragmentation process), one of the highest charged states observed by femtosecond laser ionisation for common hydrocarbons.[77] On the other hand, chemical reductions with different Group 1 metals (e.g., Li, Na and K) at –70 °C is an efficient way of creating radical anions from different isomers of benzofluorene

which decay over time (following a second order rate dependence) as the temperature is raised to their respective and more stable, fully aromatic anions, confirmed by EPR and UV–vis absorption monitoring.[78] The 3,4-dibenzofluorene anion also readily forms complexes with other metals such as manganese and iron.[79] Similarly, the electron affinities of π-extended fluorenyls increases with the benzannulation.[80]

On a related note, the acidity of the methylene protons (i.e., the ease with which protons can be deprotonated to form a fluorenyl anion) in 1,2-, and 3,4- di-[81] and benzofluorene[82] increases compared to fluorene (i.e., the pK_a of those protons is smaller than in fluorene) due to the extended conjugation, however the opposite is true for 2,3-benzofluorene (Figure 1.8a). A similar trend was observed for phenyl-substituted dibenzofluorenes (R=Ph),[81] where the head-group phenyl substitution resulted in an increase in the acidity throughout (Figure 1.8a) compared to simple dibenzofluorenes (R = H).

a

22
R = H; pK_a = 22.9
R = Ph; pK_a = 18.5

23
R = H; pK_a = 17.5
R = Ph; pK_a = 17.3

24
R = H; pK_a = 21.4
R = Ph; pK_a = 19.1

25
R = H; pK_a = 16.8
R = Ph; pK_a = 14.8

b

26
$\tau_{1/2}$ = 5.6 days

27
$\tau_{1/2}$ = 7 days

28
$\tau_{1/2}$ = 3.5 days

29
$\tau_{1/2}$ = 43 days

c

27   **28**   **29**
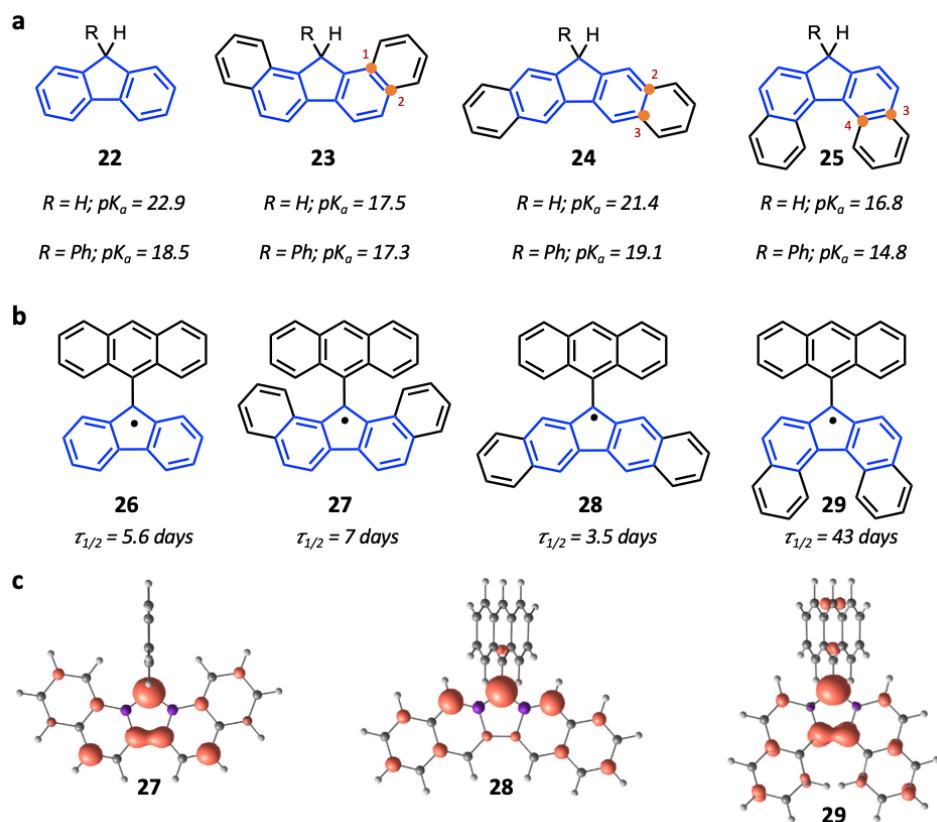
Figure 1.8 Structures of aryl head-substituted π-extended fluorenyls, with (a) the resulting pK_a highlighted underneath each structure, giving an indication of the stability of their conjugate anions or (b) the lifetime of the decay of their neutral organic radicals along with (c) spin-density plots determined by DFT (UB3LYP/6-31G(d,p)) that highlight the (de)localisation of the radical species.

Finally, Tian and co-workers[83] studied a series of π-extended fluorenyl radicals including a [5]helicene (**29**, Figure 1.8b, helicenes are discussed in more detail in Section 1.4.1). The anthracene head-unit was found to be crucial for stabilising the radical kinetically whereas π-extension provided thermodynamic stability. The *ortho* π-extended fluorenyl analogue **29** was found to display remarkable stability compared to its regioisomers owing to delocalisation resonance structures that constrained a majority

of the spin denisty to the 5-membered cyclopentadienyl ring (compared to **27** and **28**) which is effectively sterically blocked by anthracene[83] (spin-density plots are shown in Figure 1.8c). Trends in pK_a (i.e., indicating the relative stability of anionic species of dibenzofluorenyls) match the trends observed for the lifetimes of the respective neutral organic radical – i.e., 3,4-dibenzofluorenes stabilise neutral and anionic states better than other symmetric regioisomers. Researchers have recognised the ability of fluorenes and its π-extended analogues to hold and release charge in different charged and neutral states effectively and have therefore sought to extract this functionality in diverse applications,[84] e.g., as cation-hosting organic anode materials in rechargeable alkali metal-ion batteries.[85]

In addition to simple benzannulation, researchers have tended to favour the synthesis and properties analysis of indenofluorenes (IF; Figure 1.9a) that consist of two alternating 5-membered cyclopentadienyl and 6-membered benzene rings fused together (in a 6-5-6-5-6 fashion). Arranging these alternating cyclopentadienyl and benzene rings in different geometries results in 6 different possible regioisomers (Figure 1.9a) each with different conjugation/delocalisation patterns, aromatic vs antiaromatic behaviour in different redox states (depending on the sp^2 vs sp^3 hybridisation of the bridging carbons) and ground state redox structures (e.g., they are able to form both biradical open-shell or quinoidal closed shell electronic structures).[86,87]
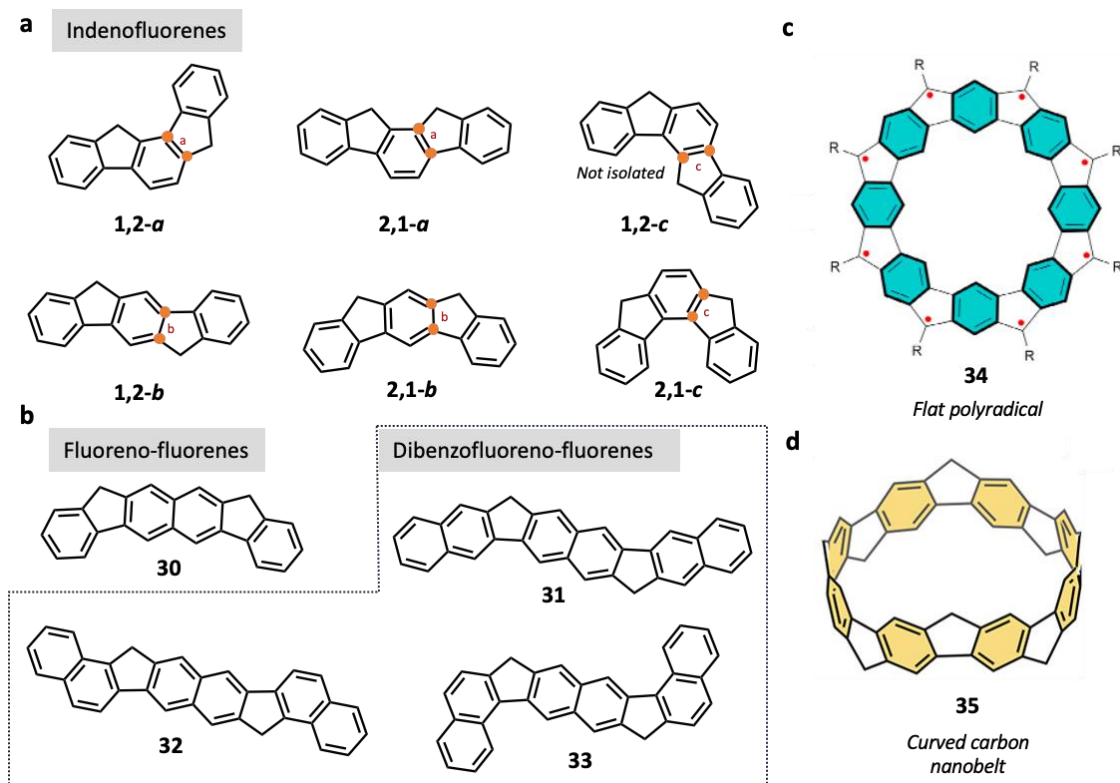
Figure 1.9 Chemical structures of different regioisomers of (a) indenofluorenes (**1,2-c** has never been isolated before) and (b) fluoreno- and dibenzofluoreno-fused fluorenes. (c) Structures of the planar and (d) non-planar macrocycles that can be synthesised by extending the π-surface of fluorene.

Introducing an additional benzene ring in the middle of **2,1-b** (i.e., to synthesise a more representative fluoreno-fluorene fused dimer **30**; Figure 1.9b) results in the expected red-shifting of its optical properties.[88] The redox properties of a series of dibenzofluoreno-fluorene diradicaloids **31–33** (Figure 1.9b) were studied and shed light on the modes of stabilisation for different charged and neutral radical states of π-extended multicomponent fluorenes. Hayashi, H. et al. found that their radical cations and neutral diradicals were stabilised thermodynamically, while radical anions were stabilised by the newly formed aromatic cyclopentadienyl rings.[89] In fact, researchers have been testing the boundaries to the number of fused alternating 5- and 6- membered rings that are possible in the neutral and polyradical states. Owing to the inherent non-linear V-shape in the structure of fluorene, fused expansion in the 2,3-positions inevitably results in macrocycles of different sizes that are both flat[90] (e.g., **34**; Figure 1.9c) and curved in geometry (e.g., **35**, also referred to as a carbon nanobelt; Figure 1.9d) with resulting polyradicals that display global aromaticity with enhanced optoelectronic and magnetic properties compared to linear derivatives.[91,92]

In addition to macrocycles, π-extended fluorenes have also been incorporated into other exotic non-planar and twisted structures. For example, fragments of C_{60}-fullerenes (also known as "buckyballs") such as corannulenes and smaller fragments[93] like **36** (Figure 1.10a) possess structures that are inherently curved due to the embedding of a cyclopentadienyl 5-membered ring into a polyaromatic nanographene analogue. In particular, **36** structurally incorporates a 9,9'-bifluorenylidene dimer (also referred to as a fulvalene) that is fused together in the 1,1-position (Figure 1.10a) and serves as a tool to understand the fundamental reactivity of fullerenes. Unfused bifluorenylidenes and their π-extended structural analogues such as **37** (Figure 1.10b) are highly strained in the neutral ground state and act as strong electron-acceptors in order to relieve steric strain to form fully aromatic systems and are suitable candidates for use in organic photovoltaic devices.[18] In addition, dibenzofluorenylidenes such as **38** (Figure 1.10c) have been used to achieve red-shifted visible-light-driven molecular motors[94] where photodissociation enables controllable unidirectional motion about the C–C double bond.
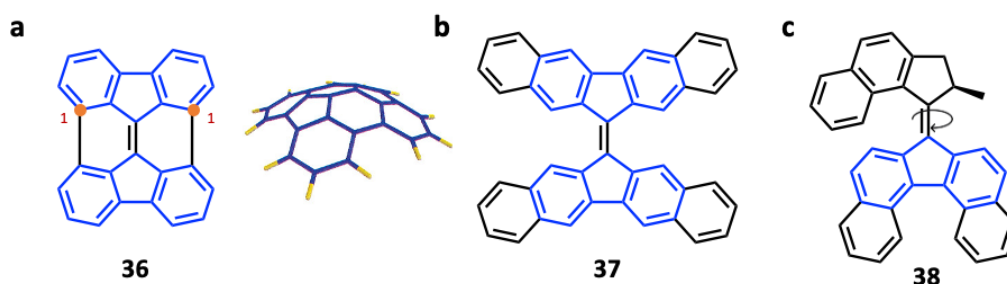
Figure 1.10 Chemical structures of non-planar (a) curved or (b) and (c) twisted π-extended analogues of benzannulated fluorenes

1.4 NON-PLANAR FLUORENYL POLYAROMATICS

1.4.1 ORGANIC SMALL-MOLECULE CHIRALITY AND HELICENES

As has been hinted at in certain parts of above sections, there is a great advantage in creating 3D π-conjugated and twisted structures in order to induce additional emergent functionality. For example, researchers have been able to develop materials that are chiral despite not containing a stereogenic point, i.e., a stereogenic carbon centre. Instead, these materials contain stereogenic axes or planes (Figure 1.11a) which render their enantiomers as non-superimposable images of each other.[95] Chiral molecules are starting to gain relevance in the development of functional organic materials as researchers aim to make use of the tuneable chiral properties that are possible as a result of their structural variety.
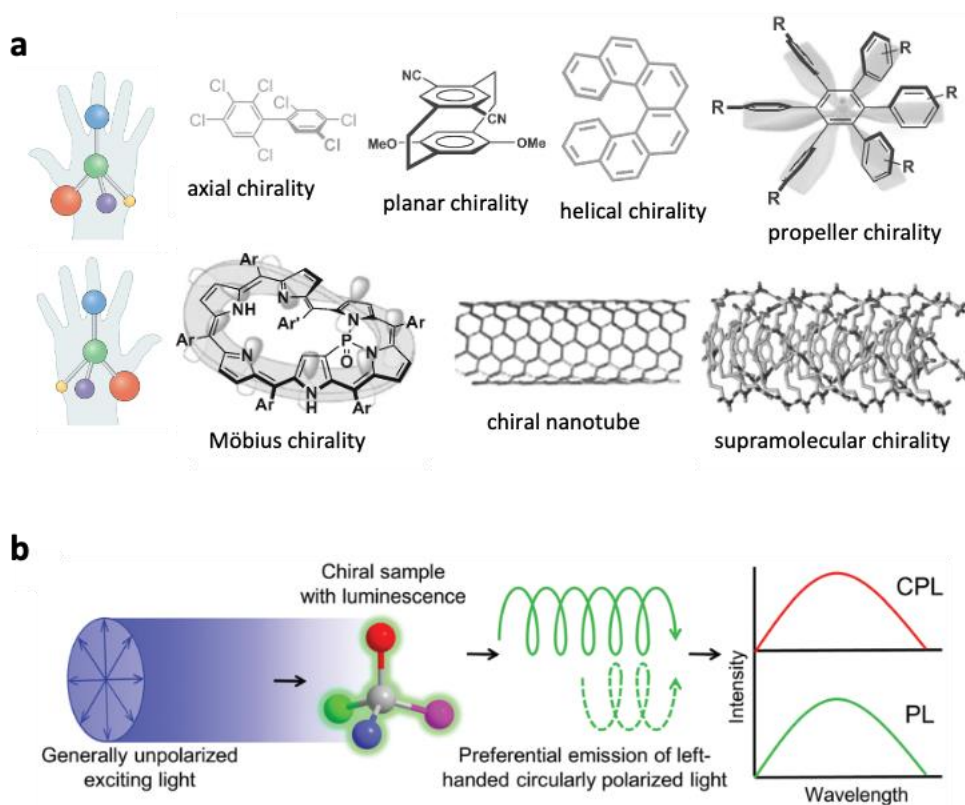
Figure 1.11 (a) Diversity in the types of chirality that can exist.[95,98] (b) Chiral molecules preferentially emit light of one handedness, and the output is circularly polarised luminescence[99]

Light is chiral as a result of the two quantum states that photons exist in[96] which when propagated form right-handed and left-handed helixes of light. Hence an enantiomer will interact differently with right-handed light *vs* left-handed light depending on its chirality. The interaction between chiral molecules and light, either by absorption or emission, can be studied, detected and quantified by circular dichroism (CD) and circularly polarised luminescence (CPL) respectively. Studying chiral small molecules for their emission of circularly polarised light (Figure 1.11b) is particularly intriguing because of how little is known thus far. Emission by organic molecules is only possible for a small

proportion of molecules and research has tended to focus more on the ability of the molecules to emit rather than the extent to which this light is circularly polarised.[97] Such a property is likely to be sought after in light-emitting device applications and in chiral probing/sensing applications. The difference in the intensity of right-handed light to left-handed light that is emitted by a small molecule is measured by the luminescence dissymmetry factor g_{lum}, defined by Equation 1, that normally has a value between +2 and –2.[96]

$$|g_{lum}| = \frac{2(I_L - I_R)}{I_L + I_R} \qquad (Eq.\,1)$$

The challenge to overcome in the design of chiral molecules that effectively emit light for chiroptical applications is to make sure that the molecule has a high g_{lum} without any sacrifices to the PLQY. Helicenes for example, are worthwhile candidates for studying CPL and have been found to have some of the largest g_{lum} values reported for organic small molecules while also boasting reasonably large quantum yield efficiencies.[96,100] Helicenes are polycyclic *ortho*-fused organic molecules that, although aromatic, adopt a non-planar helical structure in order to avoid steric repulsions between atoms positioned in the *fjord* region (orange circles shown in Figure 1.12a). The helical twist that is formed around a stereogenic axis renders helicenes as inherently chiral since either a left-handed helix (*M*–) or a right-handed helix (*P*–) can exist (Figure 1.12a).[101] Typical structural features of helicenes that are discussed in the literature include the distance between atoms in the *fjord* region (d_{H-H}), the average torsional angle (θ) and the interplanar angle (φ).[102] Extensive research has been conducted on a series of carbohelicenes (helicenes containing only carbon in its backbone) with the longest helicene reported to date formed of 16 fused aromatic units[103] (named [16]helicene).

The interplay between the steric repulsion of atoms in the terminal regions of a helicene and the ring strain that is induced to reduce the aforementioned repulsion means that smaller helicenes are flexible and tend to interconvert between enantiomers on a time scale of between minutes to a few days under ambient conditions[102] (Figure 1.12). The Gibbs free activation energy of enantiomerization $\Delta G^{\ddagger}(T)$, of [6]helicene is $\Delta G^{\ddagger}(503) \sim 44$ kcal mol^{-1} and is configurationally stable.[102] Although enantiomers of [5]helicene can be separated at low temperatures by chiral high performance liquid chromatography (HPLC), they racemize over several days under ambient conditions.[103] Introducing steric bulk in the *fjord* position can drastically increase the configurational stability of a [5]helicene[102] and therefore enables our ability to exploit its chiroptical properties for use in advanced light-emitting technologies.
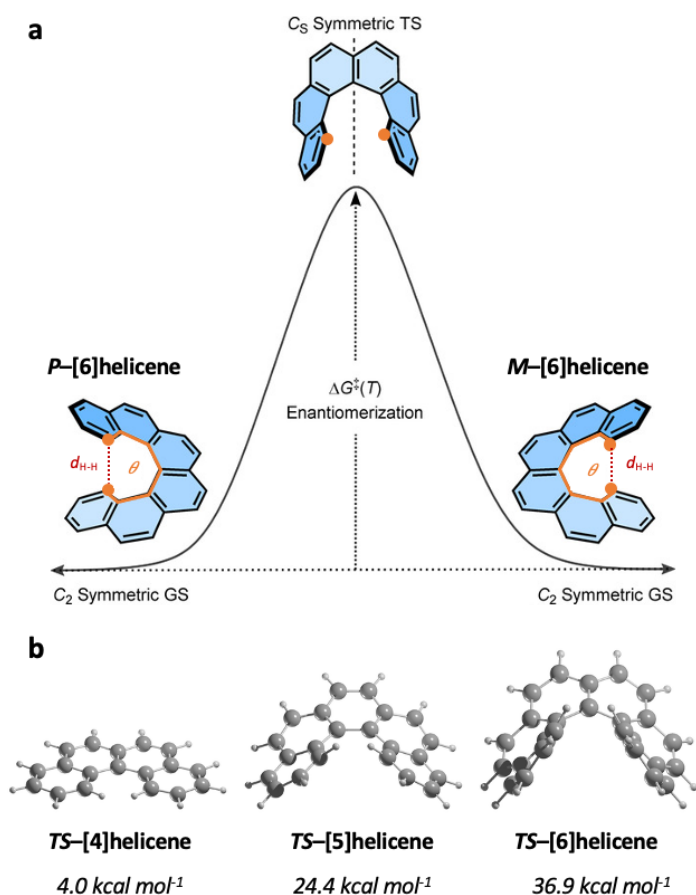
Figure 1.12 (a) *P*- and *M*- enantiomers of [6]helicene and the energy path that they follow to interconvert through a transition state (TS).[104] (b) DFT calculated geometries of the TS of a series of carbohelicenes along with their associated energy barrier.[105]

1.4.2 FLUORENYL-EMBEDDED HELICENES AND THEIR DERIVATIVES

The 5-membered cyclopentadienyl ring orients itself perfectly for building helical structures upon π-extension hence, the incorporation of the fluorenyl motif into helically chiral organic small molecules presents an attractive strategy for both enhancing inherent luminescence properties as well as enabling access to stimuli-responsive behaviour. However, there are only few reports incorporating this motif into helicene scaffolds. Research by Oyama, H. et al.[106] and Sawada, Y. et al.[107] attempted to embed a fluorene unit into a [7]helicene structure (**39** and **40**, Figure 1.13) in order to improve its PLQY and enhance its chiroptical response and g_{lum} value. Compared to the PLQY of [7]helicene (0.02),[108] both fluorene-embedded helicenes showed marked increases in quantum yields (PLQY = 0.40 and 0.32 for **39** and **40** respectively) along with reasonably high g_{lum} values in their CPL signals. Synthetic variety enables fluorenes to be incorporated into different parts of helicenes (for example at the end of a non-symmetric helicene, e.g., in **41**[109]) and in more than just one position[110] (e.g., **42** and **43**), building up to exotic helical structures containing more than one stereogenic axis (e.g., **44**[111] also known as a multihelicene; Figure 1.13). In fact, helicenes containing more than just a single embedded fluorenyl unit enables the study of polyradicaloid helicenes (e.g., from **44**), highlighting the breadth of opportunity available to take advantage of with such types of helicenes.

It should be noted that it has been recognised that 3,4-dibenzofluorenes and their derivatives, e.g., **25** (discussed in Section 1.3) possess a non-planar backbone in their crystal structures and thus exist as two enantiomers. Pammer, F. et al.[79] calculated the theoretical racemisation barrier of the anion of 3,4-dibenzofluorene (18.76 kJ mol^{-1}) to assess the viability of using this system as a ligand in metal catalysed enantioselective synthesis. They discuss from their theoretical calculations that the species are rapidly interconverting at room temperature and that these barriers are significantly lower than similar helical analogues containing methylene bridged 6-membered rings. When substituted in the *fjord* with fluorine atoms however, these theoretical barriers increase 6-fold, suggesting configurationally stable analogues of the anion of 3,4-dibenzofluorene are attainable.[79]
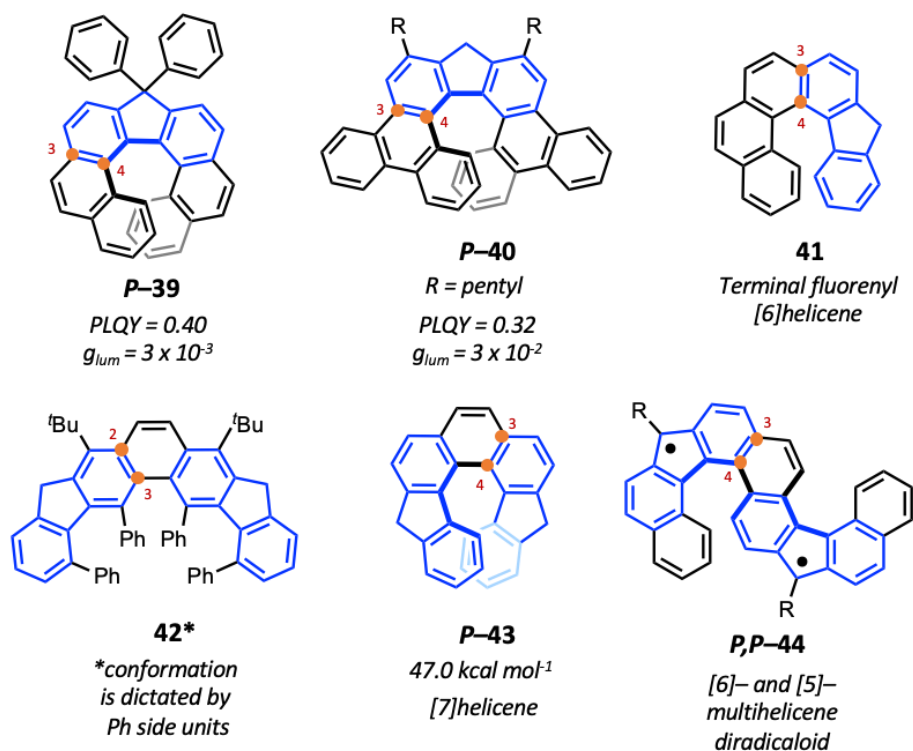
Figure 1.13. Chemical structures of a variety of helicenes that have been synthesised previously (and in some cases analysed for their chiroptical properties) bearing a fluorene moiety in various parts of the helical backbone.

Instead of building helicenes with methylene-bridged 5-membered rings, researchers have found more success with heteroatom-bridged 5-membered rings using a variety of heteroatoms including N, O, B, Si, P, and S[112–118] to create helicenes with a variety of helicene lengths, e.g., from [6]- to [9]helicenes and even a "superhelicene" (Figure 1.14). In particular, focus has been devoted to developing synthetic methodology to either enable the synthesis of enantiopure heterohelicenes (which is historically very difficult to do) or to achieve facile swapping of the heteroatom in the bridge-position, giving access to multiple functional helicene derivatives from a single helicene[113] (an example is shown in Figure 1.14a). In the small number of cases where researchers have investigated the properties of these heterohelicenes, the incorporation of the heteroatom into the helical backbone has led to the introduction of additional functional properties that were lacking in the carbon-only analogues. For

example, the PLQY of a silole-bridged [7]helicene **45**, was found to be up to 0.17 in the solid state[116] (Figure 1.14b) which was matched by an azaborole helicene (PLQY = 0.24 in the solid state). This azaborole helicene was used in the fabrication of extrinsic circularly polarised light emitting diodes with an electroluminescence dissymmetry factor g_{EL} of up to 0.54.[117] In addition, the synthesis of two hexabenzocoronenes fused together into a helicene by a central 5-membered ring (Figure 1.14c) with varying bridge-position heteroatoms allowed for easy tuning of its optoelectronic properties. This study enabled the identification of **46** as a hole-transporting material that displayed highly isotropic hole-mobilities, the highest computed for other similar heteroatom helicenes.[118]
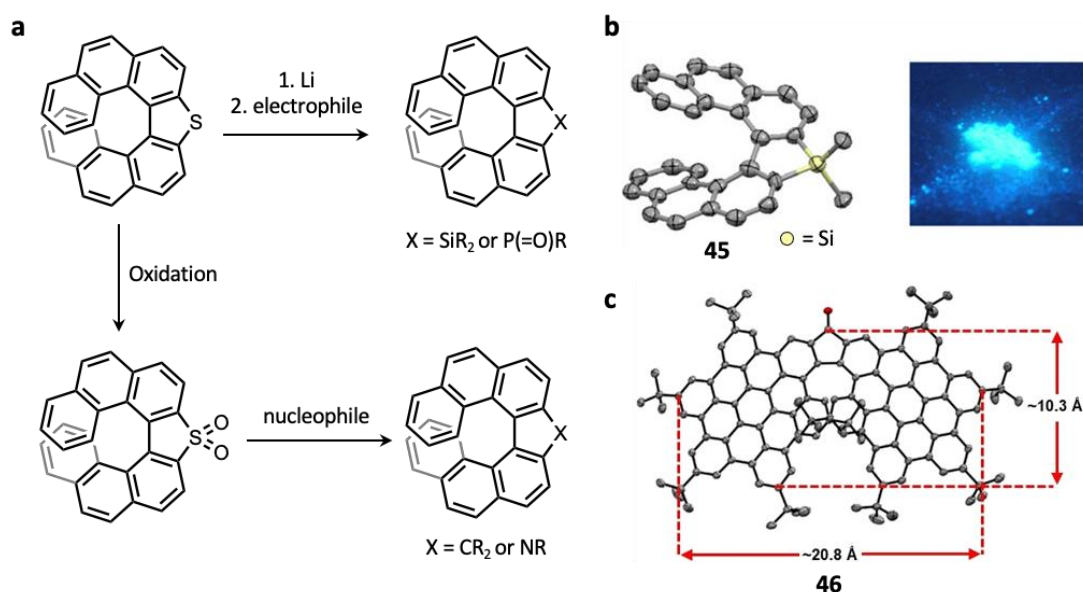
Figure 1.14. (a) Synthetic scheme highlighting the ease with which the atom in the bridge position can be swapped out to enable a variety of heteroatom-embedded [7]helicenes. X-Ray crystal structure of (b) silole-[7]helicene **45** and a picture of its emissive abilities in the solid state and (c) superhelicene **46** that has hole transporting abilities.

While there appears to be great scope in developing non-planar π-extended fluorenyl-embedded helicenes (or instead based on 5-membered heteroatom-containing rings), the difficulty in their synthesis and the isolation of enantiopure analogues appears to be hindering progress towards understanding their fundamental chiroptical properties and therefore their incorporation into device applications.

1.4.3 TETRABENZOFLUORENES

A four-fold fusion around the fluorenyl core has been achieved previously in the 1,2- and 2,3-positions where the resulting 5-membered cyclopentadienyl ring is flanked by two phenalene-derived units to make **47**[119] (Figure 1.15b), or in the 1,2- and 3,4-positions to create a fully benzannulated tetrabenzo[*a,c,g,i*]fluorene (**TBF**; Figure 1.15a). There has only been one report discussing the properties analysis of neutral organic radicals obtained from **47** that display stability under ambient conditions due to extended conjugation into the phenalenyl units (i.e., thermodynamic stability). On the

other hand, there are a few more reports focussed on **TBF**. **TBF** and its derivatives are synthesised from bromophenanthrene in three high yielding and easily scalable steps[120] involving a Grignard reaction with a formate to create the methylene carbon bridge, followed by a facile acid-promoted ring-closing reaction to sculpt the 5-membered ring (Figure 1.15a). Less efficient syntheses have been reported on smaller scales from 9,10-bifunctionalised phenanthrenes by first dimerising through an Ullmann coupling before stitching the methylene bridge together over 10 steps.[67]
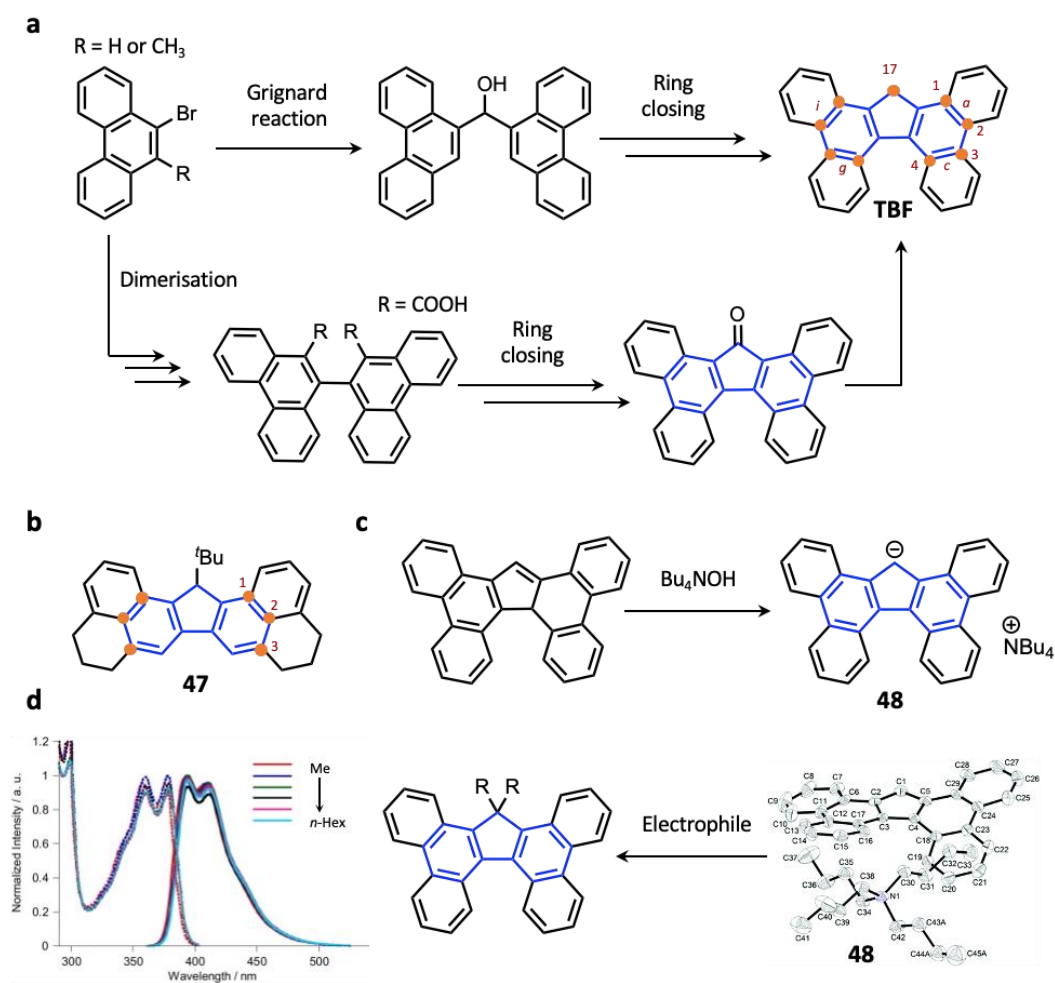
Figure 1.15 (a) Synthetic schemes from the literature that have been used to synthesise **TBF**. (b) Structure of a tetra-extended fluorene; (c) Synthesis of stable **TBF** ammonium salts (including a crystal structure) and the following synthesis to functionalise the head position of TBFs. (d) UV–vis and emission profiles of alkyl head-substituted **TBF**s.

Although the increased π-surface area decreases the solubility of TBFs in common organic solvents compared to fluorene, they can be easily functionalised in the 17-methylene carbon bridge position to introduce a variety of solubilising groups. A popular route to 17-functionalised TBFs occurs *via* ammonium salts complexed with anionic **TBF** which display remarkable stability in water at room temperature (a crystal structure of **48** is shown in Figure 1.15c). A simple nucleophilic substitution with these **TBF**-ammonium salts enables the introduction of a wide range of alkyl and benzyl groups under mild conditions.[121] Head-functionalised TBFs have found use as anchoring groups to support the solid and solution phase synthesis of biologically relevant molecules[120] because of their structural similarities

to the Fmoc protecting group.[122] In addition, **TBF** has been used to support the enantiomeric resolution of pharmaceutical compounds[123] due to its ability to be adsorbed strongly to porous graphitised carbon (i.e., charcoal) because of its relatively large π-surface.[124]

Substituents can also be introduced to the aromatic wings of **TBF** in the 3,14-positions by a simple double bromination in good yields (up to 98%) with *N*-bromosuccinimide (NBS) followed by subsequent Suzuki-Miyaura cross coupling reactions[125] (Figure 1.16a). Careful choice of substituents decorating the TBF moiety enables a tuning of its optical properties in both the solution and the solid state. For example, head group substitution with longer alkyl chains disrupts aggregate and therefore solid-state packing effectively to enable solid-state PLQYs of up to unity[126] (emission spectra of these TBFs are shown in Figure 1.15d). On the other hand, introducing electron-withdrawing substituents to the 3,14-positions of **TBF** (Figure 1.16a) leads to bathochromic absorption shifts and a lowering of PLQY efficiencies in both the solution and solid state (up to 0.70). Notably, large solvatofluorochromism ($\Delta\lambda_{em} = 67$ nm) is experienced by all 3,14-substituted derivatives (e.g., **50** in Figure 1.16a) studied by Ueda, Y. et al.[125] due to intramolecular charge transfer processes between the electron rich **TBF** core and the electron-withdrawing X groups. In addition, polymorphism in single crystals of a formyl derivative result in drastically differing optical properties (e.g., yellow *vs* green emission with solid-state PLQYs of 0.70 and 0.17 respectively from the two polymorphs). These results highlight the importance of intermolecular interactions in supporting and enabling solid-state emission of TBFs with the AIE mechanism[127] (more in-depth discussions of AIE and specific mechanisms are presented in Chapter 2). As a result, TBFs bearing electron-withdrawing substituents have been identified as turn-on fluorescent sensors for cyanide ions, displaying an intense blue-green fluorescence in the presence of cyanide ions.[128]

Although a study into the fundamental redox properties of TBFs has not been conducted in detail, researchers have identified the similarities of TBFs to cyclopentadienyls in the development of metal-organic complexes for catalytic applications. In particular, **TBF**-titanium(III)- and (IV)-complexes can be synthesised from **TBF** anions following lithiation,[129,130] where the **TBF**-titanium compound prefers to form half-sandwich complexes (a crystal structure of one such complex is shown in Figure 1.16b). These complexes are stable under ambient conditions displaying the effective stability gain of the **TBF** anion due to the benzannulation. Relatedly, due to the high affinity of TBFs for charcoal (described above), they have been utilised as covalent anchors[131] to attach Zn-porphyrins to graphene electrodes in the development of molecular wires for use in single-molecule junctions.[132] In a different example, the **TBF** was anchored non-covalently through π-π interactions which drastically improved current readings in the single-molecule transistors performance (Figure 1.16c) due to efficient overlap between the anchor **TBF** group and the graphene electrodes.[133] The results highlight the efficiency with which TBFs are able to conduct and transport charge in carbon-based materials. Separately, tetrabenzofluorenones and tetrabenzofluroenylidenes (i.e., TBF dimers connected with a C-C double

bond in the head-position) have been synthesised and studied because of their attractive electron-accepting abilities.[134,135]
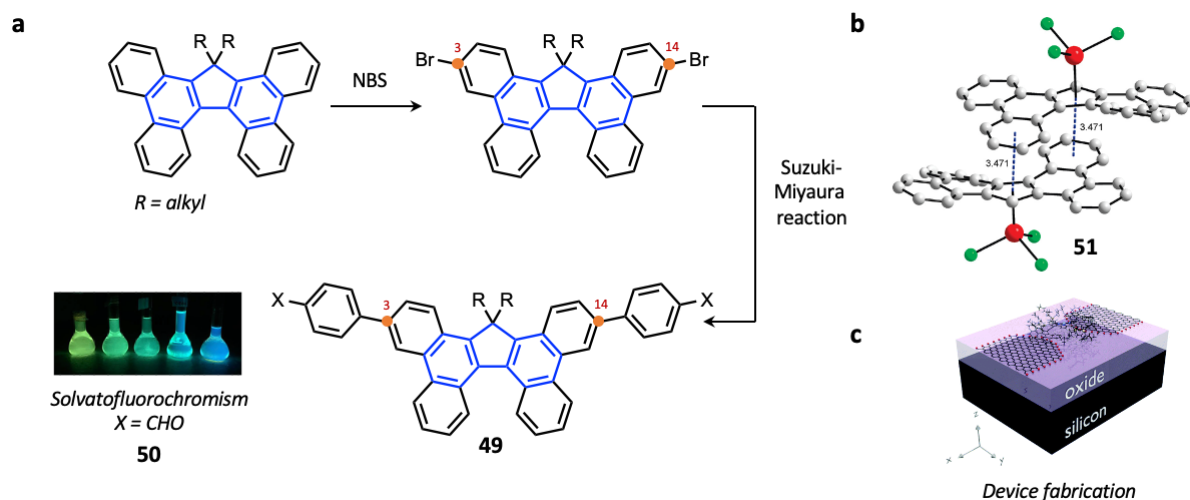
Figure 1.16 (a) Synthesis of functionalised derivatives of **TBF** through bromination and Suzuki-Miyaura couplings, where X is a range of electron-withdrawing groups. When X=CHO, i.e., compound **50**, it experiences polymorphism in its crystal-packing. (b) Crystal structure of a TBF-TiCl$_3$ complex (grey = carbon, red = Ti, green = Cl). (c) Conceptual figure of the device fabrication of non-covalent TBF-porphyrin single-molecule junctions in transistors.

The butterfly shaped structure of **TBF** and its derivatives assumes a [5]helicene-like structure and X-ray crystal structures confirm its non-planarity (e.g., Figure 1.15c and Figure 1.16b).[121,126,129,130] However, although presenting itself as an attractive AIE-active target capable of CPL and tackling challenges related to solid-state emission, TBF has yet to be developed as a chiroptical material, presumably due to its relatively low inversion barriers ($\Delta G^{\ddagger} = 14.1$ kcal mol^{-1} by variable temperature NMR)[126] rendering TBF configurationally unstable. However, as mentioned previously, there exist strategies to increase the configurational stability of such a helical structure by increasing the steric bulk of the atoms located in the *fjord* region.[102] Studying fluorene-embedded helicenes such as **TBF**, therefore presents itself as a great opportunity to understand structure-property relationships to enhance the chiroptical response of CPL-active helicenes and access solid-state emission and charge transporting properties.

1.5 THESIS OVERVIEW

In the development of organic materials that have suitable optoelectronic properties for use in advanced OLED and OFET devices, candidates that efficiently emit light in the solution and solid-state together with the ability to transport charge effectively and with high mobilities are required. Although fluorenes have surfaced as suitable organic materials and have been incorporated into polymers for use in such optoelectronic devices, their benzannulated analogues are less well studied despite their attractive features. In particular, *ortho*-fused π-extended helical derivatives based on fluorene introduce additional functionality as a result of the intrinsic chirality of their twisted aromatic backbone rendering them able to selectively emit light of single handedness when enantiopure. Such a property is highly sought after

in the development of advanced light-emitting technologies. Specifically, the efficiencies of these devices are drastically improved since there is no longer a need to use anti-glare filters that filter out 50% of polarised light emitted from conventional organic light emitters.[98]

This Chapter therefore focussed on discussing examples where researchers have studied the fundamental optoelectronic properties of fluorenes and their π-extended benzannulated analogues. The Chapter puts specific emphasis on connecting these properties with the resulting applications with which these molecules have been tested in, to set the context for the research presented in the following Chapters of this Thesis and to highlight the gaps in the current state of research. The rest of the Chapters in this Thesis therefore focus on unravelling the fundamental optoelectronic properties of non-planar organic small molecules based on the structure of TBFs. Particular focus is placed on investigating the ability of head-substituted TBFs to emit in the solid/aggregate state (Chapter 2) and studying their redox properties including in charged and neutral radical states (Chapter 3). Then, the structures of configurational stable derivatives of TBFs (predicted by DFT calculations) are pursued synthetically in Chapter 4. Finally, TBF molecules that incorporate heteroatoms into their structure by head substitution or directly into the aromatic wings are studied in Chapter 5. This Thesis serves the purpose of presenting TBFs and their derivatives as multifunctional non-planar organic small molecules that allow us to understand fundamental structure-property relationships in order to aid with the design of organic materials that are suitable for use in a range of advanced optoelectronic devices applications.

1.6 REFERENCES

1. (a) Berthelot, M.; Fluorene, *Ann. Chim. Fiz.* **1867**, *12*, 222. (b) Rieveschl, G Jr.; Ray, F. E.; The Chemistry of Fluorene and its Derivatives, *Chem. Rev.* **1938,** *23*, 287–389.

2. Barbier, P.; *Compt. Rend.* **1874**, *79*, 1151.

3. Jiao, H.; Schleyer, P. V. R; Mo, Y.; McAllister, M. A.; Tidwell, T. T. Magnetic Evidence for the Aromaticity and Antiaromaticity of Charged Fluorenyl, Indenyl and Cyclopentadienyl Systems, *J. Am. Chem. Soc.* **1997**, *30*, 7075–7083.

4. Belsky, V. K.; Zavodnik, V. E.; Vozzhennikov, V. M. Fluorene, $C_{13}H_{10}$. *Acta. Cryst.* **1984**, *C40*, 1210–1211.

5. Burns, D. M.; Iball, J. Molecular Structure of Fluorene, *Nature*, **1954**, *173*, 635.

6. Gerkin, R. E.; Lunstedt, A. P.; Reppart, W. J.; Structure of Fluorene, $C_{13}H_{10}$, at 159 K. *Acta. Cryst.* **1984**, *C40*, 1892–1894.

7. Das, A. S.; Nair, A. R.; Sreekumar, A.; Sivan, A. Approaches to Obtaining Fluorenes: An Alternative Perspective, *ChemistrySelect.* **2022**, *7*, e202201097.

8. Bordwell, F. G. Equilibrium Acidities in Dimethyl Sulfoxide Solution, *Acc. Chem. Res.* **1988**, *21***,** 456–463

9. De La Harpe, C.; van Dorp, W. A. Ueber Die Einwirkung Des Erhitzten Bleioxyds auf Fluoren, *Ber*, **1875**, *8*, 1048–1050.

10. Sieglitz, A. Studien in der Fluoren-Reihe, *Ber*, **1920**, *53*, 1232–1241.

11. Courtot, MM. Ch.; Geoffroy, R. Fluorene – About Tetreahydroxyfluorene 2.7.9.9. *Compt. Rend.* **1925**, *180*, 1665–1667.

12. Ruiz, N. *Anales. Asoc. Quím. Argentina.* **1928**, *16*, 187.

13. Kumar, D.; Thomas, K. R. J.; Lee, C.-P.; Ho, K.-C. Organic Dyes Containing Fluorene Decorated with Imidazole Units for Dye–Sensitized Solar Cells, *J. Org. Chem.* **2014**, *79*, 3159–3172.

14. Ziarani, G. M.; Moradi, R.; Lashgari, N.; Kruger, H. G. Chapter 9 – Fluorene Dyes. In *Metal-Free Synthetic Organic Dyes.* **2018**, 153–164.

15. Becker, F. F.; Mukhopadhyay, C.; Hackfield, L.; Banik, I.; Banik, B. K. Polycyclic Aromatic Compounds as Anticancer Agents: Synthesis and Biological Evaluation of Dibenzofluorene Derivatives, *Bioorg. Med. Chem.* **2000**, *8*, 2693–2699.

16. Zhou, G.; Cheng, Y.; Wang, L.; Jing, X.; Wang, F. Novel Polyphenylenes Containing Phenol-Substituted Oxadiazole Moieties as Fluorescent Chemosensors for Fluoride Ion, *Macromolecules*. **2005**, *38*, 2148–2153.

17. Zhou, G.; Qian, G.; Ma, L.; Cheng, Y.; Xie, Z.; Wang, L.; Jing, X.; Wang, F. Polyfluorenes with Phosphonate Groups in the Side Chains as Chemosensors and Electroluminescent Materials, *Macromolecules*. **2005**, *38*, 5416–5425.

18. Brunetti, F. G.; Gong, X.; Tong, M.; Heeger, A. J.; Wudl, F. Strain and Hückel Aromaticity: Driving Forces for a Promising New Generation of Electron Acceptors in Organic Electronics, *Angew. Chem. Int. Ed.* **2010**, *49*, 532–536.

19. Wong, K.-T.; Chen, R.-T.; Fang, F.-C.; Wu, C.-C.; Lin, Y.-T. 4,5-Diazafluorene-Incorporated Ter(9,9-diarylfluorene): A Novel Molecular Doping Strategy for Improving the Electron Injection Property of a Highly Efficient OLED Blue Emitter, *Org. Lett.* **2005**, *7*, 1979–1982.

20. Omer, K. M.; Ku, S.-Y.; Wong, K.-T.; Bard, A. J. Efficient and Stable Blue Electrogenerated Chemiluminescence of Fluorene-Substituted Aromatic Hydrocarbons, *Angew. Chem. Int. Ed.* **2009**, *48*, 9300–9303.

21. Yzambart, G.; Rincón-García, L.; Al-Jobory, A. A.; Ismael, A. K.; Rubio-Bollinger, G.; Lambert, C. J.; Agraït, N.; Bryce, M. R. Thermoelectric Properties of 2,7-Dipyridylfluorene Derivatives in Single-Molecule Junctions, *J. Phys. Chem. C.* **2018**, *122*, 27198–27204.

22. Kurdyukova, I. V.; Ishchenko, A. A. Organic Dyes Based on Fluorene and its Derivative, *Russ. Chem. Rev.* **2012**, *81*, 258–290.

23. Seidel, P.; Seichter, W.; Schwarzer, A.; Mazik, M. Fluorene Derivatives Bearing Two to Seven Phthalimidomethyl Groups: Syntheses, Crystal Structures and Conversion to Amines, *Eur. J. Org. Chem.* **2021**, *2021,* 2901–2914.

24. Abbel, R.; Schenning, A. P. H. J.; Meijer, E. W. Fluorene-Based Materials and Their Supramolecular Properties, *J. Polym. Sci. Part. A: Polym. Chem.* **2009**, *47*, 4215–423.

25. Li, Y.; Wang, Z.; Li, X.; Xie, G.; Chen, D.; Wang, Y.-F.; Lo, C.-C.; Lien, A.; Cao, Y.; Su, S.-J. Highly Efficient Spiro[fluorene-9-9'-thioxanthene] Core Derived Blue Emitters and Fluorescent/Phosphorescent Hybrid White Organic Light-Emitting Diodes, *Chem. Mater.* **2015**, *27*, 1100–1109.

26. Du, B.; Zhang, K.; Wang, P.; Wang, X.; Wang, S.; Shao, S.; Wang, L. Spirofluorene-Locked Carbazole Based Multiple Resonance Thermally Activated Delayed Fluorescence Emitters for Efficient Solution-Processed Narrowband Green OLEDs, *J. Mater. Chem. C.* **2023**, *11*, 9578–9585.

27. Gu, Z.-B.; Cui, Y.-M.; Li, M.-J. Hao, Z.-S. Synthesis and Characterisation of 2',7'-Diarlyspiro[cyclopentane-1,9'-fluorene] Derivatives, *Monatsh. Chem.* **2015**, *146*, 1519–1527.

28. Carbas, B. B. Fluorene Based Electrochromic Conjugated Polymers: A Review, *Polymer.* **2022**, *254*, 125040.

29. Bernius, M.; Inbasekaran, M.; Woo, E.; Wujkowski, L. Fluorene-Based Polymers: Preparation and Applications, *J. Mater. Sci: Mater. Electron.* **2000**, *11*, 111–116.

30. Wei, Y.; Yan, Y.; Li, X.; Xie, L.; Huang, W. Covalent Nanosynthesis of Fluorene-Based Macrocycles and Organic Nanogrids, *Org. Biomol. Chem.* **2022**, *20,* 73–97.

31. Shaya, J.; Corridon, P. R.; Al-Omari, B.; Aoudi, A.; Shunnar, A.; Mohideen, M. I. H.; Qurashi, A.; Michel, B. Y.; Burger, A. Design, Photophysical Properties, and Applications of Fluorene-Based Fluorophores in Two-Photon Fluorescence Bioimaging: A Review, *J. Photchem. Photobiol. C: Photochem.* **2022**, *52*, 100529.

32. Eakins, G. L.; Alford, J. S.; Tiegs, B. J.; Breyfogle, B. E.; Stearman, C. J. Tuning HOMO–LUMO Levels: Trends Leading to the Design of 9-Fluorenone Scaffolds with

Predictable Electronic and Optoelectronic Properties, *J. Phys. Org. Chem.* **2011**, *24*, 1119–1128.

33. Shaya, J.; Deschamps, M.-A.; Michel, B. Y.; Burger, A. Air-Stable Pd Catalytic Systems for Sequential One-Pot Synthesis of Challenging Unsymmetrical Aminoaromatics, *J. Org. Chem.* **2016**, *81*, 7566–7573.

34. Nguyen, W. H.; Bailie, C. D.; Burschka, J.; Moehi, T.; Grätzel, M.; McGehee, M. D.; Sellinger, A. Molecular Engineering of Organic Dyes for Improved Recombination Lifetime in Solid-State Dye-Sensitized Solar Cells, *Chem. Mater.* **2013**, *25*, 1519–1525.

35. Cheng, J.-Z.; Lin, C.-C.; Chou, P.-T.; Chaskar, A.; Wong, K.-T. Fluorene as the π-Spacer for New Two Photon Absorption Chromophores, *Tetrahedron.* **2011**, *67*, 734–739.

36. Thomas, K. R. J.; Baheti, A. Fluorene Based Organic Dyes for Dye Sensitised Solar Cells: Structure–Property Relationships, *Mater. Tech.* **2013**, *28*, 71–87.

37. Kim, S.; Lee, J. K.; Kang, S. O.; Ko, J.; Yum, J.-H.; Fantacci, S.; Angelis, F. D.; Censo, S. S.; Nazeeruddin, M. K.; Grätzel, M. Molecular Engineering of Organic Sensitizers for Solar Cell Applications, *J. Am. Chem. Soc.* **2006**, *128*, 16701–16707.

38. Feng, X. J.; Peng, J.; Xu, Z.; Fang, R.; Zhang, H.-R.; Xu, X.; Li, L.; Gao, J.; Wong, M. S. AIE-Active Fluorene Derivatives for Solution-Processable Nondoped Blue Organic Light-Emitting Devices (OLEDs), *ACS. Appl. Mater. Interfaces.* **2015**, *7*, 28156–28165.

39. Wang, J.; Wang, C.; Gong, Y.; Liao, Q.; Han, M.; Jiang, T.; Dang, Q.; Li, Y.; Li, Q.; Li, Z. Bromine-Substituted Fluorene: Molecular Structure, Br–Br Interactions, Room-Temperature Phosphorescence, and Tricolor Triboluminescence, *Angew. Chem. Int. Ed.* **2018**, *57*, 16821–16826.

40. Shigeta, M.; Morita, M.; Konishi, G.-I. Selective Formation of Twisted Intramolecular Charge Transfer and Excimer Emissions on 2,7-bis(4-Diethylaminophenyl)-fluorenone by Choice of Solvent, *Molecules*, **2012**, *17*, 4452–4459.

41. Neelambra, A. U.; Govind, C.; Devassia, T.; Somashekharappa, G. M.; Karunakaran, V. Direct Evidence of Solvent Polarity Governing the Intramolecular Charge and Energy Transfer: Ultrafast Relaxation Dynamics of Push-Pull Fluorene Derivatives, *Phys. Chem. Chem. Phys.* **2019**, *21*, 11087–11102.

42. Hapiot, P.; Lagrost, C.; Floch, F. L.; Raoult, E.; Rault-Berthelot, J. Comparative Study of the Oxidation of Fluorene and 9,9-Disubstituted Fluorenes and Their Related 2,7'-Dimers and Trimer, *Chem. Mater.* **2005**, *17*, 2003–2012.

43. Casson, D.; Tabner, B. J. Radical-Anion Intermediates. Part I. The Fluorene Radical Anion, *J. Chem. Soc. B.* **1969**, 887–892.

44. Perepichka, I. F.; Popov, A. F.; Orekhova, T. V.; Bryce, M. R.; Adrievskii, A. M.; Batsanov, A. S.; Howard, J. A. K.; Sokolov, N. I. Electron Acceptors of the Fluorene Series. 10.[1] Novel Acceptors Containing Butylsulfanyl, Butylsulfinyl, and Butylsulfonyl Substituents: Synthesis, Cyclic Voltammetry, Charge-Transfer Complexation with Anthrancene in Solution, and X-Ray Crystal Structures of Two Tetrathiafulvalene Complexes, *J. Org. Chem.* **2000**, *65*, 3053–3063.

45. Azuma, N.; Ozawa, T.; Yamauchi, J. Molecular and Crystal Structures of Complexes of Stable Free Radical BDPA with Benzene and Acetone, *Bull. Chem. Soc. Jpn.* **1994**, *67*, 31–38.

46. Zeng, Z.; Sung ,Y. M.; Bao, N.; Tan, D.; Lee, R.; Zafra, J. L.; Lee, B. S.; Ishida, M.; Ding, J.; Navarrete, J. T. L.; Li, Y.; Zeng, W.; Kim, D.; Huang, K.-W.; Webster, R. D.; Cascado, J.; Wu, J. Stable Tetrabenzo-Chichibabin's Hydrocarbons: Tunable Ground State and Unusual Transition between Their Closed-Shell and Open-Shell Resonance Forms, *J. Am. Chem. Soc.* **2012**, *134*, 14513–14525.

47. Nishiuchi, T.; Ito, R.; Takada, A.; Yasuda, Y.; Nagata, T.; Stratmann, E.; Kubo, T. Anthracene-Attached Persistent Tricyclic Aromatic Hydrocarbon Radicals, *Chem. Asian. J.* **2019**, *14*, 1830–1836.

48. Sugita, H.; Lu, Y.; Aoki, D.; Otsuka, H.; Mikami, K. Theoretical and Experimental Investigations of Stable Arylfluorene-Based Radical-Type Mechanophores, *Chem. Eur. J.* **2022**, *29*, e202203249.

49. Zhang, H.-N.; Lin, Y.-J.; Jin, G.-X. Selective Construction of Very Large Stacking-Interaction-Induced Molecular 8_{18} Metalla-knots and Borromean Ring Using Curved Dipyridyl Ligands, *J. Am. Chem. Soc.* **2021**, *143*, 1119–1125.

50. Liu, W.-J.; Zhou, Y.; Zhou, Q.-F.; Ma, Y.; Pei, J. Shape-Persistent Elliptical Macrocycles Composed of Polycyclic Aromatic Hydrocarbons: Synthesis and Photophysical Properties, *Org. Lett.* **2008**, *10*, 2123–2126.

51. Fomina, N.; Hogen-Esch, T. E. Synthesis and Characterisation of Macrocyclic Poly(fluorene-2,6-diyl), *Macromolecules*, **2008**, *41*, 3765–3768.

52. Song, Y.; Xu, W.; Zhu, D. Synthesis and Properties of Cyclic Ethylene-Bridged 3,6-Fluorene Dimer and its Linear Analogues, *Tetrahedron. Lett.* **2010**, *51*, 4894–4897.

53. Lu, X.; Lee, S.; Hong, Y.; Phan, H.; Gopalakrishna, T. Y.; Herng, T. S.; Tanaka, T.; Sandoval-Salinas, M. E.; Zeng, W.; Ding, J.; Casanova, D.; Osuka, A.; Kin, D.; Wu, J. Fluorenyl Based Macrocyclic Polyradicaloids, *J. Am. Chem. Soc.* **2017**, *139*, 13173–13183.

54. Ogumi, K.; Nagata, K.; Takimoto, Y.; Mishiba, K.; Matsuo, Y.; Inkjet Printing of Mechanochromic Fluorenylidene-Acridane, *Sci. Rep.* **2022**, *12*, 16997.

55. Suzuki, T.; Okada, H.; Nakagwa, T.; Komatsu, K.; Fujimoto, C.; Kagi, H.; Matsuo, Y. A Fluorenylidene-Acridane that Becomes Dark in Color Upon Grinding – Ground State Mechanochromism by Conformational Change, *Chem. Sci.* **2018**, *2*, 475–482.

56. Matsuo, Y.; Wang, Y.; Ueno, H.; Nakagawa, T.; Okada, H. Mechanochromism, Twisted/Folded Structure Determination, and Derivatisation of (N-Phenylfluorenylidene)acridane, *Angew. Chem. Int. Ed.* **2019**, *58*, 8762–8767.

57. Kazaryan, A.; Kistemaker, J. C. M.; Schafer, L. V.; Browne, W. R.; Feringa, B. L.; Filatov, M. Understanding the Dynamics Behind the Photoisomerization of a Light-Driven Fluorene Molecular Rotary Motor, *J. Phys. Chem. A.* **2010**, *114*, 5058–5067.

58. Keene, B. R. T.; Schofield, K. The Synthesis of 3:4-Benzofluorene and Some of its Monomethyl Derivatives, *J. Chem. Soc.* **1957**, 3181–3186.

59. Large, B.; Prim, D. On the Shape and Synthesis of Extended Fluorenones: Recent Advances and Upcoming Challenges, *Eur. J. Org. Chem.* **2022**, *4*, e202101032.

60. Saint-Ruf, G.; Buu-Hoi, N. P.; Jacquignon, P. 10. The Synthesis of Some Hexa-, Hepta- and Octa-Cyclic Hydrocarbons Derived from Fluorene, *J, Chem. Soc.* **1958**, 48–51.

61. Nishida, M.; Shintani, R. Convergent Synthesis of Fluorene Derivatives by a Rhodium-Catalysed Stitching Reaction/Alkene Isomerization Sequence. *Chem. Eur. J.* **2019**, *25*, 7475–7479.

62. Schmittel, M.; Strittmatter, M.; Vollmann, K.; Kiau, S. Intramolecular Formal Diels-Alder Reaction in Enyne Allenes. A New Synthetic Route to Benzofluorenes and Indeno[1,2-*g*]quinolines, *Tetrahedron. Lett.* **1996**, *37*, 999–1002.

63. Dong, W.; Hu, Z.; Wang, Z.; Sun, B.; Zhang, X.; Zhang, F.-L. One-Pot Synthesis of Benzofluorene Fused Aromatic Hydrocarbons, *Tetrahedron. Lett.* **2019**, *60*, 151299.

64. Wang, W.-Z.; Zhu, R.; Fan, Q.-L.; Xu, G.; Hou, L.-T.l Cao, Y.; Huang, W. Synthesis, Photophysics and Electroluminescence of Poly(dibenzofluorene)s, *Macromol. Rapid. Commun.* **2006**, *27*, 1142–1148.

65. Régimbald-Krnel, M.; Wentrup, C. On the Di-1-naphthylcarbene-Dibenzofluorene Rearrangement and the Ethylenization of Diarylcarbinols, *J. Org. Chem.* **1998**, *63*, 8417–8423.

66. Harvey, R. G.; Pataki, J.; Cortez, C.; Raddo, P. D.; Yang, C. X. A New General Synthesis of Polycyclic Aromatic Compounds Based on Enamine Chemistry, *J. Org. Chem.* **1991**, *56*, 1210–1217.

67. De Ridder, R.; Martin, R. H. Synthèses Dans Le Domaine Des Composés Polycycliques Aromatique, *Bull. Soc. Chim. Belg.* **1960**, *69*, 534–548.

68. Kazlauskas, K.; Kreiza, G.; Bobrovas, O.; Adoméniené, O.; Adoménas, P.; Jankauskas, V.; Juršénas, S. Fluorene- and Benzofluorene-Cored Oligomers as Low Threshold and High Gain Amplifying Media, *Appl. Phys. Lett.* **2015**, *107*, 043301.

69. Jeon, S.-O.; Jeon, Y.-M.; Kim, J.-W.; Lee, C.-W.; Gong, M.-S. Blue Organic Light-Emitting Diode with Improved Colour Purity Using 5-Naphthyl-spiro[fluorene-7-9'-benzofluorene], *Org. Electron.* **2008**, *9*, 522–532.

70. Jeon, S. O.; Yook, K. S.; Lee, J. Y. Pyridine Substituted Spirofluorene Derivative as an Electron Transport Material for High Efficiency in Blue Organic Light-Emitting Diodes, *Thin. Film. Solids.* **2010**, *519*, 890–893.

71. Layton Jr, E. M. Spectral Characteristics of Several Series of More Unusual Aromatic Hydrocarbons, *J. Mol. Spectrosc.* **1961**, *5*, 181–198.

72. Orchin, M.; Friedel, R. A. Structure of Benzfluorenes and Benzfluorenones, *J. Am. Chem. Soc.* **1949**, *71*, 3002–3005.

73. Kazlauskas, K.; Kreiza, G.; Radiunas, E.; Adoménas, P.; Adoméniené, O.; Karpavičius, K.; Bucevičius, J.; Jankauskas, V.; Juršénas, S. Concentration Effects on Spontaneous and Amplified Emission in Benzo[*c*]fluorenes, *Phys. Chem. Chem. Phys.* **2015**, *17*, 12935–12948.

74. Allen, T. W.; Hurtubise, R. J.; Silver, H. F. Characterisation of Polycyclic Aromatic Hydrocarbons and Hydroaromatics in a Distillable Coal-Derived Solvent by Chromatography and Corrected Fluorescence Methods, *Anal. Chim. Acta.* **1982**, *141*, 411–417.

75. Mandal, M.; Balamurugan, R. Efficient Sensing of Trinitrotoluene Using a Photoluminescent Benzo[*a*]fluorenone Derivative, *ChemistrySelect.* **2019**, *4*, 10164–10168.

76. Mukherjee, T. K. Charge-Transfer Donor Abilities of o,o'-Bridged Biphenyls, *J. Phys. Chem.* **1969**, *73*, 3442–3445.

77. Yatsuhashi, T.; Nakashima, N. Formation and Fragmentation of Quadruply Charged Molecular Ions by Intense Femtosecond Laser Pulses, *J. Phys. Chem. A.* **2010**, *114*, 7445–7452.

78. Casson, D.; Tabner, B. J. Radical-Anion Intermediates. Part II. Radical Anions of Some Benzofluorenes, *J. Chem. Soc. B.* **1970**, 1560–1564.

79. (a) Pammer, F.; Sun, Y.; May, C.; Wolmershäuser, G.; Kelm, H.; Krüger, H.-J. Theil, W. R. Dibenzo[*c,g*]fluorene: The Combination of Cyclopentadiene and 1,1'-Binaphthyl in One Ligand, *Angew. Chem. Int. Ed.* **2007**, *46*, 1270–1273. (b) Pammer, F.; Sun, Y.; Weismann, D.;

Sitzman, H.; Thiel, W. R. Exploring the Concept of Aromaticity on Complexes of a Fourfold Benzannulated Cyclopentadienyl Ligand, *Chem. Eur. J.* **2010**, *16*, 1265–1270.

80. Gonzales, J. M.; Barden, C. J.; Brown, S. T.; Schleyer, P. R.; Schaefer, H. F.; Li, Q.-S. Cyclopentadiene Annulated Polycyclic Aromatic Hydrocarbons: Investigations of Electron Affinities, *J. Am. Chem. Soc.* **2003**, *125*, 1064–1071.

81. Kuhn, R.; Rewicki, D. Die Acidität von Dibenzofluorenen, *Liebigs. Ann. Chem.* **1967**, *704*, 9–14.

82. Streitwieser Jr, A.; Brauman, J. I.; Hammons, J. H.; Pudjaatmaka, A. H Equilibrium Acidities of Hydrocarbon Acids in Cyclohexylamine[1], *J. Am. Chem. Soc.* **1965**, *87*, 384–386.

83. Tian, Y.; Uchida, K.; Kurata, H.; Hirao, Y.; Nishiuchi, T.; Kubo, T. Design and Synthesis of New Stable Fluorenyl-Based Radicals, *J. Am. Chem. Soc.* **2014**, *136*, 12784–12793.

84. Murto, P.; Bronstein, H. Electro-Optical π-Radicals: Design Advances, Applications and Future Perspectives, *J. Mater. Chem. C.* **2022**, *10*, 7368–7403.

85. Zhao, S.; Bian, Z.; Liu, Z.; Wang, Y.; Cui, F.; Wang, H.-G.; Zhu, G. Bottom-Up Construction of Fluorene-Based Porous Aromatic Frameworks for Ultrahigh-Capacity and High-Rate Alkali Metal-Ion Batteries, *Adv. Funct. Mater.* **2022**, *32*, 2204539.

86. Fukuda, K.; Nagami, T.; Fujiyoshi, J.-Y.; Nakano, M. Interplay Between Open-Shell Character, Aromaticity, and Second Hyperpolarizabilities in Indenofluorenes, *J. Phys. Chem. A.* **2015**, *199,* 10620–10627.

87. Can, A.; Facchetti, A.; Utsa, H. Indenofluorenes for Organic Optoelectronics: the Dance of Fused Five- and Six-Membered Rings Enabling Structural Versatility, *J. Mater. Chem. C.* **2022**, *10*, 8496–8535.

88. Miyoshi, H.; Miki, M. Hirano, S.; Shimizu, A.; Kishi, R.; Fukuda, K.; Shiomi, D.; Sato, K.; Takui, T.; Hisaki, I.; Nakano, M.; Tobe, Y. Fluoreno[2,3-*b*]fluorene vs Indeno[2,1-*b*]fluorene: Unusual Relationship between the Number of π Electrons and Excitation Energy in *m*-Quinodimethane-Type Singlet Diradicaloids, *J. Org. Chem.* **2017**, *82*, 1380–1388.

89. Hayashi, H.; Barker, J. E.; Valdivia, A. C.; Kishi, R.; MacMillan, S. N.; Gómez-García, C. J.; Miyauchi, H.; Nakamura, Y.; Nakano, M.; Kato, S.-I.; Haley, M. M. Casado, J. Monoradicals and Diradicals of Dibenzofluoreno[3,2-*b*]fluorene Isomers: Mechanisms of Electronic Delocalization, *J. Am. Chem. Soc.* **2020**, *142,* 20444–20455.

90. Das, S.; Herng, T. S.; Zafra, J. L.; Burrezo, P. M.; Kitano, M.; Ishida, M.; Gopalakrishna, T. Y.; Hu, P.; Osuka, A.; Casado, J.; Ding, J.; Casanova, D.; Wu, J. Fully Fused Quinoidal/Aromatic

Carbazole Macrocycles with Poly-Radical Characters, *J. Am. Chem. Soc.* **2016**, *138*, 7782–7790.

91.   Liu, C.; Sandoval-Salinas, M. E.; Hong, Y.; Gopalakrishna, T. Y.; Phan, H.; Aratani, N.; Herng, T. S.; Ding, J.; Yamada, H.; Kim, D.; Casanova, D.; Wu, J. Macrocyclic Polyradicaloids with Unusual Super-Ring Structure and Global Aromaticity, *Chem.* **2018**, *4*, 1586–1595.

92.   Kono, H.; Li, Y.; Zanasi, R.; Monaco, G.; Summa, F. F.; Scott, L. T.; Yagi, A.; Itami, K. Methylene-Bridged [6]-, [8]-, and [10]Cycloparaphenylenes: Size-Dependent Properties and Paratropic Belt Currents, *J. Am. Chem. Soc.* **2023**, *145*, 8939–8946.

93.   Bronstein, H. E.; Choi, N.; Scott, L. T. Practical Synthesis of an Open Geodesic Polyarene with a Fullerene-type 6:6-Double Bond at the Center: Diindeno[1,2,3,4-*defg*;1',2',3',4'-*mnop*]chrysene, *J. Am. Chem. Soc.* **2002**, *124*, 8870–8875.

94.   Leeuwen, T. V.; Pol, J.; Roke, D.; Wezenberg, S. J.; Feringa, B. L. Visible-Light Excitation of a Molecular Motor with an Extended Aromatic Core, *Org. Lett.* **2017**, *19*, 1402–1405.

95.   Mori, T. *Circularly Polarized Luminescence of Isolated Small Organic Molecules*; Springer, Singapore: Singapore, 2020.

96.   Sánchez-Carnerero, E. M.; Agarrabeitia, A. R.; Moreno, F.; Maroto, B. L.; Muller, G.; Ortiz, M. J.; De La Moya, S. Circularly Polarized Luminescence from Simple Organic Molecules. *Chem. Eur. J.* **2015**, *21*, 13488–13500.

97.   Burrezo, M. P.; Jiménez, V. G.; Blasi, D.; Ratera, I.; Campaña, A. G.; Veciana, J. Organic Free Radicals as Circularly Polarized Luminescence Emitters. *Angew. Chem. Int. Ed.* **2019**, *58*, 16282–16288.

98.   Brandt, J. R.; Salerno, F.; Fuchter, M. J. The Added Value of Small-Molecule Chirality in Technological Applications. *Nat. Rev. Chem.* **2017**, *1*, 0045.

99.   Sang, Y.; Han, J.; Zhao, T.; Duan, P.; Liu, M. Circularly Polarized Luminescence in Nanoassemblies: Generation, Amplification, and Application. *Adv. Mater.* **2020**, *32*, 1900110.

100.   MacKenzie, L. E.; Pålsson, L. O.; Parker, D.; Beeby, A.; Pal, R. Rapid Time-Resolved Circular Polarization Luminescence (CPL) Emission Spectroscopy. *Nat. Commun.* **2020**, *11*, 1676.

101.   Rickhaus, M.; Mayor, M.; Juríček, M. Strain-Induced Helical Chirality in Polyaromatic Systems, *Chem. Soc. Rev.* **2016**, *45*, 1542–1556.

102.   Ravat, P.; Hinkelmann, R.; Steinebrunner, D.; Prescimone, A.; Bodoky, I.; Juríček, M. Configurational Stability of [5]Helicenes. *Org. Lett.* **2017**, *19*, 3707–3710.

103.   Mori, K.; Murase, T.; Fujita, M. One-Step Synthesis of [16]Helicene. *Angew. Chem. Int. Ed.* **2015**, *54*, 6847–6851.

104. Ravat, P. Carbo[*n*]helicenes Restricted to Enantiomerize: An Insight into the Design Process of Configurationally Stable Functional Chiral PAHs, *Chem. Eur. J.* **2021**, *27*, 3957–3967.

105. Barroso, J.; Cabellos, J. L.; Pan, S.; Murillo, F.; Zarate, X.; Fernandez-Herrera, M. A.; Merino, G. Revisiting the Racemization Mechanism of Helicenes, *Chem. Commun.* **2018**, *54*, 188–191.

106. Oyama, H.; Akiyama, M.; Nakano, K.; Naito, M.; Nobusawa, K.; Nozaki, K. Synthesis and Properties of [7]Helicene-like Compounds Fused with a Fluorene Unit. *Org. Lett.* **2016**, *18*, 3654–3657.

107. Sawada, Y.; Furumi, S.; Takai, A.; Takeuchi, M.; Noguchi, K.; Tanaka, K. Rhodium-Catalyzed Enantioselective Synthesis, Crystal Structures, and Photophysical Properties of Helically Chiral 1,1′-Bitriphenylenes. *J. Am. Chem. Soc.* **2012**, *134*, 4080–4083.

108. Donckt, E. V.; Nasielski, J.; Greenleaf, J. R.; Birks, J. B. Fluorescence of the Helicenes, *Chem. Phys. Lett.* **1968**, *2*, 409–410.

109. Borkent, J. H.; Diesveld, J. W.; Laarhoven, W. H. Conformational Studies on Helicenes–IX[1]: A Hexahelicene Containing an Aromatic Carbocyclic, Five-Membered Ring, *Tetrahedron*, **1982**, *38*, 1809–1811.

110. Dai, W.; Peterson, J. L.; Wang, K. K. Synthesis and Strucutre of a Helical Diindenophenanthrene with Four Congested Phenyl Substituents as a Molecular Spiral Staircase, *Org. Lett.* **2004**, *6*, 4355–4357.

111. Borissov, A.; Chmielewski, P. J.; García, C. J. G.; Lis, T.; Stępień, M. Dinor[7]Helicene and Beyond: Divergent Synthesis of Chiral Diradicaloids with Variable Open-Shell Character, *Angew. Chem. Int. Ed.* **2023**, *62*, e202309238.

112. Uematsu, K.; Noguchi, K.; Nakano, K. Synthesis and Properties of [7]helicene and [7]helicene-like Compounds with a Cyclopenta[1,2-*b*:4,5-*b*']dithiophene of dithieno[2,3-*b*:3',2'-*d*]heterole skeleton, *Phys. Chem. Chem. Phys.* **2018**, *20*, 3286–3295.

113. Uematsu, K.; Hayasaka, C.; Takase, K.; Noguchi, K.; Nakano, K. Transformation of Thia[7]helicene to Aza[7]helicenes and [7]Helicene-like Compounds via Aromatic Metamorphosis, *Molecules*, **2022**, *27*, 606.

114. Hossain, S.; Akter, M.; Shahbuddin, M.; Salim, M.; Iimura, K.-I.; Karikomi, M. Synthesis of Enantiomerically Pure Oxa[9]helicene Derivatives by a Nucleophilic Cyclodehydration Reaction of Helical 1,1'-Bibenzo[*c*]phenanthrenylidene-2,2'-dione, *Synlett*, **2022**, *33*, 277–282.

115. Nakano, K.; Hidehira, Y.; Takahashi, K.; Hiyama, T.; Nozaki, K. Stereospecific Synthesis of Hetero[7]helicenes by Pd-Catalyzed Double *N*-Arylation and Intramolecular *O*-Arylation, *Angew. Chem. Int. Ed.* **2005**, *44*, 7136–7138.

116. Oyama, H.; Nakano, K.; Harada, T.; Kuroda, R.; Naito, M.; Nobusawa, K.; Nozaki, K. Facile Synthetic Route to Highly Luminescent Sila[7]helicene, *Org. Lett.* **2013**, *15*, 2104–2107.

117. Full, J.; Wildervanck, M. J.; Dillmann, C.; Panchal, S. P.; Volland, D.; Full, F.; Meerholz, K.; Nowak-Król, A. Impact of Truncation on Optoelectronic Properties of Azaborole Helicenes, *Chem. Eur. J.* **2023**, e202302808.

118. Reger, D.; Haines, P.; Amsharov, K. Y.; Schmidt, J. A.; Ullrich, T.; Bönisch, S.; Hampel, F.; Görling, A.; Nelson, J.; Jelfs, K. E.; Guldi, D. M.; Jux, N. A Family of Superhelicenes: Easily Tunable, Chiral Nanographenes by Merging Helicity with Planar π Systems, *Angew. Chem.* **2021**, *133*, 18221–18229.

119. Kubo, T.; Katada, Y.; Shimizu, A.; Hirao, Y.; Sato, K.; Takui, T.; Uruichi, M.; Yakushi, K.; Haddon, R. C. Synthesis, Crystal Structure, and Physical Properties of Sterically Unprotected Hydrocarbon Radicals, *J. Am. Chem. Soc.* **2011**, *133*, 14240–14243.

120. Hay, A. M.; Hobbs-Dewitt, S.; MacDonald, A. A.; Ramage, R. Use of Tetrabenzo[*a,c,g,i*]fluorene as an Anchor Group for the Solid-Solution Phase Synthesis of Ciprofloxacin, *Tetrahedron. Lett.* **1998**, *39*, 8721–8724.

121. Frey, O. N.; Stalling, R.; Schlüter, F.; Saak, W.; Schmidtmann, M.; Haase, D.; Beckhaus, R. Remarkable Stability of Tetrabenzo[*a,c,g,i*]fluorenyl Ammonium Salts in Water: Syntheses, Reactions, and Crystal Structures, *Dalton. Trans.* **2016**, *45*, 1085–1092.

122. Ramage, R.; Raphy, G. Design on an Affinity-Based N$^\alpha$-Amino Protecting Group For Peptide Synthesis: Tetrabenzo[*a,c,g,i*]fluorenyl-17-methyl Urethanes (Tbfmoc), *Tetrahedron. Lett.* **1992**, *33*, 385–388.

123. Dutton, J. K.; Knox, J. H.; Radisson, X.; Ritchie, H. J.; Ramage, R. Synthesis of 17*H*-Tetrabenzo[*a,c,g,i*]fluorene Derivatives as Chiral Selectors for Enantiomeric Separation by HPLC on Porous Graphitised Carbon, *J. Chem. Soc., Perkin. Trans.* **1995**, *1*, 2581–2587.

124. Assali, M.; Leal, M. P.; Fernández, I.; Romero-Gomez, P.; Baati, R.; Khiar, N. Improved Non-Covalent Biofunctionalization of Multi-Walled Carbon Nanotubes Using Carbohydrate Amphiphiles with a Butterfly-Like Polyaromatic Tail, *Nano. Res.* **2010**, *3*, 764–778.

125. Ueda, Y.; Tanigawa, Y.; Kitamura, D.; Ikeda, H.; Yoshimoto, Y.; Tanaka, M.; Mizuno, K.; Kurata, H.; Kawase, T. 3,14-Bis(*p*-nitrophenyl)-17,17-dipentyltetrabenzo[*a,c,g,i*]-fluorene: A New Fluorophore Displaying Both Remarkable Solvatochromism and Crystalline-Induced Emission, *Chem. Asian. J.* **2012**, *8*, 392–399.

126. Kitamura, C.; Tanigawa, Y.; Kobayashi, T.; Naito, H.; Kurata, H.; Kawase, T. 17,17-Dialkyltetrabenzo[*a,c,g,i*]fluorenes with Extremely High Solid-State Fluorescent

Quantum Yields: Relationship Between Crystal Structure and Fluorescent Properties, *Tetrahedron*, **2012**, *68*, 1688–1694.

127. Ueki, M.; Kimura, Y.; Yamamoto, Y.; Nishida, J.-I.; Kitamura, C.; Tanaka, M.; Ikeda, H.; Kawase, T. 3,14-Bis(4-formylphenyl)-17,17-di(*n*-pentyl)tetrabenzo[*a,c,g,i*]fluorene Showing Solvatochromism and Crystallochromism in Fluorescence, *Tetrahedron*, **2017**, *73*, 1170–1176.

128. Kimura, Y.; Kawajiri, I.; Ueki, M.; Morimoto, T.; Nishida, J.-I.; Ikeda, H.; Tanaka, M.; Kawase, T. A New Fluorophore Displaying Remarkable Solvatofluorochromism and Solid-State Light Emission, and Serving as a Turn-on Fluorescent Sensor for Cyanide Ions, *Org. Chem. Front.* **2017**, *4*, 743–749.

129. Schröder, K.; Haase, D.; Saak, W.; Beckhaus, R.; Kretschmer, W. P.; Lützen, A. Tetrabenzo[*a,c,g,i*]fluorenyltitanium(III) and –(IV) Complexes: Syntheses, Reactions, and Catalytic Application, *Organometallics,* **2008**, *27*, 1859–1868.

130. Schröder, K.; Haase, D.; Saak, W.; Lützen, A.; Beckhaus, R.; Wichmann, S.; Schellenbeg, J. Tetrabenzo[*a,c,g,i*]fluorenyllithium and η^5-Tetrabenzo[*a,c,g,i*]fluorenyltitanium Complexes, *Organometallics*, **2006**, *25*, 3824–3826.

131. Limburg, B.; Thomas, J. O.; Holloway, G.; Sadeghi, H.; Sangtarash, S.; Hou, I. C.-Y.; Cremers, J.; Narita, A.; Müllen, K.; Lambert, C. J.; Briggs, G. A. D.; Mol, J. A.; Anderson, H. L. Anchor Groups for Graphene-Porphyrin Single Molecule Transistors, *Adv. Funct. Mater.* **2018**, *28*, 1803629.

132. Sadeghi, H.; Sangtarash, S.; Lambert, C. Robust Molecular Anchoring to Graphene Electrodes, *Nano. Lett.* **2017**, *17*, 4611–4618.

133. Mol, J. A.; Lau, C. S.; Lewis, W. J. M.; Sadeghi, H.; Roche, C.; Cnossen, A.; Warner, J. H.; Lambert, C. J.; Anderson, H. L.; Briggs, G. A. D. Graphene-Prophyrin Single-Molecule Transistors, *Nanoscale,* **2015**, *7*, 13181–13185.

134. Yamada, K.; Shibamoto, H.; Tanigawa, Y.; Ishikawa, H.; Nishida, J.-I.; Kitamura, C.; Kurata, H.; Kawase, T. Fulvalene Derivatives Containing a Tetrabenzofluorene Unit: New Nonplanar Fulvalenes with High Electron Affinity, *Synlett*. **2016**, *27*, 2085–2090.

135. Kang, H.-W.; Liu, Y.-C.; Shao, W.-K.; Wei, Y.-C.; Hsieh, C.-T.; Chen, B.-H.; Lu, C.-H.; Yang, S.-D.; Cheng, M.-J.; Chou, P.-T.; Chiang, M.-H.; Wu, Y.-T. Synthesis, Structural Analysis, and Properties of Highly Twisted Alkenes 13,13'-Bis(Dibenzo[*a,i*]fluorenylidene) and its Derivatives, *Nat. Commun.* **2023**, *14*, 5248.

CHAPTER 2 |
AGGREGATE EMISSION IN HEAD-MODIFIED TETRABENZOFLUORENES

SYNOPSIS
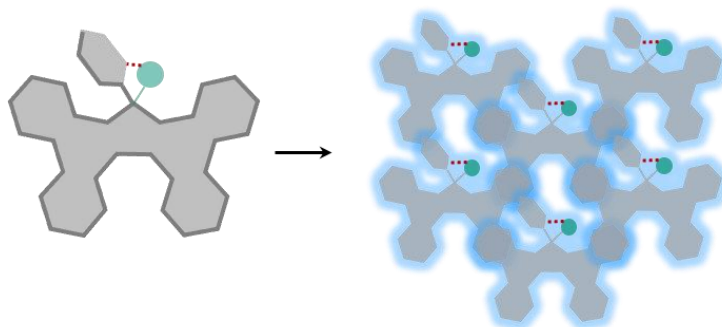
The design of organic light emitters for brighter, sustainable and more energy-efficient display technologies has benefitted greatly from advances in the field of aggregation-induced and enhanced emission (AIE/AEE). However, although we nowadays accept synthetic design approaches, e.g., constructing highly twisted and sterically bulky chromophoric structures as conventional wisdom for encouraging the intermolecular effects required for AIE/AEE, our fundamental understanding of how finer <u>intra</u>molecular interactions influence the emergence of aggregate emission remains rather limited. In addition, there does not seem to be a clear distinction in the literature of how these design features either enhance AIE *vs* sterically supress aggregation-caused quenching (ACQ) effects in isolated but structurally similar molecules. This Chapter discusses the synthesis and properties analysis of a library of non-symmetric head-substituted tetrabenzofluorenes (TBF) that display aggregate and solid-state emission. An in-depth study of their structural features, intermolecular packings and optical behaviours shed light on the specific mechanisms that enable this observed solid-state emission. Bulky and rigid anthracenyl-substituted TBFs experience AEE in particular due to intramolecular interactions (e.g., an anthracenyl-hydroxy C–H···O interaction). However, in general, these anthracenyl-substituted TBFs perform less efficiently (i.e., lower PLQYs) than butyl-substituted TBFs whose solid-state emission is enabled by a lack of π-π interactions (i.e., a suppression of ACQ). The Chapter therefore encourages future AIE/AEE works to consider the effects of reducing ACQ *vs* enabling AEE separately with careful interrogations of steric *vs* intra- and intermolecular interactions in the development of solid-state light emitters for advanced technological applications.

ACKNOWLEDGEMENTS

2.1 INTRODUCTION

Since the first report of aggregation-induced emission (AIE) from an organic small molecule in 2001,[1] research into AIE-active molecules has blossomed as researchers aim to increase the functional relevance of organic emitters in device applications by enhancing their solid-state light-emitting properties.[2] Prior to the emergence of this phenomenon, organic chromophores were designed to contain typically planar aromatic surfaces, enabling the efficient stacking and assembly of individual chromophores, which although display efficient emission in solution, suffer from aggregation-caused quenching (ACQ) effects and therefore exhibit no solid-state emissive capabilities.[3] On the other hand, aggregation-induced[2] or enhanced emission (AEE)[4] occurs when a molecule experiences a turn on and/or increase in emission intensity upon aggregation. The mechanism for this emission "switch on" has been postulated to be due to a restriction of intramolecular motions (RIM[5]), i.e., either rotations[6] and/or vibrations,[7] that limit the number of non-radiative pathways (e.g., vibrational relaxation). For example, hexaphenylbenzene and tetraphenylethene (TPE; Figure 2.1a) are AIE-active as a result of restricted intramolecular rotations of peripheral phenyl groups upon aggregation.[8] Therefore, AIE-active systems have generally been designed to have twisted and highly sterically hindered structures to interfere with and restrict intramolecular motions. Simultaneously, these twisted monomeric structures are less likely to prefer to pack in close proximity to each other leading additionally to reduced ACQ effects in the aggregate state.[9] Yet at the same time, larger, sterically bulky π-functional groups can contribute to denser aggregate packing and ultimately emission quenching. Therefore, although both AIE and ACQ phenomena have been known for a while now, the field of solid-state emission lacks clarity on the precise interplay of the structural effects influencing the two phenomena. Deciphering the role that sterically bulky groups play towards enabling solid-state emissive properties by X-ray analysis, i.e., whether they operate by enforcing RIM or by discouraging ACQ (both of which are conceptually different, but afford the same outcome), is complex and clarifying these insights would help to inform future rational design of solid-state emitters.
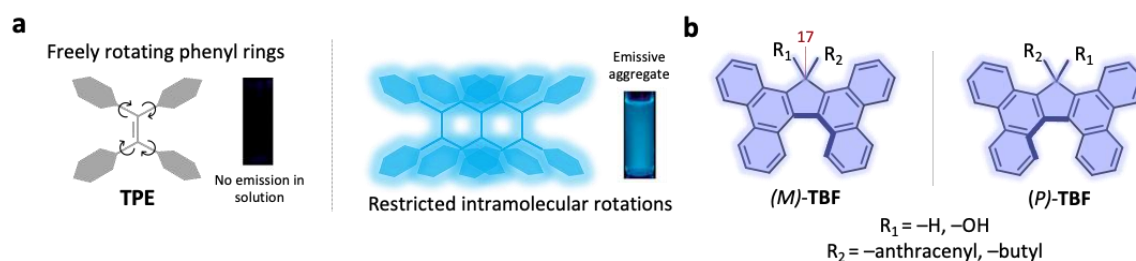
Figure 2.1 (a) AIE exemplified in TPE. (b) General structure of the two enantiomers of tetrabenzofluorenes (TBF)

Non-covalent intermolecular interactions that are present in the single-crystal X-ray packing structures of molecules have been typically used to justify observations of aggregation induced or enhanced emission.[10] Though it is understood that solution-emissive aggregates may not necessarily pack with

the same motifs as in the solid-state (e.g., due to differing solvent interactions and greater degrees of freedom in solution), these inspections can nevertheless provide some insight into the possible intermolecular interactions that could give rise to aggregate emission and strengthens claims to support a particular mechanism for the solid-state emission (i.e., either restricted motion and hence AIE, or disrupted packing and hence ACQ). Intermolecular interactions such as π⋯π interactions usually lead to ACQ type mechanisms, rendering its solid and aggregate state non-emissive. Therefore sterically disruptive design elements e.g., the introduction of long alkyl chains, reduces ACQ by disfavouring close packing of individual chromophores.[3] On the other hand, reports suggest that intermolecular interactions such as CH⋯π interactions help facilitate restricted motions and disrupt close packing upon aggregation (and hence enable AIE).[11] In addition, while the effect that intermolecular interactions have on aggregate emission is relatively well studied, the role of intramolecular interactions has received much less attention.

Structurally dynamic tetrabenzofluorene (TBF; Figure 2.1b, introduced in Chapter 1) and its derivatives have been studied as aggregation enhanced emitters in a couple of examples.[12,13] TBFs present themselves as a convenient scaffold with an easily functionalisable sp^3 methylene head 17-position (position highlighted in Figure 2.1b) to understand how intramolecular interactions and steric effects modulate efficient solid-state emission. Research into the effects that dialkyl chain lengths in the 17-position have on the solid-state emissive properties of TBFs has been conducted,[14] and the importance of longer dialkyl groups acting as spacers and disrupting the formation of π⋯π interactions was discussed. Therefore, it is understood that the primary mechanism supporting the solid-state emission for simple head-substituted TBFs is through the suppression of ACQ rather than AIE.

This Chapter describes a library of TBFs that were synthesised in order to discern the effect that subtle substitution changes at the 17-position of tetrabenzofluorenes have on their ability to be emissive in both the solution and the aggregate state. The TBFs (i.e., **A-OH**, **A-H**, **B-OH** and **B-H**; Figure 2.1b) are substituted with bulky/rigid (R_2 = anthracenyl) or flexible (R_2 = butyl) groups paired with R_1 = –OH, –H. The anthracenyl group is intrinsically photoactive, therefore butyl analogues serve the additional purpose of aiding to unravel the complex interplay of fluorenyl *vs* anthracenyl photophysics. NMR spectroscopy of these non-symmetrically substituted TBF derivatives was used to identify specific intramolecular non-covalent interactions that arise as a result of the presence of the large anthracenyl head group. X-Ray crystallographic analyses reveal that TBFs have a non-planar aromatic helical surface and highlight intramolecular interactions between R_1 and R_2 of varying distances (and hence strengths) depending on the steric bulk of the R groups. Solution-state PLQY values of the TBF library range from 0.03–0.48, with the PLQY of **B-OH** in particular being a lot lower than expected (0.04), revealing that when appended with the flexible butyl chain, the –OH group serves to quench monomeric emission. Aggregation behaviours were studied by emission spectroscopy in solvent mixtures of varying THF and H_2O compositions to reveal that anthracene-substituted TBFs **A-OH** and

A-H more readily undergo AEE due to an intramolecular CH···O and intermolecular CH···π interactions respectively, which rigidifies the structures. However, despite the structural rigidification introduced by the anthracene, this moiety was also found to contribute to a lower relative PLQY compared to butyl-substituted TBF derivates irrespective of the accompanying substituent at the head position. On the other hand, butyl-substituted TBF **B-H** was observed to display aggregate emission as a result of the flexible alkyl group preventing ACQ, resembling behaviour previously observed for alkyl-substituted TBFs. These results suggest that there is a balance to be struck between the size of a bulky π-surface and the desired efficiency in the resulting solid-state emission. The results additionally highlight the impact that intramolecular, intermolecular, and steric interactions can have on molecular motions and packing motifs of aggregates thereby affecting emissive abilities in their monomeric *vs* aggregate form.

2.2 RESULTS AND DISCUSSION

2.2.1 SYNTHESIS AND STRUCTURAL ANALYSES

To obtain **A-OH**, **A-H**, **B-OH** and **B-H**, the TBF core was first synthesised, after which –R group functionalisation at the fluorenyl 17-position was achieved (Scheme 2.1). A common route to preparing tetrabenzofluorenes, reported by Hay, A. et al.[15] proceeds *via* a Grignard-mediated dimerisation of 9-bromophenanthrene **1** to afford alcohol **2**, followed by an acid-mediated cyclisation and a base-catalysed tautomerisation of **3** to form the central 5-membered cyclopentadienyl ring. In order to install additional functionality and to enable organolithium carbon–carbon bond forming chemistries, **3** was then subjected to mild oxidation conditions by bubbling air through the reaction to form ketone **TBF=O** in an 94% yield adapted from a procedure reported by Yamada, K. et al.[16] From **TBF=O**, **A-OH** and **B-OH** were synthesised by reaction with 9-lithioanthracene (generated *in situ*) or *n*-BuLi respectively in THF at –78 °C. The isolated yield of **A-OH** is low (28%) owing to (i) steric crowding around the 17-fluorenyl ketone position from periphery aromatic rings in **TBF=O** and (ii) reaction with a sterically bulky anthracenyl group, resulting in unreacted ketone starting material remaining in solution even after 24 hours. In addition, other alkyl-containing TBF products are isolated in the reaction to synthesise **A-OH**, formed from a reaction with bromobutane which is present after lithium exchange in the presence of *n*-BuLi, supporting the low yields. Nonetheless, **A-OH** was isolated by trituration of the crude reaction material in *n*-hexanes to precipitate and remove ketone starting material **TBF=O**, followed by automated column chromatography (SiO$_2$: 0–10% EtOAc in *n*-hexanes), confirmed by mass analysis and NMR spectroscopy. **A-OH** was then reduced with Et$_3$SiH and TFA in CH$_2$Cl$_2$ to form **A-H** in 50% yield. The isolated yield of **B-OH** is poor as well (15%) due to a preferential elimination of H$_2$O to form **TBF-B** as the major product, isolated in 54% yield. The synthesis of **B-H** was trialled from **B-OH** under similar reduction reaction conditions as those used to form **A-H** and

through a reduction of **TBF-B** with H_2 gas in the presence of Pd/C in EtOAc, however the starting material remained unreacted following both procedures. **B-H** was finally synthesised from the deprotonation of **3** with tetrabutylammonium hydroxide (TBAH) which enabled a nucleophilic substitution reaction of the resulting highly air-sensitive deprotonated salt **TBF⁻BuN₄⁺** with bromobutane in a 17% yield.
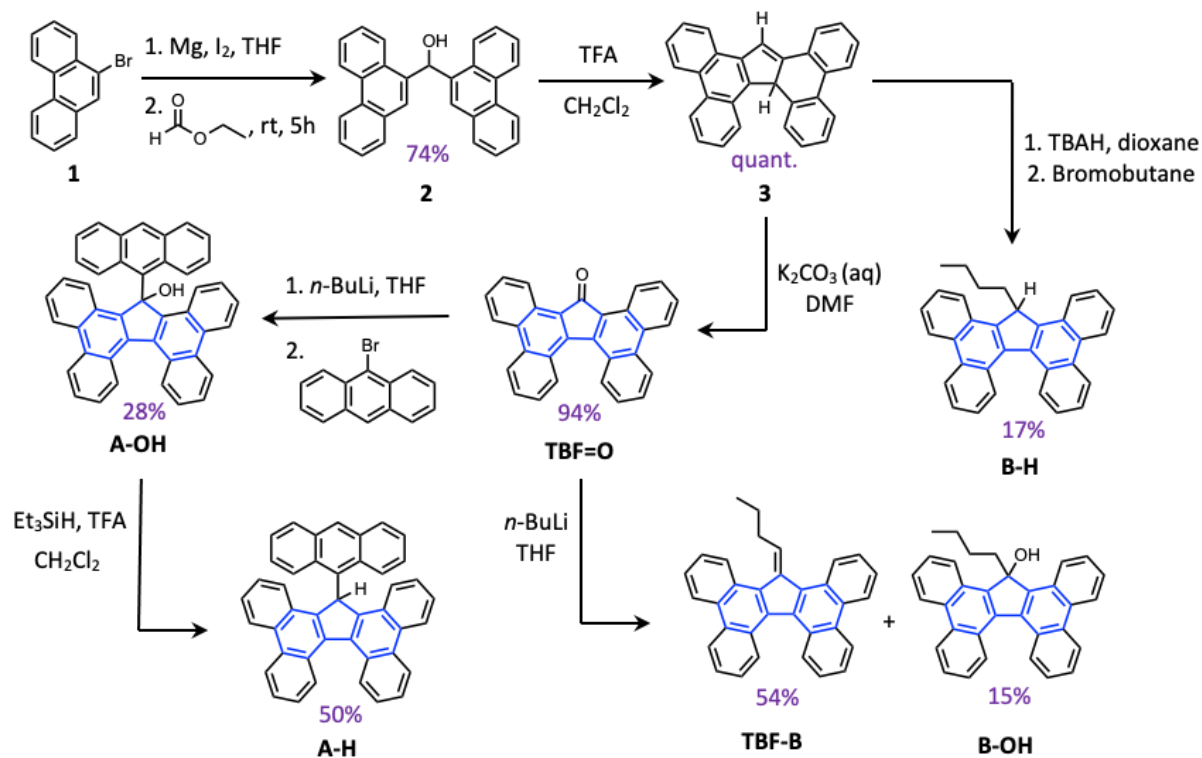
Scheme 2.1 Synthesis of a library of TBF molecules including **A-OH**, **A-H**, **B-OH**, **B-H** and **TBF-B** starting from 9-bromophenanthrene (**1**). Yields are highlighted in purple.

All TBFs were isolated as racemates under fast exchange. The novel TBF products were confirmed by ^{1}H NMR analyses (Figure 2.2) which, apart from **TBF-B**, suggest that each molecule contains a non-symmetric structure on account of a complex aromatic region that contains two sets of aromatic proton environments arising from both the anthracene and the TBF units (indicated with a pink circle or a green star respectively; Figure 2.2). These NMR spectra have been fully assigned with the aid of ^{1}H–^{1}H COSY, ^{1}H–^{1}H NOESY, ^{1}H PSYCHE, ^{1}H–^{1}H TOCSY NMR (provided in Section 2.4.3) and D_2O exchange experiment analyses (Section 2.4.3; Figure S2.2) together with single crystal X-ray data (Figure 2.3a and c *vide infra*).
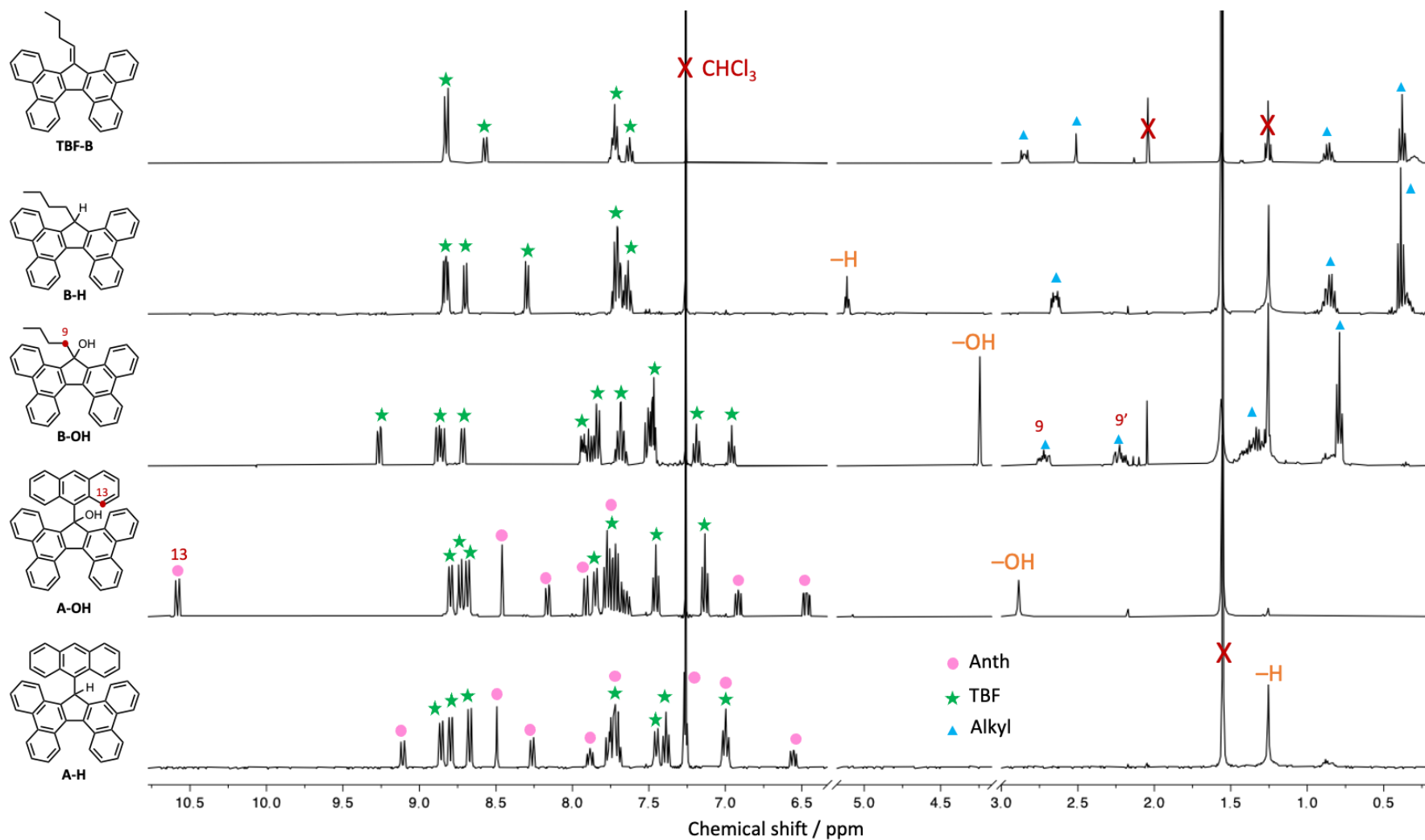
Figure 2.2 Stacked ¹H NMR (CDCl₃, 400 MHz, 298 K) spectra from bottom: **A-H**, **A-OH**, **B-OH**, **B-H** and **TBF-B**. Anthracenyl protons are represented with a pink circle, TBF protons with a green star and alkyl protons with a blue triangle; all other proton signals are labelled in orange.

Notably, the ^{1}H NMR spectrum of **A-OH** reveals a remarkably deshielded aromatic proton at a chemical shift value >10.5 ppm assigned as anthracenyl proton, H[13] (see Section 2.4.3 for full ^{1}H NMR spectroscopy characterisation). Upon closer inspection of the X-ray crystal data (Figure 2.3a), there is clear evidence of a short CH···O intramolecular interaction (2.04 Å) between the –OH group and H[13] in **A-OH** that may manifest in the downfield aromatic peak observed. In fact, ^{1}H–^{1}H NOESY NMR spectroscopy (Section 2.4.3; Figure S2.6) of **A-OH** reveals a through-space correlation between the –OH proton environment and a proton situated on both the anthracene and phenanthrene TBF core highlighting the closeness in distance between the proton environments. The furthest deshielded aromatic proton in **A-H** is also assigned to H[13] on the anthracene, where its X-ray structure highlights a short CH···H distance (1.87 Å), however, the deshielding is less pronounced compared to **A-OH** because CH···H interactions are typically described as a weaker dispersion interaction.[17] The CH···O interaction in **A-OH** is also present in its DFT-optimised structure (2.02 Å; B3LYP(G3BJ)/6-31G(d,p) in CH_2Cl_2; structure shown in Section 2.4.6; Figure S2.35a) which generally predicts the experimental solid-state structure well. Finally, owing to the steric repulsive interactions between the bulky TBF and anthracene units related by an sp[3] carbon centre, **A-OH** and **A-H** adopt highly twisted structures, with the anthracene group bent away from orthogonality and pointing towards only a single face of the TBF backbone, thus breaking planes of symmetry across the molecule (Figure 2.3a and c respectively) resulting in the more complex aromatic proton region observed in their NMR spectra.

For **B-OH**, the methylene protons on the butyl chain (H[9]) are also shifted downfield for alkyl protons (δ (H[9]) >2.0 ppm) due to their close proximity with the –OH group despite being three bonds away, albeit not as significantly as observed for alkyl protons in common alcohols (δ >3.0 ppm) presumably due to weaker non-specific interactions of the –OH group with the flexible alkyl chain. An X-ray structure (Figure 2.4b; *vide infra*) and the DFT-optimised structure of **B-OH** (Section 2.4.6; Figure S2.35c) further confirm that there is no evidence of any intramolecular interactions influencing the arrangement of the butyl group in the solid state. The asymmetry of the structure of the molecule is further highlighted by two unique proton signals for these diastereotopic protons (H[9] and H[9']; at 2.72 and 2.23 ppm respectively) compared to the similar proton environment in **B-H**. The ^{1}H NMR spectrum of **B-H** reveals a much more 'apparent' symmetry of the TBF backbone compared to **B-OH**, despite the minute change in structure, likely due its butyl group benefitting from faster and more flexible movement on the NMR timescale as a result of the less sterically bulky –H group rendering both phenanthrene wings in similar proton environments. In addition, the acidity of the proton in the head position in **B-H** is highlighted by its downfield shift (5.11 ppm). **TBF-B**, on the other hand, possesses a symmetric structure due to its unsaturated alkenyl 17-position resulting in fewer aromatic environments from overlapping protons. **TBF-B** represents the case of a TBF void of any intramolecular interactions and serves as a useful structure to compare further optical properties of saturated TBFs against.

The X-ray crystal structures of **A-OH**, **A-H** and **B-OH** were analysed in more detail to study their helical parameters (summarised in Table 2.1) and compared to geometry optimised DFT models of **A-OH**, **A-H**, **B-OH** and **B-H**, calculated at the B3LYP(GD3BJ)/6-31G(d,p) level of theory in CH_2Cl_2, (DFT structures and parameters shown in Section 2.4.6, Figure S2.35 and Table S2.2). Two different polymorphs were obtained for **A-OH**. Single crystals of polymorph **A-OH(1)** were grown from evaporation from EtOAc/*n*-hexanes while polymorph **A-OH(2)** was grown by evaporation from a CHCl₃ solution. Three different polymorphs of **A-H** were obtained. Polymorph **A-H(1)** and **A-H(3)** were grown from layering of CH_2Cl_2 and MeOH and polymorph **A-H(2)** was grown from evaporation from CH_2Cl_2. The following discussions centre around a representative **A-H(1)** (Figure 2.4 a,c) while structures and discussions of other polymorphs can be found in Section 2.4.4. Meanwhile **B-OH** is grown by evaporation from a solution of **TBF-B** in CH_2Cl_2/*n*-hexanes/MeOH. Unfortunately, single crystals of **B-H** grown from a layering of PhMe and MeOH, were not large enough to cause a strong enough diffraction pattern.

All TBFs comprise of a non-planar [5]helical backbone as a result of steric repulsive interactions between opposing inner hydrogens on the terminal benzene rings (d_{HH} 2.21 Å in **A-OH**, 2.22 Å in **A-H** and 2.12 Å in **B-OH** Figure 2.3 a,c and Figure 2.4 a,c), leading to average torsional angles (θ) around the inner *fjord* of 16.5°–17.2° and interplanar angles (φ) of 38.6°–41.7°. Helical parameters in the solid state appear to be slightly influenced by the substitution pattern at the fluorenyl head position, where TBFs containing the sterically bulky and rigid anthracene groups (**A-OH** and **A-H**) appear to have greater helical strain (larger d_{HH} and average torsional angles θ) compared to the butyl appended TBFs. However, it is difficult to deconvolute effects of substitution pattern with solvent interactions present in the X-ray packing which ultimately will influence solid-state structure. For context, the torsional and interplanar angles of [5]helicene[18] are 22.1° and 47.3° respectively determined by X-ray structural analysis (summarised in Table 2.1). The differences in helical structures between [5]helicenes and the TBF library highlight the influence of replacing a 6-membered benzene ring (in [5]helicene) with a 5-membered cyclopentadienyl ring (in TBFs). The chemical and structural alteration alleviates helical strain by widening *fjord* bond angles (i.e., from 125.2° in [5]helicene to 131.1° in **A-OH**). In fact, helical parameters of the TBFs more closely resemble that of [4]helicenes[19] and remain consistent with those of other disubstituted TBF molecules reported in the literature.[13] In addition, the more bulky –OH group paired with the intramolecular CH···O interaction in **A-OH** results in a twist of the anthracene group towards the TBF core, away from the hydroxy group, with a smaller torsional twisting (49.8°) compared to **A-H** (62.6°). These solid-state structural analyses support ¹H NMR conclusions that even in solution, the library of TBFs adopt highly twisted, non-planar and non-symmetric structures, governed by the steric bulkiness of the groups substituted at the fluorenyl head position.
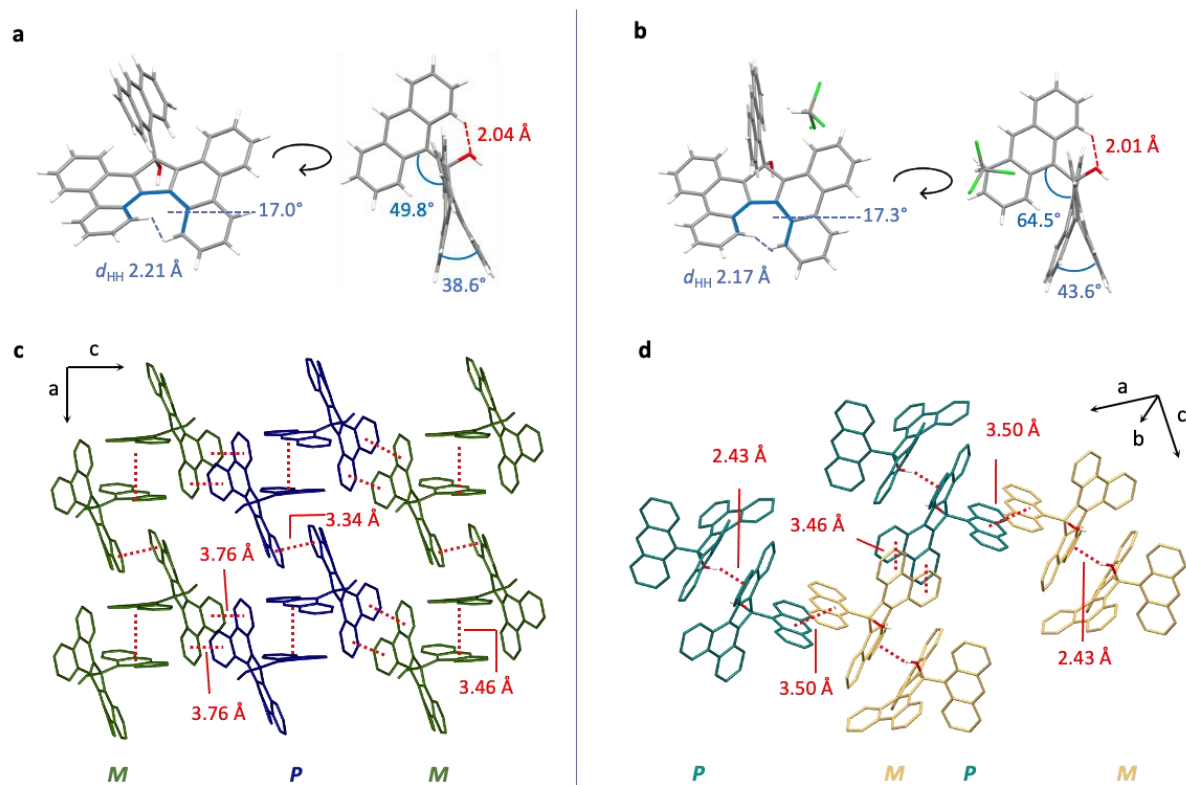
Figure 2.3. X-Ray crystal structures of polymorphs (a) *rac*-**A-OH(1)** and (b) *rac*-**A-OH(2)**. Front and side views of **A-OH(1)** and **A-OH(2)** are shown, with helical parameters highlighted. Packing structure of (c) **A-OH(1)** as viewed down the *b*-axis and (d) **A-OH(2)** with stabilising interactions highlighted in red. Segregated rows/sheets/layers of *M*- and *P*-helical enantiomers are stabilised by mutual π–π interactions (3.34–3.76 Å centroid-to-centroid distances) between TBF and anthracene π-surfaces in **A-OH(1)**. Homochiral dimers of **A-OH(2)** are additionally stabilised by a strong dimeric OH–π interaction (2.43 Å). Solvent molecules and non-interacting hydrogen atoms have been omitted for clarity.
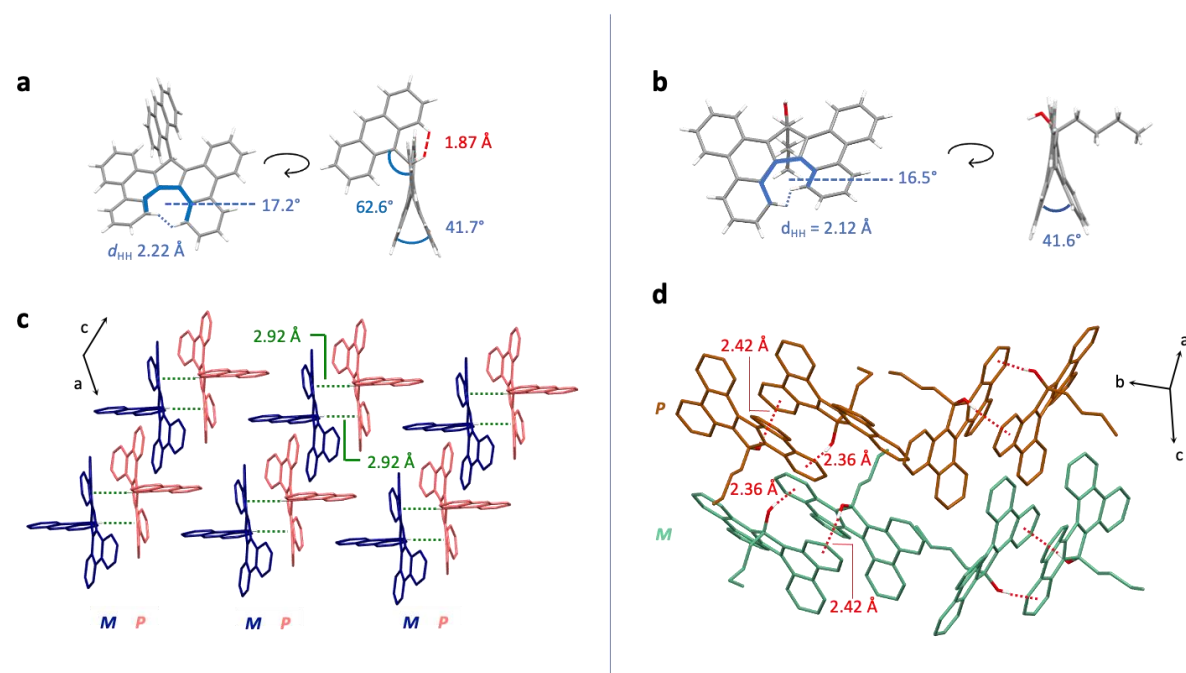
Figure 2.4. X-Ray crystal structures of (a) *rac*-**A-H(1)** and (b) *rac*-**B-OH**. Front and side view of **A-H** and **B-OH** are shown, with helical parameters highlighted. Packing structure of (c) **A-H(1)** and (d) **B-OH** are shown with stabilising interactions highlighted in green and red respectively. Heterochiral dimers in **A-H(1)** are stabilised by cooperative CH–π interactions (2.92Å). Homochiral dimers of **B-OH** are stabilised by a strong cooperative OH–π interactions (2.36–2.43 Å). Solvent molecules and non-interacting hydrogen atoms have been omitted for clarity.

Table 2.1 Comparison of TBF single crystal X-ray structural parameters with [5]helicene.

Compound	A-OH$_{avg}$[d]	A-H$_{avg}$[d]	B-OH	[5]helicene[18]
d_{HH}[a] / Å	2.21	2.22	2.12	2.60
θ[b] / °	17.0	17.2	16.5	22.1
φ[c] / °	38.6	41.7	41.6	47.3
d_{R1R2}[e] / Å	2.04	1.87	-	-

[a] d_{HH} is the distance between the hydrogen atoms on the terminal benzene rings; [b] θ is the average torsional angle around the inner *fjord*; [c] φ is the interplanar angle between planes located at the terminal *fjord* benzene rings; [d] The parameters quoted for **A-OH$_{avg}$** and **A-H$_{avg}$** are an average of all polymorphs of the compounds grown; [e] distance between R$_1$ (–OH or –H) and H[13] in R$_2$ (–anthracenyl), typically indicating a CH···X interaction, where X = O or H.

Interrogating the packing structures of **A-OH(1)** and **A-OH(2)** reveals that the supramolecular assembly of **A-OH** in both polymorphs is predominantly stabilised by π···π interactions. The superstructural packing of **A-OH(1)** (Figure 2.3c) consists of alternating homochiral layers of **A-OH** that form one dimensional chains along the *a* axis. These homochiral sheets are held together by intermolecular π-interactions between two anthracene groups (3.46 Å) and two phenanthrene units (3.34 Å). Alternating pairs of *M*-and *P*-enantiomers along the *c* axis are held together by intermolecular π-stacks involving the remaining free phenanthrene unit on TBF (3.76 Å). While polymorph **A-OH(2)** (Figure 2.3d) is also primarily held together by π···π interactions between adjacent anthracenyl groups (3.50 Å) and between the phenanthrene wings (3.46 Å) of TBF cores with differing chirality, a strong intermolecular OH···π hydrogen bond[20] (2.43 Å) exists between homochiral TBF pairs due to the electron rich nature of the TBF core. **A-H(1)** crystallises out into heterochiral dimers that are stabilised by cooperative CH···π interactions (2.92 Å) while there is no evidence of any stabilising π···π interactions, despite three different solvent polymorphs of **A-H** being grown. The superstructure of **B-OH** packs (Figure 2.4d) in a more compact manner than **A-OH** and **A-H** because of the less bulky butyl group compared to the anthracene, held together by much stronger OH···π cooperative hydrogen bonds (2.36 Å and 2.43 Å) between homochiral pairs.

Hirschfeld analyses (Section 2.4.5, Figure S2.34) of the different crystal structures of the TBF library reinforce the conclusions made from the packing analyses. Crystal structures of **A-OH** contain mostly close C···C (up to 7.7% i.e., π–π) and H···C (up to 35.2%, mostly from OH···π interactions) interactions displayed by white or red on the surfaces, i.e., regions where the intermolecular contacts are equal to or less than the sum of their van der Waals radii respectively. Similarly, crystal structures of **A-H** show mostly C···H (up to 40.6%) and H···H (up to 52.2%) interactions and **B-OH** contains mostly C···H (33.8% from OH···π interactions) and H···H (57.9%) interactions. The results together suggest that differing intramolecular and steric interactions between head group substituents (e.g., CH···O (2.02 Å) *vs* CH···H (1.87 Å)) affect the resulting packing structures with differing intermolecular stabilising interactions (π···π interactions (3.34 Å–3.76 Å) in **A-OH** *vs* CH···π interactions (2.92 Å) in **A-H** *vs*

OH···π interactions (2.36–2.43 Å) in **B-OH**) and could ultimately impact the respective optical properties of the TBFs in both the solution and solid state.

2.2.2 OPTICAL PROPERTIES OF TBFS

The absorption profiles of **A-OH** and **A-H** (Figure 2.5a, green and blue lines respectively) reveal that they absorb more broadly than other dialkylated TBF structures in THF.[14] Owing to the electronic communication that exists between the fluorene core and anthracene, evident on analysis of their LUMO orbitals (Figure 2.5d), it is possible that some electron density is delocalised from the anthracene into the fluorenyl moiety resulting in the broader absorption. Notably, **A-OH** has a more red-shifted absorption onset (> 20 nm) than **A-H** likely because the weak intramolecular CH···O interaction in **A-OH** is electronically stabilising and it allows **A-OH** to adopt a more vibrationally relaxed geometry in its excited state in solution compared to all other TBFs in the library.[21] Furthermore, there is more evident electronic communication/delocalisation between the anthracene and fluorenyl parts of **A-OH** highlighted in its HOMO/LUMO orbital depictions (Figure 2.5d) in comparison to **A-H** further justifying the red-shifted nature of absorption for **A-OH**.
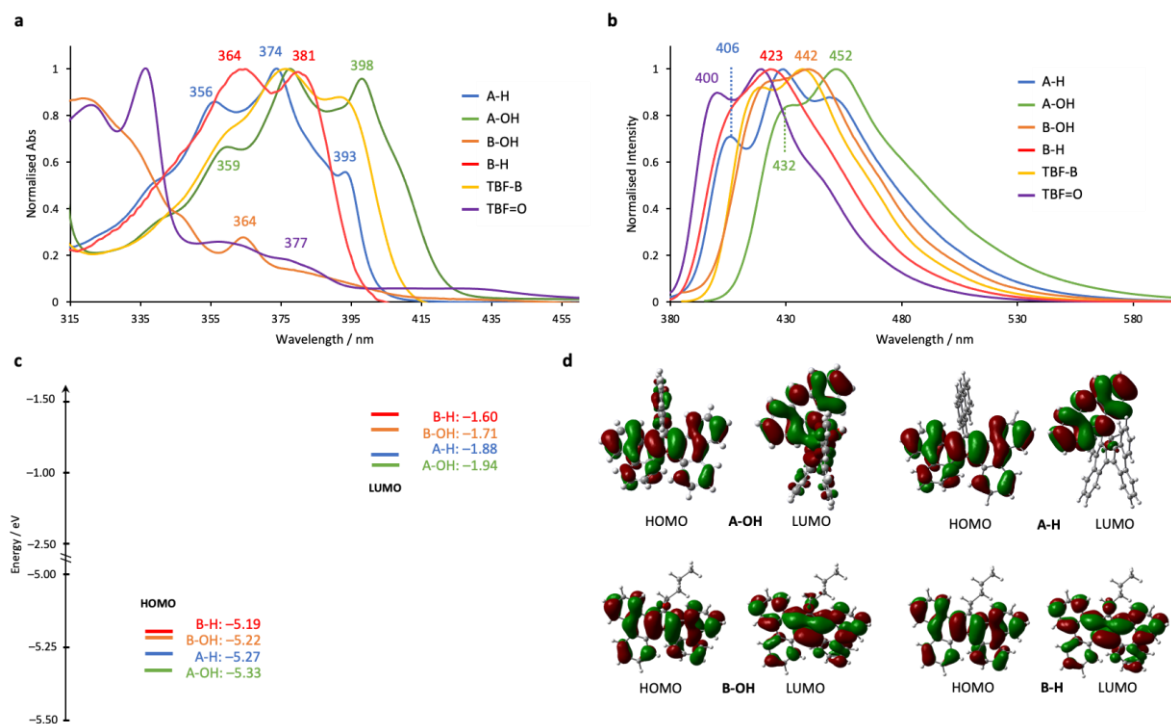
Figure 2.5. Normalised (a) UV–vis absorption and (b) emission spectra in THF (10 μM). (c) Frontier molecular orbital (FMO) energy levels for **A-OH** (green line), **A-H** (blue line), **B-OH** (orange line), **B-H** (red line) (d) DFT structures and depictions of the frontier molecular orbitals of the TBF library

In order to further elucidate the nature of these electronic interactions, Time-Dependent DFT (TD-DFT) analysis was performed at the B3LYP(GD3BJ)/6-31G(d,p) level of theory in CH_2Cl_2. The results from this calculation revealed for **A-OH** a complex first excited state (433 nm) involving transitions from the HOMO–1→LUMO, HOMO→LUMO and HOMO→LUMO+1 (Figure 2.6a, blue vertical lines), where electron density is shared across both TBF and anthracene moieties obscuring interpretation.

45

Natural transition orbital (NTO) analysis was then performed to simplify analyses by providing a more intuitive depiction of the first excited state orbital contributions for states with oscillator frequencies >0.1. NTO analysis for **A-OH** (Figure 2.6c) reveals a clear π–π* transition between a fluorene-dominant HONO and LUNO (i.e., natural orbitals with 96% occupancy) at 433 nm. It is only at the higher energy states (i.e., shorter wavelengths) that occupancies on anthracene are observed. These data imply that low energy excited state transitions are dominated by the fluorene core despite the presence of other potential chromophores.
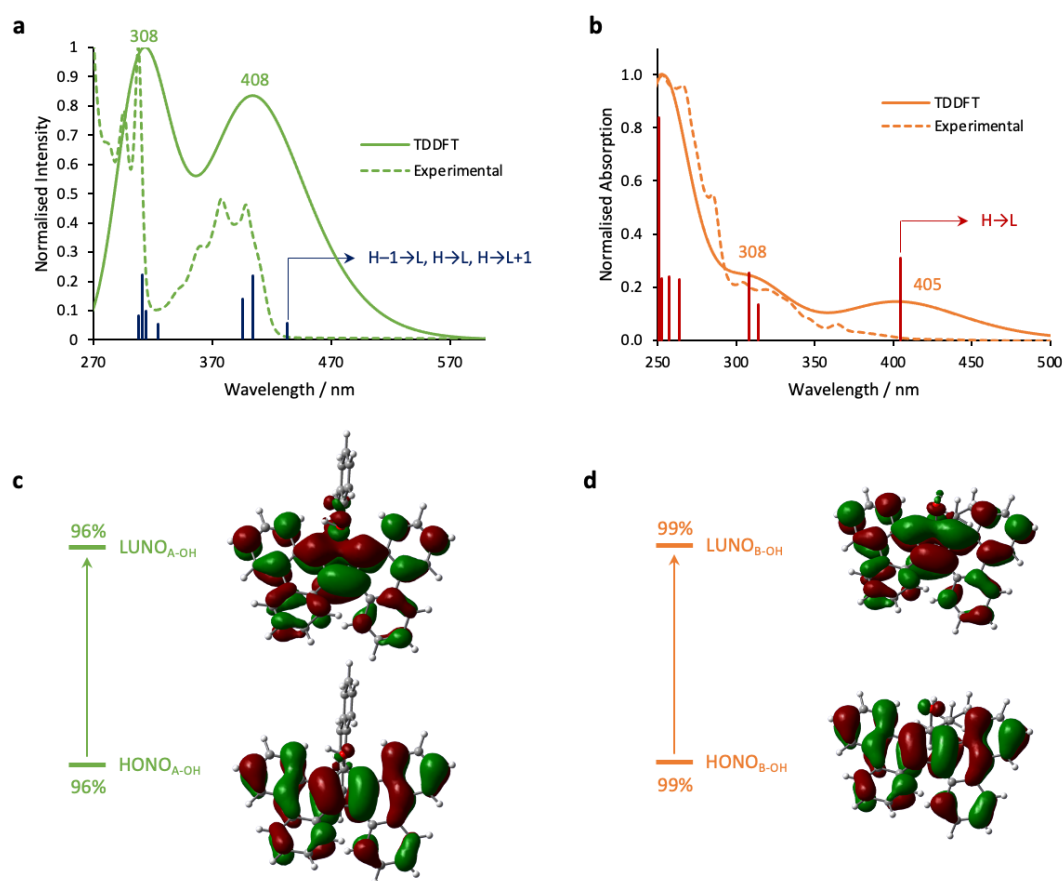
Figure 2.6. Normalised UV–vis absorption spectra measured in THF (10 μM; dashed lines) against TD-DFT simulated absorption spectra (B3LYP-GD3BJ/6-31G(d,p) in CH$_2$Cl$_2$; solid lines) for (a) **A-OH** and (b) **B-OH.** The vertical lines represent TD-DFT calculated excited state transitions with an oscillator frequency, f>0.05. NTO models for (c) **A-OH** and (d) **B-OH** showing significant (96% vs 99%) HONO/LUNO occupations of the fluorene core in the first excited state.

Compared to **A-H** and **A-OH**, the absorption bands of **B-H** and **B-OH** (red and orange line respectively, Figure 2.5a) are blue-shifted, highlighting the lesser extent of conjugation. The vibronic transitions in the absorption of **B-H** are much broader than the other TBFs studied indicating an increase in motion due to the more flexible butyl group which increases the vibrational states present for the TBF chromophore to occupy upon excitation. The absorption band of **B-OH** is notably quite different compared to the rest of the TBF library and more closely resembles the absorption profile of the synthetic intermediate bearing a ketone at the TBF 17-position **TBF=O**. It is likely that the electron-withdrawing oxygen atom in both **TBF=O** and **B-OH** results in a less intense n-π* transition involving the oxygen atom[22] which is more prominent than the TBF-centred π-π* transition. TD-DFT

analyses suggest that the lowest energy excited-state transition is dominated by a HOMO→LUMO transition for **B-OH** (at 405 nm) – NTO analyses (Figure 2.6d) confirm a large proportion of electron density situated on the oxygen atom in this transition supporting its quenching effect.

Given the propensity of 17,17'-dialkylated TBF compounds to display bright solution (and solid-state) luminescence,[12–14] emission spectroscopy of the TBF library along with measurements of their solution-state PLQYs were carried out to determine how fluorescence properties are influenced by intramolecular interactions of TBFs with differing –R group substituents. Exciting a solution of **A-H** in THF at various wavelengths between 285 and 380 nm afforded a broad emission profile (Figure 2.5b; λ_{ex} = 355 nm), extending into the visible region, as far as 580 nm, which is notably further ($\Delta\lambda_{em}$ = 100 nm) than 17,17'-dialkylated derivatives. All other TBFs display a similar looking emission profile with a higher intensity long wavelength vibronic band and a lower intensity shorter wavelength vibronic band that are red-shifted for **A-OH** (432 and 452 nm) and blue-shifted for **B-H** (406 and 423 nm) compared to **B-OH** due to the presence and absence of the intramolecular interactions discussed previously respectively. The effect of the –R group substituent at the fluorenyl head position is again portrayed by the broadness or comparative sharpness of the vibronic fine structure of the emission bands confirming the flexibility and rigidity of the excited states of the butyl- and anthracenyl-appended TBFs respectively. Excitation experiments (Section 2.4.7.1; Figure S2.36a–d *vide infra*) were conducted for each of the emission maxima and returned excitation spectra that were similar to their absorption, suggesting a molecular origin to the fluorescence of **A-OH**, **A-H**, **B-H** and **TBF-B** (i.e., as opposed to the presence of aggregate species) in THF solution. However, excitation experiments (Section 2.4.7.1; Figure S2.36e and f) collected for the emission maxima in **B-OH** and **TBF=O** returned excitation spectra that resemble the excitation spectra for the rest of the TBF library highlighting that the emission of these compounds originates from their TBF core.

Interrogation of the solution-state PLQYs measured relative to quinine sulfate dihydrate as a standard (results summarised in Table 2.2; see Section 2.4.7.2 for details on sample preparation and data handling) reveals that introduction of the anthracene group to the TBF core results in some solution-state emission quenching of **A-H** (0.03) relative to **B-H** (0.48). At the same time, the electron-withdrawing –OH group is observed to quench TBF emission in the absence of the anthracenyl moiety (PLQY (**B-OH**) = 0.04). The PLQY of **A-OH** (0.12) does not suffer as much from hydroxyl or anthracenyl quenching due to the effect of the intramolecular CH···O interaction suggesting that the anthracenyl rigidifies the structure in solution which reduces the number of non-radiative, vibrational and rotational relaxation decay pathways.

2.2.3 AGGREGATION ANALYSES

Suitable solvent conditions to induce aggregation for the TBF library were initially obtained by varying the relative amounts of two solvents of differing polarity and measuring the resulting absorption profiles. For instance, varying PhMe/EtOH compositions with **A-OH** samples resulted in the same absorption profile indicating no signs of aggregation up to 95% EtOH in PhMe. However, a red-shifted absorption in 80% H_2O in THF (compared to in THF, Section 2.4.7,1, Figure S2.38a and b) confirmed the suitability of these solvent conditions to induce aggregation and therefore study whether any changes to emission behaviours are observed. The observation of aggregation was further supported by dynamic light scattering (DLS) experiments with Z_{avg} values ranging from 158.6–194.0 nm for the TBF library (results summarised in Table 2.2; see Section 2.4.8 for full results). DLS measurements of the 80% H_2O in THF solvent mixtures for all TBFs suggest that **A-OH** forms the largest aggregates on average, while **B-OH** forms the smallest aggregates on average (Table 2.2). Importantly there is no indication by DLS that smaller monomeric species exist under these solvent conditions.

Table 2.2. Summary of PLQY, lifetime parameters and DLS (reported as an average value over three runs) for the TBF library

	$\Phi_X{}^a$	ε^a / $\times 10^4$ dm^3 mol^{-1} cm^{-1}	$\tau_{monomer}{}^a$ / ns	$\tau_1{}^b$ / ns	$\tau_2{}^b$ / ns	$Z_{avg}{}^b$ / nm
A-OH	0.12	1.57	1.84	0.79	1.50	194.0 ± 7.4
A-H	0.03	1.94	3.86	1.38	2.26	182.9 ± 3.0
B-OH	0.04	0.28	2.08	0.79	2.14	158.6 ± 1.8
B-H	0.48	1.33	2.67	1.12	3.12	194.0 ± 1.6

[a]Measurements of Φ_X, ε and $\tau_{monomer}$ were conducted in THF (i.e., for monomers of the TBF library), while [b]measurements of τ_1, τ_2 and Z_{avg} were conducted in 80% H_2O in THF solutions (i.e., aggregates)

Therefore, solution-state aggregation of the TBF library was probed by emission spectroscopy (Figure 2.7a, b, d, e) in varying THF/H_2O mixtures (10 μM) to understand how substitution at the 17-position affects the ability of TBF to be emissive in the aggregate state. For all compounds, aggregation from 80% H_2O in THF mixtures manifests in red-shifted emission profiles (compared to monomeric emission in THF). Notably, the emission profiles of **A-H** evolve as the H_2O content increases such that at 80% H_2O in THF, an increase in emission intensity is observed (Figure 2.7b) with a red-shifted emission peak at λ=431 nm (compared to its monomeric emission), suggesting the formation of electronically stabilised aggregates that are AEE active. While **A-OH** does experience an increase in emission intensity at 80% H_2O in THF from 70% H_2O in THF (Figure 2.7a), this non-remarkable relative intensity increase of **A-OH** aggregate emission could simply be an effect of solubility causing the material to precipitate or it could be due to a slight aggregation caused quenching (ACQ) effect. Regardless, qualitatively, the solid material of **A-OH** is emissive under short wavelength light (365

nm). Similar to **A-OH** and **A-H**, **B-H** experiences an increase in emission intensity up to a 70% H_2O in THF mixture supporting reports in the literature that a butyl group is sufficient to enabling solid-state emission of TBF molecules.[3,14] Meanwhile, **B-OH** experiences emission quenching upon aggregation suggesting that the quenching effects of the electron deficient oxygen experienced by **B-OH** in its monomeric emission are carried forward into the aggregate-state.
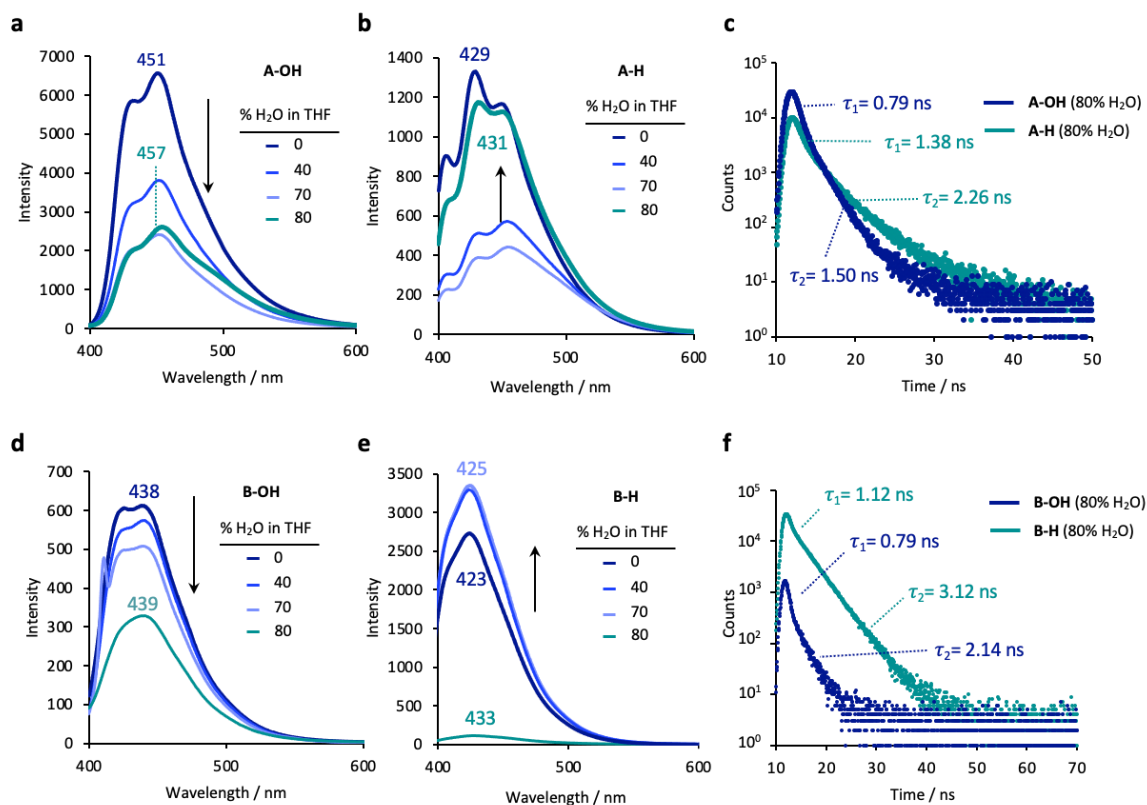
Figure 2.7. Aggregation studies in THF/H_2O mixtures for (a) **A-OH**, (b) **A-H**, (d) **B-OH** and (e) **B-H** and lifetime studies of 80% H_2O in THF mixtures for (c) **A-OH** and **A-H** and (f) **B-OH** and **B-H**

The X-ray packing structures of both compounds inform us that **A-H** readily forms strong dimeric CH···π interactions (2.92 Å), whereas the superstructure of **A-OH** is stabilised by weaker π···π interactions (3.34–3.76 Å). Hence, it is possible that a more rigid aggregate structure in **A-H** is responsible for its higher aggregate emission efficiency whereas in **A-OH**, π···π interactions may lead to the slight quenching effect observed. The smaller steric burden of the –H in the head-position in **A-H** together with the weak intramolecular non-covalent CH···H interaction (1.87 Å) results in a twisted structure with a torsional angle between the anthracene and TBF parts of 62.6°, (Figure 2.4a *vide supra*). This twisting of the two π-systems positions them in a manner where they are unable to interact intermolecularly through π···π interactions, that would normally lead to ACQ. On the other hand, the intramolecular CH···O interaction in **A-OH** (2.04 Å) enforces its structural geometry such that the torsional angle between the anthracene and TBF parts (49.8°; Figure 2.3a *vide supra*) is smaller than in **A-H** and therefore positions the anthracene such that it is able to interact intermolecularly through π···π interactions resulting in the quenched aggregate emission. Although a crystal structure of **B-H** has yet

to be grown, inspection of the packing structure of 17,17-dibutyl-TBF[14] (Section 2.4.4 Figure S2.33) confirms that it is devoid of any $\pi\cdots\pi$ interactions. Therefore, it is not too far-fetched to assume that this lack of $\pi\cdots\pi$ intermolecular interactions might exist in **B-H** to explain its aggregate and solid-state emission capabilities. Here, the butyl group could help disrupt the formation of any $\pi\cdots\pi$ interactions and help suppress ACQ in the solid-state.

Emission lifetimes were measured for each TBF in THF (Section 2.4.7.1, Figure S2.38c) and in 80% H_2O in THF solutions (10 µM; Figure 2.7 c and f) to understand how their fluorescence lifetimes might be affected in their monomeric *vs* aggregate forms. In THF, the emission intensity for each TBF decays with simple first order kinetics over time. The fitted lifetimes reveal that **A-H** and **B-H** have the longest monomeric fluorescence lifetimes of the TBF library (3.86 ns and 2.67 ns respectively) compared to **A-OH** and **B-OH** (1.84 ns and 2.08 ns respectively; values summarised in Table 2.2). The longer lifetimes indicate that the excited states of **A-H** and **B-H** monomers are more stabilised in THF than their hydroxylated analogues because of more favourable solvent interactions with THF in the excited state. Aggregates display two lifetime decay processes (τ_1 and τ_2) in 80% H_2O in THF that are thought to be associated with emissive TBF monomers and higher order aggregates in solution, respectively (Table 2.2). This reasoning is supported by literature precedent[23] and by our own DLS studies which suggest a distribution of aggregates present in an 80% H_2O in THF mixture. Literature suggests that the lifetimes of aggregate species should be larger than their monomeric counterparts, and while this is the case for the butyl-appended TBFs, the anthracenyl-TBF aggregates have shorter lifetimes than their monomers.

Attempts were made to measure neat thin-film emission (Section 2.4.7.1 Figure S2.37a–f) and PLQYs of the TBF library as additional confirmation of the enhanced emission upon aggregation. Neat thin-films were prepared from purified TBF materials by dissolving the material in PhMe (at a consistent concentration of 2.0 mM) and drop-casting onto a quartz disc, before slowly evaporating the solvent on a heating plate. Unfortunately, most TBFs showed PLQYs that were experimentally indistinguishable from zero (i.e., given the level of error from the instrument, it was difficult to differentiate between the TBF library). It is thought that the crystalline phase of the thin films is different to the aggregates formed in THF/H_2O mixtures leading to the discrepancies observed. For example, by qualitative observations, an orange-coloured emission was observed for the thin-film made from **A-H**, which is different to the blue emission that has been observed in its powdered form. These results need to be confirmed by X-ray diffraction studies. All thin-film emission spectra are red shifted compared to their emission spectra in 80% H_2O in THF (Section 2.4.7.1 Figure S2.37), highlighting the effect of extended aggregation in these films. Notably, **A-H** displays an additional new emission band at 600 nm that is thought to arise from solvent-solute interactions in the thin-film from the possible formation of a charge transfer/exciplex type of aggregate. More in depth emission studies on these thin films as well

as attempting to form the thin films using different methods (e.g., solvents, annealing) should help clarify these observations.

2.3 CONCLUSIONS

Four 17-anthracenyl TBFs, **A-OH**, **A-H**, **B-OH**, and **B-H** were synthesised – whose structures differ by substitution at the 17-position – and their structures and optical properties were analysed in their monomeric and aggregate forms. All TBFs exist with a non-planar [5]helicene-like backbone. The torsional angle between the anthracene and TBF parts in **A-OH** and **A-H** were found to be dependent upon the steric bulk and the directing non-covalent intramolecular interactions between the anthracene and the –OH or –H group in the 17-position (49.8° *vs* 62.6° respectively) resulting in differently twisted structures. An electronically stabilising intramolecular CH⋯O interaction in **A-OH** appears to lead to a wider absorption range and a narrower emission range compared to **A-H**. A smaller steric repulsion experienced by R-groups substituted at the head-position in **A-H** affect its supramolecular packing by promoting a strong intermolecular dimeric CH⋯π interaction. These intermolecular interactions lead to the formation of a rigid aggregate with restricted intramolecular motions in solution resulting in a more emissive aggregate. On the other hand, the possibility of **A-OH** forming π⋯π interactions may contribute to the aggregate quenching effect observed. The butyl group in **B-H** and **B-OH** is more flexible than the anthracene in **A-OH** and **A-H**, therefore there is no indication of any intramolecular or steric effect from the head group substituents on the structures of **B-H** and **B-OH**. Instead, the butyl group disrupts the formation of close π⋯π intermolecular interactions and lends itself to more efficient suppression of ACQ in **B-H** compared to anthracenyl-TBFs. The hydroxy group plays two roles: in **B-OH** it (i) quenches emission in both the solution- and solid-state whereas in **A-OH** it (ii) rigidifies the structure and enables an emissive solid through AEE.

These results more generally suggest that alkyl groups are effective at disrupting π⋯π interactions and hence reducing effects of ACQ. On the other hand, a hydroxy group in the presence of a bulky and rigid group such as anthracene in close proximity (such that they are able to interact intramolecularly) aids in the rigidification of the structure and therefore supports AEE mechanisms. As an extra consideration, in the case of TBFs, the anthracene chromophore competes with TBF as the main contributor of the photophysical properties of the molecule and because of its large π-surface, encourages the formation of π-interactions. Therefore, an alternative bulky group such as a ᵗbutyl group or a smaller aromatic benzene moiety might facilitate more efficient observations of aggregate-emission.

This Chapter reinforces the need for a shift in the way that the AIE/AEE community discusses mechanisms of aggregate emission to distinguish between reducing effects of ACQ *vs* enabling AEE. In addition, a careful consideration of steric *vs* intramolecular interactions is required in the development of solid-state light emitters for advanced technological applications. Furthermore, if the

chiral properties of TBF can be cultivated from the synthesis of a more sterically hindered TBF, derivatives of **A-H** and **A-OH** will be good candidates for accessing aggregation-enhanced circularly polarised luminescence properties from a TBF-derived helicene.

2.4 SUPPLEMENTARY INFORMATION

2.4.1 MATERIALS AND METHODS

Materials. Unless stated, all chemicals and reagents were purchased from commercial suppliers (Sigma Aldrich, Fisher Scientific, Alfa Aesar and Fluorochem) and used without further purification. Before use, *n*-BuLi was titrated as described by Burchat, A. F et al.[24] to obtain its active concentration. Anhydrous solvents were obtained from a neutral alumina Solvent Purification System under nitrogen and stored over activated (>250 °C at 0.01 mbar overnight) 3 Å molecular sieves under a dry Ar atmosphere.

Product confirmation. Analytical thin-layer chromatography (TLC) was performed on aluminium-backed silica gel plates and visualised under UV irradiation (254 and 365 nm). Automated flash column chromatography was performed using a Teledyne ISCO Combiflash NextGen 300+ with detectors using broad range UV–vis (200-800 nm) and evaporative light scattering (ELS) under N_2 gas and pre-filled Redisep™ Gold cartridges (normal phase: SiO_2). High-resolution mass spectra were measured on a Bruker compact QTOF Atmospheric Pressure Ionisation Time of Flight instrument using an ESI or APCI source. Nuclear magnetic resonance (NMR) spectra were recorded on a JEOL ECS400D spectrometer (working frequencies of 400 MHz and 101 MHz for ^{1}H and ^{13}C nuclei) or a Bruker Neo spectrometer equipped with a triple-resonance room temperature probe (working frequencies of 700 MHz and 176 MHz for ^{1}H and ^{13}C nuclei). Chemical shifts (δ) are reported in parts per million (ppm) relative to the signals corresponding to residual non-deuterated solvents (CDCl$_3$: δ_H 7.26 ppm; δ_c 77.23 ppm; DMSO-d_6: δ_H 2.50 ppm; δ_C 39.57 ppm). Coupling constants (J) are reported in Hertz (Hz) and ^{1}H multiplicities are reported in accordance with the following convention: s = singlet, d = doublet, t = triplet, q = quadruplet, p = pentet, m = multiplet. Assignment of ^{1}H and ^{13}C NMR signals were accomplished with the aid of 'pure-shift' yielded chirp excitation (PSYCHE) and two-dimensional ^{1}H–^{1}H COSY, ^{1}H–^{13}C HSQC and ^{1}H–^{13}C HMBC NMR spectroscopies. NMR spectra were processed using MestReNova software, Version 14.

Sample analysis. Single crystal X-ray diffraction data were collected on a single-crystal Oxford Diffraction SuperNova with dual Mo and Cu sources. A suitable crystal was selected and mounted (oil on 100 μm mount) on a SuperNova Dual, Cu at home/near, Eos diffractometer. The crystal was kept at 110.00(10) K during data collection. Using Olex2,[25] the structure was solved with the SHELXT[26] structure solution program using Intrinsic Phasing and refined with the SHELXL[27] refinement package

using Least Squares minimisation. Hirschfeld analyses of crystal structures were performed using CrystalExplorer 17.5 software.

Absorption spectra were recorded on a Shimadzu UV-2401 PC spectrophotometer or on an Agilent Technologies Cary 5000 UV–vis–NIR spectrophotometer using standard 10 mm path length quartz cuvettes at room temperature. Solution-state fluorescence spectroscopy was carried out on a Hitachi F-4500 fluorimeter equipped with a 150 W Xe lamp using standard photoluminescence quartz cuvettes. Samples for solution-state spectroscopy had an optical density (O.D.) <0.1 in anhydrous and degassed solvent to allow for the measurements of solution-state photoluminescent quantum yields (PLQYs). Time-resolved photoluminescence lifetime decay measurements were carried out using a Dept. of Edinburgh FLS980 Fluorescence spectrophotometer mounted with an EPL picosecond pulsed diode laser (λ_{ex}= 375.0 nm). Quantum yields (Φ_X) were obtained by the relative method, using quinine sulfate (Φ_{ST} = 0.55 in 0.5 M H_2SO_4)[28] as an external reference. Dynamic light scattering (DLS) experiments were performed on a Zetasizer Nano (Malvern Instruments Ltd., Worcestershire, UK) measuring backscattered light fluctuations at an angle of 173° and a calculation of an autocorrelation function. The samples were measured at 25 °C and adjusted to this temperature for 2 minutes prior to the measurement. Autocorrelation functions were analysed using the DTS v5.1 software provided by Malvern. Measurements were performed in triplicate with 15–20 runs per single measurement and the calculated mean values (based on intensity distribution) were used. Thin films for solid-state emission were prepared by drop-casting a solution of emissive material (2.0 mM) in PhMe onto a quartz substrate at 65 °C to facilitate solvent evaporation. Emission spectra of the films were collected using a Horiba- Jobin Yvon Fluorolog-3 spectrofluorometer equipped with a 450 W Xe lamp as the light source.

Density functional theory (DFT) calculations were prepared on GaussView 6.0 and submitted to the University of York Viking High Performance Computing cluster and run on Gaussian 16 using Becke's three-parameter exchange functional with the gradient-corrected correlation formula of Lee, Yang and Parr (B3LYP)[29,30] paired with the split valence double-zeta 6-31G(d,p) basis set, PCM solvation model (CH_2Cl_2) and dispersion corrections (D3BJ)[31] unless stated otherwise.

2.4.2 SYNTHETIC DETAILS
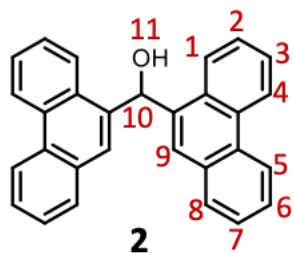
Bis(phenanthren-9-yl)methanol 2: Magnesium turnings (0.20 g, 8.22 mmol, 1.05 equiv.) and a catalytic amount of iodine were added to a flame-dried two-necked round bottomed flask with a stirrer bar and the flask was cycled under an Ar atmosphere. A solution of 9-bromophenanthrene (2.02 g, 7.84 mmol, 1.0 equiv.) in dry THF (3 mL) was added to the reaction mixture dropwise over 20 min at room temperature over which time a colour change from green to brown was observed. After stirring for 3 h, a solution of ethyl formate (0.31 mL, 3.89 mmol, 0.5 equiv.) in dry THF (1 mL) was added to the reaction mixture dropwise over 20 minutes.

The reaction mixture turned yellow-brown and was left to stir overnight. Once complete (confirmed by crude ^{1}H NMR analysis), a 1 M aqueous solution of HCl (6 mL) was slowly added to quench the reaction mixture followed by additional HCl solution (4 mL) to destroy any leftover Mg turnings. The resulting precipitate was collected by filtration and washed in diethyl ether to yield **2** (1.10 g, 2.86 mmol, 74%) as a pale yellow solid.

^{1}**H NMR** (CDCl$_3$, 400 MHz, 298 K): δ_H 8.79 (dd, J = 8.4, 1.3 Hz, 2H[8]), 8.71 (d, J = 8.3 Hz, 2H[4]), 8.14 (dd, J = 8.3, 1.3 Hz, 2H[5]), 7.82 (s, 2H[9]), 7.76 (dd, J = 7.8, 1.4 Hz, 2H[1]), 7.71–7.63 (m, 4H[6,7]), 7.59–7.53 (m, 4H[2,3]), 7.33 (s, 1H[10]), 2.52 (br, 1H[11]); ^{13}**C NMR** (CDCl$_3$, 101 MHz, 298 K): δ_C 136.5, 136.0, 131.5, 131.1, 130.6, 130.3, 129.3, 127.2, 126.9, 126.7, 126.4, 124.6, 123.5, 122.6, 70.0; **ESI–HRMS** (νe+, CH$_2$Cl$_2$) calculated for C$_{29}$H$_{20}$O: m/z = 407.1412 [M+Na]$^+$; found 407.1417 [M+Na]$^+$. Spectroscopic data matched that reported in the literature.[15]

3
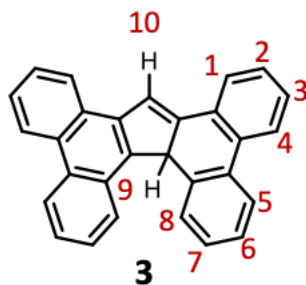
H-**Tetrabenzo[*a,c,g,i*]fluorene 3:** A round bottomed flask equipped with a stirrer bar was charged with **2** (0.52 g, 1.36 mmol, 1.0 equiv.) and CH$_2$Cl$_2$ (4 mL). Trifluoroacetic acid (TFA, 0.85 mL) was added dropwise over 5 min to afford a yellow suspension that was stirred at room temperature for an additional 20 min. CH$_2$Cl$_2$ was removed under reduced pressure and the resulting yellow solid was triturated in diethyl ether,

filtered, washed with the minimum amount of diethyl ether and dried under high vacuum to give **3** (0.42 g, 1.16 mmol, 85%) as a yellow solid.

^{1}**H NMR** (CDCl$_3$, 400 MHz, 298 K): δ_H 8.84–8.77 (m, 2H[8,5]), 8.31–8.25 (m, 1H[8']), 8.14–8.08 (m, 1H[5']), 7.99 (dd, J = 7.3, 1.8 Hz, 1H[1']), 7.85 (d, J = 7.8 Hz, 1H[1]), 7.76–7.62 (m, 5H[3',4',6',7',9]), 7.50–7.38 (m, 4H[2',4,6,7]), 7.37–7.31 (t, J = 7.6 Hz, 1H[2]), 7.13 (dd, J = 7.6 Hz, 1H[3]), 5.43 (s, 1H[10]); **APCI–HRMS** (νe+, CH$_2$Cl$_2$) calculated for C$_{29}$H$_{18}$: m/z = 367.1409 [M+H]$^+$; found 367.1489 [M+H]$^+$. Spectroscopic data matched that reported in the literature.[15]

TBF
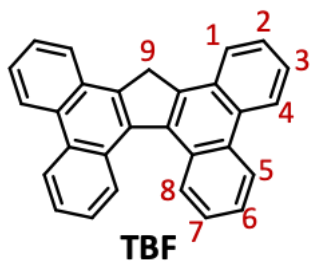
Tetrabenzo[*a,c,g,i*]fluorene TBF: To a stirred suspension of **3** (0.406 g, 1.11 mmol, 1.0 equiv.) in CH$_2$Cl$_2$ (20 mL) in a round bottomed flask, Et$_3$N (0.1 mL) was added. After 30 min, the reaction mixture was concentrated and the crude solid triturated in diethyl ether to yield **TBF** (0.35 g, 0.95 mmol, 87%) as a yellow solid.

^{1}**H NMR** (CDCl$_3$, 400 MHz, 298 K): δ_H 8.84–8.81 (m, 2H[8]), 8.78 (dd, J = 7.5, 1.5 Hz, 2H[5]), 8.73 (dd, J = 8.2, 1.4 Hz, 2H[4]), 8.24–8.21 (m, 2H[1]), 7.74–7.61 (m, 8H[2,3,6,7]), 4.67 (s, 2H[9]); **APCI–HRMS** (νe+, CH$_2$Cl$_2$) calculated for C$_{29}$H$_{18}$: m/z = 367.1409 [M+H]$^+$; found 367.1489 [M+H]$^+$ Spectroscopic data matched that reported in the literature.[32]

Tetrabenzo[a,c,g,i]fluoren-17-one TBF=O: Using a literature modified procedure,[16] a round bottomed flask with a stirrer bar was charged with **3** (0.812 g, 2.21 mmol, 1.0 equiv.), DMF (45 mL), saturated aq. K_2CO_3 (1.5 mL) with air bubbling through the solution. The reaction was heated to reflux overnight. After 18 h, the reaction mixture was cooled to room temperature, then a solution of saturated aq. NH_4Cl (30 mL) was added to precipitate out a solid which was filtered and washed with water followed by diethyl ether to yield **TBF=O** (0.786 g, 2.07 mmol, 93%) as a dark brown solid.

^{1}H NMR (CDCl$_3$, 400 MHz, 298 K): δ_H 9.25–9.20 (m, 2H[8]), 8.81–8.77 (m, 2H[5]), 8.71–8.67 (m, 2H[4]), 8.31 (dd, J = 8.3, 1.3 Hz 2H[1]), 7.81 (ddd, J = 8.3, 6.9, 1.3 Hz, 2H[2]), 7.73 (ddd, J = 8.2, 6.9, 1.3 Hz, 2H[3]), 7.70–7.64 (m, 4H[6,7]); **^{13}C NMR** (CDCl$_3$, 101 MHz, 298K): δ_C 147.1, 134.9, 131.8, 129.1, 128.7, 128.6, 127.8, 127.1, 126.8, 126.6, 126.1, 125.0, 124.1, 122.9; **APCI–HRMS** (ve+, CH$_2$Cl$_2$) calculated for $C_{29}H_{16}O$: m/z = 381.1201 [M+H]$^+$; found 381.1266 [M+H]$^+$. Spectroscopic data matched that reported in the literature.[16]

A-OH: A solution of 9-bromoanthracene (0.122 g, 0.47 mmol, 1.75 equiv.) in anhydrous and degassed THF (5 mL) under an Ar atmosphere was cooled to –78 °C and n-BuLi (2.5 M in n-hexane, 0.25 mL, 2.3 equiv.) was added slowly to eventually afford a bright orange coloured solution indicative of Li insertion. The solution was stirred at –78 °C under Ar for 45 min before a solution containing **TBF=O** (0.104 g, 027 mmol, 1.0 equiv.) in dry and degassed THF (75 mL) under Ar was slowly transferred dropwise to the reaction flask. The reaction mixture was allowed to warm up to room temperature, stirred overnight and monitored by TLC (20% EtOAc/n-hexanes). Water (40 mL) was added slowly to quench the reaction and the reaction mixture was extracted into EtOAc (3 x 50 mL). The combined organic layers were washed with saturated aq. NH$_4$Cl (50 mL) followed by brine (50 mL), dried over MgSO$_4$ and concentrated. The crude solid was washed with the minimum amount of acetone and the filtrate was concentrated. Automated column chromatography (SiO$_2$: 5% EtOAc in n-hexanes) afforded the desired product **A-OH** (43.5 mg, 0.078 mmol, 28%) as a yellow solid.

^{1}H NMR (CDCl$_3$, 400 MHz, 298 K): δ_H 10.58 (d, J = 9.4 Hz, 1H[13]), 8.80 (d, J = 8.2 Hz, 2H[5]), 8.73 (dd, J = 8.1, 1.5 Hz, 2H[8]), 8.69 (d, J = 8.4 Hz, 2H[4]), 8.46 (s, 1H[9]), 8.19–8.14 (m, 1H[10]), 7.93–7.89 (m, 1H[10']), 7.85 (d, J = 8.3 Hz, 2H[1]), 7.81–7.61 (m, 8H[6,7,11,12,13']), 7.45 (ddd, J = 8.3, 6.9, 1.3 Hz, 2H[2]), 7.13 (ddd, J = 8.2, 6.9, 1.1 Hz, 2H[3]), 6.92 (ddd, J = 8.4, 6.5, 1.0 Hz, 1H[11']), 6.47 (ddd, J = 9.4, 6.5, 1.5 Hz, 1H[12']), 2.89 (s, OH); **^{13}C NMR** (CDCl$_3$, 101 MHz, 298K): δ_C 133.1, 132.6, 132.1, 131.8, 130.6, 130.2, 129.1, 128.8, 128.4, 128.1, 127.6, 127.2, 126.8, 126.6, 126.4, 125.6, 125.6, 125.0, 124.6, 124.4, 123.9, 123.3, 91.0; **APCI–HRMS** (ve+, CH$_2$Cl$_2$) calculated for $C_{43}H_{26}O$: m/z = 559.6800 [M+H]$^+$; found 559.2048 [M+H]$^+$ and 541.1932 [M-H$_2$O]$^+$
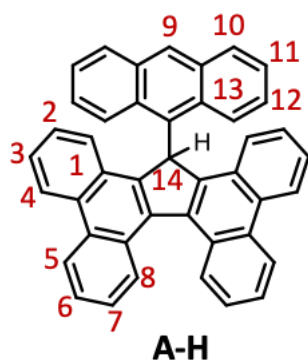
A-H: Et_3SiH (0.1 mL) and TFA (0.1 mL) were added dropwise to a solution of **A-OH** (20.2 mg, 0.036 mmol, 1.0 equiv.) in anhydrous CH_2Cl_2 (10 mL) under a N_2 atmosphere. The reaction mixture was allowed to stir at room temperature overnight and monitored by TLC (20% EtOAc in *n*-hexanes). On complete consumption of the starting material, the reaction mixture was extracted with H_2O (3 x 10 mL). The combined organic layers were dried with Na_2SO_4, concentrated and the crude solid purified by automated column chromatography (SiO_2: 10% EtOAc in *n*-hexanes) to yield **A-H** (10.1 mg, 0.019 mmol, 50%) as a yellow solid.

^{1}H NMR (CDCl$_3$, 400 MHz, 298 K): δ_H 9.11 (d, J = 9.0 Hz, 1H[13]), 8.88–8.83 (m, 2H[5]), 8.80 (d, J = 8.0 Hz, 2H[8]), 8.69–8.65 (m, 2H[4]), 8.49 (s, 1H[9]), 8.26 (d, J = 8.5 Hz, 1H[10]), 7.92–7.85 (m, 1H[12]), 7.79–7.67 (m, 6H[6,7,10',11]), 7.45 (d, J = 8.3 Hz, 2H[1]), 7.41–7.36 (m, 2H[3]), 7.28–7.24 (m, 1H[11']), 7.00 (m, 3H[2,13']), 6.59–6.52 (m, 1H[12']), 1.25 (s, 1H[14]); **^{13}C NMR** (CDCl$_3$, 101 MHz, 298K): δ_C 131.5, 131.0, 130.7, 129.6, 128.9, 128.8, 128.4, 128.0, 127.7, 127.0, 126.2, 126.0, 126.0, 125.4, 124.7, 124.5, 123.8, 123.3, 41.6*; **APCI–HRMS** (*v*e+, CH_2Cl_2) calculated for $C_{43}H_{26}$: *m/z* = 543.2107 [*M*+H]$^+$; found 543.2094 [*M*+H]$^+$; *limited by concentration
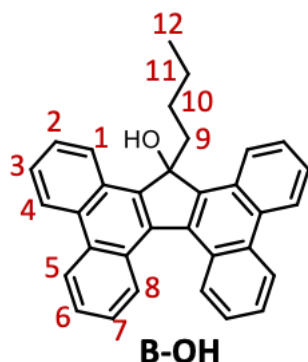
B-OH: A solution of **TBF=O** (252 mg, 0.66 mmol, 1.0 equiv.) in anhydrous and degassed THF (200 mL) under an Ar atmosphere was cooled to –78 °C and *n*-BuLi (2.44 M in *n*-hexanes, 0.32 mL, 1.2 equiv.) was added slowly. The reaction mixture was allowed to slowly warm up to room temperature and then stirred at room temperature overnight. The reaction was quenched slowly with dropwise addition of water. The reaction mixture was extracted with EtOAc (100 mL) and water (50 mL). The organic layer was dried with Na_2SO_4, filtered and concentrated. The crude solid was washed with the minimum amount of *n*-hexanes (to avoid dissolving starting material **TBF=O**) and the filtrate concentrated. Automated column chromatography (SiO_2: 5% EtOAc in *n*-hexanes) afforded the desired product, **B-OH** (39.0 mg, 0.089 mmol, 14%) as a yellow solid.

^{1}H NMR (CDCl$_3$, 400 MHz, 298 K): δ_H 9.28–9.24 (m, 1H[5]), 8.90–8.83 (m, 2H[4,5']), 8.74–8.70 (m, 1H[8]), 7.96–7.81 (m, 4H[1',2,3,6']), 7.73–7.64 (m, 2H[6,7]), 7.54–7.45 (m, 4H[1,4',7',8']), 7.19 (td, J = 7.6, 1.2 Hz, 1H[2]), 6.99–6.93 (m, 1H[3]), 4.24 (s, OH), 2.72 (ddd, J = 15.4, 11.0, 4.7 Hz, 1H[9]), 2.28–2.17 (m, 1H[9']), 1.49–1.28 (m, 4H[10,11]), 0.79 (t, J = 7.0 Hz, 3H[12]); **^{13}C NMR** (CDCl$_3$, 101 MHz, 298K): δ_C 203.4, 158.8, 142.3, 134.5, 132.6, 131.9, 131.4, 131.4, 130.7, 130.5, 129.4, 128.5, 128.4, 128.3, 128.3, 128.1, 127.8, 127.7, 127.6, 127.4, 125.4, 124.7, 124.2, 123.8, 122.5, 53.2, 38.3, 29.9, 27.5, 23.0; **APCI–HRMS** (*v*e+, CH_2Cl_2) calculated for $C_{33}H_{26}O$: *m/z* = 439.2056 [*M*+H]$^+$; found 439.2072 [*M*+H]$^+$
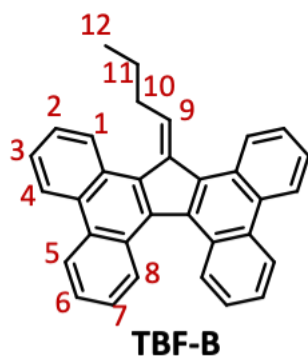
TBF-B: A solution of **TBF=O** (174.7 mg, 0.46 mmol, 1.0 equiv.) in anhydrous and degassed THF (150 mL) under an Ar atmosphere was cooled to –78 °C and *n*-BuLi (2.44 M in *n*-hexanes, 0.75 mL, 4.0 equiv.) was added slowly. The reaction mixture was allowed to slowly warm up to room temperature and then stirred at room temperature overnight. The reaction was quenched slowly with dropwise addition of NaOH (4N, 10 mL) followed by H$_2$O (50 mL). The reaction mixture was extracted with EtOAc (2 x 75 mL), then the combined organic layers were washed with brine, dried over Na$_2$SO$_4$ and concentrated. The crude solid was washed with the minimum amount of *n*-hexanes and the filtrate concentrated to remove as much **TBF=O** as possible from the crude. The desired product, **TBF-B**, was then isolated by automated column chromatography (SiO$_2$: 5% EtOAc in *n*-hexanes) as a yellow solid (101.4 mg, 0.24 mmol, 52%).

^{1}H NMR (CDCl$_3$, 400 MHz, 298 K): δ_H 8.86–8.79 (m, 6H[4,5,8]), 8.57 (dd, *J* = 8.2, 1.4 Hz, 2H[1]), 7.76–7.69 (m, 6H[3,6,7]), 7.63 (ddd, *J* = 8.2, 6.9, 1.2 Hz, 2H[2]), 2.90–2.81 (m, 2H[10]), 2.51 (s, 1H[9]), 0.86 (q, *J* = 7.4 Hz, 2H[11]), 0.38 (t, *J* = 7.3 Hz, 3H[12]); **APCI–HRMS** (*v*e+, CH$_2$Cl$_2$) calculated for C$_{33}$H$_{24}$: *m/z* = 421.1958 [*M*+H]$^+$; found 421.1966 [*M*+H]$^+$
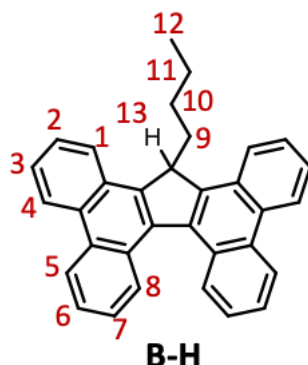
B-H: **3** (106.3 mg, 0.29 mmol, 1.0 eq.) was dissolved in degassed dioxane (5 mL) and heated to reflux. A solution of tetrabutylammonium hydroxide (40% w/w in H$_2$O, 78.0 mg, 0.30 mmol, 1.0 eq.) in degassed dioxane (2 mL) was added and a yellow precipitate was formed immediately. The salt was filtered under N$_2$ and washed with warm degassed dioxane (3 x 5 mL) followed by Et$_2$O (3 x 5 mL). The salt was resuspended in degassed dioxane (5 mL) and a solution of bromobutane (36.7 mg, 0.27 mmol, 0.9 equiv.) in degassed dioxane (2 mL) was added to the reaction mixture and heated to reflux for 6 h. Once the reaction was complete (confirmed by TLC in 10% EtOAc in *n*-hexanes), the solvent was removed, and the residue redissolved in CH$_2$Cl$_2$ (20 mL) and separated with water (20 mL). The organic layer was dried with Na$_2$SO$_4$ and concentrated. The desired product, **B-H**, was isolated as a mixture with **TBF=O** by automated column chromatography (SiO$_2$: 1% EtOAc in *n*-hexanes). The product mixture was redissolved in the minimum amount of hot hexanes and hot-filtered to remove any remaining **TBF=O**. The filtrate was finally concentrated to yield pure **B-H** (19.4 mg, 0.046 mmol, 17%) as a yellow solid.

^{1}H NMR (CDCl$_3$, 400 MHz, 298 K): δ_H 8.87–8.78 (m, 4H[5,8]), 8.70 (d, *J* = 8.2 Hz, 2H[4]), 8.30 (dd, *J* = 7.5, 1.8 Hz, 2H[1]), 7.75–7.61 (m, 8H[2,3,6,7]), 5.11 (t, *J* = 4.5 Hz, 1H[13]), 2.65 (dt, *J* = 12.7, 4.5 Hz, 2H[9]), 0.91–0.78 (m, 3H[12]), 0.41–0.33 (m, 4H[10,11]); **APCI–HRMS** (*v*e+, CH$_2$Cl$_2$) calculated for C$_{33}$H$_{24}$: *m/z* = 422.2035; found 423.2101 [*M*+H]$^+$

2.4.3 NMR DATA
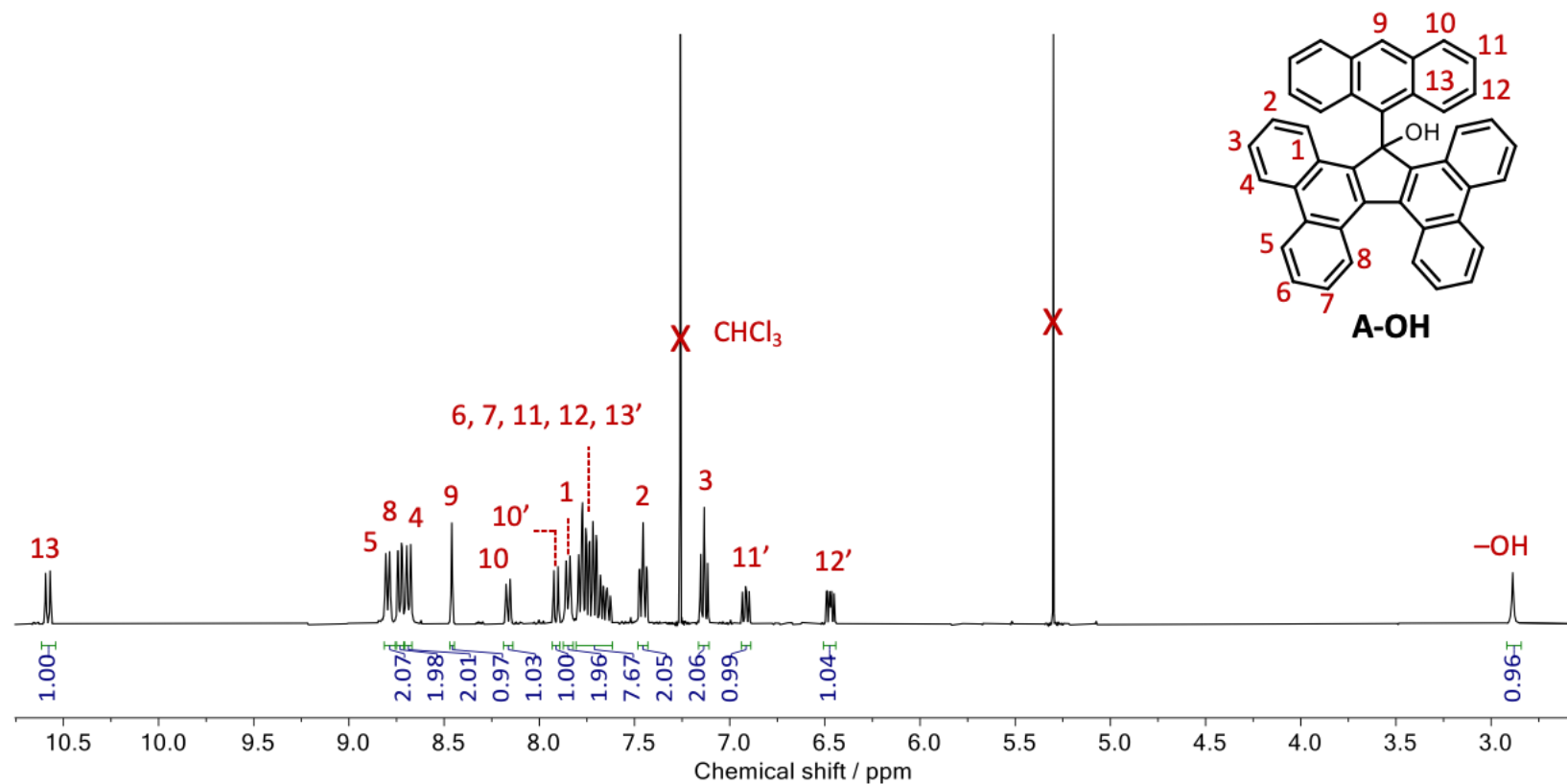
Figure S2.1 ^{1}H NMR (CDCl$_3$, 400 MHz, 298K) spectrum of **A-OH**
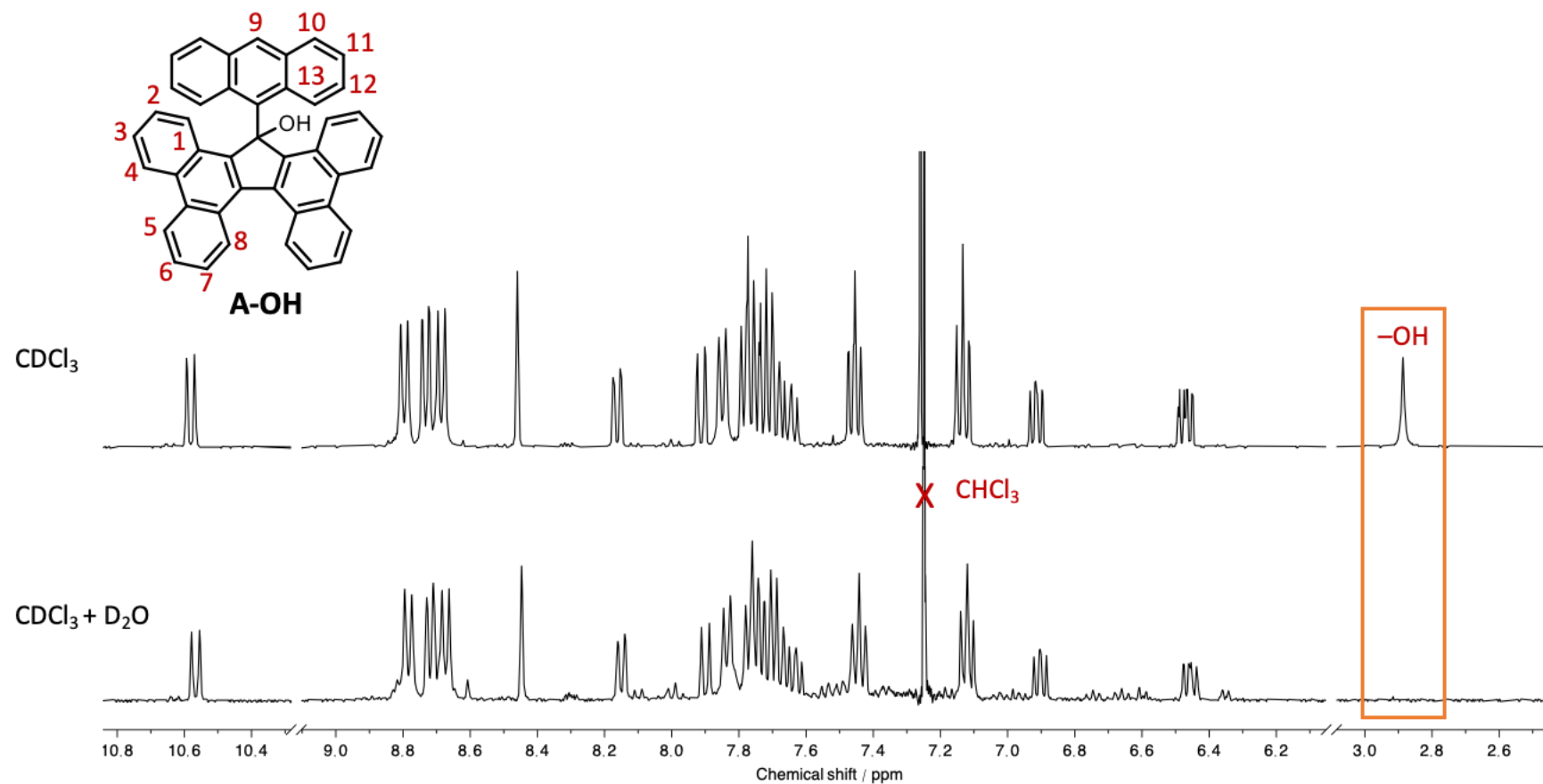
Figure S2.2 ^{1}H NMR (CDCl₃, 400 MHz, 298K) spectrum of **A-OH** before (top) and after (bottom) addition of D₂O
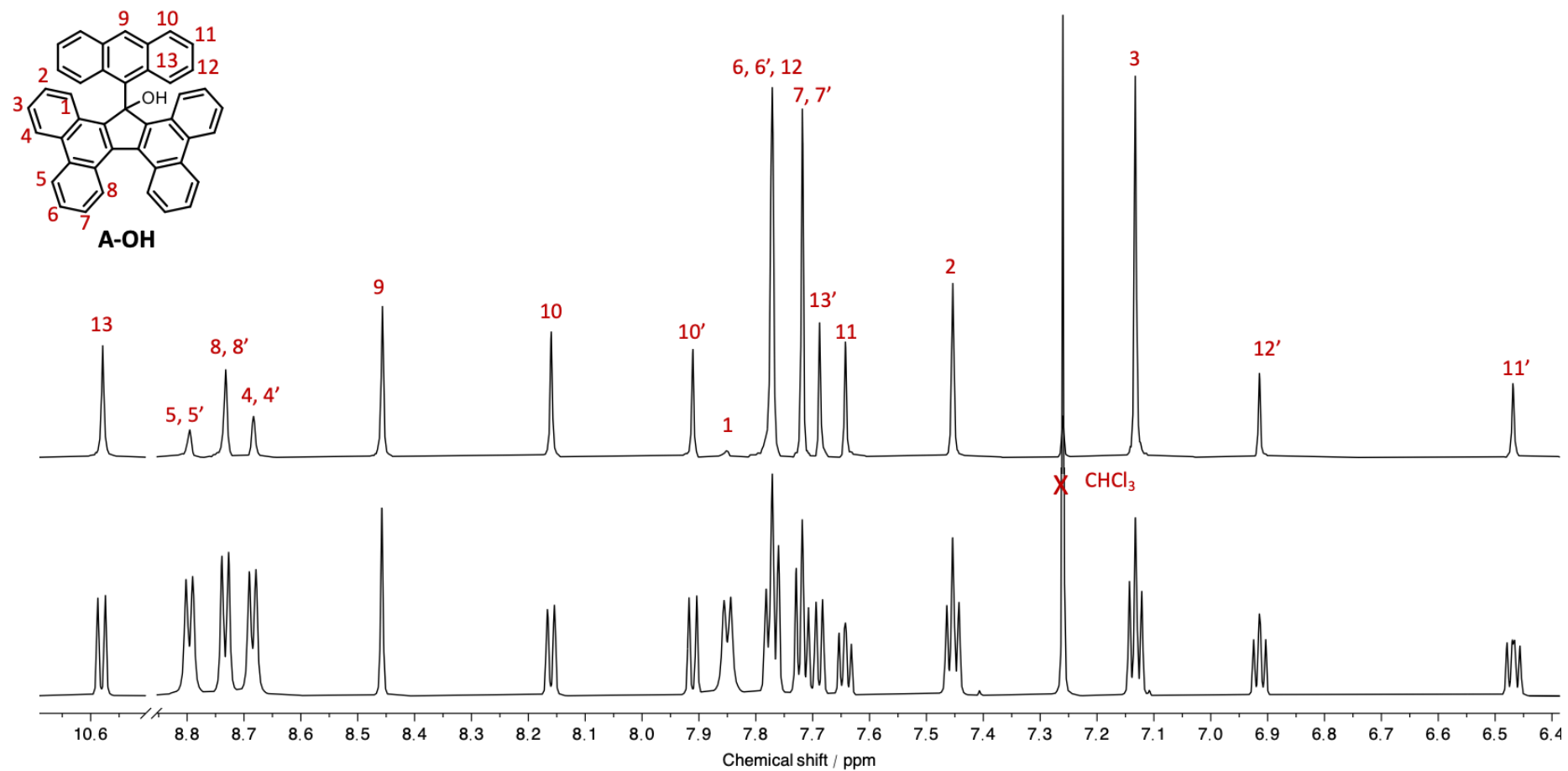
Figure S2.3 Stacked ^{1}H PSYCHE (top) and ^{1}H NMR (bottom; CDCl$_3$, 700 MHz, 298K) spectra of **A-OH**
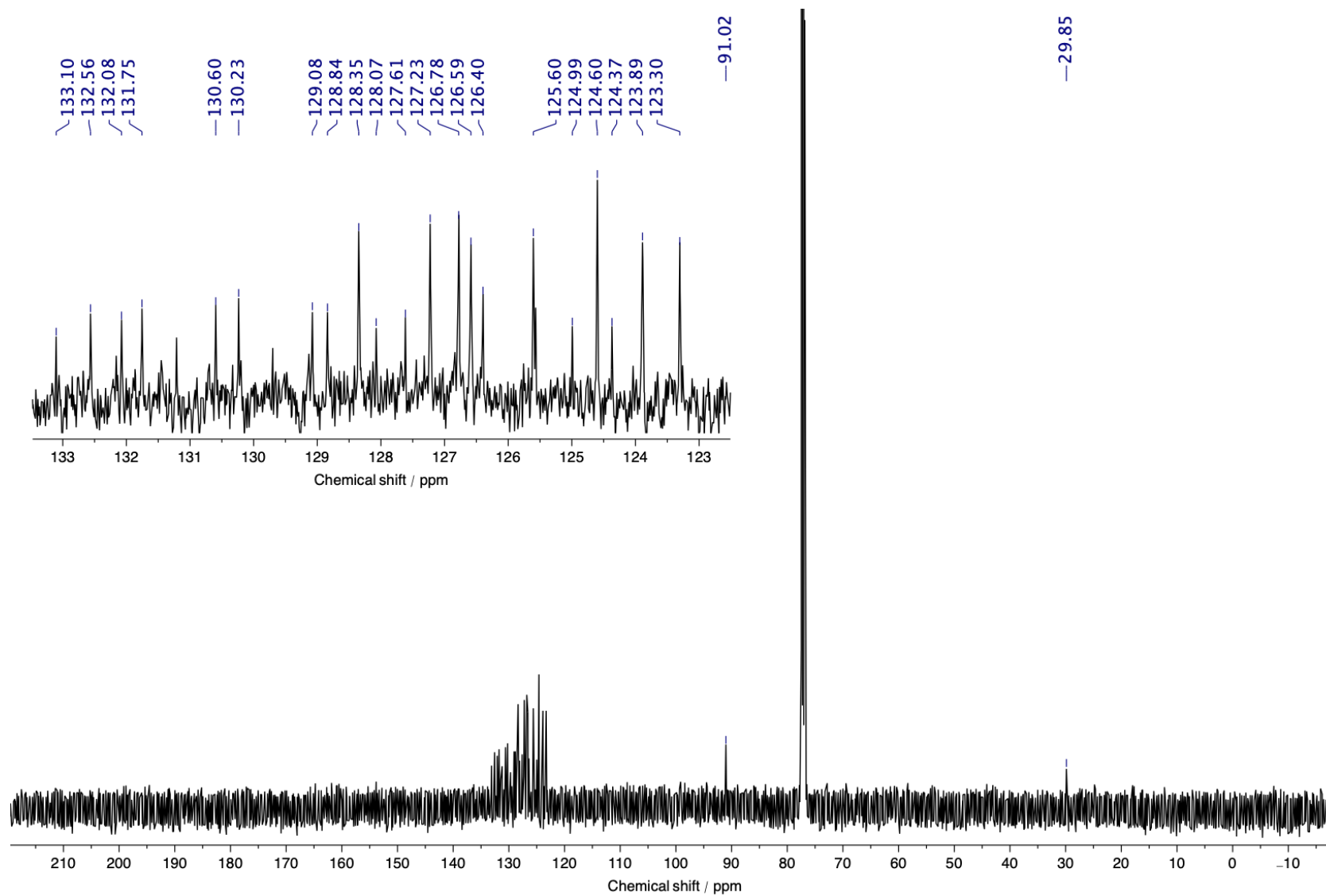
Figure S2.4 ^{13}C NMR (CDCl$_3$, 101 MHz, 298K) spectrum of **A-OH**

Figure S2.5 Annotated ^1H–^1H COSY NMR (CDCl$_3$, 700 MHz, 298K) spectrum of **A-OH**
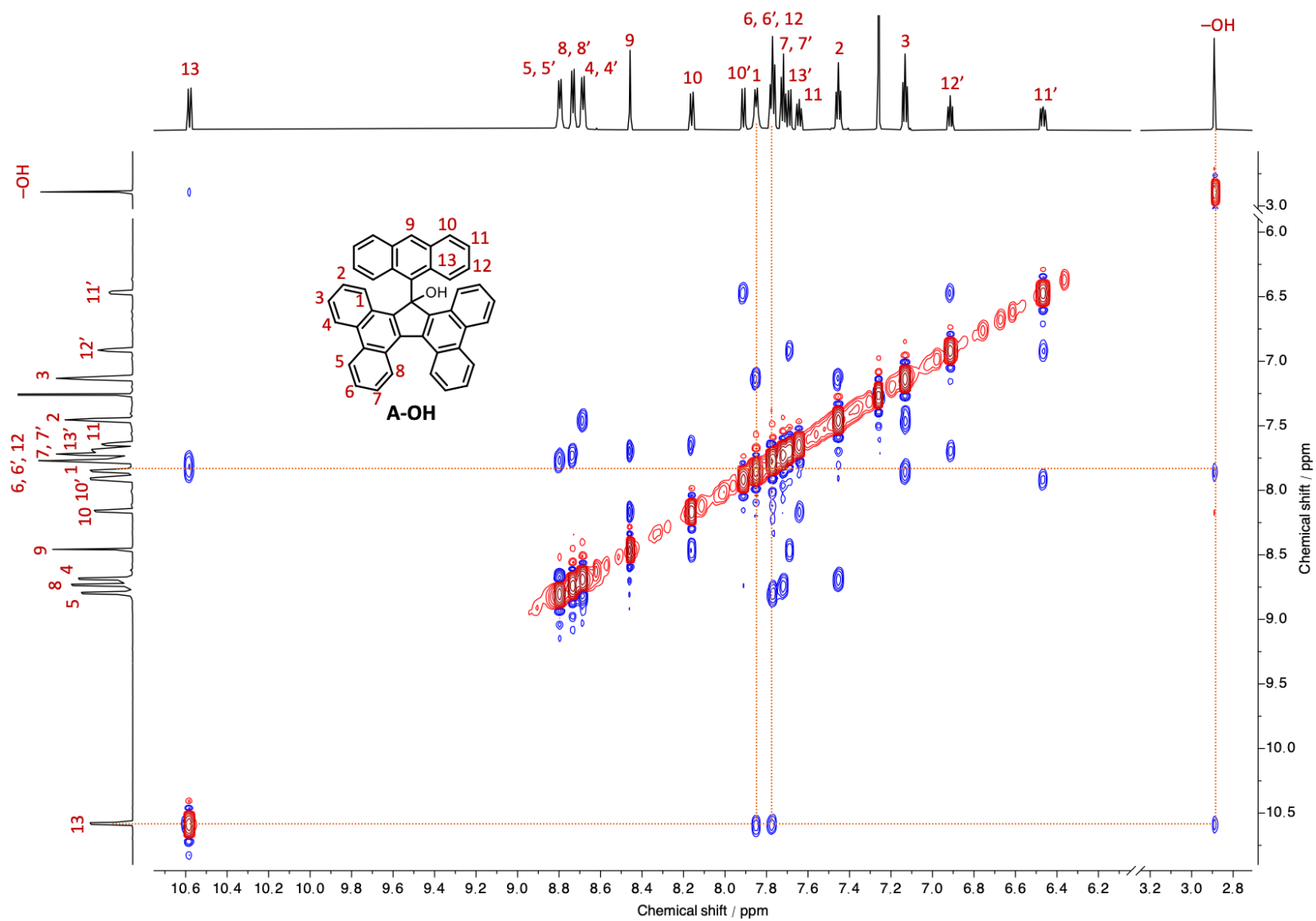
Figure S2.6 Annotated ^{1}H–^{1}H NOESY NMR (CDCl$_3$, 700 MHz, 298K) spectrum of **A-OH**
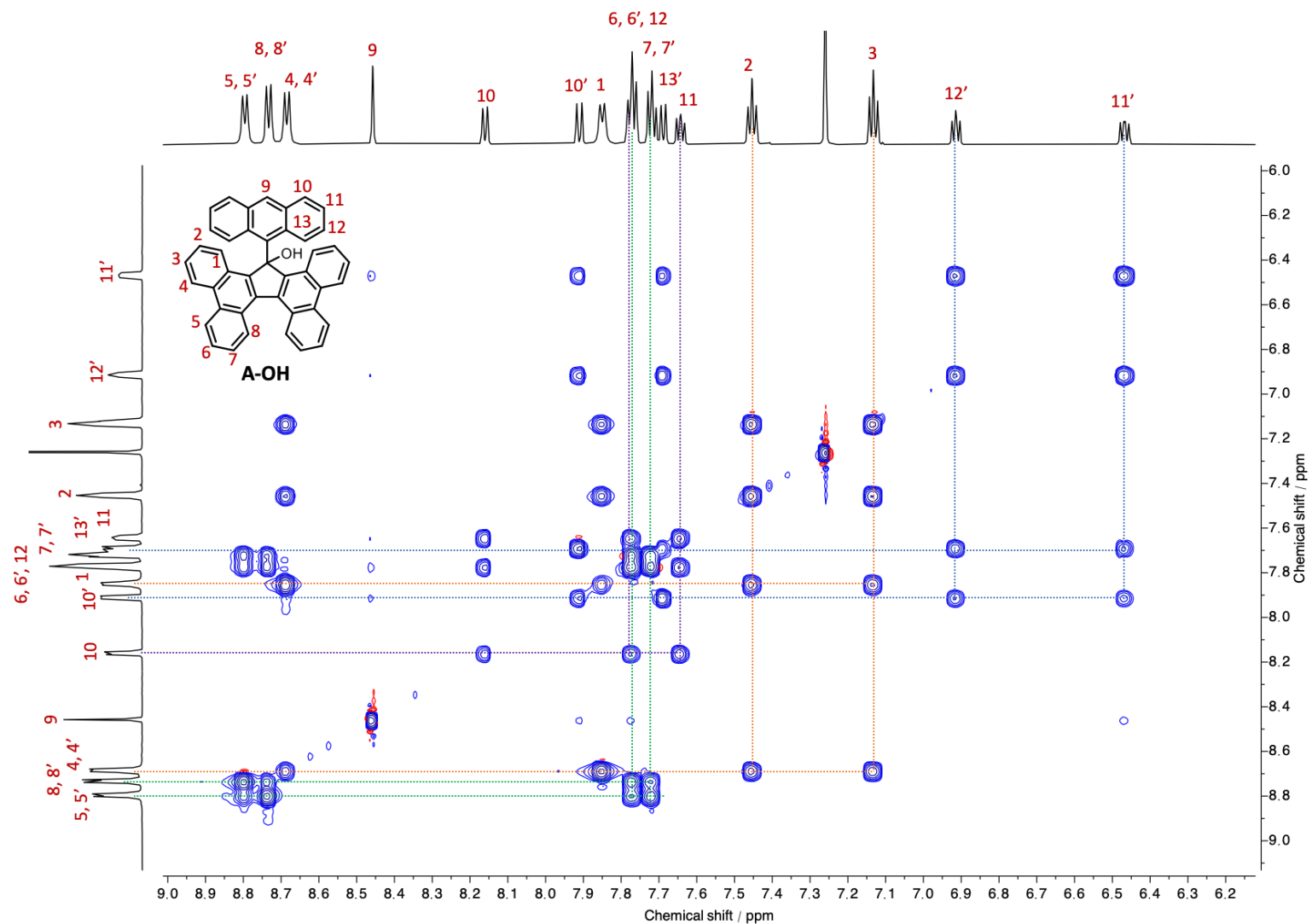
Figure S2.7 Annotated ^{1}H–^{1}H TOCSY NMR (CDCl$_3$, 700 MHz, 298K) spectrum of **A-OH**
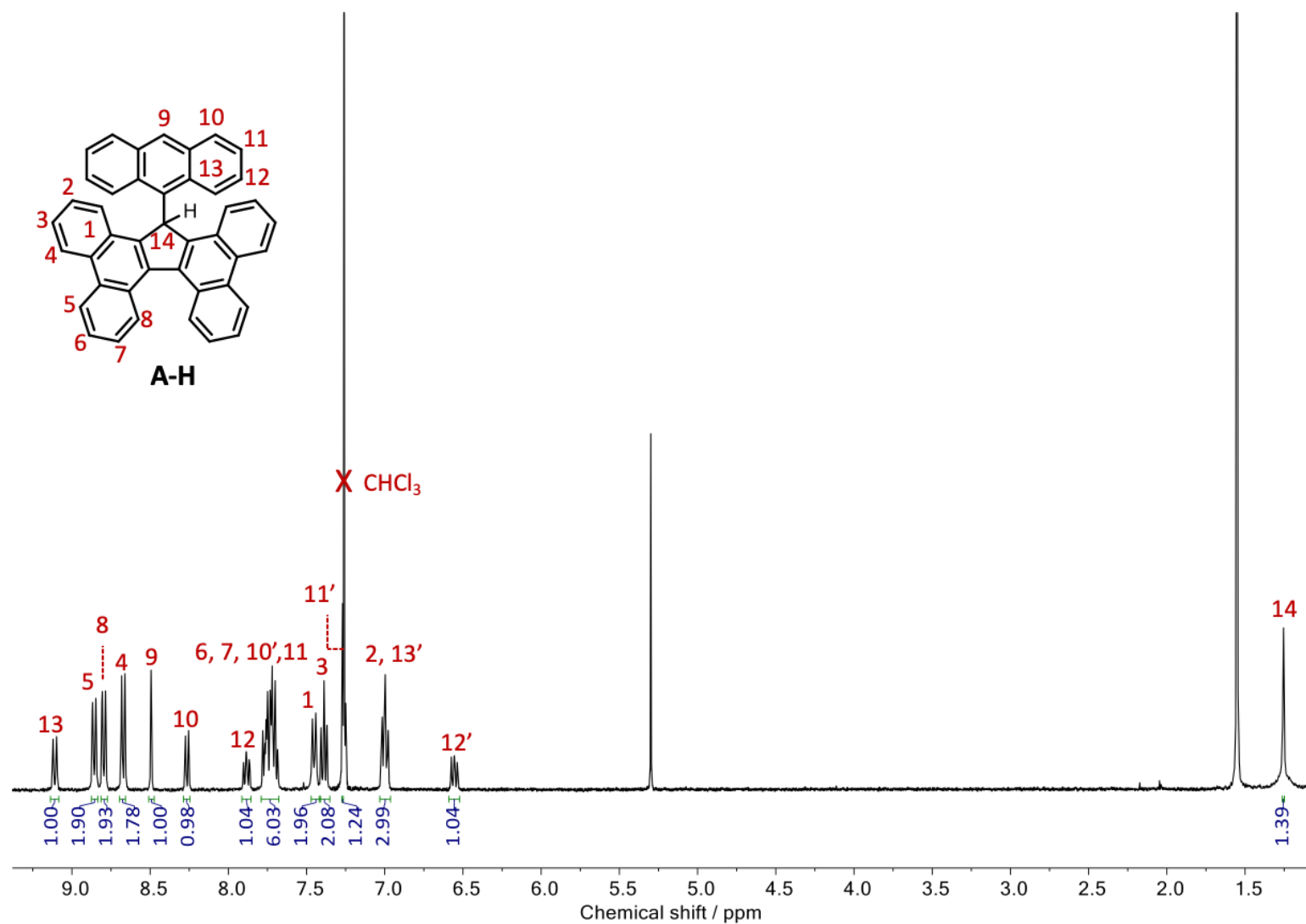
Figure S2.8 ^{1}H NMR (CDCl$_3$, 400 MHz, 298K) spectrum of **A-H**
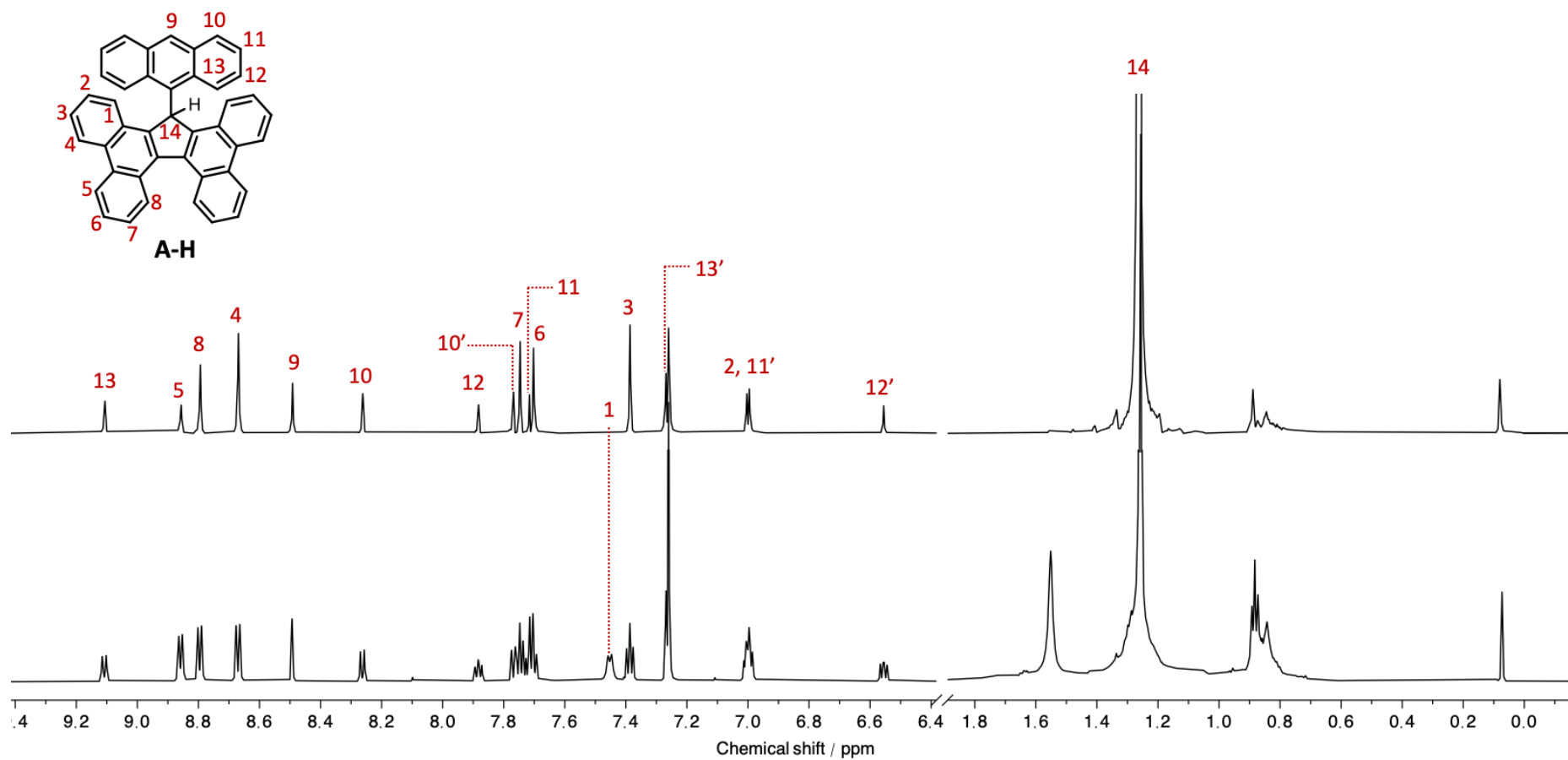
Figure S2.9 Stacked ^{1}H PSYCHE (top) and ^{1}H NMR (bottom; CDCl$_3$, 700 MHz, 298K) spectra of **A-H**
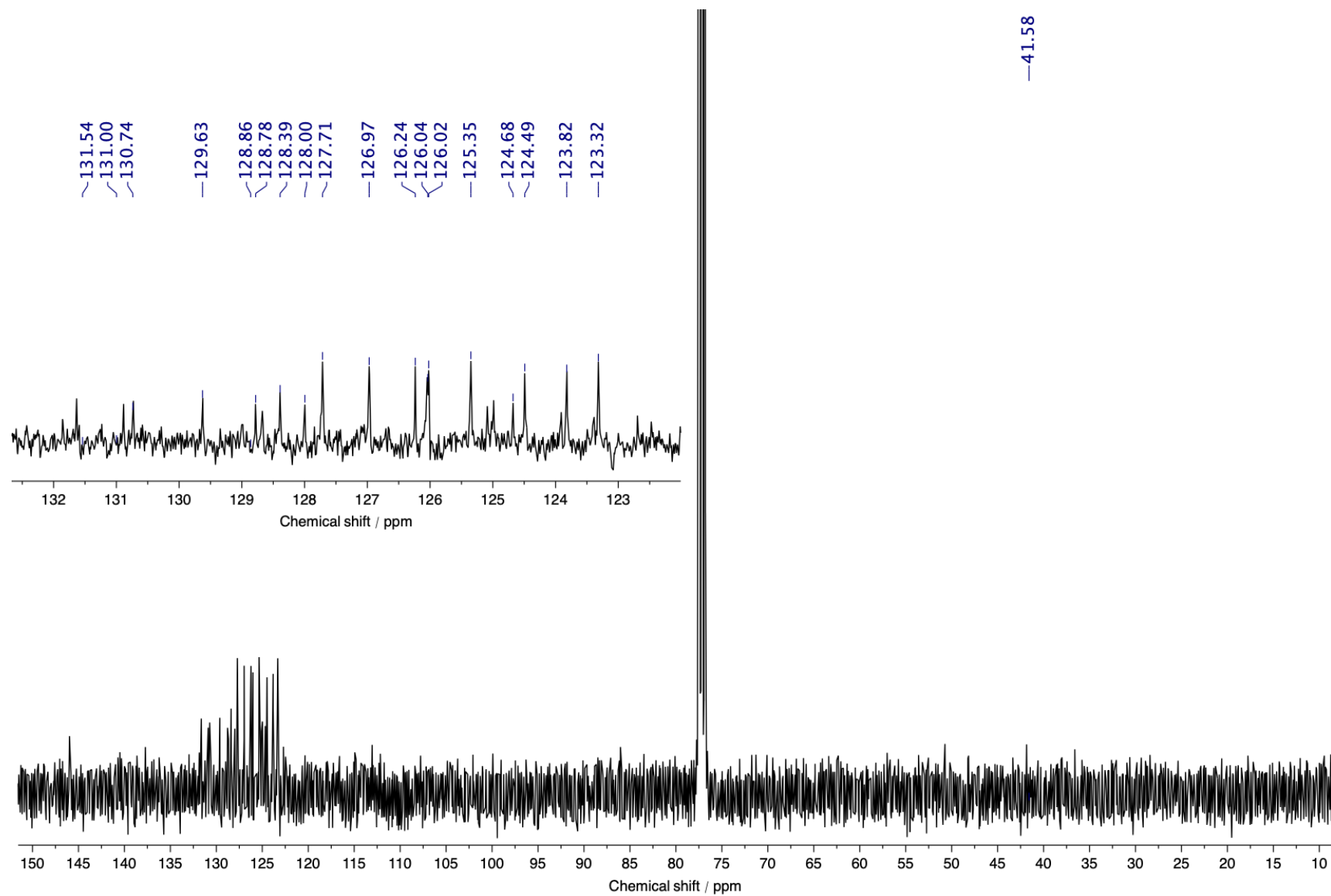
Figure S2.10 ^{13}C NMR (CDCl$_3$, 101 MHz, 298K) spectrum of **A-H**
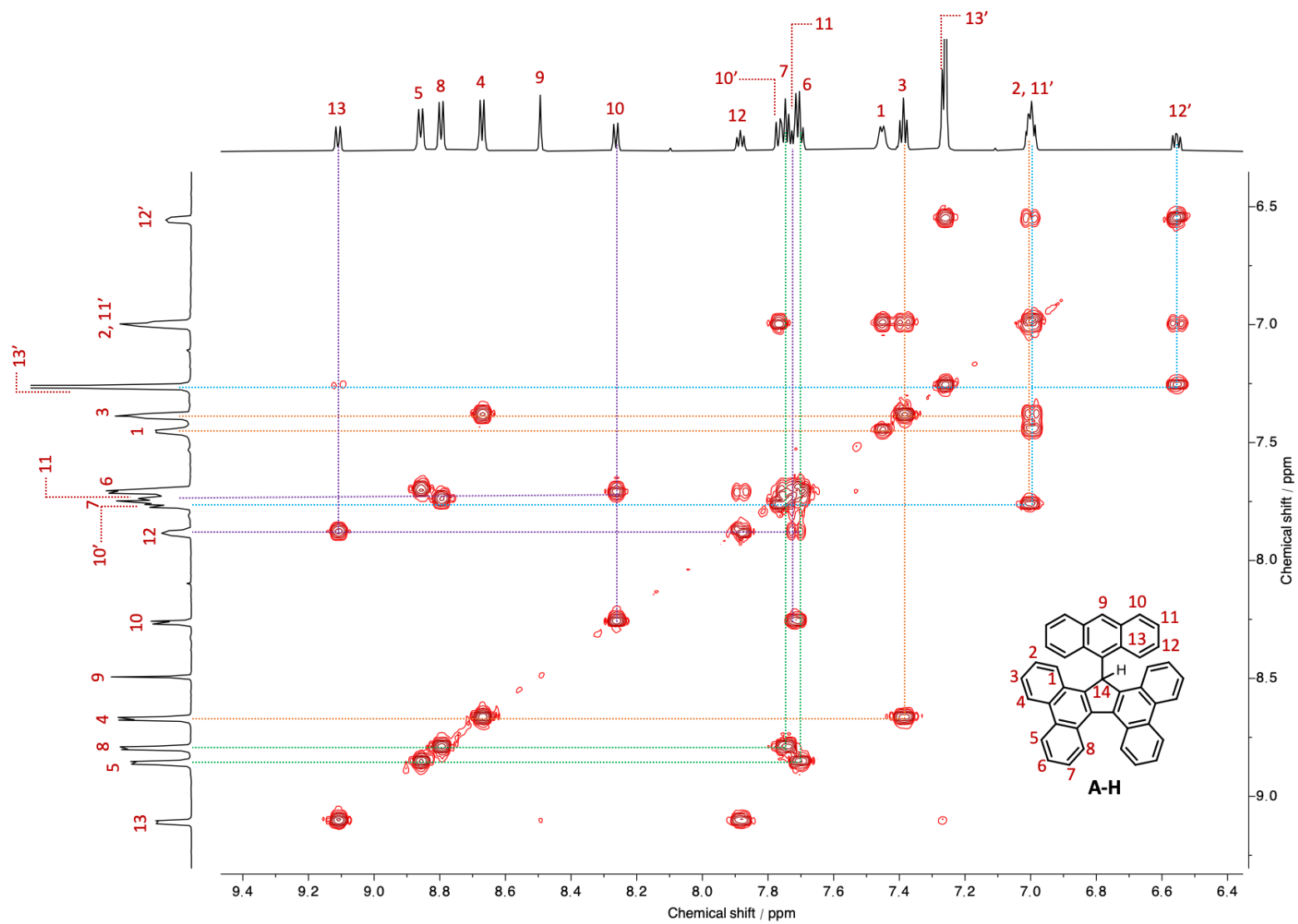
Figure S2.11 Annotated ^{1}H–^{1}H COSY NMR (CDCl$_3$, 700 MHz, 298K) spectrum of **A-H**
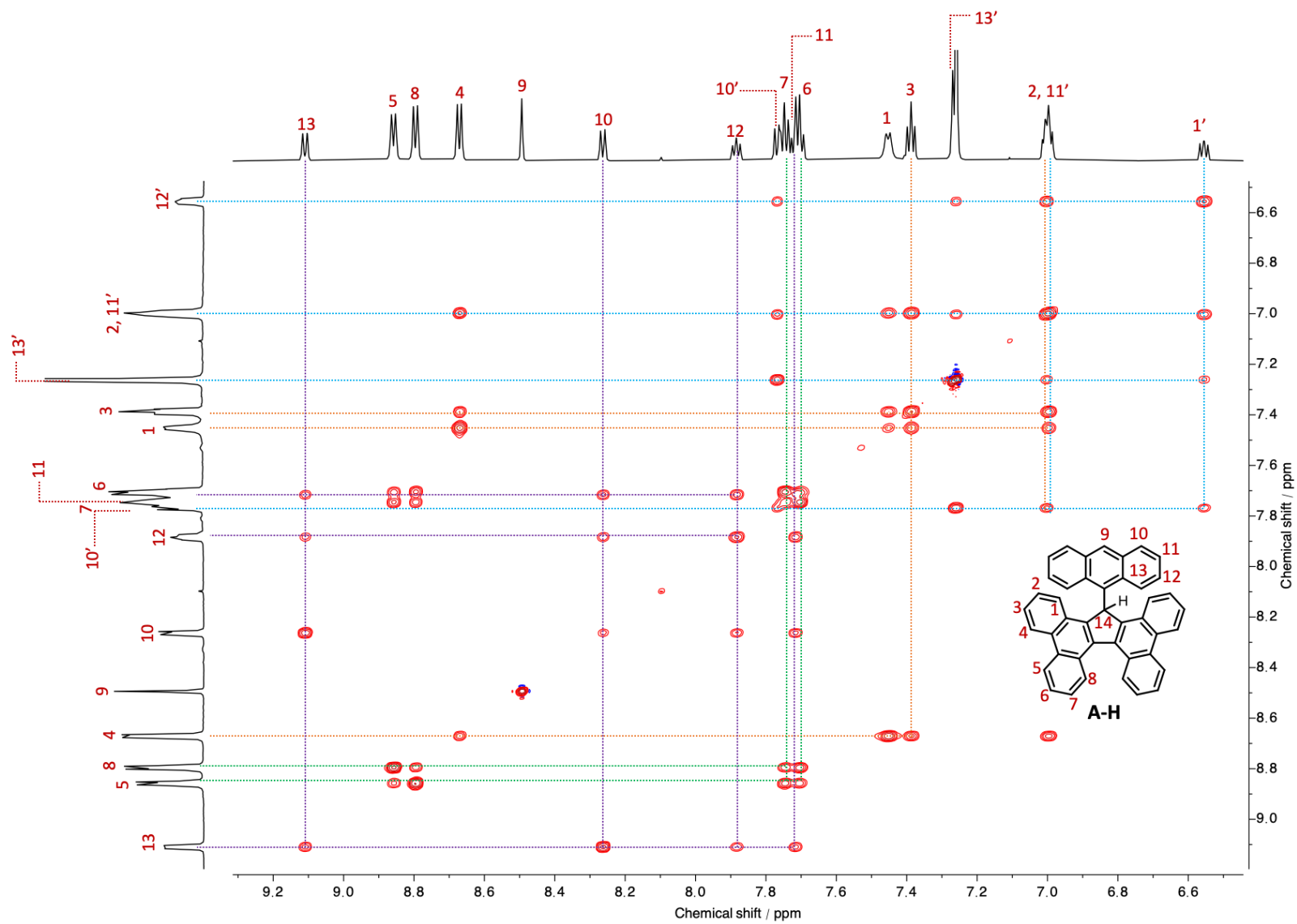
Figure S2.12 Annotated ^{1}H–^{1}H TOCSY NMR (CDCl$_3$, 700 MHz, 298K) spectrum of **A-H**
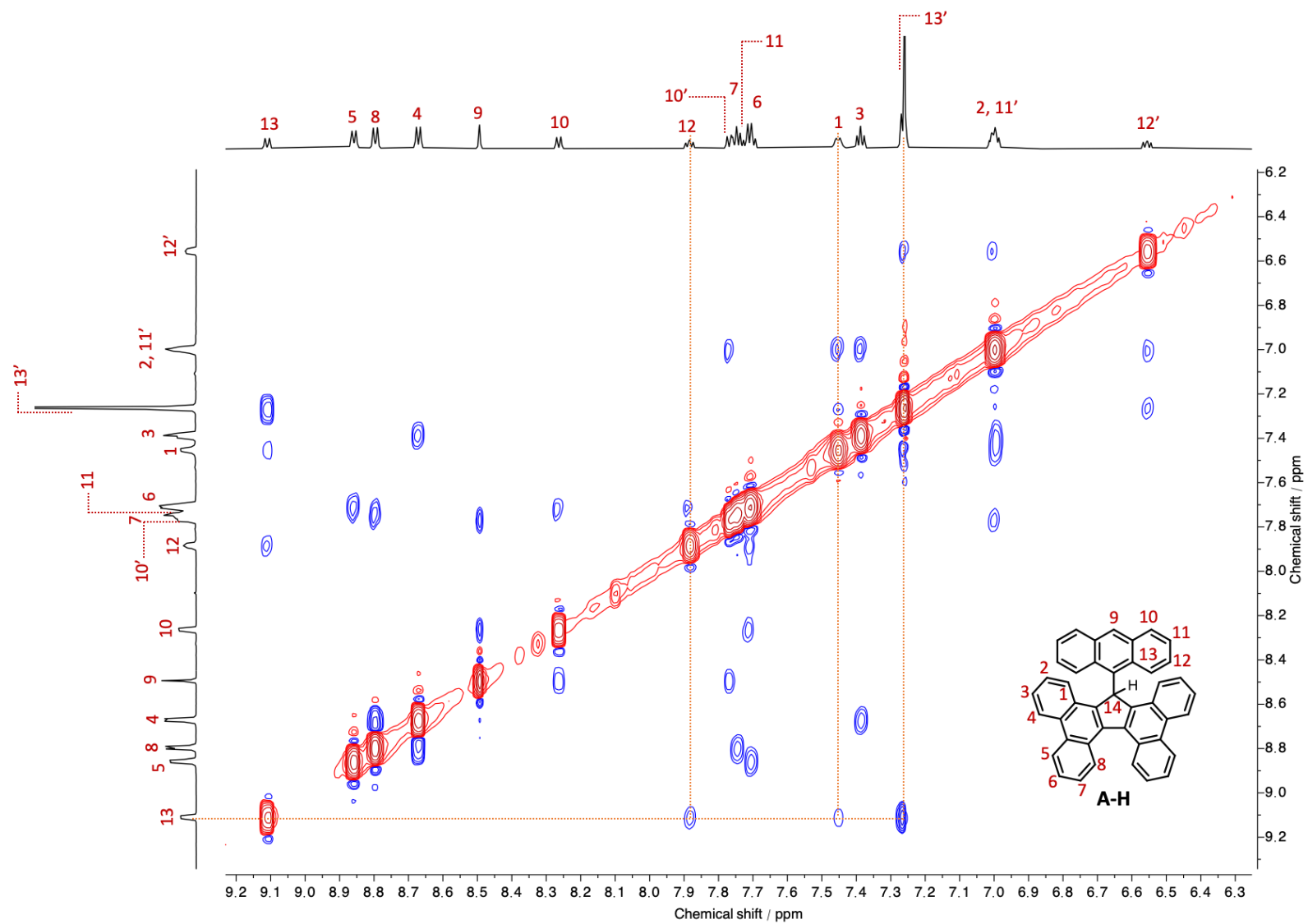
Figure S2.13 Annotated ¹H–¹H NOESY NMR (CDCl₃, 700 MHz, 298K) spectrum of **A-H**
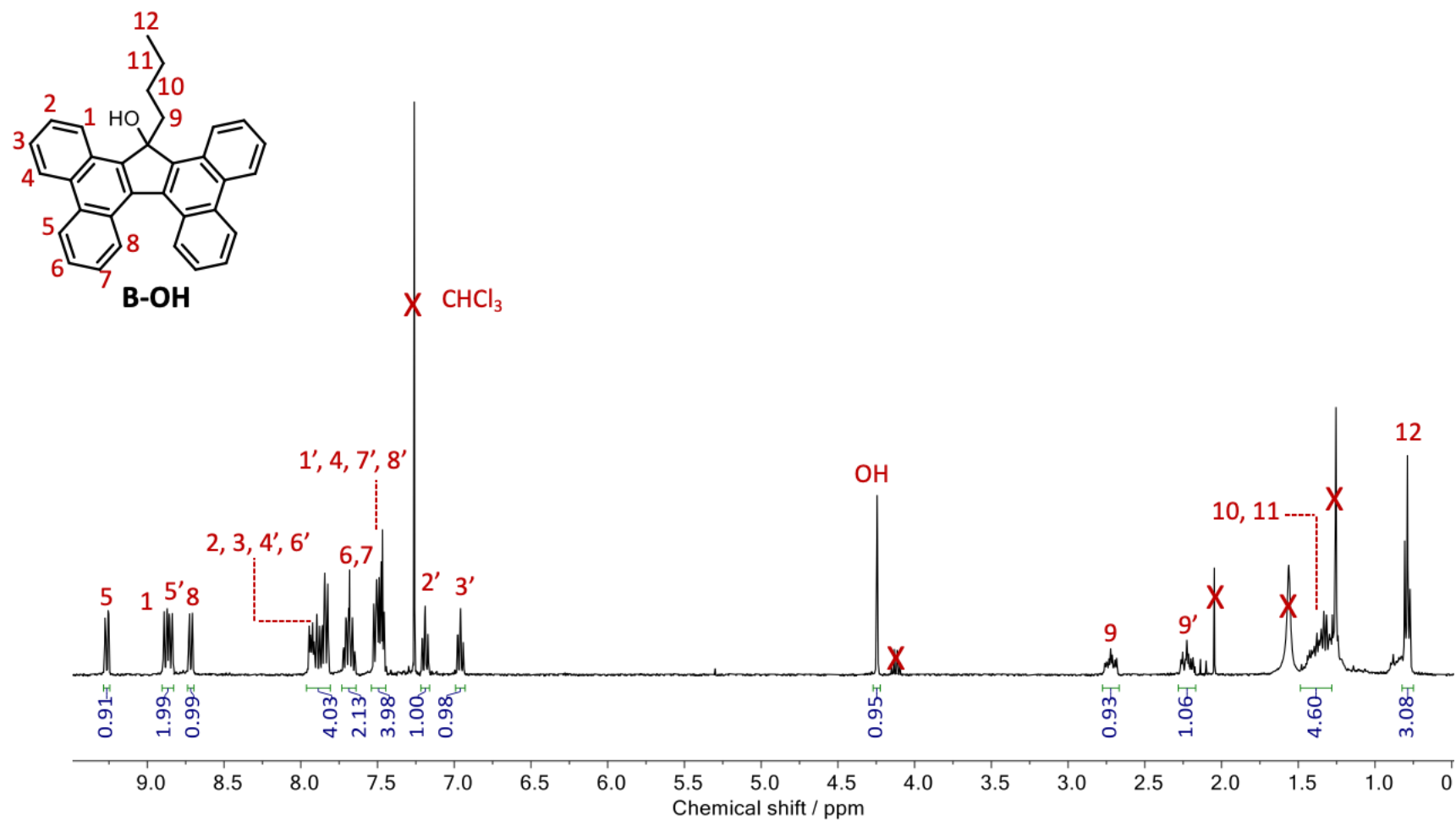
Figure S2.14 ^{1}H NMR (CDCl$_3$, 400 MHz, 298K) spectrum of **B-OH**
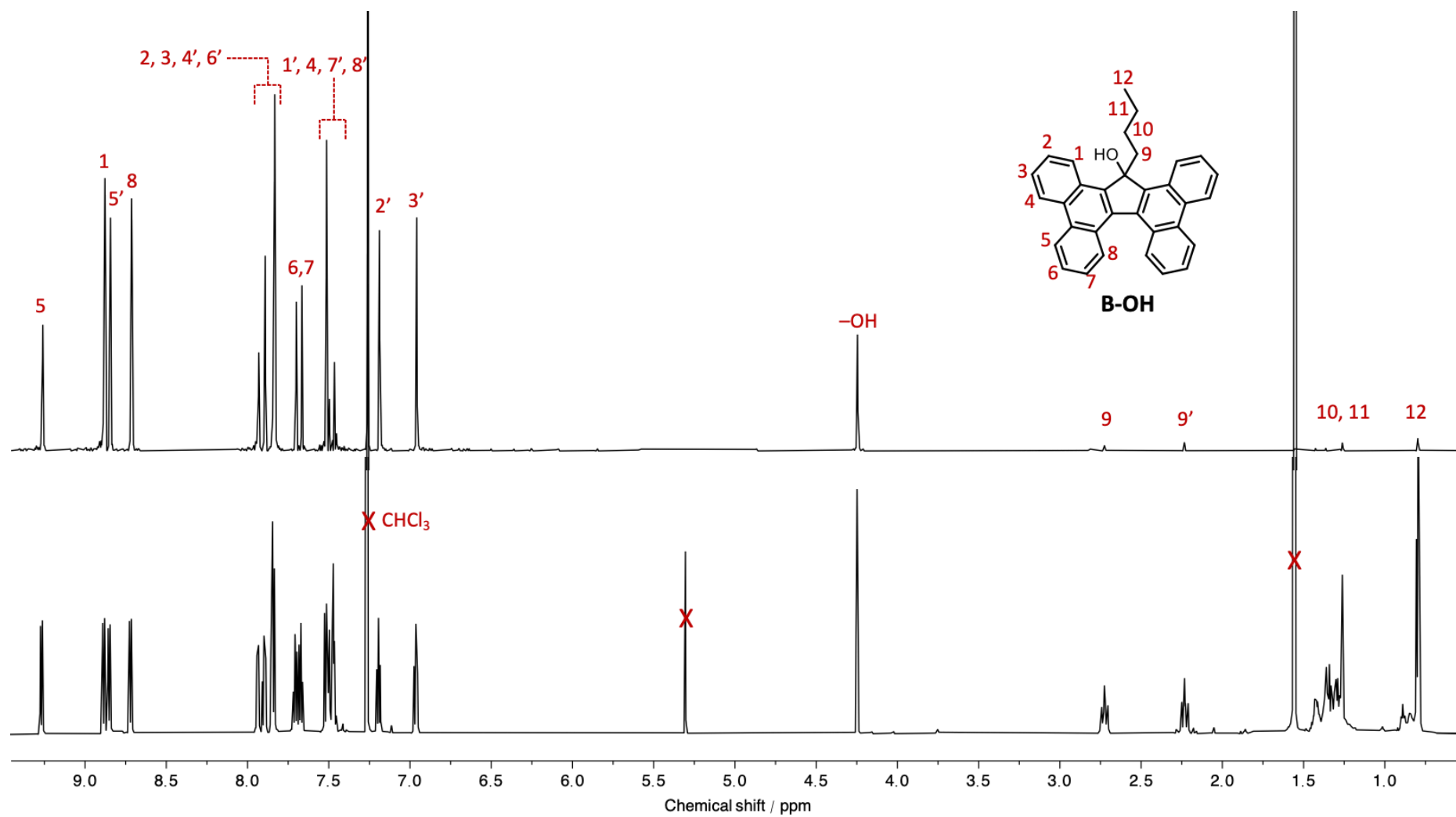
Figure S2.15 Stacked ^{1}H PSYCHE (top) and ^{1}H NMR (bottom; CDCl$_3$, 700 MHz, 298K) spectra of **B-OH**
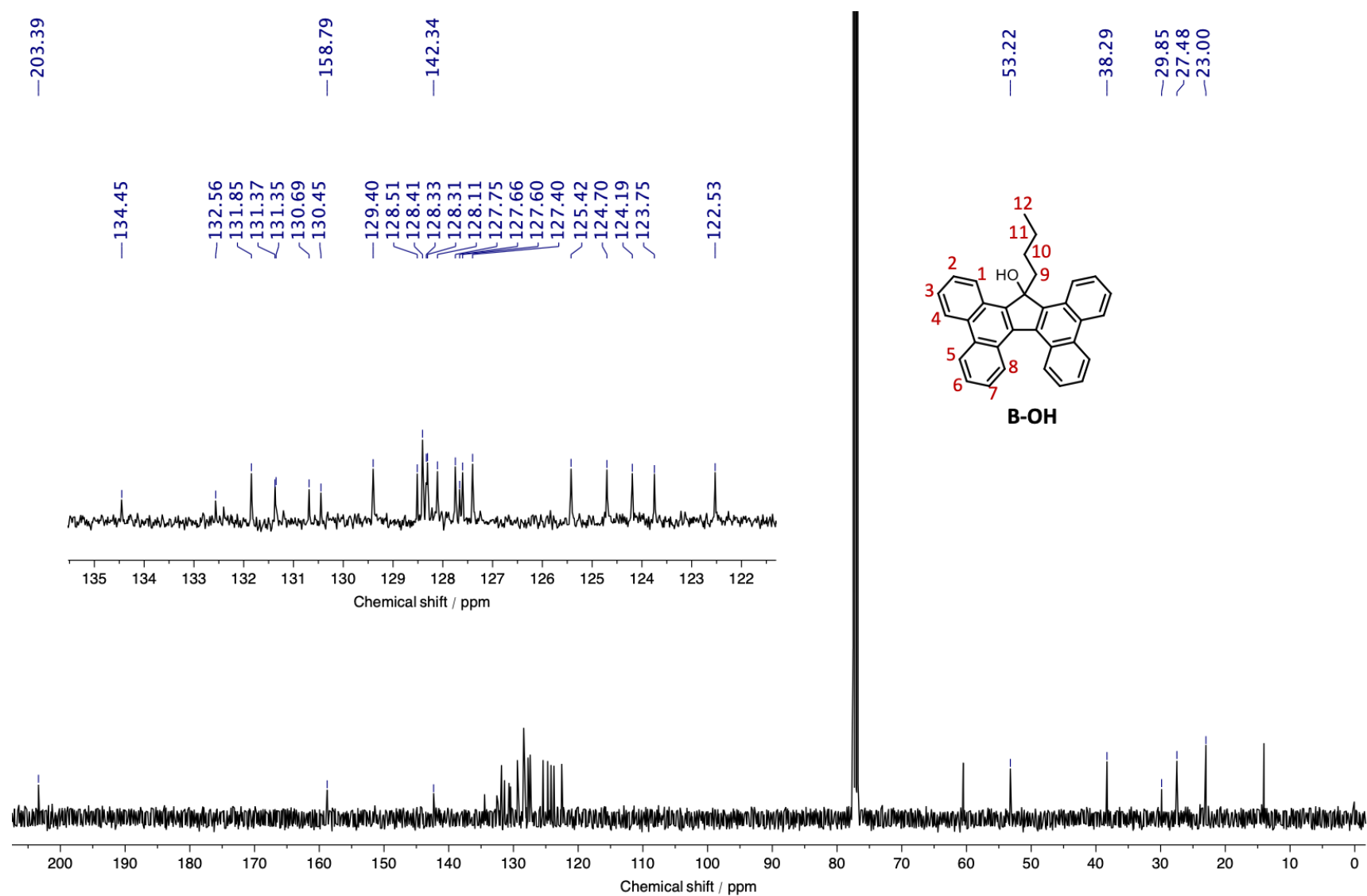
Figure S2.16 ^{13}C NMR (CDCl$_3$, 101 MHz, 298K) spectrum of **B-OH**
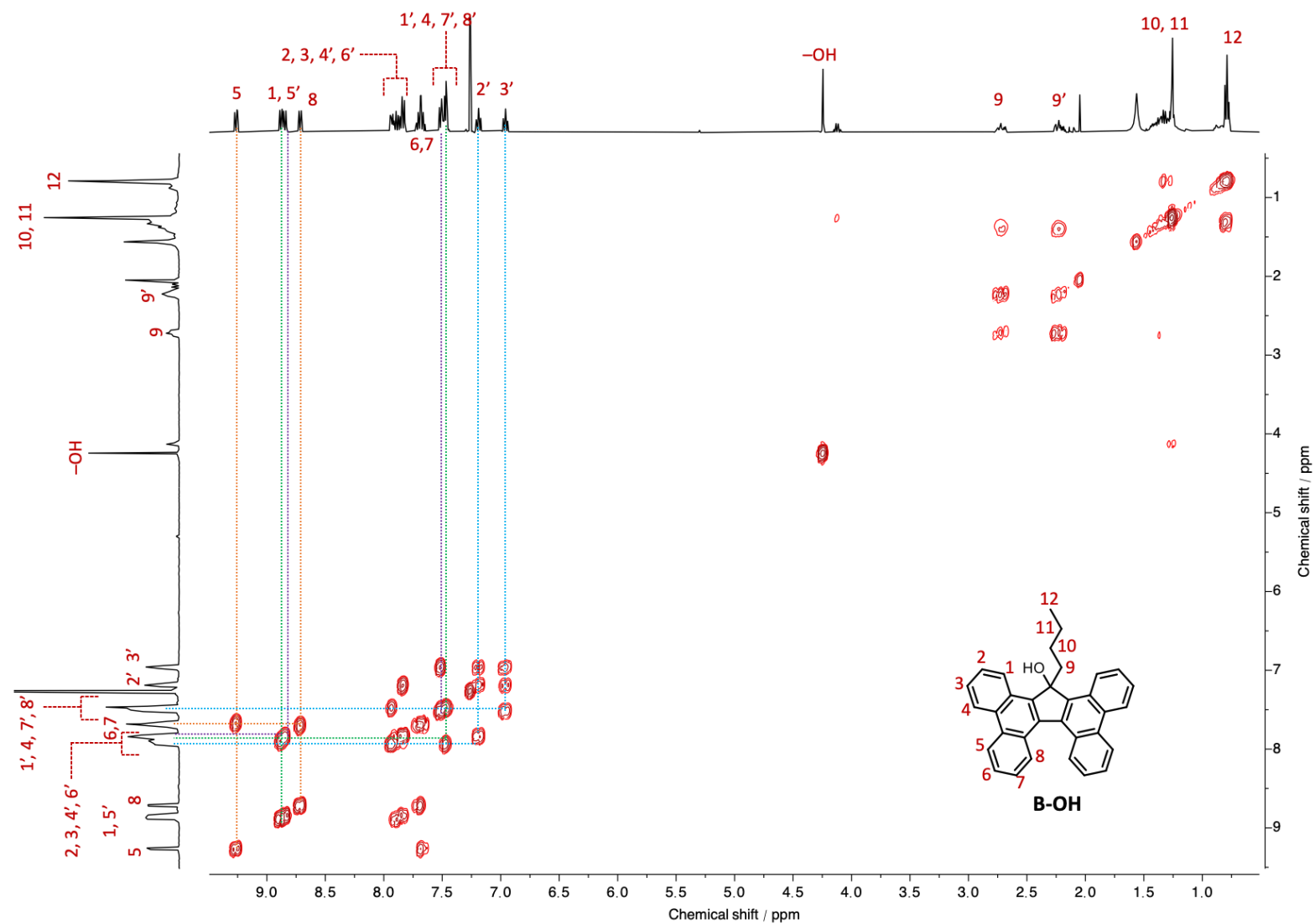
Figure S2.17 Annotated ^1H–^1H COSY NMR (CDCl$_3$, 400 MHz, 298K) spectrum of **B-OH**
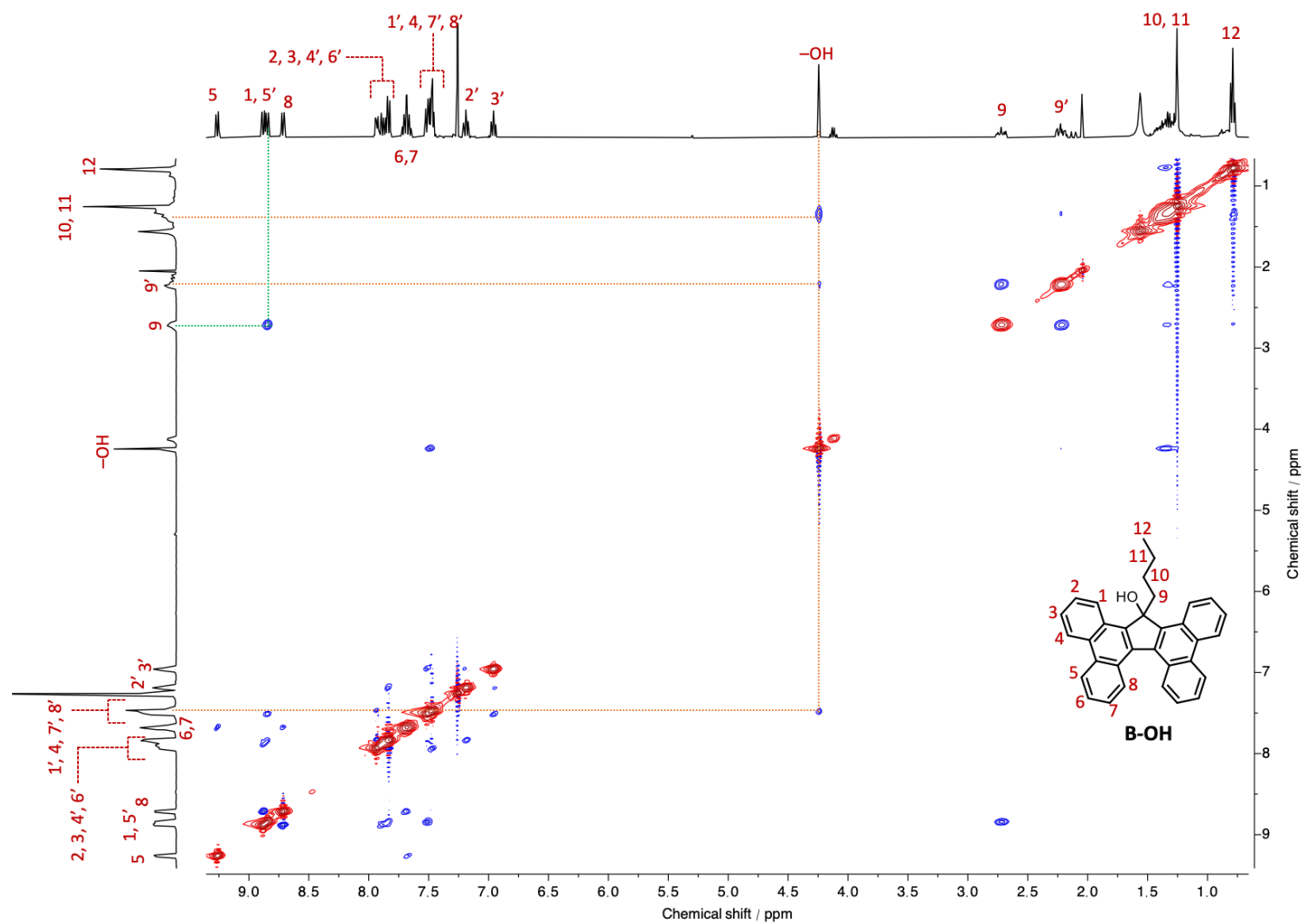
Figure S2.18 Annotated ^{1}H–^{1}H NOESY NMR (CDCl$_3$, 400 MHz, 298K) spectrum of **B-OH**
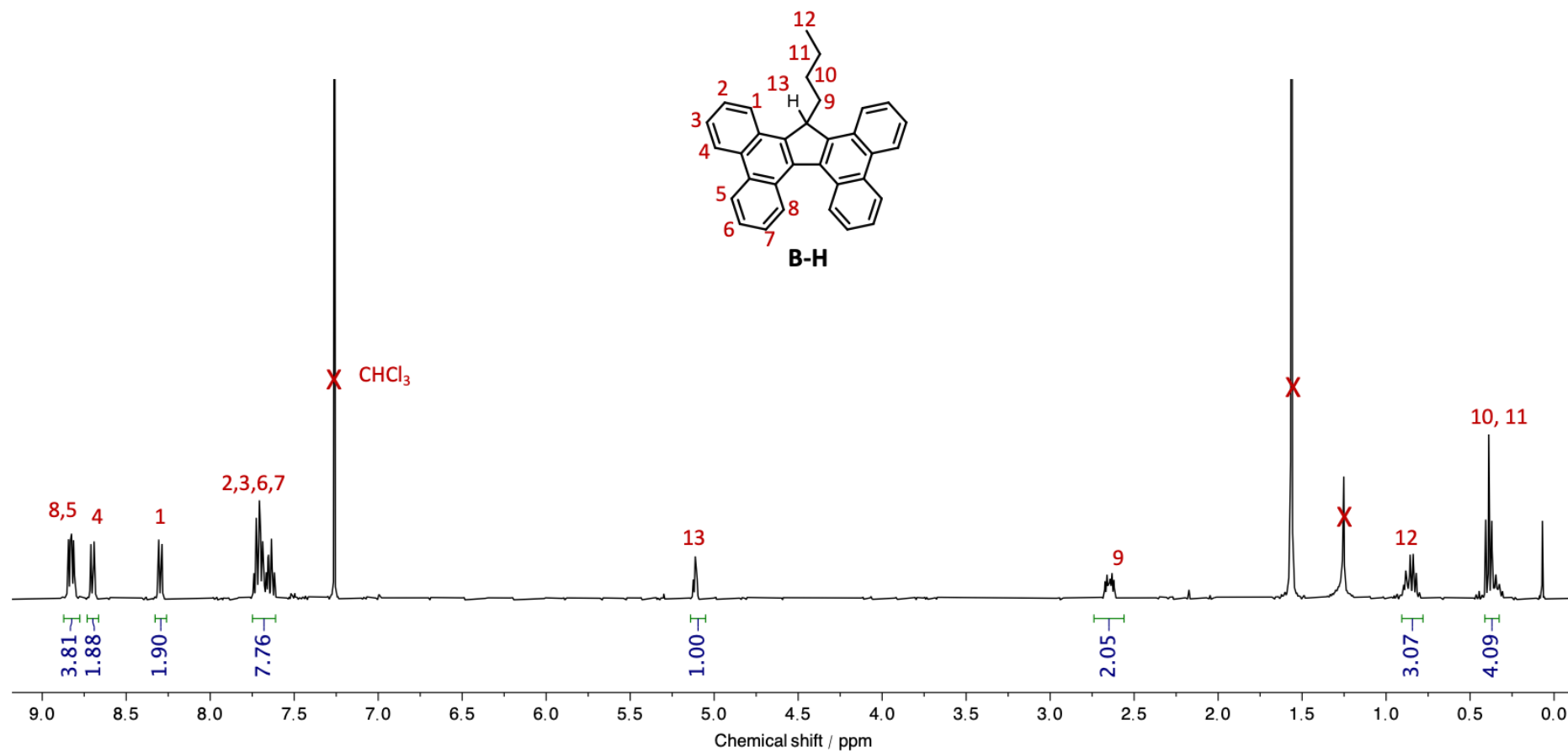
Figure S2.19 ^{1}H NMR (CDCl$_3$, 400 MHz, 298K) spectrum of **B-H**
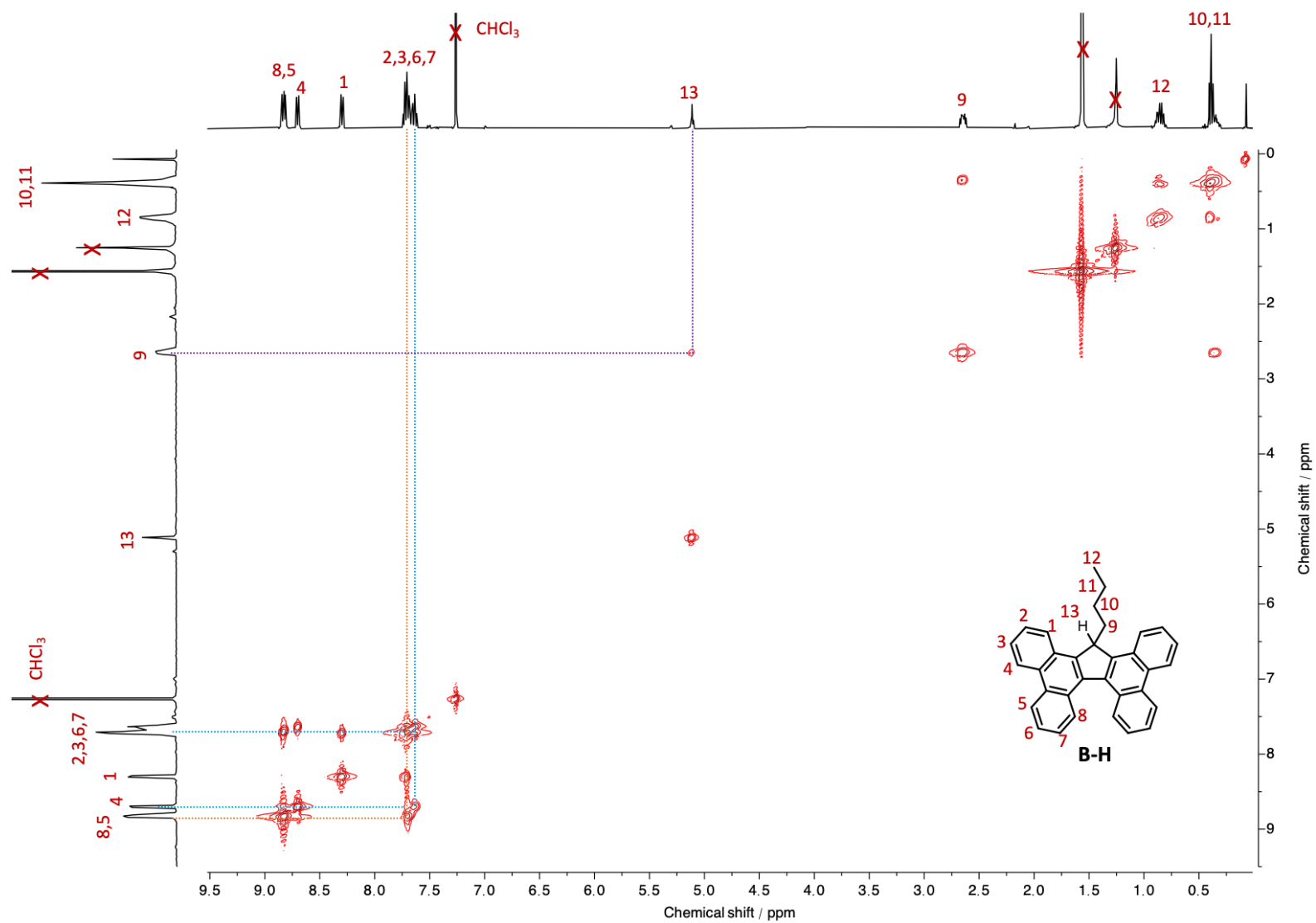
Figure S2.20 Annotated ^{1}H–^{1}H COSY NMR (CDCl$_3$, 400 MHz, 298K) spectrum of **B-H**
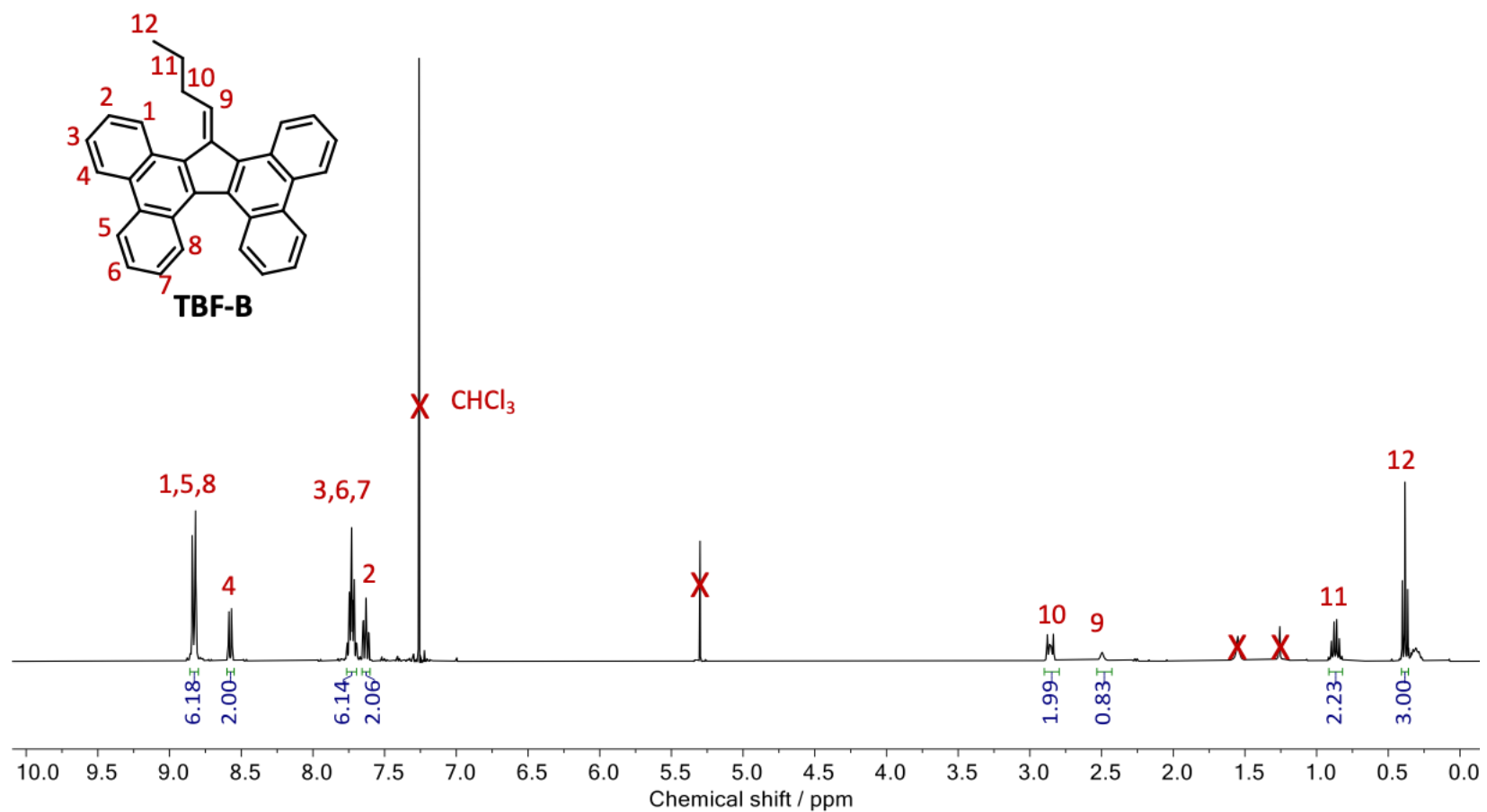
Figure S2.21 ^{1}H NMR (CDCl$_3$, 400 MHz, 298K) spectrum of **TBF-B**
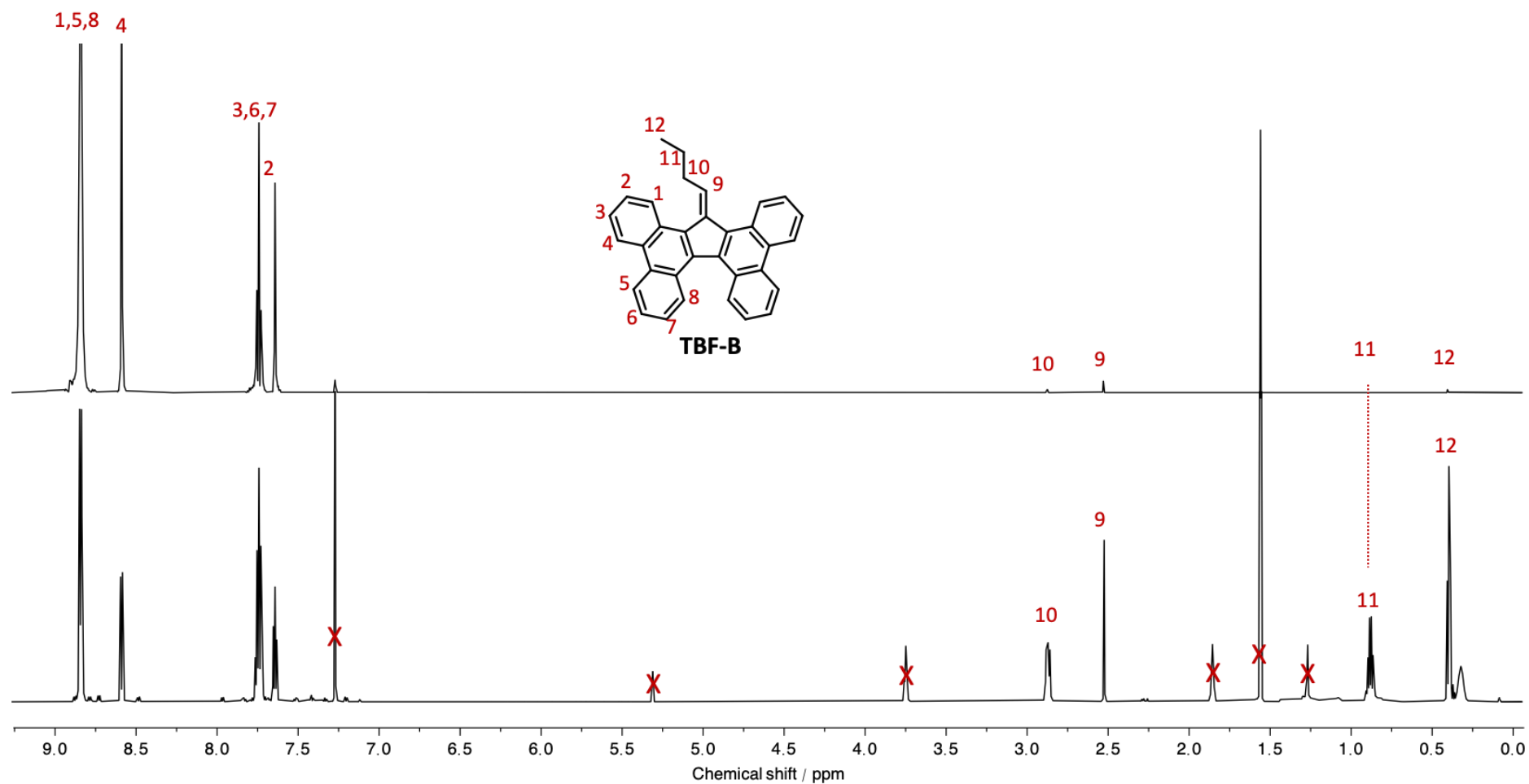
Figure S2.22 Stacked ¹H PSYCHE (top) and ¹H NMR (bottom; CDCl₃, 700 MHz, 298K) spectra of **TBF-B**
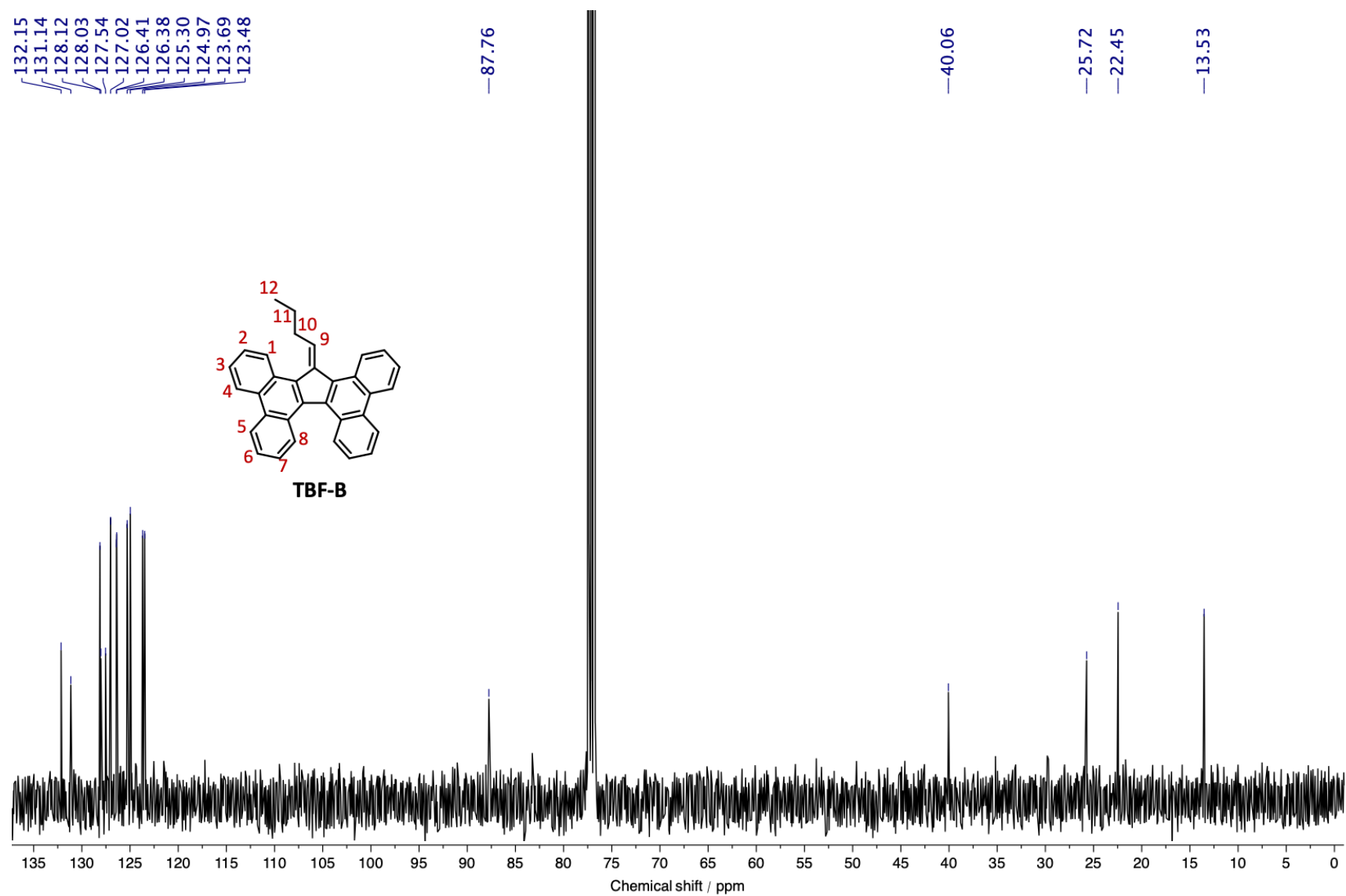
Figure S2.23 ^{13}C NMR (CDCl₃, 101 MHz, 298K) spectrum of **TBF-B**
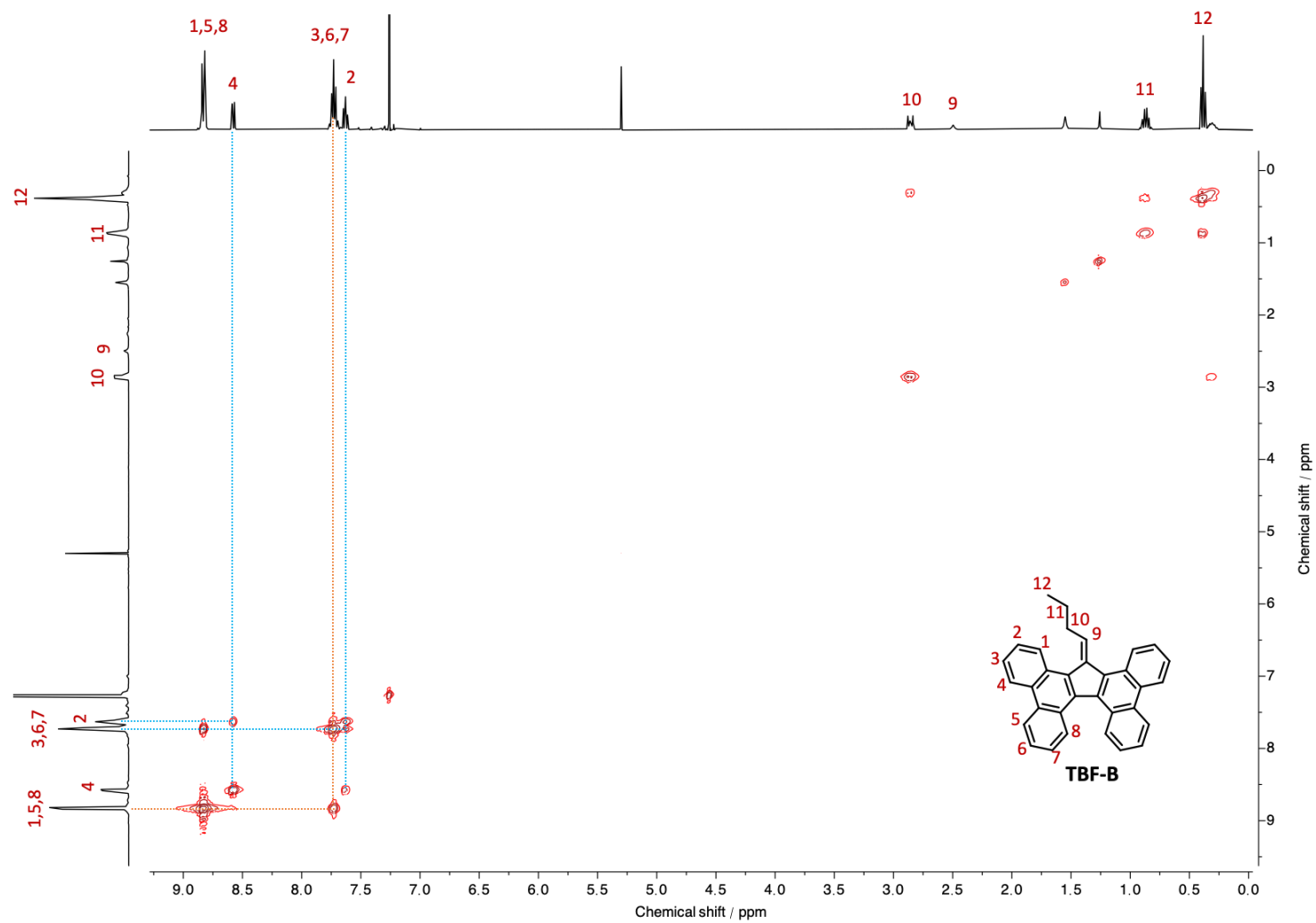
Figure S2.24 Annotated ^1H–^1H COSY NMR (CDCl$_3$, 400 MHz, 298K) spectrum of **TBF-B**
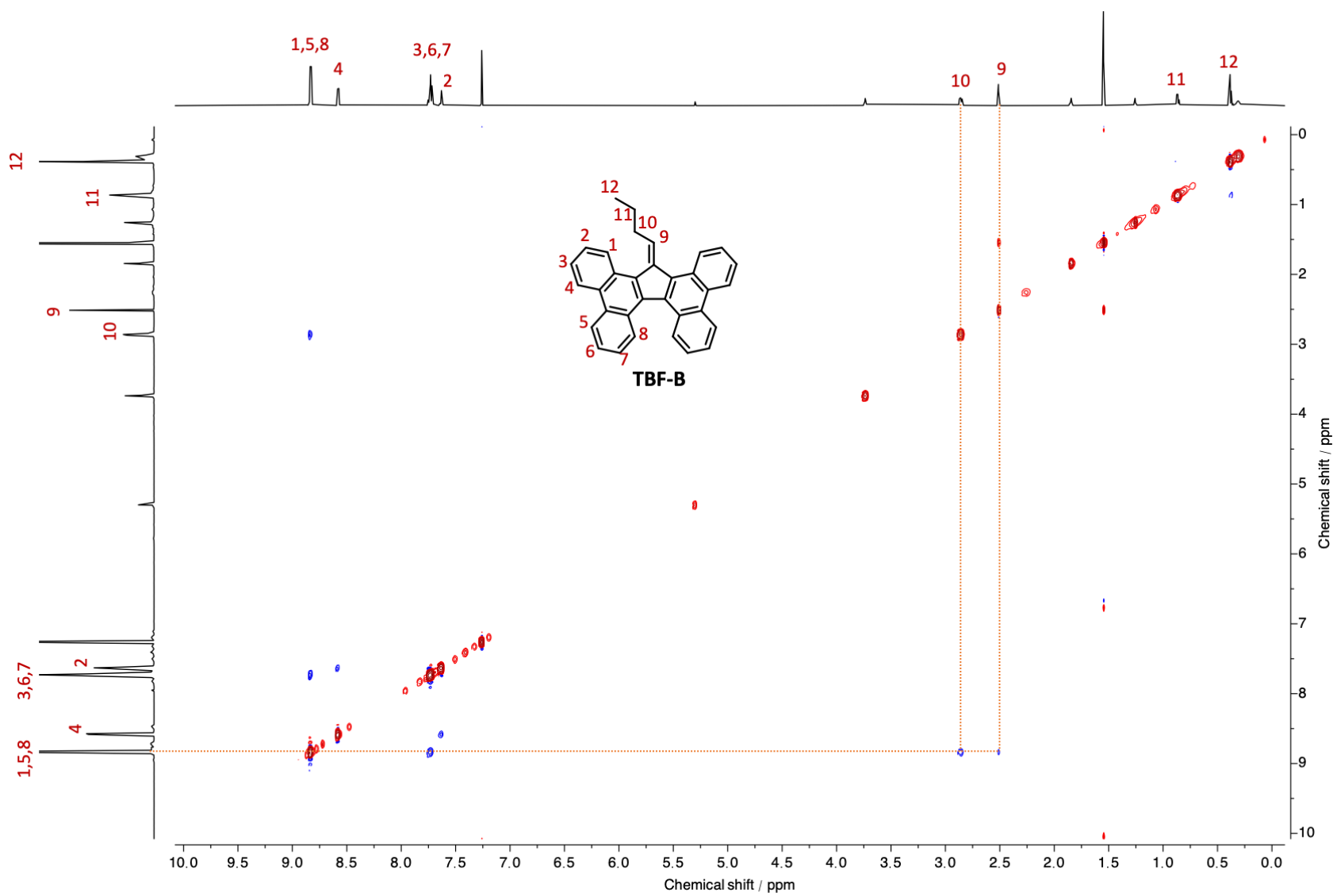
Figure S2.25 Annotated ^{1}H–^{1}H NOESY NMR (CDCl$_3$, 400 MHz, 298K) spectrum of **TBF-B**

2.4.4 X-RAY DIFFRACTION ANALYSES

Tetrabenzofluorenone **TBF=O**

Single crystals of **TBF=O** (aja22022) were grown from THF by slow evaporation.
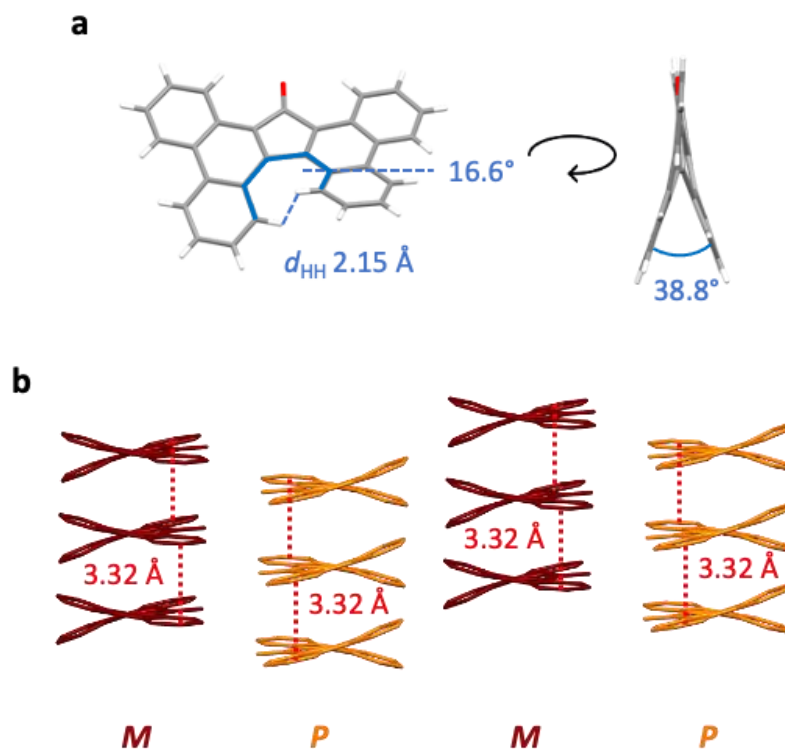
Figure S2.26 (a) Structural parameters of a representative *M*-**TBF=O** highlighted in blue and (b) the supramolecular packing of the racemate. Non-interacting H atoms have been omitted for clarity.

Crystal data for $C_{29}H_{16}O$ (M = 380.42 g/mol): monoclinic, space group P2/c (no. 13), a = 18.2583(3) Å, b = 5.07710(10) Å, c = 19.1389(3) Å, β = 90.3210(10)°, V = 1774.13(5) Å^3, Z = 4, T = 110.00(10) K, μ(Cu Kα) = 0.659 mm^{-1}, D_{calc} = 1.424 g/cm^3, 11113 reflections measured (9.242° $\leq$ 2θ $\leq$ 142.942°), 3420 unique (R_{int} = 0.0214, R_{sigma} = 0.0198) which were used in all calculations. The final R_1 was 0.0378 (I > 2σ(I)) and wR_2 was 0.1005 (all data).

Tetrabenzofluorene **A-OH(1)**

Single crystals of polymorph **A-OH(1)** suitable for X-ray diffraction (aja21017) were grown from 5% EtOAc in *n*-hexanes solution. The crystal contained solvent channels running parallel to the *b*-axis. From the difference map it was apparent that there was a mixture of ethyl acetate and hexane present and there were at least 4 different sites for the solvents within the asymmetric unit. A suitable discrete model for this solvent could not be achieved, therefore a solvent mask was used. The solvent mask estimated 34 electrons per asymmetric unit which is equivalent to approximately about two-thirds of a molecule of solvent.
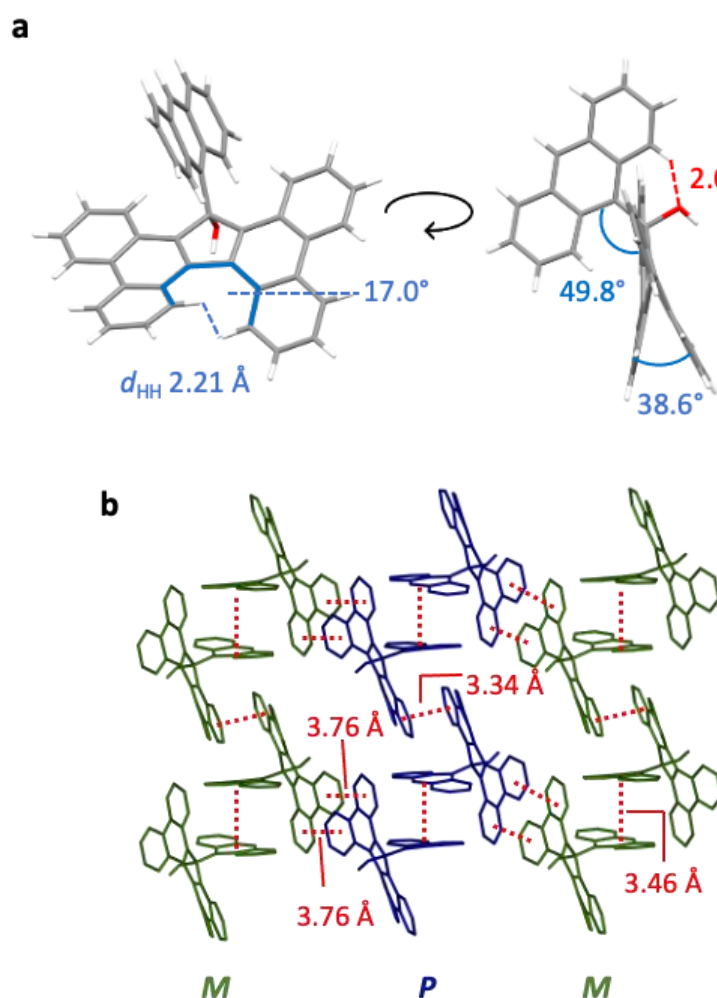
Figure S2.27. (a) Structural parameters of a representative *P*-**A-OH(1)** highlighted in blue and (b) the supramolecular packing or the racemate. Non-interacting H atoms have been omitted for clarity.

Crystal data for $C_{43}H_{26}O$ (M = 558.64 g/mol): monoclinic, space group $P2_1$/c, a = 12.47104(9) Å, b = 10.36805(9) Å, c = 23.90930(17) Å, β = 90.1508(6)°, V = 3091.47(4) Å^3, Z = 4, T = 110.00(10) K, μ(Cu Kα) = 0.542 mm^{-1}, D_{calc} = 1.200 g/cm^3, 22473 reflections measured (7.088° $\leq$ 2θ $\leq$ 134.146°), 5528 unique (R_{int} = 0.0217, R_{sigma} = 0.0182) which were used in all calculations. The final R_1 was 0.0338 (I > 2σ(I)) and wR_2 was 0.0919 (all data).

Tetrabenzofluorene **A-OH(2)**

Single crystals of polymorph **A-OH(2)** suitable for X-ray diffraction (aja21043) were also grown from chloroform. The chloroform molecules exhibited disorder and was modelled with Cl3 and C44 in two positions in a refined ratio of 0.937:0.063(3). For the minor component, the C-Cl bond lengths were restrained to be 1.76 angstroms and the Cl-C-Cl distances restrained to be 2.9 angstroms. The atomic displacement parameters (ADP) of Cl3 & Cl3a were constrained to be equal as were the ADPs of C44 & C44a. The hydroxy hydrogen was located by difference map and allowed to refine.
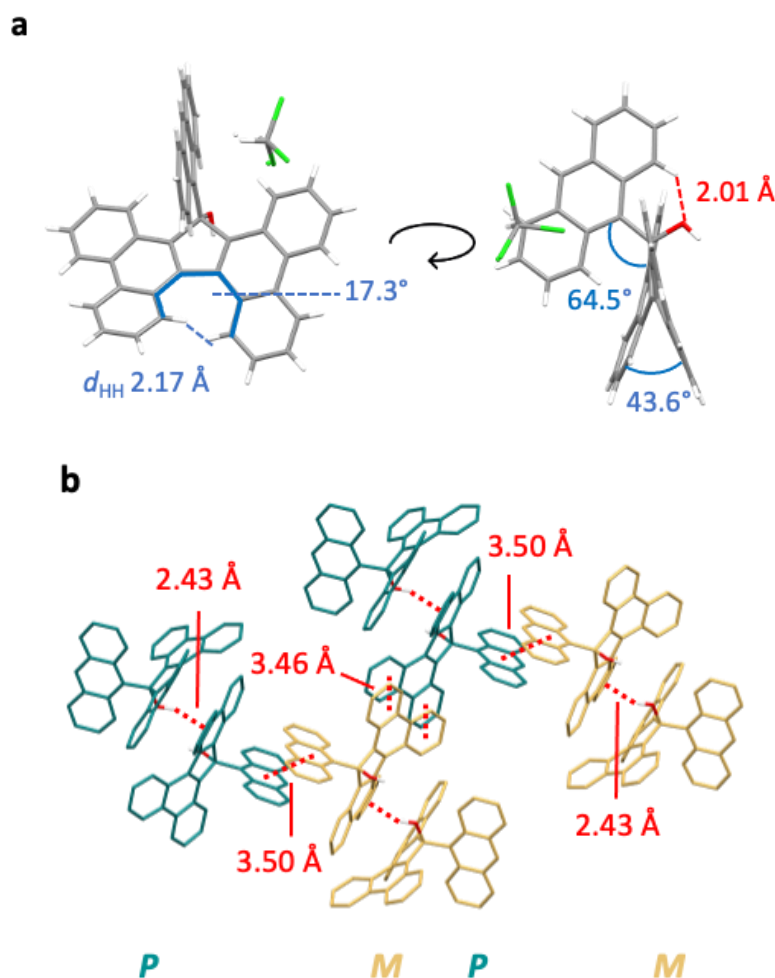
Figure S2.28. (a) Structural parameters of a representative P-**A-OH(2)** highlighted in blue and (b) the supramolecular packing of the racemate. Non-interacting H atoms and solvent molecules have been omitted for clarity.

Crystal data for $C_{44}H_{27}Cl_3O$ (M = 678.00 g/mol): monoclinic, space group P2$_1$/n (no. 14), a = 15.6722(3) Å, b = 10.8852(3) Å, c = 18.8283(4) Å, β = 96.5397(19)°, V = 3191.11(12) Å^3, Z = 4, T = 110.00(10) K, μ(Cu Kα) = 2.883 mm^{-1}, D_{calc} = 1.411 g/cm^3, 11941 reflections measured (6.96° $\leq 2\theta \leq$ 134.156°), 5687 unique (R_{int} = 0.0247, R_{sigma} = 0.0338) which were used in all calculations. The final R_1 was 0.0366 (I > 2σ(I)) and wR_2 was 0.0970 (all data).

Tetrabenzofluorene **A-H(1)**

Single crystals of polymorph **A-H(1)** suitable for X-ray diffraction (aja21050) were grown from CH_2Cl_2 and MeOH by solvent layering. There was a partially occupied solvent void containing dichloromethane. This was disordered and modelled in 4 positions with refined occupancies of 0.353(2): 0.345(3): 0.148(3): 0.0675(15). All C-Cl bond lengths were restrained to be equal and Cl-Cl distances restrained to be 2.9 Å. The ADP of equivalent disordered atoms were constrained to be equal (e.g., Cl1a, Cl1b, Cl1c and Cl1d). Forcing the occupancies to sum to unity significantly reduced the quality (e.g., R_1 worsened by 0.45%).
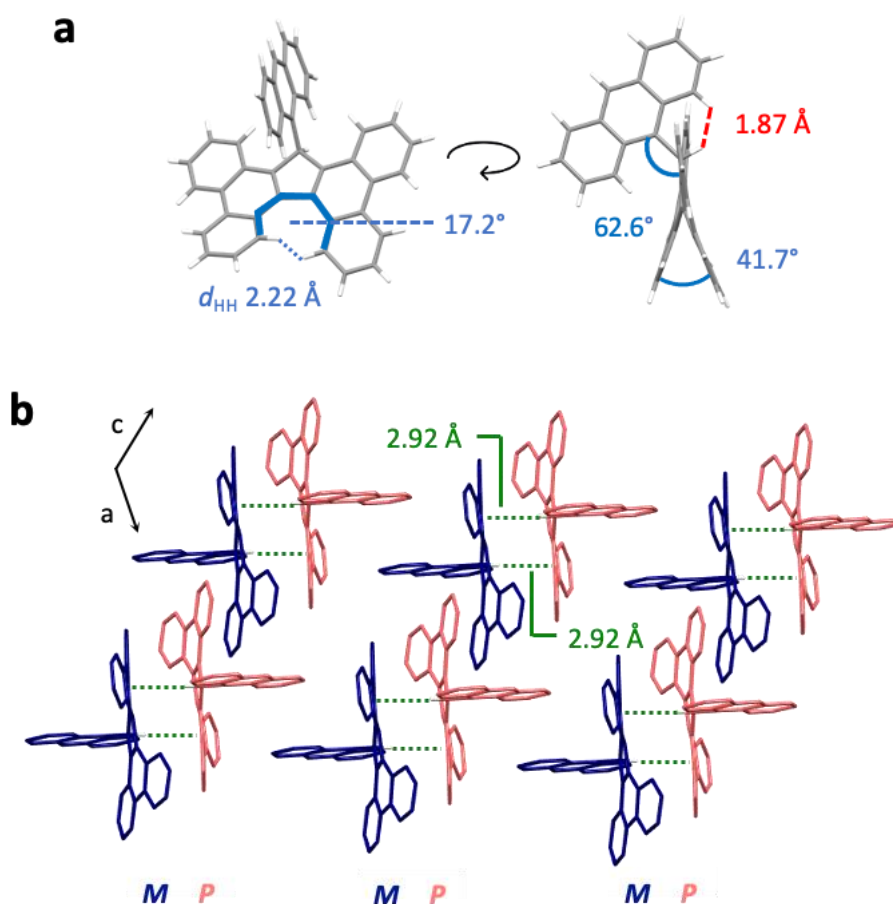
Figure S2.29. (a) Structural parameters of representative *P*-**A-H(1)** highlighted in blue and (b) the supramolecular packing of the racemate. Non-interacting H atoms and solvent molecules have been omitted for clarity.

Crystal data for $C_{43.915}H_{27.825}Cl_{1.825}$ (M =620.16 g/mol): triclinic, space group P-1 (no. 2), a = 11.7092(3) Å, b = 12.5917(4) Å, c = 12.6199(4) Å, α = 115.994(3)°, β = 90.434(3)°, γ = 109.212(3)°, V = 1553.83(10) Å^3, Z = 2, T = 110.00(10) K, μ(Cu Kα) = 1.976 mm^{-1}, D_{calc} = 1.326 g/cm^3, 21595 reflections measured (7.922° $\leq 2\theta \leq$ 134.136°), 5534 unique (R_{int} = 0.0272, R$_{sigma}$ = 0.0241) which were used in all calculations. The final R_1 was 0.0423 (I > 2σ(I)) and wR_2 was 0.1160 (all data).

Tetrabenzofluorene **A-H(2)**

Single crystals of polymorph **A-H(2)** suitable for X-ray diffraction (aja21047) were grown from CH_2Cl_2 solution by slow evaporation. The dichloromethane was disordered and modelled in two positions in a refined ratio of 0.638:0.362(7). The ADPs of C87a &C87b were constrained to be equal as were the ADPs of Cl2a & Cl2b.
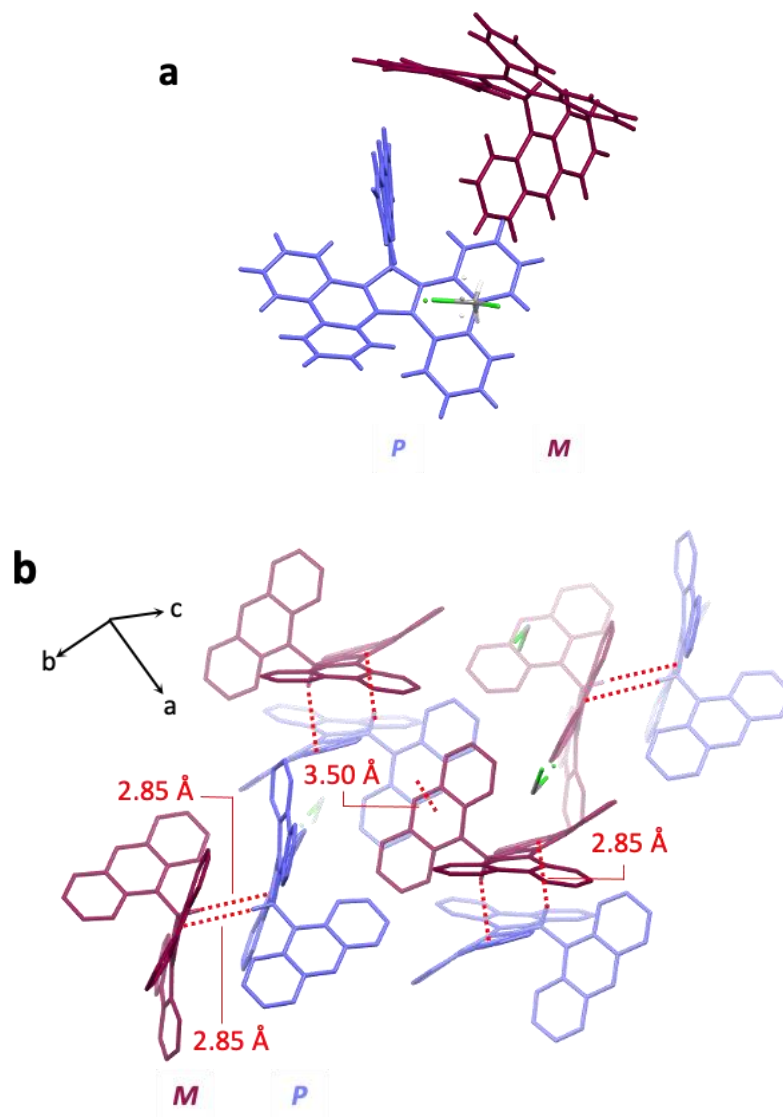
Figure S2.30 (a) Unit cell of *P*-**A-H(2)** and *M*-**A-H(2)** and (b) its supramolecular packing. Non-interacting H atoms have been omitted for clarity.

Crystal data for $C_{87}H_{54}Cl_2$ (*M* =1170.20 g/mol): triclinic, space group P-1 (no. 2), *a* = 12.1074(5) Å, *b* = 13.6029(6) Å, *c* = 17.7307(6) Å, *α* = 91.918(3)°, *β* = 90.342(3)°, *γ* = 98.692(3)°, *V* = 2884.9(2) Å^3, *Z* = 2, *T* = 110.00(10) K, μ(Cu Kα) = 1.410 mm^{-1}, D_{calc} = 1.347 g/cm^3, 19108 reflections measured (6.578° ≤ 2θ ≤ 134.158°), 10305 unique (R_{int} = 0.0350, R_{sigma} = 0.0564) which were used in all calculations. The final R_1 was 0.0465 (I > 2σ(I)) and wR_2 was 0.1233 (all data).

Tetrabenzofluorene polymorph **A-H(3)**

Single crystals of **A-H(3)** suitable for X-ray diffraction (aja21049) were grown from CH_2Cl_2 and MeOH solution by solvent layering.
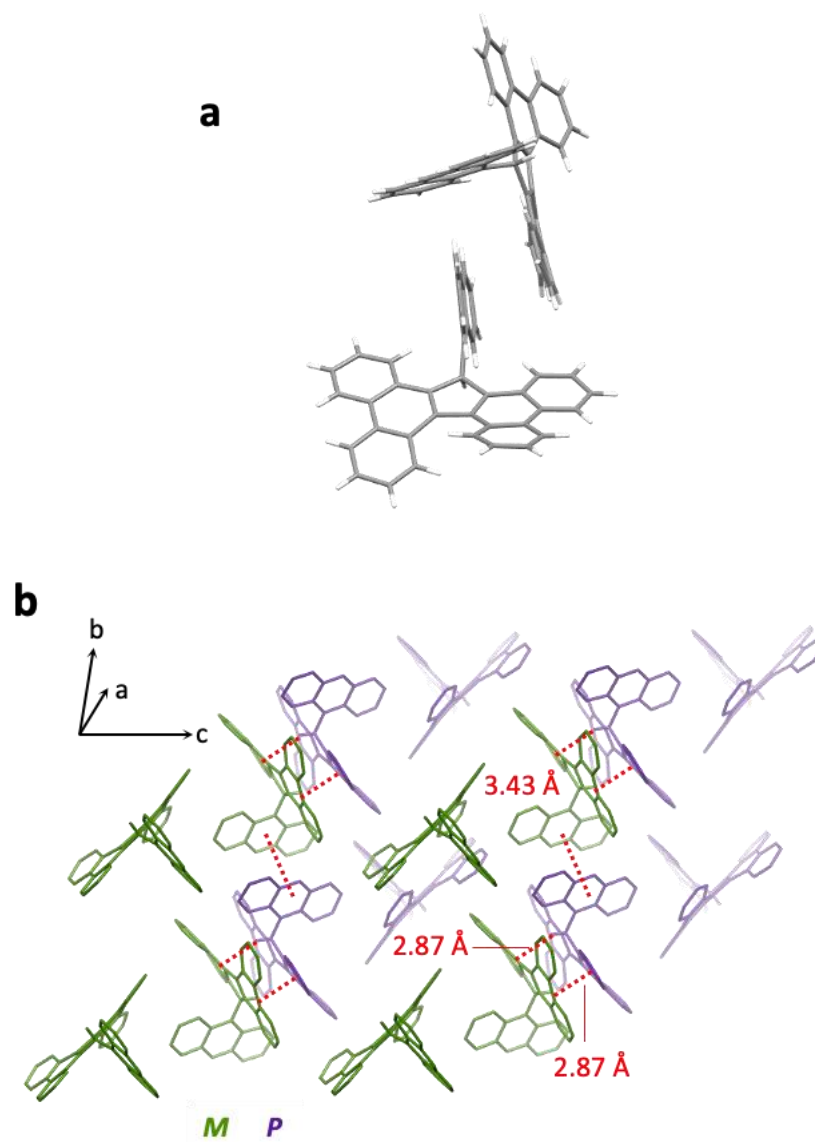
Figure S2.31. (a) Unit cell of a representative *P*-**A-H(3)** and (b) the supramolecular packing of the racemate. Non-interacting H atoms have been omitted for clarity.

Crystal data for $C_{43}H_{26}$ (M =542.64 g/mol): triclinic, space group P-1 (no. 2), a = 12.6766(3) Å, b = 13.0047(5) Å, c = 18.3093(7) Å, α = 76.845(3)°, β = 77.638(3)°, γ = 70.453(3)°, V = 2738.31(17) Å^3, Z = 4, T = 110.00(14) K, μ(Cu Kα) = 0.567 mm^{-1}, D_{calc} = 1.316 g/cm^3, 18354 reflections measured (7.32° $\leq 2\theta \leq$ 134.148°), 9767 unique (R_{int} = 0.0201, R_{sigma} = 0.0278) which were used in all calculations. The final R_1 was 0.0337 (I > 2σ(I)) and wR_2 was 0.0878 (all data).

Tetrabenzofluorene **B-OH**

Single crystals of **B-OH** suitable for X-ray diffraction (aja23018) were grown from a solution of **TBF-B** in CH_2Cl_2, *n*-hexanes and MeOH by vapour diffusion. The crystal contained disordered dichloromethanes, two per asymmetric unit. One was modelled in two positions with refined occupancies of 0.684:0.316(3). The ADPs of pairs of disordered atoms were constrained to be equal (Cl2 & Cl2A, C133 & C134) and C-Cl bond-lengths restrained to be the same (Cl1-C133, C1-C134, Cl2-C133, Cl2-C134). A discrete atom model could not be obtained for the other dichloromethane therefore a solvent mask was used which calculated 42 electrons in a volume of 180 Å^3 per asymmetric unit. Two of the butyl side chains were disordered. For one, the terminal ethyl group was modelled in two positions in a refined ratio of 0.817:0.183(5). The ADPs of disordered pairs of atoms were constrained to be equal (C65 & C65a, C66 & C66a) and C-C bond-lengths restrained to be 1.52 Å (C64-C65, C64-C65a, C65-C66 & C65a-C66a). For the other disordered butyl group, the whole side chain was modelled in two positions in a refined ratio of 0.556:0.444(7).
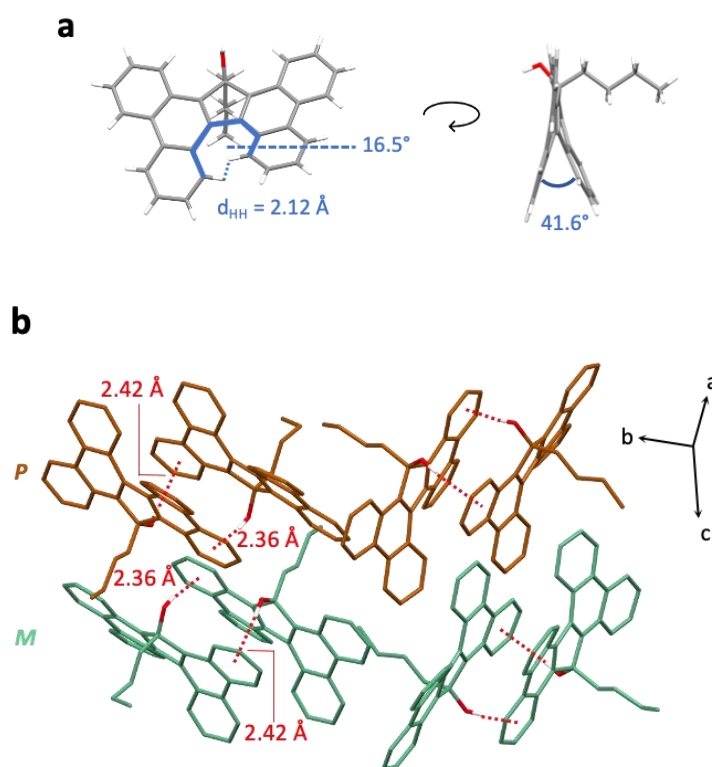
Figure S2.32. (a) Structural parameters of a representative *P*-**B-OH** highlighted in blue and (b) the supramolecular packing of the racemate. Non-interacting H atoms and solvent molecules have been omitted for clarity.

Crystal data for $C_{133}H_{106}Cl_2O_4$ (M =1839.07 g/mol): triclinic, space group P-1 (no. 2), a = 17.4084(2) Å, b = 18.4113(2) Å, c = 19.3835(3) Å, α = 117.4140(13)°, β = 110.8594(12)°, γ = 93.8416(10)°, V = 4949.77(13) Å^3, Z = 2, T = 110.00(14) K, μ(Cu Kα) = 1.039 mm^{-1}, D_{calc} = 1.234 g/cm^3, 54499 reflections measured (7.242° ≤ 2θ ≤ 134.158°), 17625 unique (R_{int} = 0.0174, R$_{sigma}$ = 0.0192) which were used in all calculations. The final R_1 was 0.0551 (I > 2σ(I)) and wR_2 was 0.0585 (all data).

Tetrabenzofluorene **17,17-dibutylTBF**[14] (CCDC 792538)

The X-ray crystal structure of 17,17-dibutylTBF was analysed in order to draw conclusions about intermolecular interactions that are likely to present in the crystal structure of **B-H**.
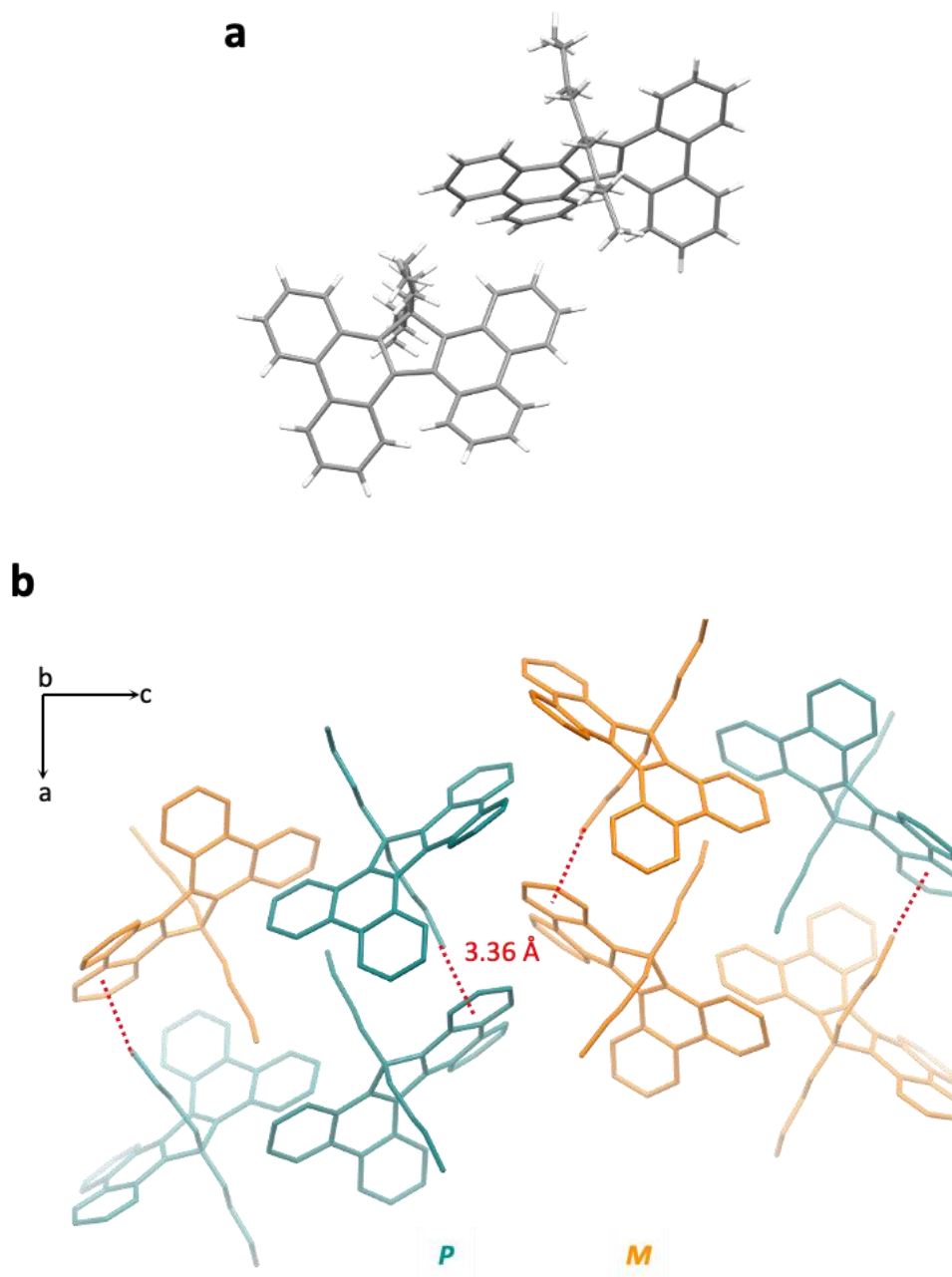
Figure S2.33. (a) Unit cell of *P*-**A-H(3)** and (b) its supramolecular packing

2.4.5 HIRSCHFELD ANALYSES

Table S2.1 Summary of the contributions (%) of intermolecular interactions for crystals structures of the TBF library determined by Hirschfeld analyses.

Interaction Type	A-OH(1)	A-OH(2)	A-H(1)	A-H(2)	A-H(3)	B-OH
C···C	6.3	7.7	6.8	6.8	9.6	3.3
C···H	35.2	31.7	38.1	40.6	38.2	33.8
H···H	45.8	59.8	45.4	49.1	52.2	57.9

Not all atom interactions are shown in the table above (e.g., interactions with solvent Cl atoms and O atoms are not given, hence not all percentages will add to 100%)
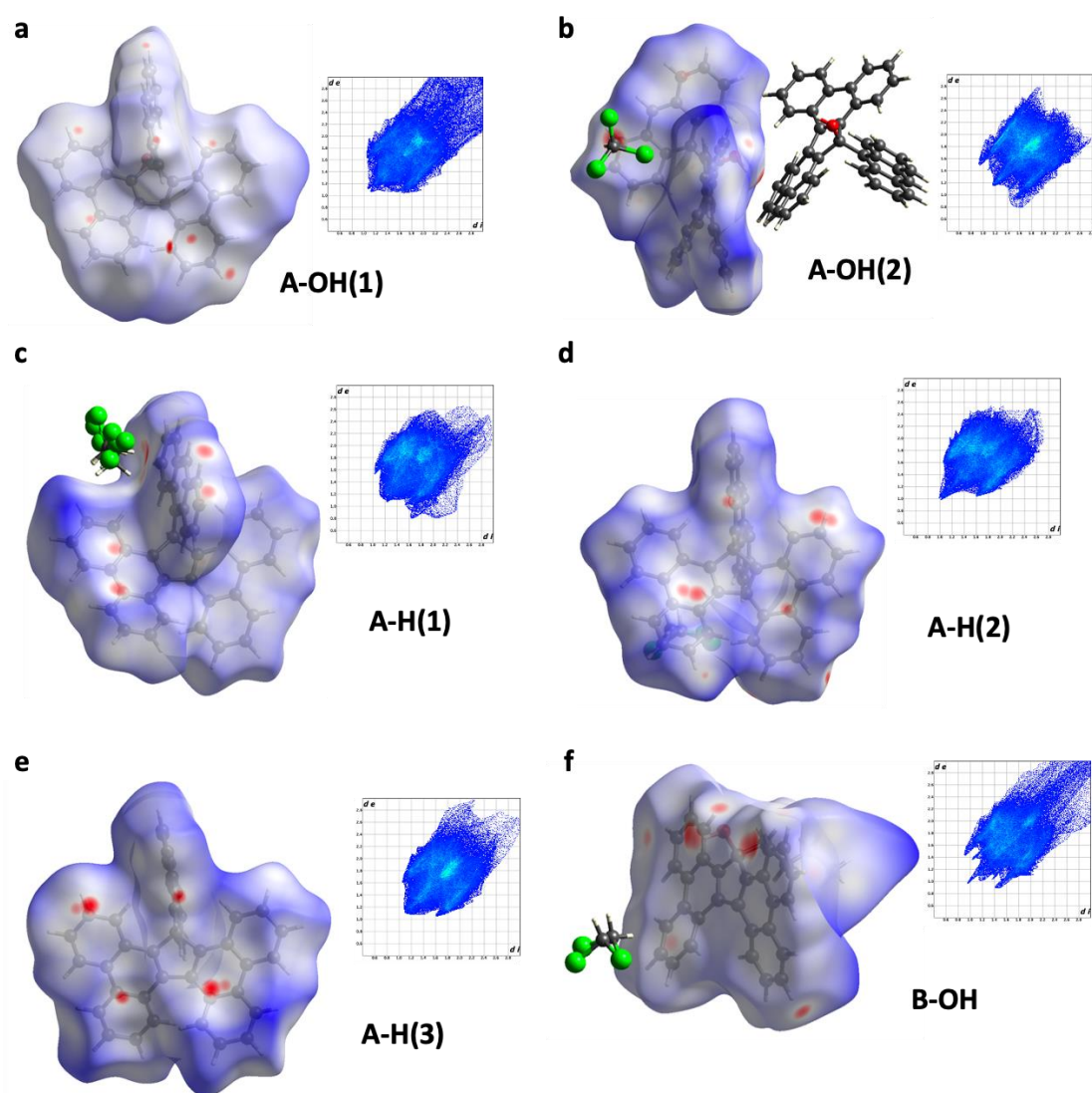
Figure S2.34. Hirschfeld surfaces along with their fingerprint regions for (a) **A-OH(1)**, (b) **A-OH(2)**, (c) **A-H(1)**, (d) **A-H(2)**, (e) **A-H(3)** and (f) **B-OH**.

2.4.6 DFT ANALYSES

DFT calculations were performed to obtain geometrically optimised structures of both enantiomers (only one representative enantiomer is shown in Figure S2.35) of **A-OH**, **A-H**, **B-OH** and **B-H** using B3LYP(GD3BJ)/6-31G(d,p) in a CH_2Cl_2 solvent model. Ground state geometries were verified by convergence to a minimum stationary point and no negative vibrational frequencies observed. Time-dependent DFT (TD-DFT) calculations were performed for the first 20 states of each compound using B3LYP(GD3BJ)/6-31G(d,p) in a CH_2Cl_2 solvent model and in some cases natural transition orbital (NTO) analysis was performed on specific excited states to understand qualitatively what occupations of orbitals gave rise to those excited state transitions.
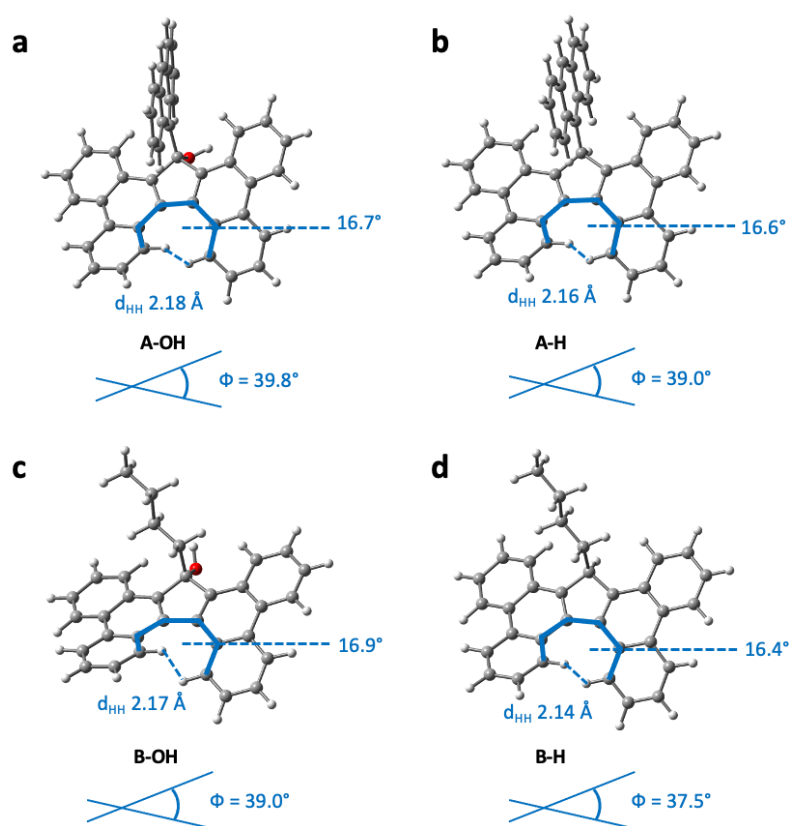
Figure S2.35. DFT optimised structures (B3LYP-GD3BJ/6-31G(d,p) in CH_2Cl_2) with key structural parameters highlighted in blue for a representative *P*-enantiomer (a) **A-OH**, (b) **A-H**, (c) **B-OH** and (d) **B-H**

Table S2.2 Comparison of DFT structural parameters from a representative *P*-enantiomer for each compound in the TBF library

Compound	A-OH	A-H	B-OH	B-H
d_{HH}[a] / Å	2.18	2.16	2.17	2.14
θ[b] / °	16.7	16.6	16.9	16.4
Φ[c] / °	39.8	39.0	39.0	37.5

2.4.6.1 CARTESIAN COORDINATES

P-**A-OH**

C	-6.739712	5.415108	3.613778
C	-6.150542	4.534695	2.728217
C	-6.632112	4.387174	1.404865
C	-7.681578	5.248445	0.955055
C	-8.279537	6.119596	1.895111
C	-7.834537	6.193309	3.201098
H	-6.346244	5.514853	4.620296
H	-9.081663	6.777148	1.583778
H	-8.308300	6.880177	3.895138
C	-7.259707	4.547427	-1.398815
C	-6.228978	3.695261	-0.902227
C	-8.051924	5.271678	-0.452731
C	-9.137554	6.035170	-0.937206
C	-7.557354	4.660265	-2.778679
C	-9.418810	6.114407	-2.288398
H	-9.774123	6.569440	-0.242577
C	-8.615431	5.429502	-3.217607
H	-6.955698	4.123601	-3.496216
H	-10.260935	6.707878	-2.629882
H	-8.831874	5.496221	-4.279126
C	-6.018385	3.500064	0.446752
C	-5.237240	2.856330	-1.717749
C	-4.391576	2.218560	-0.598970
C	-4.982952	2.450526	0.621788
C	-3.264558	1.359723	-0.762183
C	-4.631101	1.635083	1.757734
C	-2.745471	0.705795	0.400129
C	-2.620060	1.168967	-2.010868
C	-5.443147	1.540037	2.913679
C	-3.477343	0.794688	1.656546
C	-1.565833	-0.058370	0.261318
H	-3.008514	1.663254	-2.891736
C	-1.483274	0.392439	-2.112471
C	-5.087754	0.735542	3.977983
C	-3.127898	0.003987	2.775976
C	-0.944182	-0.213856	-0.964382
H	-1.128073	-0.538177	1.128080
H	-0.999512	0.264098	-3.075425

C	-3.901881	-0.016270	3.920342
H	-5.731509	0.675409	4.849652
H	-2.253102	-0.632812	2.732026
H	-0.038747	-0.807710	-1.037423
H	-3.610999	-0.641837	4.758150
C	-2.402420	5.888412	-0.521019
C	-3.356456	4.998024	-0.939737
C	-3.468837	4.589841	-2.309569
C	-2.533083	5.195546	-3.228910
C	-1.542592	6.110537	-2.754751
C	-1.468807	6.450080	-1.433003
C	-4.426706	3.645714	-2.779659
C	-2.595692	4.876129	-4.582661
C	-3.579270	4.026337	-5.081517
C	-4.535550	3.405530	-4.182218
C	-5.544999	2.596965	-4.818498
H	-6.315960	2.150326	-4.214265
C	-5.579144	2.403709	-6.175073
C	-4.606724	2.983978	-7.032423
C	-3.638014	3.778249	-6.488822
H	-2.367376	6.174317	0.525684
H	-4.054552	4.628363	-0.210778
H	-0.853492	6.534154	-3.479587
H	-0.716568	7.148344	-1.080445
H	-1.875186	5.314540	-5.267784
H	-6.373389	1.797957	-6.600719
H	-4.647055	2.808580	-8.102579
H	-2.891222	4.255596	-7.116694
O	-6.006713	1.761364	-2.247583
H	-5.382977	1.081772	-2.544824
H	-6.376270	2.085660	2.947549
H	-5.282692	3.970015	3.039280

M-**A-OH**

C	-6.739712	5.415108	-3.613778
C	-6.150542	4.534695	-2.728217
C	-6.632112	4.387174	-1.404865
C	-7.681578	5.248445	-0.955055
C	-8.279537	6.119596	-1.895111
C	-7.834537	6.193309	-3.201098

H	-6.346244	5.514853	-4.620296
H	-9.081663	6.777147	-1.583778
H	-8.308300	6.880177	-3.895138
C	-7.259707	4.547427	1.398815
C	-6.228978	3.695261	0.902227
C	-8.051924	5.271678	0.452731
C	-9.137554	6.035170	0.937206
C	-7.557354	4.660265	2.778679
C	-9.418810	6.114407	2.288398
H	-9.774123	6.569440	0.242577
C	-8.615431	5.429502	3.217607
H	-6.955698	4.123601	3.496216
H	-10.260935	6.707878	2.629882
H	-8.831874	5.496221	4.279126
C	-6.018385	3.500064	-0.446752
C	-5.237240	2.856330	1.717749
C	-4.391576	2.218560	0.598970
C	-4.982952	2.450526	-0.621788
C	-3.264558	1.359723	0.762183
C	-4.631101	1.635083	-1.757734
C	-2.745471	0.705795	-0.400129
C	-2.620060	1.168966	2.010868
C	-5.443147	1.540037	-2.913679
C	-3.477343	0.794688	-1.656546
C	-1.565833	-0.058370	-0.261318
H	-3.008514	1.663254	2.891736
C	-1.483274	0.392439	2.112471
C	-5.087754	0.735542	-3.977983
C	-3.127898	0.003987	-2.775976
C	-0.944182	-0.213856	0.964382
H	-1.128073	-0.538177	-1.128080
H	-0.999512	0.264098	3.075425
C	-3.901881	-0.016270	-3.920342
H	-5.731509	0.675409	-4.849652
H	-2.253102	-0.632812	-2.732027
H	-0.038747	-0.807710	1.037423
H	-3.610999	-0.641837	-4.758150
C	-2.402420	5.888411	0.521019
C	-3.356456	4.998024	0.939737
C	-3.468837	4.589841	2.309569
C	-2.533083	5.195546	3.228910

C	-1.542592	6.110537	2.754751
C	-1.468807	6.450080	1.433003
C	-4.426706	3.645714	2.779659
C	-2.595692	4.876129	4.582661
C	-3.579270	4.026337	5.081517
C	-4.535550	3.405530	4.182218
C	-5.544999	2.596965	4.818498
H	-6.315959	2.150326	4.214265
C	-5.579144	2.403709	6.175073
C	-4.606724	2.983978	7.032423
C	-3.638014	3.778249	6.488822
H	-2.367376	6.174317	-0.525684
H	-4.054552	4.628363	0.210778
H	-0.853492	6.534154	3.479587
H	-0.716568	7.148344	1.080445
H	-1.875186	5.314540	5.267784
H	-6.373389	1.797957	6.600719
H	-4.647055	2.808580	8.102579
H	-2.891222	4.255596	7.116694
O	-6.006713	1.761364	2.247583
H	-5.382977	1.081771	2.544824
H	-6.376270	2.085660	-2.947549
H	-5.282692	3.970015	-3.039280

P-**A**-**H**

C	-6.715486	5.421910	3.623602
C	-6.145631	4.520967	2.744855
C	-6.586738	4.416039	1.404230
C	-7.571398	5.340559	0.933347
C	-8.150921	6.232923	1.864348
C	-7.749013	6.266283	3.186300
H	-6.351528	5.485694	4.644157
H	-8.902977	6.938897	1.534182
H	-8.207245	6.970665	3.873226
C	-7.119319	4.646557	-1.415720
C	-6.136426	3.746676	-0.901667
C	-7.899382	5.400026	-0.485535
C	-8.933803	6.217640	-0.992883
C	-7.383679	4.767210	-2.801608
C	-9.179067	6.313493	-2.350578
H	-9.561539	6.779297	-0.311758

94

C	-8.393780	5.587004	-3.263394
H	-6.797286	4.192354	-3.505598
H	-9.982932	6.948398	-2.709401
H	-8.587928	5.660550	-4.328790
C	-5.981192	3.513492	0.450552
C	-5.157477	2.897886	-1.698161
C	-4.426610	2.141203	-0.598824
C	-5.015171	2.405725	0.623573
C	-3.336916	1.229088	-0.743710
C	-4.715387	1.565638	1.760045
C	-2.852215	0.563347	0.425015
C	-2.696429	1.001671	-1.986440
C	-5.549839	1.495318	2.900828
C	-3.595576	0.680638	1.673235
C	-1.700361	-0.245133	0.300767
H	-3.077306	1.487932	-2.874163
C	-1.586268	0.186038	-2.075021
C	-5.244229	0.672947	3.967715
C	-3.295435	-0.128230	2.793878
C	-1.074554	-0.429262	-0.918690
H	-1.288371	-0.735985	1.174115
H	-1.104217	0.029004	-3.034781
C	-4.087834	-0.123692	3.926164
H	-5.904958	0.633995	4.827906
H	-2.446326	-0.799660	2.759401
H	-0.190332	-1.055587	-0.981479
H	-3.835189	-0.764134	4.765215
C	-2.420474	6.075392	-0.595115
C	-3.272088	5.064505	-0.955136
C	-3.453905	4.690152	-2.325466
C	-2.691755	5.419704	-3.313007
C	-1.815717	6.469968	-2.897195
C	-1.681140	6.794471	-1.575480
C	-4.327695	3.654347	-2.733148
C	-2.819489	5.090854	-4.662695
C	-3.664128	4.063491	-5.084088
C	-4.434957	3.322673	-4.108292
C	-5.273080	2.274185	-4.615157
H	-5.867732	1.675913	-3.936736
C	-5.349630	1.991256	-5.954117
C	-4.592590	2.732276	-6.902717
C	-3.773298	3.738639	-6.471569
H	-2.306868	6.331132	0.453770
H	-3.811845	4.537897	-0.184913
H	-1.257621	7.003229	-3.661402
H	-1.013233	7.593278	-1.269228
H	-2.247094	5.644436	-5.402121
H	-5.995899	1.188566	-6.294776
H	-4.667456	2.494161	-7.958722
H	-3.183245	4.315769	-7.177630
H	-5.740238	2.133261	-2.219322
H	-6.461885	2.076290	2.921884
H	-5.320829	3.906501	3.077714

M-**A**-**H**

C	-6.715485	5.421913	-3.623600
C	-6.145628	4.520970	-2.744854
C	-6.586736	4.416041	-1.404229
C	-7.571398	5.340560	-0.933346
C	-8.150923	6.232922	-1.864348
C	-7.749014	6.266283	-3.186299
H	-6.351526	5.485698	-4.644155
H	-8.902981	6.938894	-1.534183
H	-8.207247	6.970664	-3.873226
C	-7.119321	4.646555	1.415720
C	-6.136426	3.746676	0.901667
C	-7.899383	5.400025	0.485535
C	-8.933806	6.217638	0.992884
C	-7.383683	4.767206	2.801609
C	-9.179071	6.313488	2.350579
H	-9.561541	6.779296	0.311759
C	-8.393785	5.586998	3.263394
H	-6.797289	4.192350	3.505599
H	-9.982937	6.948392	2.709402
H	-8.587934	5.660543	4.328791
C	-5.981190	3.513493	-0.450551
C	-5.157477	2.897886	1.698162
C	-4.426610	2.141204	0.598825
C	-5.015170	2.405726	-0.623573
C	-3.336916	1.229086	0.743711
C	-4.715386	1.565640	-1.760045
C	-2.852215	0.563346	-0.425014

C	-2.696432	1.001667	1.986442
C	-5.549836	1.495322	-2.900829
C	-3.595575	0.680640	-1.673235
C	-1.700363	-0.245136	-0.300766
H	-3.077309	1.487928	2.874165
C	-1.586273	0.186032	2.075024
C	-5.244226	0.672951	-3.967716
C	-3.295433	-0.128228	-2.793878
C	-1.074558	-0.429268	0.918693
H	-1.288373	-0.735988	-1.174114
H	-1.104223	0.028996	3.034784
C	-4.087832	-0.123689	-3.926165
H	-5.904954	0.634001	-4.827908
H	-2.446325	-0.799660	-2.759401
H	-0.190337	-1.055594	0.981482
H	-3.835186	-0.764130	-4.765216
C	-2.420473	6.075391	0.595112
C	-3.272088	5.064506	0.955134
C	-3.453905	4.690153	2.325465
C	-2.691753	5.419705	3.313005
C	-1.815715	6.469969	2.897192
C	-1.681139	6.794471	1.575476
C	-4.327695	3.654350	2.733148
C	-2.819487	5.090856	4.662693
C	-3.664126	4.063494	5.084087
C	-4.434957	3.322675	4.108291
C	-5.273079	2.274188	4.615158
H	-5.867733	1.675916	3.936738
C	-5.349629	1.991260	5.954118
C	-4.592587	2.732280	6.902717
C	-3.773295	3.738642	6.471568
H	-2.306867	6.331130	-0.453773
H	-3.811846	4.537897	0.184912
H	-1.257618	7.003229	3.661399
H	-1.013231	7.593276	1.269223
H	-2.247091	5.644438	5.402119
H	-5.995898	1.188571	6.294777
H	-4.667452	2.494165	7.958723
H	-3.183241	4.315772	7.177629
H	-5.740236	2.133261	2.219324
H	-6.461882	2.076295	-2.921886

H	-5.320826	3.906506	-3.077712

P-**B-OH**

C	-6.685427	5.463082	3.649650
C	-6.128002	4.572957	2.752781
C	-6.660239	4.406067	1.451406
C	-7.737447	5.250665	1.036603
C	-8.298079	6.135770	1.986197
C	-7.798414	6.232840	3.271019
H	-6.251765	5.578361	4.637929
H	-9.115010	6.785578	1.696891
H	-8.244208	6.930147	3.973179
C	-7.415996	4.516090	-1.321814
C	-6.314667	3.726124	-0.868740
C	-8.185504	5.228802	-0.348323
C	-9.334121	5.926540	-0.783831
C	-7.824628	4.546357	-2.679300
C	-9.707764	5.944599	-2.114871
H	-9.950230	6.451826	-0.064022
C	-8.945104	5.250004	-3.071084
H	-7.265088	3.969662	-3.401669
H	-10.597345	6.487495	-2.418119
H	-9.246582	5.252098	-4.113841
C	-6.069480	3.522604	0.474980
C	-5.214506	3.043762	-1.684481
C	-4.569663	2.141426	-0.633489
C	-5.082945	2.421411	0.612889
C	-3.519788	1.195866	-0.838645
C	-4.732546	1.592105	1.741709
C	-2.985543	0.521940	0.303969
C	-2.970784	0.927510	-2.118110
C	-5.488087	1.561745	2.938371
C	-3.641258	0.678291	1.596039
C	-1.870843	-0.325815	0.116578
H	-3.422294	1.385416	-2.987287
C	-1.891952	0.079378	-2.266255
C	-5.129603	0.750055	3.996643
C	-3.284753	-0.118772	2.708674
C	-1.326350	-0.538487	-1.136664
H	-1.422381	-0.824845	0.966960
H	-1.481534	-0.109580	-3.253192

C	-3.997957	-0.075796	3.891419	H	-7.265088	3.969663	3.401669
H	-5.730719	0.741940	4.900294	H	-10.597346	6.487495	2.418120
H	-2.455527	-0.810871	2.630162	H	-9.246583	5.252098	4.113842
H	-0.468367	-1.193946	-1.247346	C	-6.069481	3.522604	-0.474980
H	-3.703806	-0.708082	4.723112	C	-5.214506	3.043762	1.684481
H	-6.382687	2.164244	3.011666	C	-4.569663	2.141426	0.633489
H	-5.244205	4.017109	3.035194	C	-5.082945	2.421412	-0.612889
C	-4.158788	4.106748	-2.113307	C	-3.519788	1.195866	0.838645
H	-3.821660	4.611085	-1.202337	C	-4.732546	1.592106	-1.741709
H	-3.290207	3.563133	-2.503023	C	-2.985543	0.521940	-0.303970
C	-4.597643	5.155950	-3.137501	C	-2.970784	0.927510	2.118110
H	-4.992226	4.678653	-4.046017	C	-5.488088	1.561745	-2.938371
H	-5.415701	5.759109	-2.732750	C	-3.641258	0.678291	-1.596039
C	-3.438884	6.074628	-3.539872	C	-1.870843	-0.325815	-0.116578
H	-2.620816	5.469312	-3.951736	H	-3.422294	1.385416	2.987287
H	-3.037963	6.559447	-2.640317	C	-1.891952	0.079378	2.266255
C	-3.857153	7.138741	-4.556050	C	-5.129603	0.750055	-3.996644
H	-3.016624	7.785384	-4.826431	C	-3.284753	-0.118772	-2.708675
H	-4.234417	6.677890	-5.475829	C	-1.326350	-0.538487	1.136664
H	-4.653643	7.774436	-4.153883	H	-1.422381	-0.824845	-0.966960
O	-5.690445	2.283431	-2.799666	H	-1.481534	-0.109580	3.253192
H	-5.343107	2.679238	-3.609201	C	-3.997957	-0.075796	-3.891419

M-B-OH

				H	-5.730719	0.741940	-4.900295
				H	-2.455527	-0.810871	-2.630163
C	-6.685428	5.463083	-3.649650	H	-0.468367	-1.193946	1.247346
C	-6.128002	4.572957	-2.752781	H	-3.703806	-0.708082	-4.723112
C	-6.660239	4.406067	-1.451407	H	-6.382687	2.164244	-3.011667
C	-7.737448	5.250665	-1.036603	H	-5.244206	4.017109	-3.035194
C	-8.298079	6.135771	-1.986197	C	-4.158788	4.106748	2.113307
C	-7.798415	6.232841	-3.271019	H	-3.821660	4.611086	1.202337
H	-6.251765	5.578361	-4.637930	H	-3.290207	3.563133	2.503023
H	-9.115011	6.785578	-1.696891	C	-4.597643	5.155950	3.137501
H	-8.244209	6.930147	-3.973180	H	-4.992226	4.678654	4.046017
C	-7.415996	4.516091	1.321814	H	-5.415701	5.759109	2.732751
C	-6.314667	3.726124	0.868740	C	-3.438884	6.074629	3.539873
C	-8.185504	5.228802	0.348323	H	-2.620816	5.469312	3.951736
C	-9.334122	5.926541	0.783831	H	-3.037963	6.559448	2.640318
C	-7.824629	4.546357	2.679300	C	-3.857153	7.138742	4.556050
C	-9.707765	5.944599	2.114871	H	-3.016625	7.785384	4.826431
H	-9.950231	6.451827	0.064022	H	-4.234417	6.677891	5.475829
C	-8.945105	5.250004	3.071084	H	-4.653643	7.774437	4.153883

O	-5.690445	2.283431	2.799667
H	-5.343107	2.679238	3.609201

P–**B-H**

C	-6.810069	5.403894	3.752254
C	-6.210436	4.547738	2.848726
C	-6.698305	4.407804	1.527520
C	-7.776464	5.247390	1.103339
C	-8.379980	6.097496	2.058062
C	-7.922664	6.166892	3.360632
H	-6.408465	5.498234	4.756230
H	-9.197703	6.742525	1.759913
H	-8.401152	6.837770	4.067026
C	-7.375832	4.583216	-1.261100
C	-6.270288	3.803937	-0.800901
C	-8.186071	5.255645	-0.294564
C	-9.338781	5.934981	-0.747349
C	-7.749888	4.624919	-2.626674
C	-9.679006	5.967232	-2.087735
H	-9.986365	6.431736	-0.034765
C	-8.877568	5.307227	-3.036908
H	-7.151059	4.088080	-3.352509
H	-10.574021	6.493372	-2.404161
H	-9.153628	5.320178	-4.086520
C	-6.061098	3.560938	0.544990
C	-5.183626	3.132677	-1.615152
C	-4.554680	2.214252	-0.589695
C	-5.074150	2.461866	0.665708
C	-3.518770	1.260124	-0.818283
C	-4.723771	1.598705	1.771099
C	-2.987885	0.549249	0.301520
C	-2.993604	1.012097	-2.110888
C	-5.475474	1.537519	2.968671
C	-3.633701	0.686297	1.601351
C	-1.895441	-0.318838	0.079023
H	-3.433482	1.512435	-2.966133
C	-1.937581	0.142157	-2.295240
C	-5.112683	0.703189	4.008073
C	-3.271256	-0.132934	2.695774
C	-1.372982	-0.514437	-1.186820
H	-1.449440	-0.851604	0.910071

H	-1.543780	-0.033169	-3.291337
C	-3.979178	-0.116801	3.882430
H	-5.711562	0.674282	4.912858
H	-2.439418	-0.819820	2.599858
H	-0.533193	-1.188086	-1.324418
H	-3.679549	-0.764922	4.699871
H	-6.371413	2.135601	3.058429
H	-5.325194	4.000388	3.143116
C	-4.122982	4.175903	-2.090574
H	-3.816257	4.754042	-1.210779
H	-3.236385	3.623194	-2.418067
C	-4.546600	5.125283	-3.210210
H	-4.903817	4.544490	-4.072116
H	-5.387211	5.746811	-2.885624
C	-3.397777	6.033995	-3.659797
H	-2.555442	5.415569	-3.997212
H	-3.031170	6.603987	-2.795866
C	-3.808474	6.998227	-4.774422
H	-2.974453	7.638250	-5.079235
H	-4.152222	6.452098	-5.660124
H	-4.628131	7.648443	-4.448908
H	-5.561083	2.576944	-2.481777

M–**B-H**

C	-6.810069	5.403894	-3.752253
C	-6.210435	4.547738	-2.848725
C	-6.698305	4.407804	-1.527519
C	-7.776464	5.247390	-1.103338
C	-8.379980	6.097496	-2.058061
C	-7.922664	6.166892	-3.360631
H	-6.408465	5.498235	-4.756229
H	-9.197703	6.742525	-1.759912
H	-8.401152	6.837770	-4.067025
C	-7.375832	4.583215	1.261101
C	-6.270287	3.803936	0.800901
C	-8.186071	5.255645	0.294564
C	-9.338781	5.934980	0.747350
C	-7.749888	4.624919	2.626675
C	-9.679006	5.967231	2.087736
H	-9.986365	6.431735	0.034766
C	-8.877568	5.307226	3.036909

H	-7.151059	4.088080	3.352509	C	-3.808474	6.998229	4.774419
H	-10.574021	6.493371	2.404162	H	-2.974453	7.638252	5.079232
H	-9.153628	5.320177	4.086521	H	-4.152223	6.452101	5.660122
C	-6.061097	3.560938	-0.544990	H	-4.628132	7.648444	4.448905
C	-5.183626	3.132676	1.615152	H	-5.561083	2.576943	2.481778
C	-4.554680	2.214251	0.589695				
C	-5.074150	2.461866	-0.665707				
C	-3.518770	1.260124	0.818283				
C	-4.723771	1.598705	-1.771099				
C	-2.987885	0.549249	-0.301520				
C	-2.993605	1.012096	2.110888				
C	-5.475474	1.537520	-2.968671				
C	-3.633701	0.686297	-1.601351				
C	-1.895442	-0.318839	-0.079023				
H	-3.433483	1.512434	2.966133				
C	-1.937582	0.142156	2.295240				
C	-5.112682	0.703190	-4.008073				
C	-3.271255	-0.132933	-2.695774				
C	-1.372983	-0.514439	1.186820				
H	-1.449441	-0.851606	-0.910070				
H	-1.543781	-0.033170	3.291337				
C	-3.979177	-0.116800	-3.882431				
H	-5.711561	0.674283	-4.912858				
H	-2.439417	-0.819819	-2.599858				
H	-0.533195	-1.188088	1.324419				
H	-3.679547	-0.764920	-4.699871				
H	-6.371413	2.135602	-3.058429				
H	-5.325193	4.000389	-3.143115				
C	-4.122982	4.175902	2.090575				
H	-3.816255	4.754041	1.210779				
H	-3.236385	3.623193	2.418068				
C	-4.546600	5.125283	3.210209				
H	-4.903817	4.544492	4.072115				
H	-5.387211	5.746811	2.885623				
C	-3.397777	6.033996	3.659795				
H	-2.555442	5.415570	3.997211				
H	-3.031170	6.603987	2.795864				

2.4.7 SUPPLEMENTARY OPTICAL DATA

2.4.7.1 ABSORPTION, EMISSION AND EXCITATION SPECTRA

Samples were prepared using anhydrous and spectroscopic grade solvents with the aid of sonication to afford complete dissolution. Absorption and fluorescence spectra were recorded at room temperature (298 K) in quartz cuvettes (10 mm path length) and baseline corrected with respect to pure solvent (in the case of absorption spectroscopy).
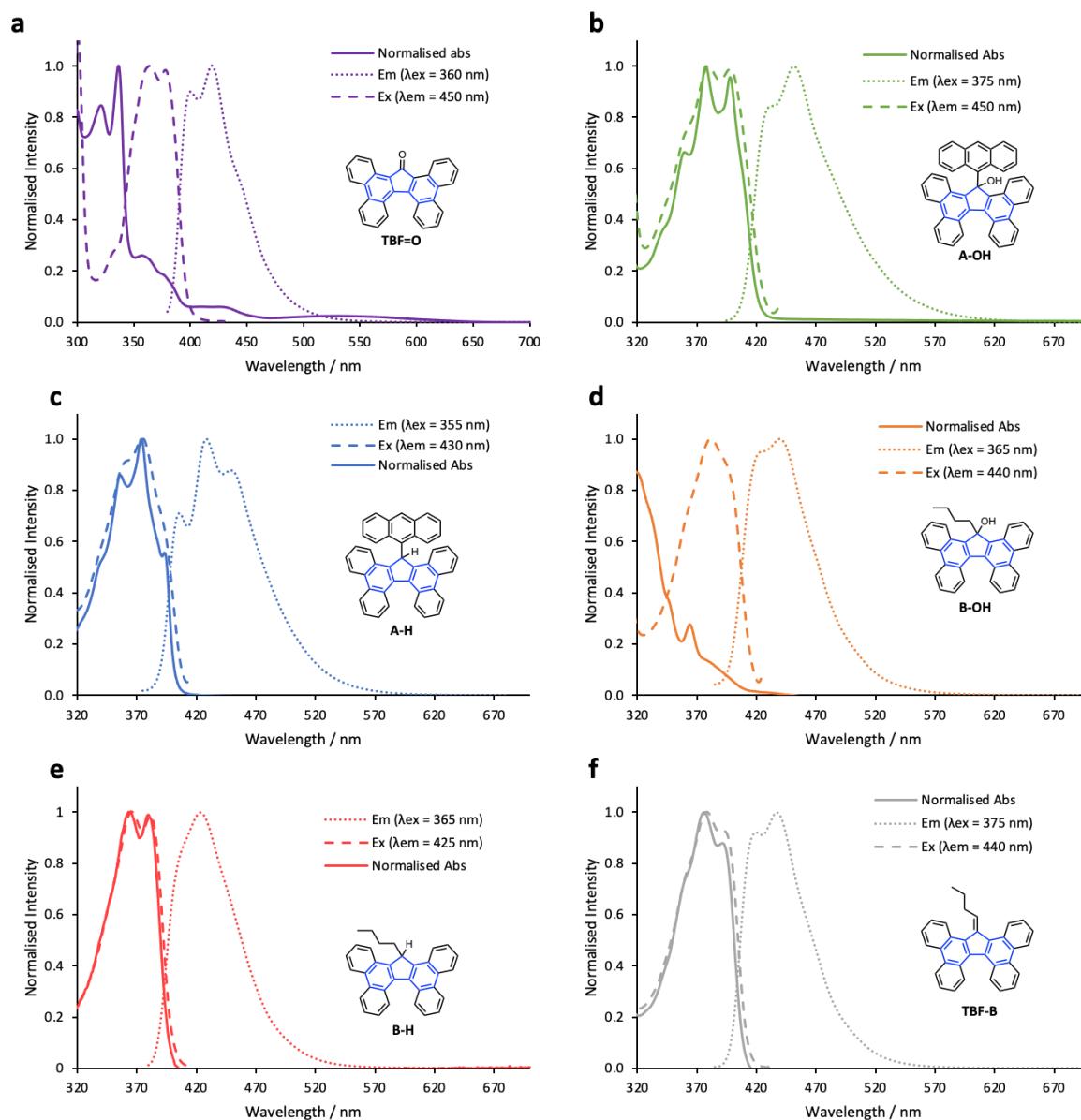
Figure S2.36. Normalised absorption (solid), emission (dotted) and excitation (dashed) spectra of (a) **TBF=O**, (b) **A-OH**, (c) **A-H**, (d) **B-OH**, (e) **B-H**, (f) **TBF-B** measured in THF (10 µM).
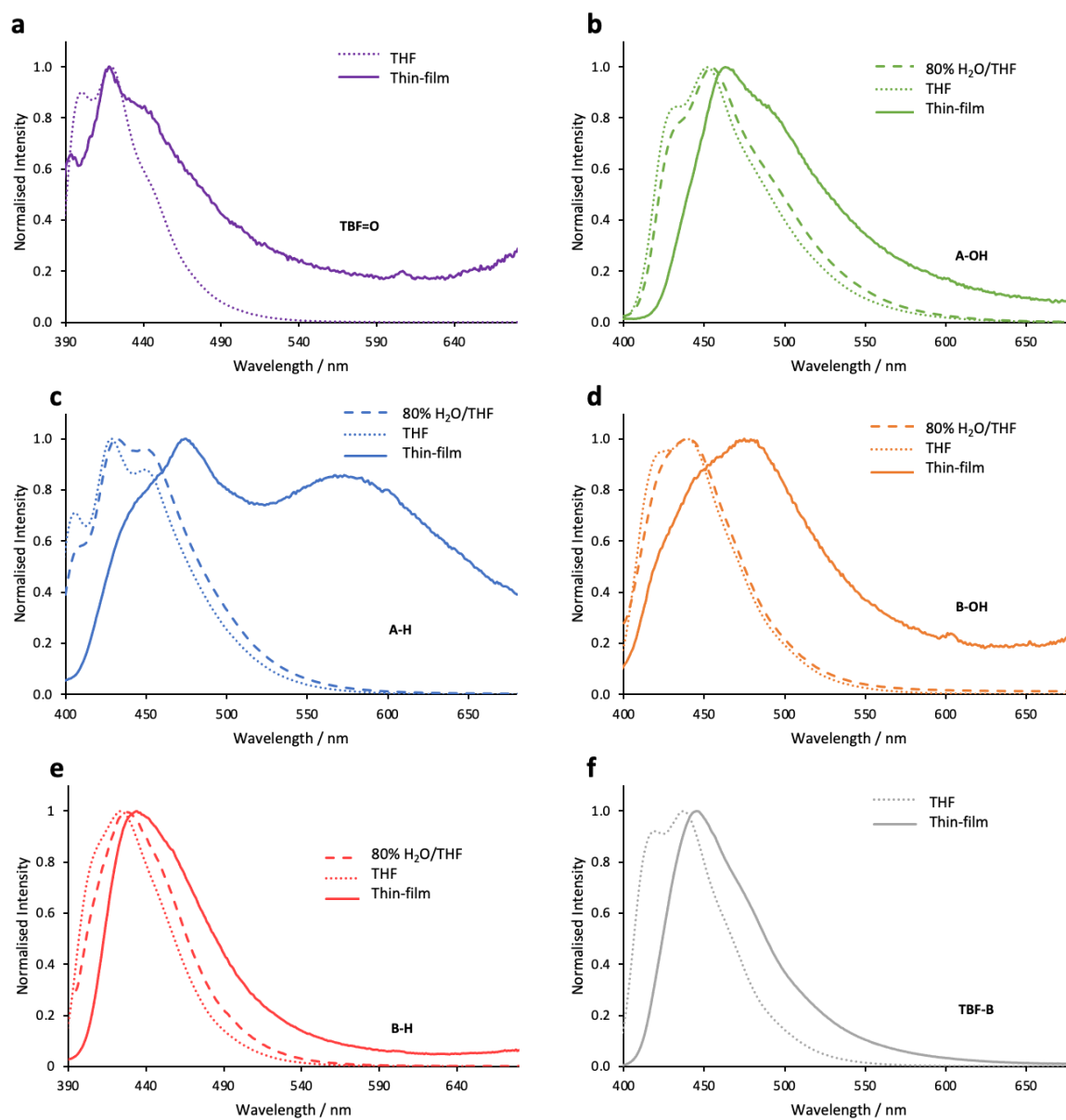
Figure S2.37. Normalised solution-state emission (dotted), aggregate emission (dashed) and thin-film emission (solid) spectra of (a) **4**, (b) **A-OH**, (c) **A-H**, (d) **B-OH**, (e) **B-H**, (f) **TBF-B**.
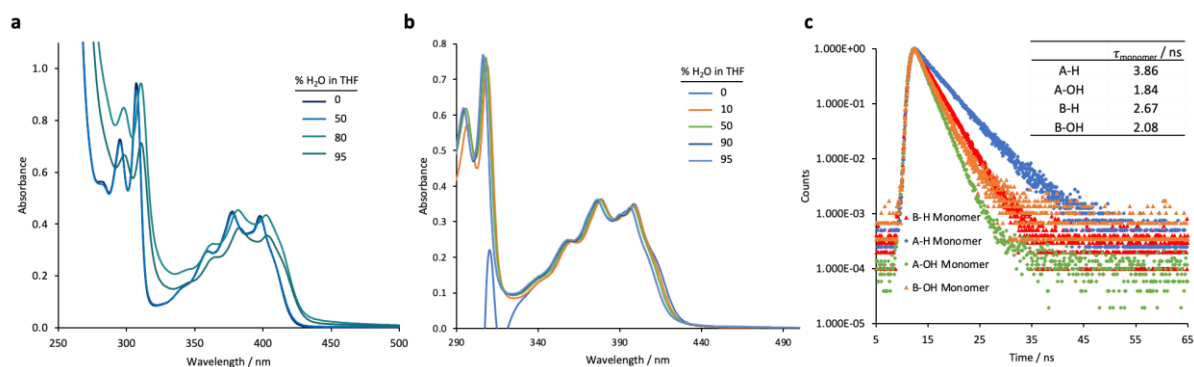
Figure S2.38. Aggregation studies by absorption spectroscopy in (a) THF–H$_2$O mixtures and (b) PhMe–EtOH mixtures. (c) Lifetime measurements of the TBF library in THF (i.e., as monomers)

2.4.7.2 PLQY DETERMINATION

Concentration-dependent absorption spectroscopy was collected in dry and degassed THF to confirm sample concentrations of optical densities < 0.1 a.u at the excitation wavelength (365 nm). Concentration-dependent emission spectra of the TBF library were collected in anhydrous and degassed THF, exciting at 365 nm (with a 5 nm slit width). The area under the emission curves was determined by the software and plotted against the absorption at 365 nm at the same concentrations. A scatter plot was generated with a line of best fit, where the gradient for each compound was used to calculate their quantum yields (Φ_X) relative to quinine sulfate dihydrate (QS; Φ_{ST}=0.55)[29] using Equation S1 where X refers to the TBF compound, ST refers to the QS, η refers to the refractive index of the solvent used (i.e., η_X=1.41 for THF and η_{ST}=1.35 for 0.5 M sulfuric acid).

$$\Phi_X = \Phi_{ST} \left(\frac{Grad_X}{Grad_{ST}} \right) \left(\frac{\eta_X^2}{\eta_{ST}^2} \right) \qquad (Eq.\,S1)$$
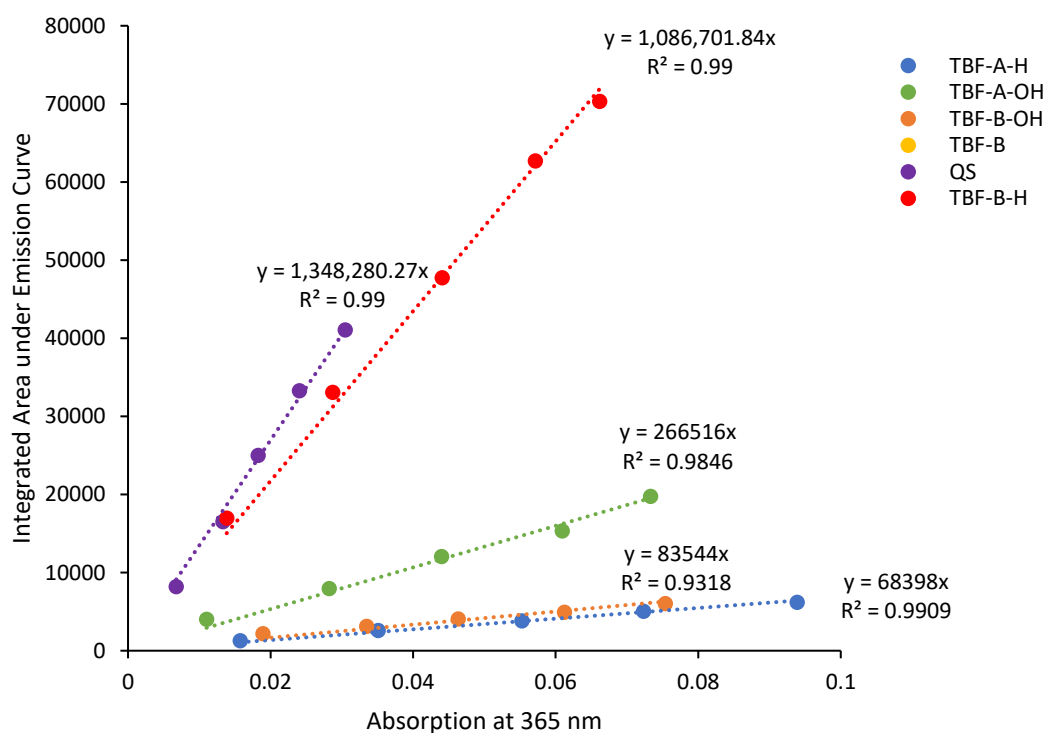
Figure S2.38. Straight line graphs of the integrated area under the emission curves of **A-OH**, **A-H**, **B-OH**, **B-H** and the standard quinine sulfate QS against the emission at 365 nm in order to calculate relative PLQY values

2.4.8 DYNAMIC LIGHT SCATTERING (DLS)

DLS experiments were conducted in a standard quartz cuvette (10 mm path length). Samples were prepared in either 70% or 80% H$_2$O and THF mixtures (10 μM) and filtered through an Acrodisc 0.45 μm filter before addition to the cuvettes. Data was collected at 298 K.
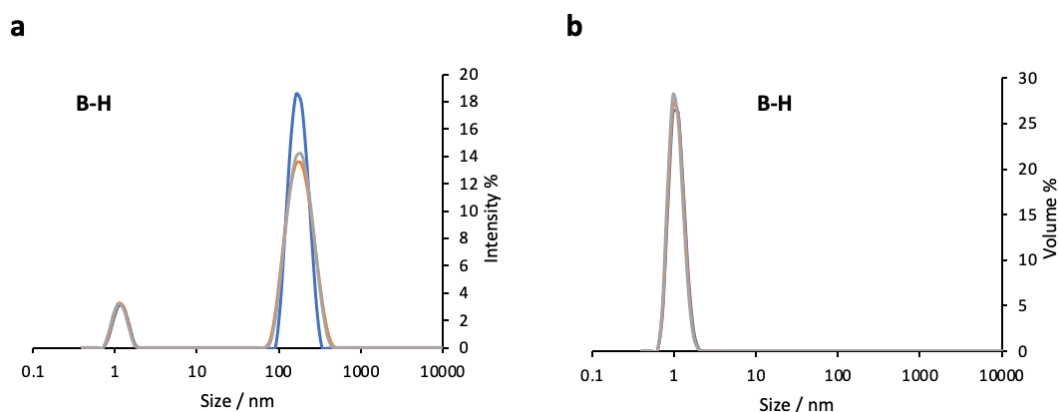
Figure S2.40. (a) Size distribution with respect to sample intensity (%) of **B-H** and (b) size distribution with respect to volume (%) of **B-H** in 70% H$_2$O and THF mixtures at 10 μM, run in triplicate. Mean particle diameter = 142.3 nm, st.d = 4.91 for **B-H**
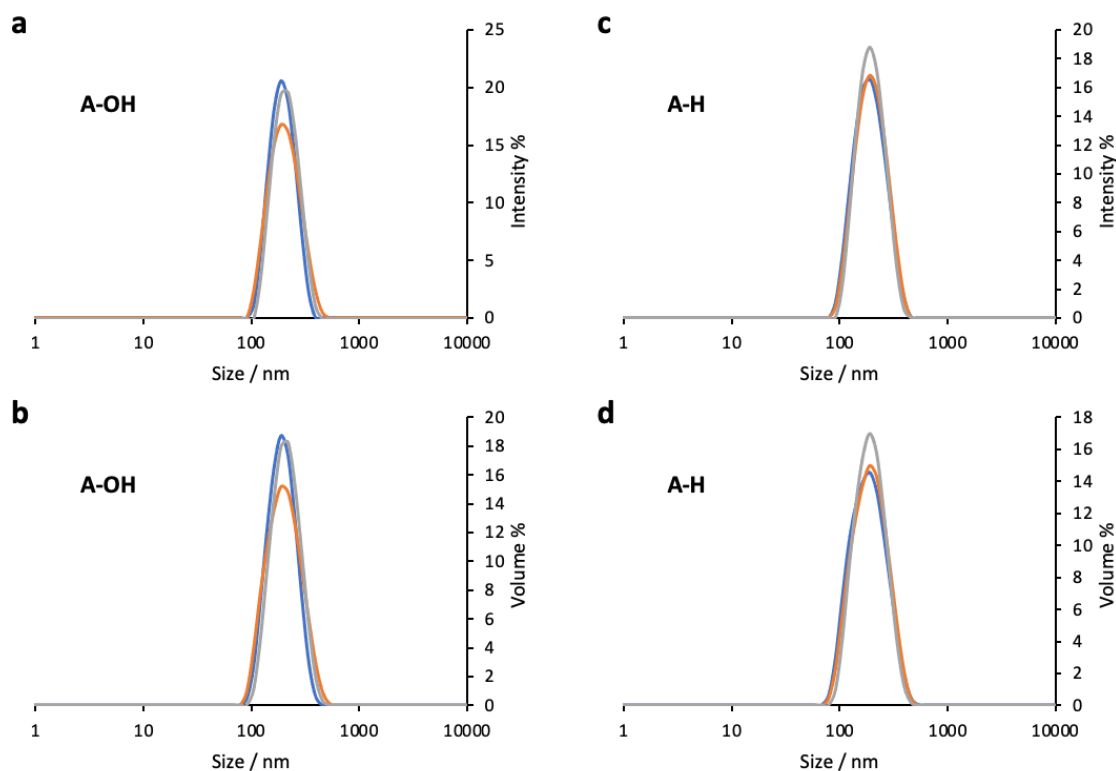
Figure S2.41. Size distribution with respect to sample intensity (%) of (a) **A-OH**, (c) **A-H** and size distribution with respect to volume (%) of (b) **A-OH** and (d) **A-H** in 80% H$_2$O and THF mixtures at 10 μM, run in triplicate. Mean particle diameter = 194.0 nm, st.d = 7.43 for **A-OH** and mean particle diameter = 182.9 nm, st.d = 3.02 for **A-H**
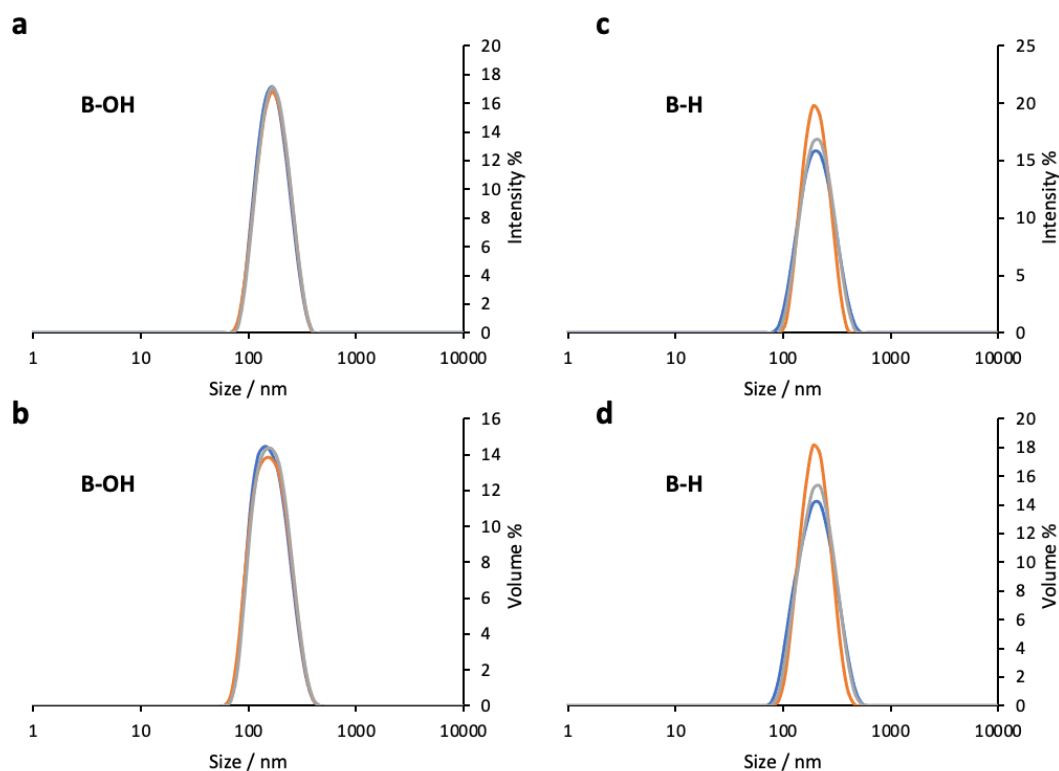
Figure S2.42. Size distribution with respect to sample intensity (%) of (a) **B-OH**, (c) **B-H** and size distribution with respect to volume (%) of (b) **B-OH** and (d) **B-H** in 80% H_2O and THF mixtures at 10 μM, run in triplicate. Mean particle diameter = 158.6 nm, st.d = 1.82 for **B-OH** and mean particle diameter = 194.0 nm, st.d = 1.64 for **B-H**

2.5 REFERENCES

1. Luo, J.; Xie, Z.; Lam, J. W. Y.; Cheng, L.; Chen, H.; Qiu, C.; Kwok, H. S.; Zhan, X.; Liu, Y.; Zhu, D.; Tang, B. Z. Aggregation-Induced Emission of 1-Methyl-1,2,3,4,5-Pentaphenylsilole. *Chem. Commun.* **2001**, *18*, 1740–1741.

2. Mei, J.; Leung, N. L. C.; Kwok, R. T. K.; Lam, J. W. Y.; Tang, B. Z. Aggregation-Induced Emission: Together We Shine, United We Soar! *Chem. Rev.* **2015**, *115*, 11718–11940.

3. Huang, Y.; Xing, J.; Gong, Q.; Chen, L.-C.; Liu, G.; Yao, C.; Wang, Z.; Zhang, H.-L.; Chen, Z.; Zhang, Q. Reducing Aggregation Caused Quenching Effect Through Co-Assemble of PAH Chromophores and Molecular Barriers, *Nat. Commun.* **2019**, *10*, 169.

4. An, B.-K.; Kwon, S.-K.; Jung, S.-D.; Park, S. Y. Enhanced Emission and Its Switching in Fluorescent Organic Nanoparticles, *J. Am. Chem. Soc.* **2002**, *124*, 14410–14415.

5. Wang, H.; Zhao, E.; Lam, J. W. Y.; Tang, B. Z. AIE Luminogens: Emission Brightened by Aggregation, *Mater. Today.* **2015**, *18*, 365–377.

6. Chen, J.; Law, C. C. W.; Lam, J. W. Y.; Dong, Y.; Lo, S. M. F.; Williams, I. D.; Zhu, D.; Tang, B. Z. Synthesis, Light Emission, Nanoaggregation, and Restricted Intramolecular Rotation of

1,1-Substituted 2,3,4,5-Tetraphenylsiloles, *Chem. Mater*. **2003**, *15*, 1535–1546.

7.   Liu, Y. Y.; Zang, X.; Li, K.; Peng, Q. C.; Qin, Y. J.; Hou, H. W.; Zang, S. Q.; Tang, B. Z. Restriction of Intramolecular Vibration in Aggregation-Induced Emission Luminogens: Applications in Multifunctional Luminescent Metal-Organic Frameworks, *Angew. Chem. Int. Ed.* **2021**, *60*, 22417–22423.

8.   Hu, R.; Lam, J. W. Y.; Liu, Y.; Zhang, X.; Tang, B. Z. Aggregation-Induced Emission of Tetraphenylethene-Hexaphenylbenzene Adducts: Effects of Twisting Amplitude and Steric Hindrance on Light Emission of Nonplanar Fluorogens. *Chem. Eur. J.* **2013**, *19*, 5617–5624.

9.   Zhang, G.; Tan, J.; Zhou, L.; Liu, C.; Liu, J.; Zou, Y.; Narita, A.; Hu, Y. S-Shaped Double Helicene Diimides: Synthesis, Self-Assembly, and Mechanofluorochromism. *Org. Lett.* **2021**, *23*, 6183–6188.

10.   Wang, C.; Li, Z. Molecular Confromation and Packing: Their Critical Roles in the Emission Performance of Mechanochromic Fluorescence Materials, *Mater. Chem. Front.* **2017**, *1*, 2174–2194.

11.   Mei, J.; Hong, Y.; Lam, J. W. Y.; Qin, A.; Tang, Y.; Tang, B. Z. Aggregation-Induced Emission: The Whole Is More Brilliant Than the Parts, *Adv. Mater.* **2014**, *26*, 5429–5479.

12.   Kimura, Y.; Kawajiri, I.; Ueki, M.; Morimoto, T.; Nishida, J. I.; Ikeda, H.; Tanaka, M.; Kawase, T. A New Fluorophore Displaying Remarkable Solvatofluorochromism and Solid-State Light Emission, and Serving as a Turn-on Fluorescent Sensor for Cyanide Ions. *Org. Chem. Front.* **2017**, *4*, 743–749.

13.   Ueda, Y.; Tanigawa, Y.; Kitamura, D.; Ikeda, H.; Yoshimoto, Y.; Tanaka, M.; Mizuno, K.; Kurata, H.; Kawase, T. 3,14-Bis(*p*-nitrophenyl)-17,17-dipentyltetrabenzo[*a,c,g,i*]-fluorene: A New Fluorophore Displaying Both Remarkable Solvatochromism and Crystalline-Induced Emission, *Chem. Asian. J.* **2012**, *8*, 392–299.

14.   Kitamura, C.; Tanigawa, Y.; Kobayashi, T.; Naito, H.; Kurata, H.; Kawase, T. 17,17-Dialkyltetrabenzo[a,c,g,i]Fluorenes with Extremely High Solid-State Fluorescent Quantum Yields: Relationship between Crystal Structure and Fluorescent Properties. *Tetrahedron* **2012**, *68*, 1688–1694

15.   Hay, A. M.; Hobbs-Dewitt, S.; MacDonald, A. A.; Ramage, R. Use of Tetrabenzo[*a,c,g,i*]fluorene as an Anchor Group for the Solid-Solution Phase Synthesis of Ciprofloxacin, *Tetrahedron. Lett.* **1998**, *39*, 8721–8724.

16. Yamada, K.; Shibamoto, H.; Tanigawa, Y.; Ishikawa, H.; Nishida, J. I.; Kitamura, C.; Kurata, H.; Kawase, T. Fulvalene Derivatives Containing a Tetrabenzofluorene Unit: New Nonplanar Fulvalenes with High Electron Affinity. *Synlett* **2016**, *27*, 2085–2090.

17. Danovich, D.; Shaik, S.; Neese, F.; Echeverría, J.; Aullón, G.; Alvarez, S. Understanding the Natures of the CH⋯HC Interactions in Alkanes, *J. Chem. Theory. Comput.* **2013**, *9*, 1977–1991.

18. Martin, R. H.; Marchant, M. J. Resolution and Optical Properties ($[\alpha]_{max}$, ORD and CD) of Hepta-, Octa- and Nonahelicene. *Tetrahedron* **1974**, *30*, 343–345.

19. Rickhaus, M.; Mayor, M.; Juríček, M. Strain-Induced Helical Chirality in Polyaromatic Systems. *Chem. Soc. Rev.* **2016**, *45*, 1542–1556.

20. Kazim, M.; Guan, L.; Chopra, A.; Sun, R.; Siegler, M. A.; Lectka, T. Switching a HO⋯π Interaction to a Nonconventional OH⋯π Hydrogen Bond: A Completed Crystallographic Puzzle, *J. Org. Chem.* **2020**, *85*, 9801–9807.

21. (a) Czernek, J.; Brus, J.; Czernerková, V.; Kobera, L. Quantifying the Intrinsic Strength of C–H⋯O Intermolecular Interactions, *Molecules*, **2023**, *28*, 4478. (b) Samanta, A. K.; Banerjee, P.; Bandyopadhyay, B.; Pandey, P.; Chakraborty, T. Antagonistic Interplay Between an Intermoelcular C–H⋯O and an Intramolecular OH⋯O Hydrogen Bond in a 1:1 Complex Between 1,2-Cyclohexanedione and Chloroform: A combined Matrix Isolation Infrared and Quantum Chemistry Study, *J. Phys. Chem. A.* **2017**, *121*, 6012–6020.

22. Eakins, G. L.; Alford, J. S.; Tiegs, B. J.; Breyfogle, B. E.; Stearman, C. J. Tuning HOMO–LUMO Levels: Trends Leading to the Design of 9-Fluorenone Scaffolds with Predictable Electronic and Optoelectronic Properties, *J. Phys. Org. Chem.* **2011**, *24*, 1119–1128.

23. Ren, Y.; Lam, J. W. Y.; Dong, Y.; Tang, B. Z.; Wong, K. S. Enhanced Emission Efficiency and Excited Stated Lifetime Due to Restricted Intramolecular Motion in Silole Aggregates, *J. Phys. Chem. B.* **2005**, *109*, 1135–1140.

24. Burchat, A. F.; Chong, M.; Nielsen, N. Titration of Alkyllithiums with a Simple Reagent to a Blue Endpoint, *J. Organomet. Chem.* **1997**, *542*, 281–283.

25. Dolomanov, O. V.; Bourhis, L. J.; Gildea, R. J.; Howard, J. A. K.; Puschmann, H. OLEX2: A Complete Structure Solution, Refinement and Analysis Program, *J. Appl. Cryst.* **2009**, *42*, 339–341.

26. Sheldrick, G. M. SHELXT-Integrated Space-Group and Crystal-Structure Determination, *Acta. Cryst.* **2015**, *A71*, 3–8.

27.   Sheldrick, G. M. Crystal Structure Refinement with SHELXL, *Acta. Cryst.* **2015**, *C71*, 3–8.

28.   Brouwer, A. M. Standards for the Photoluminescence Quantum Yield Measurements in Solution. *Pure. Appl. Chem.* **2011**, *83*, 2213–2228.

29.   Becke, A. D. Density-Functional Thermochemistry. III. The Role of Exact Exchange, *J. Chem. Phys.* **1993**, *98*, 5648–5652.

30.   Lee, C.; Yang, W.; Parr, R. G. Development of the Colle-Salvetti Correlation-Energy Formula into a Functional of the Electron Density, *Phys. Rev. B.* **1988**, *37*, 785–789.

31.   Grimme, S.; Ehrlich, S.; Goerigk, L. Effect of the Damping Function in Dispersion Corrected Density Functional Theory, *J. Comp. Chem.* **2011**, *32*, 1456–1465.

32.   Brown, A. R.; Irving, S. L.; Ramage, R.; Rapby, G. (17-Tetrabenzo[*a,c,g,i*]Fluorenyl)Methylchloroformate (TbfmocCl) a Reagent for the Rapid and Efficient Purification of Synthetic Peptides and Proteins. *Tetrahedron.* **1995**, *51*, 11815–11830.

CHAPTER 3 |
EXPLORING THE REDOX CHEMISTRIES OF TETRABENZOFLUORENES

SYNOPSIS
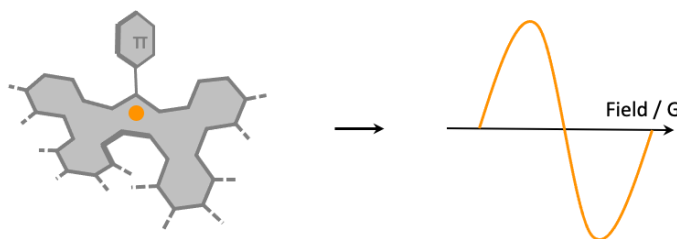
This Chapter interrogates the electrochemical and chemical redox properties of anthracenyl-appended TBFs in order to understand their fundamental behaviours under different conditions. Cyclic voltammograms of **A-H** and non-substituted **TBF** (i.e., head substituent is –H) display reversible first oxidation processes whereas **A-OH** has a quasi-reversible first oxidation. It is hypothesised that this quasi-reversibility originates from a chemical cleavage of the hydroxy group whose bond strength is predicted to decrease considerably upon oxidation of **A-OH** and results in the formation of a TBF-centred radical **TBF-A·**. Spectroelectrochemical (SEC) studies confirm the differing oxidation behaviours of **A-OH** and **A-H**. Meanwhile it is observed that once the radical cation of **A-H** is formed (**A-H·+**), this species decays over time to **TBF-A·**. The absorption profiles of **A-OH** and **A-H**, once their first oxidation species have reached electrochemical equilibrium, match confirming observations of the formation of **TBF-A·**. Following these results, CV of the TBFs is repeated under basic conditions to reveal a loss in reversibility of the first oxidation for **A-H** and **TBF** suggesting the formation of the same TBF-centred radicals. SEC under basic conditions should validate observations further. As a result of these electrochemical results, efforts to synthesise **TBF-A·** *via* chemical reduction of **A-OH** are discussed, including challenges and side products isolated. EPR spectroscopy confirms the presence of an open-shell species. The UV–vis absorption profile of this species similarly matches the oxidation equilibrium SEC absorption profiles of **A-OH** and **A-H**, thereby confirming electrochemical conclusions. TBF-centred radicals are thought to feature again when TBF ketone **TBF=O** is reduced under Grignard conditions in the presence of MgI·. A mechanism reminiscent of the synthesis of pinacols is proposed, however in the absence of a kinetically stabilising group the radical is quenched. Similarly, alcohol head-substituted TBFs (in particular **B-OH**) are shown to display an unusual reactivity leading to the isolation of a TBF dimer, **TBF-2**. This Chapter therefore highlights the various ways in which the redox chemistries of a variety of TBFs can result in exotic open-shell and closed-shell systems.

ACKNOWLEDGEMENTS

3.1 INTRODUCTION

In Chapter 2, TBFs were established as convenient scaffolds to study the emergence of the AIE/AEE phenomena as a result of intrinsic intramolecular interactions from R groups at the fluorenyl head-position. A further advantage of pursuing fluorene-based materials is their robust chemical and electrochemical redox behaviours, which allows for their use in a variety of advanced energy storage applications such as organic photovoltaic devices[1] and alkali-metal-ion batteries.[2] A thorough literature review presenting examples where researchers have investigated the ambipolar redox behaviours of fluorenes and their benzannulated analogues is presented in Chapter 1. In addition, Chapter 1 also discusses the remarkable ability of the fluorenyl core to afford stable organic neutral radicals with half-lives spanning 3–43 days under ambient conditions (Chapter 1, Figure 1.8b, *vide supra*).[3,4] In particular, sterically bulky head-substituents such as anthracene provide kinetic stability to these neutral organic radicals. As a result, upon electron transfer (e.g., oxidation in this case), fluorenes readily undergo C–H bond cleavage in favour of forming radicals (Figure 3.1a) and have been used to inspire new elementary reaction steps involving C–H bonds.[5] Long-lived persistent organic radicals such as these fluorenyl-centred radicals are sought after for their potential applications in spin electronics (also known as spintronics), molecular magnets, quantum information and other energy related applications.[6]

Organic radicals are expected to perform more efficiently than closed shell-emitters because emission arises due to spin-allowed relaxation from doublet excited states as opposed to competing singlet and triplet states of typical closed-shell organic luminophores[7] (Figure 3.1b). In addition, emission from a doublet excited state does not undergo typical fluorescence quenching experienced by closed-shell organic small molecules.[8,9] In fact, a thin film of a mesitylated trityl radical derivative displays an extremely high PLQY of 0.93 and when incorporated into a light-emitting diode boasts an external quantum efficiency of 28%.[7]
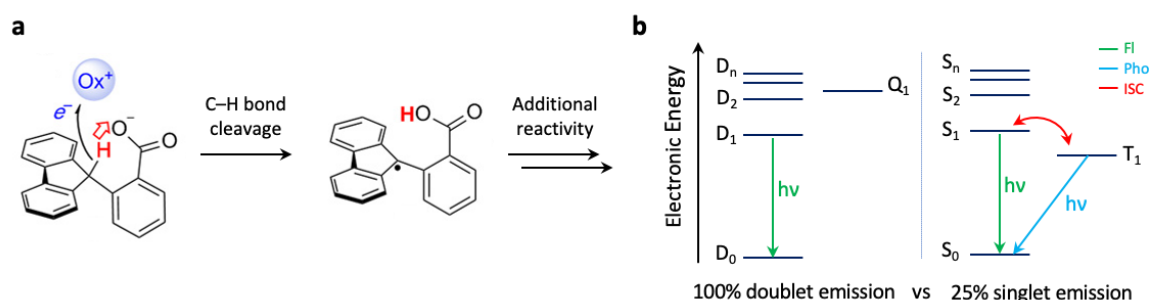
Figure 3.1 (a) Chemical structures of a fluorenyl system depicting how, upon oxidation, a C–H bond at the fluorenyl-head position is cleaved in favour of forming its organic radical analogue. In this case, the proton is transferred intramolecularly before reacting further. (b) Jablonski diagram highlighting the 100% internal quantum efficiency of doublet emission.[10]

In particular, the marriage between organic radicals, their redox behaviours and chirality has started to gain popularity among researchers. For example, chiral macrocycles have been shown to undergo redox-triggered chirality switching enabling the selective capture and release of guests.[11] Further, when

enantiopure helicenes are included in the fabrication of organic field effect transistors (OFETs), devices display a highly specific photoresponse to circularly polarised light, enhancing device performances ten-fold.[12] In addition, CPL activity from open-shell double-state systems have only been discussed in a few examples.[8,13] If configurationally stable analogues of TBF and/or their radicals can be isolated, these materials are expected to display promising chiroptoelectronic properties (e.g., chiral AIE/AEE). Therefore, the preparation of fluorenyl-embedded helicenes based off the TBF motif could afford access to novel closed- and open-shell emitters arising from the robust redox behaviour of the fluorenyl core. These redox states of configurationally stable analogues of TBF could result in materials with enhanced reactivity, high PLQYs, and even efficient solid-state optical behaviour. Research into such open-shell materials is desirable because so much is still unknown about fundamental emissive structure-property relationships and the field remains underdeveloped due to the challenge of accessing ambient stable radicals in the first place.

In this Chapter, the redox properties of anthracenyl-appended TBFs are probed in comparison to **TBF** in an effort to understand how the sterically hindered group plays a role in stabilising different redox states. Redox states are first generated electrochemically revealing an unusual quasi-reversibility of the first oxidation of **A-OH** that is not observed for **A-H**, despite the relatively minute structural modification at the head-position. Spectroelectrochemical (SEC) analyses reiterate the remarkably different mixed valence and charged states that are formed from the oxidation of both TBFs. Furthermore, cyclic voltammetry studies are repeated with an excess amount of base, and it is thought that **A-H** undergoes C–H bond cleavage as a radical cation in favour of forming **TBF-A·**. This result further suggests that the quasi-reversibility observed for the single-electron oxidation of **A-OH** is related to the formation of a similar radical species. Following these electrochemical studies, attempts to synthesise **TBF-A·** are made *via* a chemical reduction of **A-OH** with $SnCl_2$. EPR and absorption spectroscopies confirm the presence of an open-shell species, the results of which are supported by DFT calculations. Furthermore, the redox-properties of TBFs are highlighted in two separate examples resulting in the chemical reduction of a TBF ketone **TBF=O** (whose synthesis is discussed in Chapter 2) and a photoinduced dimerization to form **TBF-2**. Together, these studies support the development of ambient-stable and persistent organic radicals based on TBF. The results from these studies also suggest that the chemical reactivity of redox states of TBF can be taken advantage of to study exotic structures.

3.2 RESULTS AND DISCUSSION

3.2.1 ELECTROCHEMICALLY INDUCED REDOX STATES OF TBF

The redox properties of **A-OH** and **A-H** were firstly probed electrochemically by cyclic voltammetry (CV) and square wave voltammetry (SQWV) studies and compared to **TBF** (Figure 3.2a and c). Measurements were conducted using $TBAPF_6$ (0.1 M) as the supporting electrolyte on samples with a

concentration of 1 mM in CH$_2$Cl$_2$. A full window scan (from –1.8 V to +1.8 V; consult Supplementary Information, Section 3.4.1, Figure S3.4) for all TBFs indicates that under these conditions only the oxidative processes can be probed.
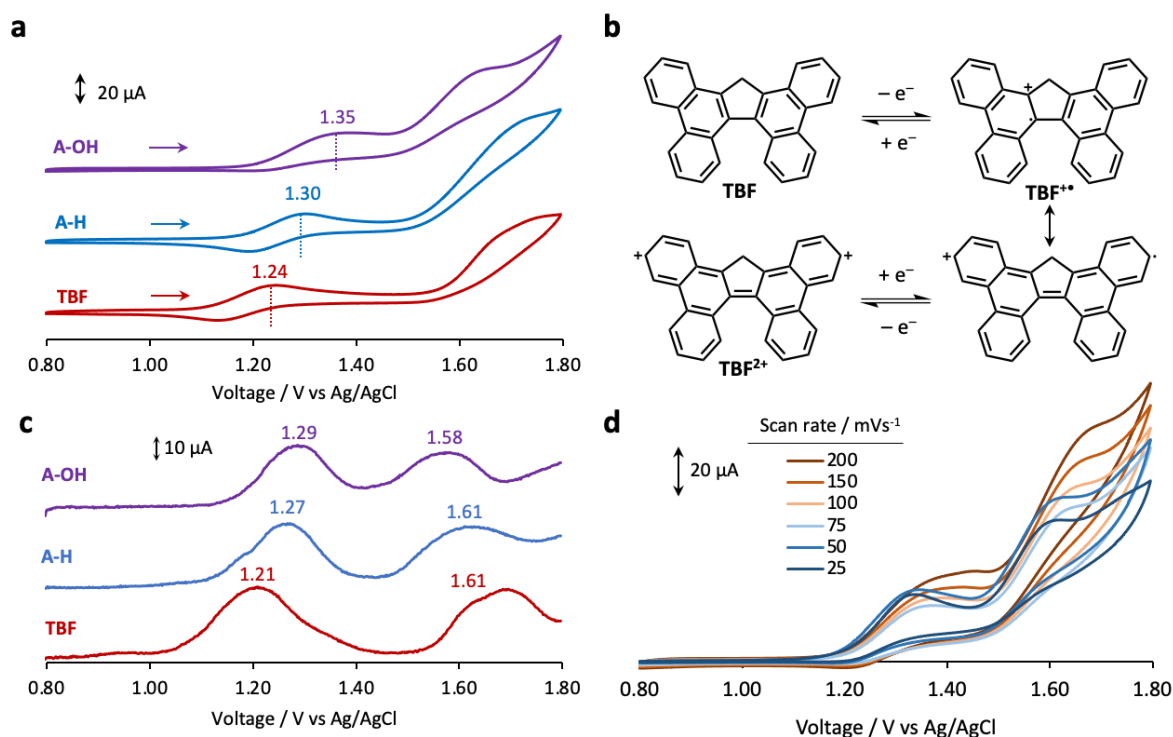
Figure 3.2 (a) Cyclic voltammograms of **A-OH**, **A-H**, and **TBF** (1 mM solutions in CH$_2$Cl$_2$ containing 0.1 M TBAPF$_6$ as the supporting electrolyte) measured at a scan rate of 100 mVs^{-1}. (b) The different oxidative states of **TBF** that are possible and a resonance structure of **TBF**$^{+\bullet}$. (c) Square wave voltammograms of **A-OH**, **A-H**, and **TBF** indicating that each oxidative process involves just a single electron; (d) Variable scan rate CV data for **A-OH** measured between 50–200 mVs^{-1}.

All TBFs display two single-electron oxidative events to form the radical cation and dicationic states (Figure 3.2b) with varying degrees of reversibility. The bulky and electron-rich anthracene groups result in a shifting of the first oxidation potential to larger positive potentials ($E^{1/2}_{ox,1}$(**A-H**) = +1.27 V vs Ag/AgCl, $E^{1/2}_{ox,1}$(**A-OH**) = +1.29 V vs Ag/AgCl) compared to **TBF** ($E^{1/2}_{ox,1}$(**TBF**) = +1.21 V vs Ag/AgCl; Figure 3.2a). These positive shifts indicate a more energetically stable radical cationic state presumably due to the lowering of the HOMO energy levels[14] of **A-OH** and **A-H** when capped with anthracene (confirmed by DFT analyses in Chapter 2). The first oxidation potential of **A-OH** is more positive than **A-H** indicating the electron-withdrawing effect from the hydroxy group, making it harder to oxidise **A-OH**. Notably, while the first oxidation potential of **TBF** and **A-H** is fully reversible (confirmed by Randles-Sevcik plots of peak current (I_P) against the square root of the scan rate ($v^{1/2}$), Section 3.4.1; Figure S3.6), this oxidation potential is quasi-reversible for **A-OH**, evident from the absence of a fully formed peak when the potential is cycled back towards zero. In fact, upon increasing the scan rate from 50 mVs^{-1} to 200 mVs^{-1} (Figure 3.2d), the first oxidation peak is observed to gradually broaden and shift to more positive potentials before the peak appears to split ever so slightly into two. These observations indicate that there is a fast chemical process occurring during the first oxidation of

A-OH which can only be observed at higher scan rates. It is known that upon oxidation, fluorenyl C–H bonds weaken and therefore can be deprotonated by a base to form fluorenyl radicals.[15] Additionally, it has been shown that benzannulation around the fluorenyl core and from head substitution lowers the pk_a of the systems significantly (e.g., the pk_a of phenyl head-substituted 3,4-dibenzofluroene is 14.8, Chapter 1, Figure 1.8).[16] Finally, it is also known that C–OH bonds are generally weaker (i.e., easier to break) than C–H bonds.[17] Therefore, it is not too far a stretch to hypothesise that upon a single-electron oxidation of **A-OH**, the head position C–OH bond may be weakened to the point that it breaks under the conditions of the CV experiment to form a TBF centred radical **TBF-A·** (a representative mechanism is shown in Figure 3.3b *vide infra*). The second oxidation peak for all TBFs is quasi-reversible, presumably due to the unstable antiaromatic nature of cationic states of fluorene (Figure 3.2b).[18]

In order to understand how the redox properties of the TBFs influence their electronic and optical properties, and to try to characterise the nature of the first oxidised species of **A-OH** in more detail, spectroelectrochemistry (SEC) was performed on **A-H** and **A-OH** whereby their first oxidation states were generated electrochemically, and their formation tracked by UV–vis–NIR absorption spectroscopy. For **A-H**, when a voltage of +1.32 V is applied, its absorption profile immediately shifts to **A-H**$_{transient}$(1) (Figure 3.3a; purple line) with a distinct vibronic absorption maximum at 515 nm and a second longer wavelength absorption band at 1095 nm. This absorption profile quickly decays over minutes to form a new charged species (Figure 3.3a; blue line) absorbing at 465 nm and 700 nm before it decays over a longer time period until the electrochemical reaction reaches equilibrium (red line). For **A-OH**, a different evolution of absorption bands is observed with fewer identifiable states generated. When a voltage of +1.37 V is applied to a solution of **A-OH**, its absorption at 380 nm drops immediately to the purple trace (Figure 3.3c) with a low intensity absorption at 1126 nm. This absorption profile decays through the blue trace (Figure 3.3c) on its way to forming a new species (red trace; Figure 3.3c) with a similar absorption profile ($\lambda_{abs} = 530$ nm) to the equilibrated oxidation species generated for **A-H**.

Due to the fast kinetics of the chemical change occurring as **A-OH** is oxidised (which was observed at faster scan rates in its CV studies), the charged states that **A-H** forms as it is oxidised are not seen in **A-OH**, presumably because they don't exist for long enough on the time scale of the experiment. In fact, the only distinct trace in the evolution of absorption spectra for **A-OH** as it is oxidised is its final state (red trace, Figure 3.3c), which following on from previous discussions about the weakened –OH bond under these electrochemical conditions has been attributed to **TBF-A·**. However this assignment needs to be confirmed by EPR spectroscopy studies once **TBF-A·** has been generated chemically and isolated. On the other hand, **A-H**$_{transient}$(1) is presumed to represent non-covalent dimers of mixed valence states (purple trace, Figure 3.3a) resulting in the long wavelength absorption band observed[19,20] which decays quickly to the blue absorption trace. This UV–vis absorption trace is presumed to be attributed to **A-H·⁺** and is blue-shifted compared to the earlier transient species (**A-OH**$_{transient}$(1)) due to

a possible structural change from a fully neutral benzenoid to an unstable quinoidal radical cationic state[21] (Figure 3.2b). Confirmation of these assignments can be made more confidently by performing *in situ* EPR spectroscopy in tandem with SEC to inform the formation of radical states (or their silence, e.g., in the formation of dimers). Due to the resemblance of the redox states formed when the electrochemical reaction has reached equilibrium upon oxidation of **A-OH** and **A-H**, the red trace for **A-H** has also been identified as originating from **TBF-A$^{\cdot}$**. Here, it is thought that trace water (pk_a = 14)[22] acts as a base to slowly deprotonate **A-H$^{\cdot+}$** to **TBF-A$^{\cdot}$** over time (Figure 3.3b).
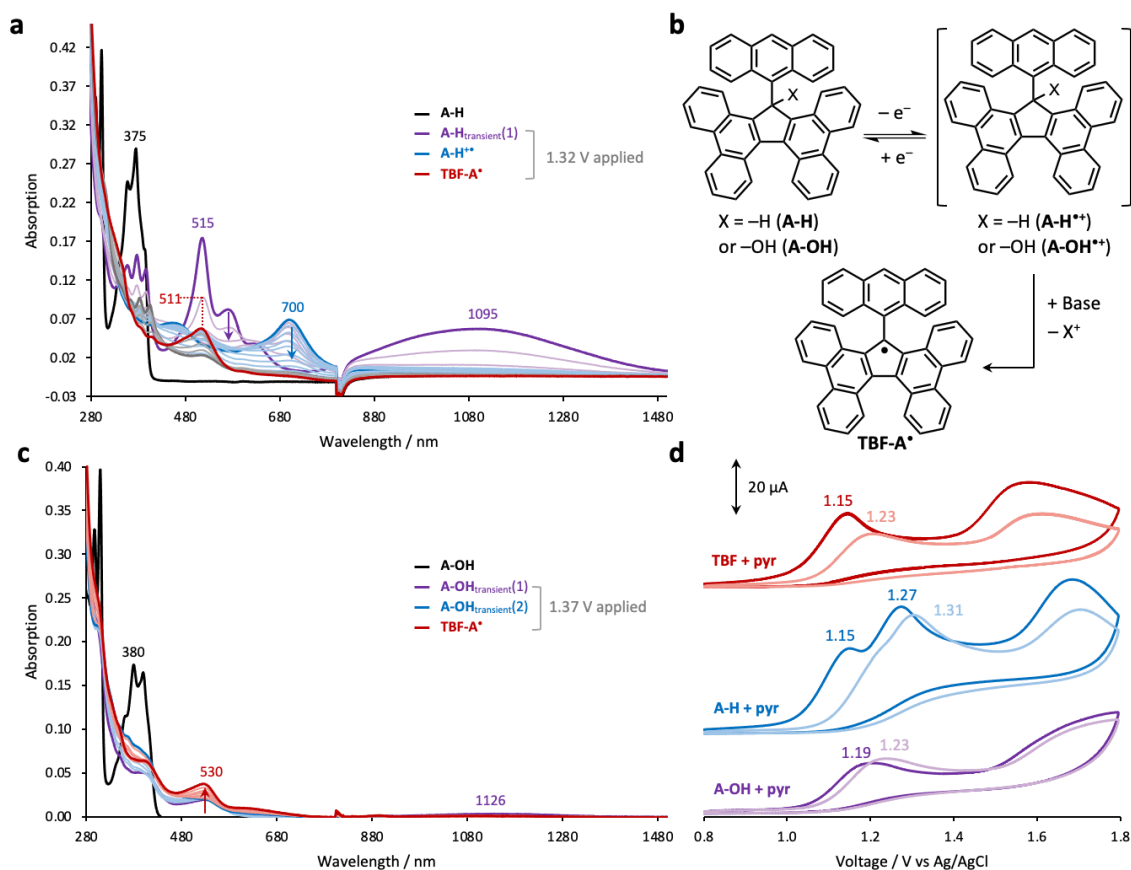
Figure 3.3 (a) Absorption spectroscopy of different transient states that are formed as **A-H** (0.5 mM solution prepared with a 0.1 M TBAPF$_6$ supporting electrolyte in CH$_2$Cl$_2$; black line) is oxidised using a constant applied voltage of +1.32 V. (b) Possible mechanism for the electrochemical generation of **TBF-A$^{\cdot}$**; (c) UV–vis absorption spectroscopy of different transient states that are formed as **A-OH** (0.5 mM solution prepared with a 0.1 M TBAPF$_6$ supporting electrolyte in CH$_2$Cl$_2$; black line) is oxidised using a constant applied voltage of +1.37 V; (d) Cyclic voltammograms of **A-OH**, **A-H**, and **TBF** when treated with pyridine (1 mM solutions prepared with a 0.1 M TBAPF$_6$ supporting electrolyte in CH$_2$Cl$_2$ measured at 100 mVs^{-1})

In order to test the stability of the oxidised states formed, CV studies were repeated in CH$_2$Cl$_2$ containing an excess of 0.3% pyridine (Figure 3.3d). Before conducting any electrochemistry, UV–vis absorption profiles for all TBFs under these conditions confirm that pyridine is not strong enough to cause deprotonation in the neutral states (Section 3.4.4.2; Figure S3.7). This particular study is inspired by experiments performed by F. G. Bordwell at al.[15] They suggest that upon oxidation of phenyl head-substituted fluorenes to the radical cation state, the bond dissociation energy of the head-position C–H bond reduces dramatically such that a base is able to deprotonate the radical cation to form a

neutral radical (potential mechanism highlighted in Figure 3.3b), evident by a loss of reversibility for the first oxidation peak. Notably, while the voltammogram of **A-OH** (purple trace, Figure 3.3d) simply shifts slightly to lower potentials compared to when no base is added, the voltammograms of **TBF** and **A-H** change dramatically. The first oxidation peaks for **A-H** and **TBF** lose their reversibility to reveal a quasi-reversible state which occurs at much lower potentials presumably due to the cleavage of the head-group C–H bond. In the absence of a kinetically stabilising anthracenyl group, as in **TBF**, it is possible that following the formation of the TBF-centred radical, dimerisation or electropolymerisation[23] occurs, quenching the radical quickly. The neutral radical that is formed as **A-H** is oxidised (**TBF-A•**) is expected to be much more stable because of the presence of the kinetically stabilising anthracene head group. Therefore, the first scan of the voltammogram of **A-H** under basic conditions (dark blue line, Figure 3.3d) is presumed to highlight two oxidation processes: the first (+1.15 V) for the oxidation of **A-H** to its radical cation which is quickly deprotonated on the timescale of the experiment to form the radical **TBF-A•** and the second oxidation process (+1.27 V) for the oxidation of **TBF-A•** to **TBF-A⁺**. As **A-H** is consumed by this chemically irreversible C–H bond cleavage, the presence of the oxidation peak at +1.15 V diminishes with successive scans (light blue traces, Figure 3.3d) The smaller change in oxidation potentials of **A-OH** under basic conditions compared to without base reveals that pyridine simply catalyses the C–OH bond cleavage that is already occurring, since we observed the quasi-reversibility of this oxidation peak from **A-OH** even in the absence of pyridine. Spectroelectrochemical studies under basic conditions need to be conducted to help to clarify the mechanism upon oxidation, and EPR studies will be necessary to confirm assignments of radical species.

3.2.2 CHEMICALLY GENERATED REDOX STATES OF TBF

TBF is a structural amalgamation of the π-extended fluorenyl radicals discussed in Chapter 1, **27** and **29** (Figure 1.8, *vide supra*) studied by Tian and coworkers[3] and therefore the TBF centred radical, **TBF-A•** is expected to exhibit an intermediate, yet still desirably long, half-life ($\tau_{1/2}$) under ambient conditions (between 7–43 days). Unrestricted DFT calculations (UB3LYP/6-31G(d,p)) of **TBF-A•** in the gas phase (Figure 3.4a) reveal that removal of the bulky –OH group at the 17-position symmetrises the overall structure of **TBF-A•** since the anthracene group is no longer being sterically or electronically influenced by an adjacent head-group substituent. In addition, removal of the –OH group has little effect on the strain in its helical backbone, since the helical parameters are relatively unchanged compared to **A-OH**. Spin density models (Figure 3.4b) clarify that the radical is predicted to be primarily situated on the cyclopentadienyl ring, with majority of the spin density (55%) sitting on the head-position carbon atom, in accordance with literature reports on π-extended fluorenyl-radicals. Unlike **29** (Chapter 1, Figure 1.8) however, there is no spin density distributed to the anthracene unit in **TBF-A•** which bodes well for its stability as there should be fewer decomposition, oxidation or dimerisation pathways

available to quench the radical. The anthracene in **TBF-A·** is therefore acting largely as a sterically bulky group, providing kinetic stability to protect the spin density that is located at the fluorene core.
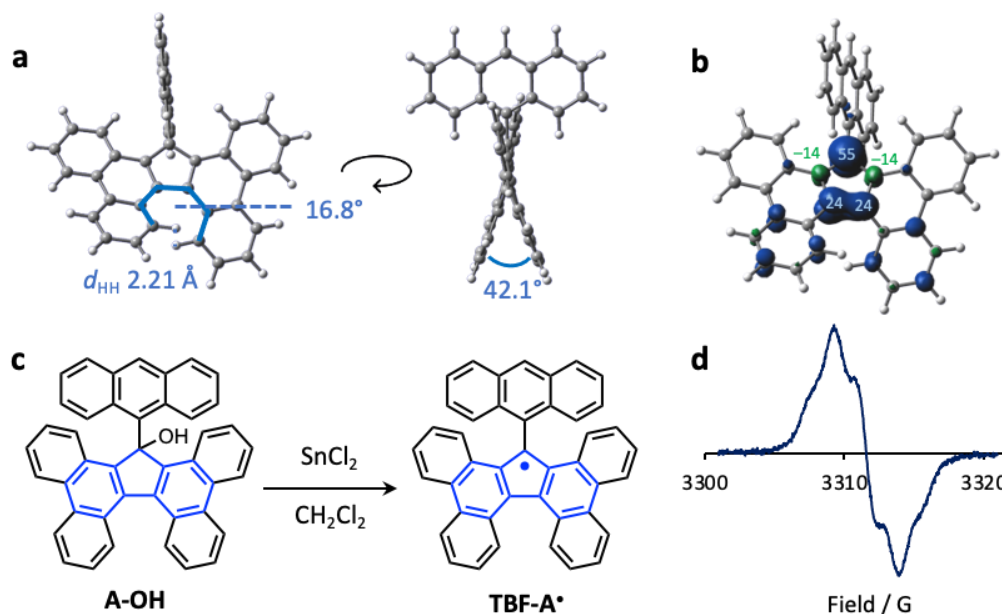
Figure 3.4 (a) Geometry optimised structure of **TBF-A·** (UB3LYP (GD3BJ)/6-31g(d,p)). (b) Spin-density DFT plots (isovalue 0.004) for **TBF-A·** where the blue and green regions represent the α and β spins of electrons respectively and the numbers represent the % of spin density on each C atom in the cyclopentadiene ring (positive and negative value for α and β spins respectively); (c) Reaction conditions for the reduction of **A-OH** by SnCl$_2$ to form **TBF-A·** (d) EPR spectrum (1000 μM, PhMe, 298 K) of an impure mixture of **TBF-A·** following column chromatography

To establish proof of concept that the TBF framework is appropriate for accessing ambient-stable organic radicals, **A-OH** was reduced with SnCl$_2$ in order to generate **TBF-A·** (Figure 3.4c). Upon treatment of **A-OH** with SnCl$_2$ and removal of heterogenous by-products and solvent, FTIR analyses (spectrum provided in Section 3.4.4.2, Figure S3.8b) of the crude material show a loss of the –OH stretching band at 3495 cm^{-1}. Relying on predictions by DFT of a relatively ambient stable radical, the crude material was purified by automated column chromatography and three separate fractions were isolated. Fraction I (not majorly coloured), which was more non-polar than the starting material, was identified by a range of techniques (including TLC, ^{1}H NMR and EPR spectroscopy and mass analyses) to contain a mixture of a closed and an open shell species. An EPR spectrum of fraction I was prepared in dry and degassed PhMe (1000 μM, Figure 3.4d) and confirms the presence of the open-shell species. The hyperfine structure of the EPR signal is broad which could be a result of multiple factors including (i) a slow relaxation time of surrounding atoms around the spin-active system, (ii) dynamic motion of the material in PhMe at room temperature, or (iii) aggregation of the material at that concentration leading to the possibility of spin hopping. The radical appears to be stable under ambient conditions since a 2-month-old crude sample of **TBF-A·** (stored in solution in a screw capped vial) still has an EPR signal (Section 3.4.4.2, Figure S3.8a), albeit with poorer resolution indicating that the radical inevitably seems to have decomposed over time. Fraction II was identified by ^{1}H NMR spectroscopy and mass spectrometry to contain starting material. Fraction III (red powder), revealed a more polar closed-shell

species that was identified by ^{1}H NMR spectroscopy and mass spectrometry to be an oxidised analogue of the starting material **A-OH** (APCI–HRMS (*v*e+, CH_2Cl_2) calculated for $C_{43}H_{26}O_2$: *m*/*z* = 575.2073 [*M*+H]$^+$; found 575.2036 [*M*+H]$^+$).

The reaction is complex to understand and control because it requires relatively long reaction times for starting material to be consumed. $SnCl_2$ reductions to yield fluorenyl-centred radicals typically occur in ~1–4 h in good yields using 5–10 equivalents of reducing agent.[3,4] Full consumption of the TBF starting material **A-OH**, under the same reaction conditions is only noticed after at least 36 h when monitoring the reaction by TLC. When **A-OH** is reduced with 10 equivalents of $SnCl_2$, the proportion of the closed-shell species isolated in fraction I increases while the amount of active radical decreases. Therefore, in a separate reduction reaction, a pure sample of this closed shell species was isolated. A ^{1}H NMR spectrum of the closed-shell species (Figure 3.5) reveals a disruption to the symmetry in the phenanthrene wings of the TBF moiety, evident by the increase in the number of aromatic proton environments observed compared to starting material. A structure of the material (**H1**) has been proposed and has been used to fully assign all the proton signals in the spectrum (with the aid of ^{1}H–^{1}H COSY NMR analyses provided in Section 3.4.3 Figure S3.2). A crystal structure of the material has been difficult to grow since **H1** transforms over time in solution to its thermodynamically stable tautomer **A-H**. It appears as though the radical is getting over reduced (by forming a radical and then accepting a further H$^•$ to form the closed-shell species). The presence of this product is not unusual since Sn is well-known for facilitating the de-aromatisation of diols under acid-free conditions.[24,25]
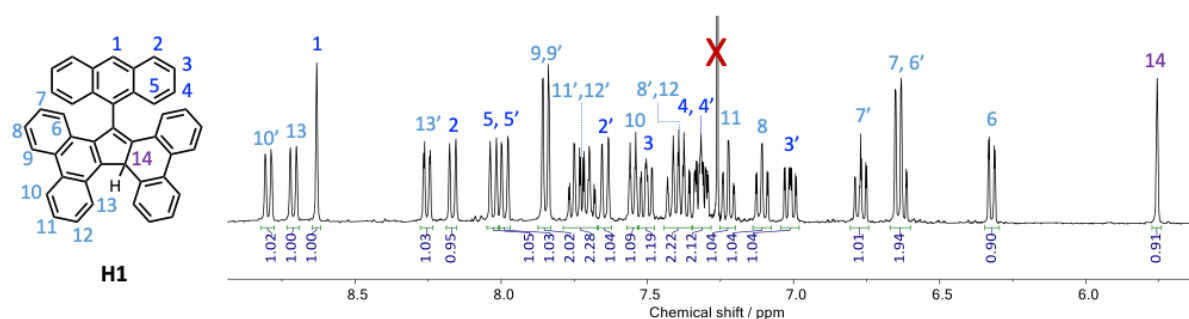
Figure 3.5. Annotated structure of the closed-shell species, **H1** that is formed as the radical decomposes along with its fully assigned ^{1}H NMR (CDCl₃, 400 MHz, 298 K) spectrum.

With a crude sample of **TBF-A$^•$** in hand, its optical properties were interrogated by measuring its UV–vis absorption profile and comparing it to a TD-DFT simulated UV–vis spectrum (Figure 3.6a). The absorption profile for the crude material shows an absorption band between 300–400 nm typical of the fluorenyl core/anthracene, with an additional broad long wavelength band between 450–700 nm which could be indicative of the radical. Notably, this absorption band matches well with the SEC analyses of **A-OH** and **A-H** (Figure 3.3a and c *vide supra*) supporting conclusions of the formation of **TBF-A$^•$** under an electrochemical stimulus. The electronic transition associated with this long wavelength absorption has been assigned to the promotion of an electron to the low lying SOMO*–β orbital (–3.42 eV) in its electronic structure (Figure 3.6b and c), determined by DFT calculations. The

accuracy of the TD-DFT model (Figure 3.6a blue dashed line) is validated by its decent fit compared to the experimental UV–vis spectrum of **TBF-A·**, albeit slightly red-shifted. Unfortunately, spin contamination limited the extent to which the TD-DFT UV–vis spectrum of **TBF-A·** could be analysed, since it typically leads to the overestimation of contributions from FMO orbitals as a result of the small SOMO–α→SOMO–β energy gap (Figure 3.7b).
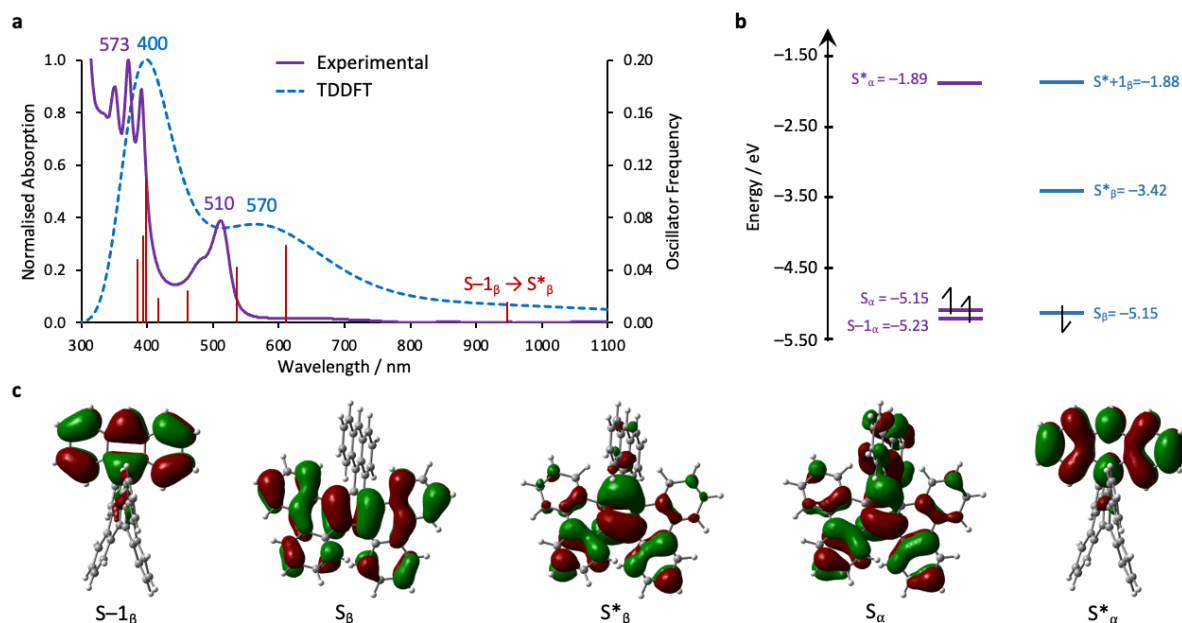
Figure 3.6. (a) UV–vis absorption profile of **TBF-A·** in CH_2Cl_2 (purple trace) compared to the TD-DFT simulated UV–vis spectrum (UB3LYP (GD3BJ) /6-31g(d,p), CH_2Cl_2 solvent model, blue dashed line). The red vertical lines represent calculated excited state transitions with an oscillator frequency, f>0.01. (b) Energy level diagram and (c) depiction of the frontier molecular orbitals (FMOs) of **TBF-A·** (isovalue = 0.02) represented separately as α and β orbitals

Apart from using $SnCl_2$ as a reducing agent, TBF centred radicals can also be accessed under Grignard reaction conditions. In the synthesis of **A-OH**, the installation of anthracene with TBF ketone **TBF=O** (introduced in Chapter 2) was attempted with a Grignard reaction (Figure 3.7) in an attempt to increase the isolated yields of **A-OH** discussed in Chapter 2. 9-Bromoanthracene was reacted with Mg turnings in the presence of I_2 to encourage formation of the Grignard reagent, followed by quenching with **TBF=O**. However, these conditions led instead to the reduction of **TBF=O** to the dihydro species **TBF=O'**, whose structure was unequivocally confirmed by single crystal X-ray analysis (Figure 3.7c). A mechanism for the reduction of **TBF=O** to **TBF=O'** has been proposed (Figure 3.7b), inspired by Gomberg and Bachmann's mechanism for the reduction of aromatic ketones to pinacols.[26] Briefly, an active MgI· species formed following Mg activation with I_2 is thought to reduce the fluorenone core to a spin-delocalised fluorenyl radical intermediate that is quickly quenched in the absence of a kinetically stabilising group. Indeed, this final step would require a H· source, however, it is well known that carbon-centred radicals readily participate in hydrogen abstractions.[6] The C-C bonds around the 5-membered ring in the single crystal X-ray structure of **TBF=O'** clearly highlight the effect of the aromatic ketone reduction. The longer C-C single bond length (1.54 Å) results in a non-planar TBF

wing such that in the supramolecular packing of **TBF=O'** (Figure 3.7d) molecules are unable to stack efficiently. Instead slip-stacked $\pi\cdots\pi$ interactions (measured as centroid-centroid distances, 3.97 Å) hold molecules together. Together, the results from this Chapter so far highlight our ability to be able to form TBF-centred radicals both electrochemically and chemically with varying degrees of stability.
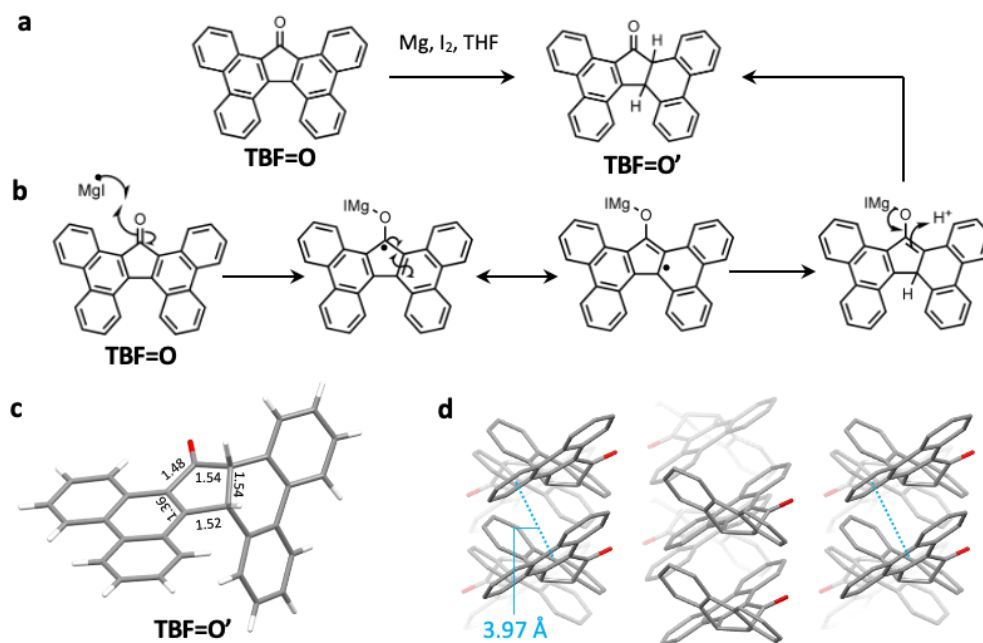
Figure 3.7 (a) Grignard reaction conditions for the reduction of **TBF=O**, *via* a (b) proposed radical-mediated pathway to form the dihydro species, **TBF=O'**. (c) Single crystal X-ray structure of **TBF=O'** with bond lengths around the 5-membered ring reported in Å along with its (d) supramolecular packing. Non-interacting hydrogen atoms have been omitted for clarity.

3.2.3 PHOTOINDUCED DIMERISATION OF TBF

The hydroxy group in head-substituted fluorenes is known to be photo-labile, since in their excited states, the C–OH bond cleaves readily to form fluorene radicals or cations.[27–30] Therefore, the photostability of alcohol-substituted TBFs were studied qualitatively by allowing solutions of **A-OH** and **B-OH** (whose synthesis and properties analysis is discussed in Chapter 2) to age over time under ambient conditions. This photostability monitoring led to the unexpected isolation of a TBF dimer, **TBF-2** as single-crystals suitable for X-ray diffraction that were grown from a solution of **B-OH** in CH$_2$Cl$_2$ with *n*-hexanes and MeOH. It is hypothesised that this chemical transformation occurs in two ways from trace amounts of a TBF substituted in the head position by a hydroxy group (i.e., R = –OH and –H). Decomposition of this TBF species is proposed to occur *via* a TBF-centred radical since fluorenyl-alcohols are known to be susceptible to a photoinduced reduction to a fluorenyl radical which dimerises quickly in the absence of kinetically stabilising groups (Figure 3.8a).[28–30] Alternatively, it is possible that trace amounts of TBF ketone **TBF=O**, follow a similar acid-catalysed decomposition pathway described previously by B. Jose and S. Prathaphan[31] (Figure 3.8b) for diazafluorene, **1** which loses a molecule of N$_2$ to form a fluorenyl cation on its way to dimer **F-2**. This TBF-dimer has in fact been isolated before[32] in pursuit of a TBF-titanium half-sandwich titanocene complex. In this case, the

dimer was formed from the oxidation of a TBF anion ligand to a radical facilitated by the reduction of Ti(IV) to Ti(III) or Ti(II).[33]
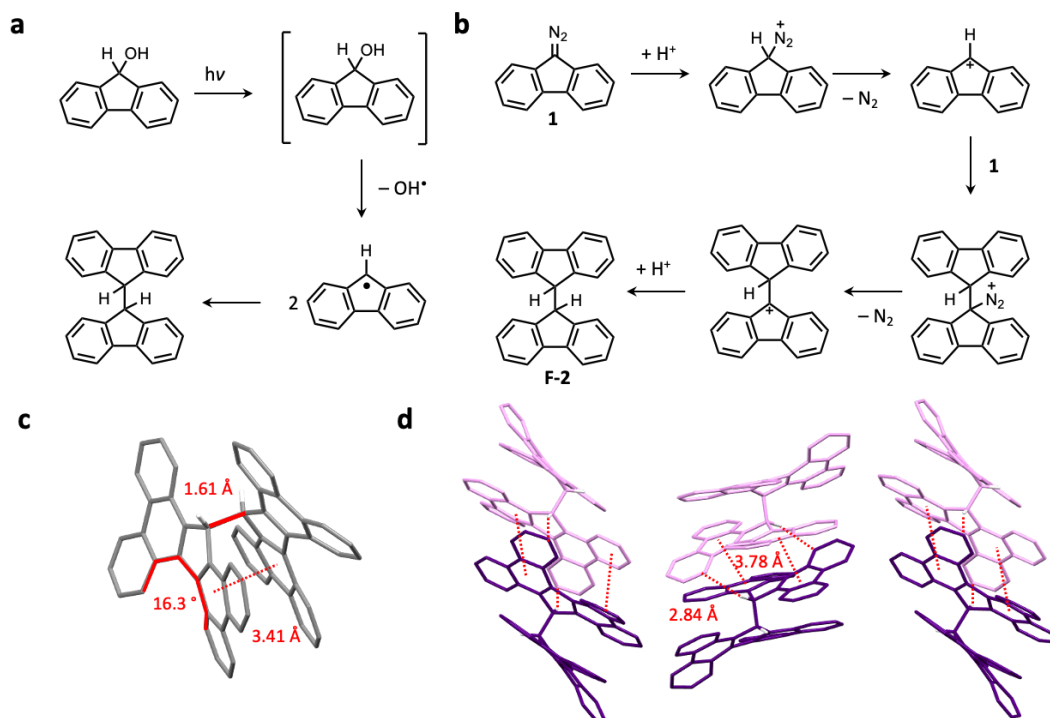
Figure 3.8. (a) Decomposition pathway that alcohol-substitutred fluorenyls are proposed to undertake when irradiated with a UV–vis light source. (b) A proposed acid-catalysed decomposition pathway of diazafluorene to **F-2** that is theorised to be a potential decomposition pathway of TBF ketone **4**; (c) X-ray crystal structure of the TBF dimer, **TBF-2** along with its (d) supramolecular crystal packing. Relevant bond lengths, angles and non-covalent interactions are highlighted in red. All non-interacting hydrogen atoms and solvent molecules have been omitted for clarity.

The X-ray crystal structure of racemic **TBF-2** (Figure 3.8c) reveals that each TBF unit within the dimer exists with the same stereochemistry, i.e., the dimer crystallises out as only *M,M*– or *P,P*–**TBF-2** (represented by purple and pink molecules respectively in Figure 3.8d). The C–C bond length between the TBFs is 1.61 Å, remarkably longer than that of a standard C–C single bond (1.54 Å). Despite the steric bulk imposed by each TBF unit in the dimer, they organise themselves in close proximity to each other in a *syn* arrangement. Each TBF in the dimer is held together by relatively strong intramolecular π···π interactions (3.41 Å) where the complementary curvature of the two TBFs favours the formation of a homochiral covalent dimer. In the supramolecular packing of the dimer (Figure 3.8d), strong dimeric CH···π and π···π interactions (2.84 Å and 3.78 Å respectively) enable a second dimer with the opposite chirality to exist in close proximity.

Since the **TBF-2** crystals were grown suspended in a solution of **B-OH**, they required purification by automated column chromatography to remove traces of **B-OH**, in order to study the structural and optical properties of **TBF-2** in solution**.** The ^{1}H NMR spectrum of **TBF-2** is broad at room temperature suggesting intermediate exchange on the time scale of the NMR experiment. However, poor resolution makes it difficult to fully analyse and assign the peaks in the spectrum at room temperature. The dynamic motion is assumed to be rotation around the elongated TBF C–C single bond and therefore,

variable temperature ^{1}H NMR spectroscopy (from 218 K to 328 K; Figure 3.9a) was performed to understand what the energy barrier for this process is. Although at lower temperatures, the peaks in its ^{1}H NMR spectrum sharpen drastically, these proton peaks do not shift by a great extent revealing that there is no conformational change to the molecule. The energy barrier for the rotation about the C–C single bond ($\Delta G^{\ddagger}$), calculated using the approximation method[34] is 18.6 kcal mol^{-1} (see Section 3.4.3.1 for full data analysis). This energy barrier is significantly higher than for typical C–C single bonds and instead is closer to the energy barrier for C=C double bonds.[35] It is presumed that the strong intramolecular π···π interaction identified in the crystal structure of **TBF-2** and the steric barrier imposed by the large π-surface of the TBF increases $\Delta G^{\ddagger}$. This experimentally calculated energy barrier is even higher than the energy barrier computed by DFT for the rotation around a C=C bond in a 1,2-dibenzofluorenylidene dimer[36] (E_{TS} = 11.6 kcal mol^{-1}) highlighting the strength of this intramolecular interaction.
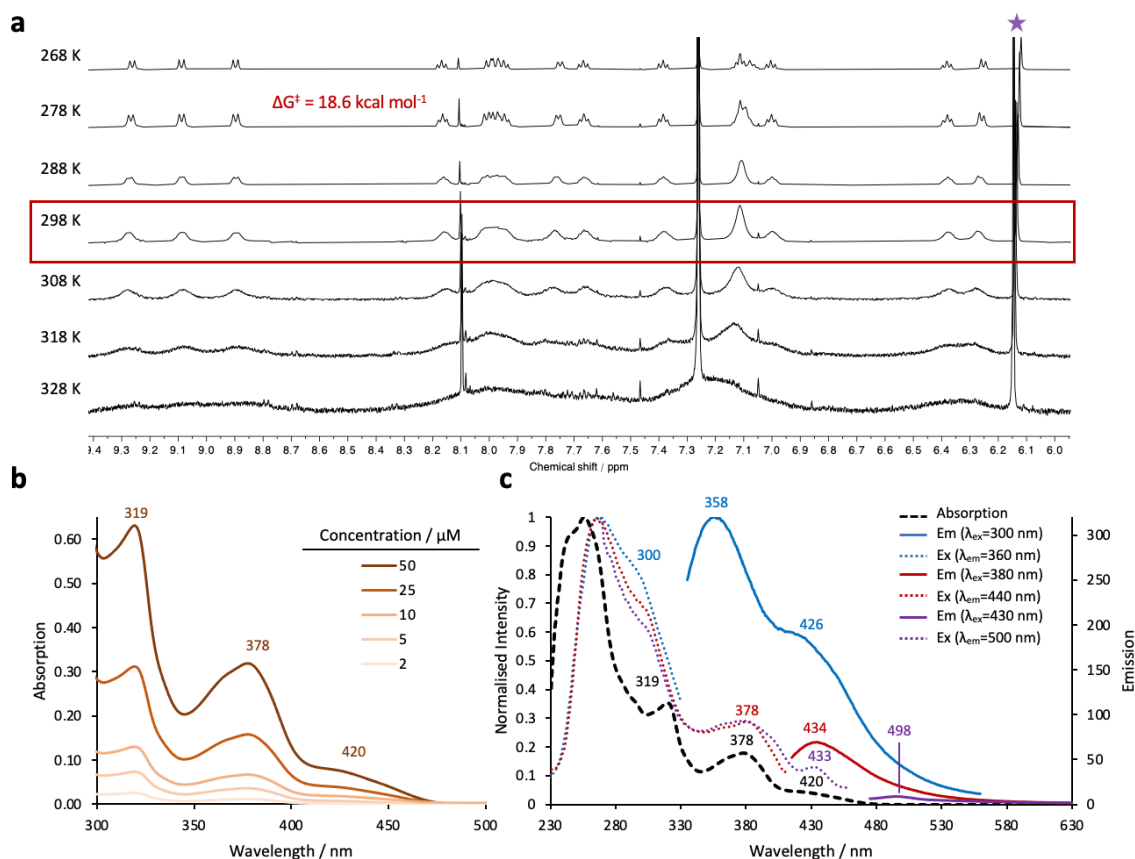
Figure 3.9 (a) VT ^{1}H NMR (CDCl$_3$, 600 MHz) spectra of **TBF-2** from 268–328 K. The spectrum for the coalescence temperature is highlighted with a red box which enabled calculations of $\Delta G^{\ddagger}$ = 18.6 kcal mol^{-1}. (b) Concentration-dependent absorption spectroscopy (CH$_2$Cl$_2$, 298 K) of **TBF-2**. (c) Emission and excitation studies of **TBF-2** (10 μM, CH$_2$Cl$_2$, 298 K)

The optical properties of the dimer were probed in order to understand how the dynamic dimeric structure of **TBF-2** impacts the absorption and emissive abilities of TBF core. The UV–vis absorption profile for **TBF-2** in CH$_2$Cl$_2$ (Figure 3.9b) is vastly different from monomeric TBF with three broad absorption bands between 300–330 nm, 345–400 nm and 400–470 nm. The featureless absorption bands indicate a system in dynamic motion on the time scale of the experiment, similar to the conclusions

reached from the ^{1}H NMR spectrum of **TBF-2** at room temperature. In addition, the new absorption band at longer wavelengths (λ_{max} = 420 nm) is indicative of a dimer that is presumably stabilised by the intramolecular $\pi\cdots\pi$ interactions identified by X-ray analyses. Emission of **TBF-2** was probed at each of the absorption bands (λ_{ex} = 300, 380 and 430 nm) resulting in broad and featureless bands (Figure 3.9c). The highest intensity emissive signal was obtained by exciting the molecule at 300 nm, resulting in two emissive bands with maxima at 358 nm and 426 nm. **TBF-2** even shows some emission upon excitation at 430 nm with a maximum at 498 nm. The resulting excitation spectra gave back signals that resemble the absorption of **TBF-2**, however some bands were more red-shifted (e.g., λ(abs) = 420 nm *vs* λ(ex) = 433 nm), indicating a relaxation of the electronic states of **TBF-2** upon excitation. VT absorption or emission studies of **TBF-2** would help confirm observations about the dynamic structure of the dimer made from VT NMR studies. The results from the properties analysis study of **TBF-2** highlight just one example of the exotic structures that can be obtained by taking advantage of the redox properties of the fluorenyl core of TBF.

3.3 CONCLUSIONS

In this Chapter, the redox properties of anthracenyl-substituted TBFs were probed first electrochemically to understand how the head group influences their ability to lose electrons. While structurally very similar, the CV of **A-H** displayed a fully reversible first oxidation wave whereas for **A-OH**, this oxidation wave was found to be quasi-reversible on account of a fast chemical process occurring. The stabilities of these oxidation states were tested by the addition of pyridine, resulting in a dramatically changed voltammogram for **A-H** in particular – losing its reversibility for the first oxidation process. Instead, it is hypothesised that upon formation of the radical cation, the base is able to deprotonate at the fluorenyl-head position to form a neutral radical **TBF-A$^•$**. Following these positive results, **TBF-A$^•$** was synthesised from **A-OH** and its structural features studied by UV–vis spectroscopy and DFT calculations, while EPR spectroscopy confirms the paramagnetic nature of the radical following the removal of the –OH group. Spin density calculations highlight the localisation of the spin on the central cyclopentadienyl ring which when compared to literature compounds allow us to infer a similar ambient stability of the radical. Synthetic efforts to remake the radical need to be made and will enable the ambient stability of **TBF-A$^•$** to be quantitatively obtained by following the loss of absorption intensity over time. Finally, interrogations of the photostability of alcohol head-substituted TBFs led to the isolation of a TBF dimer **TBF-2** that is in dynamic motion about the C–C single bond with an energy barrier of 18.6 kcal mol^{-1}, significantly higher than for typical C–C single bonds. This dynamic motion translates into its optical properties resulting in broad and featureless absorption and emission curves. This Chapter has therefore highlighted the advantage of utilising the redox properties of TBFs to study exotic structures such as ambient stable radicals and TBF dimers.

3.4 SUPPLEMENTARY INFORMATION

3.4.1 MATERIALS AND METHODS

Materials. Unless stated, all chemicals and reagents were purchased from commercial suppliers (Sigma Aldrich, Fisher Scientific, Alfa Aesar and Fluorochem) and used without further purification. Anhydrous solvents were obtained from a neutral alumina Solvent Purification System under nitrogen and stored over activated (>250 °C, at 0.01 mbar overnight) 3 Å molecular sieves under a dry Ar atmosphere. Solvents and solutions required for air-sensitive manipulations were degassed thoroughly using a minimum of three freeze–pump–thaw cycles and the flask back-filled under an Ar atmosphere.

Product confirmation. Analytical thin-layer chromatography (TLC) was performed on aluminium-backed silica gel plates and visualised under UV irradiation (254 and 365 nm). Automated flash column chromatography was performed using a Teledyne ISCO Combiflash NextGen 300+ with detectors using broad range UV–vis (200-800 nm) and evaporative light scattering (ELS) under N_2 gas and pre-filled Redisep™ Gold cartridges (normal phase: SiO_2). High-resolution mass spectra were measured on a Bruker compact QTOF Atmospheric Pressure Ionisation Time of Flight instrument using an ESI or APCI source. Nuclear magnetic resonance (NMR) spectra were recorded on a JEOL ECS400D spectrometer (working frequencies of 400 MHz and 101 MHz for ^{1}H and ^{13}C nuclei) or a Bruker AVIIIHD500 (working frequencies of 500 MHz and 126 MHz for ^{1}H and ^{13}C nuclei). Chemical shifts (δ) are reported in parts per million (ppm) relative to the signals corresponding to residual non-deuterated solvents ($CDCl_3$: δ_H 7.26 ppm, δ_c 77.23 ppm). Coupling constants (J) are reported in Hertz (Hz) and ^{1}H multiplicities are reported in accordance with the following convention: s = singlet, d = doublet, t = triplet, q = quadruplet, p = pentet, m = multiplet. Assignment of ^{1}H and ^{13}C NMR signals were accomplished with the aid of two-dimensional ^{1}H–^{1}H COSY, ^{1}H–^{13}C HSQC and ^{1}H–^{13}C HMBC NMR spectroscopies. NMR spectra were processed using MestReNova software, Version 14.

Sample analysis. Single crystal X-ray diffraction data were collected on a single-crystal Oxford Diffraction SuperNova with dual Mo and Cu sources. A suitable crystal was selected and mounted (oil on 100 μm mount) on a SuperNova Dual, Cu at home/near, Eos diffractometer. The crystal was kept at 110.00(10) K during data collection. Using Olex2,[37] the structure was solved with the SHELXT[38] structure solution program using Intrinsic Phasing and refined with the SHELXL[39] refinement package using Least Squares minimisation. Absorption spectra were recorded on an Agilent Technologies Cary 5000 UV–vis-NIR spectrophotometer using standard 10 mm path length quartz cuvettes at room temperature. Solution-state fluorescence spectroscopy was carried out on a Hitachi F-4500 fluorimeter equipped with a 150 W Xe lamp using standard photoluminescence quartz cuvettes. Samples for solution-state spectroscopy had an optical density (O.D.) <0.1 in anhydrous and degassed solvent to allow for the measurements of fluorescence spectroscopy. Cyclic voltammetry (CV) and square-wave

voltammetry (SQWV) was carried out at room temperature on Ar-purged sample solutions in anhydrous CH_2Cl_2 using a Gamry Reference 3000 Potentiostat interfaced to a PC. Tetrabutylammonium hexafluorophosphate (TBAPF$_6$; 0.1 M) was recrystallized from hot EtOH and used as the supporting electrolyte. All solution-state electrochemical experiments were performed using a glassy carbon working electrode (BASi; 0.071 cm^2). The electrode surface was polished routinely with 0.05 μm alumina–water slurry on a felt surface immediately before each use. A Pt wire was used as the counter electrode and the reference electrode was an Ag/AgCl aqueous electrode stored routinely in a 3 M KCl aqueous solution. Spectroelectrochemistry (SEC) experiments were performed at room temperature using an optically transparent thin-layer electrochemical (OTTLE) cell (path length approx. 0.2 mm with two CaF$_2$ windows separated by PTFE spacers) fitted with a Pt wire mesh working electrode, Pt wire counter electrode and a Ag wire pseudo-reference electrode. All SEC samples were prepared as Ar-purged solutions in anhydrous CH_2Cl_2 or anhydrous THF containing TBAPF$_6$ (0.1 M) as the supporting electrolyte and analysed under a constant applied voltage. Electron paramagnetic spectroscopy (EPR) spectra were recorded at X-band on a Bruker EMX-Micro spectrometer using 0.1 G modulation amplitude. EPR samples (1000 μM) were prepared and stored in an anaerobic glove box (MBraun UniLab Pro) under a dry Ar atmosphere by in anhydrous and thoroughly degassed CH_2Cl_2 or PhMe solutions. Density functional theory (DFT) calculations were prepared on GaussView 6.0 and submitted to the University of York Viking High Performance Computing cluster and run on Gaussian 16 using Becke's three-parameter exchange functional with the gradient-corrected correlation formula of Lee, Yang and Parr (B3LYP)[40,41] paired with the split valence double-zeta 6-31G(d,p) basis set, PCM solvation model (CH_2Cl_2) and dispersion corrections (D3BJ)[42] unless stated otherwise.

3.4.2 SYNTHETIC DETAILS
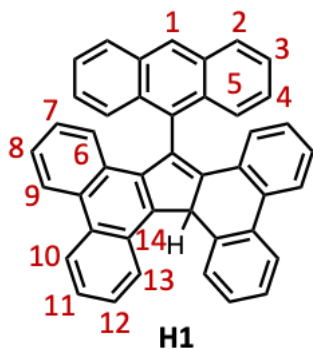
H1: To a flame-dried 2-necked round bottomed flask with a stirrer bar, SnCl$_2$ (0.187 g, 1.21 mmol, 12.3 equiv.) was added and the flask subjected to a nitrogen atmosphere by cycling under vacuum. In a separate vial, a solution of **A-OH** (55.2 mg, 0.099 mmol, 1.0 equiv.) in anhydrous and degassed CH_2Cl_2 (10 mL) was made and transferred into the reaction flask. The reaction vessel was covered with foil and left to stir at room temperature under the nitrogen atmosphere. Once a TLC (in 20% CH_2Cl_2 in *n*-hexanes) confirmed that starting material had been consumed, the reaction mixture was filtered and concentrated. **H1** was isolated by automated column chromatography (SiO$_2$: 0–20% CH_2Cl_2 in *n*-hexanes) as a white solid (26.4 mg, 0.049 mmol, 49%).

^{1}H NMR (CDCl$_3$, 400 MHz, 298 K): δ_H 8.83–8.77 (m, 1H$^{10'}$), 8.71 (d, J = 8.2 Hz, 1H^{13}), 8.63 (s, 1H^1), 8.27–8.23 (m, 1H$^{13'}$), 8.17 (d, J = 8.5 Hz, 1H^2), 8.05–7.96 (m, 2H$^{5,5'}$), 7.85 (dd, J = 7.9, 1.2 Hz, 2H$^{9,9'}$), 7.76–7.68 (m, 2H$^{11',12'}$), 7.64 (dd, J = 8.8, 1.1 Hz, 1H^2), 7.57–7.47 (m, 2H^{10,3}), 7.44–7.28 (m, 4H$^{4,4',8',12}$),

7.25–7.20 (m, 1H[11]), 7.11 (td, J = 7.6, 1.3 Hz, 1H[8]), 7.04–6.98 (m, 1H[3']), 6.77 (ddd, J = 8.2, 6.9, 1.2 Hz, 1H[7]), 6.66–6.60 (m, 2H[6',7]), 6.32 (dd, J = 7.8, 1.3 Hz, 1H[6]), 5.76 (s, 1H[14]). **APCI–HRMS** (ve+, CH$_2$Cl$_2$) calculated for C$_{43}$H$_{27}$: m/z = 542.2107 [M+H]$^+$; found 542.2100 [M+H]$^+$
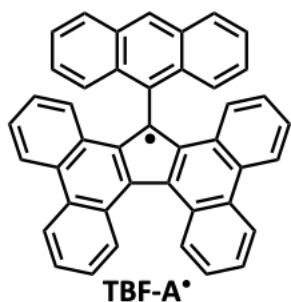
TBF-A$^\bullet$: To a flame-dried 2-necked round-bottomed flask with a stirrer bar, SnCl$_2$ (26.2 mg, 0.138 mmol, 7.8 equiv.) was added and the flask subjected to a nitrogen atmosphere by cycling under vacuum. In a separate vial, a solution of **A-OH** (19.8 mg, 0.035 mmol, 2.0 equiv.) in anhydrous and degassed CH$_2$Cl$_2$ (2.0 mL, 17.5 mM) was made and 1.0 mL of this solution transferred into the reaction flask. The reaction vessel was topped up with CH$_2$Cl$_2$ (10 mL), covered with foil and left to stir at room temperature under the nitrogen atmosphere. Once a TLC (in 20% CH$_2$Cl$_2$ in n-hexanes) confirmed that starting material had been consumed, the reaction mixture was filtered and concentrated. The desired product **TBF-A$^\bullet$** was isolated by automated column chromatography (SiO$_2$, 0–20% CH$_2$Cl$_2$ in n-hexanes) impure.

APCI–HRMS (ve+, CH$_2$Cl$_2$) calculated for C$_{43}$H$_{25}$$^\bullet$: m/z = 541.1956 [M]$^+$; found 541.1969 [M]$^+$

TBF=O': An excess magnesium turnings (17.6 mg, 0.72 mmol, 6.5 equiv.) and a catalytic amount of iodine were added to a flame-dried two-necked round bottomed flask with a stirrer bar and the flask was cycled under an Ar atmosphere. A solution of 9-bromoanthracene (50.3 mg, 0.19 mmol, 1.7 equiv.) in dry THF (1.5 mL) was added to the reaction mixture dropwise over 20 min at room temperature over which time a colour change to orange was observed. After stirring for 1 h, a solution of TBF-ketone **TBF=O** (43.1 mg, 0.11 mmol, 1.0 equiv.) in dry THF (12 mL) was added to the reaction mixture dropwise over 20 minutes. The reaction mixture was heated to 40 °C and was left to stir overnight. Once complete (confirmed by a crude ^{1}H NMR spectrum), a 1 M aqueous solution of HCl (5 mL) was added to quench the reaction mixture followed by additional HCl solution (5 mL) to destroy any leftover Mg turnings. The reaction mixture was extracted into CH$_2$Cl$_2$ (3 x 20 mL). The combined organic layers were washed with saturated aq. NaHCO$_3$ (20 mL) followed by brine (20 mL), dried over MgSO$_4$ and concentrated. The desired product **TBF=O'**, was isolated by automated column chromatography (SiO$_2$, 5% EtOAc in n-hexanes) as a yellow solid (15.9 mg, 0.042 mmol, 38%).

^{1}H NMR (CDCl$_3$, 400 MHz, 298 K): δ_H 9.20–9.12 (m, 1H[9]), 8.85 (dd, J = 8.2, 1.1 Hz, 1H[12]), 8.76–8.69 (m, 1H[16]), 8.50 (dd, J = 8.0, 1.4 Hz, 1H[13]), 7.99–7.90 (m, 2H[1,4]), 7.90–7.82 (m, 2H[2,3]), 7.75–7.65 (m, 2H[6,7]), 7.54–7.50 (m, 1H[10]), 7.48–7.40 (m, 2H[8,5]), 7.31–7.27 (m, 1H[11]), 7.23–7.19 (m, 1H[15]), 6.95 (t, J = 7.6 Hz, 1H[14]), 5.58 (d, J = 7.5 Hz, 1H[18]), 4.27 (d, J = 7.5 Hz, 1H[17]). **APCI–HRMS** (ve+, CH$_2$Cl$_2$) calculated for C$_{29}$H$_{19}$O: m/z = 383.1430 [M+H]$^+$; found 383.1434 [M+H]$^+$

3.4.3 NMR SPECTRA

Figure S3.1 ^{1}H NMR (CDCl$_3$, 400 MHz, 298K) spectrum of **H1**

Figure S3.2 Annotated ^{1}H–^{1}H COSY NMR (CDCl$_3$, 400 MHz, 298K) spectrum of **H1**

Figure S3.3 ^{1}H NMR (CDCl₃, 400 MHz, 298K) spectrum of **TBF=O'** with an attempt to assign the peaks

4.3.3.1 VT ^{1}H NMR ANALYSES

The coalescence temperature, T_C, was determined to be 298 K and the singlet proton peak at ~6.1 ppm, assigned to one of the TBF head position protons was used to calculate a change in chemical shift ($\Delta v = \delta_{328} - \delta_{218}$). The barrier to rotation about the C–C single bond, $\Delta G^{\ddagger}$ was therefore calculated using the approximation method[34,43] and Equation S1 to be around 18.6 kcal mol^{-1}.

$$\Delta G^{\ddagger} = RT_C \left[22.96 + \ln\left(\frac{T_C}{\Delta v}\right) \right] \qquad (Eq.\,S1)$$

$$\Delta v = 6.0860 - 6.147 = 0.061$$

$$T_C = 298\,K$$

$$\Delta G^{\ddagger} = 18.6\,kcal\,mol^{-1}$$

where R is the ideal gas constant.

3.4.4 SUPPLEMENTARY SPECTRA

3.4.4.1 CYCLIC VOLTAMMETRY

Cyclic voltammograms of **A-OH**, **A-H**, **TBF** were recorded at room temperature in deaerated CH$_2$Cl$_2$ solutions with 0.1 M TBAPF$_6$ as supporting electrolyte under an argon atmosphere using a standard three-electrode set up. See Section 3.4.1 for full experimental details. Table S3.1 summarises energy level and band gap parameters derived from solution-state experiments. The current intensity is directly proportional to the square-root of the scan rate for each CV experiment which reveals that the oxidation waves for **A-H** and **TBF** are highly reversible. A non-linear relationship for **A-OH** confirms the quasi-reversibility for its first oxidation process.

Figure S3.4. Full window cyclic voltammograms of **A-OH**, **A-H**, and **TBF** (1 mM solutions in a 0.1 M TBAPF$_6$ solution in CH$_2$Cl$_2$ measured at 100 mVs^{-1})

Table S3.1 Optical band gap and HOMO energy level calculations from experimental absorption and cyclic voltammetry studies in CH_2Cl_2 of **A-OH** and **A-H**

	ε / $M^{-1}cm^{-1}$	$E_{bg,opt}{}^a$ / eV	$E^{ox}_{1/2}$ / V	(E_{onset}) HOMO[b] / eV	LUMO[c] / eV
A-OH	1.57×10^4	2.67	1.29	(1.00) -5.80	-3.13
A-H	1.93×10^4	2.80	1.27	(0.99) -5.78	-2.98

[a]The optical band gap ($E_{bg,opt}$) was determined from the onset of absorption; [b]The energy of the HOMO was calculated using the equation: HOMO = $-(E_{onset,ox} + 4.80)$ eV; [c]LUMO = HOMO + $E_{bg,opt}$

The molar absorption coefficients (ε) were obtained from straight line graphs of absorption (A) at 365 nm against concentration (c) and with a path length (l) of 1 cm according to Equation S2:

$$A = \varepsilon c l \qquad (Eq.\,S2)$$

Where the gradient of these straight lines is equal to ε.

Figure S3.5. Straight line graphs of the absorption at 365 nm against the concentration of **A-OH**, **A-H**, **B-OH**, **B-H** in order to calculate molar absorption coefficients in THF.

Figure S3.6 (a) The reversibility of the first oxidation of **A-H** and **TBF** is highlighted by a linear relationship between peak current and the square root of scan rate, $\sqrt{v}$, while the first oxidation peak for **A-OH** is quasi-reversible. Variable scan rate dependent cyclic voltammograms of the first oxidation of (b) **A-H** (c) **TBF** and (d) **A-OH**

3.4.4.2 OTHER SPECTRA

Figure S3.7 (a) Absorption spectrum of **A-H** in CH_2Cl_2 with 0.3% pyridine. No difference is observed to the absorption profile of **A-H** compared to when there is no base present. The increase in intensity at 800 nm exists because of a detector change in the spectrometer.

Figure S3.8 (a) EPR spectrum of **TBF-A·** in (2-month-old crude sample stored under ambient conditions in solution in a screw capped vial, 500 μM, CH₂Cl₂). **(b)** IR spectrum of a crude material of **TBF-A·** (blue) against **A-OH** (purple trace) highlighting a loss of the peak at 3495 cm⁻¹ corresponding to an –OH stretching mode.

3.4.5 X-RAY DIFFRACTION ANALYSES

TBF=O'

Single crystals of **TBF=O'** (aja21020) were grown from a solution of CHCl₃ by slow evaporation.

Figure S3.9. (a) Structural parameters of **TBF=O'** highlighted in blue and (b) its supramolecular packing. Non-interacting H atoms have been omitted for clarity.

Crystal data for $C_{29}H_{18}O$ (M = 382.43 g/mol): monoclinic, space group P2₁/n, a = 4.56660(12) Å, b = 23.8119(7) Å, c = 16.9160(4) Å, β = 92.921(2)°, V = 1837.05(8) Å³, Z = 4, T = 110.00(10) K, μ(Cu Kα) = 0.636 mm⁻¹, D_{calc} = 1.383 g/cm³, 6298 reflections measured (9.086° ≤ 2θ ≤ 135.15°), 3293 unique (R_{int} = 0.0221, R_{sigma} = 0.0294) which were used in all calculations. The final R_1 was 0.0361 (I > 2σ(I)) and wR_2 was 0.0963 (all data).

TBF-2

Single crystals of **TBF-2** (aja23017) were grown from a solution of CH_2Cl_2 and *n*-hexanes by solvent layering.

Figure S3.10. (a) Structural parameters of a representative *P,P*-**TBF-2** highlighted in red and (b) the supramolecular packing of the racemate. Non-interacting H atoms have been omitted for clarity.

Crystal data for $C_{59}H_{36}Cl_2$ ($M =815.78$ g/mol): monoclinic, space group $P2_1/n$ (no. 14), $a = 13.83379(14)$ Å, $b = 20.02735(14)$ Å, $c = 14.92887(15)$ Å, $\beta = 110.8407(11)°$, $V = 3865.49(7)$ Å^3, $Z = 4$, $T = 110.00(10)$ K, μ(Cu Kα) = 1.843 mm^{-1}, $D_{calc} = 1.402$ g/cm^3, 25847 reflections measured (7.488° $\leq 2\theta \leq 154.194°$), 7872 unique ($R_{int} = 0.0286$, $R_{sigma} = 0.0304$) which were used in all calculations. The final R_1 was 0.0389 (I > 2σ(I)) and wR_2 was 0.1090 (all data).

3.4.6 DFT ANALYSES

DFT calculations were performed to obtain geometrically optimised structures of both enantiomers of **TBF-A•** using UB3LYP(GD3BJ)/6-31G(d,p) in a CH_2Cl_2 solvent model. Ground state geometries were verified by convergence to a minimum stationary point and no negative vibrational frequencies observed. Time dependent DFT (TD-DFT) calculations were performed for the first 20 states of each compound using UB3LYP(GD3BJ)/6-31G(d,p) in a CH_2Cl_2 solvent model.

3.4.6.1 CARTESIAN COORDINATES

P-**TBF-A•**

C	-7.367141	4.728461	3.914144
C	-6.615970	4.042649	2.982552
C	-6.726537	4.318541	1.593900
C	-7.569950	5.400175	1.170802
C	-8.334711	6.067908	2.151438
C	-8.253852	5.734427	3.491870
H	-7.257502	4.504405	4.970330
H	-8.980391	6.887904	1.863120
H	-8.850395	6.276025	4.218929
C	-6.628890	5.267332	-1.141093
C	-5.758403	4.220720	-0.665888
C	-7.581874	5.816615	-0.227822
C	-8.492524	6.783750	-0.709191
C	-6.626184	5.721743	-2.480569
C	-8.466686	7.214349	-2.022853
H	-9.242944	7.194586	-0.044957
C	-7.522930	6.679364	-2.914656
H	-5.926133	5.293768	-3.183393
H	-9.181743	7.956538	-2.363094
H	-7.504755	7.004774	-3.950106
C	-5.937656	3.647307	0.608636
C	-4.635205	3.574881	-1.295756
C	-4.170876	2.533751	-0.414896
C	-5.032617	2.482878	0.698726
C	-3.044793	1.640261	-0.527011
C	-5.042934	1.332462	1.547289
C	-2.912827	0.598768	0.443460
C	-2.036826	1.791505	-1.507752
C	-6.132081	1.021695	2.403916
C	-3.965238	0.391302	1.432946

C	-1.768899	-0.228641	0.388469
H	-2.116329	2.591633	-2.229320
C	-0.937158	0.955280	-1.540624
C	-6.128784	-0.112395	3.188929
C	-3.989696	-0.749581	2.263763
C	-0.799286	-0.062803	-0.583180
H	-1.630846	-1.006446	1.129420
H	-0.173902	1.098141	-2.299182
C	-5.035053	-0.994184	3.136651
H	-6.977535	-0.331507	3.828739
H	-3.190797	-1.477822	2.200635
H	0.069674	-0.712907	-0.596944
H	-5.024234	-1.886810	3.753830
C	-2.328743	7.137594	-1.837459
C	-3.058310	5.990866	-1.664750
C	-3.304341	5.103967	-2.758256
C	-2.751154	5.438352	-4.048166
C	-1.993422	6.642634	-4.184139
C	-1.789582	7.470819	-3.113222
C	-4.061471	3.919516	-2.611622
C	-2.965476	4.580731	-5.131839
C	-3.708877	3.403706	-4.998464
C	-4.274468	3.063095	-3.715614
C	-5.041847	1.861863	-3.610611
H	-5.478571	1.604966	-2.652337
C	-5.224657	1.045003	-4.695208
C	-4.659448	1.378295	-5.959630
C	-3.926619	2.525545	-6.104950
H	-2.155364	7.800262	-0.995497
H	-3.462046	5.740801	-0.690335
H	-1.582303	6.885089	-5.159837
H	-1.213644	8.383431	-3.229086

H	-2.544353	4.835102	-6.100837
H	-5.807889	0.135139	-4.594820
H	-4.816770	0.718486	-6.806912
H	-3.495751	2.791302	-7.065931
H	-6.997042	1.670663	2.408512
H	-5.898106	3.305424	3.315003

M-**TBF-A**[•]

C	-7.367141	4.728461	-3.914144
C	-6.615969	4.042649	-2.982552
C	-6.726537	4.318541	-1.593900
C	-7.569950	5.400175	-1.170802
C	-8.334711	6.067908	-2.151437
C	-8.253852	5.734427	-3.491870
H	-7.257501	4.504406	-4.970330
H	-8.980391	6.887905	-1.863120
H	-8.850395	6.276025	-4.218929
C	-6.628890	5.267332	1.141093
C	-5.758403	4.220720	0.665888
C	-7.581874	5.816615	0.227822
C	-8.492524	6.783749	0.709192
C	-6.626184	5.721743	2.480569
C	-8.466686	7.214348	2.022854
H	-9.242945	7.194585	0.044957
C	-7.522931	6.679363	2.914656
H	-5.926133	5.293768	3.183394
H	-9.181744	7.956537	2.363094
H	-7.504755	7.004773	3.950107
C	-5.937656	3.647307	-0.608636
C	-4.635205	3.574881	1.295756
C	-4.170876	2.533751	0.414896
C	-5.032617	2.482879	-0.698726
C	-3.044793	1.640261	0.527011
C	-5.042934	1.332462	-1.547289
C	-2.912827	0.598768	-0.443460
C	-2.036826	1.791505	1.507752
C	-6.132081	1.021695	-2.403916
C	-3.965238	0.391302	-1.432946
C	-1.768899	-0.228641	-0.388469
H	-2.116328	2.591633	2.229320

C	-0.937158	0.955280	1.540624
C	-6.128784	-0.112395	-3.188929
C	-3.989696	-0.749581	-2.263763
C	-0.799286	-0.062803	0.583181
H	-1.630847	-1.006447	-1.129419
H	-0.173902	1.098141	2.299182
C	-5.035053	-0.994184	-3.136651
H	-6.977535	-0.331507	-3.828740
H	-3.190798	-1.477822	-2.200635
H	0.069674	-0.712907	0.596944
H	-5.024234	-1.886809	-3.753831
C	-2.328743	7.137594	1.837459
C	-3.058310	5.990866	1.664750
C	-3.304341	5.103967	2.758256
C	-2.751154	5.438353	4.048166
C	-1.993422	6.642635	4.184139
C	-1.789582	7.470819	3.113222
C	-4.061470	3.919516	2.611622
C	-2.965476	4.580732	5.131838
C	-3.708877	3.403707	4.998464
C	-4.274468	3.063096	3.715614
C	-5.041847	1.861863	3.610611
H	-5.478571	1.604966	2.652337
C	-5.224657	1.045004	4.695208
C	-4.659448	1.378295	5.959630
C	-3.926619	2.525546	6.104950
H	-2.155363	7.800262	0.995496
H	-3.462045	5.740801	0.690334
H	-1.582303	6.885089	5.159837
H	-1.213644	8.383431	3.229085
H	-2.544353	4.835103	6.100837
H	-5.807889	0.135140	4.594820
H	-4.816770	0.718486	6.806912
H	-3.495751	2.791302	7.065931
H	-6.997041	1.670663	-2.408512
H	-5.898106	3.305424	-3.315003

3.5 REFERENCES

1.   Brunetti, F. G.; Gong, X.; Tong, M.; Heeger, A. J.; Wudl, F. Strain and Hückel Aromaticity: Driving Forces for a Promising New Generation of Electron Acceptors in Organic Electronics, *Angew. Chem. Int. Ed.* **2010**, *49*, 532–536.

2.   Zhao, S.; Bian, Z.; Liu, Z.; Wang, Y.; Cui, F.; Wang, H.-G.; Zhu, G. Bottom-Up Construction of Fluorene-Based Porous Aromatic Frameworks for Ultrahigh-Capacity and High-Rate Alkali Metal-Ion Batteries, *Adv. Funct. Mater.* **2022**, *32*, 2204539.

3.   Tian, Y.; Uchida, K.; Kurata, H.; Hirao, Y.; Nishiuchi, T.; Kubo, T. Design and Synthesis of New Stable Fluorenyl-Based Radicals, *J. Am. Chem. Soc.* **2014**, *136*, 12784–12793.

4.   Nishiuchi, T.; Ito, R.; Takada, A.; Yasuda, Y.; Nagata, T.; Stratmann, E.; Kubo, T. Anthracene-Attached Persistent Tricyclic Aromatic Hydrocarbon Radicals, *Chem. Asian. J.* **2019**, *14*, 1830–1836.

5.   Markle, T. F.; Darcy, J. W.; Mayer, J. M. A New Strategy to Efficiently Cleave and Form C–H Bonds using Proton-Coupled Electron Transfer. *Sci. Adv.* **2018**, *4*, eaat5776.

6.   Shaikh, A. C.; Moutet, J.; Veleta, J. M.; Hossain, M. M.; Bloch, J.; Astashkin, A. V.; Gianetti, T. L. Persistent, Highly Localized, and Tunable [4]Helicene Radicals. *Chem. Sci.* **2020**, *11*, 11060–11067.

7.   Murto, P.; Chowdhury, R.; Gorgon, S.; Guo, E.; Zeng, W.; Li, B.; Sun, Y.; Francis, H.; Friend, R. H.; Bronstein, H. Mesitylated Trityl Radicals, A Platform for Doublet Emission: Symmetry Breaking, Charge-Transfer States and Conjugated Polymers, *Nat. Commun.* **2023**, *24*, 4147.

8.   Mayorga-Burrezo, P.; Jiménez, V. G.; Blasi, D.; Ratera, I.; Campaña, A. G.; Veciana, J. Organic Free Radicals as Circularly Polarized Luminescence Emitters. *Angew. Chem. Int. Ed.* **2019**, *58*, 16282–16288.

9.   Wang, Y.; Jiang, Y.; Zhu, X.; Liu, M. Significantly Boosted and Inversed Circularly Polarized Luminescence from Photogenerated Radical Anions in Dipeptide Naphthalenediimide Assemblies. *J. Phys. Chem. Lett.* **2019**, *10*, 5861–5867.

10. Hudson, J. M.; Hele, T. J. H.; Evans, E. W. Efficient Light-Emitting Diodes from Organic Radicals with Doublet Emission. *J. Appl. Phys.* **2021**, *129*, 180901.

11. Xiao, C.; Wu, W.; Liang, W.; Zhou, D.; Kanagaraj, K.; Cheng, G.; Su, D.; Zhong, Z.; Chruma, J. J.; Yang. C. Redox-Triggered Chirality Switching and Guest-Capture/Release with a Pillar[6]arene-Based Molecular Universal Joint, *Angew. Chem. Int. Ed.* **2020**, *59*, 8094–8098.

12. Yang, Y.; da Costa, R. C.; Fuchter, M. J.; Campbell. A. J. Circularly Polarized Light Detection By a Chiral Ligand Semiconductor Transistor, *Nat. Photo.* **2013**, *7*, 634–638.

13. Mayorga-Burrezo, P.; Jiménez, V. G.; Blasi, D.; Parella, T.; Ratera, I.; Campaña, A. G.; Veciana, J. An Enantiopure Propeller-Like Trityl-Brominated Radical: Bringing Together a High Racemization Barrier and an Efficient Circularly Polarized Luminescent Magnetic Emitter. *Chem. Eur. J.* **2020**, *26*, 3776–3781.

14. Eakins, G. L.; Alford, J. S.; Tiegs, B. J.; Breyfogle, B. E.; Stearman, C. J. Tuning HOMO–LUMO Levels: Trends Leading to the Design of 9-Fluorenone Scaffolds with Predictable Electronic and Optoelectronic Properties, *J. Phys. Org. Chem.* **2011**, *24*, 1119–1128.

15. Bordwell, F. G.; Cheng, J.-P.; Bausch, M. J. Acidities of Radical Cations Derived from Remotely Substituted and Phenyl-Substituted Fluorenes, *J. Am. Chem. Soc.* **1988**, *110*, 2867–2872.

16. Kuhn, R.; Rewicki, D. Die Acidität von Dibenzofluorenen, *Liebigs. Ann. Chem.* **1967**, *704*, 9–14.

17. Trung, N. Q.; Mechler, A.; Hoa, N. T.; Vo, Q. V. Calculating Bond Dissociation Energies of X–H (X=C, N, O, S) Bonds of Aromatic Systems *via* Density Functional Theory: A Detailed Comparison of Methods, *R. Soc. Open. Sci*, **2022**, *9*, 220177.

18. Allen, A. D.; Tidwell, T. T. Antiaromaticity in Open-Shell Cyclopropenyl to Cycloheptatrienyl Cations, Anions, Free Radicals, and Radical Ions, *Chem. Rev.* **2001**, *101*, 1333–1348.

19. Brøløs, L.; Kilde, M. D.; Hammerich, O.; Nielsen, M. B. Toward Redox-Active Indenofluorene-Extended Tetrathiafulvalene Oligomers–Synthesis and Studies of Dimeric Scaffolds, *J. Org. Chem.* **2020**, *85*, 3277–3286.

20. Christensen, M. A.; Parker, C. R.; Sørensen, T. J.; de Graaf, S.; Morsing, T. J.; Brock-Nannestad, T.; Bendix, J.; Haley, M. M.; Rapta, P.; Danilov, A.; Kubatkin, S.; Hammerich, O.; Nielsen, M. B. Mixed Valence Radical Cations and Intermolecular Complexed Derived from Indenofluorene-Extended Tetrathiafulvalenes, *J. Mater. Chem. C.* **2014**, *2*, 10428–10438.

21. Nishinaga, T.; Inoue, R.; Matsuura, A.; Komatsu, K. Radical Cation and Dication of Fluorene Fully Annealated with Bicyclo[2.2.2]octene Units: Importance of the Quinoidal Resonance in the Cationic Fluorene, *Org. Lett.* **2002**, *4*, 4117–4120.

22. Silverstein, T. P; Heller, S. T. pK_a Values in the Undergraduate Curriculum: What is the Real pK_a of Water, *J. Chem. Educ.* **2017**, *94*, 690–695.

23. Hapiot, P.; Lagrost, C.; Floch, F. L.; Raoult, E.; Rault-Berthelot, J. Comparative Study of the Oxidation of Fluorene and 9,9-Disubstituted Fluorenes and Their Related 2,7'-Dimers and Trimer, *Chem. Mater.* **2005**, *17*, 2003–2012.

24. Marshall, J. L.; Lehnherr, D.; Lindner, B. D.; Tywinski, R. R. Reductive Aromatization/Dearomatization and Elimination Reactions to Access Conjugated Polycyclic Hydrocarbons, Heteroacenes, and Cumulenes, *ChemPlusChem*, **2017**, *82*, 967–1001.

25. Rose, B. D.; Vonnegut, C. L.; Zakharov, L. N.; Haley, M. M. Fluoreno[4,3-*c*]fluorene: A Closed-Shell, Fully Conjugated Hydrocarbon, *Org. Lett.* **2012**, *14*, 2426–2429.

26. Gomberg, M.; Bachmann, W. The Reducing Action of a Mixture of Magnesium Iodide (or Bromine) and Magnesium on Aromatic Ketones. Probable Formation of Magnesium Subiodide (or Subbromide). *J. Am. Chem. Soc.* **1927**, *49*, 236–257.

27. Wan, P.; Krogh, E. Evidence for the Generation of Aromatic Cationic Systems in the Excited State. Photochemical Solvolysis of Fluoren-9-ol, *J. Chem. Soc. Chem. Commun.* **1985**, 1207–1208.

28. Dyblenko, T.; Chtchemelinine, A.; Reiter, R.; Chowdhury, R. Q.; Enaya, A.; Afifi, H.; Fournier, R.; Mladenova, G.; Lever, A. B. P.; Lee-Ruf, E. Photochemical Generation of 9H-Fluorenyl Radicals, *Photochem. Photobiol.* **2013**, *90*, 470–475.

29. Kinani, S.; Souissi, Y.; Kinani, A.; Vujović, S.; Aït-Aïssa, S.; Bouchonnet, S. Photodegradation of Fluorene in Aqueous Solution: Identification and Biological Activity Testing of Degradation Products, *J. Chromatogr. A.* **2016**, *1442*, 118–128.

30. Dey, D.; Kundu, A.; Mandal, B.; Roy, M.; Adhikari, D. Deciphering the Single Electron Transfer Ability of Fluorene Under Photoredox Conditions, *Catal. Sci. Technol.* **2022**, *12*, 7322–7327.

31. Jose, B.; Prathapan, S. Acid-Catalysed Decomposition of Diazofluorene, *J. Chem. Research.* **2000**, 478.

32. Schröder, K.; Haase, D.; Saak, W.; Lützen, A.; Beckhaus, R.; Wichmann, S.; Schellenbeg, J. Tetrabenzo[*a,c,g,i*]fluorenyllithium and η^5-Tetrabenzo[*a,c,g,i*]fluorenyltitanium Complexes, *Organometallics*, **2006**, *25*, 3824–3826.

33. Knjazhanski, S. Y.; Moreno, G.; Cadenas, G.; Belsky, V. K.; Bulychev, B. M. Preparation of Bifluorenes *via* the Synthesis and Thermal Decomposition of Fluorenyltitanium(IV)trichlorides. Molecular and Crystal Structure of 9,9'-Bis(trimethylsilyl)-bi-9,9'-fluorene, *Tetrahedron*, **1999**, *55*, 1639–1646.

34. Bühringer, M. U.; Padberg, K.; Phleps, M. D.; Maid, H.; Placht, C.; Neiss, C.; Ferguson, M. J.; Görling, A.; Tykwinski, R. R. Double Bonds? Studies on the Barrier to Rotation About the Cumulenic C=C Bonds of Tetraaryl[*n*]cumulenes (*n*=3, 5, 7, 9), *Angew. Chem. Int. Ed.* **2018**, *57*, 8321–8325.

35. Fokin, A. A.; Chernish, L. V.; Gunchenko, P. A.; Tikhonchuk, E. Y.; Hausmann, H.; Serafin, M.; Dahl, J. E. P.; Carlson, R. M. K.; Schreiner, P. R. Stable Alkanes Containing Very Long Carbon–Carbon Bonds, *J. Am. Chem. Soc.* **2012**, *134*, 13641–13650.

36. Kang, H.-W.; Liu, Y.-C.; Shao, W.-K.; Wei, Y.-C.; Hsieh, C.-T.; Chen, B.-H.; Lu, C.-H.; Yang, S.-D.; Cheng, M.-J.; Chou, P.-T.; Chiang, M.-H.; Wu, Y.-T. Synthesis, Structural Analysis, and Properties of Highly Twisted Alkenes 13,13'-Bis(dibenzo[*a,i*]fluorenylidene) and its Derivatives, *Nat. Commun.* **2023**, *14*, 5248.

37. Dolomanov, O. V.; Bourhis, L. J.; Gildea, R. J.; Howard, J. A. K.; Puschmann, H. OLEX2: A Complete Structure Solution, Refinement and Analysis Program, *J. Appl. Cryst.* **2009**, *42*, 339–341.

38. Sheldrick, G. M. SHELXT-Integrated Space-Group and Crystal-Structure Determination, *Acta. Cryst.* **2015**, *A71*, 3–8.

39. Sheldrick, G. M. Crystal Structure Refinement with SHELXL, *Acta. Cryst.* **2015**, *C71*, 3–8.

40. Becke, A. D. Density-Functional Thermochemistry. III. The Role of Exact Exchange, *J. Chem. Phys.* **1993**, *98*, 5648–5652.

41. Lee, C.; Yang, W.; Parr, R. G. Development of the Colle-Salvetti Correlation-Energy Formula into a Functional of the Electron Density, *Phys. Rev. B.* **1988**, *37*, 785–789.

42. Grimme, S.; Ehrlich, S.; Goerigk, L. Effect of the Damping Function in Dispersion Corrected Density Functional Theory, *J. Comp. Chem.* **2011**, *32*, 1456–1465.

43. Huggins, M. T.; Kesharwani, T.; Buttrick, J.; Nicholson, C. Variable Temperature NMR Experiment Studying Restricted Bond Rotation, *J. Chem. Educ.* **2020**, *97*, 1425–1429.

CHAPTER 4 |
TOWARDS CONFIGURATIONALLY STABLE TETRABENZOFLUORENES

SYNOPSIS

In the design of efficient light-emitting enantiopure organic molecules for advanced chiroptical applications, helicenes – featuring *ortho*-fused polyaromatic non-planar structures – have generally performed well due to the inherent chirality of their backbones. However, the configurational stability of smaller helicenes (< six fused rings) is not sufficiently high to prevent dynamic interconversion between enantiomers at room temperature in solution. In particular, although embedding the highly photoactive fluorene should boost the solution and solid-state PLQY as well as the chiroptical response of [5]helicene-like tetrabenzofluorenes (TBFs), the central 5-membered ring appears to hamper its configurational stability even further compared to benzenoid helicenes. This Chapter discusses computational efforts to investigate the energy barriers associated with the interconversion between enantiomers ($\Delta G^{\ddagger}$) of TBFs introduced in previous Chapters. Then the effectiveness of design strategies towards increasing these interconversion barriers is examined. Increasing the steric bulk in the *fjord* region with methyl groups, or by increasing the length of the helicene structure (e.g., to a [7]helicene) is predicted by DFT calculations to achieve the desired configurational stability without affecting the optical properties of the proposed systems. Finally, synthetic efforts to isolate these helicene targets are discussed including the challenges faced and how these were overcome, with alternative synthetic routes proposed.

4.1 INTRODUCTION

As discussed in Chapter 1 (Section 1.4), research into chiral organic small molecules has gained interest over the years as researchers aim to take advantage of their structural diversity to develop chiral fluorescent materials that produce circularly polarised luminescence[1] (CPL) of single light-handedness. The performance of CPL-active molecules is evaluated by their luminescence dissymmetry factor[2] g_{lum} (Eq. 1). Such a property is likely to be sought after in light-emitting device applications and chiral probing/sensing applications.[3] Among chiral organic small molecules, helicenes have surfaced as desirable CPL-active candidates and have been found to possess some of the highest g_{lum} values owing to the inherent chirality in their helical structure.[4] Unfortunately, the photoluminescence quantum yields (PLQYs) of simple carbon-containing helicenes (i.e., carbohelicenes) are poor in both the solution- and solid-states.[5] For example, the PLQY of [5]helicene is 0.04 in solution. Similarly, a triple carbo[5]helicene, which has three helical components fused to its backbone and therefore has extended conjugation, was found to have a PLQY of only 0.062 in solution and 0.058 as a powder.[6]

$$|g_{lum}| = \frac{2(I_L - I_R)}{I_L + I_R} \quad Eq. 1$$

Despite the attractive luminescence features and potential for stimuli-responsiveness offered by fluorene, there are only a few reports that study the effectiveness of incorporating this motif into helicene scaffolds in order to boost solution-state CPL emission efficiencies.[7,8] Fluorenyl-embedded [7]helicene structures were found to be configurationally stable such that their chiroptical response could be evaluated (Figure 4.1a). Examples[7,8] showed marked increases in quantum yields (of between 0.32–0.40 compared to 0.02 for [7]helicene)[5] along with reasonably high g_{lum} values in their CPL signals. Studying fluorene-embedded helicenes therefore presents itself as a great opportunity to understand structure-property relationships that enhance the chiroptical response of CPL-active helicenes and enable access to solid-state emission properties. However, fluorenyl-embedded *ortho*-fused molecules based on TBF have not been interrogated in much detail for their CPL abilities, despite X-ray crystal structures of the butterfly-shaped molecule confirming its non-planar [5]helicene-like structure (Figure 4.1b).[9] Although presenting itself as an attractive AEE-active target[10,11] (discussed in Chapter 2), relatively low inversion barriers ($\Delta G^{\ddagger} = 14.1$ kcal mol^{-1} by VT NMR)[9] render TBF configurationally unstable.

Fortunately, there exist multiple strategies to increase the configurational stability of such helical structures. The first strategy involves (i) extending the π-conjugation to access higher order helicenes[12,13] such as the fluorene-centred [7]helicene studied by Oyama, H. et al.[7] (Figure 4.1a) which is configurationally stable. Then, (ii) increasing the steric bulk of the atoms located in the *fjord* region[14] can favourably increase $\Delta G^{\ddagger}$, where methyl groups have been shown to be highly effective steric groups[15] when substituted into the *fjord* region of carbohelicenes. Finally, (iii) increasing the chiral

complexity of helicenes by introducing multiple stereogenic axes[16] has been shown to be suitable at increasing $\Delta G^{\ddagger}$, where a triple[5]helicene is configurationally stable even though [5]helicene on its own is not. This strategy additionally lends itself to enhanced g_{lum} values. In this Chapter, initially, the configurational stability of key molecules discussed in Chapter 2 and 3 including **A-OH**, **A-H**, **B-OH** and **TBF-A**˙ (Table 4.1 and Figure 4.2) are explored by DFT calculations of transition state interconversion energy barriers. Then, structures of configurationally stable fluorenyl-embedded helicene analogues of TBF are identified, targeting each of the strategies discussed above (e.g., (i) **7HTBF**, (ii) **MeTBF**, and (iii) **TNF**, Figure 4.1c). TD-DFT calculations provide an insight into the optical properties of the target helicenes before a discussion on the synthesis of brominated precursors and attempts to isolate the helicene targets.
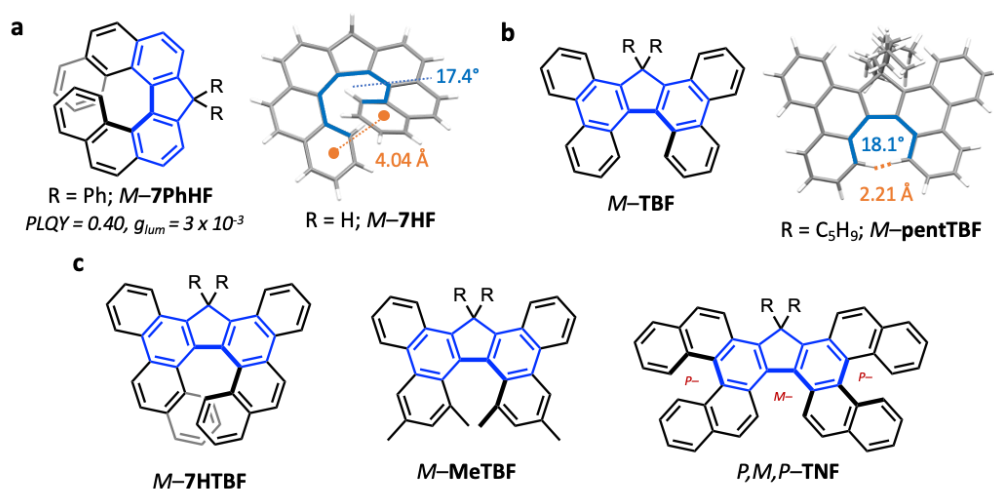
Figure 4.1 Example of (a) a fluorene-embedded [7]helicene[7] and (b) a dialkylated TBF along with their X-ray crystal structures. Typical structural helical parameters are indicated on crystal structures in blue and orange. (c) Structures of **7HTBF**, **MeTBF** and **TNF** highlighting different structural methods of increasing configurational stability. The R-group is simplified to R=H for DFT calculations.

4.2 RESULTS AND DISCUSSION

4.2.1 PREDICTING STRUCTURAL DYNAMICS

In order to investigate the chiroptical activity of fluorene-centred helicenes, it is necessary to generate systems with high configurational stability. For context, the Gibbs free energy barrier of enantiomerisation, $\Delta G^{\ddagger}$ of [5]helicene is 24.1 kcal mol^{-1} at 298 K in solution and an enantioenriched sample racemises over 29 h under ambient conditions.[13] DFT transition state optimisations for the interconversion between $M-$ and $P-$ enantiomers of **A-OH** (B3LYP(GD3BJ)/6-31G(d,p) in CH$_2$Cl$_2$) reveal an enantiomerisation energy barrier (summarised in Table 4.1) of 12.6 kcal mol^{-1}, similar to the interconversion barriers measured experimentally for dialkylated TBFs (14.1 kcal mol^{-1} at 10 °C).[9] These results imply that **A-OH** is likely to have a low configurational stability and interconverts between enantiomers at a fast rate at room temperature. In fact, the interconversion barrier for **A-OH** is

understandably smaller than the barrier for [5]helicene because the cyclopentadienyl ring causes a widened average C-C-C bond angle between the atoms within the internal *fjord* (i.e., from 125.2° in [5]helicene to 131.1°; discussed in Chapter 2). This widened *fjord* loosens the helical pitch of the fluorenyl[5]helicene structure, allowing for easier interconversion between enantiomers.

There is a slight effect on the enantiomerisation barrier from the R-group in the head position of TBF, evident by comparing the respective interconversion barriers for **A-OH**, **A-H** and **B-OH** (Table 4.1). A larger steric bulk of the combined R groups appears to increase the interconversion barrier slightly (i.e., **A-OH** > **A-H** > **B-OH**). Steric and/or electronic effects between head group substituents were found in Chapter 2 to affect anthracene-TBF torsional angles. Larger steric interactions/weaker intramolecular interactions between head-group substituents were observed to position the anthracene moiety closer to a single face of the TBF (i.e., top or bottom face). In this case, the spatial orientation of the anthracene (Figure 4.2) hinders the geometrical adjustments that the TBF backbone needs to make in order to interconvert between enantiomers resulting in a relatively larger barrier. On the other hand, the flexibility of the butyl group in the head-position avoids hindering the interconversion of the TBF backbone, resulting in relatively lower enantiomerisation barriers. Unfortunately, these results therefore suggest that **TBF-A$^{•}$** ($\Delta G^{\ddagger}$ =13.1 kcal mol^{-1}), pursued in Chapter 3, is predicted to be configurationally unstable.

Table 4.1 Summary of the Gibbs free energy of enantiomerisation, $\Delta G^{\ddagger}$, determined by DFT transition state calculations ((U)B3LYP (GD3BJ) / 6-31G(d,p) in CH$_2$Cl$_2$)

Compound	$\Delta G^{\ddagger}$ / kcal mol^{-1}
A-OH	12.6
A-H	11.8
B-OH	9.15
TBF-A$^{•}$	13.1
MeTBF	37.8
7HTBF	34.0
[5]helicene[13]	24.1

Configurationally stable TBFs were therefore targeted by following each of the three strategies discussed in the introduction. Firstly, a two-fold *ortho* π-extension of the tetrabenzofluorene [5]helicene framework into a [7]helicene-based TBF with chrysene wings, **7HTBF** (Figure 4.1c) is predicted to have a sufficiently high barrier to enantiomerisation of 34.0 kcal mol^{-1}. The transition state of this [7]helical framework adopts a highly strained, non-planar, saddle-like transition state geometry (Figure 4.2) that is consistent with that of other configurationally stable [7]helicenes in the literature.[7,8] Secondly, introducing steric bulk in the *fjord* region of the [5]helical TBF framework with methyl groups, is predicted to raise the interconversion barrier (37.8 kcal mol^{-1}; Figure 4.2)) such that **MeTBF**

is expected to be configurationally stable. It is evident that methylation is a more effective strategy of increasing the configurational stability of TBFs compared to π-extension likely because methyl groups provide greater steric bulk in the immediate inner helix *fjord* position compared to an annulated benzene ring. Similar trends are observed experimentally[13,15] for fully benzenoid helicenes – dimethylation of [5]helicene results in $\Delta G^{\ddagger}$ = 44.2 kcal mol^{-1} at 503 K while a dibenzannulated [7]helicene has $\Delta G^{\ddagger}$ = 41.2 kcal mol^{-1} at 298 K. Regardless, both strategies result in configurationally stable helicenes and if a choice needs to be made, the easier target to achieve synthetically should be pursued. For the purposes of this Chapter, starting materials to arrive at both **7HTBF** and **MeTBF** were synthesised and progress achieved to make the helicenes is described in Section 4.2.3.

| 11.8 kcal mol^{-1} | 12.6 kcal mol^{-1} | 13.1 kcal mol^{-1} |
| **A-H** | **A-OH** | **TBF-A•** |

| 9.15 kcal mol^{-1} | 34.0 kcal mol^{-1} | 37.8 kcal mol^{-1} |
| **B-OH** | **7HTBF** | **MeTBF** |
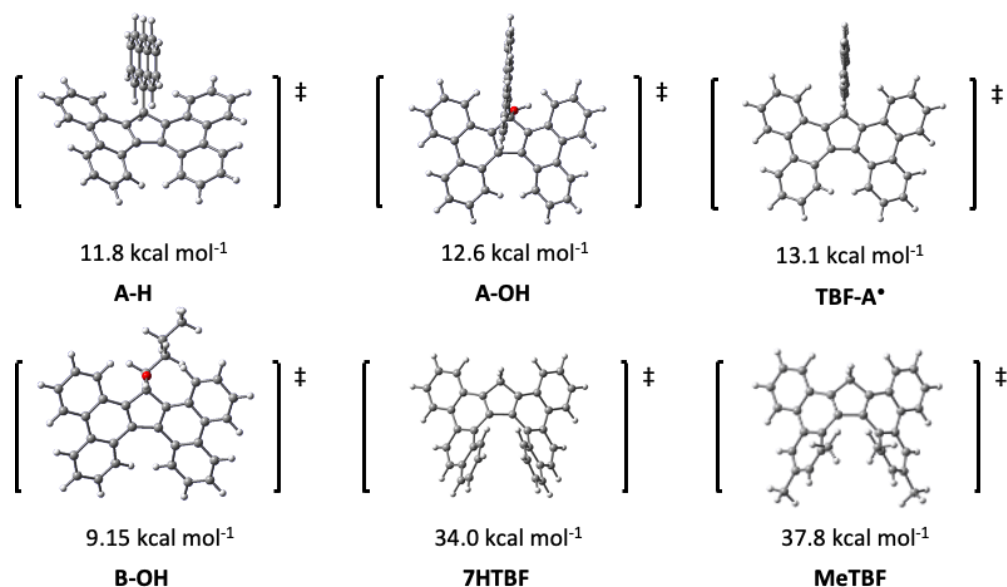
Figure 4.2. Transition-state structures ((U)B3LYP(GD3BJ)/6-31G(d,p) in CH$_2$Cl$_2$) of **A-H**, **A-OH**, **TBF-A•**, **B-OH**, **7HTBF** and **MeTBF** along with their calculated energy barriers of enantiomerisation, $\Delta G^{\ddagger}$ highlighting the difference in the transition-state structures of [5]helical TBFs, sterically bulky [5]helical TBFs and [7]helical TBFs.

Finally, the third strategy to yield configurationally stable helicenes involves increasing the chiral complexity of the system by designing a triple helicene from a four-fold π-*ortho* extension of the TBF framework. This benzannulation results in a tetranaphthafluorene (**TNF**) structure (Figure 4.1c) whose interconversion barriers are more complex to analyse. There are now three stereogenic axes, each of which can exist as either the *P*– or *M*– enantiomer. Each of these stereogenic elements of the molecule are fluxional and can interconvert to the opposite enantiomer resulting in 6 distinct isomeric structures of **TNF** all with different chirality. Out of the 6 isomers of **TNF**, DFT calculations reveal that the lowest energy pair of enantiomers exist as the *P,M,P/M,P,M* pair while the *M,M,P/P,P,M* enantiomeric pair is 1.44 kcal mol^{-1} higher in energy and the *P,P,P/M,M,M* enantiomeric pair is higher still in energy (2.73 kcal mol^{-1}) compared to the lowest energy enantiomer pair (Figure 4.3). The helical strain under which the system is put appears to be minimised when the chirality of each stereogenic axis alternates. These results are corroborated by literature DFT TS analyses of an analogous triple[5]helicene where the central 5-membered ring is replaced with a benzene ring.[6] Furthermore, an in depth transition state

analysis highlights that the interconversion of the central TBF-like [5]helicene has the lowest energy barrier (10.4 kcal mol^{-1}; Figure 4.3). This interconversion barrier is even lower than the alkylated TBFs studied above and therefore in **TNF** will be interconverting at a fast rate at room temperature. It is evident that the 5-membered cyclopentadienyl is therefore an effective design strategy to incorporate into π-extended polyaromatic molecules to relieve helical strain. On the other hand, the [5]helicene wings on the **TNF** molecule have a higher energy barrier to interconversion (21.4–20.9 kcal mol^{-1}), however still lower compared to [5]helicene. In **TNF**, the loosening of helical pitch due to the central 5-membered cyclopentadienyl ring propagates outwards to the [5]helicene wings allowing for the easier interconversion of all stereogenic helical elements. This result is different from what has been shown in the literature, where the increase in chiral complexity consolidates into greater interconversion barriers for individual [5]helicene elements in a multihelicene.
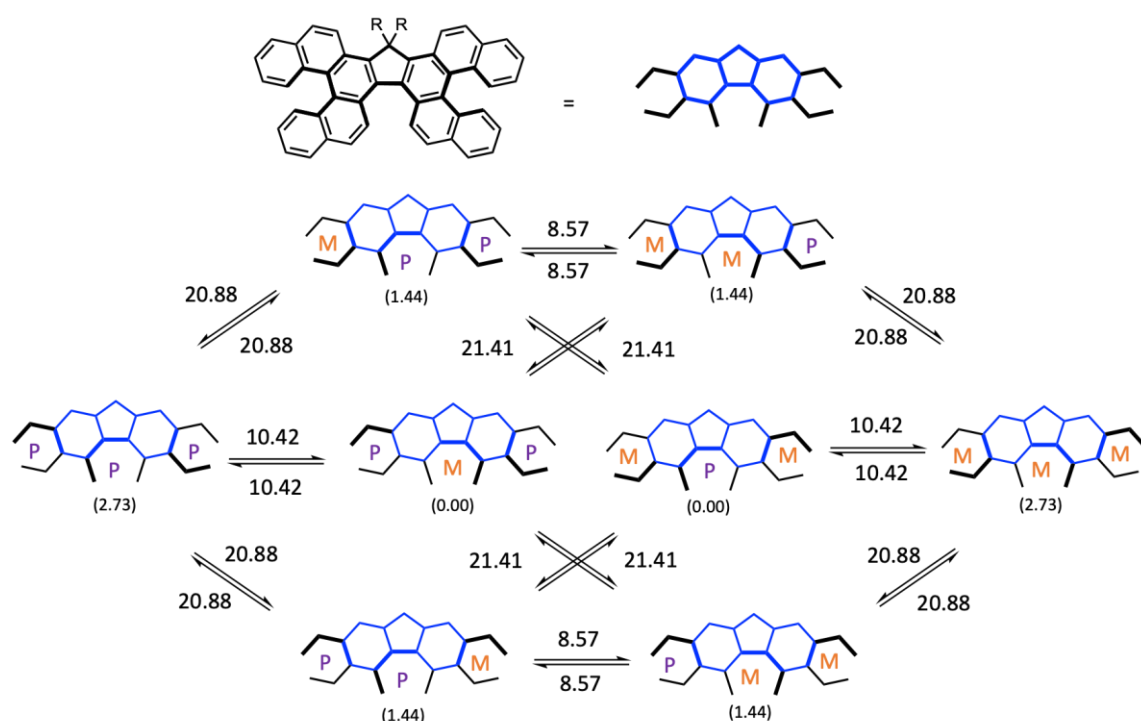
Figure 4.3 Complex transition-state interconversion analysis of the 6 possible structures of the triple helicene, which is represented by a simplified triple helicene skeleton. Note that *P*, *P*, *M* and *M*, *P*, *P* are the same as well as *P*, *M*, *M* and *M*, *M*, *P*, but are represented separately on the diagram for full comprehension. All values are quoted in kcal mol^{-1}; numbers in brackets underneath the simplified structures represent the zero-point energies of the molecules relative to the lowest energy enantiomer pair (*P*, *M*, *P* or the *M*, *P*, *M*). All other energies represent the transition state energies for the interconversion specified by the arrows, e.g., the interconversion between *P*, *P*, *P* to *P*, *P*, *M* has an energy barrier of 20.88 kcal mol^{-1}.

Due to the large difference in transition state barriers between the central and wing helicenes in **TNF**, it is unlikely that the *M,M,P/P,P,M* enantiomeric pair will be accessed thermodynamically from the lowest energy enantiomeric pair if temperatures are kept low. As a result, the full interconversion pathway from *P,M,P* to its *M,P,M* enantiomer is unlikely to occur at low temperatures. At room temperature and higher, the system is likely to be rapidly interconverting between isomers. Therefore, the structural design of this complex triple helicene may not lend itself to favourable chiroptical properties because enantiopure samples will be difficult to obtain. Nevertheless, gaining a deeper

understanding of why increased chiral complexity might not always lead to enhanced configurational stability is required for future designs of multihelicenes that can emit light with high PLQYs.

4.2.2 TD-DFT ANALYSES OF CHIROPTICAL PROPERTIES

The optical properties of the three helicene targets **MeTBF**, **7HTBF**, and **TNF** were explored by time-dependent DFT calculations (of the first 20 states; B3LYP(GD3BJ)/6-31G(d,p) in CH_2Cl_2) in order to get an understanding of what effect the structural changes to these helicenes have on their excited state behaviours compared to the closed shell TBFs explored in Chapter 2. A comparison of frontier molecular orbitals (FMOs; Figure 4.4a and b) reveals that the increase in electron density through either π-extension or methylation results in a destabilisation of both the HOMO and LUMO energy levels of all configurationally stable TBF targets compared to **A-H**. This shift in FMOs results in similar optical energy band gaps for all the materials and is supported by the TD-DFT calculations where the onset of absorption for all compounds studied (Figure 4.4c) is very similar. Notably, the greatest increase in FMO energy levels is experienced by **MeTBF** rather than the π-extended analogues **TNF** and **7HTBF**. Depictions of the FMOs (Figure 4.4b) of these configurationally stable TBFs suggest that for **7HTBF**, there is a lack of electron density around the newly introduced terminal benzene rings in the LUMO, even though this electron density exists in its HOMO. A similar observation is noticed for **TNF** where the lateral π-extended benzene rings display relatively less electron density in its LUMO compared to the parent TBF core. The results reveal that despite structural changes to these TBF analogues, the HOMO and LUMO energy levels are still mainly centred around the TBF core and therefore the optical properties of **MeTBF**, **7HTBF** and **TNF** are likely to appear quite similar.

The TD-DFT simulated UV–vis absorption profiles of **MeTBF**, **7HTBF** and **TNF** (Figure 4.4c) reveal two absorption bands for all three TBF analogues for a low energy π–π* transition and a higher energy transition (below 300 nm) involving core electrons. Meanwhile, the simulated circular dichroism (CD) spectra (Figure 4.4d and e) for two **TNF** diastereoisomers display a negative cotton effect for the long wavelength peak (350–500 nm) and a positive cotton effect for the shorter wavelength peak (250–350 nm). For *P*–**MeTBF** and *P*–**7HTBF**, the lowest energy transition occurs corresponds to a HOMO→LUMO transition that is highly localised around their fluorenyl cores. The lowest energy transition for *P,M,P*–**TNF** is a little more complex and in addition to a HOMO→LUMO transition, it involves a transition from its HOMO→LUMO+1 and HOMO–2→LUMO+1 (Figure 4.4c). In order to deconvolute the contributions of these orbital transitions to this lowest energy excited state, natural transition orbital (NTO) analysis was conducted. The results reveal a 96.1% occupancy from its highest occupied natural transition orbital (HONO) to its lowest unoccupied natural transition orbital (LUNO, Section 4.4.4, Figure S4.12), suggesting that the fluorenyl core dominates the excited state properties of **TNF** despite the lateral π-extension and consequent increase in chiral complexity of the molecule. The results in combination are positive since the photophysical properties of the fluorenyl core are

maintained in the configurationally stable helical targets, indicating that when successfully synthesised and separated out into their enantiomers, **MeTBF**, **7HTBF** and **TNF** are predicted to display absorption and emission characteristics that are similar to TBFs and with equally high PLQYs and g_{lum} values.
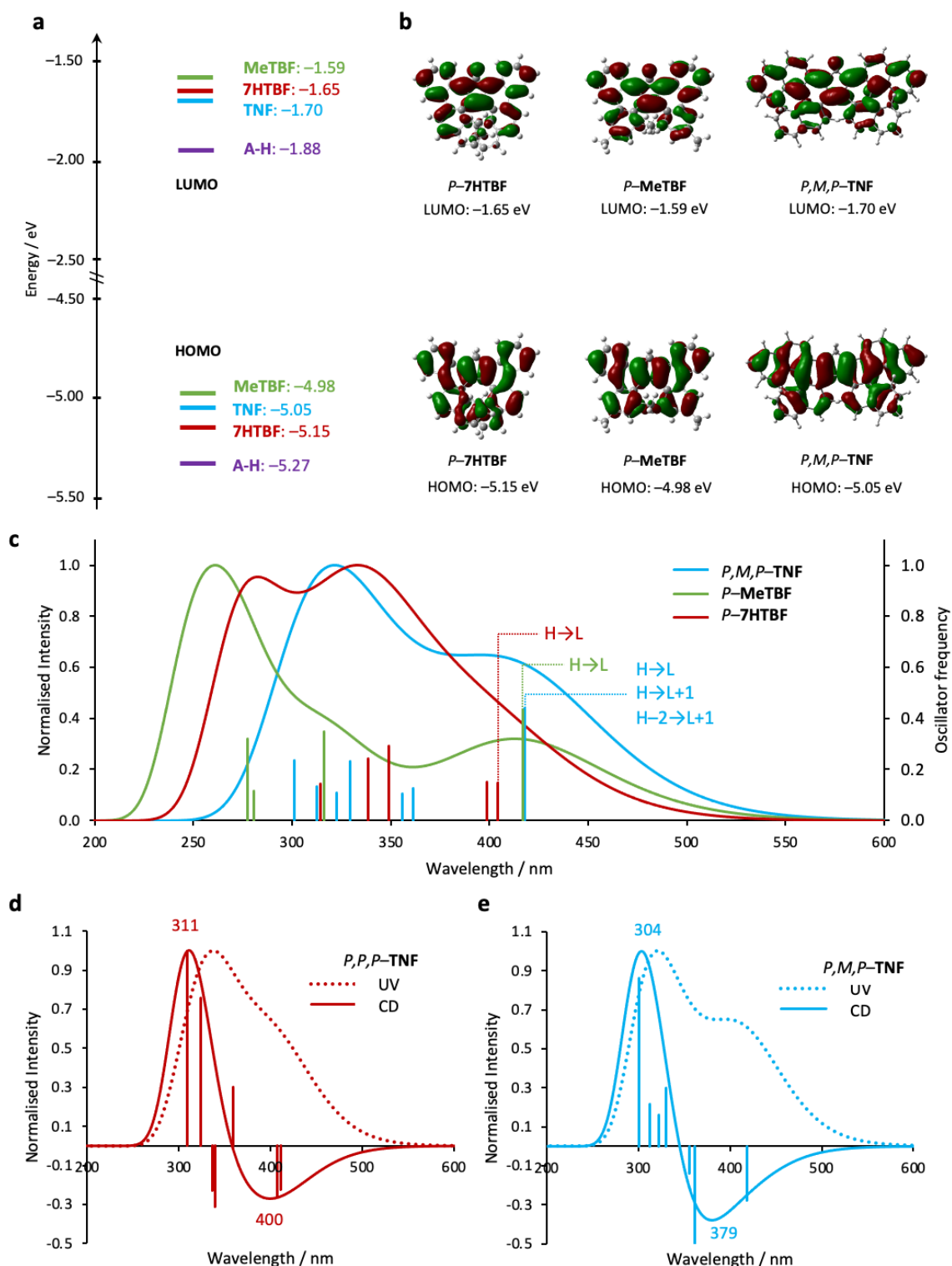
Figure 4.4 (a) HOMO and LUMO energy levels of the configurationally stable TBF targets compared to **A-H** (discussed in Chapter 2) and (b) their depictions. (c) TD-DFT of the first 20 states calculated using B3LYP(GD3BJ)/6-31G(d,p) in CH_2Cl_2 of *P*–**7HTBF**, *P*–**MeTBF**, *P,M,P*–**TNF**; Comparison of the simulated UV and CD spectra for (b) *P,P,P*– and (c) *P,M,P*-**TNF** diastereoisomers.

4.2.3 SYNTHETIC PROGRESS

The general synthetic strategy used in this Chapter attempted to sculpt the central 5-membered ring follows the synthesis outlined by Hay, A. et al.[17] described in Chapter 2 to synthesise **A-OH** starting from 9-bromophenanthrene (Scheme 2.1; *vide supra*). Monobrominated precursors bromochrysene, dimethylbromophenanthrene and bromo[5]helicene are therefore required to achieve **7HTBF**, **MeTBF**, and **TNF** respectively. Monobromochrysene **5** was synthesised from chrysene using *N*-bromosuccinimide (NBS) as a brominating agent, in anhydrous DMF with heating at 60 °C (Scheme 4.1). Monitoring the reaction by TLC (10% CH_2Cl_2 in *n*-hexanes) and ^1H NMR spectroscopy shows conversion to the desired product **5** along with some minor dibrominated species. Purification of this crude solid has been difficult because the spots all coelute, even in a 1% CH_2Cl_2/*n*-hexanes solvent system (and poor solubility in *n*-hexanes that causes streaking). An initial Grignard reaction to form a methylene bridged alcohol dimer was trialled unsuccessfully for **5** using activated magnesium turnings and I_2 in THF, followed by the addition of ethylformate or methylformate. The crude material contained unreacted starting material (confirmed by ^1H NMR spectroscopy), indicating that this electron rich brominated polyaromatic requires harsher conditions in its activation. Since there was only a small amount of material (**5**) to work with and a dibrominated impurity, effort was placed instead on synthesising bromo[5]helicene, which could be attained on much higher scales.
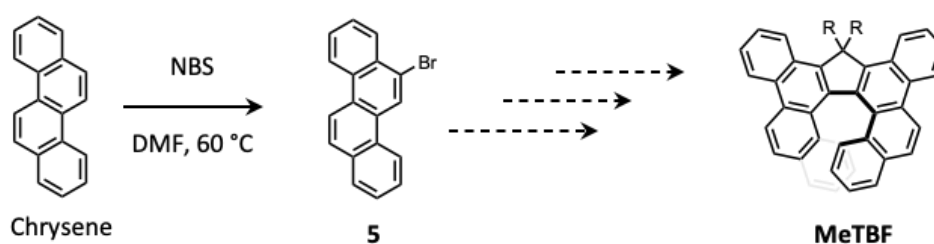
Scheme 4.1. Bromination of chrysene to form monobromochrysene **5**, which was used to form the fluorenyl core *via* a Grignard-mediated dimerisation.

The second brominated precursor, bromo[5]helicene was prepared in a 22% yield over five steps (Scheme 4.2) from *rac*-BINOL following previously reported methods.[15,21] A triflation of BINOL to introduce a good leaving group allows methyl groups to be installed *via* a Kumada coupling (**7**). Then, two radical-mediated reactions first brominate the methyl groups (using dibenzoylperoxide as the radical initiator) and facilitate ring closing to make the fully aromatised dibromo[5]helicene **9**. Finally, a reduction with zinc dust forms the monobromo[5]helicene in a 72% yield. The monobrominated [5]helicene **10**, contains non-brominated [5]helicene (14% by mass, determined by ^1H NMR spectroscopy) which has been difficult to purify due to coelution of the brominated and non-brominated species in even 100% *n*-hexanes, however its presence should not affect the outcome of any future reactions.
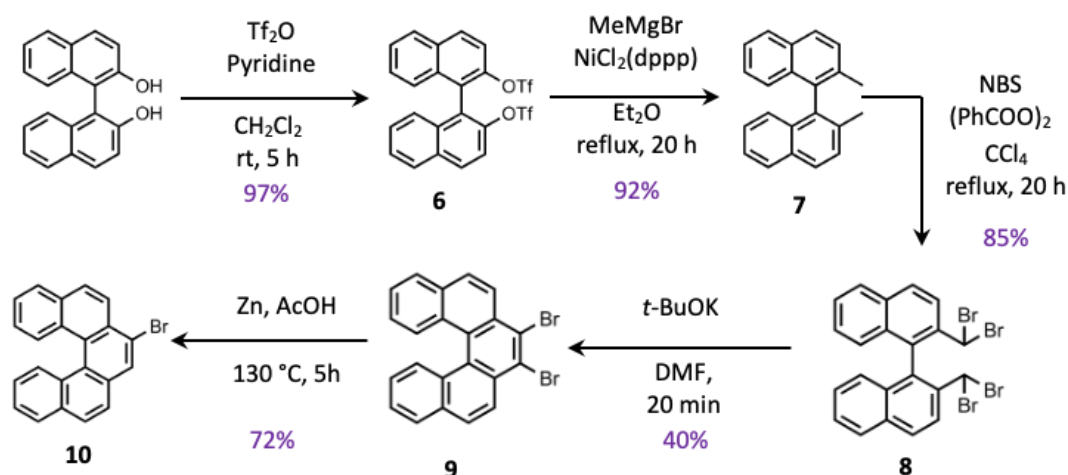
Scheme 4.2 Five-step synthetic scheme starting from *rac*-BINOL followed by a triflation to form **6**, methylation (**7**), bromination (**8**), ring-closing (**9**) and reduction to arrive at monobromo[5]helicene **10**.

An initial Grignard reaction was trialled with **10** using activated magnesium turnings and I_2 in THF, followed by the addition of ethylformate or methylformate. The results were the same as for the dimerisation of **5**, i.e., the larger aromatic surfaces in these brominated precursors require harsher conditions in their activation. Since lithiation has been used previously to activate 7-bromo[5]helicene,[22] *n*-BuLi conditions were trialled at –78 °C (Scheme 4.3) and monitored once the electrophile was added (i.e., ethylformate, methylformate or DMF). Even though activation is occurring (i.e., upon quenching of the reaction there is no starting material remaining), multiple products have been isolated, none of which are the desired dimer **11**. Notably, an intermediate aldehyde species **12**, formed by the reaction of only a single equivalent of the lithiated [5]helicene, **10a**, has been isolated as the major product in a 32% yield (Figure 4.5). This result indicates that a second addition of lithiated [5]helicene **10a** (Figure 4.5(i)) is hindered in the formation of **11**. Instead, in the same reaction pot, **12** does appear to be electrophilic enough to react with further equivalents of *n*–BuLi to form an alkylated alcohol which undergoes elimination to form two diastereomeric 9-butene[5]helicenes, **13** (Figure 4.5(ii), see Section 4.4.3, Figure S4.1 for its ^{1}H NMR spectrum).
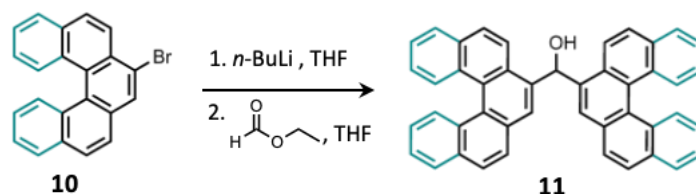
Scheme 4.3. Synthesis of dihelicene **11** from bromo[5]helicene **10**.

A reaction to encourage a second equivalent of the lithiated **10a** to react with the newly formed aldehyde **12** was set up to push the second addition in the formation of the dimer **11** (Figure 4.5(i)). Although **10a** was being consumed, majority of the aldehyde, **12** was recovered from the reaction by column chromatography suggesting that the formylhelicene **12** does not behave as a suitable electrophile when

in conjugation with the electron-rich [5]helicene backbone. The reactivity of **12** was tested by attempting a reaction of the less sterically hindered 9-bromophenanthrene with **12** which could achieve an asymmetric double helicene with a fluorene core (**15** in Figure 4.5(iii)). 9-Bromophenanthrene was reacted with *n*-BuLi in THF at –78 °C followed by the addition of **12**. Upon quenching the reaction with NH$_4$Cl and an aqueous work up, a solid that is insoluble in CH$_2$Cl$_2$ was isolated in a 47% yield with an [*M*+H]$^+$ peak in its mass spectrum that corresponds to a molecule with the structure of **14** or due to free rotation of the phenanthrene, its isomer **15** (calculated for C$_{37}$H$_{22}$: *m/z* = 467.1802 [*M*+H]$^+$; found 467.1767 [*M*+H]$^+$, Figure 4.5). The appearance of an aromatic singlet with a single proton integration in the ^{1}H NMR spectrum of this reaction attempt (Section 4.4.3, Figure S4.3), suggests that it is more likely that **14** has formed instead of **15** since an aromatic singlet only exists in **14** (indicated with an orange circle on its structure, Figure 4.5). However, the material is highly insoluble, even in DMSO, resulting in peaks that are broad and poorly resolved at high concentrations, making it hard to analyse the NMR data fully. It is possible that on quenching the reaction with NH$_4$Cl (which is slightly acidic), a dehydration occurs inducing ring closing to the thermodynamically stable 6-membered ring isomer **14** (as opposed to a more sterically strained **15**). The result suggests that the formyl helicene species **12** is reactive because there has been a successful conversion towards a dimerised product (i.e., **14**), hence it is unclear why the dimerisation of two [5]helicenes is not occurring (i.e., to form **11**). Regardless, the results from this test reaction suggests that the solubility of **TNF** is likely to be poor in common organic solvents, a key factor that needs to be addressed before future synthetic efforts.
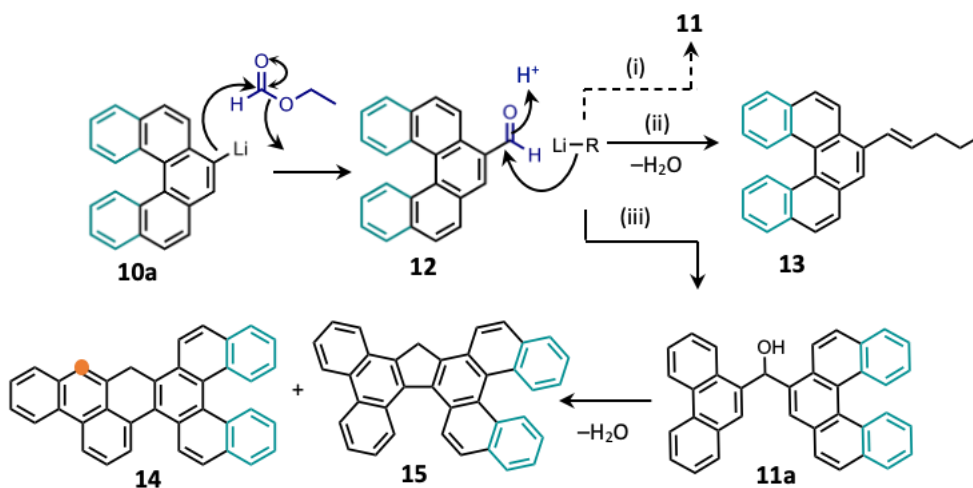
Figure 4.5 Mechanism showing how the activated lithiated [5]helicene **10a** reacts with ethyl formate to form the isolated aldehyde [5]helicene **12**, which can then be attacked by a second equivalent of a lithiated species either (i) R=[5]helicene in the synthesis of the dimer **11** (not isolated); (ii) R=butyl, which undergoes an elimination of H$_2$O to form **13**, or (iii) R=phenanthrene which forms the intermediate alcohol dimer **11a** in situ before cyclising to allow for the isolation of proposed structures **14** or **15** upon acidic workup.

The final brominated precursor dimethylbromophenanthrene **20** was synthesised over five steps, in a stepwise sequence adapted from the literature[18–20] (Scheme 4.4). First, a Suzuki–Miyaura coupling of bromobenzaldehyde and dimethylphenyl boronic acid forms **16**, followed by a Corey-Fuchs reaction to first synthesise **17** then, **18** in a 78% yield. A simple bromination with NBS followed by gold-mediated

cycloisomerisation, involving a 1,2-migration of the bromine atom,[20] yields the desired brominated precursor **20**, in an 80% yield. Although Rusali, L. E. et al.[18] encourage microwave heating for the Pd catalysed Suzuki-Miyaura reaction to form **16** and the gold-mediated cycloisomerisation reaction to form **20**, conventional heating was performed more successfully during a scale up of these reactions resulting in better yields. Due to the relatively distant location of the microwave facility in the Green Chemistry microwave facility at the University of York, reactions were never performed under pristine air-free/moisture-free conditions and therefore never reached full completion. Instead, conventional heating provided more control over these reaction conditions as well as the ability to monitor the reactions.
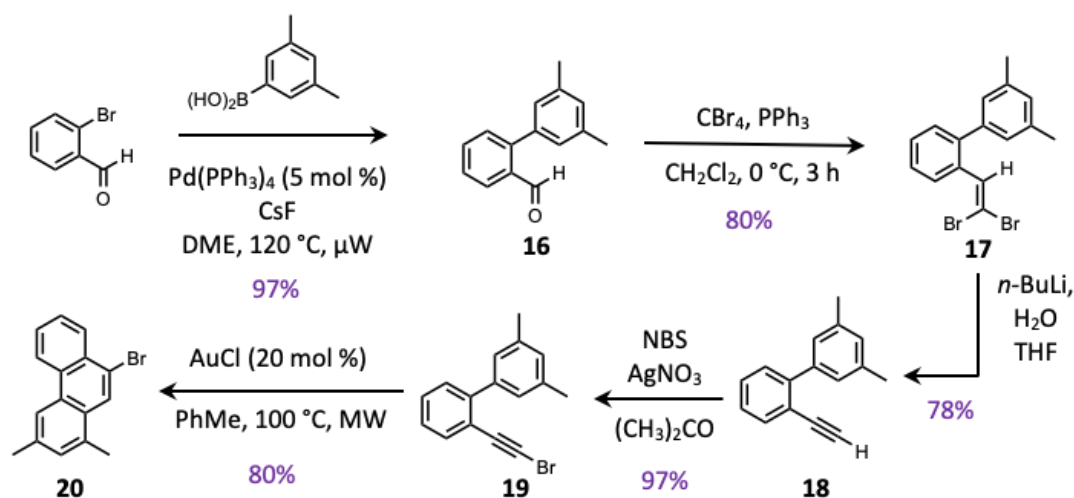
Scheme 4.4 Five-step synthetic route starting from 1,2-bromobenzaldehyde involving a Suzuki–Miyaura coupling to form **16**, a Corey-Fuchs reaction (first forming **17** then **18**), before a bromination (**19**) and gold-catalysed cycloisomerisation to form dimethylbromophenanthrene **20** which should yield a configurationally stable analogue of TBF.

Learning from previous attempts to dimerise brominated polyaromatics, the dimerisation of **20** was performed over two steps, forming aldehyde **21** initially, before reacting it with a second equivalent of **5** (after lithiation) to form alcohol dimer **22** in a 75% yield (Scheme 4.5). The successful dimerisation of **20** suggests that less electron rich and less sterically bulky brominated analogues of phenanthrene are more suitable and favour the formation of the desired dimer, unlike attempts to dimerise **10**. Subsequent attempts to ring close **22** through a simple dehydration with TFA at room temperature were unsuccessful since the isolated material (**24**) appears to have the same structure as **22**, evident from the presence of three singlet aromatic peaks with a relative integration of 2:2:2 (i.e., H[9] is still present, Figure 4.6). The NMR results, combined with qualitative observations (of a colour change to a light blue upon addition of TFA) reveal that while there is a chemical change occurring, ring closing is not favoured at room temperature. A structure of **24** has been proposed where the species chooses to react with EtOAc (presumably) used in the work up (Figure 4.6).
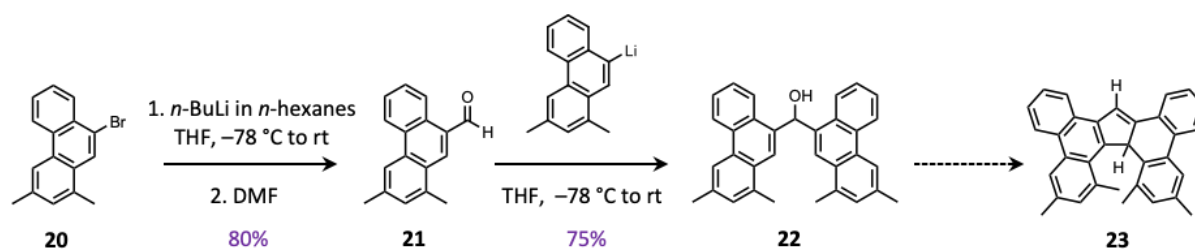
Scheme 4.5 Reaction scheme followed to synthesise dimer **22** from **20** through aldehyde **21**.

The ring closing of **22** has been attempted in CHCl₃, which is a more acidic solvent than CH₂Cl₂ and enables higher temperatures to be reached upon reflux and therefore was hypothesised to favour the formation of the desired product **23**. After a 48 h reflux, with no evidence of the formation of **23**, the reaction mixture was treated with a mild base (Et₃N) to recover a derivative of the starting material. Harsher yet conditions were attempted, using Scholl oxidation reaction conditions (DDQ and CH₃SO₃H) to push the reaction to product formation. It is difficult to say with certainty whether this reaction worked in the way that was expected because Scholl oxidations can lead to unexpected structural products all with similar molecular masses.[23–25] The ¹H NMR spectrum of the major product isolated (**25**) following automated column chromatography reveals a highly symmetric product with only three singlet peaks in the aromatic region, indicating that there is a possibility that the fully ring-closed, methylated TBF-helicene product **MeTBF** has formed. Since 2D ¹H–¹³C HMBC analyses suggest that the singlet peak at 7.3 ppm is in close proximity to the singlet aromatic peaks at 8.2 and 8.4 ppm, it will be necessary to grow single crystals suitable for X-ray diffraction in order to confirm fully the structure of the material formed after the Scholl oxidation.
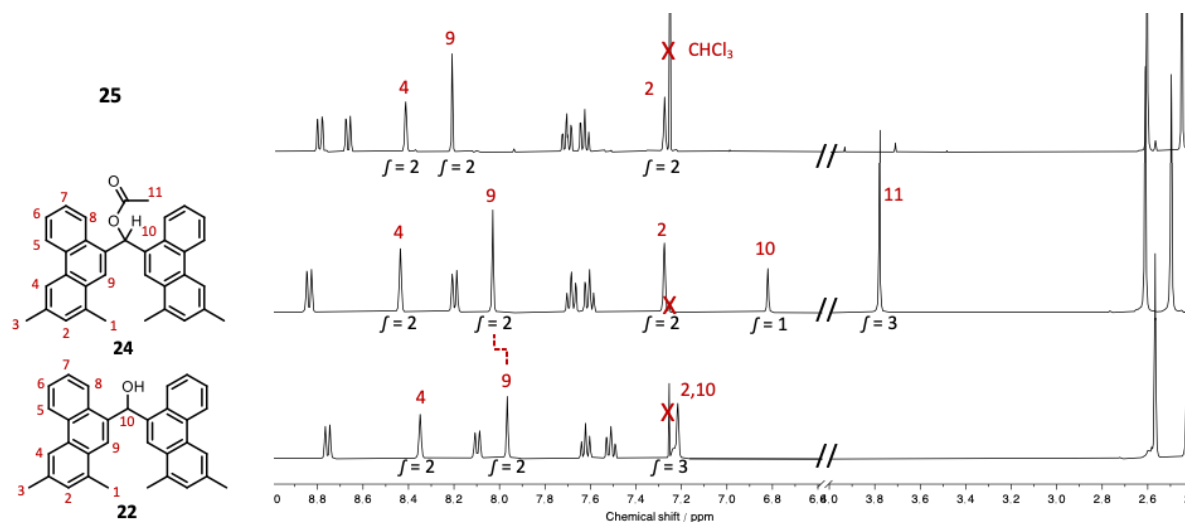
Figure 4.6 Structures and stacked ¹H NMR (CDCl₃, 400 MHz, 298 K) spectra of **22** and the major products **24** (with a proposed structure shown) and **25** isolated after attempts to encourage ring closing.

4.3 CONCLUSIONS

Three structural strategies have been adopted to synthesise topologically complex fluorenyl-embedded helicenes **7HTBF**, **MeTBF**, and **TNF** whose configurational stabilities are predicted by DFT calculations. Strategies to increase the steric bulk around the inner helix at the terminal benzene ring position (either through methylation or benzannulation) are suitable for increasing the Gibbs free energy of enantiomerisation such that the resulting helicenes are configurationally stable. In the context of trying to choose which strategy might work more reliably in pursuit of configurationally stable helicenes, methylation appears to be a more effective strategy ($\Delta G^{\ddagger}$ (**MeTBF**) = 37.8 kcal mol^{-1} compared to $\Delta G^{\ddagger}$ (**7HTBF**) = 34.0 kcal mol^{-1}). However, since both strategies achieve similar results, the strategy that is easier to implement synthetically should be adopted. Increasing the chiral complexity with a triple helicene design **TNF** does not result in a configurationally stable helicene because the configurational instability of the central fluorenyl-helicene propagates outwards toward the [5]helicene 'wings' lowering their interconversion barriers. However, the study of **TNF** is still necessary from a fundamental perspective to contribute to the underdeveloped field of multihelicenes. DFT and TD-DFT calculations provide an insight to the functional optical properties that these helical targets are predicted to have once they have been successfully synthesised. The calculations reveal that despite synthetic alterations to the TBF core in **MeTBF**, **7HTBF** and **TNF**, the fluorenyl electronic (i.e., FMOs) and optical properties (from simulated UV–vis and CD spectra) are retained. This result suggests that we can expect these TBF analogues to behave in a similar manner to the TBFs studied in previous Chapters, with efficient absorption, emission and redox characteristics.

Monobrominated precursors have been synthesised in decent yields and initial dimerization attempts have worked to varying extents. Grignard reactions were insufficient at activating the larger π-surfaces, therefore lithiation proves to be a more efficient route to forming the fluorenyl methylene bridge. The dimerisation of bromo[5]helicene does not go to completion presumably due to the increased steric bulk of the [5]helicene compared to phenanthrene. Instead, an intermediate [5]helicene aldehyde prefers to react with excess *n*–BuLi as opposed to activated Li-[5]helicene. On the other hand, dimethylated phenanthrene more readily forms the desired alcohol dimer. However, ring-closing attempts to create the 5-membered cyclopentadienyl core require extremely harsh Scholl oxidation conditions to push the reaction to completion, and there is still some uncertainty about whether the desired helicene has formed. While this Chapter has focussed on synthesising the cyclopentadienyl ring by forming the CH$_2$ bridge upon dimerisation, there are alternative routes that could be trialled to form the fluorenyl core,[26] e.g., by forming the CH$_2$ bridge after aromatic C–C dimerisation first[27] (Figure 4.7).
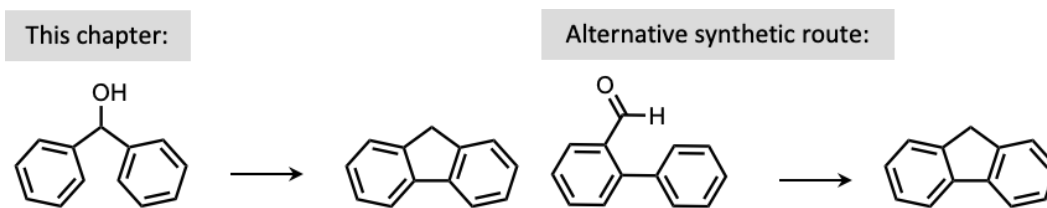
Figure 4.7 Alternative routes to forming the fluorenyl core in the synthesis of configurationally stable TBF analogues.

Tying these conclusions together with the promising results obtained in Chapter 2 with respect to efficient aggregate emission and Chapter 3 with regards to the robust redox chemistry of TBFs, the results presented in this Chapter suggest that configurationally stable TBF analogues have the potential to be efficient multifunctional helicenes that can afford redox states that are solid-state CPL-active for potential uses in advanced light-emitting and charge-transporting technologies.

4.4 SUPPLEMENTARY INFORMATION

4.4.1 GENERAL MATERIALS AND METHODS

Materials. Unless stated, all chemicals and reagents were purchased from commercial suppliers (Sigma Aldrich, Fisher Scientific, Alfa Aesar and Fluorochem) and used without further purification. Tetrakis(triphenylphospine)palladium(0) was prepared according to literature methods.[28] Before use, *n*-BuLi was titrated as described by Burchat, A. F et al.[29] to obtain its active concentration. Anhydrous solvents were obtained from a neutral alumina Solvent Purification System under nitrogen and stored over activated (>250 °C at 0.01 mbar overnight) 3 Å molecular sieves under a dry Ar atmosphere.

Product confirmation. Thin layer chromatography was performed on aluminium-backed silica gel plates and visualised under UV irradiation (254 and 365 nm). Automated flash column chromatography was performed using a Teledyne ISCO Combiflash NextGen 300+ with detectors using broad range UV–vis (200-800 nm) and evaporative light scattering (ELS) under N_2 gas and pre-filled Redisep™ Gold cartridges (normal phase: SiO_2). High-resolution mass spectra were measured on a Bruker compact QTOF Atmospheric Pressure Ionisation Time of Flight instrument using an ESI or APCI source. Nuclear magnetic resonance (NMR) spectra were recorded on a JEOL ECS400D spectrometer with working frequencies of 400 MHz for ^{1}H and 101 MHz for ^{13}C. Chemical shifts are reported in ppm relative to the signals corresponding to residual non-deuterated solvents ($CDCl_3$: δ_H 7.26 ppm, δ_C 77.23 ppm, DMSO-d_6: δ_H 2.50 ppm, δ_C 39.57 ppm). Coupling constants (J) are reported in Hertz (Hz) and ^{1}H multiplicities are reported in accordance with the following convention: s = singlet, d = doublet, t = triplet, q = quadruplet, p = pentet, m = multiplet. Assignment of ^{1}H and ^{13}C NMR signals were accomplished with the aid of two-dimensional ^{1}H–^{1}H COSY, ^{1}H–^{13}C HSQC and ^{1}H–^{13}C HMBC NMR spectroscopies. NMR spectra were processed using MestReNova software, Version 14.

Computational analysis. Density functional theory (DFT) calculations were prepared on GaussView 6.0 and submitted to the University of York Viking High performance Computing cluster and run on Gaussian 16 using Becke's three-parameter exchange functional with the gradient-corrected correlation formula of Lee, Yang and Parr (B3LYP)[30,31] paired with the split valence double-zeta 6-31G(d,p) basis set, PCM solvation model (CH_2Cl_2) and dispersion corrections (D3BJ)[32] unless stated otherwise.

4.4.2 SYNTHETIC DETAILS
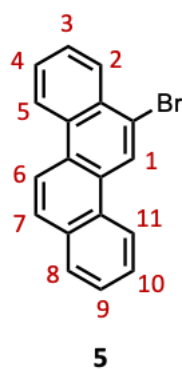
5: A flame-dried crimp-capped vial was charged with *N*-bromosuccinimide (0.0781 g, 0.44 mmol, 1.0 equiv.) and chrysene (0.101 g, 0.44 mmol, 1.0 equiv.) under an Ar atmosphere with a stirrer bar. DMF (3 mL) was added, and the reaction mixture was heated at 60 °C overnight. The reaction was cooled to room temperature and water was added to precipitate the solid. The precipitate was collected by vacuum filtration, washed with water and the minimum amount of MeOH and *n*-hexanes. Column chromatography is not a suitable separation technique to isolate pure singly brominated chrysene, nevertheless, **5** (83.8 mg, 0.27 mmol, 62%) was isolated as a mixture of singly and dibrominated chrysene, confirmed by ^{1}H NMR spectroscopy.

^{1}H NMR (CDCl$_3$, 400 MHz, 298 K) δ_H 9.04 (s, 1H^1), 8.80–8.76 (m, 1H^2), 8.71–8.64 (m, 2H^{6,8}), 8.46–8.42 (m, 1H^5), 8.04–7.97 (m, 2H^{7,9}), 7.79–7.71 (m, 3H^{3,4,11}), 7.66 (ddd, J = 8.0, 6.9, 1.2 Hz, 1H^{10}); **ESI–HRMS** (*v*e+, CH$_2$Cl$_2$) calculated for C$_{18}$H$_{11}$Br: *m*/z = 307.0122 [*M*+H]$^+$; found 307.0119 [*M*+H]$^+$ Spectroscopic data were consistent with those published previously.[33]
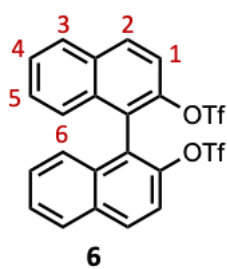
6: To a flame-dried round bottomed flask with a stirrer bar was added *rac*-BINOL (2.88 g, 10 mmol, 1.0 equiv.) and the flask was subjected to an Ar atmosphere. Anhydrous CH$_2$Cl$_2$ (80 mL) was added, and the reaction mixture was stirred before adding distilled pyridine (3 mL). The reaction vessel was cooled to 0 °C in an ice bath and trifluoromethanesulfonic dianhydride (3.5 mL) was added dropwise over 15 minutes. After stirring at room temperature for 5 hours, the reaction mixture was cooled in an ice bath to 0 °C and was quenched with HCl (1 M, 20 mL) followed by an extraction in CH$_2$Cl$_2$ (40 mL). The aqueous layer was washed once with CH$_2$Cl$_2$ (40 mL), then the combined organic layers were washed with saturated sodium bicarbonate (25 mL) followed by brine (25 mL). The combined organic layers were dried over MgSO$_4$ and concentrated to yield **6** (5.39 g, 9.79 mmol, 98%) as a white colourless solid which was dried on the Schlenk line overnight.

^{1}H NMR (DMSO-*d*$_6$, 400 MHz, 298 K): δ_H 8.47 (d, J = 9.1 Hz, 2H^1), 8.25–8.21 (m, 2H$^{3/6}$), 7.82 (d, J = 9.1 Hz, 2H^2), 7.69 (ddd, J = 8.2, 6.9, 1.2 Hz 2H$^{4/5}$), 7.52 (ddd, J = 8.4, 6.9, 1.3 Hz, 2H$^{4/5}$), 7.13–7.09 (m, 2H$^{3/6}$); **^{13}C NMR** (DMSO-*d*$_6$, 101 MHz, 298 K): δ_C 133.0, 132.4, 132.2, 128.8, 128.6, 127.7, 125.9, 122.4, 119.2; **^{19}F NMR** (DMSO-*d*$_6$, 377 MHz, 298 K): δ_F –74.51; **ESI–HRMS** (*v*e+, CH$_2$Cl$_2$) calculated

for $C_{22}H_{12}F_6O_6S_2$: $m/z = 572.9877$ $[M+Na]^+$; found 572.9864 $[M+Na]^+$ Spectroscopic data matched that reported in the literature.[15,21]
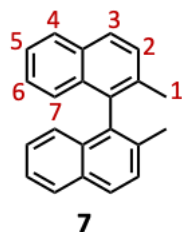
7: To a flame-dried two-necked round bottomed flask with a stirrer bar was added **6** (0.563 g, 1.02 mmol, 1.0 equiv.), Ni(dppp)Cl$_2$ (42 mg, 0.08 mmol, 0.08 equiv.) and the flask was subjected to an Ar atmosphere. Diethyl ether (8 mL) was added, and the stirred reaction mixture was cooled to 0 °C in an ice bath before methyl magnesium bromide (1.33 mL, 3.0 M in diethyl ether solution, 4.0 mmol, 4.0 equiv.) was added slowly over 5 minutes. The yellow reaction mixture was then heated to reflux overnight, and a colour change to dark red was observed. Once complete (confirmed by TLC in 5% CH_2Cl_2 in *n*-hexanes) the flask was cooled to 0 °C in an ice bath, the reaction was quenched slowly with water (10 mL) and HCl (1 M, 10 mL) and extracted with diethyl ether. The aqueous layer was washed with diethy ether (20 mL) and the combined organic layers were washed with saturated aq. NaHCO$_3$ (25 mL) followed by brine (25 mL). The combined organic layers were dried over MgSO$_4$ and concentrated to yield **7** (0.263 g, 0.932 mmol, 91%) as a yellow oil that was pure enough to use in the next step without further purification.

¹H NMR (CDCl$_3$, 400 MHz, 298 K): δ_H 7.92–7.87 (m, 4H²,⁷), 7.52 (d, $J = 8.4$ Hz, 2H³), 7.40 (ddd, $J = 8.1, 6.7, 1.2$ Hz, 2H⁶), 7.21 (ddd, $J = 8.3, 6.7, 1.3$ Hz 2H⁵), 7.07–7.04 (m, 2H⁴), 2.05 (s, 6H¹); **¹³C NMR** (DMSO-d_6, 101 MHz, 298 K): δ_C 134.3, 133.7, 132.0, 131.8, 128.6, 128.0, 127.4, 126.2, 124.9, 124.7, 19.5; Spectroscopic data matched that reported in the literature.[15,21]
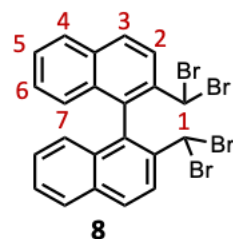
8: To a flame-dried two-necked round bottomed flask with a stirrer bar connected to a condenser was added N-bromosuccinimide (7.20 g, 40.5 mmol, 19 equiv.) and dibenzoyl peroxide (94 mg, 0.388 mmol, 0.18 equiv.). The flask was evacuated and subjected to an Ar atmosphere. A solution of **7** (0.596 g, 2.11 mmol, 1.0 equiv.) in CCl$_4$ (15 mL) was added and the reaction flask was heated to reflux for 40 hours. The reaction vessel was cooled to room temperature, filtered and the filtrate concentrated before the crude residue was taken up in CH_2Cl_2 (25 mL) and extracted with water (20 ml). The aqueous layer was extracted with CH_2Cl_2 (2 x 20 mL), the combined organic layers were washed with saturated aq. NaHCO$_3$ (2 x 30 mL), followed by water (2 x 30 mL), dried under MgSO$_4$ and concentrated. The crude residue was purified by column chromatography (silica gel, 20% CH_2Cl_2 in *n*-hexanes) to yield **8** (1.079 g, 1.80 mmol, 85%) as a pale yellow/white solid.

¹H NMR (CDCl$_3$, 300 MHz, 298 K): δ_H 8.24 (d, $J = 8.8$ Hz, 2H²), 8.15 (d, $J = 8.8$ Hz, 2H³), 7.95 (dd, $J = 8.2, 1.3$ Hz, 2H⁷), 7.53 (ddd, $J = 8.2, 6.9, 1.2$ Hz 2H⁶), 7.30 (ddd, $J = 8.3, 6.9, 1.3$ Hz, 2H⁵), 6.98, (d, $J = 8.3$ Hz, 2H⁴), 6.21 (s, 2H¹); **¹³C NMR** (CDCl$_3$, 101 MHz, 298 K): 138.3, 133.8, 130.8, 130.8, 128.3, 127.9, 127.9, 127.7, 127.6, 126.5, 39.1. Spectroscopic data matched that reported in the literature.[15,21]

9
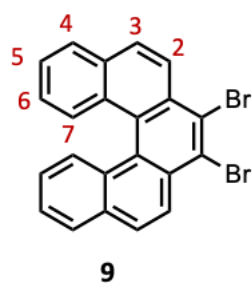
9: Into a flame-dried round bottomed flask with a stirrer bar was added **8** (0.133 g, 0.22 mmol, 1.0 equiv.) and anhydrous DMF (5 mL) and cooled in an ice bath to 0 °C. *t*-BuOK (0.3895 g, 3.47 mmol, 15 equiv.) was added slowly in portions over 15 minutes and the temperature of the flask monitored to control the exotherms. After 30 minutes the reaction mixture was poured into aq. HCl (10 mL, 0.12 M) to precipitate out the product. 1 M HCl was added until the pH dropped from 10 to 1. The precipitate was filtered and triturated with MeOH, then dried under vacuum to give a yellow powder (0.0392 g, 0.090 mmol, 39%). The filtrate and the aqueous phase were extracted with diethyl ether (3 x 30 mL) to isolate more product from the DMF, dried under $MgSO_4$ and concentrated to yield **9** as a brown/yellow powder (0.0668 g) that needs to be purified further.

¹H NMR (CDCl₃, 300 MHz, 298 K): δ_H 8.46 (d, J = 8.9 Hz, 2H[2]), 8.24 (d, J = 8.9 Hz, 2H[3]), 8.01–7.92 (m, 4H[4,7]), 7.54 (ddd, J = 8.0, 6.9, 1.1 Hz 2H[6]), 7.27–7.21 (m, 2H[5]); **APCI–HRMS** (*v*e+, CH₂Cl₂) calculated for $C_{22}H_{12}Br_2$: m/z = 434.9306 [M+H]⁺; found 434.9399 [M+H]⁺ Spectroscopic data matched that reported in the literature.[15,21]

10
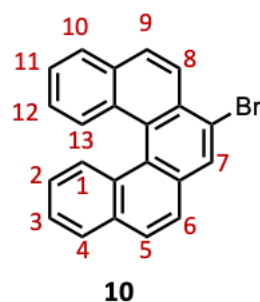
10: A flame-dried 2-necked round bottomed flask fitted with a condenser was charged with 7,8-dibromo[5]helicene, **9** (262 mg, 0.60 mmol, 1.0 equiv) and non-activated zinc dust (191 mg, 2.93 mmol, 5.0 equiv) and the flask was evacuated and back-filled with argon. Glacial acetic acid (20 mL) was added *via* syringe and the contents heated to reflux at 130 ºC for 5 h. Once the reaction was confirmed to be complete by ¹H NMR analysis of a crude sample, the reaction mixture was filtered while hot to remove any excess zinc. The filtrate was allowed to cool down to room temperature overnight over which point the desired product slowly precipitated out of solution. The light cream solid was filtered and washed with water to afford a mixture of 7-bromo[5]helicene, **10** and [5]helicene (145 mg total, 86% of total solid is the desired product).

¹H NMR (CDCl₃, 400 MHz, 298 K): 8.43 (d, J = 8.6 Hz, 1H[8]), 8.36 (dd, J = 8.7, 3.4 Hz, 2H), 8.20 (s, 1H[7]), 8.00–7.91 (m, 4H), 7.79 (d, J = 8.6 Hz, 1H[9]), 7.56–7.49 (m, 2H), 7.30–7.22 (m, 2H); **APCI–HRMS** (*v*e+, CH₂Cl₂) calculated for $C_{22}H_{13}Br$: m/z = 357.0279 [M+H]⁺; found 357.0275[M+H]⁺ Spectroscopic data matched that reported in the literature.[15,21]

12
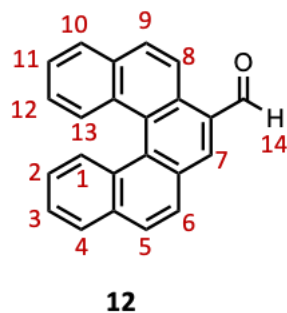
12/13: A flame-dried round-bottomed flask with a stirrer bar, under an atmosphere of N₂ was charged with **10** (0.217 g, 0.61 mmol, 1.0 equiv.) and dry THF (10 mL) and cooled to –96 °C in a liq. N₂/acetone bath. *n*-BuLi (0.35 mL, 0.88 mmol, 2.5 M in *n*-hexanes) was added dropwise to the reaction mixture and it was stirred for 2 h under N₂ and at –96 °C. A solution of ethyl formate (0.05 mL, 0.62 mmol, 1.0 equiv.) in THF (1 mL) was added to the reaction mixture dropwise and the reaction flask was allowed to slowly warm up to

room temperature. A crude ^{1}H NMR spectrum of the reaction mixture after 2 h shows consumption of starting material therefore the reaction mixture was quenched with 1 M HCl (5 mL), added slowly. The reaction mixture was extracted with CH_2Cl_2 (3 x 10 mL) before the combined organic layers were washed with sat. aq. $NaHCO_3$ (10 mL), followed by brine (10 mL). The organic layers were finally dried over Na_2SO_4 and concentrated. Product **12** (64.9 mg, 0.21 mmol, 34%) and product **13** (11.4 mg, 0.033 mmol, 5%) were isolated by automated column chromatography (SiO$_2$: 5–10% EtOAc in *n*-hexanes) as colourless solids.

12: ^{1}**H NMR** (CDCl$_3$, 400 MHz, 298 K): 10.54 (s, 1H[14]), 9.32 (d, *J* = 9.0 Hz, 1H[8]), 8.41–8.34 (m, 3H[1,7,13]), 8.12–8.06 (m, 1H[9]), 8.02–7.96 (m, 4H[4,5,6,10]), 7.63–7.52 (m, 2H[2,12]), 7.32–7.27 (m, 1H[3,11]); **APCI–HRMS** (*v*e+, CH$_2$Cl$_2$) calculated for C$_{23}$H$_{14}$O: *m*/z = 307.1123 [*M*+H]$^+$; found 307.1110 [*M*+H]$^+$ Spectroscopic data matched that reported in the literature.[22]

13
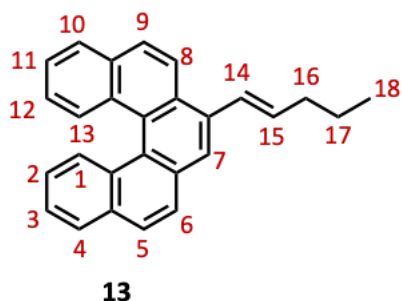
13: ^{1}**H NMR** (CDCl$_3$, 400 MHz, 298 K): 8.43 (dd, *J* = 8.7, 2.8 Hz, 2H[1]), 8.37 (dd, *J* = 9.3, 1.2 Hz, 2H[13]), 8.20 (d, *J* = 9.0 Hz, 1H[5]), 8.13 (d, *J* = 9.0 Hz, 1H[6]), 8.04 (d, *J* = 9.2 Hz, 2H[8,9]), 7.97–7.87 (m, 10H[4,5,6,7,8',9',10]), 7.51 (ddd, *J* = 7.9, 6.7, 1.2 Hz, 4H[3,11]), 7.27–7.22 (m, 4H[2,12]), 5.58 (ddd, *J* = 9.9, 8.1, 4.4 Hz, 2H[14]), 2.10–2.03 (m, 2H[15]), 1.66–1.50 (m, 4H[16]), 1.46–1.36 (m, 4H[17]), 0.95–0.90 (m, 6H[18]); **APCI–HRMS** (*v*e+, CH$_2$Cl$_2$) calculated for C$_{23}$H$_{14}$O: *m*/z = 347.1800 [*M*+H]$^+$; found 347.1794 [*M*+H]$^+$

16
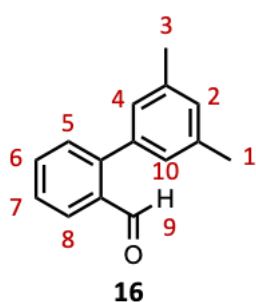
16: A flame-dried round-bottomed flask fitted with a condenser and a stirrer bar under an atmosphere of N$_2$ was charged with 2-bromobenzaldehyde (2.032 g, 11.0 mmol, 1.0 equiv.), 3,5-dimethylphenyl boronic acid (1.953 g, 13.0 mmol, 1.2 equiv.), caesium fluoride (4.651 g, 30.6 mmol, 2.8 equiv.) and tetrakis(triphenylphospine)palladium(0) (0.681 g, 0.59 mmol, 5 mol%) all dissolved in degassed, anhydrous 1,2-dimethoxyenthane (20 mL). The resulting yellow suspension was heated to 80 °C and monitored by mass spectrometry. After 4 hours, following complete consumption of 2-bromobenzaldehyde, the reaction mixture was diluted with EtOAc (50 mL) and water (50 mL) and separated. The resulting aqueous layer was washed with EtOAc (3 x 50 mL) and the combined organic layers dried over Na$_2$SO$_4$ and concentrated. The desired product **16** (2.154 g, 10.2 mmol, 97%) was isolated by automated column chromatography (SiO$_2$: 1% EtOAc in *n*-hexanes) as a colourless solid.

^{1}**H NMR** (CDCl$_3$, 400 MHz, 298 K) δ_H 10.0–9.98 (m, 1H[9]), 8.01 (dd, *J* = 7.8, 1.4 Hz, 1H[8]), 7.62 (td, *J* = 7.8, 1.4 Hz, 1H[6]), 7.51–7.40 (m, 2H[5,7]), 7.08 (s, 1H[10]), 6.99–7.00 (m, 2H[2,4]), 2.37–2.40 (m, 6H[1,3]); ^{13}**C NMR** (CDCl$_3$, 101 MHz, 298 K) δ_C 192.9, 146.5, 138.2, 137.8, 133.9, 133.6, 130.8, 129.9, 128.2, 127.7,

127.5, 21.5; **ESI–HRMS** (*v*e+, CH_2Cl_2) calculated for $C_{15}H_{14}O$: m/z = 233.0937 $[M+Na]^+$; found 233.0940 $[M+Na]^+$ Spectroscopic data matched that reported in the literature.[18–20]
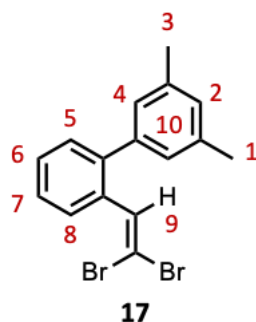
17: CBr_4 (1.554 g, 4.68 mmol, 2.7 equiv.) was added portion wise to a cooled solution of PPh_3 (2.278 g, 8.68 mmol, 5.0 equiv.) in CH_2Cl_2 (25 mL) and the resulting orange suspension was stirred for 10 minutes at 0 °C. A solution of **16** (0.361 g, 1.72 mmol, 1.0 equiv.) in CH_2Cl_2 (25 mL) was added dropwise. The reaction was kept at 0 °C for 1 h, while the reaction was monitored by TLC (5% EtOAc/*n*-hexanes). Upon completion of the reaction, the reaction mixture was quenched with brine (20 mL) and separated. The aqueous layer was washed with CH_2Cl_2 (3 x 30 mL) and the combined organic layers dried over Na_2SO_4 and concentrated. The crude solid was dissolved in hexanes and triturated (with sonication) then filtered, three times to remove traces of triphenylphosphine oxides. The combined filtrates were concentrated and purified by automated column chromatography (SiO_2: 5% EtOAc in *n*-hexanes) to yield **17** (0.500 g, 1.36 mmol, 80%) as a colourless oil.

¹H NMR (CDCl_3, 400 MHz, 298 K) δ_H 7.70–7.67 (m, 1H[8]), 7.42–7.33 (m, 3H[5,6,7]), 7.22 (d, *J* = 0.9 Hz, 1H[10]), 7.02 (s, 1H[9]), 6.96–6.94 (m, 2H[2,4]), 2.37–2.39 (m, 6H[1,3]); **¹³C NMR** (CDCl_3, 101 MHz, 298 K) δ_C 141.4, 140.1, 137.9, 137.9, 133.9, 129.9, 129.3, 129.3, 128.7, 127.6, 127.1, 90.5, 21.5. Spectroscopic data matched that reported in the literature.[18–20]
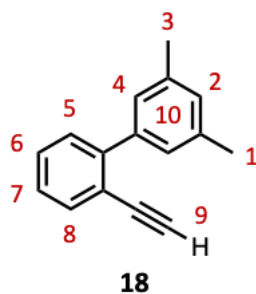
18: A flame-dried round-bottomed flask with a stirrer bar, under an atmosphere of N_2 was charged with **17** (0.651, 1.78 mmol, 1.0 equiv.) and dry THF (25 mL) and cooled to –96 °C in a liq. N_2/acetone bath. *n*-BuLi (2.4 mL, 3.55 mmol, 1.6 M in *n*-hexanes) was added dropwise to the reaction mixture and it was stirred for 2.5 h under N_2 and at –96 °C. The reaction was quenched with water (15 mL) and allowed to warm up to rt before being extracted with Et_2O (3 x 30 mL). The combined organic layers were dried with Na_2SO_4 and concentrated. The desired product **18** (0.285 g, 1.38 mmol, 78%) was isolated by automated column chromatography (SiO_2: 2% EtOAc in *n*-hexanes) as a clear oil.

¹H NMR (CDCl_3, 400 MHz, 298 K) δ_H 7.63–7.60 (m, 1H[8]), 7.42–7.35 (m, 2H[5,7]), 7.31–7.27 (m, 1H[6]), 7.23–7.21 (m, 2H[2,10]), 7.03 (s, 1H[4]), 3.05 (s, 1H[9]), 2.39–2.37 (m, 6H[1,3]); **¹³C NMR** (CDCl_3, 101 MHz, 298 K) δ_C 144.8, 140.3, 137.6, 134.0, 129.7, 129.3, 129.0, 127.2, 126.9, 120.5, 83.3, 80.1, 21.5; **APCI–HRMS** (*v*e+, CH_2Cl_2) calculated for $C_{16}H_{14}$: m/z = 207.1168 $[M+H]^+$; found 207.1165 $[M+H]^+$. Spectroscopic data matched that reported in the literature.[18,20]
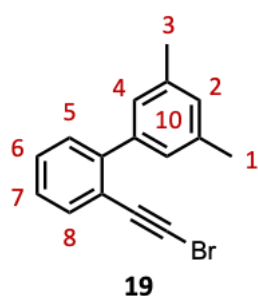
19: A flame-dried round bottomed flask under an atmosphere of N_2 was charged with **18** (0.810 g, 3.92 mmol, 1.0 equiv.) and dissolved in acetone (100 mL). N-bromosuccinimide (0.736 g, 4.13 mmol, 1.05 equiv.) and silver(I) nitrate (65.9 mg, 0.39 mmol, 0.1 equiv.) were added and the reaction allowed to proceed at room temperature under light-free conditions for 3 hours. After the reaction was complete, confirmed by TLC (5% EtOAc/n-hexanes), the reaction mixture was concentrated to dryness.

n-Hexanes (50 mL) was added to the crude material and triturated (with sonication), before being filtered through a pad of celite. The filtrate was concentrated to yield the desired product **19** (1.083 g, 3.80 mmol, 97%) as a yellow oil without any need for any further purification.

¹H NMR (CDCl₃, 400 MHz, 298 K) δ_H 7.55 (dd, J = 7.7, 1.0 Hz, 1H[8]), 7.40–7.37 (m, 2H[5,7]), 7.31–7.26 (m, 1H[6]), 7.23–7.21 (m, 2H[2,10]), 7.03 (s, 1H[4]), 2.40–2.38 (m, 6H[1,3]); **¹³C NMR** (CDCl₃, 101 MHz, 298 K) δ_C 144.7, 140.0, 137.7, 133.7, 129.6, 129.3, 129.0, 127.1, 127.0, 121.0, 79.9, 52.3, 21.5; **APCI–HRMS** (ve+, CH₂Cl₂) calculated for C₁₆H₁₃Br: m/z = 285.0273 [M+H]⁺; found 285.0260 [M+H]⁺ Spectroscopic data matched that reported in the literature.[18,20]
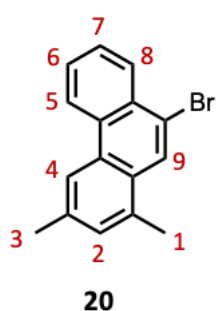
20: A flame-dried round bottomed flask fitted with a condenser and a stirrer bar, under an atmosphere of N_2 was charged with **19** (1.085 g, 3.80 mmol, 1.0 equiv.), AuCl (0.201 g, 0.86 mmol, 20 mol%) and anhydrous and degassed toluene and heated to 80 °C. A TLC of the reaction mixture (10% EtOAc in n-hexanes) confirmed the reaction was complete after 20 h. The crude material was purified by automated column chromatography (SiO₂: 5% EtOAc in n-hexanes) to yield the desired product **20** (0.942 g, 3.30 mmol, 87%) as a pale-yellow solid.

¹H NMR (CDCl₃, 400 MHz, 298 K) δ_H 8.72–8.67 (m, 1H[8]), 8.37–8.32 (m, 2H[5,9]), 8.27 (s, 1H[4]), 7.70–7.66 (m, 2H[6,7]), 7.30 (s, 1H[2]), 2.70 (s, 3H[1/3]), 2.57 (s, 3H[1/3]); **¹³C NMR** (CDCl₃, 101 MHz, 298 K): δ_C 136.6, 134.2, 131.6, 130.4, 130.3, 130.2, 129.3, 128.1, 127.4, 127.3, 127.0, 123.3, 120.9, 120.8, 22.2, 19.8; **APCI–HRMS** (ve+, CH₂Cl₂) calculated for C₁₆H₁₃Br: m/z = 285.0273 [M+H]⁺; found 285.0283 [M+H]⁺ Spectroscopic data matched that reported in the literature.[18–20]
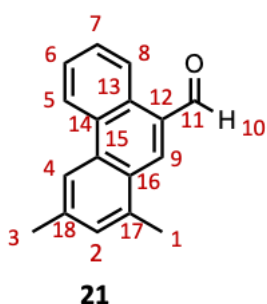
21: A flame-dried round bottomed flask with a stirrer bar, under an atmosphere of N_2 was charged with **20** (0.199 g, 0.70 mmol, 1.0 equiv.) and dry THF (15 mL) and cooled to –96 °C in a liq. N_2/acetone bath. n-BuLi (0.3 mL, 0.73 mmol, 2.5 M in n-hexanes) was added dropwise to the reaction mixture and it was stirred for 2 h under N_2 and at –96 °C. A colour change to a deep purple indicated activation of the aromatic core. Anhydrous DMF (1.1 mL, 14.0 mmol, 20 equiv.) was added to the reaction mixture and stirred for an additional 2 h at –96 °C. A colour change to yellow indicated quenching of

mixture and stirred for an additional 2 h at –96 °C. A colour change to yellow indicated quenching of

the lithiated species. The reaction mixture quenched additionally with saturated aq. NH$_4$Cl and extracted with CH$_2$Cl$_2$ (3 x 20 mL). The combined organic layers were dried over Na$_2$SO$_4$ and concentrated. The desired product **21** (0.130 g, 0.56 mmol, 80%) was isolated by automated column chromatography (SiO$_2$: 5–10% EtOAc in *n*-hexanes) as a colourless solid.

^{1}H NMR (CDCl$_3$, 400 MHz, 298 K) δ_H 10.39 (s, 1H[10]), 9.40–9.36 (m, 1H[5]), 8.74–8.69 (m, 1H[8]), 8.44 (s, 1H[9]), 8.36 (s, 1H[4]), 7.74–7.68 (m, 2H[6,7]), 7.36 (s, 1H[2]), 2.81 (s, 3H[1]), 2.61 (s, 3H[3]); **^{13}C NMR** (CDCl$_3$, 101 MHz, 298 K): δ_C 194.0[11], 140.5[18], 137.6[9], 137.0[16], 133.6[13], 130.9[14], 130.5[2], 129.4[15], 128.3[12], 128.1[7], 127.5[6], 127.2[17], 125.9[5], 123.1[8], 121.1[4], 22.6[3], 19.8[1]; **APCI–HRMS** (*v*e+, CH$_2$Cl$_2$) calculated for C$_{17}$H$_{14}$O: *m/z* = 235.1045 [*M*+H]$^+$; found 235.1062 [*M*+H]$^+$
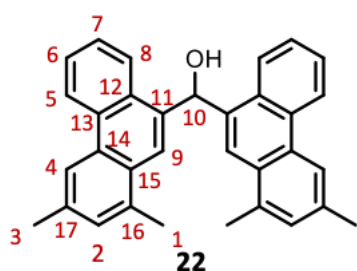
22: A flame-dried round bottomed flask with a stirrer bar, under an atmosphere of N$_2$ was charged with **20** (0.159 g, 0.56 mmol, 1.0 equiv.) and dry THF (5 mL) and cooled to –96 °C in a liq. N$_2$/acetone bath. *n*-BuLi (0.24 mL, 0.61 mmol, 2.5 M in *n*-hexanes) was added dropwise to the reaction mixture and it was stirred for 2 h under N$_2$ and at –96 °C. A colour change to a deep purple indicated activation of the aromatic core. After 2 h, a solution of **21** (0.127 g, 0.54 mmol, 1.0 equiv.) in dry THF (5 mL) was added dropwise and the reaction mixture was allowed to warm up slowly to room temperature and stirred for an additional 3 hours. A TLC (5% EtOAc/*n*-hexanes) confirmed complete consumption of **21**, after which the reaction was quenched with saturated aq. NH$_4$Cl (10 mL) and the reaction mixture extracted with EtOAc (15 mL). The aqueous layer was washed with EtOAc (3 x 15 mL), and the combined organic layers dried over Na$_2$SO$_4$ and concentrated. The desired product **22** (0.178 g, 0.40 mmol, 75%) was isolated by automated column chromatography (SiO$_2$: 5–10% EtOAc in *n*-hexanes) as a colourless solid.

^{1}H NMR (CDCl$_3$, 400 MHz, 298 K) δ_H 8.78–8.73 (m, 2H[5]), 8.35 (s, 2H[4]), 8.10 (d, *J* = 8.3 Hz, 2H[8]), 7.97 (s, 2H[9]), 7.63 (ddd, *J* = 8.3, 7.0, 1.3 Hz, 2H[7]), 7.52 (ddd, *J* = 8.3, 7.0, 1.3 Hz, 2H[6]), 7.22 (s, 3H[2,10]), 2.57 (s, 6H[1]), 2.43 (s, 6H[3]).; **^{13}C NMR** (CDCl$_3$, 101 MHz, 298 K): δ_C 136.2[17], 135.4[14], 135.3[15], 131.1[12], 130.7[11], 130.1[13], 129.9[2], 128.2[16], 126.7[6], 126.3[7], 124.6[8], 123.7[5], 122.3[9], 120.5[4], 70.7[10], 22.2[3], 19.8[1]; **APCI–HRMS** (*v*e+, CH$_2$Cl$_2$) calculated for C$_{33}$H$_{28}$O: *m/z* = 463.2032 [*M*+Na]$^+$; found 463.2041 [*M*+Na]$^+$

4.4.3 NMR SPECTRA OF SELECTED COMPOUNDS
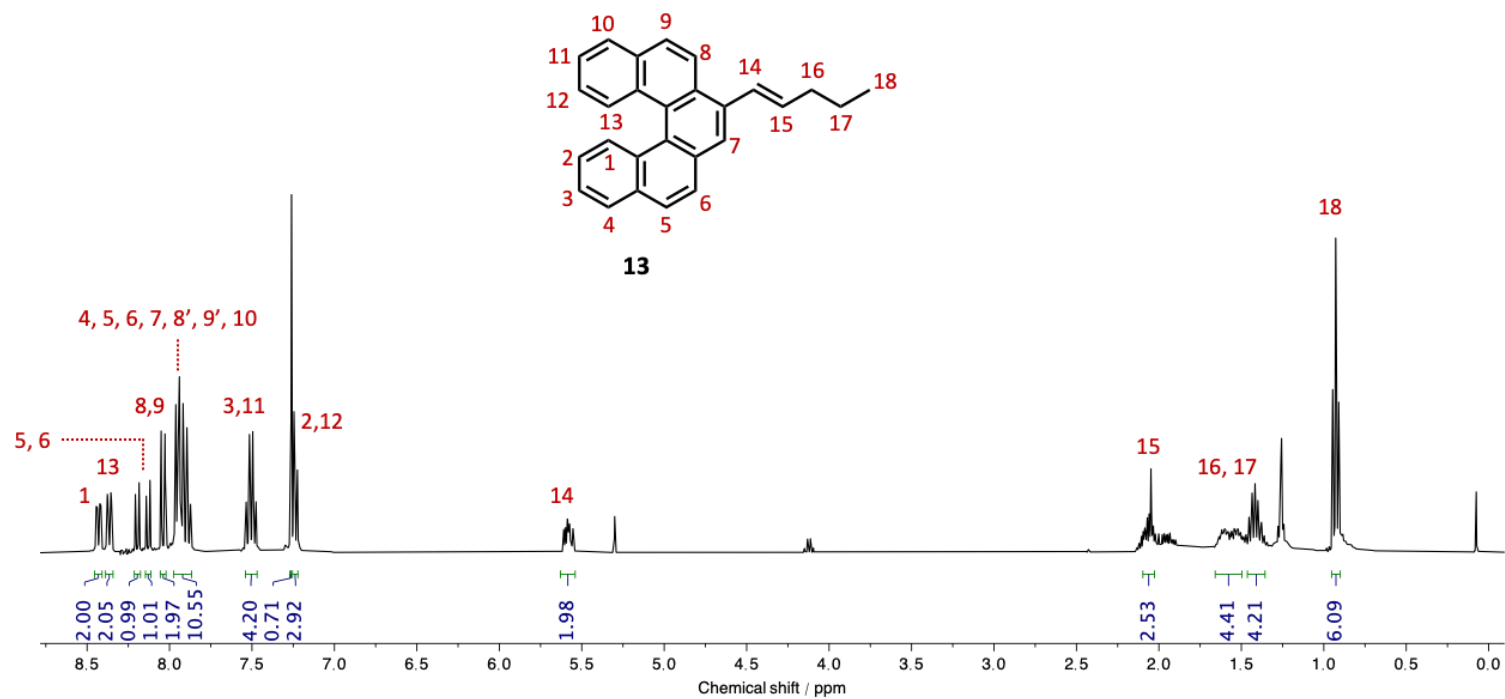
Figure S4.1 ^{1}H NMR (CDCl$_3$, 400 MHz, 298K) spectrum of **13**
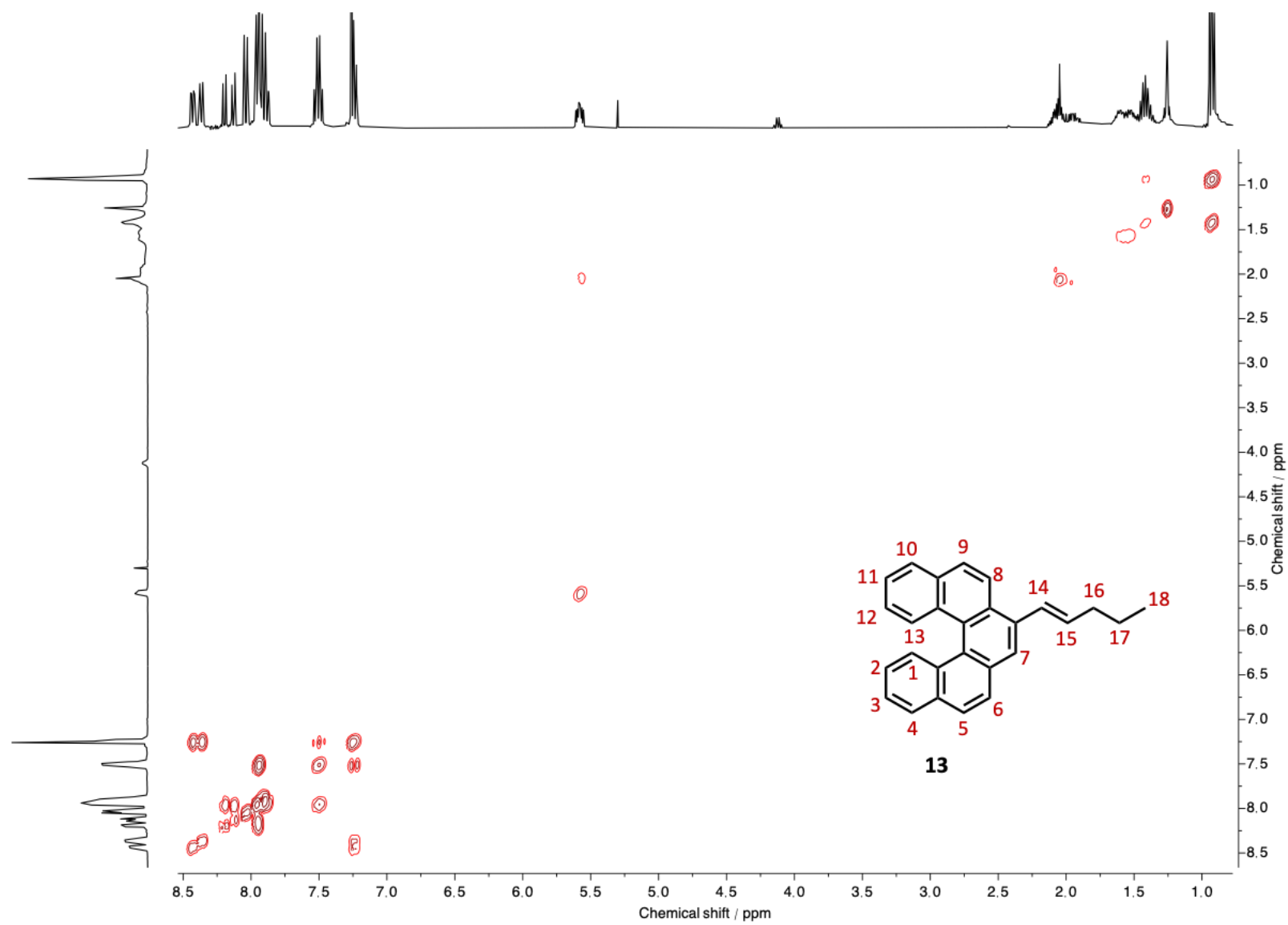
Figure S4.2 ^{1}H–^{1}H COSY NMR (CDCl$_3$, 400 MHz, 298K) spectrum of **13**

Figure S4.3 ^{1}H NMR (CDCl$_3$, 400 MHz, 298K) spectrum of **14** or **15**
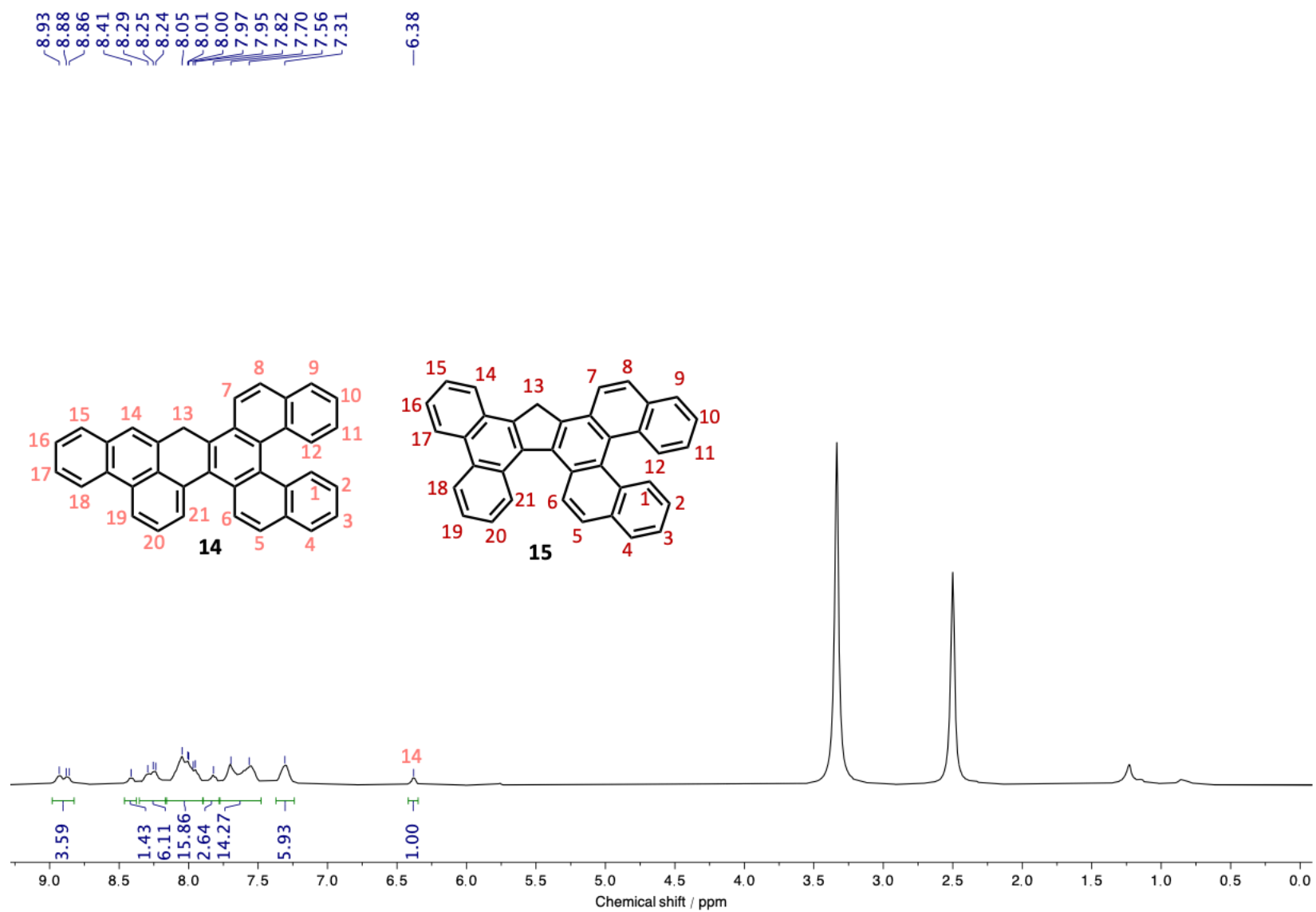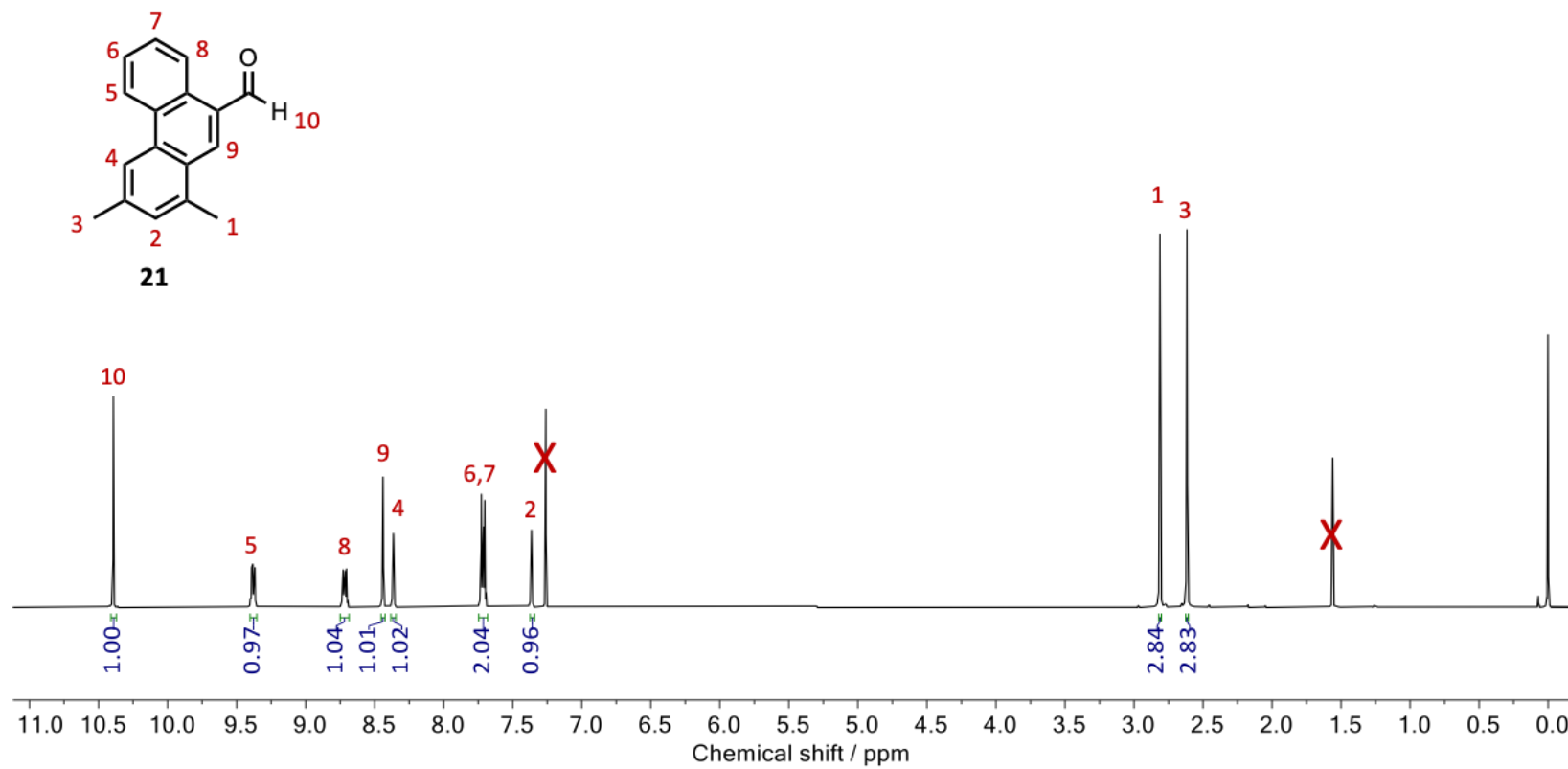
Figure S4.4 ^{1}H NMR (CDCl$_3$, 400 MHz, 298K) spectrum of **21**
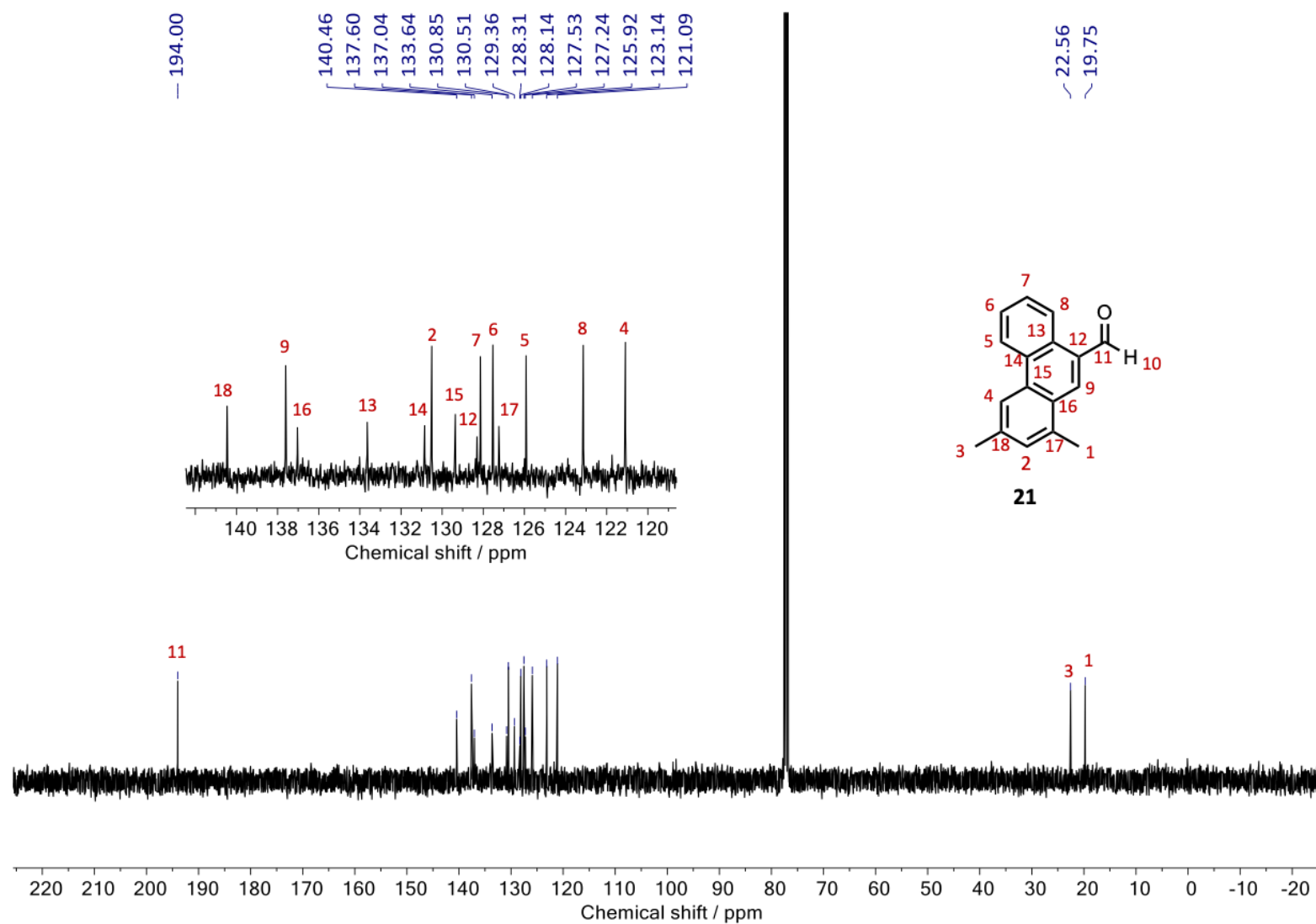
Figure S4.5 ^{13}C NMR (CDCl$_3$, 101 MHz, 298K) spectrum of **21**
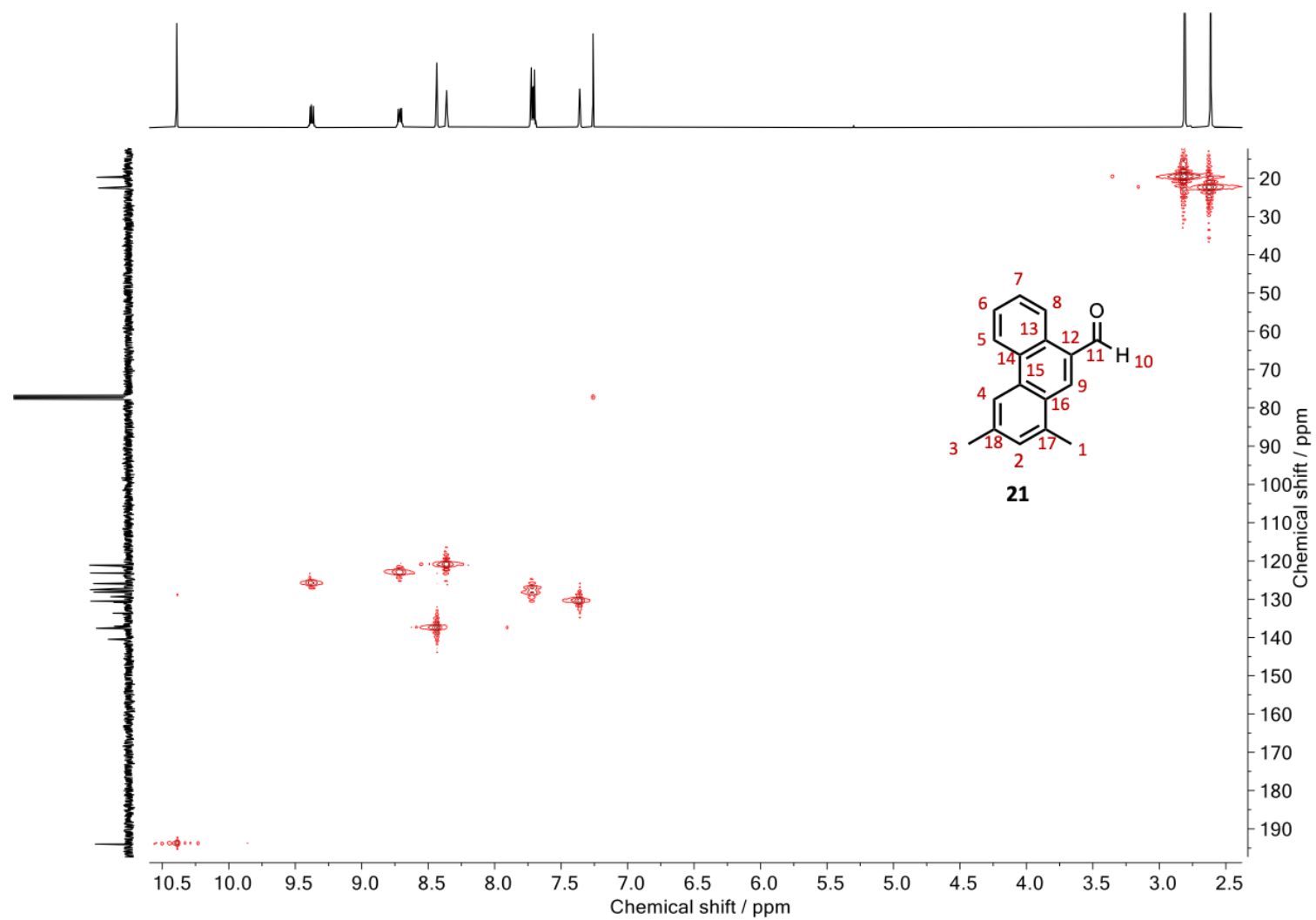
Figure S4.6 ^1H–^{13}C HSQC NMR (CDCl$_3$, 101 MHz, 298K) spectrum of **21**
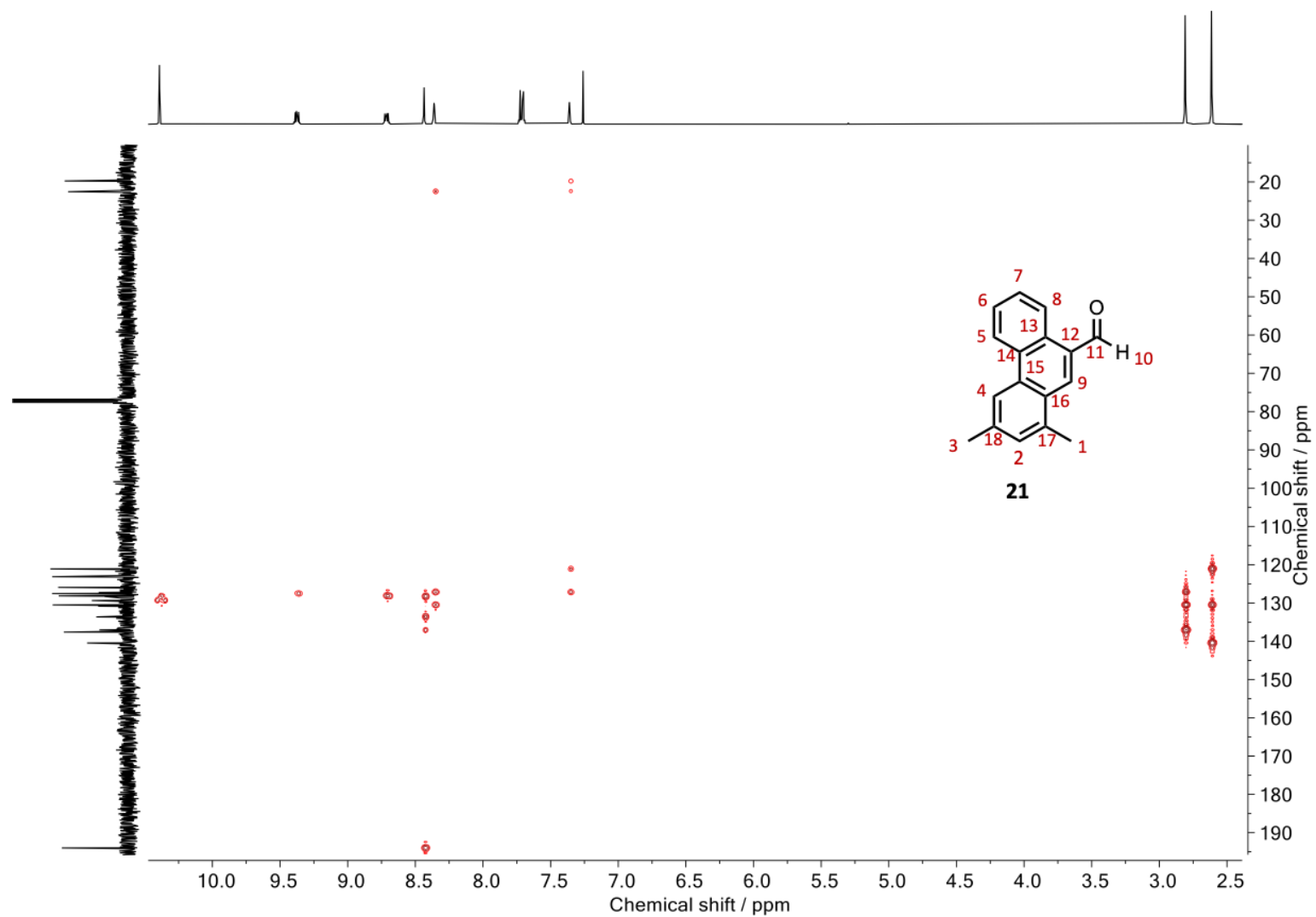
Figure S4.7 ^{1}H–^{13}C HMBC NMR (CDCl$_3$, 101 MHz, 298K) spectrum of **21**
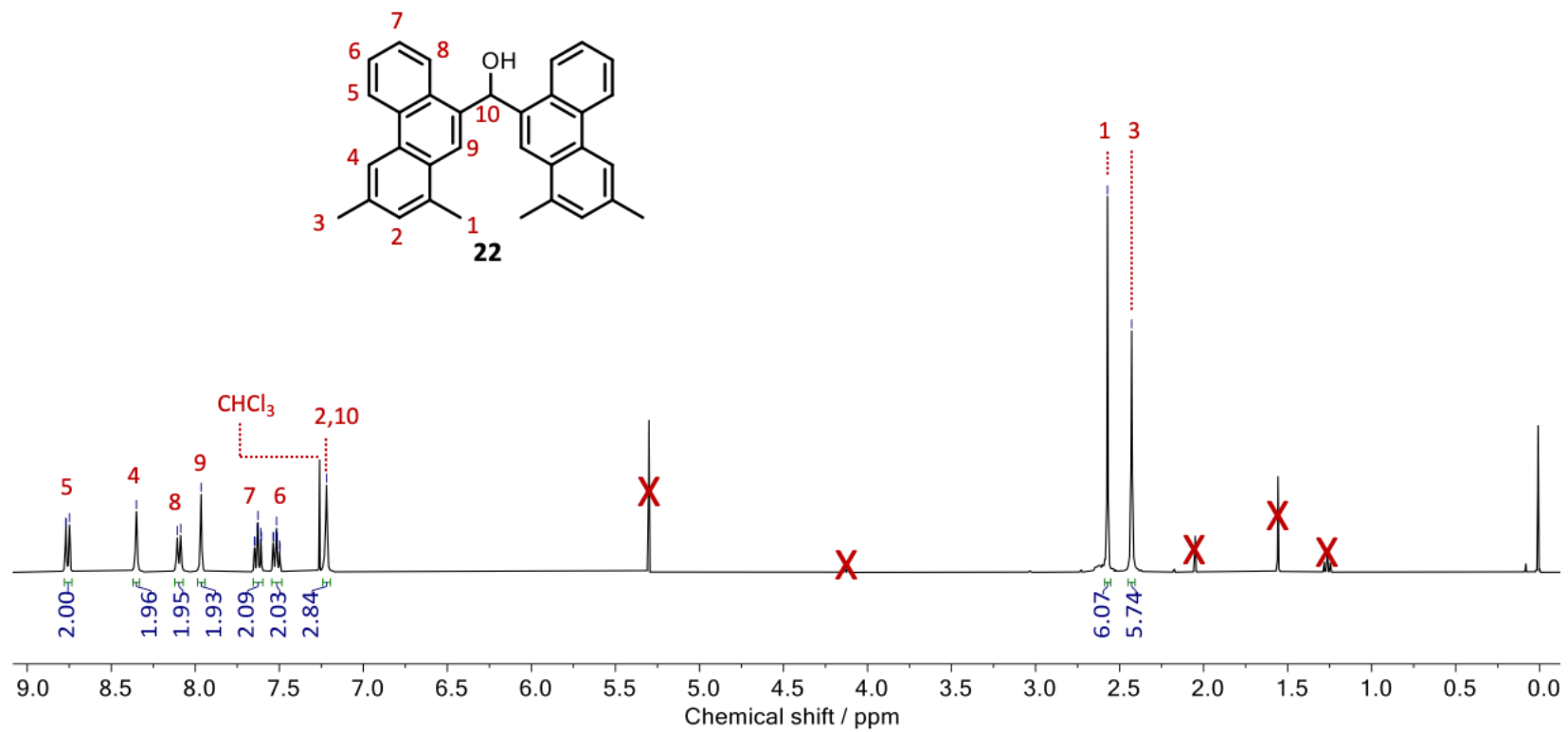
Figure S4.8 ^{1}H NMR (CDCl$_3$, 400 MHz, 298K) spectrum of **22**
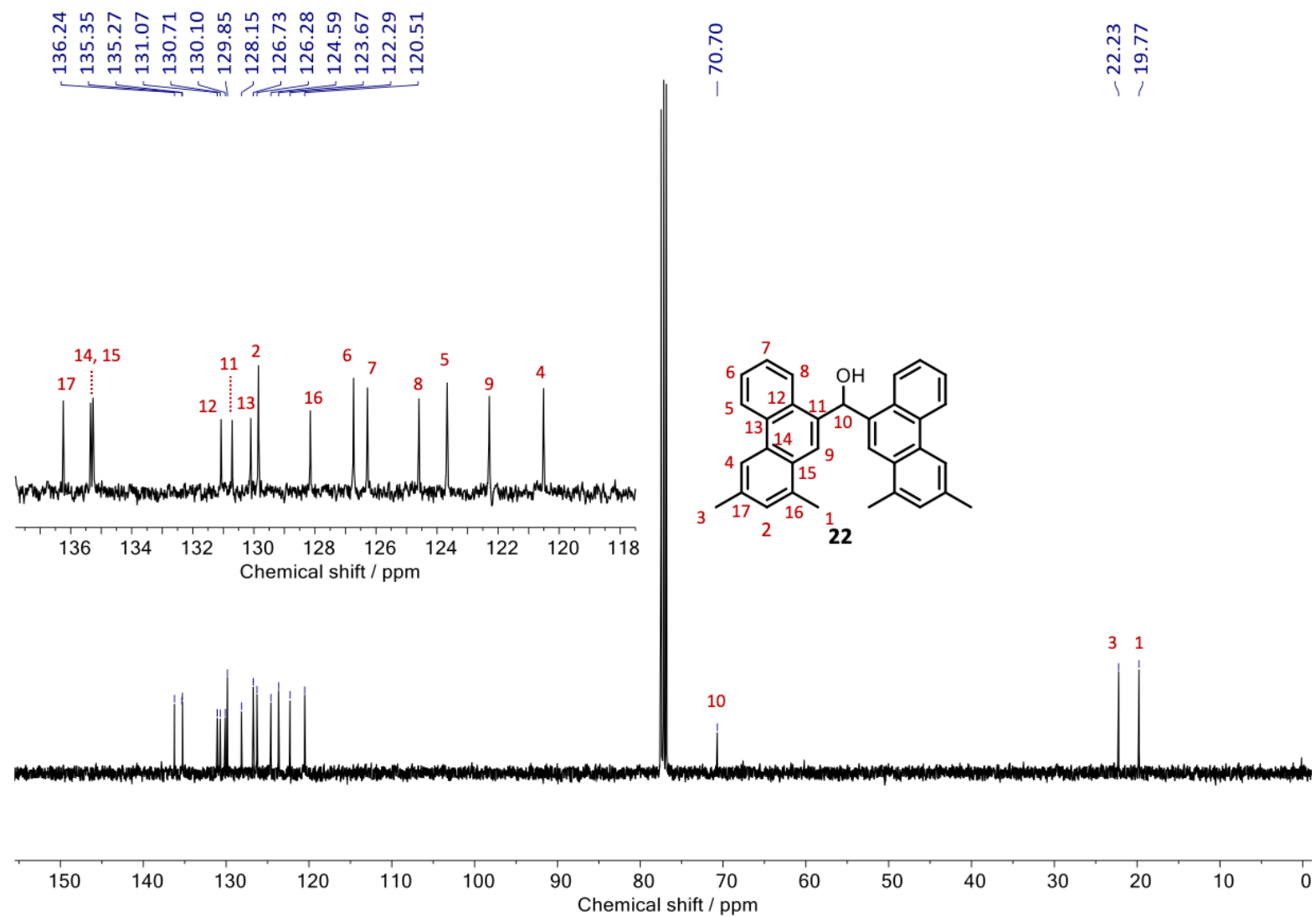
Figure S4.9 ^{13}C NMR (CDCl$_3$, 101 MHz, 298K) spectrum of **22**
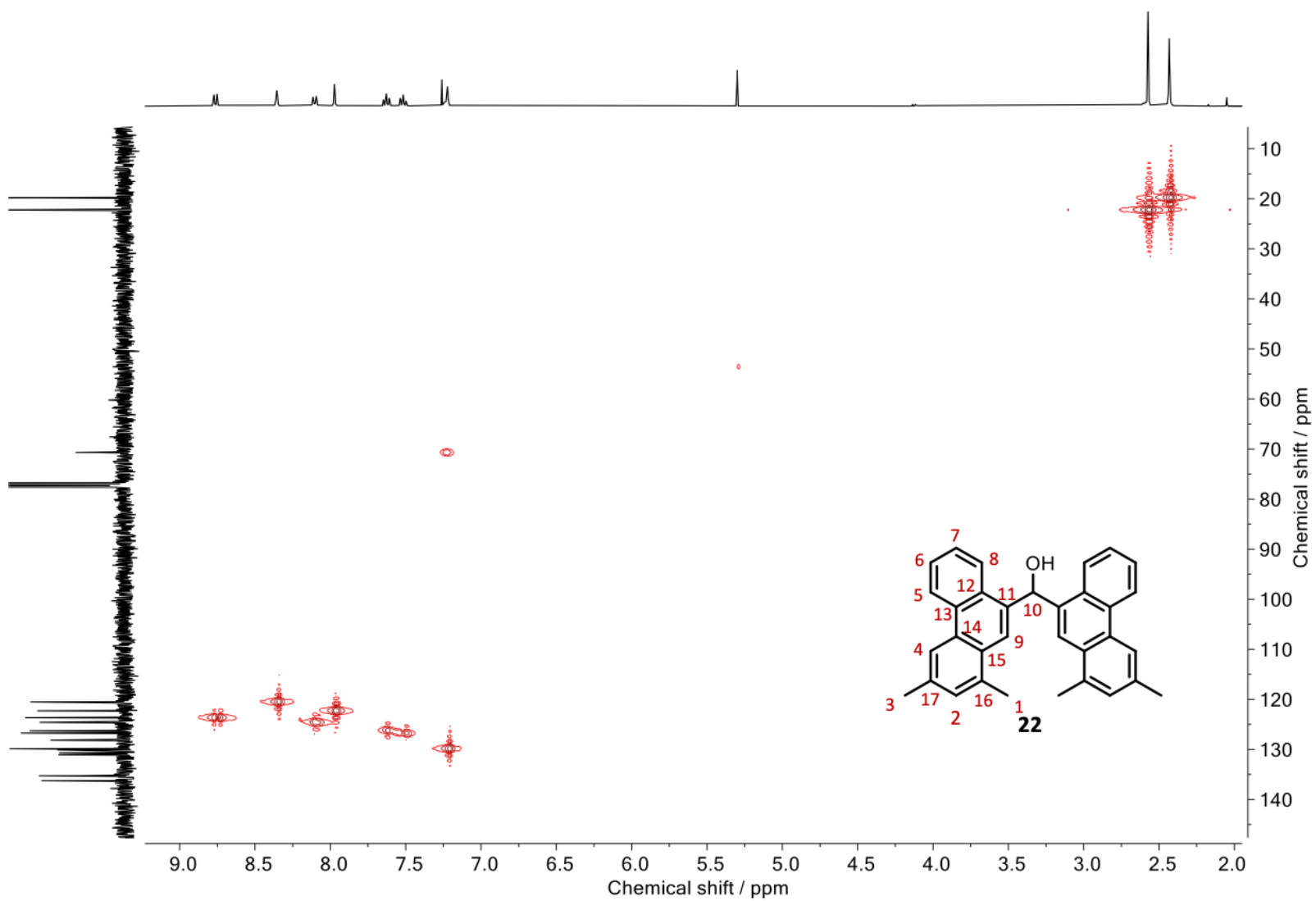
Figure S4.10 ^{1}H–^{13}C HSQC NMR (CDCl$_3$, 101 MHz, 298K) spectrum of **22**
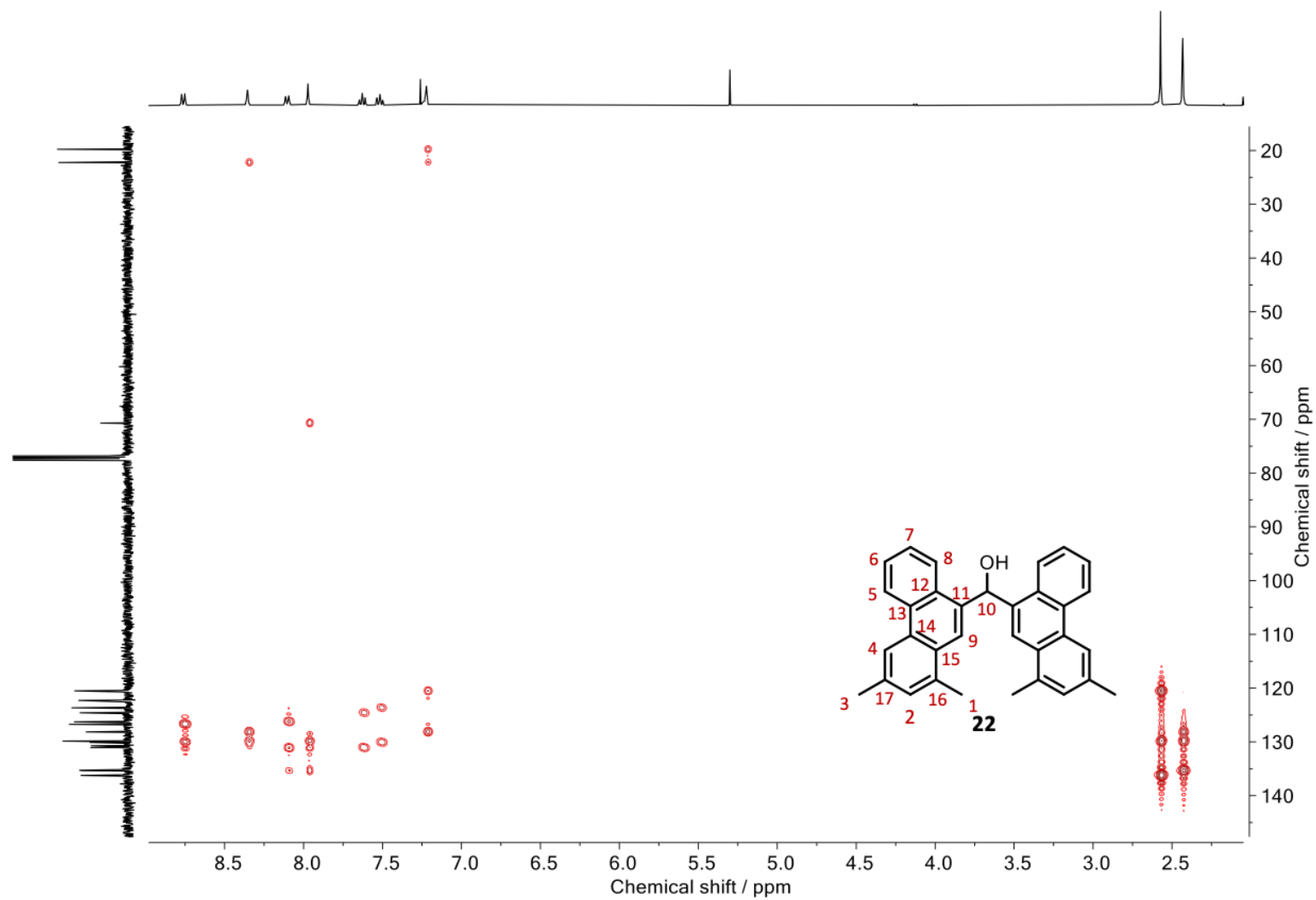
Figure S4.11 ^{1}H–^{13}C HMBC NMR (CDCl$_3$, 101 MHz, 298K) spectrum of **22**

4.4.4 DFT ANALYSES

DFT calculations were performed to obtain geometrically optimised structures of all enantiomers and the transition state structures for the interconversion between enantiomers of **A-OH**, **A-H**, **B-OH, TBF-A·**, **7HTBF, MeTBF** and **TNF** using (U)B3LYP(GD3BJ)/6-31G(d,p) in a CH_2Cl_2 solvent model or unrestricted conditions for open-shell structures. Ground state geometries were verified by convergence to a minimum stationary point and no negative vibrational frequencies observed.

Time dependent DFT (TD-DFT) calculations were performed for the first 20 states of each compound using B3LYP(GD3BJ)/6-31G(d,p) in a CH_2Cl_2 solvent model and in some cases natural transition orbital (NTO) analysis was performed on specific excited states to understand qualitatively what occupations of orbitals gave rise to those excited state transitions.

Structures of transition states for the interconversion between the *M*- and *P*- enantiomers of the TBF library were optimised using the Berny approximation[34] using (U)B3LYP(GD3BJ)/6-31G(d,p) in a CH_2Cl_2 solvent model starting from a random guess. Transition states were verified by the appearance of a negative imaginary frequency which when animated mirrored the translational motion that would depict enantiomeric interconversion. Single point energy calculations were performed so that energies of the enantiomers and transition states could be compared to determine the energy barrier for the interconversion to provide insight into the configurational stability of the studied molecules.
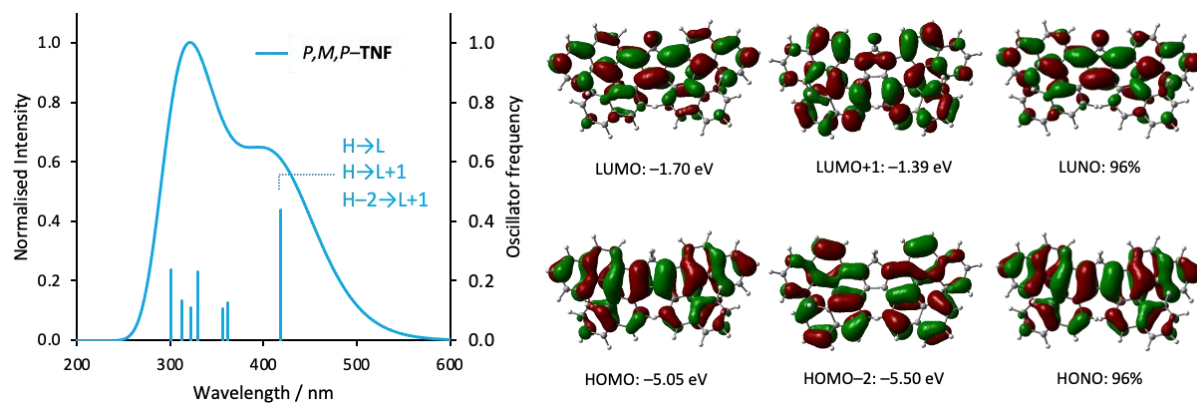
Figure S4.12. TD-DFT and NTO analyses for the first excited state of *P,M,P-***TNF**

4.4.4.1 CARTESIAN COORDINATES

Cartesian coordinates for the optimised structures of the TBF-based helicenes studied are summarised here.

4.5 REFERENCES

1. Liu, J.; Su, H.; Meng, L.; Zhao, Y.; Deng, C.; Ng, J. C. Y.; Lu, P.; Faisal, M.; Lam, J. W. Y.; Huang, X.; Wu, H.; Wong, K. S.; Tang, B. Z. What Makes Efficient Circularly Polarised Luminescence in the Condensed Phase: Aggregation-Induced Circular Dichroism and Light Emission. *Chem. Sci.* **2012**, *3*, 2737–2747.

2. Sánchez-Carnerero, E. M.; Agarrabeitia, A. R.; Moreno, F.; Maroto, B. L.; Muller, G.; Ortiz, M. J.; De La Moya, S. Circularly Polarized Luminescence from Simple Organic Molecules. *Chem. Eur. J.* **2015**, *21*, 13488–13500.

3. Sang, Y.; Han, J.; Zhao, T.; Duan, P.; Liu, M. Circularly Polarized Luminescence in Nanoassemblies: Generation, Amplification, and Application. *Adv. Mater.* **2020**, *32*, 1900110.

4. Sánchez-Carnerero, E. M.; Agarrabeitia, A. R.; Moreno, F.; Maroto, B. L.; Muller, G.; Ortiz, M. J.; De La Moya, S. Circularly Polarized Luminescence from Simple Organic Molecules. *Chem. Eur. J.* **2015**, *21*, 13488–13500.

5. Donckt, E. V.; Nasielski, J.; Greenleaf, J. R.; Birks, J. B. Fluorescence of the Helicenes, *Chem. Phys. Lett.* **1968**, *2*, 409–410.

6. Yubuta, A.; Hosokawa, T.; Gon, M.; Tanaka, K.; Chujo, Y.; Tsurusaki, A.; Kamikawa, K. Enantioselective Synthesis of Triple Helicenes by Cross-Cyclotrimerization of a Helicenyl Aryne and Alkynes via Dynamic Kinetic Resolution. *J. Am. Chem. Soc.* **2020**, *142*, 10025–10033.

7. Oyama, H.; Akiyama, M.; Nakano, K.; Naito, M.; Nobusawa, K.; Nozaki, K. Synthesis and Properties of [7]Helicene-like Compounds Fused with a Fluorene Unit. *Org. Lett.* **2016**, *18*, 3654–3657.

8. Sawada, Y.; Furumi, S.; Takai, A.; Takeuchi, M.; Noguchi, K.; Tanaka, K. Rhodium-Catalyzed Enantioselective Synthesis, Crystal Structures, and Photophysical Properties of Helically Chiral 1,1′-Bitriphenylenes. *J. Am. Chem. Soc.* **2012**, *134*, 4080–4083.

9. Kitamura, C.; Tanigawa, Y.; Kobayashi, T.; Naito, H.; Kurata, H.; Kawase, T. 17,17-Dialkyltetrabenzo[a,c,g,i]Fluorenes with Extremely High Solid-State Fluorescent Quantum Yields: Relationship between Crystal Structure and Fluorescent Properties. *Tetrahedron* **2012**, *68*, 1688–1694.

10. Ueki, M.; Kimura, Y.; Yamamoto, Y.; Nishida, J.-I.; Kitamura, C.; Tanaka, M.; Ikeda, H.; Kawase, T. 3,14-Bis(4-formylphenyl)-17,17-di(*n*-pentyl)tetrabenzo[*a,c,g,i*]fluorene Showing Solvatochromism and Crystallochromism in Fluorescence, *Tetrahedron*, **2017**, *73*, 1170–1176.

11.   Ueda, Y.; Tanigawa, Y.; Kitamura, D.; Ikeda, H.; Yoshimoto, Y.; Tanaka, M.; Mizuno, K.; Kurata, H.; Kawase, T. 3,14-Bis(*p*-nitrophenyl)-17,17-dipentyltetrabenzo[*a,c,g,i*]-fluorene: A New Fluorophore Displaying Both Remarkable Solvatochromism and Crystalline-Induced Emission, *Chem. Asian. J.* **2012**, *8*, 392–399.

12.   Barroso, J.; Cabellos, J. L.; Pan, S.; Murillo, F.; Zarate, X.; Fernandez-Herrera, M. A.; Merino, G. Revisiting the Racemization Mechanism of Helicenes, *Chem. Commun.* **2018**, *54*, 188–191.

13.   Ravat, P. Carbo[*n*]helicenes Restricted to Enantiomerize: An Insight into the Design Process of Configurationally Stable Functional Chiral PAHs, *Chem. Eur. J.* **2021**, *27*, 3957–3967.

14.   Pammer, F.; Sun, Y.; May, C.; Wolmershäuser, G.; Kelm, H.; Krüger, H.-J. Theil, W. R. Dibenzo[*c,g*]fluorene: The Combination of Cyclopentadiene and 1,1'-Binaphthyl in One Ligand, *Angew. Chem. Int. Ed.* **2007**, *46*, 1270–1273.

15.   Ravat, P.; Hinkelmann, R.; Steinebrunner, D.; Prescimone, A.; Bodoky, I.; Juríček, M. Configurational Stability of [5]Helicenes. *Org. Lett.* **2017**, *19*, 3707–3710.

16.   Li, C.; Yang, Y.; Miao, Q. Recent Progress in Chemistry of Multiple Helicenes. *Chem. Asian. J.* **2018**, *13*, 884–894.

17.   Hay, A. M.; Hobbs-Dewitt, S.; MacDonald, A. A.; Ramage, R. Use of Tetrabenzo[*a,c,g,i*]fluorene as an Anchor Group for the Solid-Solution Phase Synthesis of Ciprofloxacin, *Tetrahedron. Lett.* **1998**, *39*, 8721–8724.

18.   Rusali, L. E.; Schramm, M. P. Au-Cavitands: Size Governed Arene-Alkyne Cycloisomerization, *Tetrahedron. Lett.* **2020**, *61*, 152333.

19.   Mandrelli, F.; Blond, A.; James, T.; Kim, H.; List. B, Deracemizing α-Branched Carboxylic Acids by Catalytic Asymmetric Protonation of Bis-Silyl Ketene Acetals with Water or Methanol, *Angew. Chem. Int. Ed.* **2019**, *58*, 11479–11482.

20.   Mamane, V.; Hannen, P.; Früstner, A. Synthesis of Phenanthrenes and Polycyclic Heteroarenes by Transition-Metal Catalyzed Cycloisomerization Reactions, *Chem. Eur. J.* **2004**, *10*, 4556–4575.

21.   Goretta, S.; Tasciotti, C.; Mathieu, S.; Smet, M.; Maes, W.; Chabre, Y. M.; Dehaen, W.; Giasson, R.; Raimundo, J.-M.; Henry, C. R.; Barth, C.; Gingras, M. Expeditive Syntheses of Functionalized Pentahelicenes and NC-AFM on Ag(001). *Org. Lett.* **2009**, *11*, 3846–3849.

22.   Ravat, P.; Ribar, P.; Rickhaus, M.; Häussinger, D.; Neuburger, M.; Juríček, M. Spin-Delocalization in a Helical Open-Shell Hydrocarbon. *J. Org. Chem.* **2016**, *81*, 12303–12317.

23.   Liu, J.; Narita, A.; Osella, S.; Zhang, W.; Schollmeyer, D.; Beljonne, D.; Feng, X.; Müllen, K. Unexpected Scholl Reaction of 6,7,13,14-Tetraarylbenzo[*k*]tetraphene: Selective Formation of Five-Membered Rings in Polycyclic Aromatic Hydrocarbons, *J. Am. Chem. Soc.* **2016**, *138*, 2602–2608.

24.   Dou, X.; Yang, X.; Bodwell, G. J.; Wagner, M.; Enkelmann, V.; Müllen, K. Unexpected Phenyl Group Rearrangement During an Intramolecular Scholl Reaction Leading to an Alkoxy-Substituted Hexa-*peri*-hexabenzocoronene, *Org. Lett.* **2007**, *9*, 2485–2488.

25.   Avlasevich, Y.; Kohl, C.; Müllen, K. Facile Synthesis of Terrylene and Its Isomer Benzoindenoperylene, *J. Mater. Chem.* **2006**, *16*, 1053–1057.

26.   Nishinaga, T.; Inoue, R.; Matsuura, A.; Komatsu, K. Radical Cation and Dication of Fluorene Fully Annealated with Bicyclo[2.2.2]octene Units: Importance of the Quinoidal Resonance Structure in the Cationic Fluorene, *Org. Lett.* **2002**, *4*, 4117–4120.

27.   De Ridder, R.; Martin, R. H. Synthèses Dans Le Domaine Des Composés Polycycliques Aromatique, *Bull. Soc. Chim. Belg.* **1960**, *69*, 534–548.

28.   Carrasco, S.; Martín-Matute, B. Hydrazine-Free Facile Synthesis of Palladium-Tetrkis(Triphenylphosphine), *Eur. J. Inorg. Chem.* **2019**, *2019*, 1951–1955.

29.   Burchat, A. F.; Chong, M.; Nielsen, N. Titration of Alkyllithiums with a Simple Reagent to a Blue Endpoint, *J. Organomet. Chem.* **1997**, *542*, 281–283.

30.   Becke, A. D. Density-Functional Thermochemistry. III. The Role of Exact Exchange, *J. Chem. Phys.* **1993**, *98*, 5648–5652.

31.   Lee, C.; Yang, W.; Parr, R. G. Development of the Colle-Salvetti Correlation-Energy Formula into a Functional of the Electron Density, *Phys. Rev. B.* **1988**, *37*, 785–789.

32.   Grimme, S.; Ehrlich, S.; Goerigk, L. Effect of the Damping Function in Dispersion Corrected Density Functional Theory, *J. Comp. Chem.* **2011**, *32*, 1456–1465.

33.   Kitagawa, Y.; Kumagai, M.; Hasegawa, Y.; Nakanishi, T.; Fushimi, K. Rare-Earth Complex, Light-Emitting Material, Light-Emitting Object, Light-Emitting Device, Interlayer for Laminated Glass, Laminated Glass, Windshield for Vehicle, Wavelength Conversion Material, And Security Material. WO 2020/013087, May 19, 2021.

34.   Ayala, P. Y.; Schlegel, B. A Combined Method for Determining Reaction Paths, Minima, and Transition State Geometries, *J. Chem. Phys.* **1997**, *107*, 375–384.

CHAPTER 5 |
MULTIFUNCTIONAL HETEROATOM-DOPED HELICENES

SYNOPSIS
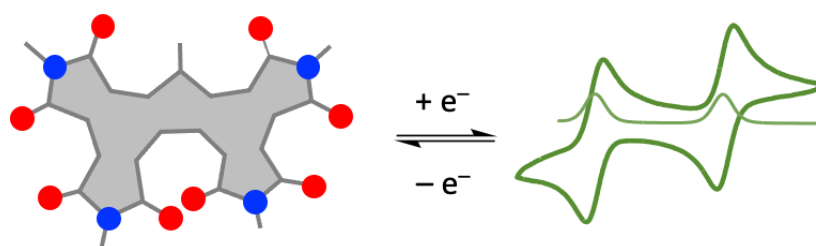
There is a limit to how well carbohelicenes can perform as efficient chiral light-emitting and charge transporting materials for advanced chiroptoelectronic applications. Therefore, heteroatoms embedded into helicenes serve the purpose of boosting their performances and introducing additional relevant functionality. This chapter discusses two synthetic targets **Acr-OH** and **MDI-TBF** that are pursued whose structures are based on the TBF framework. **Acr-OH**, where a redox-active acridine is non-conjugatively substituted in the head position of TBF, forms dimers in solution that are held together by intermolecular hydrogen bonds (H-bonds). These intermolecular dimers appear to stay intact upon excitation, resulting in large observed emission Stokes shifts ($\Delta\lambda$ = 93 nm). **Acr-OH** is quite sensitive to the addition of H_2O, which disrupts these H-bonds and breaks apart the dimers revealing the monomeric behaviour of **Acr-OH** in solution. Then, in the second part of this Chapter, the redox properties of an intermediate MDI-dimer **4** that has been isolated in the pursuit of **MDI-TBF** (where heteroatoms would be conjugated into the TBF framework) are studied. The results reveal how favourably **4** accepts electrons compared to its monomer **H₂MDI**. The ease with which **4** accepts electrons is due to extended conjugation between MDI units, enhanced by an increase in double bond character of the C–C bond that joins the MDI units in the dimer and is confirmed by SEC analyses. Interrogation of the DFT structures of the reduced states of **MDI-TBF** highlight a largening of helical *fjord* parameters upon reduction, suggesting an increase in its configurational stability. It is evident from these two examples that the embedding of heteroatoms results in fluorenyl-embedded helicenes with emergent multifunctionality that make them suitable for use as sensing or charge transporting materials.

ACKNOWLEDGEMENTS

5.1 INTRODUCTION

So far, the research Chapters this Thesis have solely discussed carbon-containing polyaromatic frameworks with non-planar and contorted structures that are based off the TBF moiety. The central 5-membered cyclopentadienyl ring has been crucial to enabling the optical and redox properties observed for the systems discussed. However, in general, without additional substituent functionalisation to the helicene framework (or through heteroatom doping), carbohelicenes suffer from relatively low PLQYs and poor charge carrier mobilities.[1,2] Chapter 1 discussed examples where researchers have been successful at introducing additional functionality to fluorenyl-based helicenes by incorporating heteroatoms into the helical framework to enable and tune multifunctional and stimuli responsive behaviours. They achieved this feat by swapping out the methylene carbon atom in fluorene for heteroatoms such as N, S, O, B, P and Si.[3–9] Therefore, there are benefits to introducing redox-active heteroatom moieties to TBF structures in order to induce new (electro)chemical responsiveness and functionality.

Since the TBF core is electron rich (due to its tetrabenzannulated wings), it seems appropriate to pair it with electron-deficient heteroatom-based moieties in order to study fundamental charge-transfer properties, as has been conducted for smaller fluorenes.[10] In particular, acridiniums (or acridines in their neutral forms) – isostructural with anthracene – exhibit profound changes to their electronic properties and/or shape upon redox, acid/nucleophile or mechanical stimuli.[11] These stimuli-dependent behaviours have enabled their development as multi-responsive recognition units[12,13] (Figure 5.1a). In addition, researchers have had success with sculpting helical aromatic systems from highly electron-deficient diimides (Figure 5.1b). These helicene diimides display typical *n*-type redox behaviours inherent to linear and flat aromatic diimides but with enhanced emission in both solution and the solid-state (PLQY$_{solid}$ of up to 0.17). While heteroatom-based non-planar systems exhibit enhanced intrinsic redox and optical properties, they also introduce novel ways for molecules to interact supramolecularly e.g., through H-bonds[14] leading to the emergence of novel bulk material properties in their aggregate forms (e.g., thin-films), which are arguably more relevant for device-like applications. To this end, the design of electron deficient heterohelicenes is required to enhance the performance of current chiral organic semiconductors and emitters for use in advanced technological applications.

In this Chapter, introducing heteroatoms to helical frameworks was approached in two different ways. Firstly, while providing kinetic stability to fluorenyl radicals, an acridine moiety is used as a substitute for anthracene (Figure 5.1c) in **Acr-OH**. The design of the structure of **Acr-OH** results in the electron-deficient acridine unit being bound non-conjugatively in the head-position of the electron rich TBF framework, which paves the way for the study of charge transfer processes. In fact, AEE studies of **Acr-OH** highlight the strong tendency for the molecule to form intermolecular H-bonds in non-polar solvents that are disrupted upon addition of polar solvents such as water which competes for these H-

bonding sites. The second method discussed in this Chapter involves sculpting diimide units around a fluorenyl core to create a highly electron accepting helical framework (Figure 5.1d). The design of this helicene introduces heteroatoms into the [5]helical framework in a mellaphanic diimide (MDI)/TBF hybrid **MDI-TBF**. Here, the flat but non-linear mellaphanic diimide replaces the electron-rich phenanthrenes as the 'wings' of the structure. The synthesis of this target has proved to be difficult to achieve, however a study of the optoelectronic properties of an MDI-dimer was undertaken and was compared to results obtained for a regioisomer of MDI based on a pyromellitic diimide (PMDI – here the diimide groups are placed *para* to each other rather than *ortho* as in MDI). The redox properties of the MDI-dimer along with DFT calculations of **MDI-TBF** revealed the potential that **MDI-TBF** has in acting as a redox-controlled chirality lock.
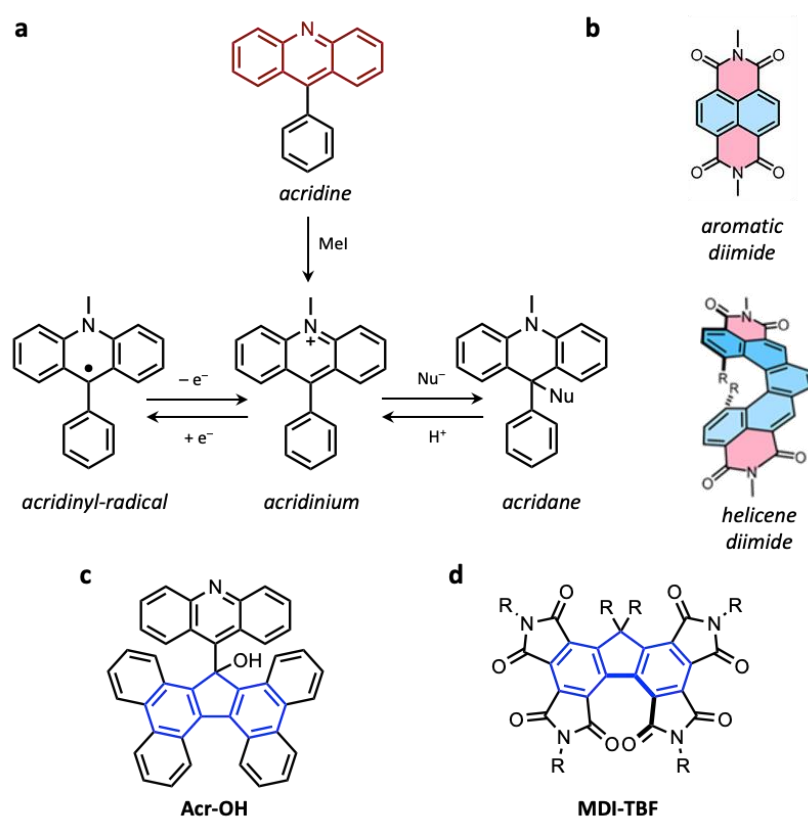
Figure 5.1 (a) Structures depicting the multi-responsive electronic properties of acridines under different stimuli. (b) Examples of linear flat aromatic diimides and analogous non-planar helicene diimides. Chemical structures of targeted hetero-substituted TBF inspired helicenes including (c) **Acr-OH** and (d) **MDI-TBF**.

5.2 RESULTS AND DISCUSSION

5.2.1 ACRIDINYL-TBFS

In Chapter 2, the synthesis, optical and aggregation behaviours of TBF moieties substituted with an anthracene were discussed. Then in Chapter 3, discussions are presented focussing on how this bulky anthracene enables ambient stable organic radicals to be isolated and studied. The swapping of an

anthracenyl head-substituent with an acridinyl head-substituent was performed to introduce a nitrogen atom *para* to the 17-position in TBF, in order to understand how the optical and aggregation properties of the resulting TBF, **Acr-OH** change compared to **A-OH** (studied in Chapter 2). Its synthesis was performed in a similar manner to **A-OH** (Scheme 5.1) using 9-bromoacridine (provided by collaborator Dr. Henri-Pierre Jacquot de Rouville at the University of Strasbourg), under *n*-BuLi conditions with the TBF ketone **TBF=O**.
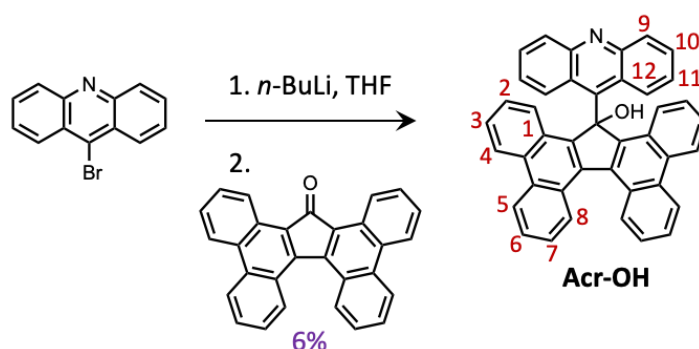
Scheme 5.1 Synthesis of **Acr-OH** from 9-bromoacridine and TBF ketone **TBF=O**

^{1}H NMR spectroscopic analyses (Figure 5.2a) reveal a non-symmetric structure on account of two sets of proton peaks on the acridine moiety (pink circles, Figure 5.2a), similar to the structural features of **A-OH**. The chemical shift corresponding to one of the H[12] protons on the acridine moiety is significantly shifted downfield suggesting a deshielding effect from the hydroxy group in close proximity. The solubility of **Acr-OH** is worse than **A-OH** in the same organic solvents and is evidenced by the poor signal-to-noise of the ^{1}H NMR spectrum, even though the sample is prepared to saturation. As a result, the proton signals in the ^{1}H NMR spectrum appear broader than in **A-OH**, potentially indicating some form of aggregation that is occurring in solution. Alternatively, the broadness of the NMR signals could be as a result of dynamic motion in solution from rotation of the acridine group around the C–C single bond in the head position.

A single-crystal X-ray structure of **Acr-OH** (Figure 5.2b) was obtained by evaporation from a solution of EtOAc and *n*-hexanes. Analysis of this structure reveals that **Acr-OH** crystallises out as a heterochiral dimer that is held together by a strong OH···N hydrogen bond (2.07 Å). The helical parameters of the non-planar TBF (i.e., its interplanar angle $\varphi = 43.7°$, average torsional angle $\theta = 18.1°$ and the distance between the inner *fjord* protons $d_{HH} = 2.23$ Å) are slightly larger than for other TBF structures studied in Chapter 2 ($\varphi = 38.6–41.7°$, $\theta = 16.5–17.2°$ and $d_{HH} = 2.12–2.22$ Å). These differences arise as a result of the different packing structures and solvent interactions in this solvate, however the structure of **Acr-OH** remains looser in helical pitch compared to [5]helicene ($\varphi = 47.3°$, $\theta = 22.1°$ and $d_{HH} = 2.60$ Å). In addition to intermolecular OH···N bonds, there exist $\pi···\pi$ interactions (3.45 Å) which hold the superstructure together in alternating *M–* and *P–* enantiomers (Figure 5.3d *vida*

infra). Hirschfeld surface analysis is a useful tool to understand what close contacts exist in a crystalline material, because it provides a straightforward visualisation of intermolecular interactions. From the surface constructed, regions in red, white and blue represent interatomic distances closer, equal or greater than the sum of their van der Waal radii. Hirschfeld analysis (Figure 5.2c) confirms that the major intermolecular interactions that contribute to red spots on the surface are from strong hydrogen bonds (which accounts for 3.7% of the entire Hirschfeld surface), while C⋯C (i.e., weak π⋯π) and C⋯H interactions contribute 8.2% and 30.8% respectively of the surface.
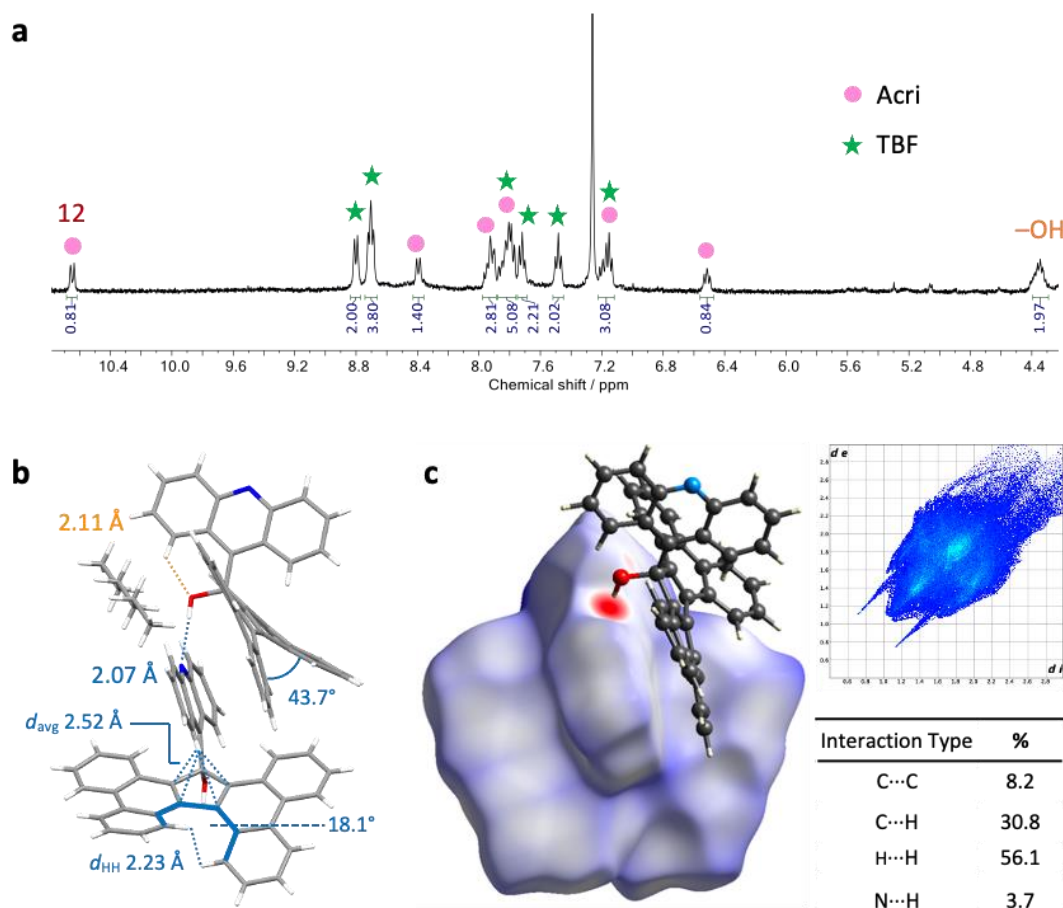
Figure 5.2. (a) Partial ^{1}H NMR (CDCl$_3$, 400 MHz, 298 K) spectrum of **Acr-OH**. Acridinyl protons are represented with a pink circle and TBF protons with a green star; all other proton signals are labelled. (b) Unit cell representation of the single crystal X-ray structure of **Acr-OH** where hydrogen bonds and distances are highlighted in orange, interplanar angles and average torsional angles in dark blue. (c) Hirschfeld surface generated for the single crystal X-ray structure of **Acr-OH** including its fingerprint region and a table highlighting the % surface area of particular atom-atom interactions to the overall surface.

The solution-state optical properties of **Acr-OH** were studied by UV–vis absorption and fluorescence spectroscopy in THF (10 µM; Figure 5.3a). **Acr-OH** absorbs between 325–435 nm (similar to other TBFs studied in Chapter 2) identified as the π-π* transition of the TBF core, revealing that the acridine moiety does not interfere with TBF photophysics. In addition, the vibrational features of the absorption band are broad indicating dynamic motion of the molecule in solution (corroborating peak broadness observed in its ^{1}H NMR spectrum). Aggregation is not observed between 5–60 µM, evidenced by a

linear concentration-dependence of the absorption spectra at 365 nm according to the Beer-Lambert relationship (see Supplementary Information, Section 5.4.5, Figure S5.21).
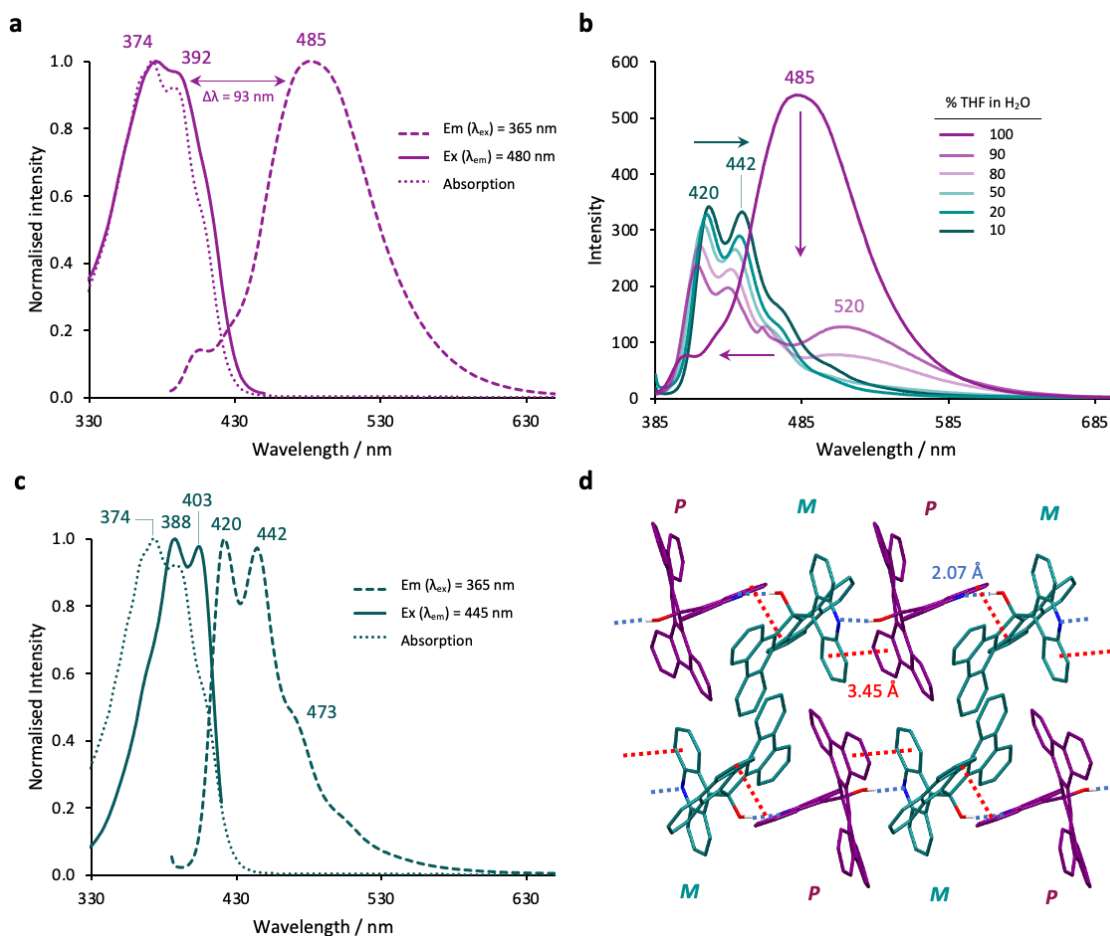
Figure 5.3 (a) Normalised absorption, emission, and excitation spectra for **Acr-OH** measured in THF (10 μM). (b) Aggregation studies in THF/H$_2$O mixtures for **Acr-OH**; (c) Normalised absorption, emission and excitation spectra for **Acr-OH** measured in 10% THF–H$_2$O (10 μM) (d) Packing structure of **Acr-OH** viewed along the *a* axis is shown highlighting H-bonds and π-π interactions that are the major non-covalent interactions taking place. *M*–enantiomers are coloured in green while *P*–enantiomers are coloured purple. All non-interacting hydrogen and solvent atoms have been omitted for clarity.

Exciting **Acr-OH** at 365 nm (Figure 5.3a) results in a broad and featureless emission band between 425–635 nm with a remarkably large Stokes shift (Δλ = 93 nm). This observed Stokes shift indicates either (i) the formation of an excited state dimer (excimer) or an excited state complex (exciplex) in the excited state[15,16] (ii) the formation of an intramolecular charge transfer (ICT)[17] complex due to the donor (TBF)-acceptor (acridine) structure of **Acr-OH** or (iii) excitation of a non-covalently bound ground-state dimer/aggregate[18,19] with an apparent excimer-like emission. Of the three possibilities described above, (i) seems least likely to occur since the excitation spectra (Figure 5.3a and Section 5.4.5.1, Figure S5.22) corresponding to emission between 400–480 nm is reminiscent of the absorption spectrum[15] of **Acr-OH**, albeit with less prominent vibronic resolution. The similarities between the excitation and absorption spectra of **Acr-OH** suggest that it is not possible for excimers or exciplexes (i.e., which are different species compared to their ground state monomers) to have formed upon excitation. On the other hand, although the electron-rich TBF core is not in conjugation with the electron deficient acridine

184

moiety, it is possible that an ICT process occurs through-space[20] given the close proximity between the two groups in the X-ray crystal structure (d_{avg}(C–H) = 2.52 Å; Figure 5.2b). Interrogation of the frontier molecular orbitals (FMOs; Supplementary Information, Section 5.4.6 Figure S5.28) of **Acr-OH** provides additional support for an ICT process since electron density in the LUMO is observed predominantly around the acridine head-group with a small amount of electron density situated on the cyclopentadienyl core. It is also possible that (iii) can occur since the X-ray structure of **Acr-OH** suggests that it can exist as a ground state dimer in THF with a strong hydrogen bond holding two **Acr-OH** molecules together (Figure 5.3d) such that when excited, its emission appears to resemble that of an excimer.

Notably, upon titration of H_2O into THF solutions of **Acr-OH** (Figure 5.3b), a dramatic reduction of the intensity of the emission peak at 485 nm is observed along with the growth of a blue shifted emission band between 390–550 nm. If the emission at 485 nm was due to an ICT process (i), the titration of a polar solvent like H_2O is expected to stabilise the charge transfer product more than non-polar solvents like THF.[20] At a 90% THF in H_2O solvent composition, a red shift of the long-wavelength emission peak is observed (from 485 nm to 520 nm) highlighting a possibly stabilised ICT state. However, the hypothesis of the ICT process is less likely to result in the new blue-shifted emission band at that same solvent composition (420 nm). This new emission data therefore appears to favour (iii). The new blue-shifted emission band shows vibronic fine structure which potentially indicates a breaking apart of the ground-state dimer/aggregate into its monomers (with has less vibrational freedom) upon titration of H_2O. Here, the sensitivity of **Acr-OH** to H_2O suggests that it is an efficient medium to compete for hydrogen bond sites on the acridine thereby allowing **Acr-OH** to exist as a monomer. Excitation experiments for the emission at 445 nm were probed in a 10% THF–H_2O mixture of **Acr-OH** (Figure 5.3c) to uncover a red-shifted excitation spectrum compared to its absorption with a much smaller Stokes shift ($\Delta\lambda = 17$ nm). These results further support the conclusion that in H_2O, **Acr-OH** exists as a monomer.

Further experiments such as solvent dependent emission spectroscopy, lifetime measurements[21] and dynamic light scattering measurements need to be conducted to help elucidate more clearly the monomeric and aggregate states in different solvent conditions. Together, the results highlight the effect that introducing heteroatoms into the structure of helical polyaromatic molecules such as **Acr-OH** has on its ability to interact intermolecularly through non-covalent interactions (H-bonds). These intermolecular interactions were previously not possible in the all carbon-containing framework. As a result, **Acr-OH** displays optical behaviours, where it exists as a dimer/aggregate in THF which is effectively destabilised in aqueous media. The decent separation between the monomeric and dimeric/aggregate emission bands warrants the use of **Acr-OH** as an effective optical H_2O sensor.

5.2.2 TOWARDS A TBF-DIIMIDE HYBRID

Since the attractive properties of helicene diimides have been discussed in the introduction of this Chapter, we thought it would be appropriate to work towards the synthesis of a hybrid diimide-TBF, **MDI-TBF** where the phenanthrene wings can be replaced by a structurally analogous non-linear mellaphanic diimide (MDI). The synthesis of **MDI-TBF** was proposed via two different routes (Scheme 5a and b). Both methods require monobrominated tetramethylbenzene, therefore a large-scale synthesis was required. Bromination of tetramethylbenzene **TMB** was conducted *via* two methods[22,23] using (i) a single equivalent of Br_2 in DMF, or (ii) milder conditions involving benzyltrimethylammonium tribromide ($BTMABr_3$) as the brominating agent with a $ZnCl_2$ catalyst. Both synthetic methods resulted in a mixture of starting material **TMB** and product **1** upon analyses of crude ^1H NMR spectra, however higher conversions to **1** were achieved with method (ii) using $BTMABr_3$ (86% yield compared to 52% with method (i)). Purification of **1** from the starting material **TMB** was attempted *via* vacuum distillation and *via* column chromatography on alumina since product degraded on silica, however both purification methods were unable to fully separate out the mixture and tended to result in lower isolated yields. The presence of **TMB** should not affect the outcome of subsequent reactions (i.e., oxidation, condensation, etc), therefore, a crude product mixture containing a 1:1.1 mixture of **TMB** and **1** was carried forward with the expectation that any remaining **TMB** could be eventually removed upon purification of later stage products.

The first synthetic route towards **MDI-TBF** (Scheme 5.2a) involves the synthesis of the monobrominated MDI 'wings' **3** of the framework first. The MDI wings are then dimerised (i.e., **4**) to construct the cyclopentadienyl core afterwards. The synthesis of novel MDI **3** from bromotetramethylbenzene **1** was adapted from the synthesis of its dibrominated-analogue,[24] while the synthesis of **4** was adapted from the synthesis of a pyromellitic diimide dimer.[25] Oxidation of the methyl groups with an excess of $KMnO_4$ afforded **2** in a 60% yield, which enabled the synthesis of monobrominated MDI **3** (17%) in a condensation reaction with hexylamine in AcOH under reflux conditions. At this stage, automated column chromatography (SiO_2: 0–100% CH_2Cl_2 in *n*-hexanes) enabled the separation of brominated (**3**) and non-brominated MDI (**H₂MDI**). Then, an Ullman coupling with activated Cu-bronze in NMP under reflux yielded dimer **4** in a 43% yield. From MDI-dimer **4**, we hypothesised that an electrophilic aromatic substitution reaction with formaldehyde should enable the formation of the cyclopentadienyl carbon bridge to synthesise **MDI-TBF**. However, the electron deficient nature of MDI would require harsh conditions and the use of TFA or a Lewis acid ($AlCl_3$) to push the reaction to completion.
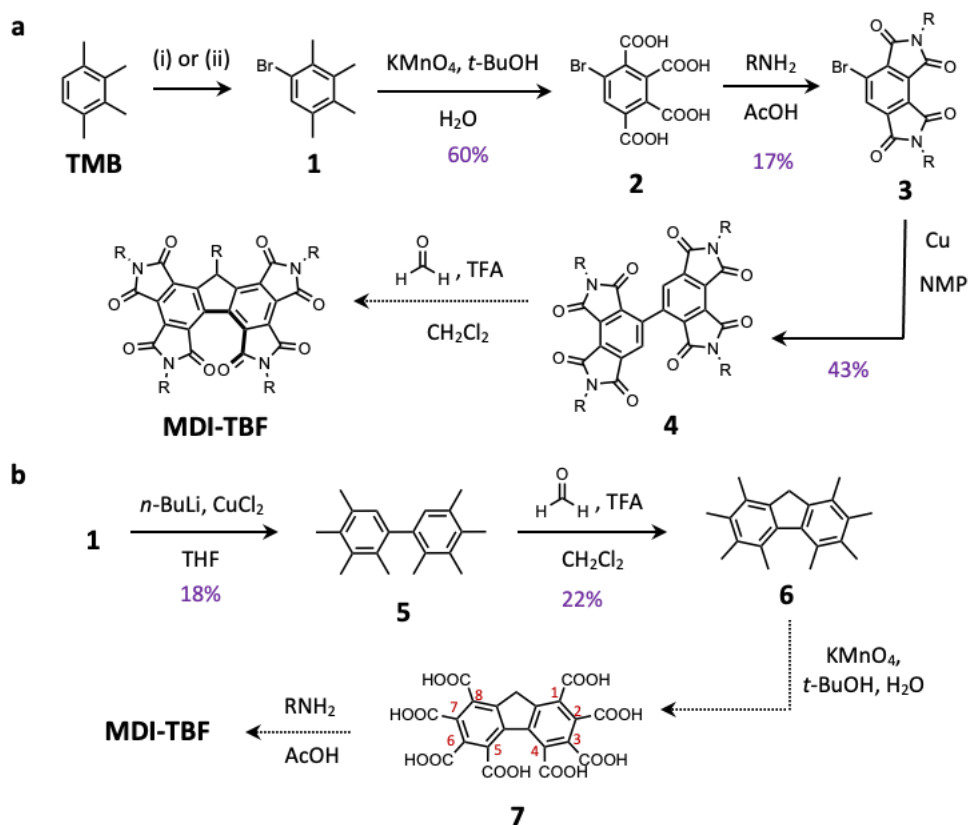
Scheme 5.2. Synthesis of **MDI-TBF** from 2,3,4,5-tetramethylbromobenzene (**TMB**) using two separate routes; (a) by constructing the diimide wings first (**1-4**) and (b) by devising the TBF core first before forming the diimide wings. Conditions for (i) Br$_2$, DMF, 52%, (ii) BTMABr$_3$, ZnCl$_2$, AcOH, 86%.

In light of these envisioned difficulties in the first synthetic route, the second route (Scheme 5.2b) approaches the synthesis of **MDI-TBF** from a different perspective. It begins with construction of the fluorenyl core to form octamethylfluorene **6**[22] first, after which an 8-fold oxidation and condensation should synthesise the desired helicene **MDI-TBF**. Commencing from the same 1:1.1 mixture of **TMB** and **1**, dimer **5** is synthesised in a homocoupling reaction under *n*-BuLi conditions, followed by the addition of CuCl$_2$. The cyclopentadienyl ring is then constructed by a simple electrophilic aromatic substitution reaction with paraformaldehyde and TFA in CH$_2$Cl$_2$ in a 22% yield. When following this route, the largely impure mixture of brominated and non-brominated tetramethylbenzene impacted purification in all stages of the small reaction tests performed thus far due to a coelution of the desired products with **TMB**. However, it is anticipated that the improved bromination method development involving BTMABr$_3$ discussed above should yield better results since there would be a smaller proportion of the **TMB** impurity. Unfortunately, time did not permit the completion of this synthesis. Moving forward, although an 8-fold oxidation might seem insurmountable, a 6-fold oxidation has been conducted previously on hexamethylbenzene.[26] This successful synthesis is precedent to suggest that the oxidation of octamethylfluorene **6** should go to completion with longer reaction times and excess equivalents of KMnO$_4$. Literature suggests that the condensation to create the four diimide wing groups is likely to lead to a distribution of products[24] where diimides can possibly form in the 2,3- and 6,7-

positions in the oxidised derivative of octamethyl fluorene (positions highlighted in Scheme 5.2b on compound **7**), instead of in the desired positions.

Despite not arriving at **MDI-TBF** yet, MDI-dimer **4** is an interesting compound to study in of itself due to the possibility of it adopting a quinoidal-type structure in its reduced states (Figure 5.5c *vide infra*), where a fairly flexible system (i.e., **4**) becomes highly rigid and planar (in both **4**$^{\bullet-}$ and **4**$^{2-}$). In addition, in its neutral state, **4** can exist in one of two conformations **4A** and **4B** (Figure 5.4), both of which are symmetric (i.e., they result in the same number of proton peaks in a ^{1}H NMR spectrum). At room temperature, there exists a single aromatic proton for the MDI core, and two sets of proton environments for the alkyl protons. The splitting of the alkyl protons into two distinct environments highlights the intrinsic non-symmetric nature of a single non-linear MDI unit in dimer **4** (i.e., the two sets of alkyl proton environments exist for the alkyl groups on the top (R) and bottom (R$_1$) face of a single MDI unit in the dimer; represented in Figure 5.4).

Variable temperature (VT) ^{1}H NMR spectroscopy (Figure 5.4) was conducted in order to gain insight on the conformation that **4** favours adopting in solution (if at all). No noticeable changes to the spectra were observed within the increased temperature range studied (298–328 K) however, the experiment was limited by the boiling point of CHCl$_3$ (stacked spectra presented in Section 5.4.3 Figure S5.18). More noticeable shifts and broadening of peaks were observed upon decreasing the temperature (298–218 K; Figure 5.4). At colder temperatures, molecular movements are slowed down such that **4** will tend towards its thermodynamically stable conformation. Of the two conformations, **4A** is likely to be more thermodynamically stable since it appears to avoid the steric interactions that are evident in **4B** between diimide carbonyl groups. In addition, **4A** is likely to be stabilised by an intramolecular CH···O interaction between an aromatic proton on the MDI with a carbonyl on the adjacent MDI unit (highlighted in Figure 5.4). The shift of the aromatic proton H^1 downfield upon lowering the temperature indicates a deshielding of that proton environment, which could be indicative of the intramolecular interaction with the electronegative oxygen atom from a carbonyl group as presented in conformer **4A**. In addition, the alkyl proton in the α-position to the nitrogen atom H$^{2'}$ appears to separate out into two environments indicating that this environment becomes diastereotopic at lower temperatures. This proton environment (i.e., the α-proton on R) has been assigned to the face of the MDI where the inner carbonyl (e.g., on C^8; Figure 5.4) interacts with the aromatic proton in **4A**, where each of the two protons in this position would be affected differently by the intramolecular CH···O interaction upon rigidification. Since the proton shifts are relatively small upon lowering temperatures, it can be concluded that the MDI-dimer **4** prefers to exist in a dynamic conformation similar to **4A** even at room temperature.
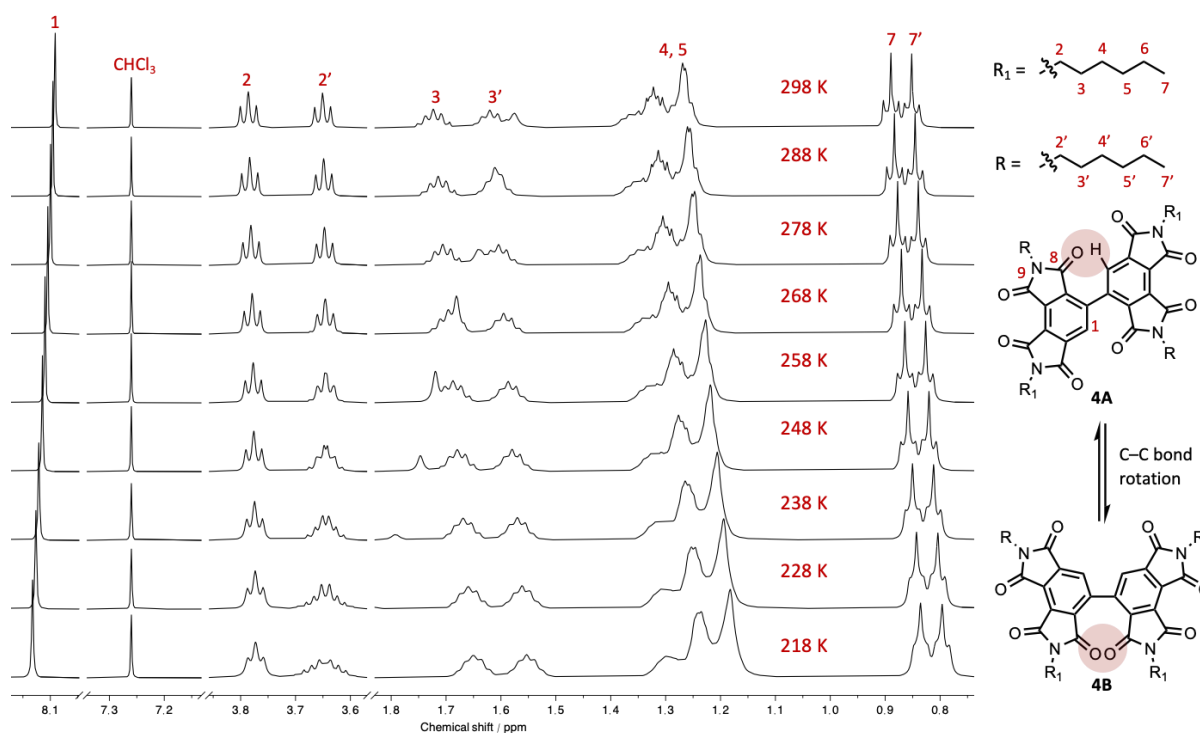
Figure 5.4 Stacked VT ^{1}H NMR (500 MHz, CDCl$_3$, 298–218 K) spectra of **4** that has been fully assigned along with structures of the two idealised planar conformations that **4** can adopt by rotation around the C–C single bond.

In order to understand how the structural dynamics of **4** are affected in its different redox states, cyclic voltammetry (CV; prepared with TBAPF$_6$ (0.1 M) as the supporting electrolyte in THF) was performed and the results compared to an MDI-monomer **H$_2$MDI** as a control compound (Figure 5.5a). The cyclic voltammogram of **H$_2$MDI** is reminiscent of symmetric, linear aromatic diimides (such as its isomer PDMI) and displays two reversible single electron reductions at –0.96 V *vs* Ag/AgCl and –1.59 V *vs* Ag/AgCl. These reduction potentials (and especially the second reduction potential) are much more negative than its linear regioisomer (e.g., E$^1_{1/2}$ of H$_2$PMDI[25] is –0.78 V and E$^2_{1/2}$ is –1.46 V *vs* Ag/AgCl) indicating that it is much harder to add electrons to this system, likely because the non-linear nature of the MDI positions charged carbonyl oxygen centres in close proximity to each other. Possible resonance structures of the reduced states of **H$_2$MDI** that confirm this hypothesis are presented in Section 5.4.5.2, Figure S5.26.

The cyclic voltammogram of **4** in THF displays four reversible single-electron reduction processes (two for each MDI unit). It is clear from the splitting of the first reduction process in **H$_2$MDI** (–0.96 V *vs* Ag/AgCl) into two distinct less negative reduction processes (–0.76 V *vs* Ag/AgCl and –0.99 V *vs* Ag/AgCl) that some electronic communication between the two MDI units in the dimer exists. The electrochemical reversibility of this first reduced state for **4** was confirmed by measuring the cyclic voltammogram at multiple scan rates (Figure 5.5b) which resulted in a straight-line relationship between the peak current *i* and the square root of the scan rate, $\sqrt{v}$ (See Section 5.4.5.2, Figure S5.27). The first reduction of MDI-dimer **4** occurs at only slightly more negative potentials than the first

189

reduction potential for its isomeric PMDI-dimer (–0.75 V *vs* Ag/AgCl under the same conditions)[25] suggesting that upon reduction, **4** has a similarly twisted and rigid structure compared to PMDI-dimer with enhanced delocalisation between the two MDI units. Upon accepting electrons, two possible resonance structures of the radical anion (and therefore the dianion) of **4** have been proposed (Figure 5.5c). Both resonance structures feature a double bond between the MDI–MDI C–C bond, providing an explanation for the increased conjugation observed by CV. **4Q**$^{2-}$ has a quinoidal-type structure where the resulting charges exist on the outer carbonyls of the diimide, whereas **4C**$^{2-}$ manages to maximise conjugation between the two charged centres ideally making it the more thermodynamically-favoured resonance structure.
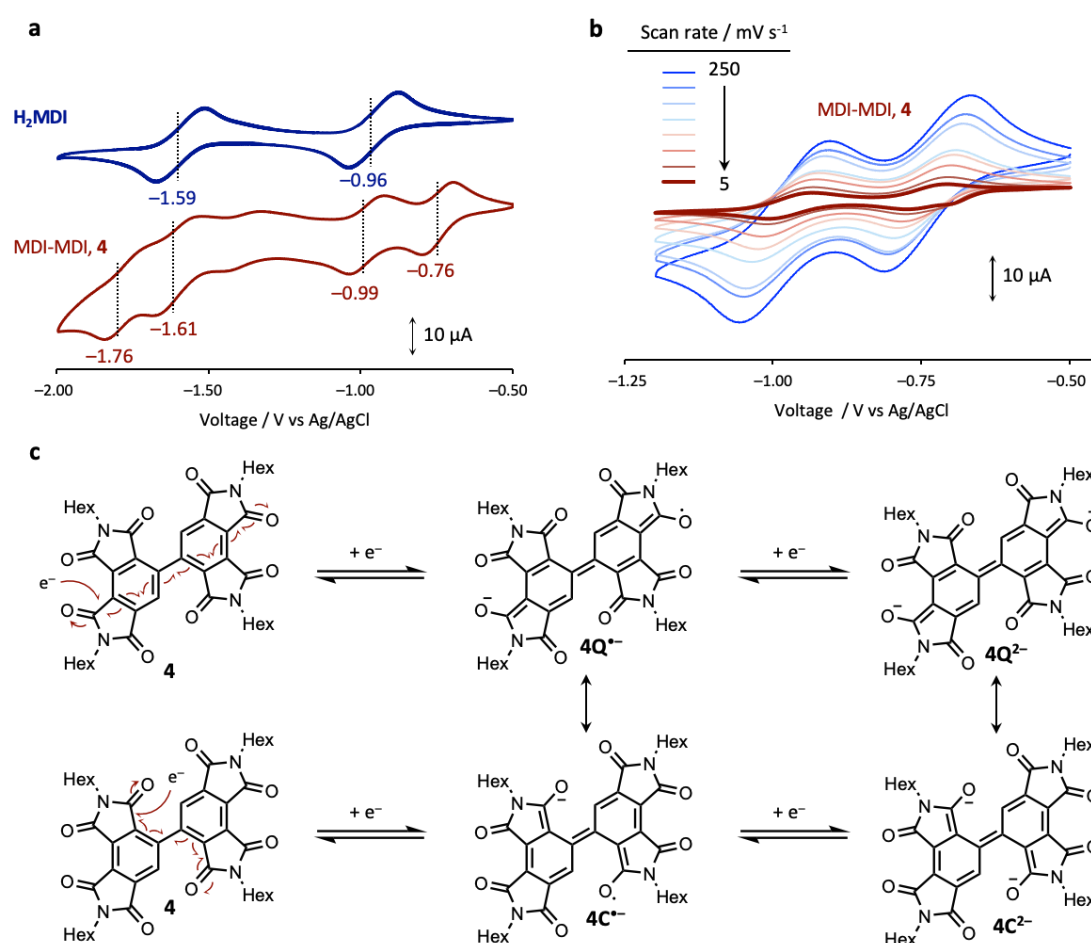
Figure 5.5 (a) Cyclic voltammograms of **H$_2$MDI** compared to MDI-dimer **4** (1 mM solutions prepared using 0.1 M TBAPF$_6$ as the supporting electrolyte in THF measured at a scan rate of 100 mVs^{-1}) with E$_{1/2}$ values indicated; (b) variable scan rate dependent cyclic voltammograms of the first two reductions of **4**. (c) Proposed resonance structures of the mono- and direduced redox states of **4**

DFT calculations for the first and second reduced states of MDI-dimer **4** provide further insight into their structures. The structures of both the first and second reduced states are highly planar where the twist angle between each MDI in the dimer is 40.4° in **4**$^{•-}$ and 31.0° in **4**$^{2-}$ compared to 57.3° for **4** (Figure 5.6). In addition, the carbon-carbon bond between the two MDI units is shorter (1.46 Å for **4**$^{•-}$ and 1.43 Å for **4**$^{2-}$; Figure 5.6a) than in the neutral state (1.48 Å) suggesting an increase in the double

bond character upon reduction. The LUMO of the neutral dimer **4**, along with the SOMO of **4•−** and the HOMO of **4²⁻** highlight electron density along the MDI–MDI C–C bond supporting the argument for extended delocalisation between the MDI units in the dimer. A representative orbital is shown with **4**_LUMO_ in Figure 5.7a (see Section 5.4.6, Figure S5.29 for other orbitals). Bond length analyses of the DFT structures of the reduced states of the dimer (Figure 5.6) suggest a bond lengthening for the four C–C bonds adjacent the central MDI-MDI C–C bond (e.g., from 1.40 Å and 1.41 Å in **4**, to 1.46 Å and 1.43 Å in **4²⁻**) and a bond shortening of the inward facing carbon–carbonyl carbon bonds (from 1.50 Å in **4**, to 1.45 Å in **4²⁻**), with the structures appearing to mirror the bonding highlighted in resonance structures **4C•−** and **4C²⁻**.
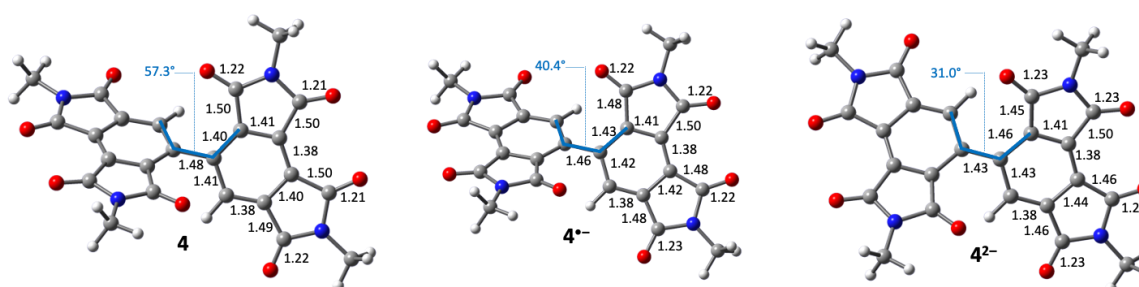
Figure 5.6 DFT optimised ((U)B3LYP-GD3BJ/6-31G(d,p) in CH₂Cl₂) geometry analysis of **4**, **4•−**, and **4²⁻** highlighting torsional angles around the central C–C bond (highlighted in blue) and bond lengths (in black). These bond lengths are mirrored along the symmetry axis.

In order to understand how the structural dynamics of **4** affect its optical properties, UV–vis absorption and fluorescence spectroscopy were conducted in different solvents (Figure 5.7b and c). The neutral dimer **4** absorbs between 300–370 nm, attributed to a π-π* transition, which appears as a shoulder to a higher energy transition below 300 nm in all solvents. The π-π* absorption band is red-shifted with less resolved vibrational features compared to a control compound Br-MDI **3** (its absorption spectrum is shown in Section 5.4.5.1; Figure S5.23) indicating that the conjugation in **4** results in an electronic stabilisation and that the dimer is more dynamic in solution respectively. There are only small shifts to the absorption of **4** in different polarity solvents (Figure 5.7b) and the spectra remain broad and with no vibrational fine structure indicating that solvent polarities don't impact the dynamic motion of the dimer. Unlike its non-emissive monomer **H₂MDI**, MDI-dimer **4** is emissive and emits between 330–600 nm in THF with an emission maximum at 367 nm (Figure 5.7c). This emission peak is red shifted in more polar solvents such as DMF (λ_{max} = 379 nm) due to greater excited state stabilisation in accordance with the Franck-Condon principle. The excitation spectra obtained for these emission peaks are similarly featureless and do not resemble the absorption spectra indicating the possibility of some structural changes in the excited state resulting in the emission. This conclusion is supported by the large Stokes shift[27] observed in both solvents ($\Delta\lambda$ = 61–71 nm).
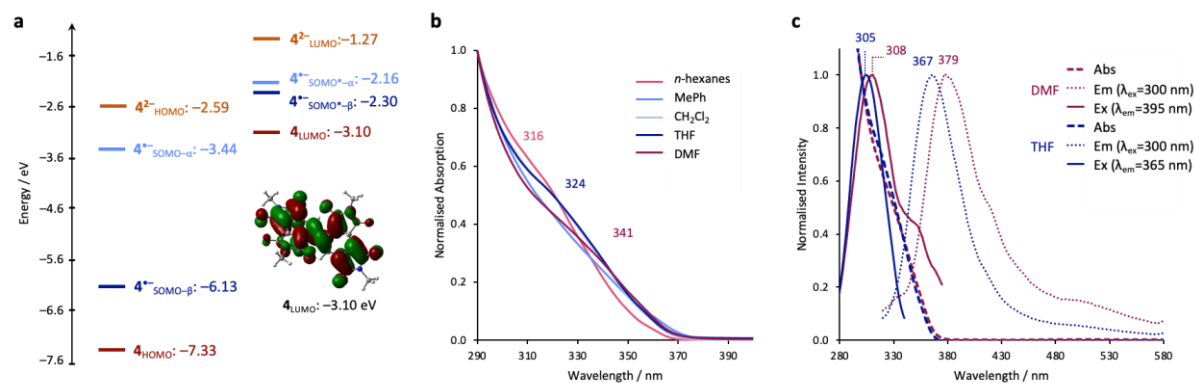
Figure 5.7. (a) Frontier molecular orbital diagram for neutral, radical anion and dianionic states of **4** obtained by DFT calculations ((U)B3LYP-GD3BJ/6-31G(d,p) in CH$_2$Cl$_2$) along with a pictorial representation of the LUMO of **4** highlighting conjugation across the central MDI–MDI C–C bond. (b) Normalised UV–vis absorption (100 µM, 298 K) spectra of **4** in a variety of polar and non-polar solvents and (c) Normalised fluorescence spectra (50 µM, 298 K) of **4** in THF and DMF.

The electronic and optical properties of the reduced states of MDI-dimer **4** were interrogated by DFT analyses of their frontier molecular orbitals (FMOs, Figure 5.7a) and by spectroelectrochemistry (SEC, Figure 5.8) to understand whether predictions by DFT of the formation of **4C$^{\bullet-}$** preferentially over **4Q$^{\bullet-}$** occur experimentally. When the neutral dimer **4** accepts an electron to become **4$^{\bullet-}$**, the new singly occupied molecular orbital (SOMO; here SOMO–α; Figure 5.7a) is actually lower in energy (–3.44 eV) compared to the LUMO of the neutral state (–3.10 eV) highlighting the stability gained from extended conjugation of the charge within the dimeric structure. SEC of **4** (Figure 5.8b) was conducted where the first and second reduced states were formed (by applying a constant voltage of –0.81 V and –1.05 V respectively) in a single experiment and the resulting changes to the absorption of the molecule monitored over time and compared to **H$_2$MDI** (Figure 5.8a) as a control. Notably, even though **4** consists of two individual **H$_2$MDI** units bonded together, the absorption traces of their analogous redox states – i.e., the radical anion and dianion – are vastly different. On its way to the absorption trace presumed to be the radical anion **4$^{\bullet-}$**, the absorption of **4** evolves through two identifiable mixed valence states, labelled as transient (1) with a broad absorption band at λ_{max} = 1257 nm which quickly (over minutes) decays to form transient (2) with an absorption maximum of 844 nm. This second absorption peak (844 nm) decays over time before growing again once the solution has fully converted to the presumed radical anion of **4** (purple line, Figure 5.8b) with a second absorption band with peaks at 567 nm and 604 nm. EPR spectroscopy of this reduced state needs to be performed to confirm its identity. The absorption curve of **4$^{\bullet-}$** decays slowly over time when the more negative potential is applied (–1.05 V) to the orange curve (Figure 5.8b) with an absorption at 557 nm for **4^{2-}**. These absorption spectra are much more red-shifted than the evolution of **H$_2$MDI** to **H$_2$MDI$^{\bullet-}$** which features an absorption at 551 nm, reminiscent of the absorption of the radical anions of linear diimides such as PMDI.[25] The radical anion of **H$_2$MDI** also decays slowly over time when the more negative potential is applied (–1.70 V) to the purple line with absorption at 384 nm and 304 nm. The red-shifted nature of the absorption of the reduced states of **4** compared to **H$_2$MDI** highlight the electronic stabilisation experienced by **4** due to

extended conjugation, similar to the resonance structures **4C**$^{•–}$ and **4C**$^{2–}$. In addition, the highly blue-shifted nature of **H₂MDI**$^{2–}$ highlights the effects of the non-linear nature of MDI which points charged carbonyl oxygen atoms towards each other (Section 5.4.5.2 Figure S5.26).
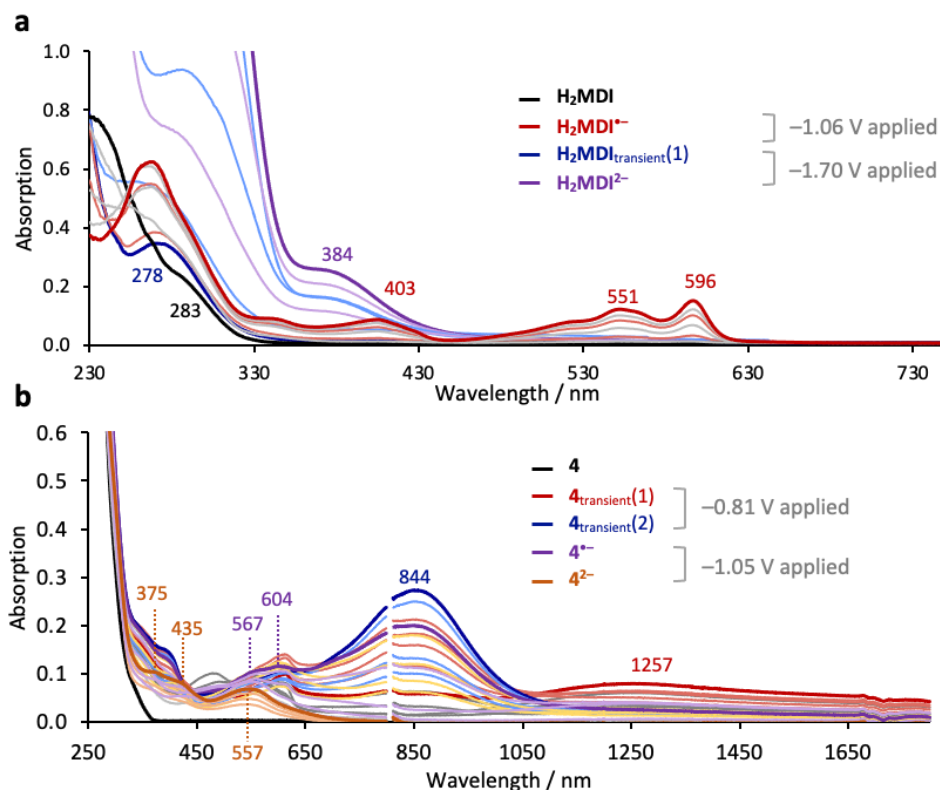
Figure 5.8. Evolution of UV–vis absorption spectra monitored over time of different transient states that are formed as (a) **H₂MDI** (0.5 mM solution in a 0.1 M TBAPF₆ in THF; black line) is reduced to a radical anion (red line) using a constant applied voltage of –1.06 V, then reduced to a dianion (purple line) using a constant applied voltage of –1.70 V and of (b) **4** (0.5 mM solution in a 0.1 M TBAPF₆ in THF; black line) is reduced to a radical anion (purple line) using a constant applied voltage of –0.81 V and then reduced to a dianion (orange line) using a constant applied voltage of –1.05 V. Absorption data at 800 nm has been manually removed where the spectrometer was changing light sources.

Together, the optoelectronic properties analysis of MDI-dimer **4** and its redox states highlight some of the behaviours and properties we might expect to see in a TBF-MDI hybrid helicene **MDI-TBF**, albeit with less rotational freedom than **4**. Therefore, hypotheses have been made that are substantiated by DFT optimised structures of **MDI-TBF** and its reduced states (Figure 5.9b). Firstly, similar to MDI-dimer **4**, it is expected that upon reduction, **MDI-TBF** will adopt bonding which favours the formation of the greatest delocalisation pathway (Figure 5.8a) which conveniently spans the entire helical backbone and the inner *fjord* carbonyl groups. As a result, DFT structures of the reduced states reveal an increase of the through-space distance between the oxygen atoms in the *fjord* (from $d_{OO} = 2.73$ Å in **MDI-TBF** to $d_{OO} = 2.91$ Å in **MDI-TBF**$^{2–}$) and an increase of the average torsional angle along the inner helix (from $\theta = 17.6°$ in **MDI-TBF** to $\theta = 20.1°$ in **MDI-TBF**$^{2–}$). The increasing repulsion between those inner *fjord* carbonyl oxygens upon reduction is expected to hamper the interconversion *M*– and *P*– enantiomers of **MDI-TBF** and therefore lead to an increased barrier, $\Delta G^{‡}$. The interconversion for the neutral state of **MDI-TBF** has been predicted by DFT calculations to be 20.7 kcal mol^{-1} which is

193

similar to the configurational stability of [5]helicene ($\Delta G^{\ddagger}$ = 24.1 kcal mol^{-1} at 298 K in solution and an enantioenriched sample will form a racemic mixture over 29 h under ambient conditions).[28,29] Here, we envision that the configurational stability of **MDI-TBF** can therefore be controlled by its different redox states. As a result, **MDI-TBF** will be able to act as a chiroptical enantiomeric lock that is governed by its charge.
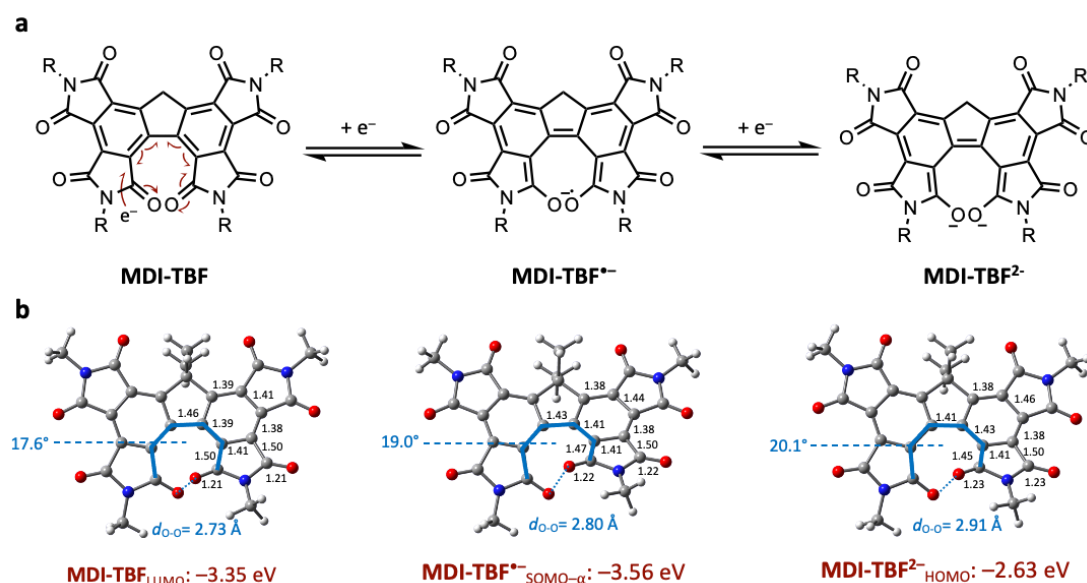
Figure 5.9. (a) Proposed delocalisation pathway for various redox states of **MDI-TBF** and (b) DFT (B3LYP(GD3BJ)/6-31G(d,p) in CH$_2$Cl$_2$) optimised geometry analysis of **MDI-TBF**, **MDI-TBF**$^{\bullet-}$, and **MDI-TBF**$^{2-}$ highlighting average torsional angles about the inner *fjord* (highlighted in blue) and bond lengths (highlighted in black). The bond lengths are mirrored along the symmetry axis.

5.3 CONCLUSIONS

This Chapter has discussed the synthetic efforts to isolate a TBF appended with an acridine moiety **Acr-OH**. The peaks in the ^{1}H NMR spectrum of the molecule are broad and poorly resolved revealing a propensity for **Acr-OH** to aggregate in CDCl$_3$. Its X-ray crystal structure highlights the non-planarity of the helical backbone. Unlike **A-OH** (discussed in Chapter 2) where an intramolecular CH···O interaction between head-group substituents is most remarkable, in **Acr-OH** a strong intermolecular hydrogen bond exists between a nitrogen atom on the acridine in one molecule with a hydroxy group of a second. The optical properties of the system were investigated by UV–vis and fluorescence spectroscopy in a single relatively non-polar solvent system (THF) to uncover an emission band that is broad and featureless and displays a notably large Stokes shift ($\Delta\lambda$ = 93 nm). However, upon titrating in a more polar solvent H$_2$O, this emission experiences a blue shift and exhibits vibrational fine structure. Together, these optical results suggest that **Acr-OH** exists as a dimer in its ground state in relatively low polarity solvents (such as CDCl$_3$ and THF), presumably held together by intermolecular H-bonds, which when excited, appear to mimic excimeric emission. H$_2$O competes for the H-bonding sites within **Acr-OH**, to break apart these dimers revealing its true monomeric emissive behaviour.

Impressively, these properties have been introduced to the system by the simple embedding of a single nitrogen atom to the TBF structure to drastically affect its optical behaviour in solvents with different polarities.

In a separate example, synthetic efforts to introduce multiple nitrogen and oxygen atoms into the backbone of a TBF [5]helicene, **MDI-TBF** are discussed, including the challenges encountered in its synthesis. Although, the desired helical product has not yet been achieved, the optoelectronic properties of an MDI-dimer **4** were studied instead. Structurally, this dimer can exist in two conformations. VT NMR spectroscopic analyses hint at the dimer existing in its sterically less hindered conformer where an intramolecular aromatic-carbonyl CH···O interaction appears to be stabilising. Its cyclic voltammogram highlights the ability of **4** to be able to accept two electrons reversibly and with a smaller energy barrier than its monomer **H₂MDI** as a result of extended conjugation between both MDI units. SEC and DFT structural analyses help to confirm that upon reduction the C–C bond that bridges the two individual units gains double bond character and leads to a planarisation of the system. Together, these results suggest that in the reduced states of **MDI-TBF**, the inner carbonyls are likely to hold these extra electrons, leading to a largening of the helical *fjord* atom-atom distances and therefore greater configurational stability. Therefore, it is suggested that **MDI-TBF** could act as a redox-controlled chirality lock, where its configurational stability is locked upon reduction. In both examples, the advantages of including heteroatoms into the TBF backbone are clear resulting in multifunctional and stimuli responsive systems with relevance in a range of applications.

5.4 SUPPLEMENTARY INFORMATION

5.4.1 GENERAL MATERIALS AND METHODS

Materials. Unless stated, all chemicals and reagents were purchased from commercial suppliers (Sigma Aldrich, Fisher Scientific, Alfa Aesar and Fluorochem) and used without further purification. Before use, *n*-BuLi was titrated as described by Burchat, A. F et al.[30] to obtain its active concentration. Anhydrous solvents were obtained from a neutral alumina Solvent Purification System under nitrogen and stored over activated (>250 °C at 0.01 mbar overnight) 3 Å molecular sieves under a dry Ar atmosphere. Solvents and solutions required for air-sensitive manipulations were degassed thoroughly using a minimum of three freeze–pump–thaw cycles and the flask back-filled under an Ar atmosphere.

Product confirmation. Analytical thin-layer chromatography (TLC) was performed on aluminium-backed silica gel plates and visualised under UV irradiation (254 and 365 nm). Automated flash column chromatography was performed using a Teledyne ISCO Combiflash NextGen 300+ with detectors using broad range UV–vis (200-800 nm) and evaporative light scattering (ELS) under N_2 gas and pre-filled Redisep™ Gold cartridges (normal phase: SiO_2). High-resolution mass spectra were measured on

a Bruker compact QTOF Atmospheric Pressure Ionisation Time of Flight instrument using an ESI or APCI source. Nuclear magnetic resonance (NMR) spectra were recorded on a JEOL ECS400D spectrometer (working frequencies of 400 MHz and 101 MHz for ^{1}H and ^{13}C nuclei) or a Bruker AVIIIHD500 (working frequencies of 500 MHz and 126 MHz for ^{1}H and ^{13}C nuclei). Chemical shifts (δ) are reported in parts per million (ppm) relative to the signals corresponding to residual non-deuterated solvents (CDCl$_3$: δ_H 7.26 ppm, δ_c 77.23 ppm). Coupling constants (J) are reported in Hertz (Hz) and ^{1}H multiplicities are reported in accordance with the following convention: s = singlet, d = doublet, t = triplet, q = quadruplet, p = pentet, m = multiplet. Assignment of ^{1}H and ^{13}C NMR signals were accomplished with the aid of two-dimensional ^{1}H–^{1}H COSY, ^{1}H–^{13}C HSQC and ^{1}H–^{13}C HMBC NMR spectroscopies. NMR spectra were processed using MestReNova software, Version 14.

Sample analysis. Single crystal X-ray diffraction data were collected on a single-crystal Oxford Diffraction SuperNova with dual Mo and Cu sources. The crystal was kept at 110.00(10) K during data collection. Using Olex2,[31] the structure was solved with the SHELXT[32] structure solution program using Intrinsic Phasing and refined with the SHELXL[33] refinement package using Least Squares minimisation. Hirschfeld analysis of crystal structures was performed using CrystalExplorer 17.5. Absorption spectra were recorded on a Shimadzu UV-2401 PC spectrophotometer or on an Agilent Technologies Cary 5000 UV–vis–NIR spectrophotometer using standard 10 mm path length quartz cuvettes at room temperature. Solution-state fluorescence spectroscopy was carried out on a Hitachi F-4500 fluorimeter equipped with a 150 W Xe lamp using standard photoluminescence quartz cuvettes. Samples for solution-state spectroscopy had an optical density (O.D.) <0.1 in anhydrous and degassed solvent to allow for the measurements of fluorescence spectroscopy. Cyclic voltammetry (CV) and square-wave voltammetry (SWQV) were carried out at room temperature on Ar-purged sample solutions in anhydrous THF using a Gamry Reference 3000 Potentiostat interfaced to a PC. Tetrabutylammonium hexafluorophosphate (TBAPF$_6$; 0.1 M) was recrystallized from hot EtOH and used as the supporting electrolyte. All solution-state electrochemical experiments were performed using a glassy carbon working electrode (BASi; 0.071 cm^2). The electrode surface was polished routinely with 0.05 μm alumina–water slurry on a felt surface immediately before each use. A Pt wire was used as the counter electrode and the reference electrode was an Ag/AgCl aqueous electrode stored routinely in a 3 M KCl aqueous solution. Spectroelectrochemistry (SEC) experiments were performed at room temperature using an optically transparent thin-layer electrochemical (OTTLE) cell (path length approx. 0.2 mm with two CaF$_2$ windows separated by PTFE spacers) fitted with a Pt wire mesh working electrode, Pt wire counter electrode and an Ag wire pseudo-reference electrode. All SEC samples were prepared as Ar-purged solutions in anhydrous THF containing TBAPF$_6$ (0.1 M) as the supporting electrolyte and analysed under a constant applied voltage. Density functional theory (DFT) calculations were prepared on GaussView 6.0 and submitted to the University of York Viking High performance Computing cluster and run on Gaussian 16 using Becke's three-parameter exchange functional with the

gradient-corrected correlation formula of Lee, Yang and Parr (B3LYP)[34,35] paired with the split valence double-zeta 6-31G(d,p) basis set, PCM solvation model (CH_2Cl_2) and dispersion corrections (D3BJ)[36] unless stated otherwise.

5.4.2 SYNTHETIC DETAILS
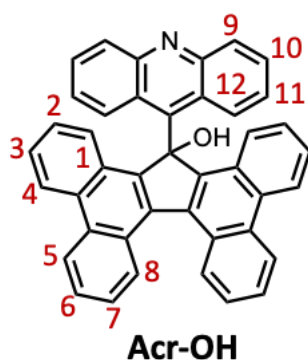
Acr-OH: A solution of 9-bromoacridine (96.7 mg, 0.375 mmol, 1.1 equiv.) in anhydrous and degassed THF (5 mL) under an Ar atmosphere was cooled to –78 °C and *n*-BuLi (1.6 M in *n*-hexane, 0.25 mL, 1.1 equiv.) was added slowly to eventually afford a bright yellow coloured solution indicative of Li insertion. The solution was stirred at –78 °C under Ar for 45 minutes before a solution containing **TBF=O** (0.134 g, 0.351 mmol, 1.0 equiv.) in dry and degassed THF (15 mL) under Ar was slowly transferred dropwise to the reaction flask. The reaction mixture was allowed to warm up to room temperature, stirred overnight and monitored by TLC (20% EtOAc/*n*-hexanes). Once complete, water (40 mL) was added slowly to quench the reaction followed by saturated aq. NH_4Cl (10 mL) and the reaction mixture was extracted into EtOAc (3 x 50 mL). The combined organic layers were dried over $MgSO_4$ and concentrated. The desired product **Acr-OH** (12.9 mg, 0.023 mmol, 6%), was isolated by automated column chromatography (SiO_2: 5% EtOAc in *n*-hexanes) as a yellow solid.

¹H NMR (CDCl₃, 400 MHz, 298 K): δ_H 10.65 (d, J = 9.3 Hz, 1H[12]), 8.80 (d, J = 8.4 Hz, 2H[5]), 8.74–8.67 (m, 4H[4,8]), 8.39 (d, J = 8.8 Hz, 1H[9]), 7.98–7.87 (m, 3H[9',10,12']), 7.87–7.76 (m, 5H[1,7,11]), 7.75–7.67 (m, 2H[6]), 7.48 (t, J = 7.7 Hz, 2H[3]), 7.23–7.12 (m, 3H[2,10']), 6.51 (t, J = 8.0 Hz, 1H[11']), 4.34 (br, OH). **APCI–HRMS** (*v*e+, CH_2Cl_2) calculated for $C_{43}H_{26}NO$: *m*/z = 560.2009 [*M*+H]⁺; found 560.2036 [*M*+H]⁺ and 542.1924 [*M*-H₂O]⁺

Bromination of tetratmethylbenzene (TMB):
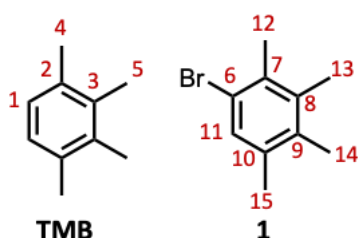
Method 1[22]: A flame-dried two-necked round bottomed flask equipped with a stirrer bar was charged with **TMB** (5.60 mL, 37.5 mmol, 1.0 equiv.) and dry DMF (25 mL) under a positive flow of N₂ gas. The flask was then wrapped in aluminium foil and the solution was cooled to 0 °C in an ice bath. A separately prepared solution containing Br₂ (1.90 mL, 37.1 mmol, 1.0 equiv.) in DMF (7.5 mL) was cooled to 0 °C and added dropwise to the stirring mixture. The reaction mixture was then allowed to warm to rt and stirred for additional 20 h. [*Safety note: Trace Br₂ on contaminated equipment (e.g., vials, pipettes, needles and syringes) was quenched with saturated aq. Na₂S₂O₃ and fumes allowed to dissipate in a well-ventilated fume hood prior to disposal*]. The reaction mixture was cooled to 0 °C

and saturated aq. $Na_2S_2O_3$ (10 mL) was added to quench any unreacted Br_2 until the orange colour dissipated and the mixture formed a white suspension. The mixture was then diluted with H_2O (10 mL) and extracted with *n*-hexanes (30 mL). The aqueous layer was washed with *n*-hexanes (2 x 30 mL). The combined organic layers were washed with H_2O (15 mL), dried (MgSO$_4$), filtered and concentrated to yield a yellow oil. ^{1}H NMR analyses revealed the isolated oil (7.18 g) to be a 50% pure mixture of the desired product **1** (4.40 g, 20.7 mmol, 52%) with an unreacted **TMB** impurity.

Method 2[23]: A single-necked round bottomed flask with a stirrer bar was charged with glacial AcOH (300 mL), **TMB** (7.2 mL, 48.3 mmol, 1.0 equiv.), anhydrous $ZnCl_2$ (7.19 g, 52.5 mmol, 1.1 equiv.) and BTMABr$_3$ (18.88 g, 48.4 mmol, 1.0 equiv.). The orange mixture was left to stir under N_2 for 20 h until the reaction mixture formed a yellow-white suspension. The mixture was diluted with H_2O (30 mL) and quenched with saturated aq. $Na_2S_2O_3$ (25 mL) until the orange colour faded. The mixture was extracted with *n*-hexanes (4 x 150 mL) before the combined organic layers were dried (MgSO$_4$), filtered and concentrated. ^{1}H NMR analysis revealed the oil (9.13 g) to be an 87% pure mixture of the desired product **1** (8.33 g, 39.1 mmol, 81%) with an unreacted **TMB** impurity.

^{1}H NMR (CDCl$_3$, 400 MHz, 298 K): δ_H 7.31 (s, 1H^{11}), 6.99 (s, 2H^1), 2.45 (s, 3H^{12}), 2.35 (s, 6H$^{4/5}$), 2.31 (s, 3H^{13}), 2.30 (s, 3H^{15}), 2.28 (s, 6H$^{5/4}$), 2.21 (s, 3H^{14}); **^{13}C NMR** (CDCl$_3$, 101 MHz, 298 K): δ_C 136.9$^{10/9}$, 135.5$^{7/6}$, 134.3$^{9/10}$, 133.2^8, 131.0^{11}, 122.3$^{6/7}$, 20.5^{15}, 20.2^{12}, 17.4^{13}, 16.1^{14}. **APCI–HRMS** (*ve*+, *n*-hexanes) calculated for C$_{10}$H$_{13}$Br: *m/z* = 213.0273 [*M*+H]$^+$, found 213.0272 [*M*+H]$^+$
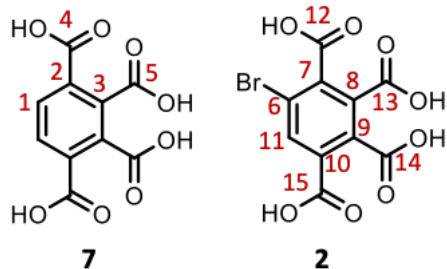
2: A two-necked round bottomed flask equipped with a stirrer bar and a condenser was charged with the 1:1.1 mixture of **1** and **TMB** (2.05 g, 11.8 mmol, 1.0 equiv.), *t*-BuOH (15 mL) and H_2O (15 mL). Following KMnO$_4$ (9.63 g, 60.9 mmol, > 5 equiv.) addition, the open necks were sealed with glass stoppers and the reaction mixture was refluxed gently at 90 °C with vigorous stirring until the purple colour of the solution faded, indicating complete consumption of KMnO$_4$. The reaction flask was removed from the heating and more KMnO$_4$ (9.54 g, 60.4 mmol, > 5 equiv.) was slowly added. The reaction mixture was refluxed gently with vigorous stirring for 2 d. Before cooling, the reaction was slowly quenched with EtOH (2 mL) until the purple colour faded. The mixture was then cooled, filtered, washed with H_2O and the filtrate concentrated. The filtrate was dried on high vacuum line (~3.5 mbar, 60 °C) overnight. The material was then redissolved in the minimum amount of water (ca. 2–5 mL) before conc. HCl (ca. 1 mL) was added dropwise until pH = 1. After the solvents had been removed by rotary evaporation, the crude material was left on a high vacuum line overnight (3.5 mbar, 60 °C). The solid was then redissolved in acetone and KCl salt was filtered off the mixture. The filtrate was concentrated to yield the desired product as a cream solid, which was dried on high vacuum before any characterisation. ^{1}H NMR

analysis revealed the isolated solid (2.17 g) to be a 48% pure mixture of the desired product **2** (1.18 g, 3.54 mmol, 60%) and 1,2,3,4-teracarboxybenzoic acid **7** (0.990 g, 3.90 mmol, 66%) by-product.

^{1}H NMR (Me$_2$CO, 400 MHz, 298 K): δ_H 8.29 (s, 1H[11]), 8.08 (s, 2H[1]). **^{13}C NMR** (Me$_2$CO, 101 MHz, 298 K): δ_C 167.9[4], 167.4[13], 166.8[5], 166.8[14], 166.2[12], 165.4[15], 140.0[8], 136.7[9], 135.5[7], 135.2[3], 134.1[2], 133.0[10], 133.0[6], 131.4[1], 120.6[11]
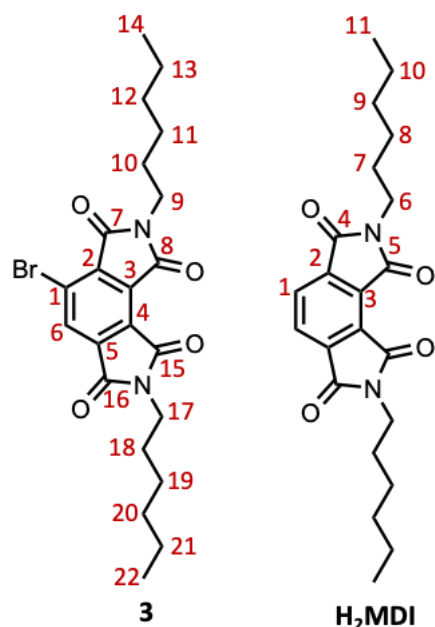
3: A flame-dried two-necked round bottomed flask with a stirrer bar and a condenser was charged with glacial AcOH (ca. 36 mL), before the 1:1.1 mixture of **2** and **7** (1.06 g, 3.62 mmol, 1.0 equiv.) was added under N$_2$ with stirring and heating at 120 °C. Upon complete dissolution, hexylamine (950 μL, 7.20 mmol, 2.0 equiv.) was added *via* micropipette and the reaction allowed to stir under N$_2$ for 16 h. More hexylamine (95 μL, 0.720 mmol, 0.2 equiv.) was added *via* micropipette push the reaction to completion and left to stir at 120 °C for 5 h. H$_2$O (ca. 35 mL) was added and a white-brown solid was collected *via* vacuum filtration. To maximise product yield, the solid was collected off the filter by dissolving in CH$_2$Cl$_2$ (ca. 50 mL) into a new receiving flask. The solution was subsequently dried (MgSO$_4$), filtered and concentrated to dryness by rotary evaporation to yield a dark-brown solid. The solid was subjected to automated flash column chromatography (SiO$_2$: 0–70% CH$_2$Cl$_2$ in *n*-hexanes) to yield BrMDI **3** as a white solid (138 mg, 0.298 mmol, 17%) and **H$_2$MDI** as a white solid (39 mg, 0.1 mmol, 5.2 %).

3: ^{1}H NMR (CDCl$_3$, 400 MHz, 298 K): δ_H 8.28 (s, 1H[6]), 3.77–3.71 (m, 4H[9,17]), 1.74–1.64 (m, 4H[10,18]), 1.38–1.23 (m, 12H[11,12,13,19,20,21]), 0.90–0.84 (m, 6H[14, 22]). **^{13}C NMR** (CDCl$_3$, 101 MHz, 298 K): δ_C 165.5[16], 165.0[7/8/15], 163.7[7/8/15], 162.8[7/8/15], 138.2[3/4], 134.2[1], 133.2[6], 130.4[3/4], 127.1[2], 124.5[5], 39.1[9/17], 39.1[9/17], 31.4[12,20], 28.3[10/18], 28.3[10/18], 26.6[11,20], 22.6[13,21], 14.1[14,22]. **APCI–HRMS** (*v*e+, CH$_2$Cl$_2$) calculated for C$_{22}$H$_{27}$BrN$_2$O$_4$: *m/z* = 463.1227 [*M*+H]$^+$, found 463.1211 [*M*+H]$^+$.

H$_2$MDI: ^{1}H NMR (CDCl$_3$, 400 MHz, 298 K): δ_H 8.18 (s, 2H[1]), 3.75 (t, *J* = 8 Hz, 4H[6]), 1.71 (q, *J* = 8 Hz, 4H[7]), 1.38–1.24 (m, 12H[8,9,10]), 0.91–0.84 (m, 6H[11]). **APCI–HRMS** (*v*e+, CH$_2$Cl$_2$) calculated for C$_{22}$H$_{28}$N$_2$O$_4$: *m/z* = 385.2127 [*M*+H]$^+$, found 385.2099 [*M*+H]$^+$. Spectroscopic data matched that reported in the literature.[24]

4: *Copper bronze activation*: Copper bronze (9.98 g) was treated with an I$_2$ solution in acetone (2.22 g in 110 mL) and stirred for 15 min. The solid was collected by vacuum filtration and rinsed with acetone a few times, before stirring in conc. HCl solution in acetone (1:1 v/v) for 15 min.

199
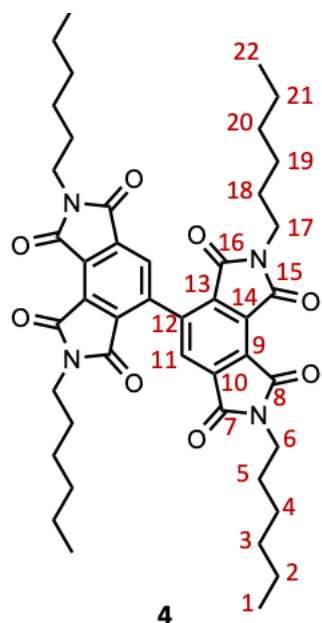
A flame-dried two-necked round bottomed flask equipped with a magnetic stir bar and a condenser was charged with **3** (90.2 mg, 0.195 mmol, 1.0 equiv.) and activated copper bronze (92.4 mg, 1.46 mmol, 7.46 equiv.) and cycled three times with Ar. Dry NMP (10 mL) was added *via* syringe and the reaction was allowed to stir at 150 °C for 3 h. The mixture was cooled to rt, before EtOAc (35 mL) and brine (30 mL) were added, and the layers separated. The organic layer was washed with water (3 x 30 mL) to remove a white precipitate and the aqueous layer was washed further with EtOAc (3 x 30 mL). The combined organic layers were dried (Na$_2$SO$_4$), filtered and concentrated to yield a brown solid. The crude material was subjected to automated column chromatography (SiO$_2$: 0–30 % CH$_2$Cl$_2$ in *n*-hexanes) to yield the product **4** as a light-brown solid (32.1 mg, 0.042 mmol, 43%).

^{1}H NMR (CDCl$_3$, 400 MHz, 298 K): δ_H 8.09 (s, 2H[11]), 3.78 (t, *J* = 7.24 Hz, 4H[6]), 3.65 (t, *J* = 7.24 Hz, 4H[17]), 1.76–1.65 (m, 4H[5]), 1.65–1.57 (m, 4H[18]), 1.32 (m, 24H[2,3,4,19,20,21]), 0.92–0.81 (m, 12H[1,22]). **^{13}C NMR** (CDCl$_3$, 101 MHz, 298 K): δ_C 166.4[16/15], 166.1[7], 163.8[8], 163.6[15/16], 137.8[9/10/12/13], 137.5[9/10/12/13], 135.3[9/10/12/13], 128.9[11], 128.7[9/10/12/13], 39.1[6], 38.9[17], 31.4[2/21], 31.4[2/21], 28.4[5], 28.3[18], 26.6[4], 26.5[19], 22.6[3/20], 22.6[3/20], 14.2[1/22], 14.1[1/22]. **APCI–HRMS** (*v*e+, CH$_2$Cl$_2$) calculated for C$_{44}$H$_{54}$N$_4$O$_8$: *m/z* = 767.4014 [*M*+H]$^+$, found 767.3989 [*M*+H]$^+$.
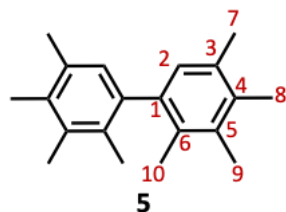
5: A flame-dried three-necked round bottomed flask was charged the 1:1.1 mixture of **1** and **TMB** (0.405 g, 1.16 mmol, 1 equiv.) under an N$_2$ atomosphere. The flask was cooled to –96 °C in an acetone/liquid N$_2$ bath before dry THF (5 mL) was added. *n*-BuLi (2.44 M in *n*-hexanes, 0.53 mL, 1.1 equiv.) was added dropwise over 5 min, after which a yellow suspension formed and the mixture was allowed to stir for 1 h at –96 °C. Anhydrous CuCl$_2$ was added (0.176 g, 1.29 mmol, 1.1 equiv.) in one portion and the reaction mixture was further stirred for 20 min at –96 °C. The mixture was exposed to air and stirred for 15 min. 1 M HCl solution (ca. 10 mL) was added, and the mixture was stirred for further 5–7 min before *n*-hexanes (25 mL) and H$_2$O (15 mL) were added and the layers separated. The aqueous layer was subsequently washed with *n*-hexanes (25 mL) and CH$_2$Cl$_2$ (15 mL). The combined organic layers were washed once more with H$_2$O (25 mL), dried (Na$_2$SO$_4$), filtered and concentrated to leave a yellow oil. The crude material was subjected to automated flash column chromatography (SiO$_2$: 0–10% CH$_2$Cl$_2$ in *n*-hexanes) to yield a white solid (0.029 g, 0.108 mmol, 18%).

^{1}H NMR (CDCl$_3$, 400 MHz, 298 K): δ_H 7.09 (s, 2H[2]), 2.33–2.28 (m, 18H[7/8/9/10]), 2.02 (s, 6H[7/8/9/10]). **APCI–HRMS** (*v*e+, CH$_2$Cl$_2$) calculated for C$_{20}$H$_{26}$: *m/z* = 267.2107 [*M*+H]$^+$, found 267.2111 [*M*+H]$^+$. Matched spectroscopic data in the literature.[22]

5.4.3 NMR Spectra
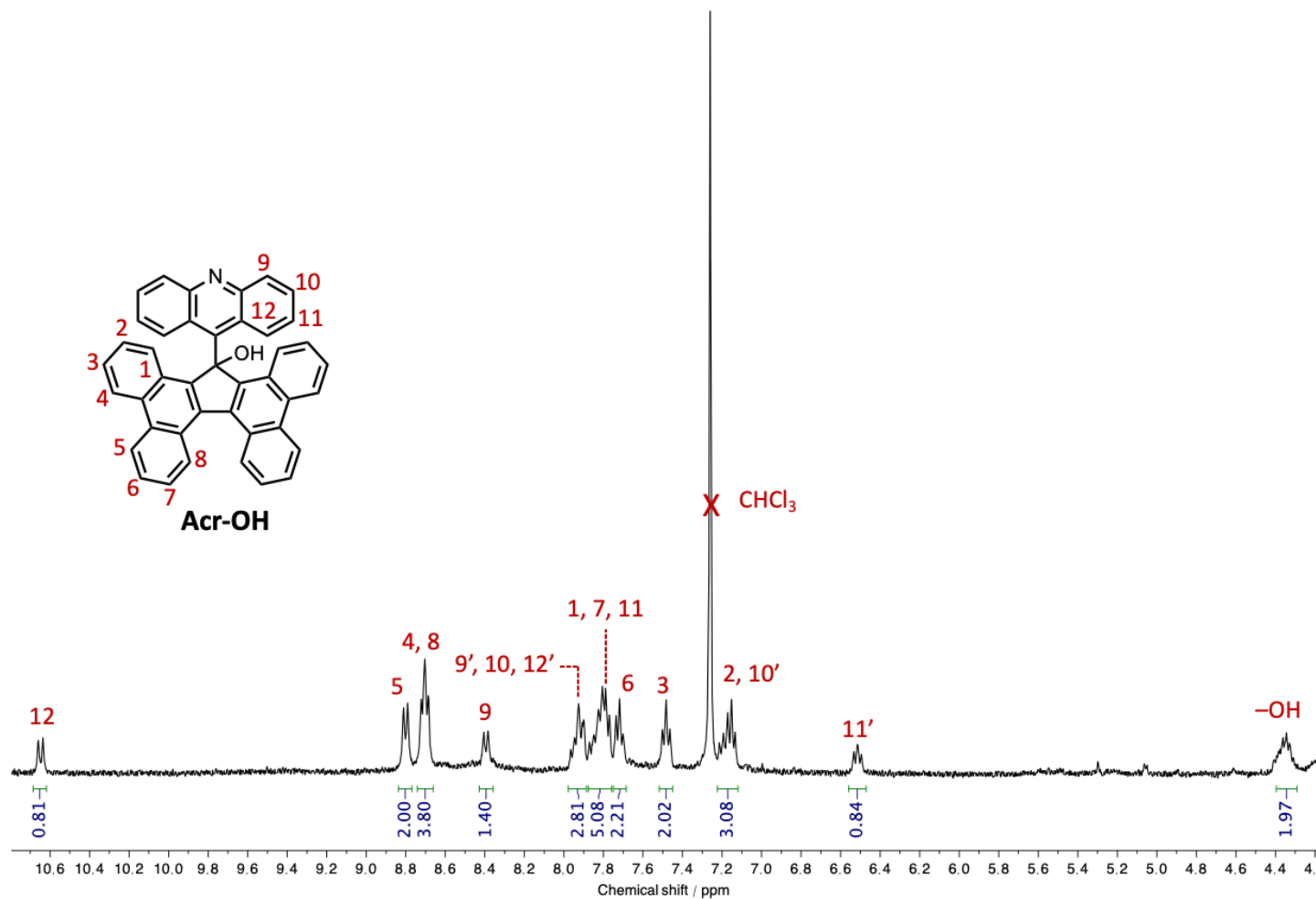
Figure S5.1 Partial ^{1}H NMR (CDCl$_3$, 400 MHz, 298K) spectrum of **Acr-OH**
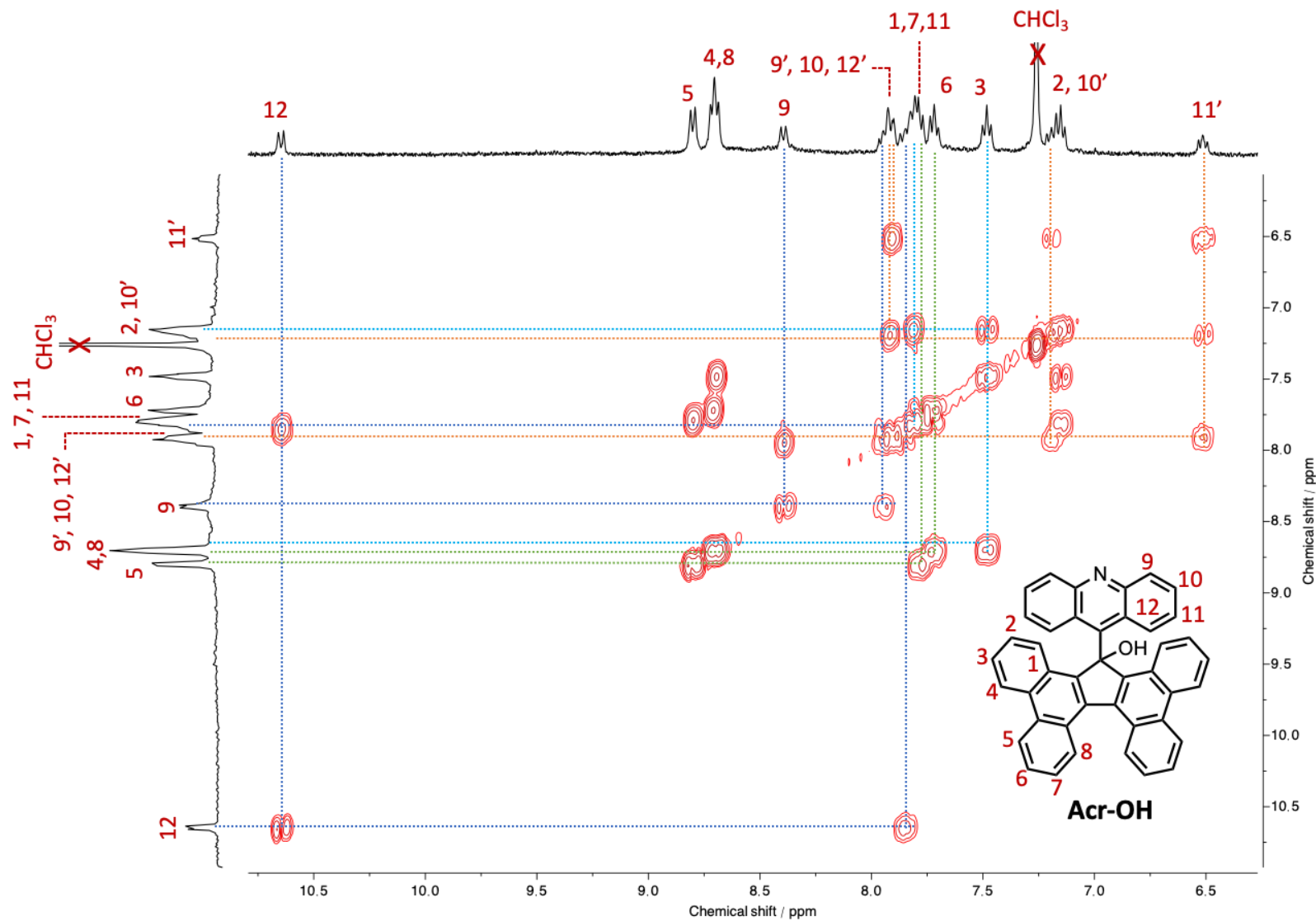
Figure S5.2 Annotated ^{1}H-^{1}H COSY NMR (CDCl$_3$, 400 MHz, 298K) spectrum of **Acr-OH**
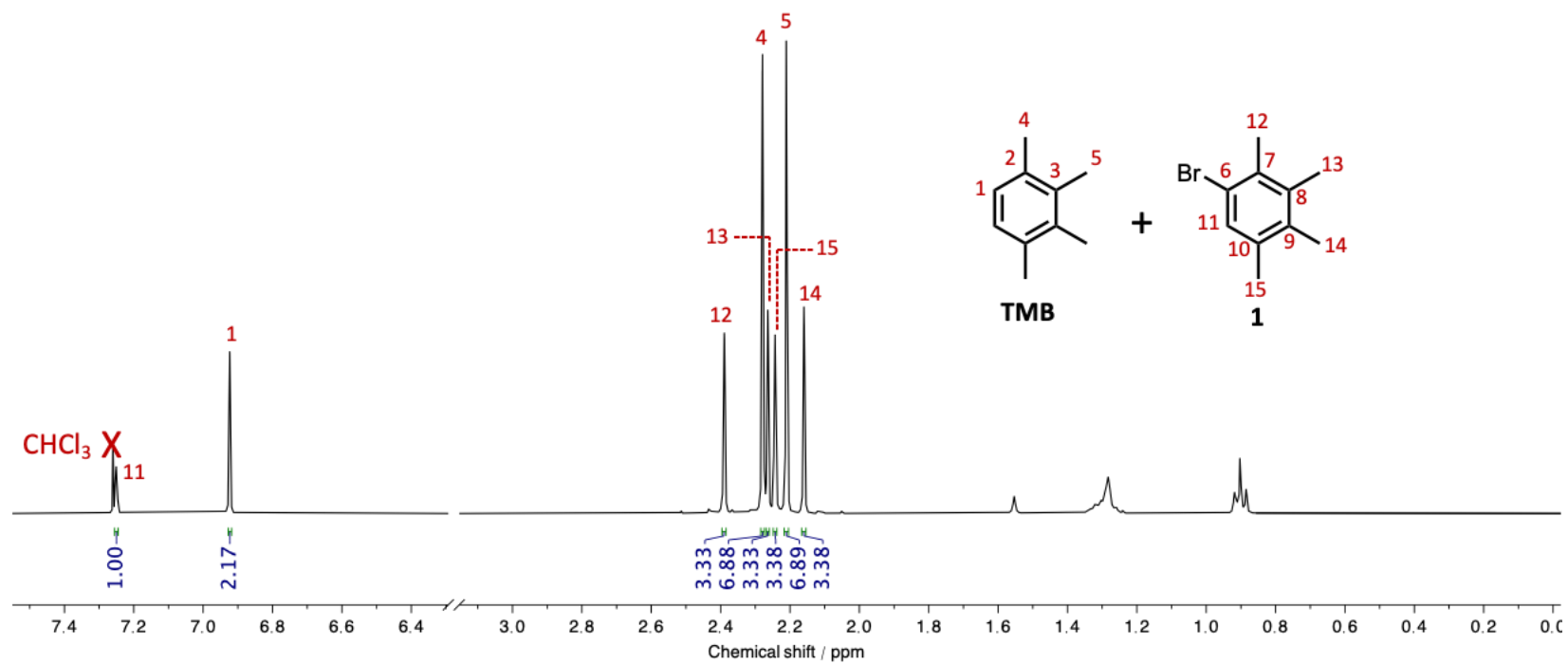
Figure S5.3 ^{1}H NMR (CDCl$_3$, 400 MHz, 298K) spectrum of a 1:1.1 mixture of **TMB** and **1**
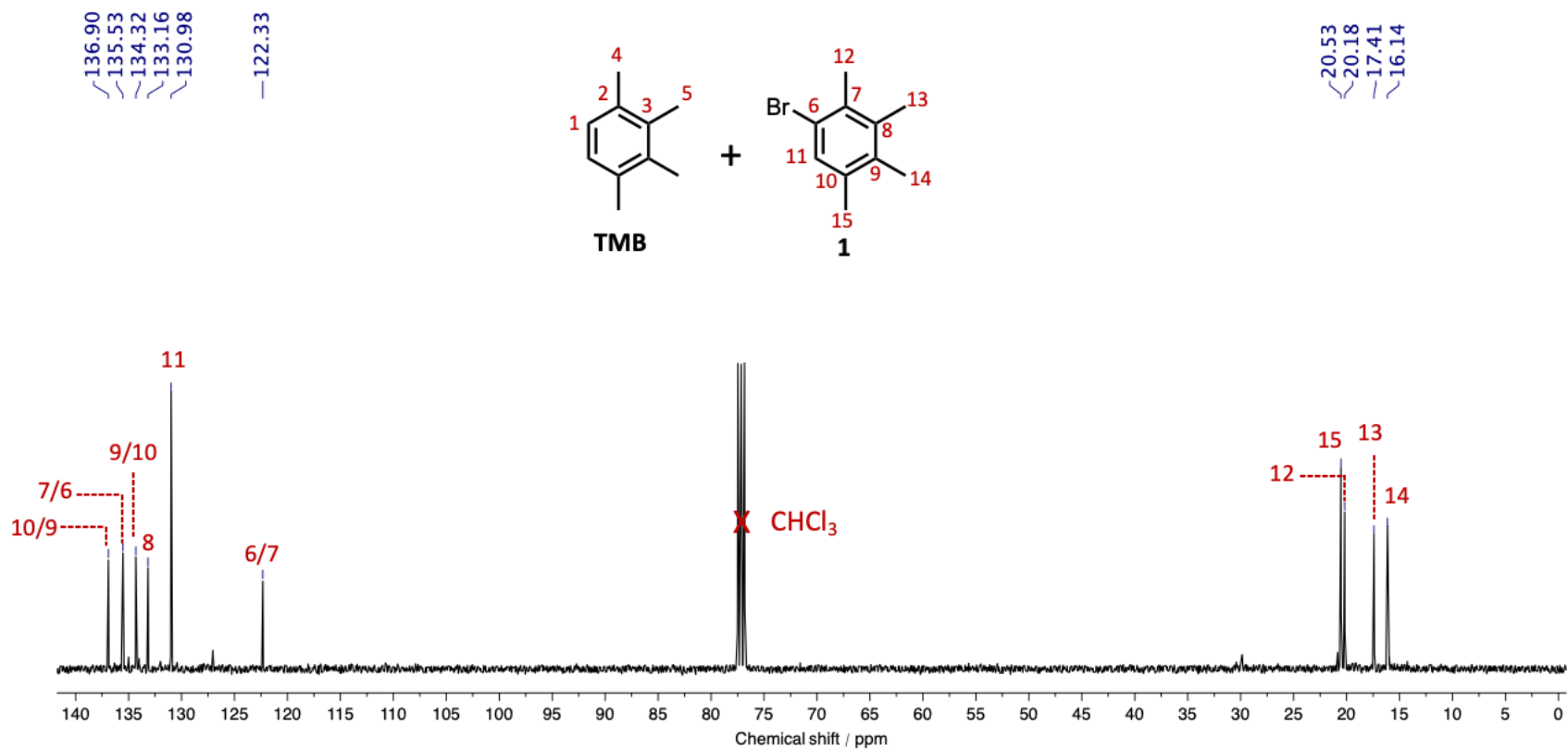
Figure S5.4 ^{13}C NMR (CDCl$_3$, 101 MHz, 298K) spectrum of a 13:87 mixture of **TMB** and **1**
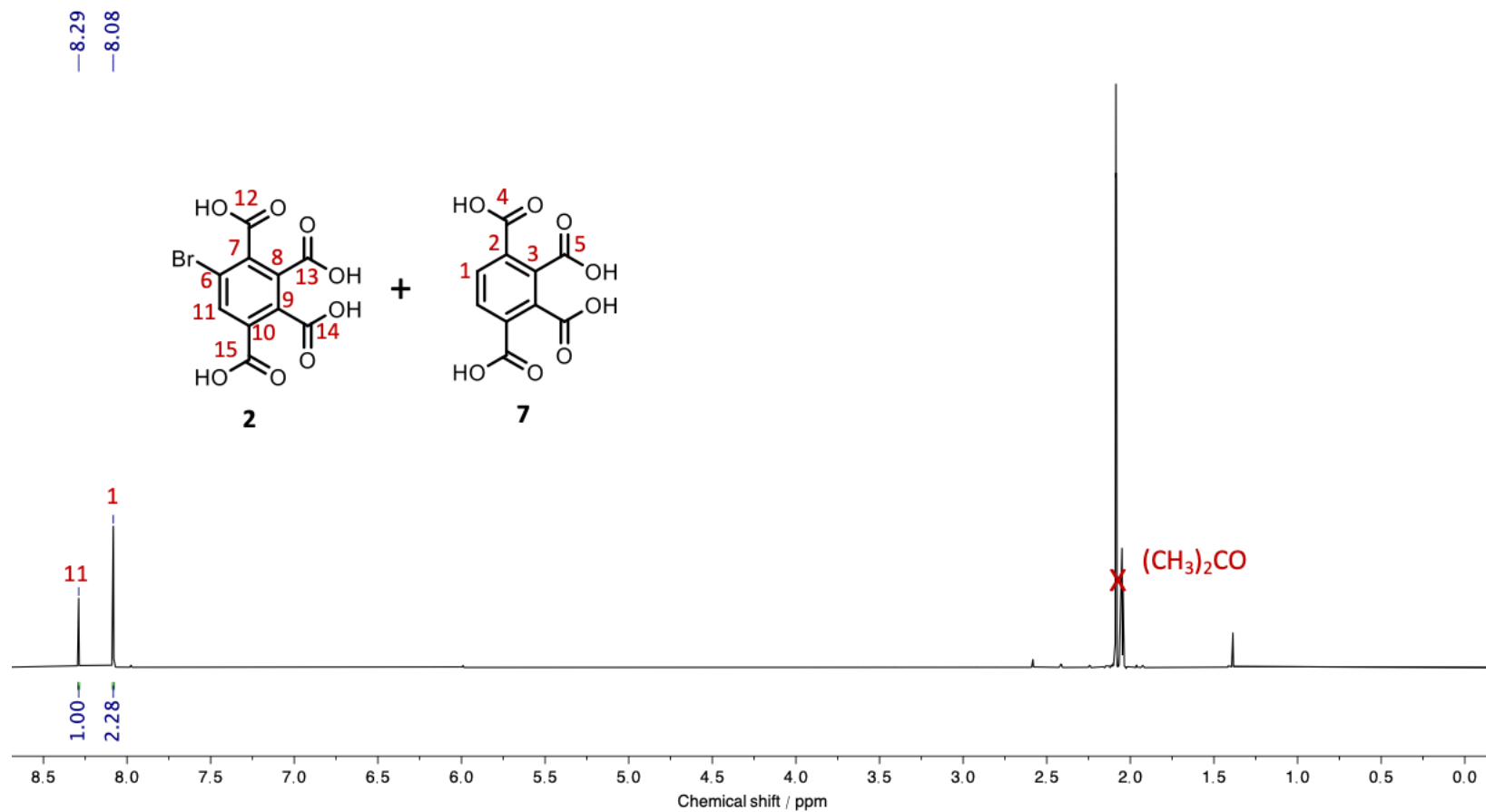
Figure S5.5 ^{1}H NMR (CDCl$_3$, 400 MHz, 298K) spectrum of a 1:1.1 mixture of **2** and **7**
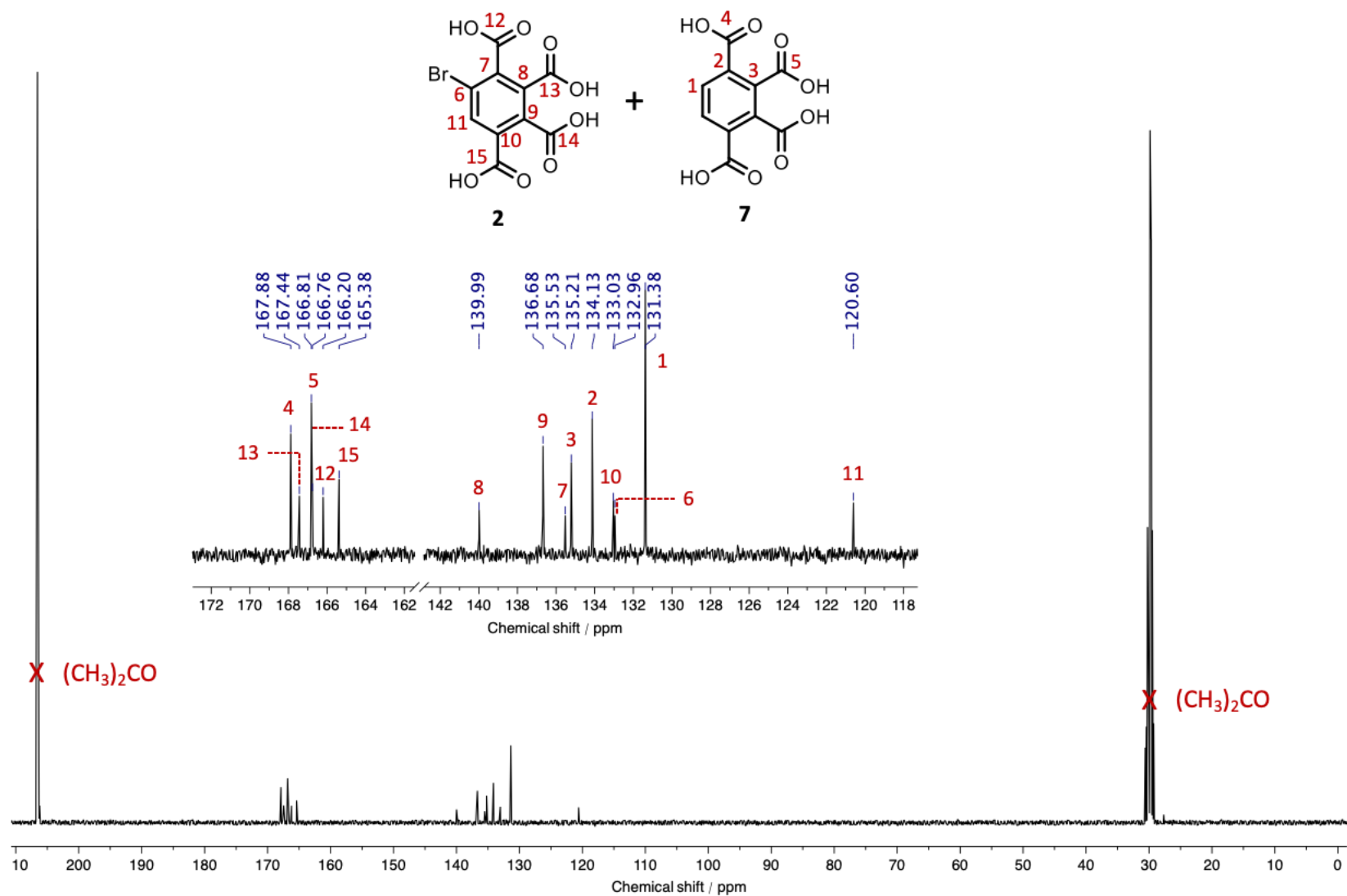
Figure S5.6 ^{13}C NMR (CDCl$_3$, 101 MHz, 298K) spectrum of a 1:1.1 mixture of **2** and **7**
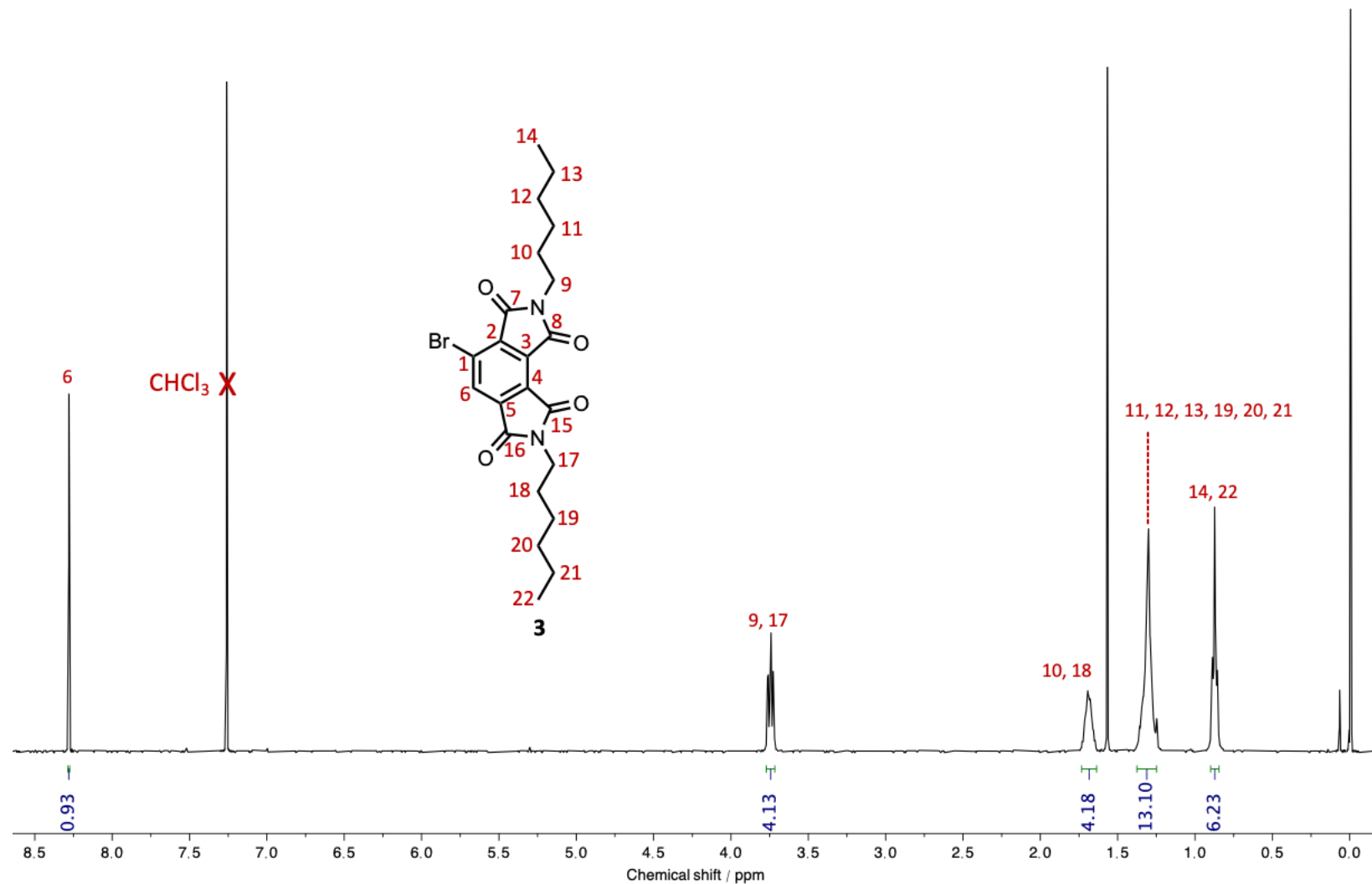
Figure S5.7 ^{1}H NMR (CDCl₃, 400 MHz, 298K) spectrum of **3**
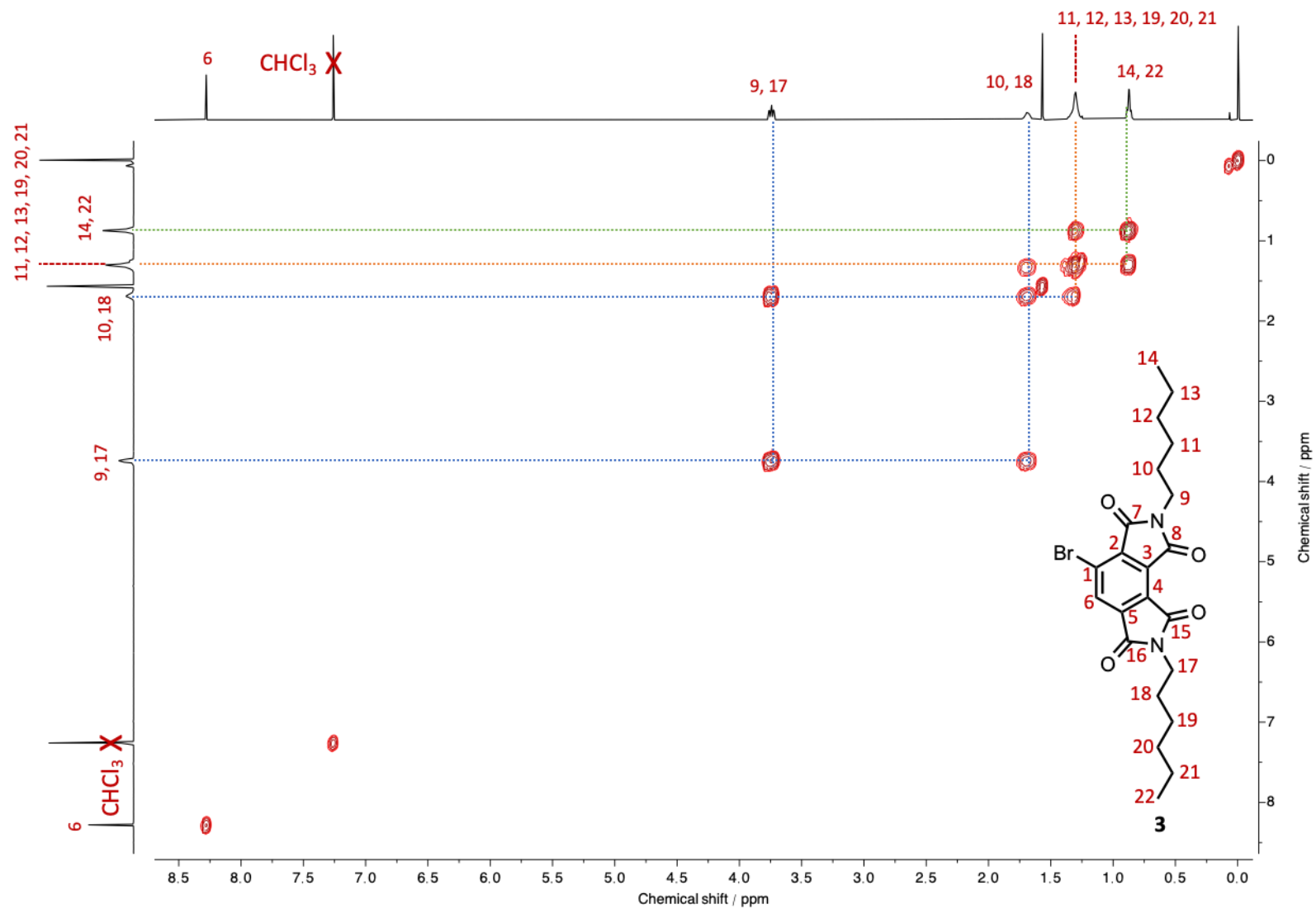
Figure S5.8 Annotated ^{1}H-^{1}H COSY NMR (CDCl$_3$, 400 MHz, 298K) spectrum of **3**
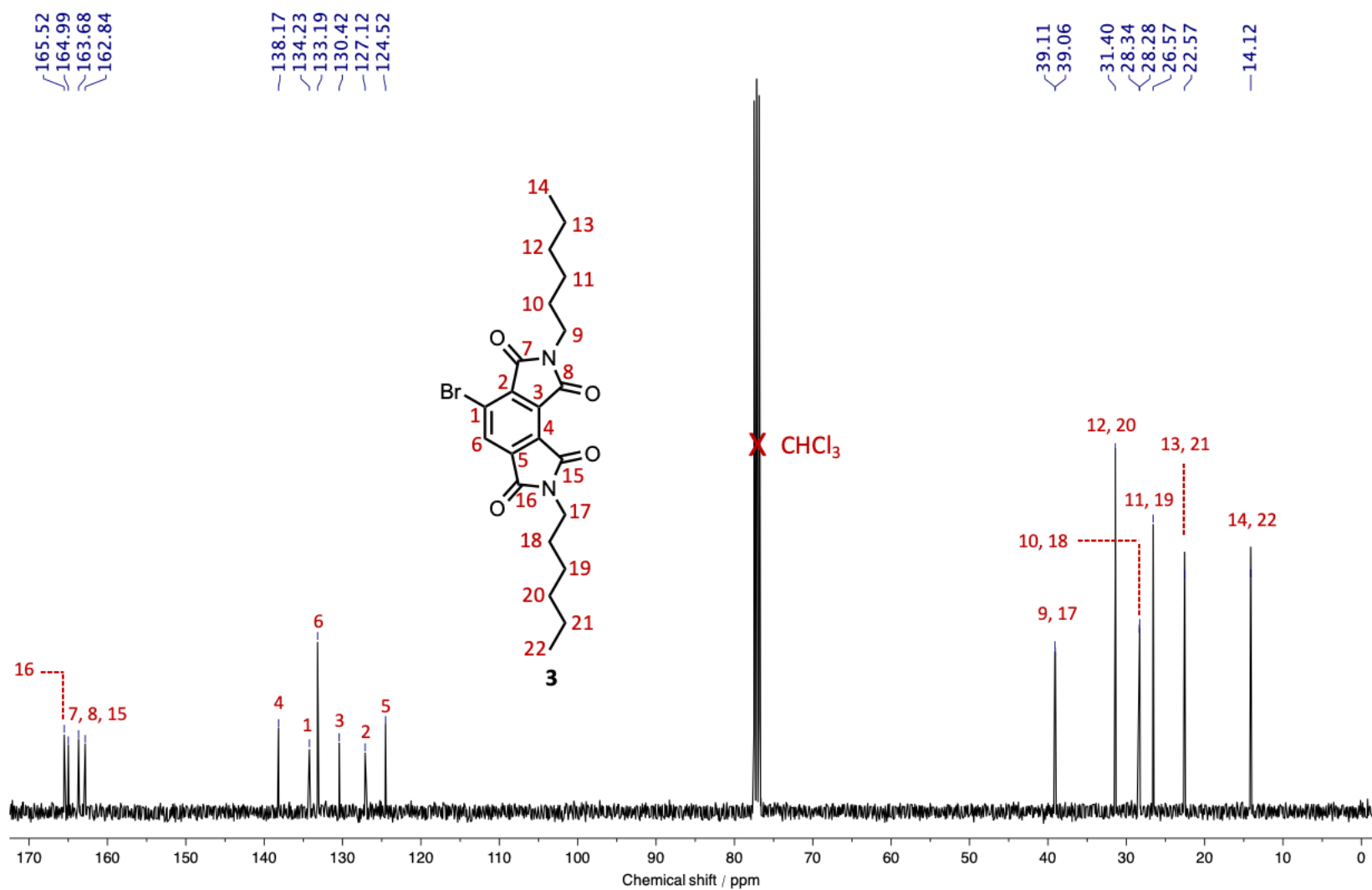
Figure S5.9 [^13]C NMR (CDCl₃, 101 MHz, 298K) spectrum of **3**
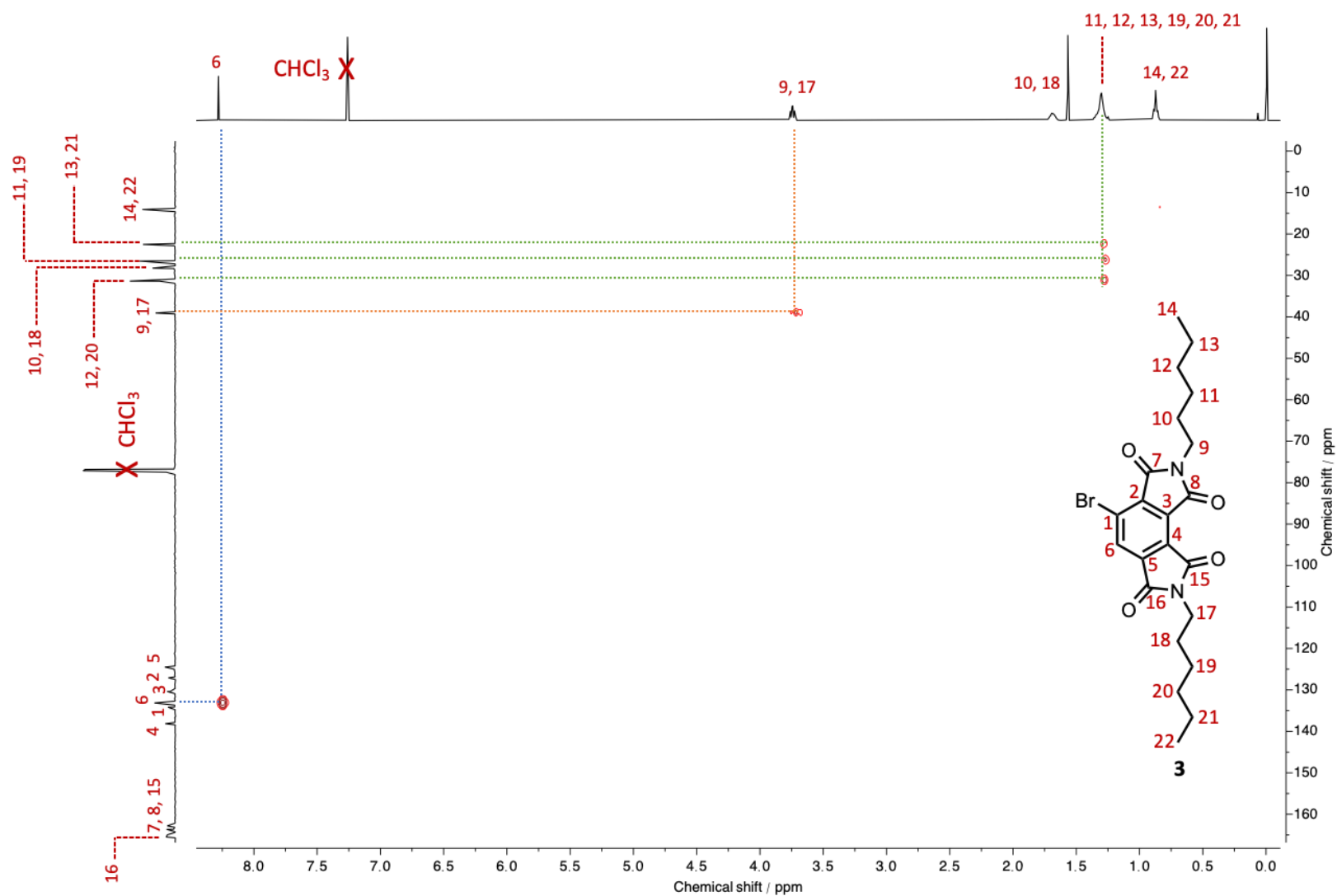
Figure S5.10 Annotated ^{1}H-^{13}C HSQC NMR (CDCl$_3$, 101 MHz, 298K) spectrum of **3**
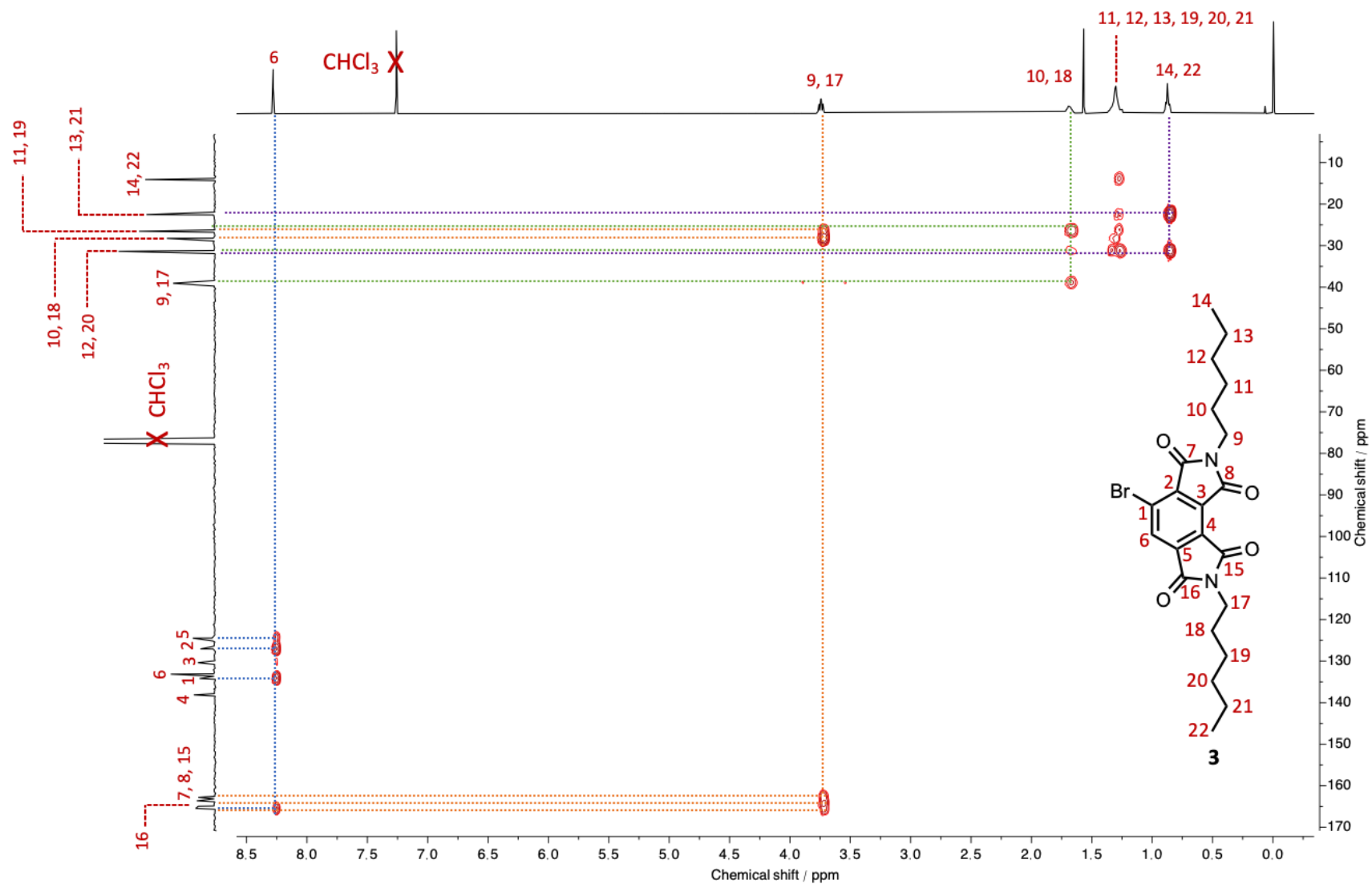
Figure S5.11 Annotated ^{1}H-^{13}C HMBC NMR (CDCl$_3$, 101 MHz, 298K) spectrum of **3**
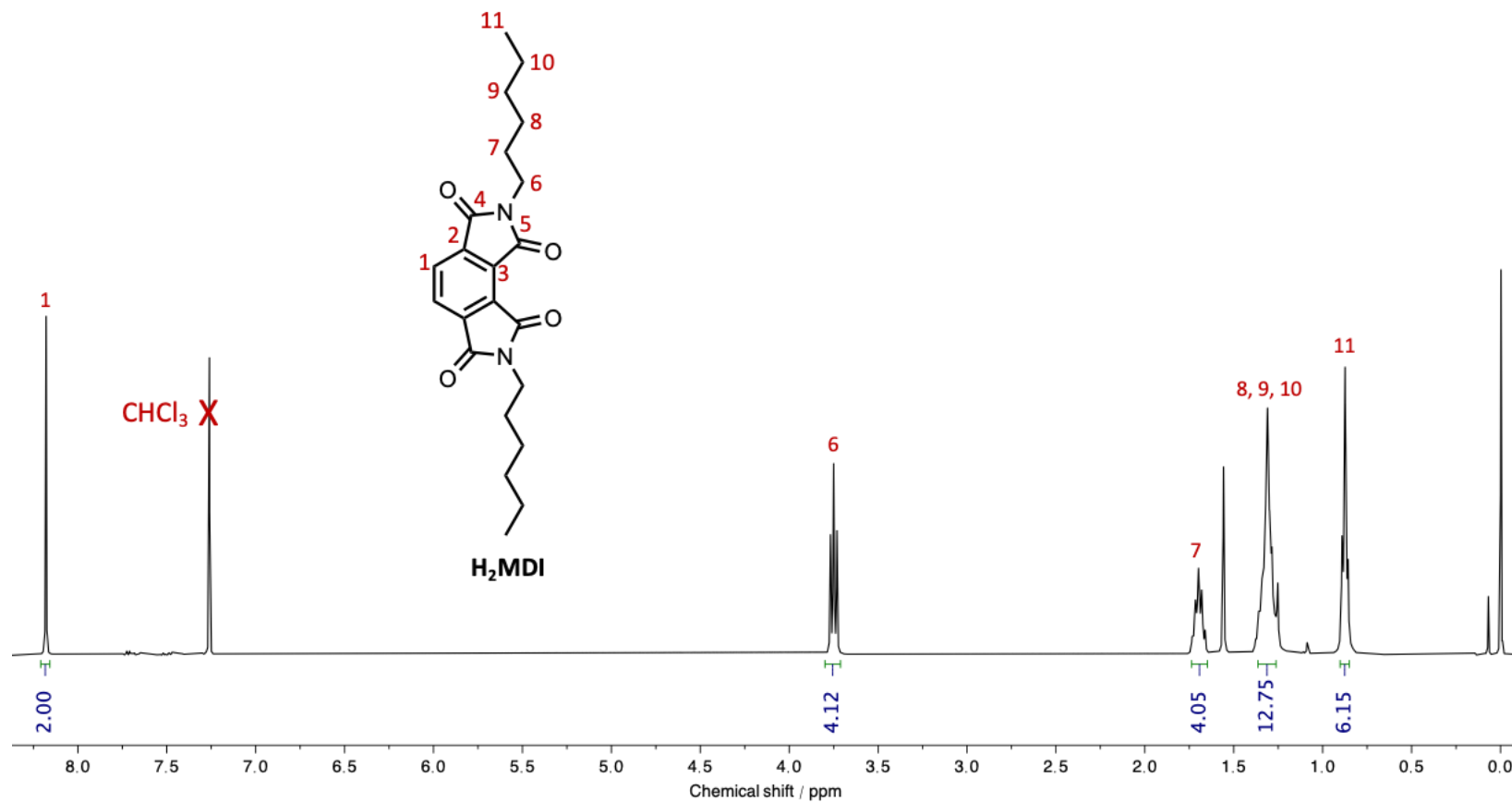
Figure S5.12 ^{1}H NMR (CDCl$_3$, 400 MHz, 298K) spectrum of **H$_2$MDI**
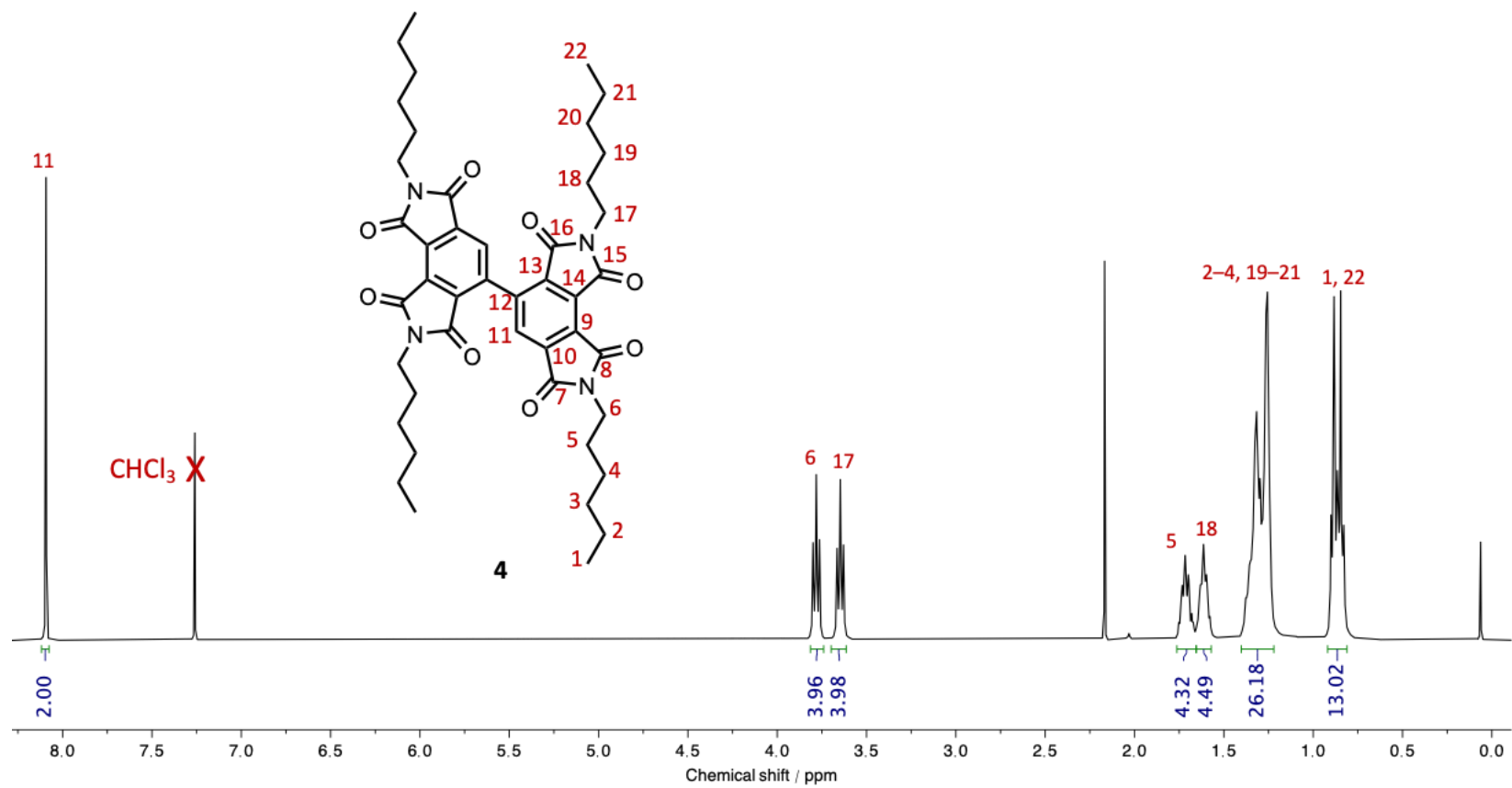
Figure S5.13 ^{1}H NMR (CDCl3, 400 MHz, 298K) spectrum of **4**
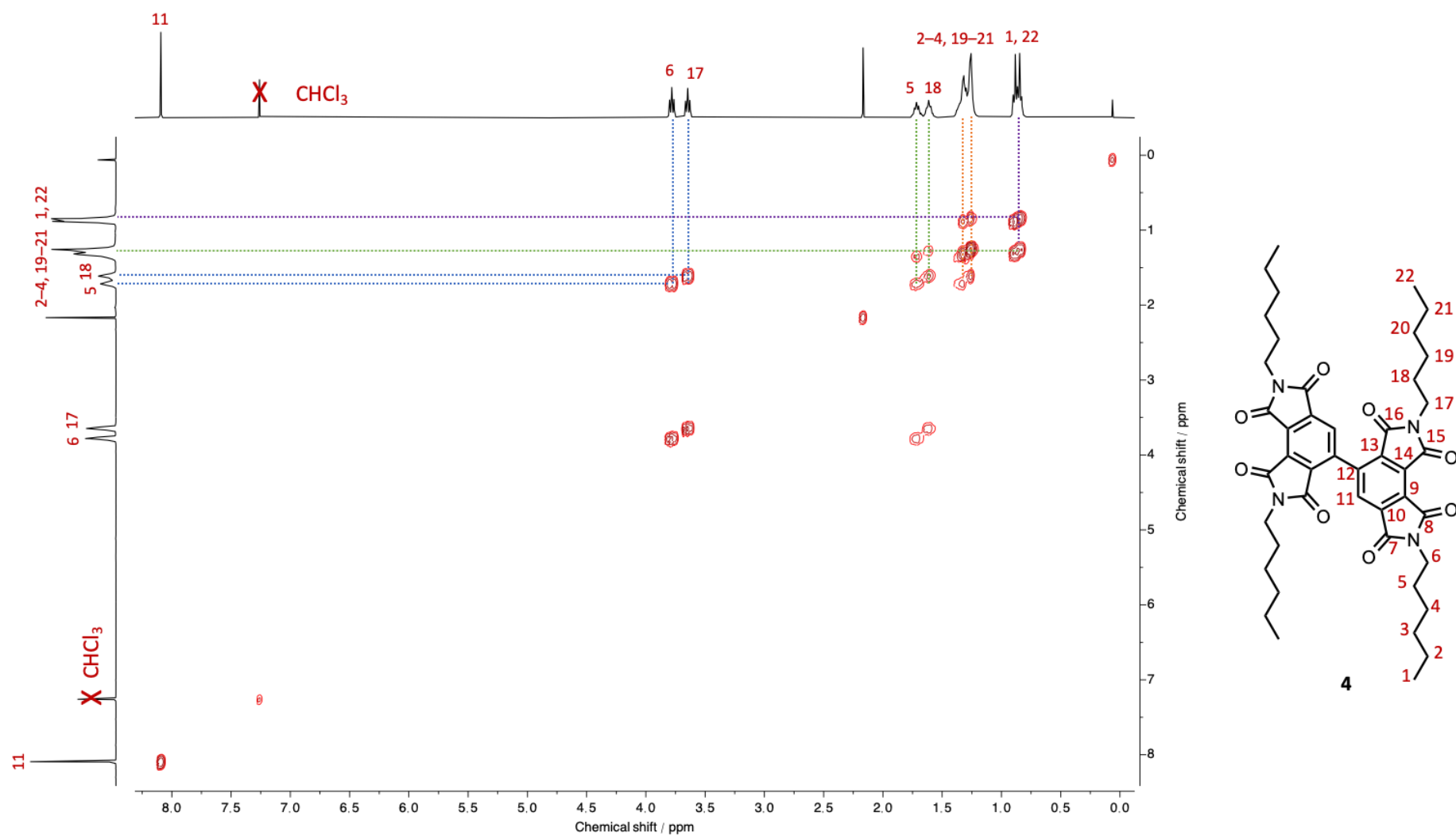
Figure S5.14 Annotated ^{1}H-^{1}H COSY NMR (CDCl$_3$, 400 MHz, 298K) spectrum of **4**
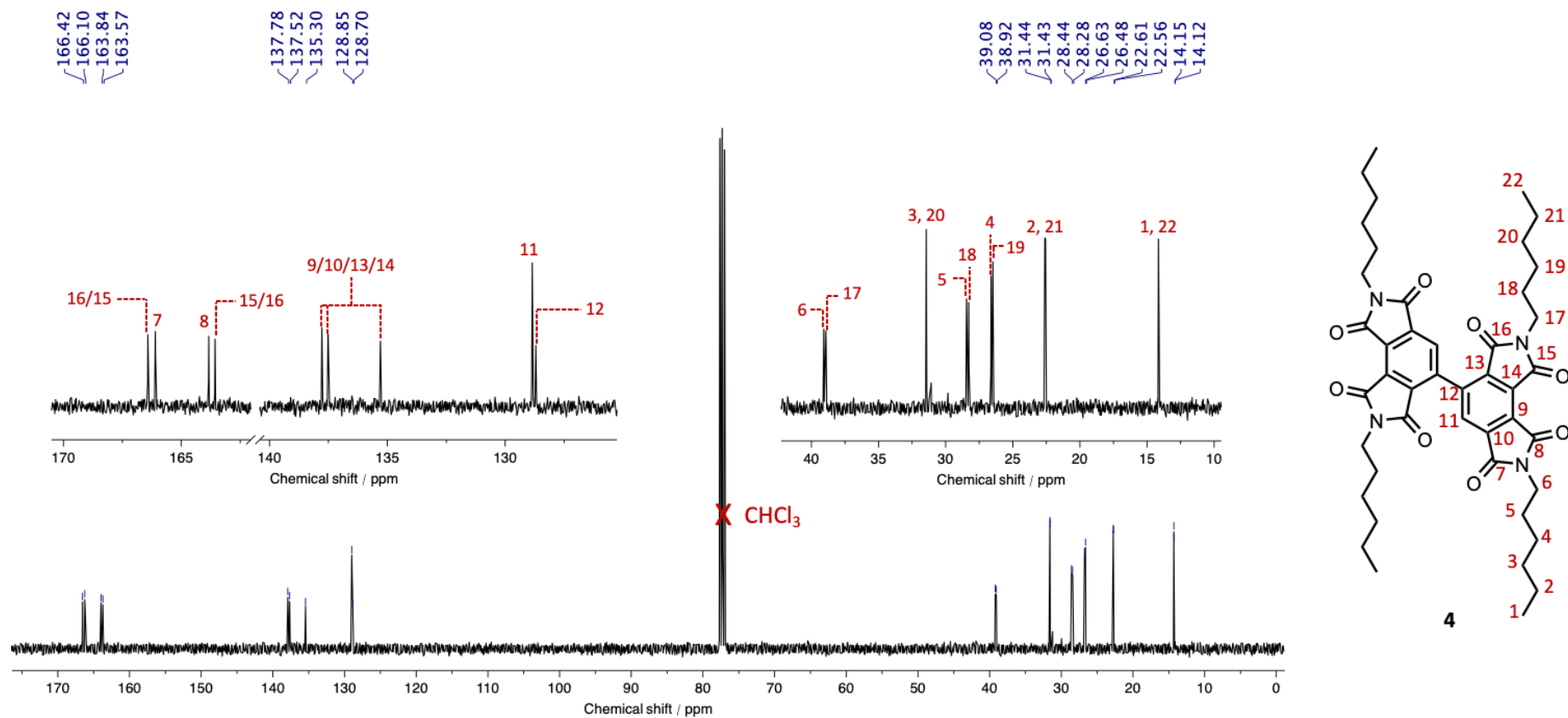
Figure S5.15 ^{13}C NMR (CDCl$_3$, 101 MHz, 298K) spectrum of **4**
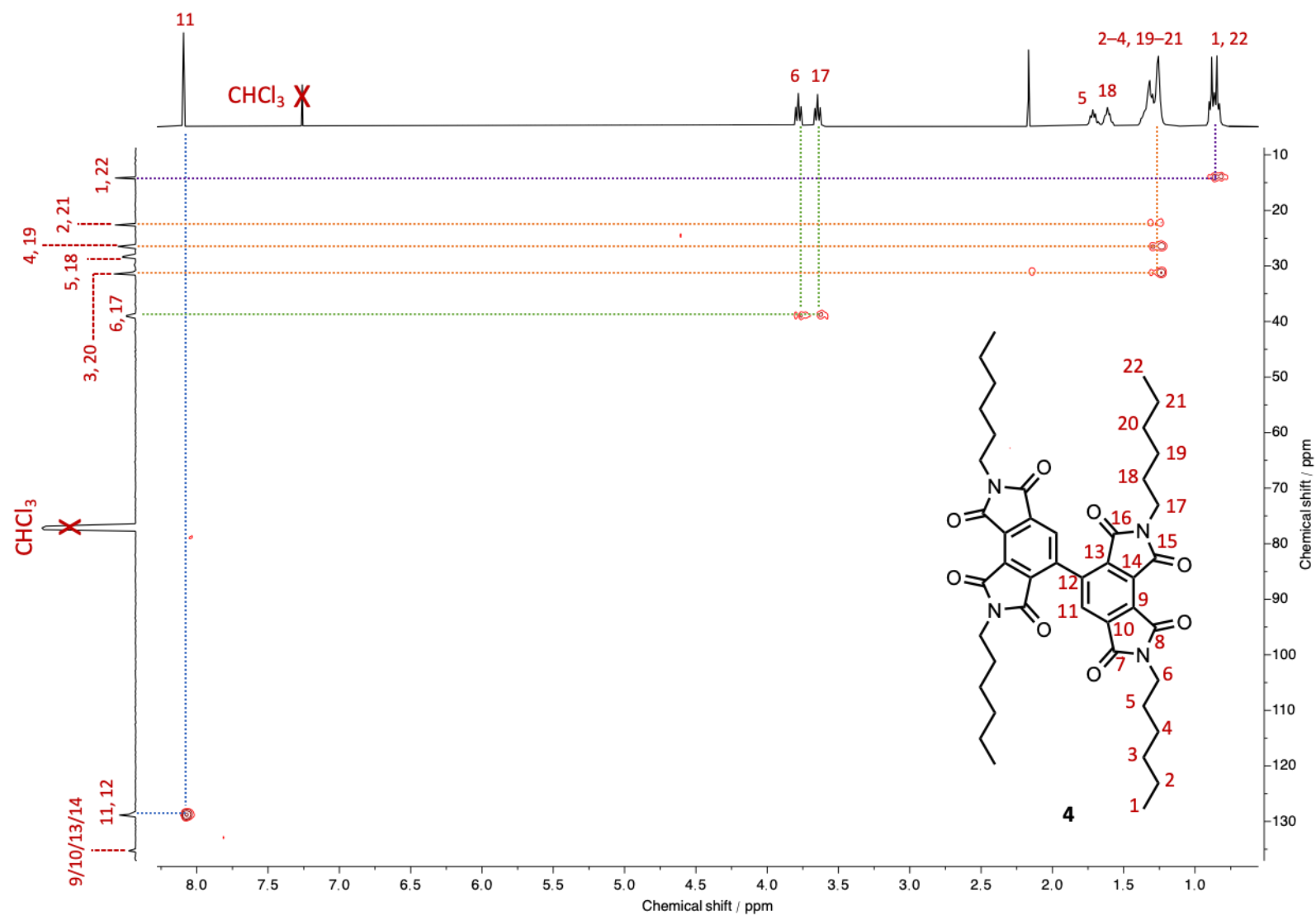
Figure S5.16 Annotated ^{1}H-^{13}C HSQC NMR (CDCl$_3$, 101 MHz, 298K) spectrum of **4**
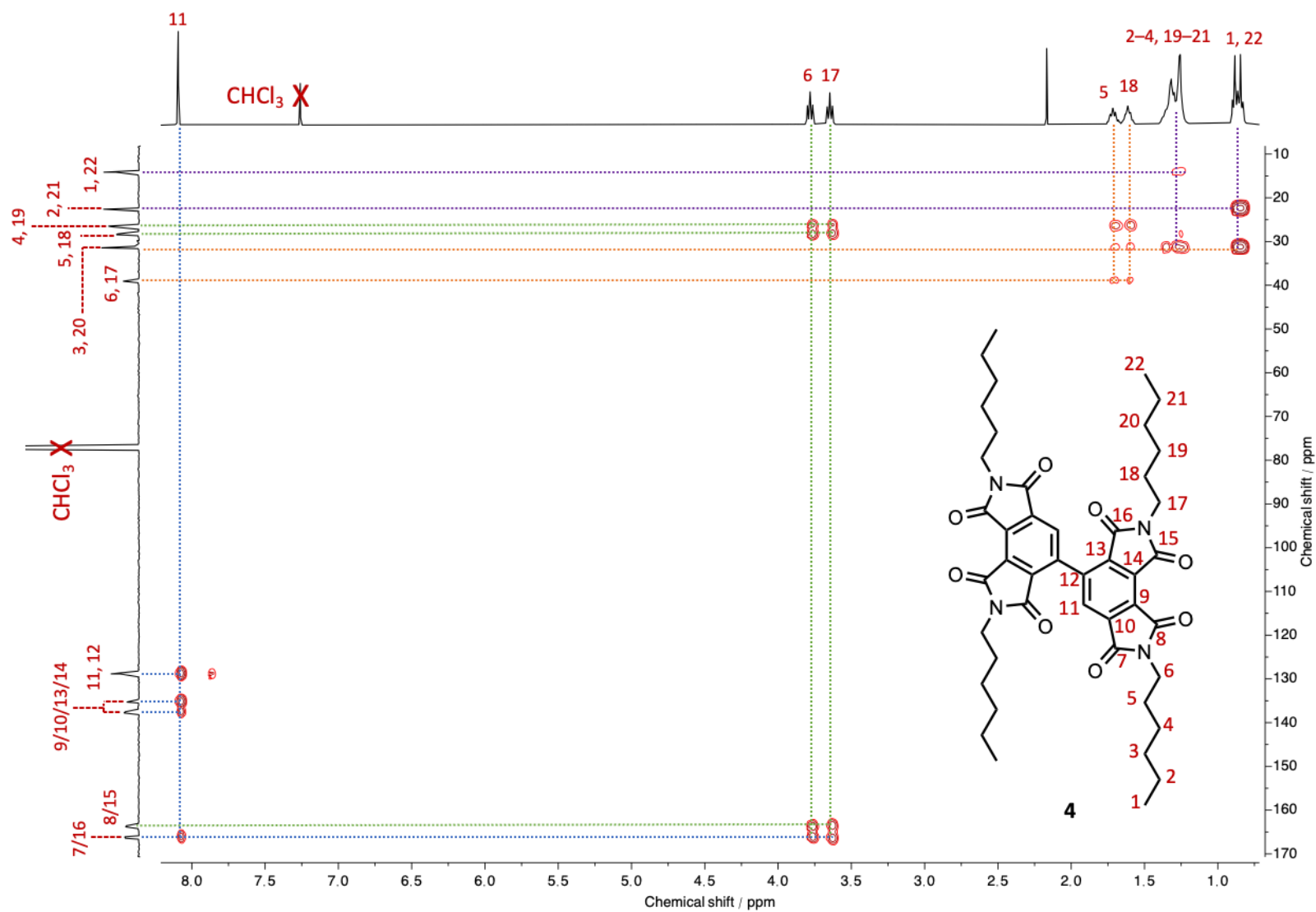
Figure S5.17 Annotated ^{1}H-^{13}C HMBC NMR (CDCl$_3$, 101 MHz, 298K) spectrum of **4**
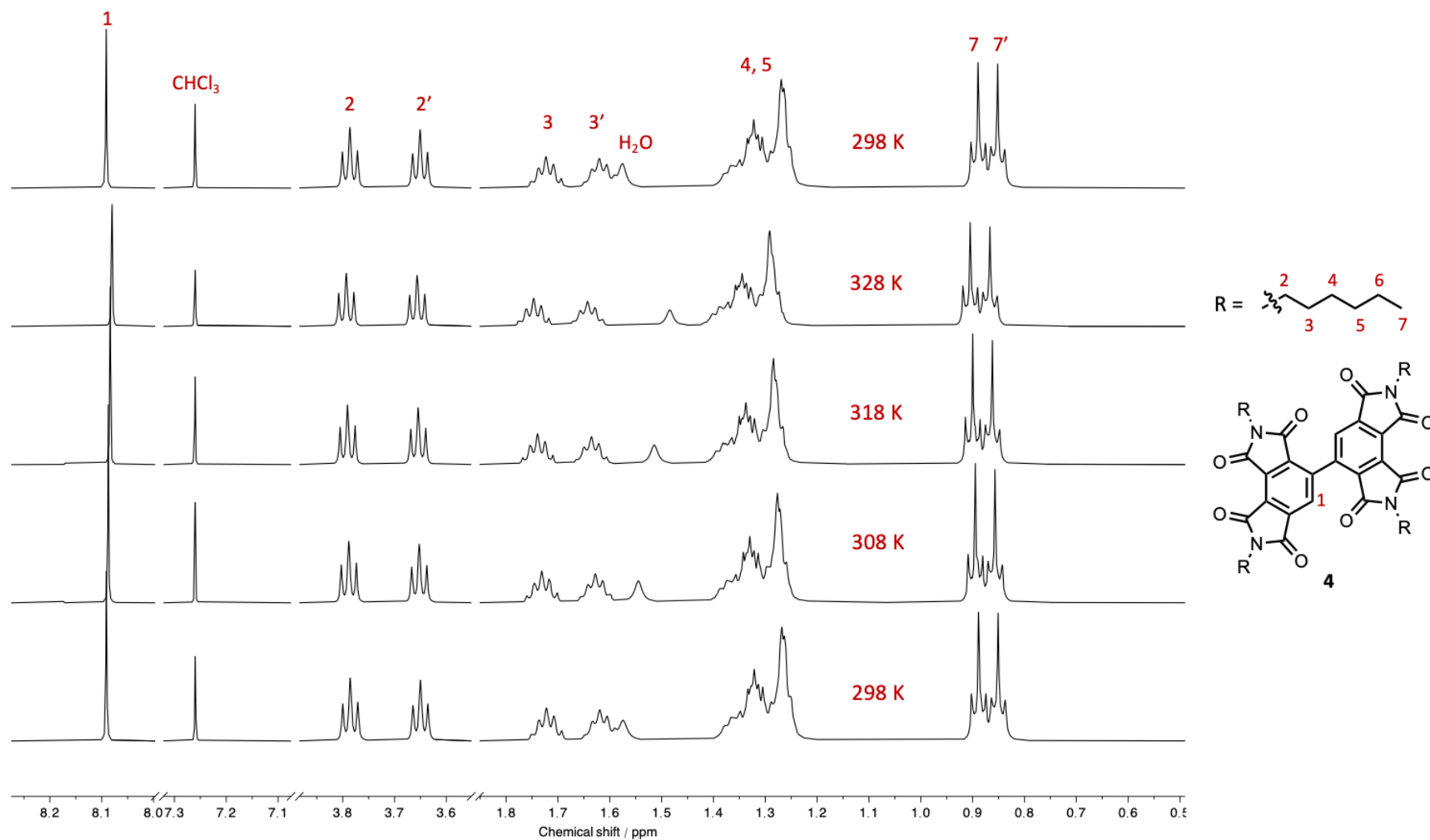
Figure S5.18 High temperature VT NMR (CDCl₃, 400 MHz, 298K) spectrum of **4**
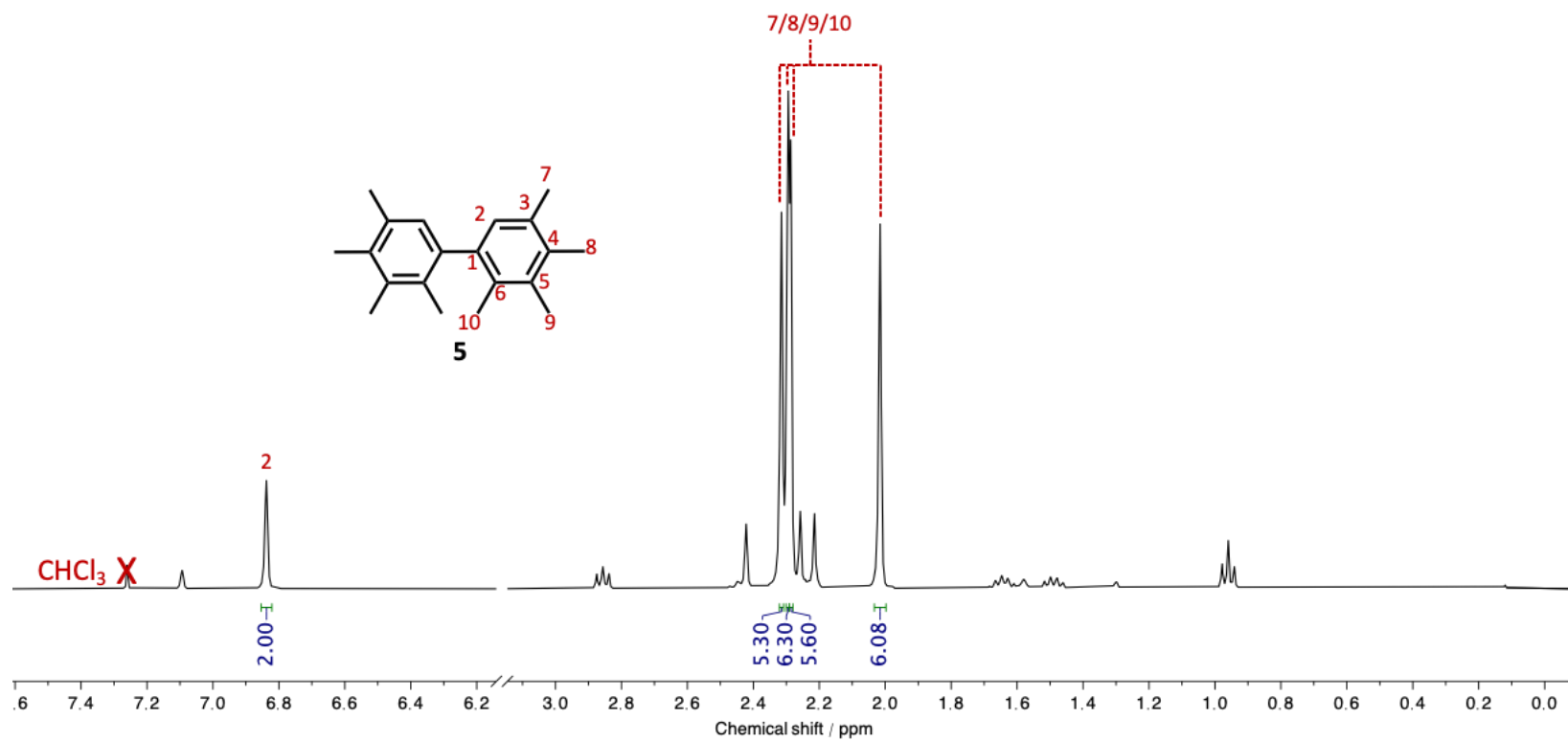
Figure S5.19 ^{1}H NMR (CDCl$_3$, 400 MHz, 298K) spectrum of **5**

5.4.4 X-RAY DIFFRACTION ANALYSIS

TBF-Acr

Single crystals of **TBF-Acr** were grown from a solution of EtOAc in *n*-hexanes. The asymmetric unit contained two channels with *n*-hexanes, one of which was well defined, and the second which was less well defined. A suitable discrete model for this solvent in the second channel could not be achieved, therefore a solvent mask was used.
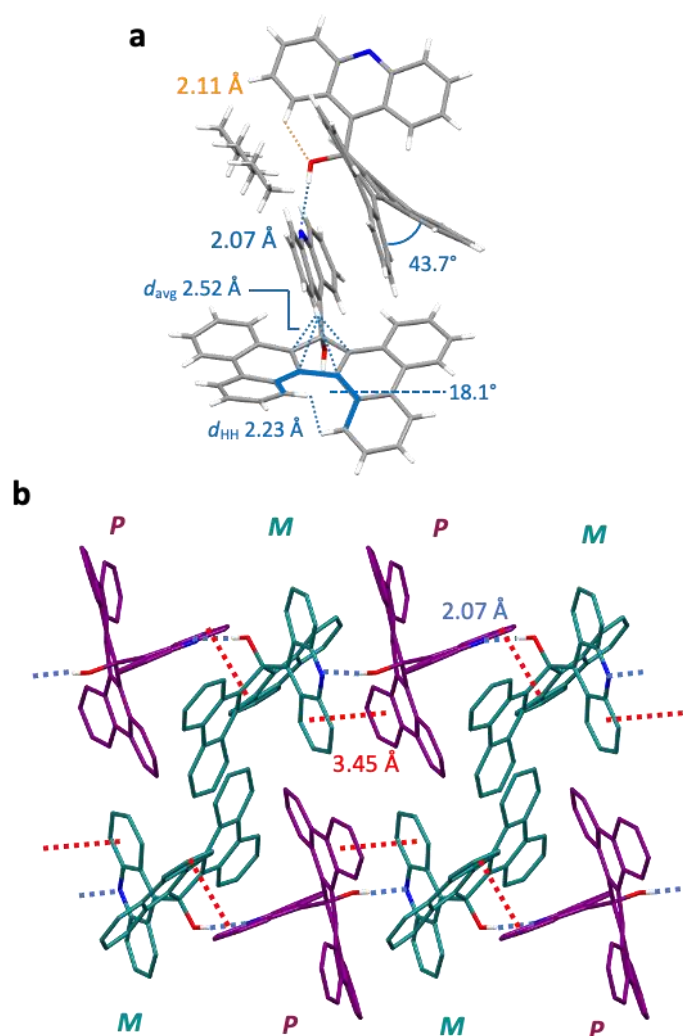
Figure S2.20 (a) Structural parameters of the unit cell packing of **TBF-Acr** highlighted in blue and orange and (b) the supramolecular packing of the racemate. Non-interacting H atoms and solvent have been omitted for clarity.

Crystal data for $C_{87}H_{57}N_2O_2$ (M =1162.34 g/mol): triclinic, space group P-1 (no. 2), a = 12.8097(10) Å, b = 13.2065(11) Å, c = 20.1413(14) Å, α = 79.779(6)°, β = 87.266(6)°, γ = 71.352(7)°, V = 3177.1(4) Å^3, Z = 2, T = 110.00(10) K, μ(Cu Kα) = 0.555 mm^{-1}, $Dcalc$ = 1.215 g/cm^3, 20270 reflections measured (7.77° ≤ 2θ ≤ 142.628°), 11946 unique (R_{int} = 0.0895, R$_{sigma}$ =

0.1472) which were used in all calculations. The final R_1 was 0.0659 (I > 2σ(I)) and wR_2 was 0.1567 (all data).

5.4.5 SUPPLEMENTARY SPECTRA

5.4.5.1 OPTICAL SPECTRA

Samples were prepared using anhydrous and spectroscopic grade solvents with the aid of sonication of afford complete dissolution. Absorption spectra were recorded at room temperature (298 K) in quartz cuvettes (10 mm path length) and baseline corrected with respect to pure solvent.
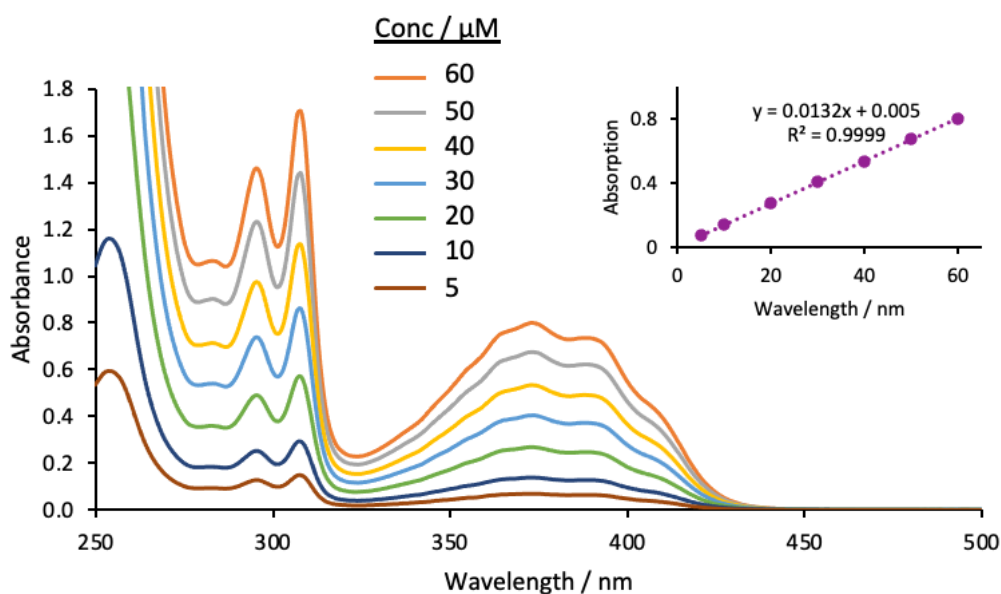
Figure S5.21 Concentration-dependent UV–vis absorption studies of **Acr-OH** in THF. Inset shows a straight-line graph highlighting observations of the Beer-Lambert law.
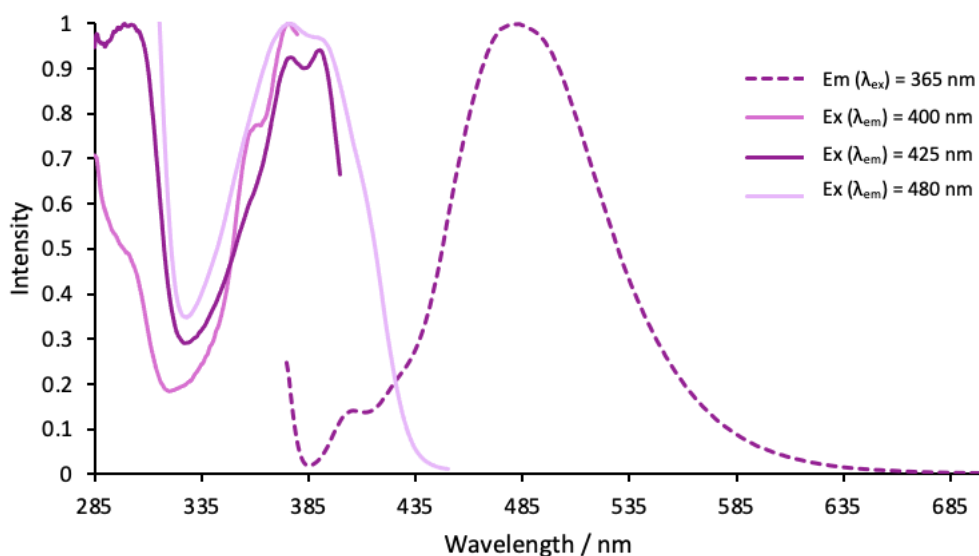
Figure S5.22 Excitation spectra of **Acr-OH** at different emission wavelengths in THF (10 µM)
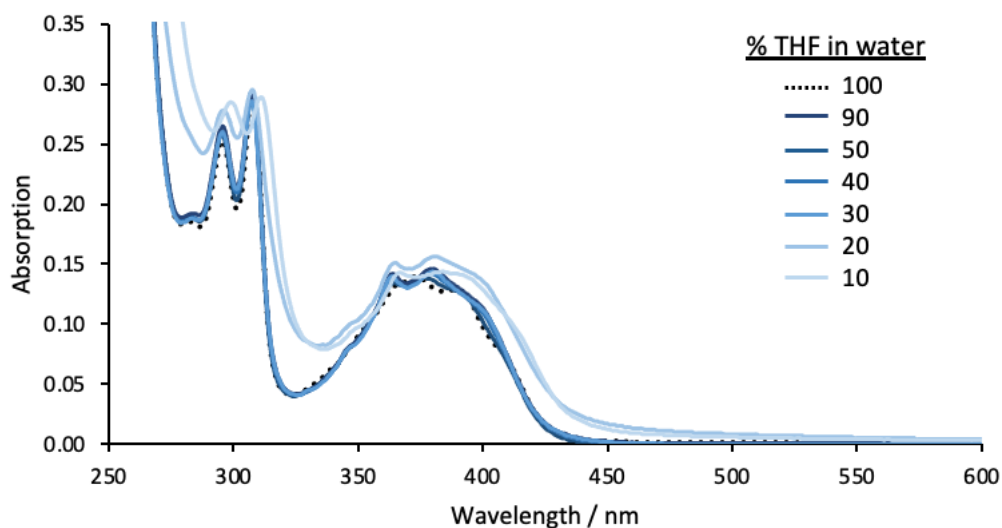
Figure S5.23 Aggregation studies by UV–vis absorption studies of **Acr-OH** in THF/H$_2$O mixtures
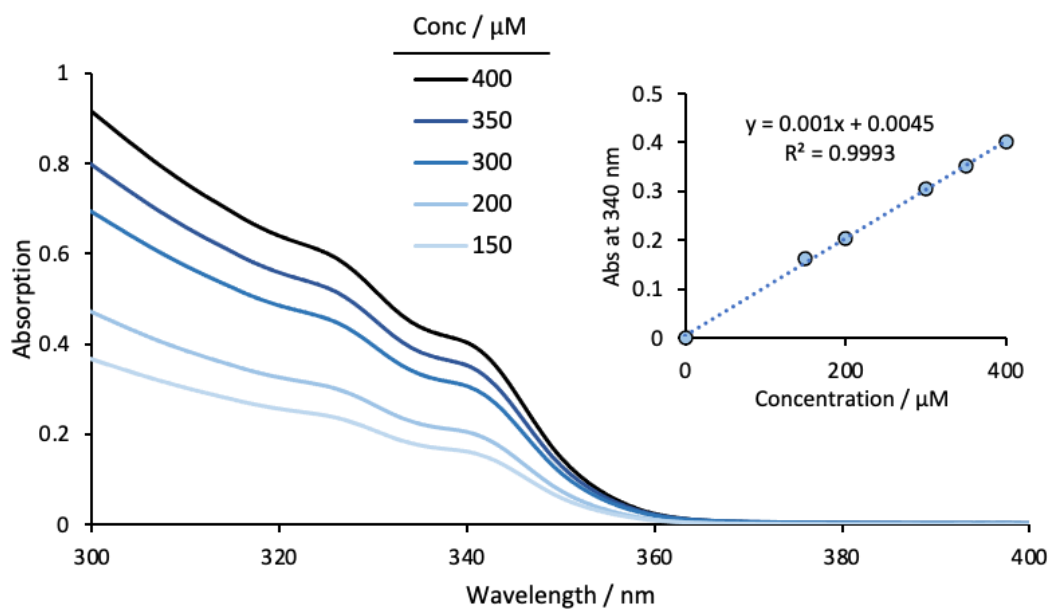
Figure S5.24 Concentration dependent UV–vis absorption studies of **Br-MDI** in THF. Inset shows a straight-line graph highlighting observations of the Beer-Lambert law.
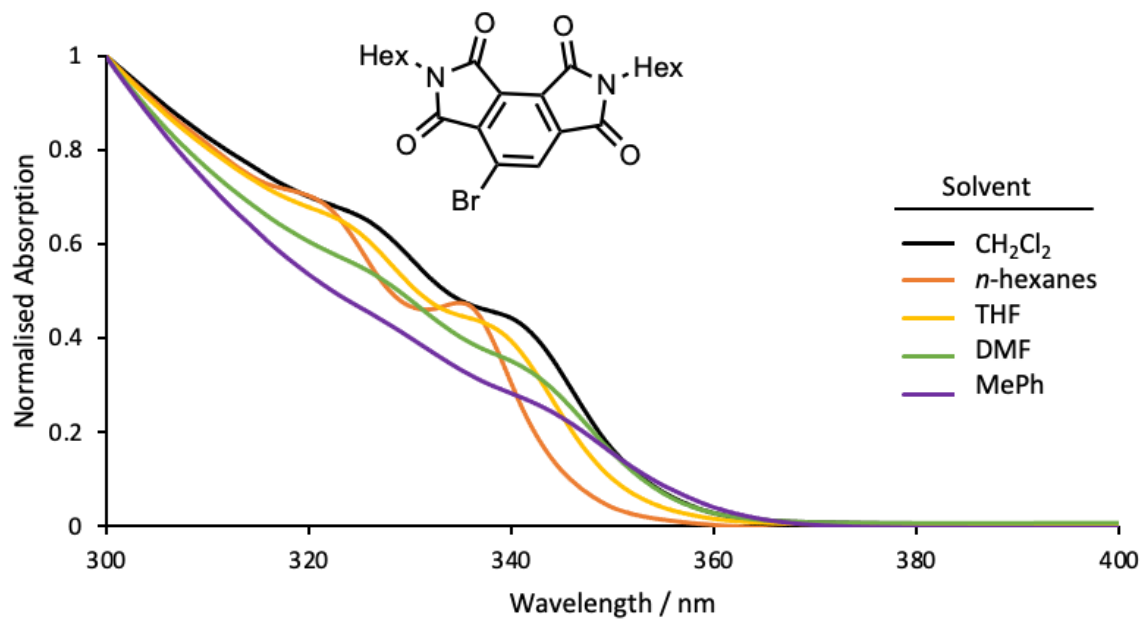
Figure S5.25 Solvent-dependent UV–vis absorption studies of **Br-MDI**.
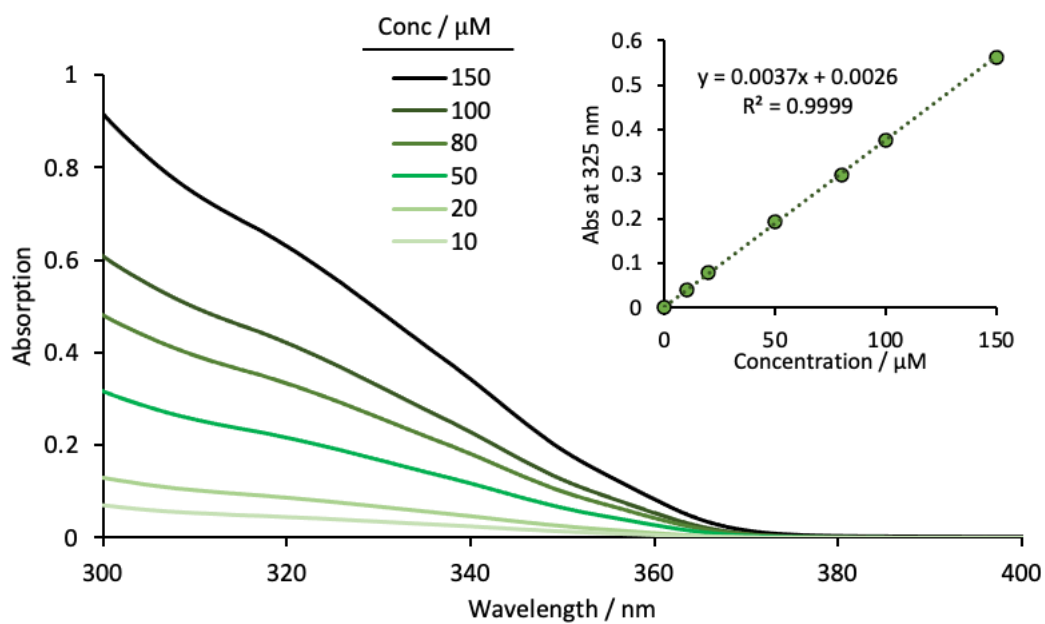
Figure S5.26 Concentration dependent UV–vis absorption studies of MDI-dimer **4** in THF. Inset shows a straight-line graph highlighting observations of the Beer-Lambert law.

5.4.5.2 CYCLIC VOLTAMMETRY

Cyclic voltammograms of **4** were recorded at room temperature in deaerated THF solutions (1 mM with solutions 0.1 M TBAPF$_6$ supporting electrolyte) under an argon atmosphere using a standard three-electrode set up. See Section 5.4.1 for full experimental details.
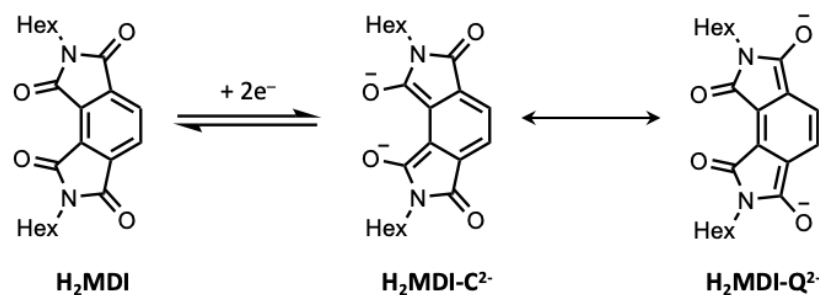
Figure S5.27 Electrochemical reduction of **H$_2$MDI** and canonical resonance forms (i.e., C = fully conjugated; Q = quinoidal) of the dianion **H$_2$MDI**$^{2-}$

The electrochemical reversibility of the first reduced state for **4** was confirmed by measuring the cyclic voltammogram at multiple scan rates which resulted in a straight-line relationship between the peak current i and the square root of the scan rate, $\sqrt{v}$.
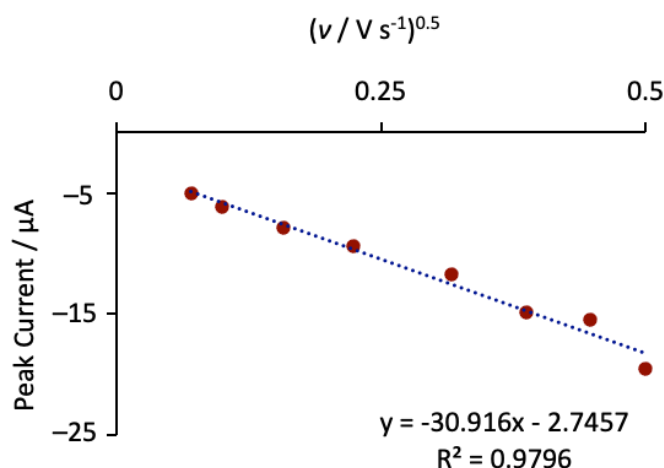
Figure S5.28 The reversibility of the first reduction of **4** is highlighted by a linear relationship between peak current and the square root of scan rate, $\sqrt{v}$

Table S4.1. Experimentally determined LUMO and band gap ($E_{bg(opt)}$) parameters of **BrMDI** and **4** from UV–vis and CV analyses in THF

	λ_{onset}/ nm	$E_{bg(opt)}$[a] / eV	$E_{onset,red}$ / V	LUMO[b] / eV	HOMO[c] / eV
BrMDI	353	3.51	−1.44	−3.36	−6.87
4	364	3.41	−1.30	−3.50	−6.91

[a]The optical band gap ($E_{\text{bg,opt}}$) was determined from the onset of absorption; [b]The energy of the LUMO was calculated using the equation: LUMO $= -(E_{\text{onset,red}} + 4.80)$ eV; [c]The energy of the HOMO was calculated using the equation: HOMO $=$ LUMO $- E_{\text{bg,opt}}$

5.4.6 DFT ANALYSES

DFT calculations were performed to obtain geometrically optimised structures of both enantiomers (**Acr-OH,** MDI-dimer **4** and its redox states and **MDI-TBF** and its redox states) and the transition state structures for the interconversion between enantiomers of **MDI-TBF** (and its redox states) using (U)B3LYP(GD3BJ)/6-31G(d,p) in a CH_2Cl_2 solvent model. Ground state geometries were verified by convergence to a minimum stationary point and no negative vibrational frequencies observed.

Structures of transition states for the interconversion between the *M*- and *P*- enantiomers of **MDI-TBF** were optimised using the Berny approximation using B3LYP(GD3BJ)/6-31G(d,p) in a CH_2Cl_2 solvent model starting from a random guess. Transition states were verified by the appearance of a negative imaginary frequency which when animated mirrored the translational motion that would depict enantiomeric interconversion. Following this optimisation, single point energy calculations were performed so that energies of the enantiomers and transition states could be compared to determine the energy barrier involved in the interconversion to provide insight into the configurational stability of the studied molecules.
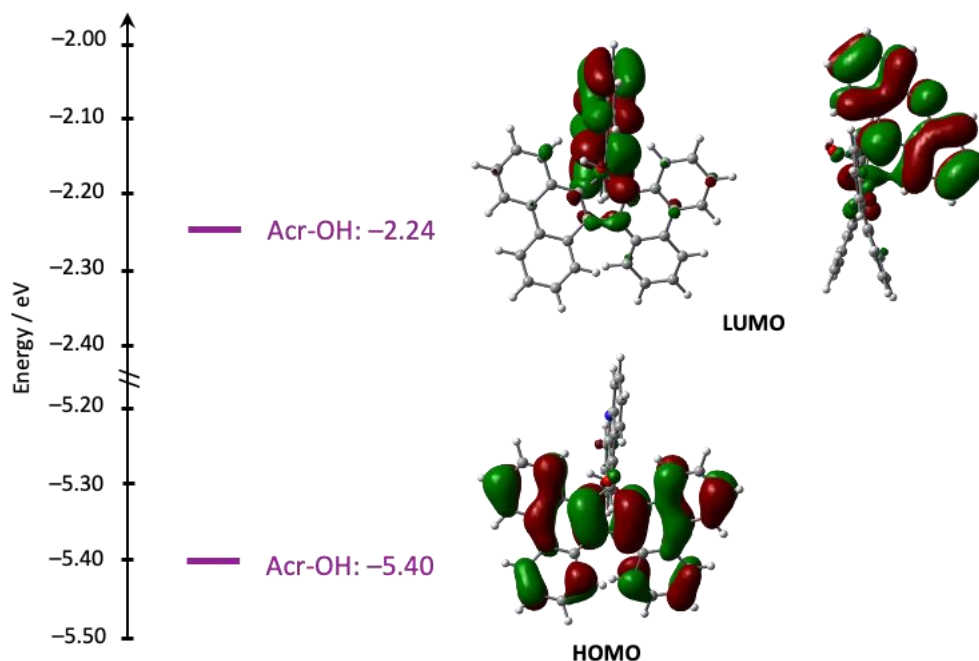
Figure S5.29 Depiction of the HOMO and LUMO energy levels of a representative enantiomer of **Acr-OH** along with pictorial representation of the electron density distribution of those energy level.

The *anti*-conformer of **4** and its redox states were found to be lower in energy than the *syn*-conformer, therefore only the *anti*-conformer is shown. The singlet states of **4²⁻** and **MDI-TBF²⁻** were predicted

to be more energetically stable than their triplet states therefore, results pertaining to only the dianion singlet states are discussed and shown in this Thesis Chapter.

Table S4.2. DFT calculated parameters for the neutral and redox states of **4** and **MDI-TBF**.*

	Relative ZPE/ eV	HOMO / eV	LUMO / eV	Band Gap / eV
4	+ 5.83	–7.37	–3.10	4.26
4$^{\bullet-}$	+ 2.48	–3.44	–2.16	1.28
4^{2-}	0.00	–2.59	–1.27	1.32
MDI-TBF	+ 6.08	–7.13	–3.35	3.78
MDI-TBF$^{\bullet-}$	+ 2.56	–3.56	–1.93	1.63
MDI-TBF^{2-}	0.00	–2.63	–1.04	1.59

*Relative zero-point energies (ZPE) are quoted by setting the minimum energy for each series of compounds to 0.00 eV. For all radical states (e.g., **4**$^{\bullet-}$) HOMO and LUMOs are represented by the highest singly occupied (SOMO) and lowest singly unoccupied (SOMO*) α-orbitals.

4_{LUMO}: −3.10 eV $4^{\bullet-}_{SOMO-\alpha}$: −3.44 eV 4^{2-}_{HOMO}: −2.59 eV

$MDI\text{-}TBF_{LUMO}$: −3.35 eV $MDI\text{-}TBF^{\bullet-}_{SOMO-\alpha}$: −3.56 eV $MDI\text{-}TBF^{2-}_{HOMO}$: −2.63 eV
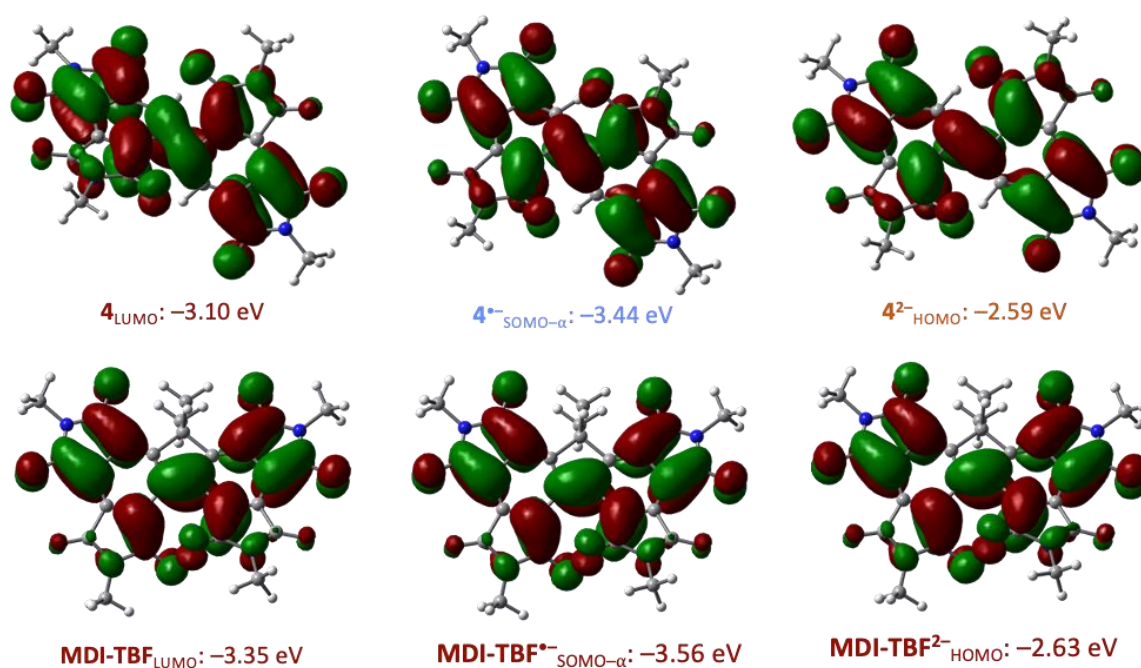
Figure S5.30. Frontier molecular orbital depictions (along with the energies of those orbitals) of selected neutral and charged states of **4** and **MDI-TBF**.

5.4.6.1 CARTESIAN COORDINATES

4

C	-3.505356	1.928830	0.853514
C	-3.433978	0.720663	1.517032
C	-2.172460	0.157496	1.780495
C	-2.305009	2.552239	0.479300
C	-0.975833	0.773602	1.409295
C	-1.059684	2.015232	0.741472
C	0.631091	-1.132128	1.127259
C	1.885930	-1.674621	1.323278
C	0.348478	0.147946	1.652452
C	2.904994	-1.019936	2.032261
C	1.364942	0.795845	2.356894
C	2.636004	0.227844	2.558160
C	-2.394409	-1.115472	2.541467
C	-2.639400	3.832062	-0.213959
C	2.410625	-2.993683	0.860158
C	1.340138	2.115848	3.067667
O	-1.881730	4.655794	-0.688835
O	-1.572370	-1.897218	2.980895
O	0.428613	2.915822	3.163555
O	1.839364	-3.850621	0.214009
C	-4.637931	2.802840	0.404998
O	-5.835688	2.647045	0.519805
C	-4.480410	-0.189697	2.082182
O	-5.689095	-0.085699	2.069039
C	3.450500	1.182607	3.376555
O	4.595878	1.091125	3.766148
C	4.108368	-1.914573	2.038538
O	5.203223	-1.745900	2.533149
N	2.606577	2.267775	3.633268
N	3.726429	-3.057607	1.324223
N	-4.034485	3.904831	-0.214705
N	-3.777771	-1.246558	2.669320
C	3.013457	3.421534	4.417226
H	3.246038	3.120037	5.440897
H	3.895885	3.883795	3.970555
H	2.184247	4.127492	4.419415
C	4.616788	-4.182781	1.097327
H	5.505215	-3.855634	0.553142

H	4.921801	-4.620612	2.050170
H	4.071986	-4.919843	0.508928
C	-4.429843	-2.353574	3.347953
H	-5.020879	-1.983667	4.188314
H	-5.085479	-2.885004	2.655085
H	-3.650673	-3.023239	3.709078
C	-4.793110	4.999256	-0.795234
H	-5.443328	4.627127	-1.589797
H	-5.404012	5.481796	-0.029420
H	-4.079792	5.713447	-1.204308
H	-0.161517	2.534326	0.430445
H	-0.121507	-1.677245	0.571214

4·⁻

C	-3.542067	1.884845	0.865155
C	-3.473336	0.619410	1.410187
C	-2.227414	0.064957	1.773902
C	-2.319403	2.596056	0.699241
C	-0.997832	0.765946	1.589570
C	-1.094633	2.075460	1.055422
C	0.558884	-1.164223	1.436630
C	1.823444	-1.700397	1.538884
C	0.311782	0.175864	1.827462
C	2.934072	-0.974826	2.056661
C	1.423613	0.894093	2.361214
C	2.710221	0.323105	2.467769
C	-2.497740	-1.216891	2.454992
C	-2.623661	3.907923	0.097452
C	2.285774	-3.048048	1.156873
C	1.475195	2.220385	3.007329
O	-1.866680	4.818453	-0.217296
O	-1.738455	-2.006756	3.000874
O	0.592371	3.043202	3.212212
O	1.658814	-3.979900	0.667303
C	-4.641904	2.750288	0.386527
O	-5.850605	2.570867	0.342291
C	-4.551663	-0.352429	1.782869
O	-5.756955	-0.286079	1.611400
C	3.619341	1.321688	3.118862
O	4.810621	1.248704	3.368484

C	4.114711	-1.865331	2.023911	C	1.548623	2.255355	3.025869
O	5.273708	-1.684152	2.368452	O	-1.884256	4.887087	0.039176
N	2.814792	2.412435	3.414883	O	-1.856610	-2.033080	3.090200
N	3.649887	-3.075840	1.476877	O	0.696898	3.098020	3.317714
N	-4.016770	3.931065	-0.055663	O	1.562237	-4.029943	0.942705
N	-3.897304	-1.407565	2.401912	C	-4.632792	2.687971	0.319484
C	3.292885	3.606766	4.080841	O	-5.839292	2.501727	0.148194
H	3.722258	3.355666	5.053953	C	-4.579583	-0.428849	1.631163
H	4.055271	4.105541	3.476578	O	-5.772029	-0.384037	1.352400
H	2.438927	4.269896	4.215227	C	3.707269	1.380065	2.991805
C	4.506338	-4.225910	1.272753	O	4.919517	1.305308	3.156760
H	5.348345	-3.964098	0.627184	C	4.121222	-1.813283	1.947008
H	4.896103	-4.589421	2.227304	O	5.323837	-1.634864	2.149534
H	3.906048	-5.003573	0.801201	N	2.932273	2.463013	3.341395
C	-4.576196	-2.565990	2.945724	N	3.607107	-3.058737	1.511021
H	-5.262164	-2.271099	3.744216	N	-4.003581	3.911182	-0.016077
H	-5.143573	-3.077353	2.164079	N	-3.968639	-1.460295	2.307927
H	-3.814045	-3.233932	3.345810	C	3.445096	3.664270	3.957366
C	-4.751208	5.049409	-0.610224	H	3.993856	3.425669	4.872988
H	-5.295887	4.743900	-1.507358	H	4.117068	4.201714	3.280028
H	-5.466687	5.436694	0.119626	H	2.589713	4.296602	4.196047
H	-4.027985	5.823758	-0.864602	C	4.445511	-4.211347	1.275981
H	-0.198222	2.657232	0.887527	H	5.281397	-3.946053	0.623438
H	-0.240194	-1.760854	1.017400	H	4.852374	-4.604111	2.213787
4²⁻				H	3.829320	-4.975711	0.801882
				C	-4.655799	-2.635815	2.789111
C	-3.564129	1.844473	0.846521	H	-5.476636	-2.359105	3.457298
C	-3.486243	0.561257	1.349850	H	-5.065908	-3.221446	1.959801
C	-2.259969	0.015880	1.795551	H	-3.927271	-3.237528	3.333074
C	-2.336925	2.607507	0.821684	C	-4.719845	5.026798	-0.589893
C	-1.008883	0.762731	1.717371	H	-5.137302	4.764479	-1.567269
C	-1.134541	2.106063	1.257367	H	-5.541481	5.335099	0.062916
C	0.524989	-1.167518	1.648207	H	-4.011466	5.847759	-0.704016
C	1.790449	-1.699115	1.670070	H	-0.253159	2.729801	1.195412
C	0.284182	0.204201	1.951695	H	-0.298669	-1.793612	1.334723
C	2.958115	-0.937064	2.049026	**MDI-TBF**			
C	1.456641	0.955137	2.387677				
C	2.747958	0.378094	2.414788	C	-3.474311	1.903763	1.011115
C	-2.560108	-1.237442	2.463551	C	-3.481494	0.745144	1.767556
C	-2.626067	3.924494	0.255983	C	-2.265548	0.105873	2.065856
C	2.216355	-3.053862	1.321590	C	-2.257439	2.385497	0.482526

C	-1.052287	0.661455	1.669155
C	-1.048816	1.772674	0.778248
C	0.355031	2.028524	0.238447
C	1.161337	0.979102	0.997501
C	2.516993	0.686432	0.971092
C	0.332534	0.272732	1.915663
C	3.082062	-0.255390	1.857232
C	0.919370	-0.540245	2.881467
C	2.292922	-0.834725	2.834687
C	-2.589331	-1.251825	2.606552
C	-2.577378	3.562793	-0.387032
C	3.626534	1.231099	0.124542
C	0.394606	-1.040700	4.191120
O	-1.827809	4.260225	-1.047874
O	-1.858957	-2.211367	2.753979
O	-0.656528	-0.784020	4.743464
O	3.585016	2.079290	-0.749445
C	0.866541	3.444086	0.591529
H	0.231091	4.186775	0.108018
H	0.847236	3.605655	1.672695
H	1.889993	3.560093	0.231974
C	0.383737	1.792134	-1.289088
H	1.407447	1.897384	-1.649846
H	0.018944	0.790912	-1.533918
H	-0.247680	2.532296	-1.782669
C	-4.579159	2.779670	0.507109
O	-5.772943	2.732147	0.718919
C	-4.592687	-0.103564	2.312300
O	-5.789107	0.098165	2.335663
C	2.616733	-1.709039	4.009446
O	3.662468	-2.240321	4.320031
C	4.548501	-0.345308	1.569095
O	5.404594	-1.035883	2.081603
N	1.433262	-1.791141	4.749019
N	4.781394	0.566700	0.533237
N	-3.958256	3.731779	-0.309127
N	-3.973268	-1.257577	2.800840
C	1.353074	-2.448493	6.041862
H	1.643173	-3.495929	5.942144
H	2.014572	-1.960797	6.762013
H	0.321754	-2.378026	6.384447

C	6.095559	0.788789	-0.045408
H	6.802824	1.073798	0.735793
H	6.451508	-0.119554	-0.536594
H	6.003352	1.591664	-0.775309
C	-4.715388	-2.400652	3.303438
H	-5.296764	-2.110871	4.180860
H	-5.392209	-2.783013	2.535874
H	-3.992622	-3.169190	3.573511
C	-4.690653	4.779673	-0.999523
H	-5.451714	4.338962	-1.646439
H	-5.174161	5.441125	-0.277342
H	-3.975633	5.343425	-1.596765

MDI-TBF_TS

C	3.464432	-0.401828	-0.188309
C	3.097077	0.926057	-0.175380
C	1.782570	1.325332	0.171592
C	2.496342	-1.369170	0.109129
C	0.754734	0.361875	0.306477
C	1.165134	-1.014397	0.277888
C	0.000001	-1.969416	0.359554
C	-1.165133	-1.014398	0.277885
C	-2.496341	-1.369172	0.109124
C	-0.754734	0.361874	0.306477
C	-3.464431	-0.401830	-0.188312
C	-1.782572	1.325330	0.171595
C	-3.097078	0.926055	-0.175376
C	1.907650	2.816536	0.415905
C	3.189871	-2.703125	0.139444
C	-3.189869	-2.703127	0.139435
C	-1.907652	2.816532	0.415916
O	2.751626	-3.808041	0.406994
O	1.231858	3.562305	1.082026
O	-1.231855	3.562298	1.082036
O	-2.751622	-3.808043	0.406986
C	-0.000001	-2.737794	1.705143
H	0.888503	-3.366627	1.761597
H	-0.000002	-2.038318	2.545415
H	-0.888505	-3.366627	1.761595
C	0.000003	-2.928726	-0.856416
H	-0.881890	-3.565435	-0.825402

H	0.000004	-2.359482	-1.790050	C	0.321499	0.282821	1.915840
H	0.881897	-3.565434	-0.825399	C	3.093639	-0.272253	1.856952
C	4.778879	-1.090284	-0.404239	C	0.918144	-0.555973	2.884488
O	5.868468	-0.643381	-0.692941	C	2.293136	-0.856782	2.821005
C	3.933966	2.133027	-0.462015	C	-2.596152	-1.243262	2.586879
O	5.074550	2.196327	-0.875815	C	-2.566453	3.533013	-0.407202
C	-3.933971	2.133026	-0.461998	C	3.613317	1.255947	0.146074
O	-5.074559	2.196327	-0.875789	C	0.409868	-1.033070	4.180894
C	-4.778876	-1.090288	-0.404252	O	-1.830764	4.232862	-1.098971
O	-5.868463	-0.643386	-0.692960	O	-1.890470	-2.230230	2.726124
N	-3.126548	3.215081	-0.149525	O	-0.632140	-0.781678	4.766246
N	-4.518803	-2.446570	-0.186792	O	3.595077	2.122825	-0.724401
N	4.518806	-2.446566	-0.186780	C	0.842716	3.448923	0.581880
N	3.126542	3.215083	-0.149547	H	0.203882	4.181017	0.085867
C	-3.601984	4.585990	-0.081000	H	0.804638	3.614966	1.662514
H	-4.584540	4.615477	-0.549693	H	1.871657	3.572876	0.239212
H	-3.675527	4.912594	0.959255	C	0.408166	1.783453	-1.291459
H	-2.915140	5.245699	-0.613946	H	1.435694	1.899416	-1.639181
C	-5.548679	-3.468926	-0.260757	H	0.060284	0.774982	-1.533770
H	-6.325732	-3.275574	0.481849	H	-0.230543	2.510605	-1.796157
H	-5.998037	-3.474134	-1.255742	C	-4.576760	2.774741	0.524391
H	-5.075708	-4.429002	-0.060697	O	-5.782003	2.764560	0.734012
C	3.601976	4.585993	-0.081035	C	-4.602817	-0.086683	2.334059
H	4.584530	4.615479	-0.549734	O	-5.802477	0.127072	2.373868
H	2.915128	5.245697	-0.613981	C	2.624001	-1.733617	3.994085
H	3.675525	4.912605	0.959218	O	3.671759	-2.279406	4.294613
C	5.548685	-3.468921	-0.260734	C	4.540194	-0.350255	1.576778
H	5.998123	-3.474052	-1.255682	O	5.424621	-1.038325	2.067905
H	6.325679	-3.275631	0.481951	N	1.457027	-1.800085	4.745708
H	5.075694	-4.429011	-0.060784	N	4.770565	0.583148	0.550543
MDI-TBF•−				N	-3.949830	3.712921	-0.314553
				N	-3.995424	-1.246496	2.799976
C	-3.490821	1.908445	1.021711	C	1.371589	-2.456930	6.033467
C	-3.485905	0.756035	1.786518	H	1.407124	-3.544028	5.919147
C	-2.273570	0.097587	2.073040	H	2.198776	-2.142835	6.674454
C	-2.253123	2.379212	0.462831	H	0.422522	-2.169063	6.485177
C	-1.040408	0.647931	1.656082	C	6.082475	0.818886	-0.016571
C	-1.053389	1.756905	0.755502	H	6.782165	1.134927	0.761266
C	0.354752	2.025559	0.233073	H	6.466868	-0.091033	-0.484829
C	1.166593	0.991665	1.007607	H	5.981920	1.604344	-0.764877
C	2.518578	0.702855	0.971793	C	-4.731954	-2.384947	3.308523

H	-5.208592	-2.142214	4.262140		O	-5.818481	0.143062	2.393949
H	-5.503172	-2.690662	2.596939		C	2.630609	-1.751843	3.989338
H	-4.019548	-3.197000	3.451968		O	3.677606	-2.319697	4.276484
C	-4.677689	4.754523	-1.009980		C	4.531866	-0.367090	1.577792
H	-5.472438	4.317652	-1.619264		O	5.443329	-1.053165	2.047921
H	-5.125678	5.453140	-0.298032		N	1.483789	-1.789640	4.757114
H	-3.969109	5.283218	-1.646664		N	4.759112	0.582667	0.556325

MDI-TBF²⁻

					N	-3.943370	3.699227	-0.314219
					N	-4.019567	-1.247303	2.781751
C	-3.508128	1.906937	1.026185		C	1.391811	-2.439552	6.042695
C	-3.491332	0.757391	1.795921		H	1.370098	-3.529894	5.939820
C	-2.282281	0.082499	2.072182		H	2.243434	-2.167647	6.672545
C	-2.250796	2.371019	0.442204		H	0.464874	-2.104198	6.509306
C	-1.031078	0.634327	1.640887		C	6.067489	0.823690	-0.006782
C	-1.057402	1.741349	0.733484		H	6.776132	1.115443	0.773928
C	0.354913	2.023022	0.227999		H	6.451994	-0.074306	-0.500362
C	1.170925	1.001087	1.015046		H	5.968657	1.628404	-0.735542
C	2.519896	0.711846	0.969584		C	-4.748302	-2.378928	3.303488
C	0.313025	0.293163	1.916621		H	-5.176112	-2.157503	4.287017
C	3.103063	-0.294383	1.855206		H	-5.561364	-2.661406	2.628200
C	0.917557	-0.564304	2.894382		H	-4.041971	-3.204807	3.394599
C	2.292082	-0.877130	2.812662		C	-4.664067	4.743858	-1.004343
C	-2.600106	-1.242689	2.558758		H	-5.369343	4.323493	-1.728442
C	-2.558317	3.508223	-0.423635		H	-5.226208	5.355697	-0.293276
C	3.601692	1.267048	0.157712		H	-3.931286	5.359804	-1.525731
C	0.427547	-1.001986	4.183863					
O	-1.834642	4.213447	-1.141010					
O	-1.916840	-2.255019	2.698509					
O	-0.599457	-0.742195	4.807798					
O	3.605533	2.151160	-0.710492					
C	0.822825	3.452121	0.576677					
H	0.180335	4.176132	0.072458					
H	0.769437	3.619145	1.657183					
H	1.856128	3.583974	0.248132					
C	0.430353	1.782595	-1.294570					
H	1.461105	1.910253	-1.629984					
H	0.097753	0.768687	-1.539024					
H	-0.214823	2.500443	-1.805755					
C	-4.578011	2.767394	0.538099					
O	-5.794343	2.791202	0.744563					
C	-4.615322	-0.082923	2.340020					

5.5 REFERENCES

1. Saal, F.; Zhang, F.; Holzapfel, M.; Stolte, M.; Michail, E.; Moos, M.; Schmiedel, A.; Krause, A.-M.; Lambert, C.; Würthner, F.; Ravat, P. [*n*]Helicene Diimides (n = 5, 6, and 7): Through-Bond versus Through-Space Conjugation. *J. Am. Chem. Soc.* **2020**, *142*, 21298–21303.

2. Upadhyay, G. M., Talele, H. R.; Bedekar, A. V. Synthesis and Photophysical Properties of Aza[n]helicenes. J. Org. Chem., **2016**, 81, 7751–7759.

3. Uematsu, K.; Noguchi, K.; Nakano, K. Synthesis and Properties of [7]helicene and [7]helicene-like Compounds with a Cyclopenta[1,2-*b*:4,5-*b*']dithiophene of dithieno[2,3-*b*:3',2'-*d*]heterole skeleton, *Phys. Chem. Chem. Phys.* **2018**, *20*, 3286–3295.

4. Uematsu, K.; Hayasaka, C.; Takase, K.; Noguchi, K.; Nakano, K. Transformation of Thia[7]helicene to Aza[7]helicenes and [7]Helicene-like Compounds *via* Aromatic Metamorphosis, *Molecules*, **2022**, *27*, 606.

5. Hossain, S.; Akter, M.; Shahbuddin, M.; Salim, M.; Iimura, K.-I.; Karikomi, M. Synthesis of Enantiomerically Pure Oxa[9]helicene Derivatives by a Nucleophilic Cyclodehydration Reaction of Helical 1,1'-Bibenzo[*c*]phenanthrenylidene-2,2'-dione, *Synlett*, **2022**, *33*, 277–282.

6. Nakano, K.; Hidehira, Y.; Takahashi, K.; Hiyama, T.; Nozaki, K. Stereospecific Synthesis of Hetero[7]helicenes by Pd-Catalyzed Double *N*-Arylation and Intramolecular *O*-Arylation, *Angew. Chem. Int. Ed.* **2005**, *44*, 7136–7138.

7. Oyama, H.; Nakano, K.; Harada, T.; Kuroda, R.; Naito, M.; Nobusawa, K.; Nozaki, K. Facile Synthetic Route to Highly Luminescent Sila[7]helicene, *Org. Lett.* **2013**, *15*, 2104–2107.

8. Full, J.; Wildervanck, M. J.; Dillmann, C.; Panchal, S. P.; Volland, D.; Full, F.; Meerholz, K.; Nowak-Król, A. Impact of Truncation on Optoelectronic Properties of Azaborole Helicenes, *Chem. Eur. J.* **2023**, e202302808.

9. Reger, D.; Haines, P.; Amsharov, K. Y.; Schmidt, J. A.; Ullrich, T.; Bönisch, S.; Hampel, F.; Görling, A.; Nelson, J.; Jelfs, K. E.; Guldi, D. M.; Jux, N. A Family of Superhelicenes: Easily Tunable, Chiral Nanographenes by Merging Helicity with Planar π Systems, *Angew. Chem.* **2021**, *133*, 18221-18229.

10. Shaya, J.; Corridon, P. R.; Al-Omari, B.; Aoudi, A.; Shunnar, A.; Mohideen, M. I. H.; Qurashi, A.; Michel, B. Y.; Burger, A. Design, Photophysical Properties, and Applications of Fluorene-Based Fluorophores in Two-Photon Fluorescence Bioimaging: A Review, *J. Photchem. Photobiol. C: Photochem*. **2022**, *52*, 100529.

11. Ogumi, K.; Nagata, K.; Takimoto, Y.; Mishiba, K.; Matsuo, Y.; Inkjet Printing of Mechanochromic Fluorenylidene-Acridane, *Sci. Rep.* **2022**, *12*, 16997.

12. Hu, J.; Ward, J. S.; Chaumont, A.; Rissanen, K.; Vincent, J.-M.; Heitz, V.; de Rouville, H.-P. J. A Bis-Acridinium Macrocycle as Multi-Responsive Receptor and Selective Phase-Transfer Agent of Perylene, *Angew. Chem. Int. Ed.* **2020**, *59*, 23206–23212.

13. de Rouville, H.-P. J.; Hu, J.; Heitz, V. N-Substituted Acridinium as a Multi-Responsive Recognition Unit in Supramolecular Chemistry, *ChemPlusChem*, **2021**, *89*, 110–129.

14. Anetai, H.; Takeda, T.; Hoshino, N.; Kobayashi, H.; Saito, N.; Shigeno, M.; Yamaguchi, M.; Akutagawa, T. Ferroelectric Alkylamide-Substituted Helicene Derivative with Two-Dimensional Hydrogen-Bonding Lamellar Phase. *J. Am. Chem. Soc.* **2019**, *141*, 2391–2397.

15. Santos, E. M.; Sheng, W.; Salmani, R. E.; Nick, S. T.; Ghanbarpour, A.; Gholami, H.; Vasileiou, C.; Geiger, J. H.; Borhan, B. Design of Large Stokes Shift Fluorescent Proteins Based on Excited State Proton Transfer of an Engineered Photobase, *J. Am. Chem. Soc.* **2021**, *143*, 15091–15102.

16. Kim, T.-I.; Jim, H.; Bae, J.; Kim, Y. Excimer Emission-Based Fluorescent Probe Targeting Caspase-3, *Anal. Chem.* **2017**, *89*, 10565–10569.

17. Wu, Y.-Y. Chen, Y.; Gou, G.-Z.; Mu, W.-H.; Lv, X.-J.; Du, M.-L.; Fu, W.-F. Large Stokes Shift Induced by Intramolecular Charge Transfer in N,O-Chelated Naphthyridine–BF$_2$ Complexes, *Org. Lett.* **2012**, *14*, 5226–5229.

18. Jones, G.; Vullev, V. I. Ground- and Excited-State Aggregation Properties of a Pyrene Derivative in Aqueous Media, *J. Phys. Chem. A.* **2001**, *105*, 6402–6406.

19. Newsome, W. J.; Chakraborty, A.; Ly, R. T.; Pour, G. S.; Fairchild, D. C.; Morris, A. J.; Uribe-Romo, F. J. J-Dimer Emission in Interwoven Metal-Organic Frameworks, *Chem. Sci.* **2020**, *11*, 4391–4396.

20. Misra, R.; Bhattacharyya, S. P. Introduction: An Overview of the ICT Process. In Intramolecular Charge Transfer: Theory and Applications; Wiley-VCH Verlag GmbH & Co. KGaA, 2018, 1–24. DOI:10.1002/9783527801916

21. Dimitriev, O. P.; Piryatinski, Y. P.; Slominskii, Y. L. Excimer Emission in J-Aggregates, *J. Phys. Chem. Lett.* **2018**, *9*, 2138–2143.

22. Bazinet, P.; Tupper, K. A.; Tilley, T. D. Octa- and Nonamethylfluorene and an Electron-Rich Permethylfluorenyl Ruthenocene Derivative. *Organometallics* **2006**, *25*, 4286–4291.

23. Kajigaeshi, S.; Kakinami, T.; Moriwaki, M.; Tanaka, T.; Fujisaki, S.; Okamoto, T. Halogenation Using Quaternary Ammonium Polyhalides. XIV. Aromatic Bromination and Iodination of Arenes by Use of Benzyltrimethylammonium Polyhalides-Zinc Chloride System, *Bull. Chem. Soc. Jpn.* **1989**, *62*, 439–443.

24. Zou, B.; Stellmach, K. A.; Luo, S. M.; Gebresilassie, F. L.; Jung, H.; Zhang, C. K.; Bass, A. D.; Janzen, D. E.; Cao, D. D. Improved Syntheses of Halogenated Benzene-1,2,3,4-Tetracarboxylic Diimides. *J. Org. Chem.* **2022**, *87*, 13605–13614.

25. Wu, Y.; Han, J. M.; Hong, M.; Krzyaniak, M. D.; Blackburn, A. K.; Fernando, I. R.; Cao, D. D.; Wasielewski, M. R.; Stoddart, J. F. X-Shaped Oligomeric Pyromellitimide Polyradicals. *J. Am. Chem. Soc.* **2018**, *140*, 515–523.

26. Fishwick, B. The Analysis of Mixtures of Benzene-Carboxylic Acids by Partition Chromatography. *J. Chem. Soc.* **1957**, 1196–1199.

27. Ren, T.-B. Xu, W. Zhang, W.; Zhang, X.-X. Wang, Z.-Y.; Xiang, Z.; Yuan, L.; Zhang, X.-B. A General Method to Increase Stokes Shift By Introducing Alternating Vibronic Structures, *J. Am. Chem. Soc.* **2018**, *140*, 7716–7722.

28. Ravat, P.; Hinkelmann, R.; Steinebrunner, D.; Prescimone, A.; Bodoky, I.; Juríček, M. Configurational Stability of [5]Helicenes. *Org. Lett.* **2017**, *19*, 3707–3710.

29. Ravat, P. Carbo[*n*]helicenes Restricted to Enantiomerize: An Insight into the Design Process of Configurationally Stable Functional Chiral PAHs, *Chem. Eur. J.* **2021**, *27*, 3957–3967.

30. Burchat, A. F.; Chong, M.; Nielsen, N. Titration of Alkyllithiums with a Simple Reagent to a Blue Endpoint, *J. Organomet. Chem.* **1997**, *542*, 281–283.

31. Dolomanov, O. V.; Bourhis, L. J.; Gildea, R. J.; Howard, J. A. K.; Puschmann, H. OLEX2: A Complete Structure Solution, Refinement and Analysis Program, *J. Appl. Cryst.* **2009**, *42*, 339–341.

32. Sheldrick, G. M. SHELXT-Integrated Space-Group and Crystal-Structure Determination, *Acta. Cryst.* **2015**, *A71*, 3–8.

33. Sheldrick, G. M. Crystal Structure Refinement with SHELXL, *Acta. Cryst.* **2015**, *C71*, 3–8.

34. Becke, A. D. Density-Functional Thermochemistry. III. The Role of Exact Exchange, *J. Chem. Phys.* **1993**, *98*, 5648–5652.

35. Lee, C.; Yang, W.; Parr, R. G. Development of the Colle-Salvetti Correlation-Energy Formula into a Functional of the Electron Density, *Phys. Rev. B.* **1988**, *37*, 785–789.

36. Grimme, S.; Ehrlich, S.; Goerigk, L. Effect of the Damping Function in Dispersion Corrected Density Functional Theory, *J. Comp. Chem.* **2011**, *32*, 1456–1465.

CHAPTER 6 |
SUMMARY AND OUTLOOK

This Thesis has primarily focused on studying the optoelectronic properties of derivatives of tetrabenzofluorenes (TBFs), a non-planar, helically twisted polyaromatic framework that is built from a fluorene core. Chapter 1 lays out the foundations for the rest of the thesis by presenting a thorough literature review of the field, starting from the discovery of the highly fluorescent organic small molecule fluorene, before building up to larger benzannulated analogues. Initially, fluorene is presented as a highly desirable functional organic molecule for use in the development of advanced light-emitting and charge transporting technologies, due to the enforced planarity of its biphenyl moiety due to a methylene bridge. This planarity enhances conjugation within the molecule enabling both its inherent fluorescence and ambipolar charge transporting behaviours. Substitution of electron-donating or electron-withdrawing substituents around the periphery of the molecule allows for the facile tuning of these properties for the desired outcome. Benzannulation to form mono-, di-, tri- or tetrabenzofluorenes only enhances these properties further by extending delocalisation pathways resulting in bathochromically shifted optical behaviours and thermodynamically stable charged and neutral redox species. In addition, *ortho*-fused fluorenyl-based polyaromatics such as TBFs, are noticed to possess a non-planar screw-shaped backbone, indicating the potential to exploit these structures for properties related to their inherent chirality. In light of these findings, the remainder of this thesis discussed research that I have conducted during the three years of my PhD to investigate the fundamental properties of multifunctional derivatives of TBFs.

In Chapter 2, a series of non-symmetric, head-substituted TBFs are synthesised and the mechanism for their solid-state emission is probed by optical and time-resolved spectroscopies. In particular, the Chapter strives for clarity on the impact of sterically bulky, rigid aromatic substituents compared to flexible but disruptive alkyl head groups and specifically how the nature of these substituents affects the mechanism for the aggregate emission. Anthracenyl-TBFs are observed to undergo AEE as a result of restricted motions, e.g., due to an intramolecular CH···O interaction observed by X-ray crystal structure analyses. The anthracene also appears to compete with the photophysical properties of the TBF core resulting in lower overall solution-state PLQY values. Butyl-appended TBFs emit light more efficiently in solution with relatively higher PLQYs and display aggregate emission due to the effective disruption of TBF π-interactions by flexible butyl groups which hinder ACQ effects. An adjacent hydroxy head-group (which for anthracenyl-TBFs helps enforce aggregate rigidity and reduce intramolecular motions) appears to negatively impact solution and aggregate-emission of butyl appended TBFs as a result of its electron-withdrawing nature. This Chapter has therefore helped to build a strong fundamental understanding of TBF aggregate emission such that these learnings can be applied to similar functional organic molecules to enhance their solid-state emissive behaviours. Given these findings, future endeavours to study surface morphologies (e.g., using electron microscopy techniques) and emissive behaviours of derivatives of TBF as thin-films or powders would serve this line of research well to highlight the use of these TBF materials in organic light-emitting applications.

Apart from their ability to absorb and emit light efficiently, TBFs should be able to donate and accept charge readily, similar to fluorene. However, a fundamental study of the redox properties of head-substituted TBFs has never been conducted. Chapter 3 therefore describes efforts to probe the electrochemical, chemical, and photochemically induced redox states of derivatives of TBFs. Despite minimal structural differences between hydroxy- and hydrogen anthracenyl head-substituted TBFs, the hydroxy-derivative is found to display a quasi-reversible first oxidation. This quasi-reversibility is observed presumably due to the cleavage of a weakened C–OH bond following oxidation to a radical cation state after which a TBF centred-radical is proposed to form. SEC analyses confirm the evolution of different redox states between the two TBF derivatives. The TBF-centred radical was then pursued by a chemical reduction of the hydroxy derivative. EPR spectroscopy confirms the presence of an open-shell molecule, after which absorption studies of the material match the profiles generated by electrochemical oxidation of the hydroxy- and hydrogen anthracenyl head-substituted TBFs confirming earlier hypotheses. TBF centred radicals are also hypothesised to be generated under Grignard conditions (i.e., in the presence of MgI$^{•}$) from a TBF head-substituted ketone. However, in this case, the absence of kinetically stabilising groups leads to the reduction of the aromatic core. In addition, upon exposure to visible light, hydroxy-substituted TBFs are observed to decompose to a TBF dimer with a relatively large carbon-carbon single bond between the two TBFs. The mechanism for this decomposition is proposed to take place *via* either a cationic, anionic, or radical TBF state. The results from this Chapter reveal the complexity of the redox behaviours of TBFs, and the breadth of opportunities available to take advantage of them to achieve ambient stable neutral organic radicals. While the TBF radical has been isolated in this Chapter, this line of research would benefit from further in-depth studies of this organic radical, including quantifying its half-life stability, studying its emissive properties in both the solution and solid-state and attempting to grow single crystals.

In Chapter 4, the configurational stability of the [5]helicene-like backbone of the TBF framework is addressed through DFT calculations. The Gibbs free energy barrier of enantiomerisation ($\Delta G^{\ddagger}$) for head-substituted TBFs are predicted to be low, similar to experimental analyses of this barrier that have previously been reported. These results confirm that in solution, TBFs will be rapidly interconverting between enantiomers at room temperature. Three strategies to increase this barrier are discussed, with varying degrees of success. Elongating the helical framework through *ortho*-benzannulation and adding steric bulk to the *fjord* through methylation are predicted to be appropriate methods of increasing $\Delta G^{\ddagger}$. On the other hand, the design of a triple-helicene based on the TBF framework with increased chiral complexity is not predicted to achieve the desired results. TD-DFT calculations further predict that these structural changes should not affect the photophysical properties of the targets. Syntheses of these targets reveal the challenge associated with isolating configurationally stable TBF derivatives. However enough progress has been made so that the next researcher who continues this work should be able to isolate and study configurationally stable derivatives of TBF. With the enantiopure helicenes based on

TBF, together with conclusions made in Chapter 2, we have a framework for accessing solid-state emission of single-handedness for the development of more efficient and advanced organic light-emitting technologies. In addition, while Chapter 4 focused solely on configurationally stable analogues based on the TBF structure, there would also be advantages of attempting to generate organic radicals from other [7]helicene fluorenyl-embedded helicenes reported in the literature to study their chiroptical properties.

The final experimental Chapter in this thesis discusses efforts to introduce additional functionality to the TBF core by incorporating known *n*-type redox-active units such as acridines and diimides into the design of the electron-rich TBF. Acridines are head-substituted non-conjugatively to the TBF core and result in strong intermolecular hydrogen bonded dimers. As a result, the optical properties of the acridinyl-TBF display large Stokes shifts due to the excitation of ground state dimers, while the true monomeric optical behaviours are revealed upon addition of water. Even with the observation of these remarkable optical behaviours, the full potential of acridines have not yet been realised. There are still further opportunities to synthesise the acridinium (i.e., a charged analogue of the acridine) and to then explore its sensitivity to other stimuli such as pH, redox and light. In the second example presented in this Chapter, a non-linear aromatic diimide unit, mellaphanic diimide (MDI) is used to sculpt the wings of the TBF framework, and an MDI-dimer is isolated as an intermediate towards synthesising the MDI-TBF helicene hybrid. This dimer is observed to adopt one of two conformations, presumably stabilised by an intramolecular aromatic-carbonyl CH$\cdots$O interaction, in its neutral and reduced states. Compared to its monomer, the dimer accepts charges easily due to extended conjugation between the two MDI units, aided by an increase in double bond character of the MDI-MDI C–C bond. This enhanced conjugation endows the dimer with emissive capabilities (even though monomers of MDI are non-emissive). These results together with DFT calculations highlight the potential for the structure of the MDI-TBF dimer to deliver a highly electron-deficient emissive helicene. Upon reduction of this MDI-TBF hybrid helicene, its configurational stability is expected to increase allowing for a selective and controllable lock and release of the configuration of the helicene. Therefore, synthetic efforts to isolate this diimide helicene are expected to reap interesting results and should be pursued further.

This Thesis therefore presents the TBF framework as a multifunctional platform that can be tuned in a controllable manner in order to extract a desired outcome. A thorough fundamental analysis of the properties of TBFs has enabled us to understand clearly, how its structural and electronic features can be tweaked to enhance either its solid-state emissive properties or its ability to stabilise charged and neutral redox states. I envision that a marriage of all the potential characteristics of TBFs that are tackled in previous Chapters, including its configurational stability, highlights an avenue for research that will deliver a highly impactful organic functional molecule that can possibly revolutionise the fields of organic light-emitting and charge-transporting materials in our ever rapidly evolving technological world.

APPENDIX |

CONTENTS

A.1 INTRODUCTION

Throughout my PhD, I have also been more widely involved in other collaborative projects with researchers in the Avestro Group that don't necessarily focus on the specific goals of my PhD. These projects include (i) my involvement in the synthesis, optoelectronic properties analysis and DFT analyses of azole-substituted naphthalene diimides as through-space charge transporting materials. I was first involved in this project during my BSc research project, and I have been helping to push the research to completion during my PhD. In a second project, my involvement has included (ii) DFT calculations to model transition states for the interconversion of *M*- and *P*- enantiomers of charged helicenes derived from naphthalene diimides and performing aromaticity calculations such as nucleus independent chemical shift (NICS), anisotropy induced current density (AICD) and isomagnetic shielding analysis (IMS, with Peter Karadakov). My involvement in this project was extended to study (by DFT) some elongated structures based on these helicenes with redox-controlled conformational changes. Finally, I was involved in a third project to help study by DFT, (iii) the structures of functionalised shape-persistent 3-conjugated triangular macrocycles based off pyromellitic diimides and their non-linear regioisomer mellaphanic diimide. This appendix summarises my involvements in these projects outside of the scope of my PhD Thesis and discusses some of the results collected.

A.2 CHARGE MOBILITIES OF AZOLE-SUBSTITUTED NAPHTHALENE DIIMIDES

Collaborators and contributors: Grant M. Brown, Philip A. Hope, Fraser H. N. Arnold, Adam C. Carrick and Jamie A. Gould.

The discussions below are adapted from a manuscript in preparation for which I am a co-first author.

A series of four naphthalene diimides were synthesised bearing either a 4-pyrazole, 3,5-dimethylpyrazole, 3-pyrazole and 4,5-dimethylpyrazole (to make **1**, **2**, **3**, and **4** respectively) in the *N,N'*-position as a hydrogen bond directing substituent (Figure A.1a). Solvent-free crystal structures (Figure A.1b–e) of the four diimides reveal that the aromatic surfaces organise and orient themselves with different degrees of π-overlap despite minute differences to the *N*-group substituents. The sterically bulky diimides **2** and **4** displayed packings with virtually no π···π interactions. Sterically unhindered diimide **1** orders π-surfaces in a thermodynamically favoured slip-stacked configuration ($d_{\pi-\pi} = 3.24$ Å), however with a relatively low degree of π-contact. Notably, the highest degree of NDI–NDI overlap is observed for NDI **3** where aromatic surfaces orient themselves co-facially with each layer related by S_2 symmetry. This arrangement of π-surfaces results in π–π distances (3.47 Å) greater than NDI **1**.

To understand whether the orientation and area of overlap is more energetically favourable and conducive to charge transport in NDI **3** or in NDI **1**, the energy and orbital overlap of the LUMO of a

representative dimer (Figure A.1, dimer LUMO orbital inset; isovalue 0.01) was compared. It is clear that the twisted orientation of NDI surfaces in **3** promotes efficient orbital lobe matching (and therefore, spatial orbital overlap) in its dimer compared to the parallel orientation of π-surfaces in **1**. Therefore, **3** possesses a lower energy dimer LUMO (E_{LUMO} of **1** = –3.5 eV *vs* E_{LUMO} of **3** = –3.7 eV, Figure A.1a and c respectively) despite the larger π-π distance. Following these results, we envisaged that NDI **3** would transport charge most efficiently, followed by NDI **1**, then either of NDI **2** or **4**. This hypothesis was confirmed by experimental conductivity measurements on as-synthesised micro-crystalline powders of the respective NDIs.
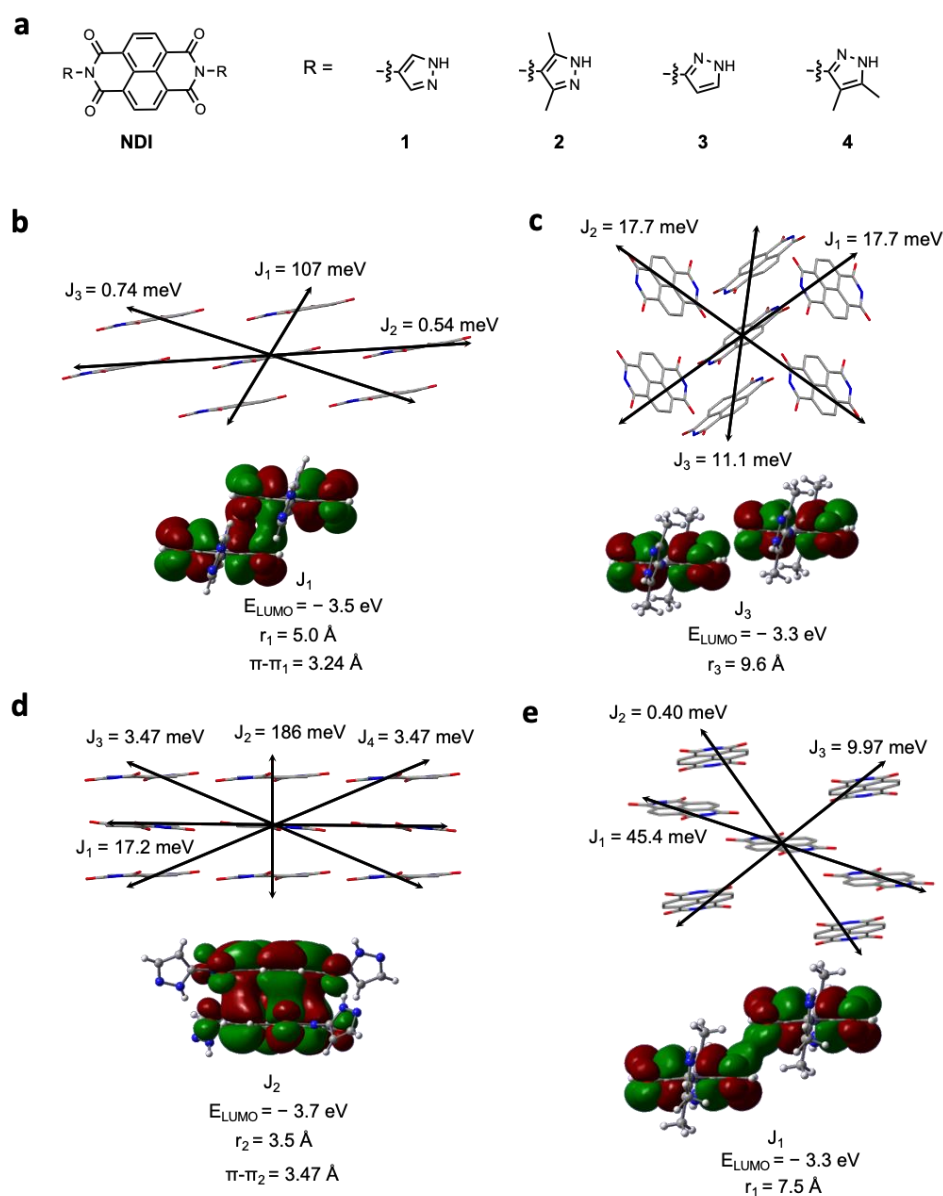
Figure A.1 (a) Chemical structures of the NDIs studied in this work. Charge transfer pathways and the resulting charge transfer integrals in each specified direction for solvent-free X-ray crystal structures of NDI b) **1**; c) **2**; d) **3** and e) **4**. For each compound, the LUMO of the dimer (isovalue 0.01) with the largest *J* value is shown along with the energy of this LUMO and the centroid-centroid distance r_i (or the plane-plane distance, π-$π_i$ where appropriate). Pyrazole groups and H atoms have been omitted for clarity.

To understand what particular aspects (i.e., distance, orientation, symmetry) of the solid-state packing of each NDI lead to the conductivity results obtained experimentally, theoretical charge mobility calculations were carried out (supported by DFT calculations and CATNIP[1]). Charge transfer pathways were determined within the de-solvated crystal packing structures for each compound and the charge transfer integral, J_i, was evaluated in each of these directions using the dimer projection method (Figure A.1, black arrows highlight charge transport pathways).[2,3] The rate of charge transport in each direction k_i, was then calculated according to the Marcus equation (Eq. 1) using the calculated values of J_i, and the calculated reorganization energy, λ (Eq. 2). Finally, the charge mobility of electron transport, μ, which is dependent upon the rate of charge transfer in all directions, k_i, and the centroid-centroid distance between dimers, r_i (Eq. 3), was calculated and summarised in Table A.1.

$$k_i = \frac{2\pi}{\hbar} J_{eff\_i}^2 \left(\frac{1}{4\pi\lambda k_B T}\right)^{\frac{1}{2}} e^{-\frac{\lambda^2}{4\lambda k_B T}} \qquad Eq.\,1$$

where $\hbar$ is reduced Planck's constant, k_B is Boltzmann's constant, T is room temperature i.e., 298 K.

$$\lambda = E_N^- - E_N^0 + E_C^0 - E_C^- \qquad Eq.\,2$$

where E_N^0 and E_C^- are the energies of the neutral and singly charged NDIs. E_N^- is the energy of the neutral species in the optimised geometry of the charged species, and E_C^0 is the energy of the charged species in the optimised geometry of the neutral species.

$$\mu = \frac{eD}{k_B T} = \frac{e}{6k_B T} \sum_i k_i r_i^2 p_i \qquad Eq.\,3$$

where e is electron charge, D is the charge diffusion coefficient, r_i is the centroid-centroid NDI-NDI distance between dimers in the ith direction and p_i is the probability of charge moving in this specified direction, i.e., $p_i = \frac{k_i}{\sum_i k_i}$.

Table A.1. Summary of the charge mobility, μ for each NDI

NDI	μ / cm^2 J^{-1} s^{-1}
1	0.24
2	0.36
3	0.09
4	0.05

The results from these calculations approximately match the trends observed in the experimental conductivity measurements (NDI **3** > **1** and **4** $\approx$ **2**; Table A.1). Significant charge transfer pathways (i.e., J_i >20 meV) include the slip stacked NDI–NDI π-interaction in NDI **1** (Figure A.1a, J_1=108 meV) and the co-facial overlap in NDI **3** which results in the greatest charge transfer integral (Figure A.1c, J_2 = 182 meV). Despite the closer π-π distance in NDI **1**, the charge transfer calculations reveal that this charge transfer pathway (J_1 in NDI **1**) does not contribute to the overall charge mobility as much as the co-facial dimer in NDI **3** (J_2 in NDI **3**) as a result of poorer spatial overlap between orbitals in

the LUMO of the dimer. NDI **3** therefore displays the greatest theoretical charge mobility, larger than theoretical values that have previously been reported in the literature for some NDI materials.[4]

This result is further highlighted in distance dependent calculations where the vertical distance, d_v between the dimers in NDI **1** and **3** were altered and the resulting charge transfer integral, J calculated and plotted (Figure A.2a). The results reveal that at any distance, NDI **3** is more susceptible to transfer charge than NDI **1** due to the more efficient spatial overlap in the twisted and co-facial arrangement of NDIs in **3**. The results, in combination with experimental conductivity properties, suggest that the area/extent of LUMO π-orbital overlap is a significant factor to consider in achieving high conductivity materials as it maximizes the surface area of the most straightforward charge transfer pathway(s) in a material. Additionally, although twisted in an S_2 symmetry, the LUMO orbital lobe matching and hence overlap in NDI **3** seems to be maximized in comparison to the parallel arrangement of NDI surfaces in NDI **1**.
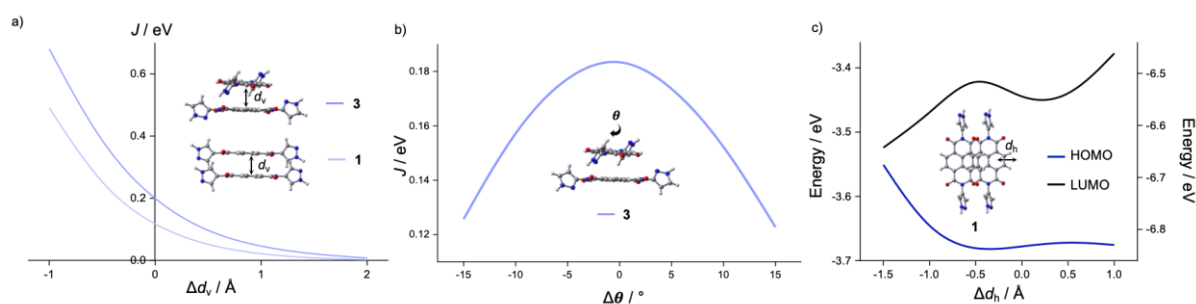
Figure A.2 (a) A comparison of the absolute charge transfer integral, $|J|$, between the slip-stacked dimer in **1** and the co-facial dimer in **3** at varying vertical distances (Δd_v) away from the distance of the dimers obtained in the respective crystal structures (defined as 0 Å); (b) Dependence of J on the twist angle (θ) between monomers in the co-facial dimer in **3** where 0° is the crystal structure defined angle between the two monomers; (c) Variation of HOMO and LUMO energies of the resulting dimers as one molecule in the dimer is horizontally translated away from the crystal structure defined distance ($d_h = 0$) to alter the degree of slip-stacking in **1**.

To test these hypotheses, first the area/extent of orbital overlap was probed further – the horizontal distance, d_h between NDIs in the slip-stacked dimer in NDI **1** was altered away from the crystal structure defined distance (set to 0 Å) and the resulting energy of the HOMO and LUMO of the dimer plotted (Figure A.2c). Similar to what has been reported previously,[5] the energy of the HOMO and LUMO show alternating increases and decreases in energy attributed to the symmetry alignment and then breaking of orbital overlap as the extent of slip-stacking is either increased or decreased. The results hint at the criticality of quantum chemical symmetry alignments in enabling charge to flow. This result is further substantiated when the orientation of the arrangement of π-surfaces in NDI **3** is probed in more detail – the twist angle between two NDIs in the co-facial dimer in **3** was altered and the resulting charge transfer integral calculated and plotted (Figure A.2b). At the crystal structure defined angle (set to 0°), the charge transfer integral is at its maximum and steeply falls away as the angle is altered in either a clockwise or anticlockwise manner away from 0°. Evidently, the S_2 twisted orientation of NDIs maximizes the electronic and quadrupolar interactions through efficient π-orbital overlap due to

quantum mechanical orbital symmetry matching in the dimer and hence allows for a superior charge transport in comparison to NDI **1**. Through this systematic study, we have therefore shown that consideration of factors in addition to the distance between π-surfaces such as the orientation of π-surfaces and quantum mechanical symmetry factors (which impact the efficiency of orbital overlap) can dictate the resulting charge transport.

A.3 DFT CALCULATIONS OF NAPHTHALENE DIIMIDE-DERIVED HELICENES

Collaborators and contributors: Venkata S. Mothika, Matteo L. Albino, Pavan K. Yerramsetti, Biman Bhunia, Shana Noureen, Connor Prior and Peter Karadakov.

For context, this project is work I am doing as part of a larger group where my role is to collect the DFT data including optimised structures of neutral and charged states (of **H1, H3** and **TH**), conformational and transition state (TS) analyses. Initially, the aromaticity of helicenes derived from a diketone diimide (DKDI) – a product of the oxidation of a naphthalene diimide (NDI; Figure A.3a) – is studied computationally by AICD[6], IMS[7] and NICS[8] analyses. These analyses are important to conduct because they support experimental claims for the observation (for the first time!) of a Zimmerman-Möbius aromatic stabilised species in the reduced states of **H1** and **H3**. IMS results are highlighted in Figure A.3b, where the isosurfaces generated are an intuitive way to visualise Clar's rule. Aromatic rings that appear like distinct donuts exhibit a strong magnetic shielding and therefore are aromatic. Upon reduction to the dianion, **H1**, is predicted to experience an increase in aromaticity between atoms in the helicene's *fjord* region (highlighted in orange in Figure A.3b), as a result of a through-space Zimmerman-Möbius aromatic interaction.
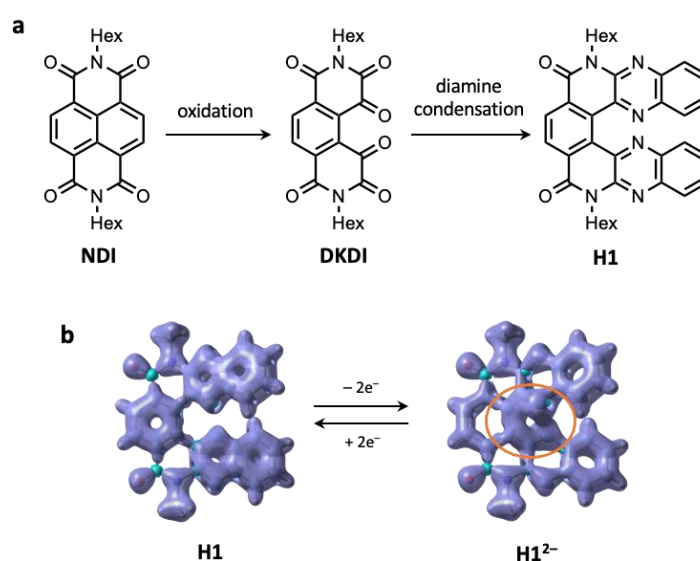
Figure A.3 (a) Structures of synthetic precursors used to isolate NDI-based helicenes studied in our group such as **H1**. (b) IMS calculation results where an isosurface has been generated to highlight an increased aromatic character through-space between the nitrogen atoms in the *fjord* (highlighted in orange).

In a related project, **H1** has been laterally extended with a thianthrene moiety to test the boundaries of this observed Zimmerman-Möbius aromaticity and redox-induced intraannular *fjord* electronic interactions. Following a screen of different functionals (B3LYP, PBE0, M06-2X) and basis sets (6-31G(d,p), 6-31G+(d,p), 6-311G(d,p), 6-311G+(d,p), cc-pvtz, aug-cc-pvtz), B3LYP(GD3BJ)/6-311G(d,p) in CH_2Cl_2 was chosen as the most suitable functional and basis set pairing which estimated band gap values and LUMO energies that were close to experimental values while also having a manageable computational expense. Since the thianthrene moiety is non-aromatic and hence kinked in its geometry in its neutral state, there are three possible conformers of **TH** that can exist with the two arms of the helicene (Figure A.4a). Of the three conformers of thianthrene, DFT confirms that the conformer which preferentially crystallises out (*P*–TH$_A$; Figure A.4a) has the lowest zero-point energy. The difference in energy between the conformers is between 0.31–2.31 kcal mol^{-1} (i.e., 0.01–0.10 eV) and the transition-state energy barrier for the interconversion between conformers is low (4.28 kcal mol^{-1} or 0.19 eV) suggesting that in solution an average of all three conformations is observed.
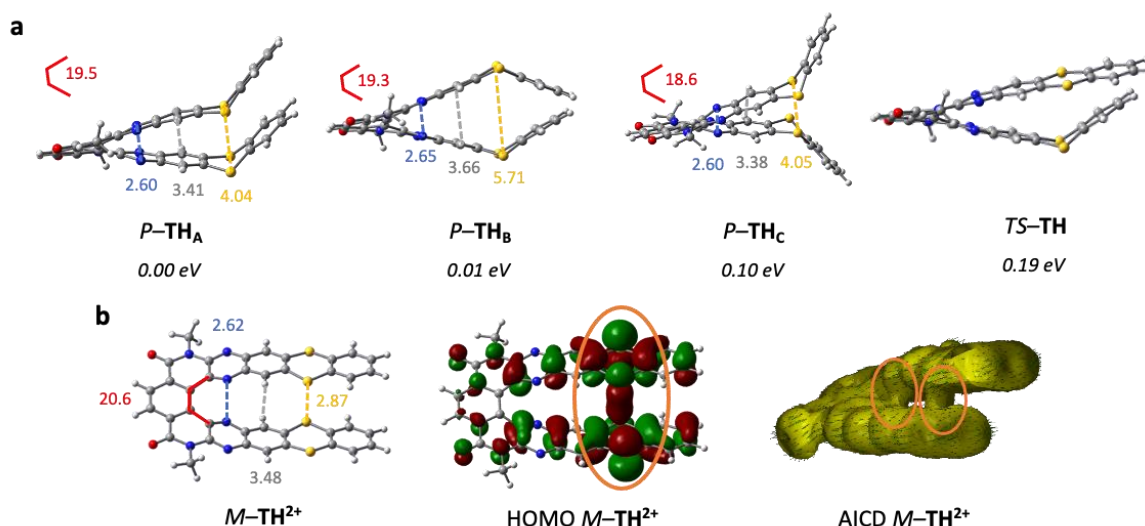
Figure A.4. (a) Structures of three conformers of *P*-**TH** that can exist along with the transition state energy for the interconversion between conformers, *TS*–**TH**. All energies are quoted in eV. (b) Optimised structure, HOMO and AICD plots of the dicationic state of **TH** highlighting the potential for through-space S–S bonding interactions.

DFT calculations of the oxidised **TH^{2+}** state reveal a highly planar laterally extended analogue of **H1**, notably with a shortened S–S distance of 2.87 Å. Its HOMO displays through-space electron delocalisation between the two sulfur atoms indicating a bonding-type interaction. The implications of these structural changes on the aromaticity of the molecule are evaluated by AICD calculations which highlight an isosurface with current density occupying the through-space regions of both the *fjord* N–N atoms as well as the S–S atoms. Work to obtain experimental evidence to support these DFT calculations is ongoing.

A.4 DFT CALCULATIONS OF MOLECULAR TRIANGLES

Collaborators and Contributors: Fraser H. N. Arnold, William Glover-Humphreys, Mariia Kuznetsova, Paul McGonigal

My involvement in this project has included the optimisation of the geometries of functionalised molecular triangles based on pyromellitic diimides (PMDIs) and frustrum shaped rigid macrocycles built from non-linear mellaphanic diimides (MDIs). This Section will therefore appear more like a Supplementary Information section from a manuscript.

Calculations to optimise the geometries of ground states of a range of triangles were carried out using density functional theory (DFT) with Becke's three-parameter exchange functional with the gradient-corrected correlation formula of Lee, Yang and Parr (B3LYP)[9,10] paired with the triple zeta valence plus polarisation def2tzvp[11] basis set, PCM solvation model (CH_2Cl_2) and dispersion corrections (D3BJ).[12] Ground state geometries were verified by convergence to a minimum stationary point and no negative vibrational frequencies observed. Tri-functionalised triangles result in the formation of atropisomers therefore, the structures Δ a (for the *syn*-conformer i.e., all groups pointing in the same direction) and Δ b (for the *anti*-conformer) were optimised as well.
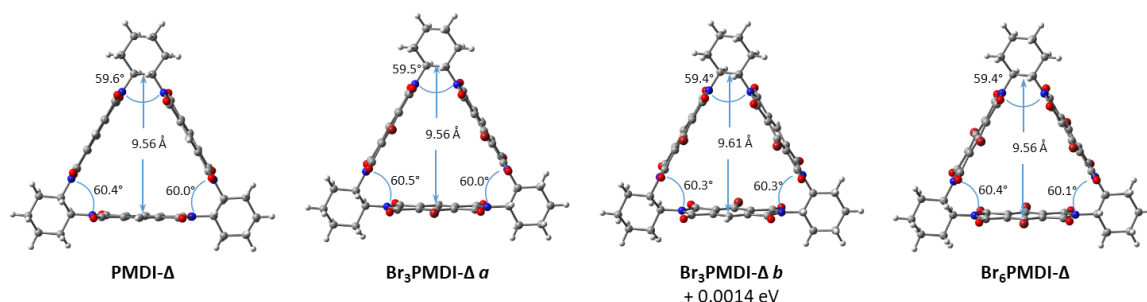
Figure A.5 Geometry optimised structures of simple brominated molecular triangles based on PMDI. Vertex angles were measured as the angle between two PMDI planes, and the height of the cavity is quoted as an average height of centroid-centroid distance between a PMDI centroid and a centroid bisecting the cyclohexane C–C bond.

The PMDI planes in aryl- and pyridyl-triangles are more twisted than simpler functionalised PMDI triangles (e.g., brominated triangles shown in Figure A.5) whose triangular sides are more planar. To avoid steric repulsions, these aryl- or pyridyl- groups are twisted away from the plane of the PMDI with torsional angles between 52.5–62.3º. In addition, Py$_3$PMDI-Δ a and Ar$_3$PMDI-Δ a appear to display some stabilising intramolecular CH···π interactions (2.72 Å and 2.71 Å respectively – quoted as an average value) between aryls and pyridyls in close proximity. These intramolecular aryl–π interactions result in a macrocyclic geometry change where there is less access to the triangular cavity from one face of the triangle.
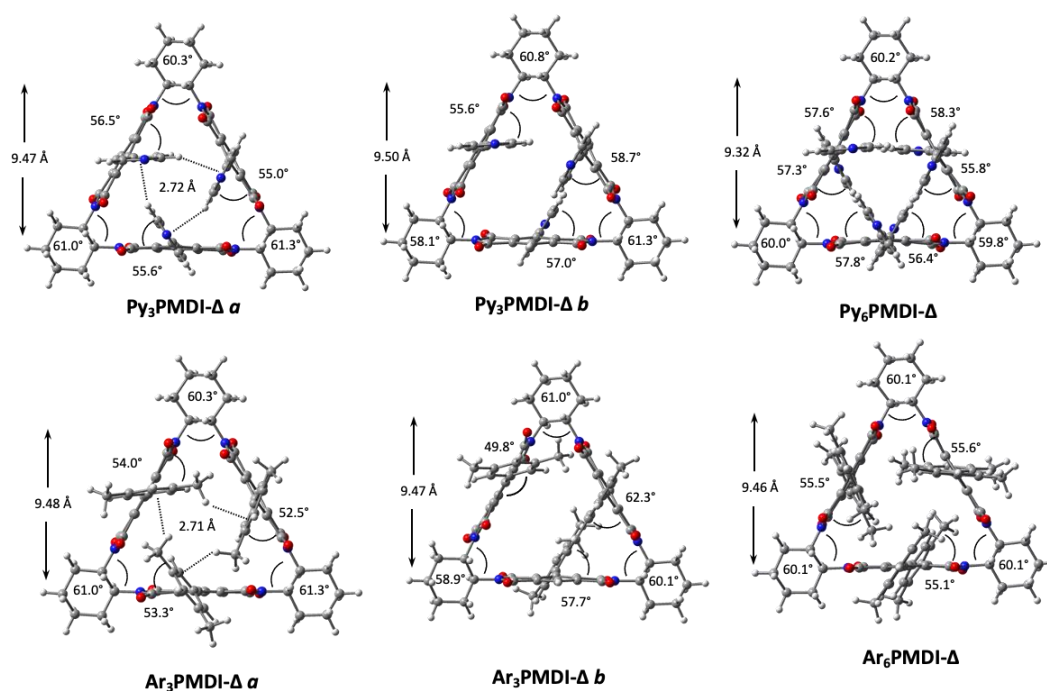
Figure A.6 Geometry optimised structures of tri- and hexa-substituted aryl- (Ar) and pyridyl- (Py) molecular triangles based on PMDI. Vertex angles were measured as the angle between two PMDI planes, and aryl or pyridyl torsional twists are quoted as an average. The height of the cavity is quoted as an average height of centroid-centroid distance between a PMDI centroid and a centroid bisecting the cyclohexane C–C bond.

Creating molecular triangles from non-linear and non-symmetric aromatic diimides such as mellaphanic diimides (MDI) reveal two DFT optimised structures of conformers (Figure A.7a and b) where carbonyls from the diimides are placed in much closer proximity than its linear and symmetric triangular isomer (PMDI, presented in Figures A.5). As a result, the cavity of the *syn* triangle appears widened and much more accessible from once face of the triangle, whereas the highly electron-rich oxygen atoms in the carbonyls suggest a strong possibility of binding metals similar to crown-ethers.
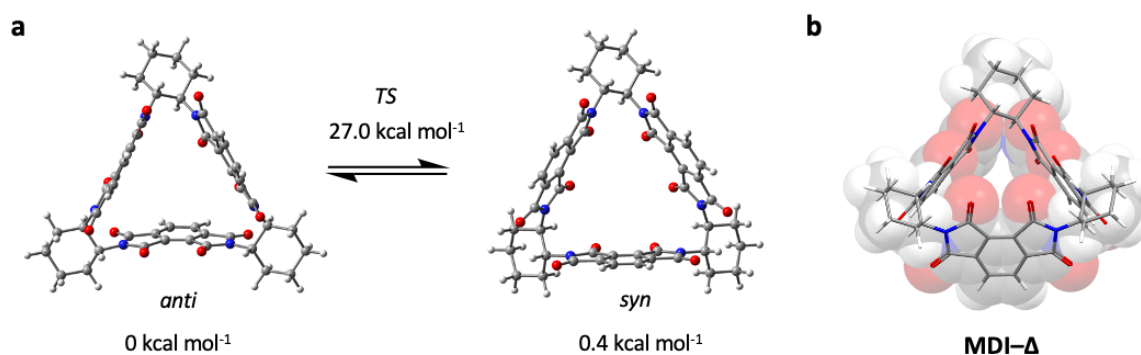
Figure A.7 (a) Geometries of two conformers that can be synthesised from the condensation reaction involving a non-symmetric diimide, MDI, including the transition state energy barrier involved in the interconversion between conformers. (b) A space-fill model of the *syn* conformer to highlight the close proximity of the carbonyls.

DFT coordinates for all systems discussed in this Appendix can be viewed here.

247

A.5 REFERENCES

1. Brown, J. S. (2018). CATNIP (Version 1.9). [Software]. Available from https://github.com/JoshuaSBrown/QC_Tools

2. Valeev, E. F.; Coropceanu, V.; da Silva Filho, D. A.; Salman, S.; Brédas, J.-L. Effect of Electronic Polarization on Charge-Transport Parameters in Molecular Organic Semiconductors. *J. Am. Chem. Soc.* **2006**, *128*, 9882–9886.

3. Baumeier, B.; Kirkpatrick, J.; Andrienko, D. Density-Functional Based Determination of Intermolecular Charge Transfer Properties for Large-Scale Morphologies. *Phys. Chem. Chem. Phys.* **2010**, *12*, 11103–11113.

4. Komissarova. E. A.; Dominskiy. D. I.; Zhulanov. V. E.; Abashev. G. G.; Siddiqui. A.; Singh. A. P.; Sosorev. A. Y.; Paraschuk. D. Y. Unravelling the Unusual Effect of Fluorination on Crystal Packing in an Organic Semiconductor, *Phys. Chem. Chem. Phys.* **2020**, *22*, 1665–1673.

5. Brédas. J. L.; Calbert. J. P.; da Silva Filho. D. A.; Cornil. J. Organic Semiconductors: A Theoretical Characterization of the Basic Parameters Governing Charge Transport, *Proc. Natl. Acad. Sci. U.S.A.* **2002**, *99*, 5804–5809.

6. Geuenich. D.; Hess. K.; Köhler. F.; Herges. R. Anisotropy of the Induced Current Density (AICD), a General Method To Quantify and Visualize Electronic Delocalisation, *Chem. Rev.* **2005**, *105*, 3758–3772.

7. Lampkin. B. J.; Karadakov. P. B.; VanVeller. B. Detailed Visualization of Aromaticity Using Isotropic Magnetic Shielding, *Angew. Chem. Int. Ed.* **2020**, *58*, 19275–19281.

8. Chen. Z.; Wannere. C. S.; Corminboeuf. C.; Puchta. R.; Schleyer. P. v. R. Nucleus-Independent Chemical Shifts (NICS) as an Aromaticity Criterion, *Chem. Rev.* **2005**, *105*, 3842–3888.

9. Becke. A. D. Density-Functional Thermochemistry. III. The Role of Exact Exchange, *J. Chem. Phys.* **1993**, *98*, 5648–5652.

10. Lee. C.; Yang. W.; Parr. R. G. Development of the Colle-Salvetti Correlation-Energy Formula into a Functional of the Electron Density, *Phys. Rev. B.* **1988**, *37*, 785–789.

11. Weigend, F.; Ahlrichs, R. Balanced Basis Sets of Split Valence, Triple Zeta Valence and Quadruple Zeta Valence quality for H to Rn: Design and Assessment of Accuracy, *Phys. Chem. Chem. Phys.* **2005**, *7*, 3297–3305.

12. Grimme. S.; Ehrlich. S.; Goerigk. L. Effect of the Damping Function in Dispersion Corrected Density Functional Theory, *J. Comp. Chem.* **2011**, *32*, 1456–1465.

Ruhee Dawood, AMRSC

ruhee.dawood4@gmail.com

Education

PhD in Chemistry, University of York, UK   Oct 2020–Oct 2023
Thesis title: Multifunctional Fluorenyl-Embedded Helicenes
Supervisor: Dr. Alyssa-Jennifer Avestro

BSc in Chemistry, University of York, UK   Sept 2017–Jun 2020
Awarded result: 82% (1st class, with distinction; top in class)
Option modules: Year 2 The Material World: Chemistry and Applications,
                          Year 3 Reaction Intermediates and Mechanisms

International Baccalaureate, Aga Khan Academy Senior School, Nairobi, Kenya   Aug 2015–Jul 2017
Diploma result: 44 points out of 45 (99th percentile worldwide, highest scorer in school)
Chemistry higher level (HL) – 7/7   Maths HL – 7/7   English Lang & Lit standard level (SL) – 7/7
Physics HL – 7/7   Economics HL – 7/7   French SL – 6/7 (+3 extra points)

Publications

1) Dessent, C. E. H*; Dawood, R. A; Jones, L. C; Matharu, A. S; Smith, D. K.*; Uleanya, K. O. "Decolonizing the Undergraduate Chemistry Curriculum: An Account of How to Start," *The Journal of Chemical Education*, **2022**, *99*, 5–9, DOI:10.1021/acs-jchemed.1c00397

2) Dawood, R. A; Avestro, A.-J.* "A New Equilibrium for Supramolecular Chemists," *Nature Chemistry*, **2021**, *13*, 1164–1165, DOI:10.1038/s41557-021-00849-1. (Invited contribution to report on the inaugural Women in Supramolecular Chemistry workshop)

3) Brown, G[†]; Dawood, R. A.[†]; Arnold, F. H. N; Carrick, A. C; Gould, J. A; Avestro, A.-J.* "Azole-mediated π-assembly of redox-active rylenes", Manuscript in preparation. [†]Equal author contributions

Awards and Prizes

Roger J Mawby Demonstrating Award (£150)   Jun 2023
Awarded to recognise graduate teaching assistants (GTA) who have made a significant contribution to undergraduate teaching.

Johnson Matthey Poster Competition (£500)   Mar 2023
Awarded in the Chemistry Department's 3rd year poster competition for engaging poster presentation and discussions.

Funds For Women Graduates Foundation Main Grant (£5500) – link   Oct 2022
Awarded an additional Professor Elizabeth Slater Award

Royal Society Representative at the 71st Nobel Laureate Meeting in Lindau Jun 2022
One of 611 to be selected to attend the meeting that was held in late June 2022

Yorkshire Asian Young Achiever Award in the School/College category – link 1, 2   Nov 2021
Awarded to recognise hard-work and determination among South Asians in Yorkshire

York Chemistry Whinfield Medal (£150)   Jul 2020
Awarded to top achiever in class (82%); received £150 and a Whinfield Medal

York Chemistry Wild Fund Platinum Scholarship (£66k over 3 years)   Jun 2020
3-years fully funded overseas PhD tuition, awarded based on academic merit

York Futures Scholarship (£1000)   Dec 2019
Awarded for demonstrating ambition, and commitment towards professional development

University of York Chemistry Departmental Scholarship (£500)   Feb 2018
1 of 20, for clearly expressing chemical interests and academic merit

Sharifah Sofia Albukhary Scholarship (£20k over 3 years)   May 2017
1 of 10, awarded based on academic merit and need

University of York Chemistry Excellence Award For Overseas Students (£2000) Feb 2017
Awarded on the basis of outstanding academic ability

Conferences Attended with Presentation

RSC's Macrocyclic and Supramolecular Chemistry Conference, University of Nottingham   Dec 2022
Poster presented: Fluorenyl-embedded helicenes as aggregation-enhanced emitters
Won a poster prize sponsored by Aggregate OA

RSC's Early Career Researcher's Macrocyclic and Supramolecular Chemistry   Jul 2022
Conference, Loughborough University
Title of oral presentation: Fluorenyl-embedded helicenes as aggregation-enhanced emitters

Women in Supramolecular Chemistry (WISC) Workshop, University of Cagliari – link   July 2021
Poster presented: Fluorene-centred helicenes and their stable radicals

SCI National Undergraduate Poster Competition   Jun 2020
Poster presented: Azole-mediated self-assembly of redox-active rylenes

RSC's Macrocyclic and Supramolecular Chemistry Conference, University of Kent – link   Dec 2019
Poster presented: Azole-mediated assembly of redox-active rylenes

Teaching and Research Experience

Research Mentor, Avestro Group   Oct 2022–Jun 2023
Designed a BSc research project which I managed and directed. Served as the primary mentor for the undergraduate student to enable their proficiency of the necessary skills to work independently.

Graduate Teaching Assistant – Dept of Chemistry, University of York   Oct 2020–Jun 2023
Served as a laboratory demonstrator in the undergraduate teaching labs advising undergraduates on best practices for key laboratory skills.

Semlyen Bursary Researcher (£1585), Dept of Chemistry, University of York   Jul 2019–Aug 2019
Achieved the microwave-assisted synthesis, purification, and optoelectronic properties characterisation of azole-functionalised electron acceptors to probe self-assembly directed processes in the solid and solution state for charge transport applications.

Service, Mentoring & Outreach

Postgraduate Applications Mentor, Dept of Chemistry, University of York   Oct 2021–Oct 2022
Advised undergraduate chemistry students at York about PhD applications, including tips for picking a project and supervisor, CV and personal statement guidance and interview question examples.

Mentor: STEMi Women Kuongoza Project   Aug 2020–Oct 2022
Served as a mentor for women and girls from Africa who are passionate about STEM to help them access opportunities, build networks, and inspire them to pursue studies further.

Postgraduate representative: Equality and Diversity Group   Nov 2019–Oct 2021
Attended termly meetings that address the importance of equal participation and success of members of the Department of Chemistry, University of York in the working, learning, social and living environment. Co-authored an article focusing on decolonisation efforts taking place in the department.

Skills

Lab Skills:
Proficient at carrying out basic laboratory procedures, (e.g acid-base workup, reflux, etc). Experience with manual and automated column chromatography (CombiFlash); distillation, working under an inert (N_2/Ar) atmosphere and performing manipulations in a glovebox. Exposure to characterisation techniques such as IR, melting point determination, HPLC, GC, NMR, TLC, mass spectrometry, elementary analysis. Schlenk line technique; liquid nitrogen handling; freeze-pump-thaw technique and solvent degassing; growing single-crystals suitable for X-ray diffraction analysis; powder XRD sample preparation; cyclic voltammetry; UV-Vis and fluorescence spectroscopy, microwave-assisted synthesis.

Technical Skills:
Well versed in Microsoft Office, familiar with software for processing spectra such as ACD Labs/Spectrus, SPSS, MestReNova and Mercury. Experience with Gaussian and CATNIP for DFT and computational chemistry.

Language Skills:
English (fluent), French (intermediate), Swahili (basic), Gujarati (basic)